Applied Bionics and Biomechanics

Biologically Inspired and Rehabilitation Robotics

Lead Guest Editor: Liwei Shi
Guest Editors: Yong Yu, Nan Xiao, and Dongming Gan

Biologically Inspired and Rehabilitation Robotics

Applied Bionics and Biomechanics

Biologically Inspired and Rehabilitation Robotics

Lead Guest Editor: Liwei Shi
Guest Editors: Yong Yu, Nan Xiao, and Dongming Gan

Editorial Board

Contents

Hindawi
Applied Bionics and Biomechanics
Volume 2019, Article ID 2428707, 2 pages
https://doi.org/10.1155/2019/2428707

Editorial

Biologically Inspired and Rehabilitation Robotics

Liwei Shi ,[1] Yong Yu,[2] Nan Xiao,[1] and Dongming Gan [3]

[1]*The Institute of Advanced Biomedical Engineering System, School of Life Science, Beijing Institute of Technology, No. 5, Zhongguancun South Street, Haidian District, 100081 Beijing, China*
[2]*Kagoshima University, Kagoshima, Japan*
[3]*Khalifa University Center for Autonomous Robotics Systems and Department of Mechanical Engineering, Khalifa University of Science and Technology, PO Box, 127788 Abu Dhabi, UAE*

Correspondence should be addressed to Liwei Shi; shiliwei@bit.edu.cn and Dongming Gan; dongming.gan@ku.ac.ae

Received 30 December 2018; Accepted 30 December 2018; Published 13 March 2019

Intelligent robots will soon be ready to serve in our home, hospital, office, and outdoors. One key approach to the development of such intelligent and autonomous robots draws inspiration from behavior demonstration of biological systems. In fact, using this approach, a number of new application areas have recently received significant interests in the robotics community, including rehabilitation robots, service robots, medical robots, and entertainment robots. It is clear that bioinspired methods are becoming increasingly important in the face of the complexity of today's demanding applications. Biological inspiration in robotics is leading to complex structures with sensory-motor coordination, in which learning often plays an important role in achieving adaptation. In addition, rehabilitation robotics has produced exciting new ideas and novel human assistive devices in the growing field of biomedical robotics. The science and technology of rehabilitation robotics will progress through the collaboration among robotic researchers, medical doctors, and patients.

This special issue focuses on the theoretical and technological challenges of evolutionary transformation from biological systems to intelligent robots. There were 33 submissions received, and 18 original research papers were finally accepted in this special issue after formal peer reviews. The accepted papers can be further classified into three related topics, namely, exoskeleton systems for human assisting and rehabilitation, bioinspired manipulator design for fine manipulation and surgery, and bioinspired sensing system development for human-centered applications.

Among the exoskeleton works, a big focus was on the lower limb applications. A. Yatsugi et al. studied the feasibility of neurorehabilitation using a hybrid assistive limb for patients who underwent spine surgery. Treatment indices were introduced, and real patient subject experiments were conducted to prove that neurorehabilitation therapy using lower limb exoskeleton is feasible following spine surgery. For the similar application, Q. Chen et al. proposed a novel gait planning approach, which is aimed at providing a reliable and balance gait during walking assistance. The exoskeleton and patient were modeled together as a linear inverted pendulum (LIP), and the patients' intention was obtained through an orbital energy diagram. Experimental results demonstrated the effectiveness of the proposed new method. Y. Liu et al. developed a wearable powered foot orthosis with metatarsophalangeal joint which is considered a critical component in human locomotion. The experimental results also suggested that the designed system could offer promise in certain rehabilitation applications and clinical treatment. A soft robotic suit was also developed by S. Jin et al. to assist hip flexion for energy-efficient walking of elderly persons in daily life activities, on metabolic cost reduction in the long-distance level and inclined walking. Experiment results show that, for a 79-year-old healthy male subject, the robotic suit significantly reduced metabolic cost in the condition of the robotic suit worn and powered on compared with the condition of worn but powered off. To assist customized gait planning for stable motion in variable terrains in lower limb exoskeleton-based rehabilitation walking, C. Yue et al.

developed a novel wearable sensing system employing 7 force sensors as a sensing matrix to achieve high accuracy of ground reaction force detection. By fusing force and angular velocity data, four typical terrain features are able to be recognized successfully, and the recognition rate can reach up to 93%. For the upper limb rehabilitation, W. Wei et al. developed a soft arm exoskeleton-based Bowden cable-driven system. The movement of the shoulder skeletal system through a mathematical model based on the Bowden cable transmission was explored, and the experimental results show that man-machine interaction force can be reduced when the number of bearing force points is increased and the bearing force point is away from the elbow. To fully understand the human shoulder mechanism to rehabilitation exoskeleton design, a new skeleton model and the motion rhythm analysis for human shoulder complex were proposed by S. Zhibin et al. Experimental data were analyzed and proved the proposed model effectiveness. One of the big topics in exoskeleton research is the human-robot interfacing. EMG has been widely used, and B. Gao et al. studied the real-time evaluation of the sEMG signal processing in an upper arm exoskeleton system for rehabilitation. The experimental results showed that the recognition accuracy of sEMG was 94%, and the average delay time was 300 ms, which met the requirements in the real rehabilitation process.

Biology systems have showed good references and inspiration for engineers to develop new manipulation and sensing systems. A critical review was conducted by H. Al-Shuka et al. with focus on active impedance control of bioinspired motion robotic manipulators. Different strategies were summarized and compared for future reference of new system control development. By learning from human anatomy and the muscle control system, a muscle coordination control for an asymmetrically antagonistic-driven musculoskeletal robot using attractor selection was developed by S. Ide and A. Nishikawa. A virtual antagonistic muscle structure was revealed in the experiments to show the effective control method. By fully exploring the human elbow joint complex, kinematic decoupling analysis was conducted, and a new biomimetic robotic elbow joint was designed by B. Cui et al. Detailed kinematics and design were explained followed by simulation tests. Similarly, a full 7-DOF prosthetic arm was built for shoulder disarticulation with the objective of low cost. A 3D printed method was recommended with the final prototype weighing 1350 g, and assessment was conducted to show the effectiveness in daily living activities. Other than prosthesis, a bioinspired catheter system was also developed by Y. Jiang et al. for endovascular treatment with force feedback. An initial clinical trial was conducted and showed the feasibility of the developed system. Apart from a human, a soft robotic fish was presented by W. Zhao et al. by using piezoelectric fiber composite (PFC) as flexible actuator based on numerical coupling analysis. On the bioinspired sensing side, a novel micro-photoionization detector for rapid volatile organic compound measurement was developed by Q. Zhou et al. The testing results showed that the ion collection efficiency reached 91% at a bias voltage of 150 V. To target microdistance and force perception, a magnetostrictive bioinspired whisker sensor based on the galfenol composite cantilever beam was developed to realize bidirectional tactile perception. In the experiment, the designed whisker, compared with a traditional unimorph whisker, displayed an output voltage range of -240 to 240 mV, the distance was 0-22 mm, with the microforce sensing range of 9.8-2,744 mN, the average distance of 10.90 mm/mV, and the force sensitivity of 11.4 mN/mV. The experimental results show that the proposed whisker sensor can realize the bidirection tactile perception in one-dimensional space. The automatic measurement, especially for products with complex shapes, has always been one of the most important application areas of robots. Aiming at the challenge of measuring residual stress under the curved surface, Q. Pan et al. proposed a robotic system for the residual stress ultrasonic measuring based on combining industrial robot technology with residual stress ultrasonic nondestructive measuring technology. Irregular vibration of the vocal cords corresponding to a variety of voice disorders can be observed with electronic laryngoscope to assist diagnosing vocal cord disease. However, laryngoscopy examination is invasive, and the outcomes are relatively subjective. Acoustic analysis can complement and in some cases replace the other invasive methods, which are based on direct vocal fold observation. Based on this, X. Zhang et al. designed a pathological voice source analysis system by integrating nonlinear dynamics with an optimized asymmetric two-mass model to explore nonlinear characteristics of vocal cord vibration. Changes in acoustic parameters, such as fundamental frequency, caused by distinct subglottal pressure and varying degrees of vocal cord paralysis are analyzed. Experimental results validate the applicability of the proposed model to reproduce vocal cord vibration with high accuracy and show that a paralyzed vocal cord increases the model coupling stiffness.

Therefore, this special issue presents the most recent advances in modeling, design, analysis, implementation, and therapeutic testing of the human assistive rehabilitation robotic exoskeletons, bioinspired prosthesis, manipulators, and sensing systems. We hope the knowledge and information will be good references and basis for further development in those fields for human-centered science and technology.

Conflicts of Interest

We all guest editors have no conflict of interest.

Liwei Shi
Yong Yu
Nan Xiao
Dongming Gan

Hindawi
Applied Bionics and Biomechanics
Volume 2019, Article ID 2797896, 8 pages
https://doi.org/10.1155/2019/2797896

Research Article

Robotic Ultrasonic Measurement of Residual Stress in Complex Curved Surface Components

Qinxue Pan[1,2] **Chang Shao**[1,2] **Dingguo Xiao**[1,2] **Ruipeng Pan**[1,2] **Xiaohao Liu**[1,2] **and Wei Song**[1,2]

[1] *School of Mechanical Engineering, Beijing Institute of Technology, Beijing 100081, China*
[2] *Key Laboratory of Fundamental Science for Advanced Machining, Beijing Institute of Technology, Beijing 100081, China*

Correspondence should be addressed to Qinxue Pan; panqx@bit.edu.cn

Received 1 May 2018; Revised 21 November 2018; Accepted 4 December 2018; Published 3 March 2019

Guest Editor: Dongming Gan

The automatic measurement, especially for products with complex shapes, has always been one of the most important application areas of robots. Aiming at the challenge of measuring residual stress under curved surface, in this paper, the residual stress ultrasonic measuring robot system with two manipulators is constructed, which is based on combining industrial robot technology with residual stress ultrasonic nondestructive measuring technology. The system is mainly composed of a motion control system, an ultrasonic detection system, and a data processing system. The robotic arm controls the movement of the two ultrasonic transducers along the set scanning path which is based on the geometric model of components and adjusts the transducer's posture in time according to the shape of the workpiece being measured. The configuration information based on workpiece coordinate system is transformed into a position data that takes into consideration the first critical angle and can be recognized by the robot. Considering the effect of curvature, the principle model of residual stress measuring by the critical refraction longitudinal wave is established. The measured signal including the stress state of the measured region, as well as the actual position and posture information of the transducers, is processed by the computer in real time, which realizes automatic nondestructive measurement of residual stress under curved surface.

1. Introduction

Currently, complex surface components have been widely used in aviation, aerospace, marine, automobile, and molds industry and have played an extremely important role, such as in engine blades and propellers, which is directly related to the reliability and safety of the equipment. The manufacturing process of complex surface components is cumbersome and complex, which will inevitably produce residual stress on the surface [1]. Even after a certain process, for example, heat treatment, the residual stress is also difficult to eliminate completely. On the other hand, these complex surface components will also have residual stresses due to impact loads, thermal loads, and corrosion during long-term service. The existence of this residual stress not only seriously affects the shape and mechanical properties of the components but also promotes the generation and propagation of cracks, causing the components to suddenly break under the working load, leading to malfunctions and even serious safety accidents [2]. Therefore, it is very important to measure and evaluate the residual stress of complex surface components.

Ultrasonic detection technology based on acoustic elasticity principle is one of the reliable and effective methods for residual stress nondestructive measuring. Residual stress ultrasonic measuring technology is more and more widely used in the inspection of residual stress of regular-shaped members such as rails, pipes, gears, and hubs due to its advantages of nondestructivity, harmlessness, reliability, accuracy, and convenience. Duquennoy et al., of the University of Valensina, France, used Rayleigh waves that excited by laser and received by PZT to measure the residual stress on the pipe surface [3]. Using the similar method, Wanwan et al. measured the residual stress in a cast iron brake disc

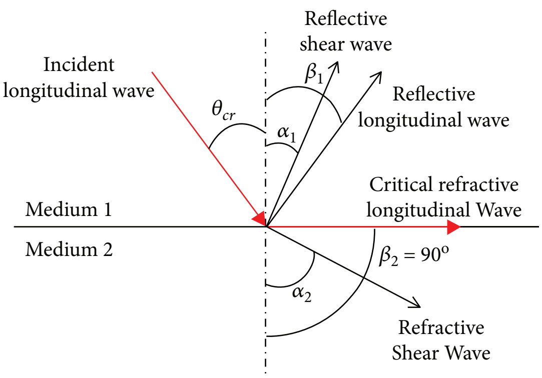

Figure 1: Wave conversion.

and compared with that measured by X-ray stress analyser [4]. In general, the research hotspots of ultrasonic nondestructive testing of residual stress mainly focus on different application objects and different ways of ultrasonic signal excitation and reception in recent years [5–8].

The residual stress ultrasonic measuring has a strict requirement on the incident and receiving angles of the transducer. However, for a complex curved surface component, the change of curvature will seriously affect the incidence, propagation, and reception of the ultrasonic signal, which poses great challenges to ultrasonic measuring of residual stress in complex surface components. The traditional manual measurement not only is difficult to ensure the necessary position and posture of the ultrasonic transducer but also has disadvantages such as low efficiency, large labor intensity, poor detection accuracy, and difficulty in quantitative analysis.

The development of high-precision, multi-degrees-of--freedom robots has brought a new support to the ultrasonic measurement for complex surface components [9, 10].

In this paper, an ultrasonic residual stress measurement method based on robot technology is proposed, which takes full advantage of a robot's precise control of ultrasonic transducer position and automatic scanning. It adjusts the posture of the ultrasonic transducer in real time according to the detection position. The actual posture information of the ultrasonic transducers and the ultrasonic signal at this position is processed by the computer to obtain the residual stress value of the measured area.

2. Materials and Methods

2.1. Ultrasonic Measuring Principle of Residual Stress in Curved Surface Components. The main basis for the ultrasonic measurement of stress is the acoustic elasticity theory, that is, the stress state in the elastic solid will affect the propagation speed of the ultrasonic wave in a material [11, 12]. Theoretical and experimental studies show that the ultrasonic longitudinal wave with the propagation direction being consistent with the stress direction is most sensitive to the change of stress. Therefore, it is necessary to generate a longitudinal wave propagating along the surface. By measuring the change of the longitudinal wave speed, we can realize the nondestructive detection of the tangential residual stress state in the propagation direction in the surface layer.

As shown in Figure 1, when the longitudinal wave propagates from a medium with a slower wave velocity to a medium with a faster wave velocity (such as from water to metal material), according to Snell's theorem, there is an incident angle so that the refracted longitudinal wave has a refraction angle of 90 degrees. This refracted longitudinal wave will propagate along the surface of the second medium. This incident angle is called the first critical angle (θ_{cr}), and the resulting refracted longitudinal waves are called critical refraction longitudinal wave (L_{cr}).

The first critical angle can be obtained by Snell's theorem:

$$\theta_{\mathrm{cr}} = \sin^{-1}\frac{V_{1L}}{V_{2L}}, \tag{1}$$

where V_{1L} is the longitudinal wave velocity of medium 1 and V_{2L} is the longitudinal wave velocity of medium 2.

For complex surface components, in order to excite and receive the critical refracted longitudinal wave at the surface of the component, it must be ensured that the ultrasonic transducer is tilted by a certain angle. The angle between the excitation transducer and the normal of incident point is equal to a positive critical angle, and the receive transducer and the normal of exit point is equal to a negative critical angle. It must also ensure that the exciting and receiving transducers are in the same plane as the refracted longitudinal wave propagation path. The excitation, propagation, and reception process of critical refraction longitudinal wave along the surface is shown in Figure 2.

In order to overcome the diffusion of the ultrasonic beam in the coupling agent and improve the detection sensitivity and resolution of the curved surface workpiece, the focal transducer is used for detection, which is shown in Figure 3. The focus position of the transducer in water can obtained by calculation or experiment.

According to the principle of ultrasound, the focal length of the transducer in water is calculated as follows:

$$F = \frac{R}{1 - C_2/C_1}, \tag{2}$$

where F, R, C_1, and C_2 are the focal length of the transducer in water, curvature radius of the acoustic lens, ultrasound speed in the lens, and ultrasound speed in water, respectively.

Based on the theory of acoustic elasticity, the relationship between ultrasonic longitudinal wave velocity and stress can be simplified as follows:

$$V_{\mathrm{L}\sigma} = V_{\mathrm{L}0}(1 - K_{\mathrm{L}}\sigma), \tag{3}$$

where $V_{\mathrm{L}\sigma}$ represents the longitudinal wave velocity when the stress is σ, $V_{\mathrm{L}0}$ is the longitudinal wave velocity in the absence of stress, and K_{L} is the acoustic elastic coefficient of longitudinal wave.

Suppose that the propagation path is s, the propagation time is t and the tangential stress on the path is σ. Because the velocity is difficult to measure directly, the different time

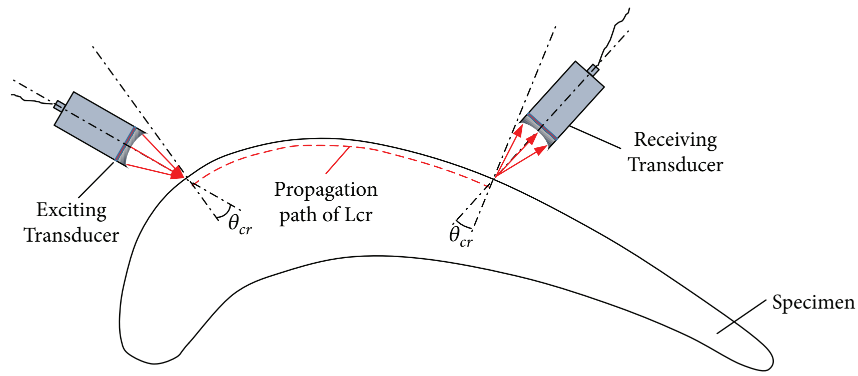

Figure 2: Critical refracted longitudinal waves propagating in a curved surface.

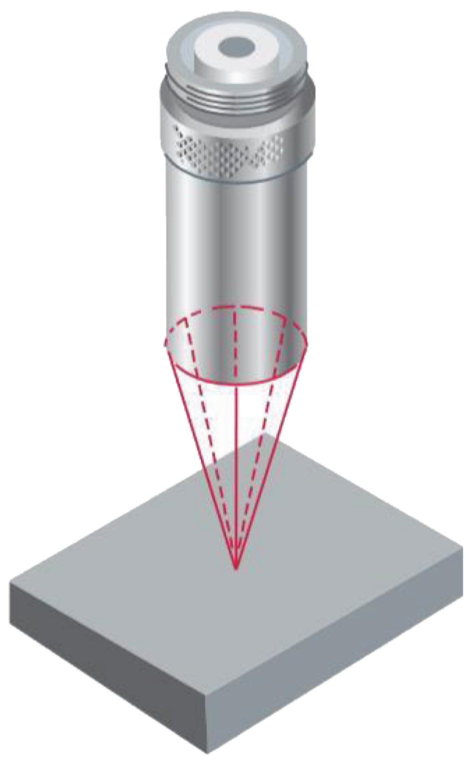

Figure 3: Spherical focus transducer.

that ultrasound travels the same distance is used to calculate the stress state on the path:

$$\Delta t = \frac{s}{V_{L0}[1-K_L\sigma]} - \frac{s}{V_{L0}} = \frac{sK_L\sigma}{V_{L0}[1-K_L\sigma]}, \quad (4)$$

$$\sigma = \frac{\Delta t \cdot V_{L0}}{K_L(s+\Delta t \cdot V_{L0})}. \quad (5)$$

2.2. Trajectory Planning. According to the principle of ultrasonic measurement of residual stress for curved surface components, it must be ensured that the exciting and receiving transducers move along the set path with a specific posture. Therefore, it is necessary to perform trajectory planning on the measured surface to obtain the controlled movement point of the manipulator. Based on the CAD model of the component, the computer-aided manufacturing (CAM) numerical simulation software is used to obtain the position and normal vector of the scanning trajectory points in the Cartesian coordinate system.

As shown in Figure 4, the robot arm that holds the exciting transducer is defined as the master manipulator and the robot arm that holds the receiving transducer as the slave manipulator.

Both the master manipulator and slave manipulator move in the zig-zag scanning mode, and the slave manipulator always keeps a certain distance from the master manipulator in the stepping direction, which determines the spatial resolution of the detection. Figure 5 shows two different zig-zag scan modes for surface workpiece. Through this two different scanning methods, we can get the stress components in two directions, and then according to the principle of force synthesis, we can determine the stress vector in the surface direction.

2.3. Coordinate Transformation. Considering the requirements for transducer position orientation, the pose information in the Cartesian coordinate system of workpiece cannot be directly recognized and used by the robot controller. We need to convert that into point and the orientation data of the transducer based on the coordinate system of the robot.

As shown in Figure 6, taking the master manipulator motion control as an example, set the reference coordinate system of the robot as $\{W\}$ and the tool coordinate system as $\{M\}$. The tool coordinate system translated along the z-axis to the focus of the ultrasonic transducer is $\{C\}$, the workpiece coordinate system is $\{A\}$, and the measured discrete coordinate system is $\{B\}$. The origin of the $\{B\}$ coordinate system is specified at the scanning point. The Z-axis is along the normal direction of the scanning point, the X-axis goes along the incident point to the exit point, and the Y-axis direction is determined according to the right-hand rule.

Through the CAM simulation software, we can easily get the position and normal information of the discrete points on the surface of the workpiece in the workpiece coordinate system. Considering the location parameters of transducer installation, scanning path and the requirements of incident or exit direction of ultrasonic wave, the purpose of coordinate transformation is to transform the position and normal

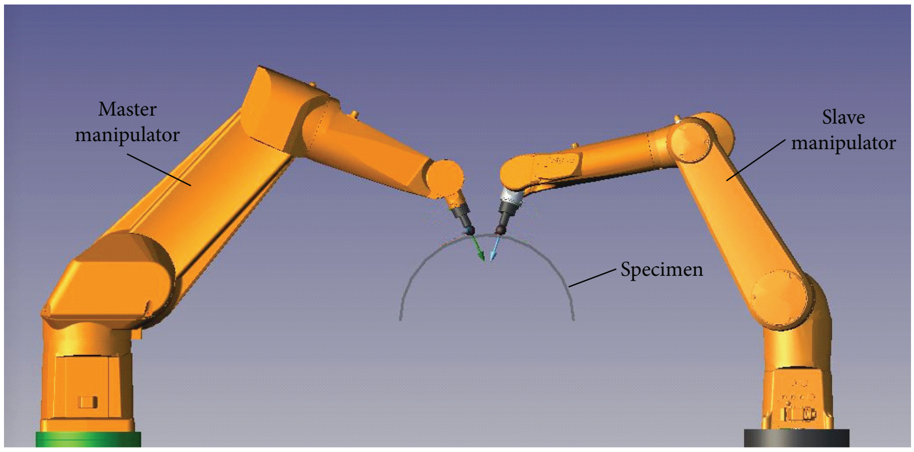

FIGURE 4: Manipulator distribution.

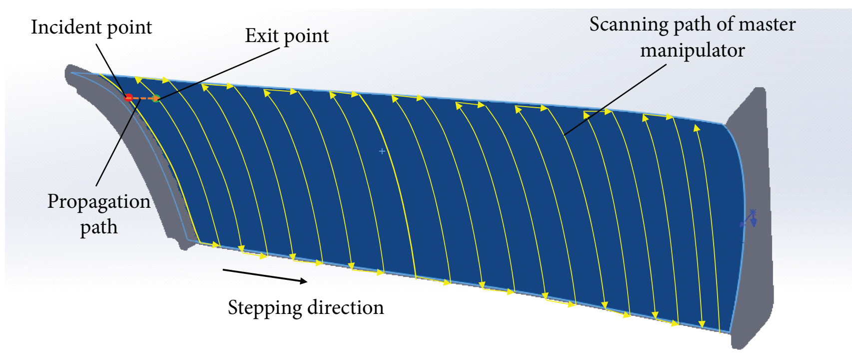

(a)

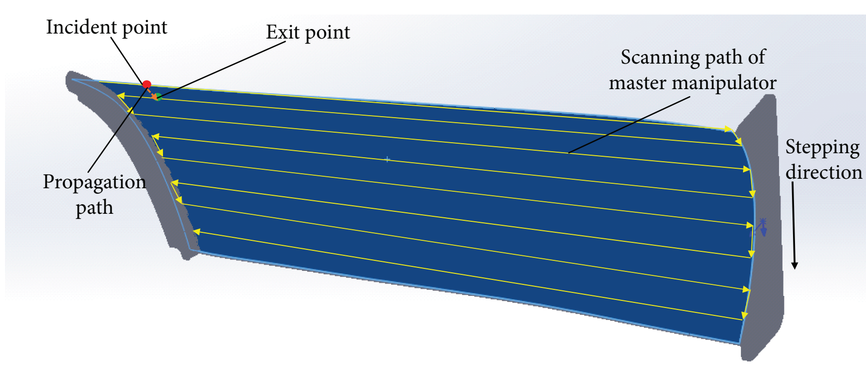

(b)

FIGURE 5: Different zig-zag scan modes for surface workpiece.

direction information of discrete points and the deflection angle of transducer into the position and posture of trajectory points in the coordinate system of the robots.

For a space vector P, let its position in the coordinate system $\{A\}$, $\{B\}$, $\{C\}$, and $\{W\}$ be expressed as ${}^{A}P$, ${}^{B}P$, ${}^{C}P$, and ${}^{W}P$, respectively. According to the principle of robot kinematics, we need to identify the posture of transducers in the coordinate system of the robot $\{W\}$ based on the pose information in the Cartesian coordinate system of workpiece $\{A\}$. According to the principle of coordinate transformation,

$$ {}^{W}P = {}^{W}_{A}T\,{}^{A}_{C}T\,{}^{C}P, \tag{6} $$

$$ {}^{A}_{C}T = \begin{bmatrix} {}^{A}_{C}R & {}^{A}P_{\mathrm{CORG}} \\ 0 & 1 \end{bmatrix} = \left[\begin{array}{ccc|c} \multicolumn{3}{c|}{{}^{A}_{B}R\,{}^{B}_{C}R} & {}^{A}_{B}R\,{}^{B}P_{\mathrm{CORG}} + {}^{A}P_{\mathrm{BORG}} \\ \hline 0 & 0 & 0 & 1 \end{array}\right], \tag{7} $$

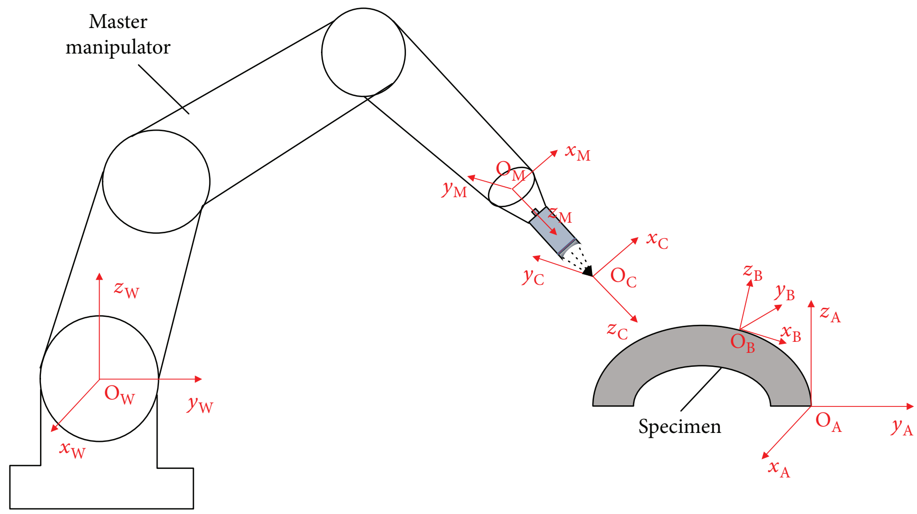

Figure 6: Definition of the coordinate systems in the master manipulator.

where

$$ {}_{B}^{A}R = \begin{bmatrix} \xi_X & \xi_Y & \xi_Z \\ \varphi_X & \varphi_Y & \varphi_Z \\ \psi_X & \psi_Y & \psi_Z \end{bmatrix}, \tag{8} $$

$[\xi_X, \xi_Y, \xi_Z]$ is the direction vector of the X-axis of coordinate system $\{B\}$ in the coordinate system $\{A\}$; $\varphi = [\varphi_X, \varphi_Y, \varphi_Z]$ is the direction vector of the Y-axis of coordinate system $\{B\}$ in the coordinate system $\{A\}$; and $\psi = [\psi_X, \psi_Y, \psi_Z]$ is the direction vector of the Z-axis of coordinate system $\{B\}$ in the coordinate system $\{A\}$. Supposing that the location of the incident point is P_i and the location of the out point is P_o at some time, their positions and normal directions in the coordinate system $\{A\}$ can be expressed as

$$ \begin{aligned} {}^{A}P_i &= [x_i, y_i, z_i, nx_i, ny_i, nz_i]^{T}, \\ {}^{A}P_o &= [x_o, y_o, z_o, nx_o, ny_o, nz_o]^{T}, \end{aligned} \tag{9} $$

where $[x, y, z]$ represents the position information and $[nx, ny, nz]$ represents the normal vector.

According to the definition of axes in coordinate system $\{B\}$,

$$ \begin{aligned} \psi &= [\psi_X, \psi_Y, \psi_Z] = [nx_i, ny_i, nz_i], \\ \varphi &= [\varphi_X, \varphi_Y, \varphi_Z] = \frac{\psi \times [x_o - x_i, y_o - y_i, z_o - z_i]}{|\psi \times [x_o - x_i, y_o - y_i, z_o - z_i]|}, \\ \xi &= \varphi \times \psi = \frac{\psi \times [x_o - x_i, y_o - y_i, z_o - z_i] \times [nx_i, ny_i, nz_i]}{|\psi \times [x_o - x_i, y_o - y_i, z_o - z_i]|}. \end{aligned} \tag{10} $$

In order to ensure that the focal point of the receiving transducer coincides with the measured point and that the acoustic axis deviates from the θ_{cr} of the incident point normal within the plane formed by the incident axis and the propagation path, the measured discrete coordinate system $\{B\}$ and transducer coordinate system $\{C\}$ should satisfy the following relationship:

$$ \begin{aligned} {}_{C}^{B}R &= \begin{bmatrix} 1 & 0 & 0 \\ 0 & -1 & 0 \\ 0 & 0 & -1 \end{bmatrix} \begin{bmatrix} \cos\theta_{cr} & 0 & -\sin\theta_{cr} \\ 0 & 1 & 0 \\ \sin\theta_{cr} & 0 & \cos\theta_{cr} \end{bmatrix} \\ &= \begin{bmatrix} \cos\theta_{cr} & 0 & \sin\theta_{cr} \\ 0 & -1 & 0 \\ \sin\theta_{cr} & 0 & -\cos\theta_{cr} \end{bmatrix}, \end{aligned} \tag{11} $$

$$ {}^{B}P_{CORG} = 0. \tag{12} $$

Bring equations (8), (11), and (12) into equation (7):

$$ \begin{aligned} {}_{C}^{A}R &= \begin{bmatrix} \xi_X & \xi_Y & \xi_Z \\ \varphi_X & \varphi_Y & \varphi_Z \\ \psi_X & \psi_Y & \psi_Z \end{bmatrix} \begin{bmatrix} \cos\theta_{cr} & 0 & \sin\theta_{cr} \\ 0 & -1 & 0 \\ \sin\theta_{cr} & 0 & -\cos\theta_{cr} \end{bmatrix} \\ &= \begin{bmatrix} \xi_X c\theta_{cr} + \xi_Z s\theta_{cr} & -\xi_Y & \xi_X s\theta_{cr} - \xi_Z c\theta_{cr} \\ \varphi_X c\theta_{cr} + \varphi_Z s\theta_{cr} & -\varphi_Y & \varphi_X s\theta_{cr} - \varphi_Z c\theta_{cr} \\ \psi_Y c\theta_{cr} + \psi_Y s\theta_{cr} & -\psi_Y & \psi_Y s\theta_{cr} - \psi_Y c\theta_{cr} \end{bmatrix}, \\ {}^{A}P_{CORG} &= {}^{A}P_{CORG} = \begin{bmatrix} x_i \\ y_i \\ z_i \end{bmatrix}. \end{aligned} \tag{13} $$

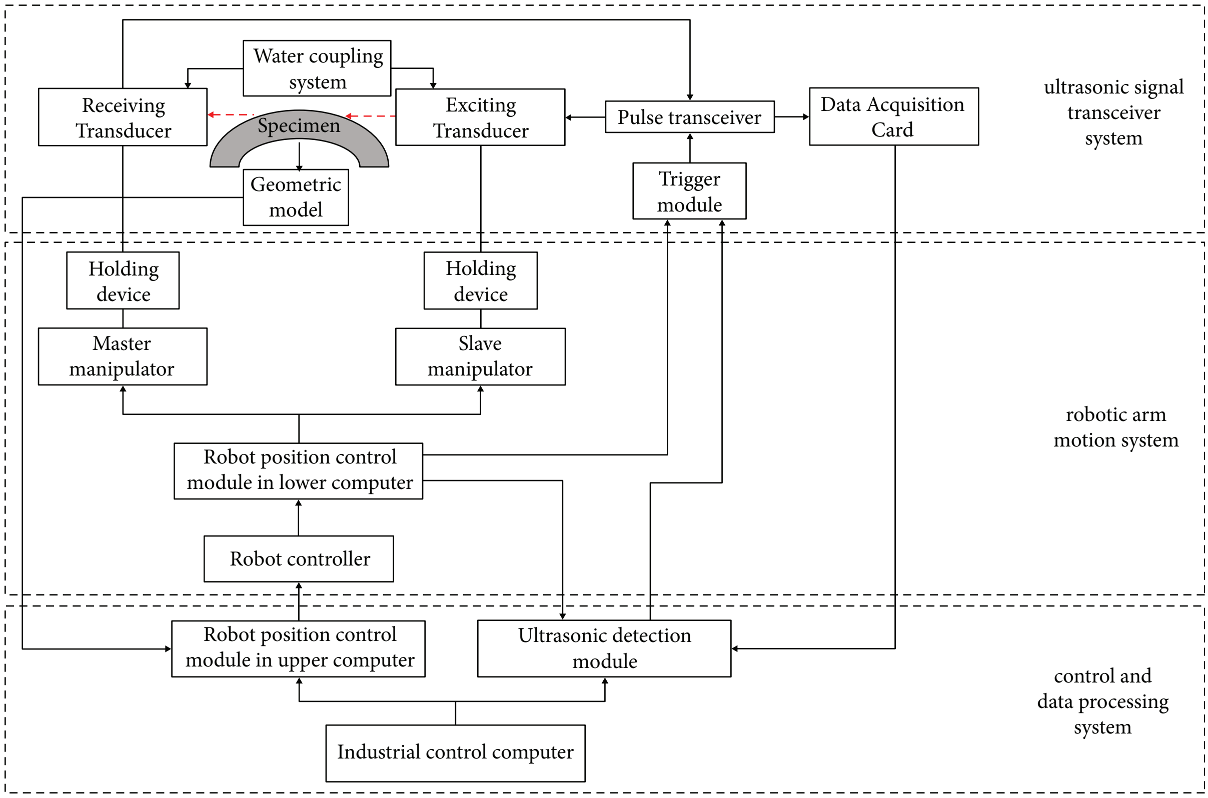

Figure 7: Ultrasonic measuring robot system.

cos and **sin** are abbreviated as **c** and **s**, respectively.

$$
\begin{aligned}
{}^{W}_{C}R &= {}^{W}_{A}R\,{}^{A}_{C}R \\
&= {}^{W}_{A}R \begin{bmatrix} \xi_X \mathbf{c}\theta_{cr} + \xi_Z \mathbf{s}\theta_{cr} & -\xi_Y & \xi_X \mathbf{s}\theta_{cr} - \xi_Z \mathbf{c}\theta_{cr} \\ \varphi_X \mathbf{c}\theta_{cr} + \varphi_Z \mathbf{s}\theta_{cr} & -\varphi_Y & \varphi_X \mathbf{s}\theta_{cr} - \varphi_Z \mathbf{c}\theta_{cr} \\ \psi_Y \mathbf{c}\theta_{cr} + \psi_Y \mathbf{s}\theta_{cr} & -\psi_Y & \psi_Y \mathbf{s}\theta_{cr} - \psi_Y \mathbf{c}\theta_{cr} \end{bmatrix},
\end{aligned}
\tag{14}
$$

$$
{}^{W}P_{CORG} = {}^{W}_{A}R\,{}^{A}P_{CORG} + {}^{W}P_{AORG} = {}^{W}_{A}R \begin{bmatrix} x_i \\ y_i \\ z_i \end{bmatrix} + {}^{W}P_{AORG}. \tag{15}
$$

Although the workpiece coordinate system $\{A\}$ is unknown, its position and posture is fixed in the detection process. Therefore, we can calibrate the coordinate system $\{A\}$ by several characteristic points to determine the transformation matrix ${}^{W}_{A}R$ and ${}^{W}T_{AORG}$ between the workpiece coordinate system $\{A\}$ and the reference coordinate system of the robot $\{W\}$. Bringing the ${}^{W}_{A}R$ and ${}^{W}T_{AORG}$ into equations 14 and 15, we can calculate the position and posture of the excitation transducer in coordinate $\{W\}$.

The pose determination method of the receiving transducer is similar to that of the transmitting transducer. The only differences between them are the establishment of coordinate system $\{B\}$ and the deflection direction of transducer.

In this case,

$$
\begin{aligned}
\psi &= [\psi_X, \psi_Y, \psi_Z] = [nx_o, ny_o, nz_o], \\
\varphi &= [\varphi_X, \varphi_Y, \varphi_Z] = \frac{\psi \times [x_i - x_o, y_i - y_o, z_i - z_o]}{|\psi \times [x_i - x_o, y_i - y_o, z_i - z_o]|}, \\
\xi &= \varphi \times \psi = \frac{\psi \times [x_i - x_o, y_i - y_o, z_i - z_o][nx_o, ny_o, nz_o]}{|\psi \times [x_i - x_o, y_i - y_o, z_i - z_o]|}, \\
{}^{A}_{C}R &= \begin{bmatrix} \xi_X & \xi_Y & \xi_Z \\ \varphi_X & \varphi_Y & \varphi_Z \\ \psi_X & \psi_Y & \psi_Z \end{bmatrix} \begin{bmatrix} \mathbf{cos}\,(-\theta_{cr}) & 0 & \mathbf{sin}\,(-\theta_{cr}) \\ 0 & -1 & 0 \\ \mathbf{sin}\,(-\theta_{cr}) & 0 & -\mathbf{cos}\,(-\theta_{cr}) \end{bmatrix}, \\
{}^{A}P_{CORG} &= {}^{A}P_{BORG} = \begin{bmatrix} x_o \\ y_o \\ z_o \end{bmatrix}.
\end{aligned}
\tag{16}
$$

3. Results and Discussion

Ultrasonic measuring robot for residual stress of complex surface components includes hardware system and software system. As shown in Figure 7, the hardware system is mainly composed of three parts: the robotic arm motion mechanism, the ultrasonic signal transceiver system, and the control and data processing system. Two six-DOF industrial robots are used to implement the gripping, position, and

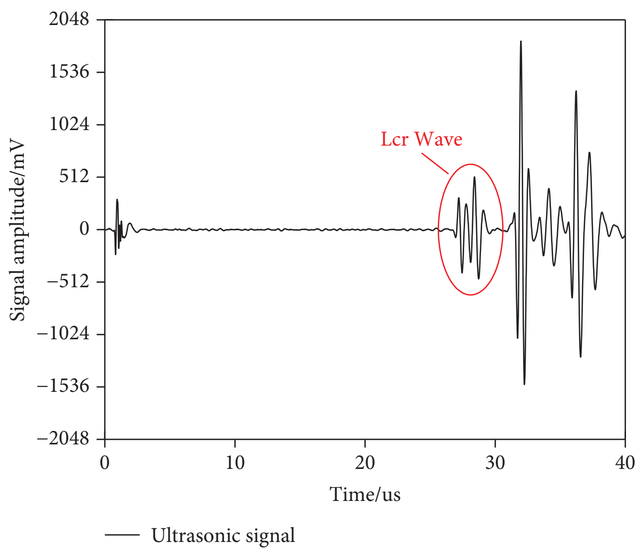

Figure 8: Ultrasonic signal.

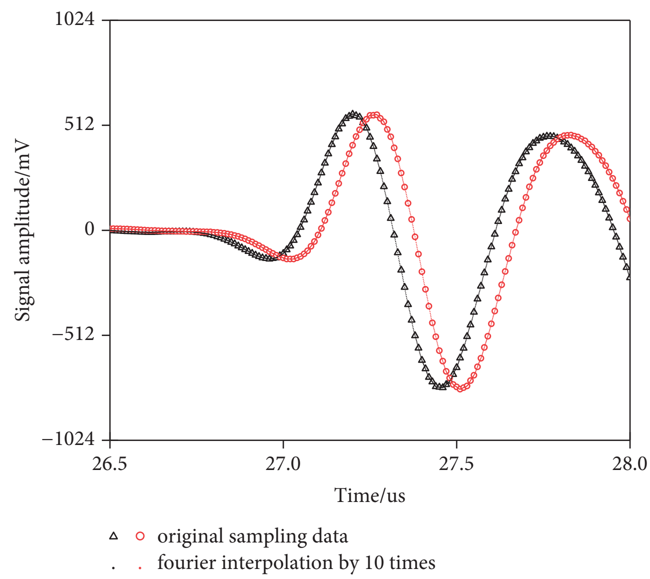

Figure 9: Ultrasonic signals before and after interpolation in different stress states.

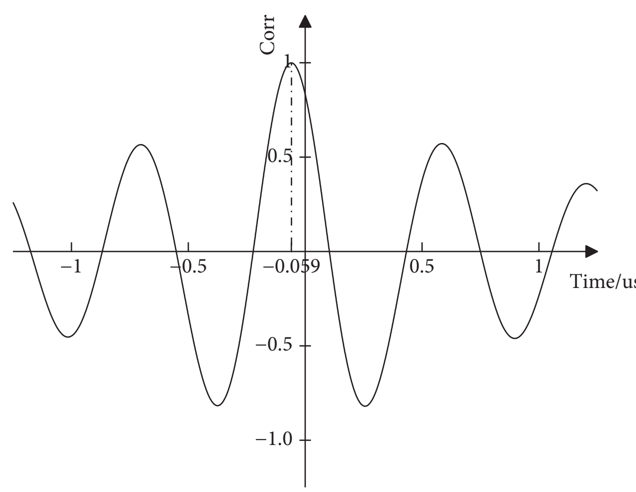

Figure 10: Cross-correlation of ultrasonic signals under two different stress states.

posture control of the ultrasonic transducers and automatic scanning; the ultrasonic signal transceiver system mainly includes a pulse transceiver, a high-frequency data acquisition card, two ultrasonic transducers, and a water coupling system. The role of this system is to excite and receive ultrasonic signals at the detection location. The control and processing system is the "brain" of the entire measuring robot, realizing the core tasks of motion control and ultrasonic signal processing.

The software system consists of the upper computer software subsystem and the lower computer software subsystem. The two subsystems cooperate with each other to jointly perform functions such as communication and control of the ultrasonic signal transceiver system and the manipulator movement system. The upper computer software is implemented in the industrial control computer to complete the trajectory planning and coordinate transforming. Another core task of the upper computer software is to process the ultrasonic transducer posture data and ultrasonic signals to obtain residual stress results. The ultrasonic signal is shown in Figure 8. The lower computer software refers to the software system implemented in the controller of the robot and is mainly responsible for robot motion control, external triggering ultrasonic pulse transceiver, and reading and transferring the robot position information.

According to equation 5, the time difference directly determines the accuracy of the results. For acoustic time method of measuring residual stress, we are only interested in the effect of stress on the ultrasonic signal in the time domain. Hence, as shown in Figures 9 and 10, we combine interpolation and time-delayed autocorrelation theory to improve the accuracy of time measurement and calculate the delay of two sets of signals.

4. Conclusions

In this paper, a new ultrasonic measuring robot system with two manipulators was designed, which can realize the nondestructive automatic detection of the residual stress in the surface of a complex curved surface component by using critical refracted longitudinal wave.

(1) Deduced an ultrasonic measuring principle and calculation formula of residual stress in curved surface components

(2) Proposed a trajectory planning strategy for the robot with two manipulators

(3) Established a coordinate transformation formula between the workpiece coordinate system and the robot coordinate system in consideration of the first critical angle

(4) A system architecture of ultrasonic measuring robot for residual stress in complex curved surface components was proposed

Data Availability

The data used to support the findings of this study are available from the corresponding author upon request.

Disclosure

The authors declare that this funding does not lead to any conflict of interests regarding the publication of this manuscript.

Conflicts of Interest

The authors declare that there is no conflict of interest regarding the publication of this paper and there is no any other possible conflict of interests in the manuscript.

Acknowledgments

This research and publication is supported by the project of Basic Technology Research which is funded by Technology and Quality Division of the Ministry of Industry and Information Technology (grant no. JSZL2017602B002).

References

[1] Z. Hong, H. Xiao, C. Yanyan, W. Yangzhong, and W. Linfeng, "Finite Element analysis of milling surface residual stresses," *Machine and Hydraulics*, vol. 5, pp. 49–52, 2013.

[2] X. Juan, "Aeroengine blade processing deformation analysis and control measures," *China's New Technology and New Products*, vol. 17, pp. 60-61, 2018.

[3] M. Duquennoy, M. Ouaftouh, M. L. Qian, F. Jenot, and M. Ourak, "Ultrasonic characterization of residual stresses in steel rods using a laser line source and piezoelectric transducers," *NDT & E International*, vol. 34, no. 5, pp. 355–362, 2001.

[4] F. Wanwan, Y. Pan, R. Dongheng, W. Hao, and Y. Yuanfeng, "Residual stress in cast iron brake disc measured by laser-generated surface wave technique," *Materials for Mechanical Engineering*, vol. 9, pp. 78–82, 2018.

[5] J. Wong, *Laser Ultrasonic Nondestructive Testing of Metal Surface Defects and Rail Tread Residual Stress*, Beijing Jiaotong University, 2016.

[6] R. Murayama and H. Nishino, "A pipe inspection using a circumferential SH-mode plate wave generated in a pipe by an electromagnetic acoustic transducer (EMAT)," *World Journal of Engineering and Technology*, vol. 6, no. 3, pp. 671–683, 2018.

[7] N. Nakamura, K. Ashida, T. Takishita, H. Ogi, and M. Hirao, "Inspection of stress corrosion cracking in welded stainless steel pipe using point-focusing electromagnetic-acoustic transducer," *NDT & E International*, vol. 83, pp. 88–93, 2016.

[8] C. Xu, W. Junfeng, S. Jianfeng, T. Haibing, L. Lianpo, and R. Xin, "Ultrasonic nondestructive testing and in situ regulation technology of residual stress for oil and gas pipelines," *Petroleum Science Bulletin*, vol. 1, no. 3, pp. 442–449, 2016.

[9] T. Chunlei, *Research on Several Detection Problems of Multi--Degree-of-Freedom Ultrasonic Automatic Detection System*, Zhejiang University, 2011.

[10] Y. Xiuchao, *3D Reconstruction Technology for Flaw Detection of Aero-Engine Blades*, Lanzhou University of Technology, 2015.

[11] D. S. Hughes and J. L. Kelly, "Second-order elastic deformation of solids," *Physics Review*, vol. 92, no. 5, pp. 1145–1149, 1953.

[12] J. L. Rose, *Ultrasound in Solids*, Science Press, 2004.

Hindawi
Applied Bionics and Biomechanics
Volume 2018, Article ID 5697408, 12 pages
https://doi.org/10.1155/2018/5697408

Research Article

Development of High-Performance Soft Robotic Fish by Numerical Coupling Analysis

Wenjing Zhao[1], **Aiguo Ming**[2] **and Makoto Shimojo**[2]

[1] College of Mechanical Engineering, Zhejiang University of Technology, Hangzhou 310014, China
[2] Department of Mechanical Engineering and Intelligent Systems, The University of Electro-Communications, Tokyo 182-8585, Japan

Correspondence should be addressed to Wenjing Zhao; jinjin83205181@163.com

Received 22 March 2018; Accepted 3 July 2018; Published 27 November 2018

Academic Editor: Nan Xiao

To design a soft robotic fish with high performance by a biomimetic method, we are developing a soft robotic fish using piezoelectric fiber composite (PFC) as a flexible actuator. Compared with the conventional rigid robotic fish, the design and control of a soft robotic fish are difficult due to large deformation of flexible structure and complicated coupling dynamics with fluid. That is why the design and control method of soft robotic fish have not been established and they motivate us to make a further study by considering the interaction between flexible structure and surrounding fluid. In this paper, acoustic fluid-structural coupling analysis is applied to consider the fluid effect and predict the dynamic responses of soft robotic fish in the fluid. Basic governing equations of soft robotic fish in the fluid are firstly described. The numerical coupling analysis is then carried out based on different structural parameters of soft robotic fish. Through the numerical analysis, a new soft robotic fish is finally designed, and experimental evaluation is performed. It is confirmed that the larger swimming velocity and better fish-like swimming performance are obtained from the new soft robotic fish. The new soft robotic fish is developed successfully for high performance.

1. Introduction

With the development of interdisciplinary sciences, including the science of electronic information and biological technology, biomimetic robots have made a lot of irreplaceable contributions in human life [1, 2]. Many researchers have been dedicated to the fields of biomimetic robots, especially on the development of a biomimetic robotic fish by mimicking the real fish [3–7]. The biomimetic robotic fish, expressed as high efficiency, good mobility, and small disturbance, will be widely available for the rescue, exploration and observation of the seabed, and other special tasks.

In order to fulfil some special work in the complicated or unknown environment accurately and reliably, the biomimetic robotic fish should be designed as soft as the real fishes, and the actuation strategy using a soft structure is needed due to the obvious advantages of smooth propulsion, high safety, and high mobility. It has been proven difficult to reproduce the fish-like smooth propulsion by using conventional rigid mechanisms, causing a relatively complex and unreliable propulsion structure with low efficiency and mobility [8, 9]. A soft robotic fish combining soft behaviors of real fishes with robotics is thus gradually turning up [6, 7, 10–13]. As a young field, the relative theories and technologies have not yet been defined in a general method and activities of robot development are still exploring the new ways [8, 13]. Therefore, it motivates us to challenge the design and control of the soft robotic fish by biomimetic approach for the development of a high-performance soft robot. Many soft robots use flexible actuators with smart materials for smooth propulsion, such as shape memory alloy (SMA), electrostatic film, PZT film, ionic polymer metal composite (IPMC), or PFC. Based on the propulsion mechanism using flexible actuators, the soft robotic fish can obtain relatively better propulsion performances similar to those of real fishes.

When designing a soft robotic fish, it must consider a surrounding fluid. The fluid increases the system mass, stiffness, and damping and changes the dynamic characteristics of the

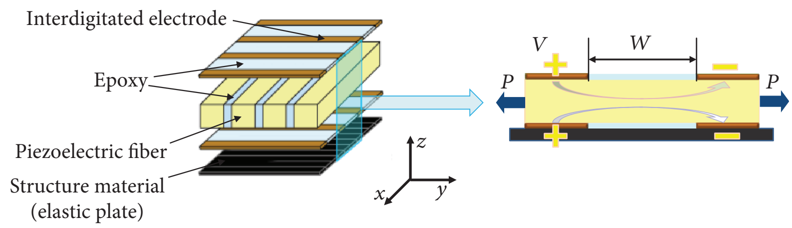

Figure 1: Structure and driving model of MFC.

soft robotic fish. The fluid-structural coupling analysis considering the interaction between the flexible structure and the surrounding fluid is performed in the design of dynamic behaviors of the soft robotic fish. Most of fluid-structural coupling problems involve a fluid without significant flow, and the main concern in the fluid is pressure wave propagation. The acoustic fluid-structure coupled method considering the sound pressure can thus be utilized to solve these coupling problems and predict their dynamic responses. According to the coupling analysis using finite element method (FEM), Ai and Sun [14] studied the vibration response of underwater cylindrical shells, Sung and Nefske [15] analyzed dynamic responses of an automobile compartment, and Djojodihardjo and Safari [16] achieved the characteristics of spacecraft structures, etc. These researches provided a basis of flow formulation and boundary conditions. However, the coupling problem is very difficult to be solved, and the design and control of the soft robotic fish have not been established due to large deformation and complicated coupling dynamics with fluid. It is necessary to investigate the design and control problems of the soft robotic fish by analytical simulation with a coupling effect.

In the present research, the fish's body and/or caudal fin (BCF) propulsion is focused. PFC can be constructed to a simple structure with high energy conversion efficiency and large displacement response and is utilized as a soft actuator to develop a BCF-propulsion prototype. In the paper, the acoustic fluid-structural coupling using FEM is applied to predict dynamic responses of the soft robotic fish in the fluid. Through the coupling analysis, a new soft robot structure is proposed, and a well-established experiment is performed to evaluate dynamic behaviors with the coupling method. From the results, it is confirmed that the new soft robotic fish with larger velocity and better fish-like swimming performance is achieved by the established coupling method. The new high-performance soft robotic fish is developed successfully.

2. Materials and Methods

2.1. Piezoelectric Fiber Composite. In this study, macrofiber composite (MFC) [17], one of the typical PFC, was adopted as a soft actuator. Figure 1 shows the structure model of MFC. The piezoceramic fiber was embedded in epoxy to make a rectangular plate. The plate was sandwiched by two pieces of polyimide film on which the interdigitated electrodes were placed. When a voltage from −500 V to +1500 V was applied, the strain and stress would be generated, and an equivalent driving load could be finally obtained by (1) for expansion and contraction in the direction of the fibers [18]:

$$\begin{Bmatrix} P_x \\ P_y \end{Bmatrix} = \frac{1}{1 - \nu_{xy}\nu_{yx}} \begin{bmatrix} E_x & E_x\nu_{yx} \\ E_y\nu_{xy} & E_y \end{bmatrix} \begin{Bmatrix} d_{33} \\ d_{31} \end{Bmatrix} \frac{V}{W}, \tag{1}$$

where E_x and E_y are the tensile modulus in the X and Y directions, respectively, ν_{xy} and ν_{yz} are Poisson's ratio, d_{33} and d_{31} are the piezoelectric constants, V is the voltage, W is the distance between the electrodes, and P is the driving load.

When MFC combined with a thin elastic plate, the bending deformation generated due to resonance. The characteristics of bending deformation were utilized to design the soft robotic fish with BCF propulsion. The carbon-fiber-reinforced polymer (CFRP) was adopted as the thin elastic plate in the research.

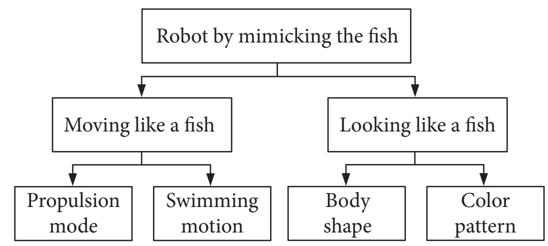

Figure 2: Decomposition of functions for a soft robot mimicking the fish.

2.2. Design Method and Numerical Coupling System of Soft Robotic Fish. The biomimetic approach has been used to design the soft robotic fish in the unknown or complicated environments. Through mimicking the real fish, the concerned functions of the soft robot can be classified into two types: moving like a fish and looking like a fish, described in Figure 2. The type of moving like a fish focuses on the propulsion modes and motions similar to those of real fishes. The swimming performances such as velocity and swimming number are adopted to evaluate the propulsion performance of the soft robot. For the type of looking like a fish, it concerns a fish species by matching its body shape and color pattern [19]. In the study, the function of moving like a fish was mainly focused.

In the research, the main research purpose is to develop the high-performance soft robotic fish by a biomimetic method. The design method based on numerical analysis is presented. It takes into account the interaction between the

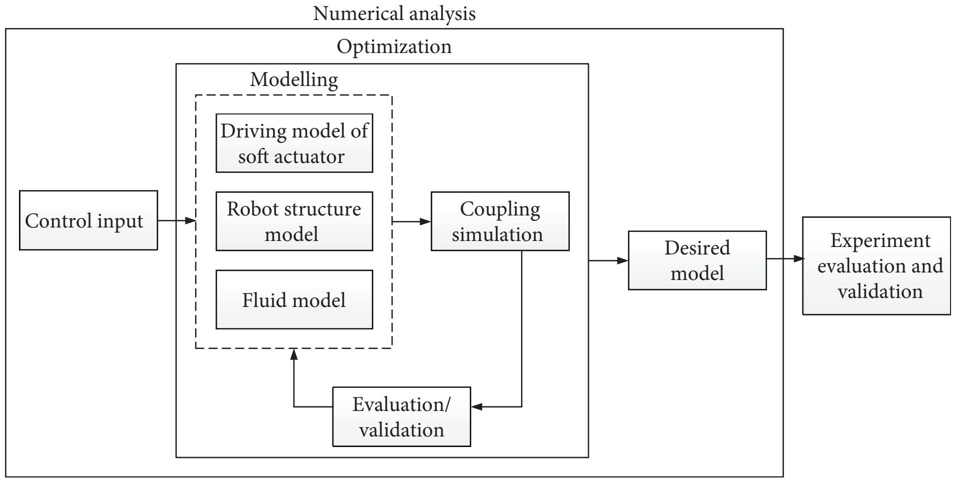

Figure 3: Design procedure of the soft robotic fish.

flexible structure and the surrounding fluid. Figure 3 shows the design procedure of the soft robotic fish. The desired robot model is firstly proposed through the coupling analysis. The manufacture and experiment evaluation are then carried out for validation. In the research, the fish with subcarangiform type such as trout fish is focused. The propulsion motion is dominated by the inertial force of the fluid [20]. The driving model based on an MFC soft actuator is described, in which the control input is considered. Through the driving model, the modelling of the soft robotic fish including the surrounding fluid is presented, and the corresponding material properties are defined. Based on the modelling, the numerical coupling simulation is performed to establish the fish-like propulsion motion, and then the robot structure is optimized by the established coupling simulation for improvement until the achievement of the desired model. When the desired model is achieved, the experiment evaluation will be done by using the actual prototype.

2.3. Approach of Acoustic Fluid-Structural Coupling. In this paper, the FEM approach was used to deal with the acoustic coupling problems through ANSYS software. Acoustic elements, four degrees of freedom (DOF): three for optional displacement and one for pressure, accomplished the required fluid-structural coupling. A consistent matrix coupling was set up between structural and fluid elements in which strongly coupled physics caused no convergence problems.

In the fluid-structural coupling, a flexible robot structure was in contact with an enclosed fluid. The differential motion equation of a continuum body in finite element formulation was used to model the flexible robot structural domain. The fluid domain presented by the acoustic wave equation met the basic conditions: inviscid, compressible, no mean flow, no heat transfer process, and relatively small pressure. The amplitude in the fluid domain was relatively small for small variation in fluid density. The mean density and pressure were uniform throughout the fluid domain. The interaction between the flexible robot structure and the surrounding fluid at the interface caused the fluid pressure to exert a force applied to the flexible robot structure, and the structure motion produced an effective load acting on the fluid. The coupling boundary conditions at the interface met the continuity of displacement and fluid pressure between two domains. Through the coupling boundary condition and algorism, the soft robotic fish's coupling problem could be described by an unsymmetrical system in a finite element matrix equation shown as (2). Both structural and fluid loads were transferred at the interface. The nodes on the interface had both displacement and pressure DOF. If the body force F_S is zero, (2) will become the equation of coupled modal analysis:

$$\begin{bmatrix} M_S & 0 \\ \rho R^T & M_F \end{bmatrix} \begin{Bmatrix} U \\ P \end{Bmatrix} + \begin{bmatrix} K_S & -R \\ 0 & K_F \end{bmatrix} \begin{Bmatrix} U \\ P \end{Bmatrix} = \begin{Bmatrix} F_S \\ F_F \end{Bmatrix}, \tag{2}$$

where M and K are the structural element mass matrix and stiffness matrix, respectively, F is the body force, U is the displacement, P is the fluid pressure, ρ is the fluid density, and subscript S and F are expressed as the structural domain and fluid domain, respectively. R, the fluid-structure coupled matrix, represents the effective surface area associated with each node on the fluid-structure interface and considers the direction of the normal vector defined for each pair of coincident fluid and structure element faces that comprises the interface surface.

3. Structure Design Based on Coupling Analysis

3.1. Structure of Soft Robotic Fish. Figure 4 shows the structure of the soft robotic fish. The robot body was made by a CFRP plate and two MFC plates. Two MFC plates using M-8528-P1 type sandwiched the CFRP plate as an actuator structure. The weight made by steel was placed on the robot head to increase the displacement of the tail end. The height of the robot body was varied toward the tail end, and it was smallest at the place of the caudal peduncle. The material properties of the soft robotic fish are shown in Table 1.

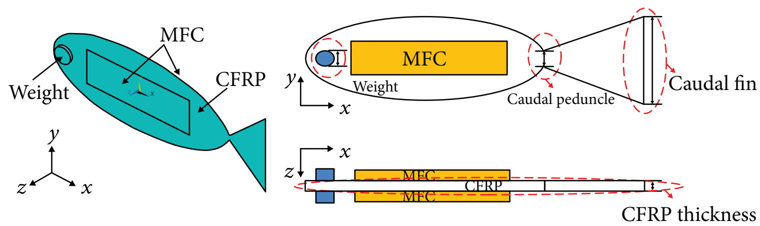

Figure 4: Structure of the soft robotic fish.

Table 1: Material properties of soft robotic fish.

Item	Weight	CFRP
Density (kg/m^3)	7850	1643
Elastic modulus (GPa)	20	20.5
Poisson's ratio	0.3	0.3
Thickness (m)	0.0025	0.0002

Table 2: Range of key structural parameters of the soft robot.

Key structural parameters of soft robot	Range of optimization
A: caudal peduncle height (m)	0.001~0.064
B: caudal fin height (m)	0.001~0.064
C: body thickness (CFRP thickness) (m)	0.0001~0.001
D: radius of head weight (m)	0.001~0.007
Entire robot body length (m)	0.175

3.2. Design Scheme of Soft Robotic Fish. The real fishes move forward by making transformation waves generated by a meandering motion. The transformation is obtained by the bending moment generated from the muscles along the body axis of real fishes. In the meandering motion of the real fish, the inertia force apparent increase in fluid mass becomes a propulsive force in the increased amplitude case. The net positive force can be obtained at the locomotion direction when the motion amplitude is increased toward the tail [20]. Moreover, in the propulsion of the trout fish [20], the undulation amplitude is limited anteriorly and increases only in the posterior half of the fish body; that is to say, there is increased amplitude from anterior to posterior of the fish body. Therefore, to design a soft robotic fish with large propulsive velocity, the motion amplitude needs to be increased toward the tail, and the maximum value should be located at the caudal fin end.

The main bending propulsion motion and the motion amplitude at the caudal fin end were focused in the design. To achieve the fish-like propulsion motion with large velocity, the structure design on larger amplitude at the tail end was carried out by the coupling analysis. The caudal fin shape, head weight, and body thickness of the soft robot played the important role in the propulsion [20, 21], and they were viewed as the key structural parameters in the design. The dashed lines in Figure 4 described the detailed locations of the design. The caudal peduncle height and caudal fin height were considered in the design of caudal fin shape. The CFRP plate as the main body of the actuation structure was important for large bending amplitude. Weight placed on the robot head was utilized to increase the amplitude of the tail end. These key parameters were allowed to vary within a certain range presented in Table 2. The caudal peduncle and caudal fin height were in the range of 1 mm~64 mm. The body thickness was ranged from 0.1 mm to 1 mm, and the radius of head weight was in the range of 1 mm~7 mm. These key parameters were arranged and combined at random to achieve the maximum displacement of the caudal fin end for improvement.

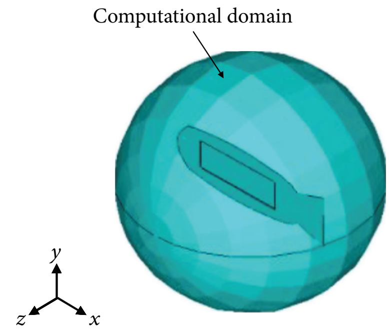

Figure 5: Computational domain of the soft robot fish in the fluid.

3.3. Fluid-Structural Coupling Analysis. The coupled transient analysis was utilized to identify the dynamic behaviors of the soft robot in the fluid. The robot structural domain was described by three-dimensional (3-D) SOLID186 elements, and 3-D FLUID30 elements were used to model the fluid domain and coupled interface. As shown in Figure 5, a spherical surface was set as the boundary of the computational fluid domain, whose diameter was 220 mm. The soft robot was placed in the middle of the static fluid domain. Due to a high voltage of MFC, which could reach up to 2000 V, the Fluorinert Electronic Liquid FC3283 was adopted as insulating liquid, whose dielectric strength range was larger than 35 KV and density was 1820 kg/m^3. It was a fully fluorinated liquid, and composition would not shift with time, which insured the fluid transport properties were stable.

In the coupling analysis, the driving load of 3 Hz ranging from −500 V to +1500 V in sine waveform was applied. The simulation results on the displacement of the caudal fin end based on different parameter arrays are described in Figure 6(a). It could be known that the maximum displacement of the caudal fin end was about 62 mm. Based on this maximum value, the corresponding structural parameters could be identified, which were the caudal peduncle height of 3 mm, caudal fin height of 20 mm, body thickness of

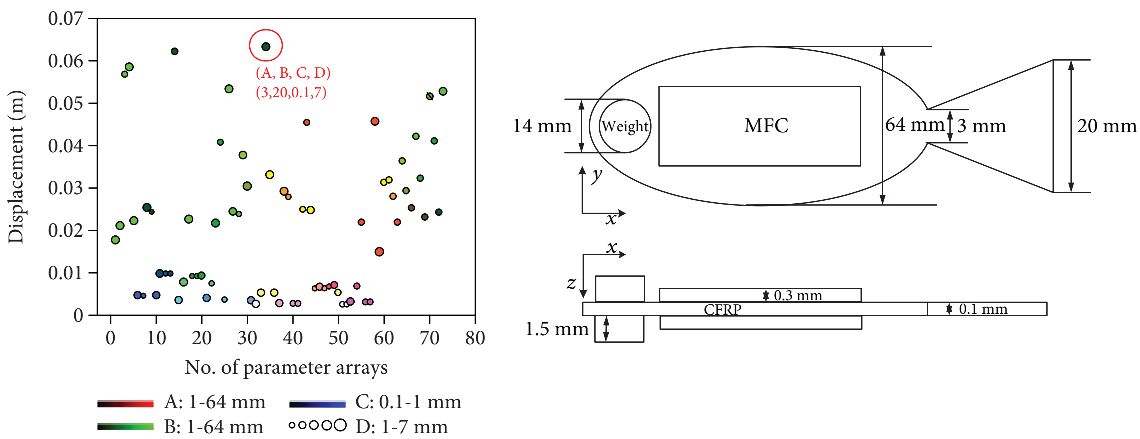

(a) (b)

Figure 6: Model of the soft robot. (a) Displacement of caudal fin end based on different parameter arrays. (b) New model of the soft robot.

Table 3: Bending mode frequencies of the new soft robot in the fluid.

Item	Mode shape	Frequency (Hz)
1st mode	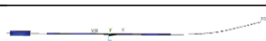	2.5
2nd mode		9.5
3rd mode		11.8

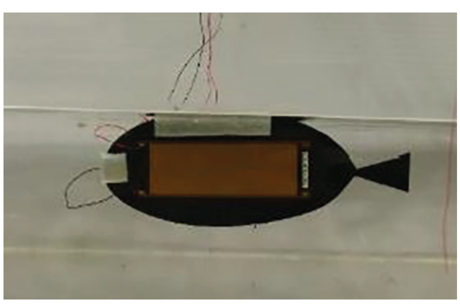

Figure 7: Prototype of the new soft robotic fish.

0.1 mm, and radius of head weight of 7 mm. A new robot model was therefore designed and is shown in Figure 6(b).

The bending mode frequencies of the new robot model in the fluid are shown in Table 3, where the first three modes were presented. The first bending mode frequency was about 2.5 Hz, and its maximum deformation occurred at the tail end. The second bending mode similar to S-shape was obtained at about 9.5 Hz. If the frequency was close to 12 Hz, the third bending mode occurred.

4. Experiment Evaluation

Figure 7 presents the prototype of the new soft robot. The low-density blowing agent as the float was placed on the robot head and top part to balance the robot weight in the fluid. The detailed specifications are shown in Table 4. The epoxy 3M-DP460 was used to make the MFC and CFRP plates bond together.

Table 4: Specifications of the new soft robotic fish.

Item	Specification
Caudal peduncle height (m)	0.003
Caudal fin height (m)	0.02
Radius of head weight (m)	0.007
Maximum body height (m)	0.064
Type of actuator	MFC 8528P1 × 2
Actuator dimensions (m)	0.103 × 0.035
Actuator active area (m)	0.085 × 0.028
Actuator for adhering	CFRP
Entire body length (m)	0.175
Adhesion bond	Epoxy 3M-DP460
Weight (kg)	0.0141

Figure 8 presents the experiment platform and driving system of the prototype. A cubical fluid tank filled with Liquid FC-3283 and a high-speed camera (Digital Camera EX-F1 from Casio Company) were utilized in the experiment. The main signal generation was controlled by a computer, and basic signal waveforms such as sine wave were designed. The signal processing circuit used a voltage follower between a high-voltage amplifier (AMP PA05039) and a computer to reduce output impedance. The high-voltage amplifier was capable of delivering an output voltage of −500 V to +1500 V at an output current up to 50 mA DC. The high-voltage output was controlled by the amplifier whose input voltage was −2.5 V~7.5 V DC or peak AC corresponding to −500 V~+1500 V output. In the experiment, the input voltage was ranged from −500 V to +1500 V and the frequency was in the range of 1 Hz~20 Hz.

The bending mode frequencies of the prototype in the fluid are shown in Table 5. The main bending propulsion mode occurred at about 2 Hz, and the second and third bending modes generated at the frequency larger than 10 Hz. The simulation results were validated by the experiment.

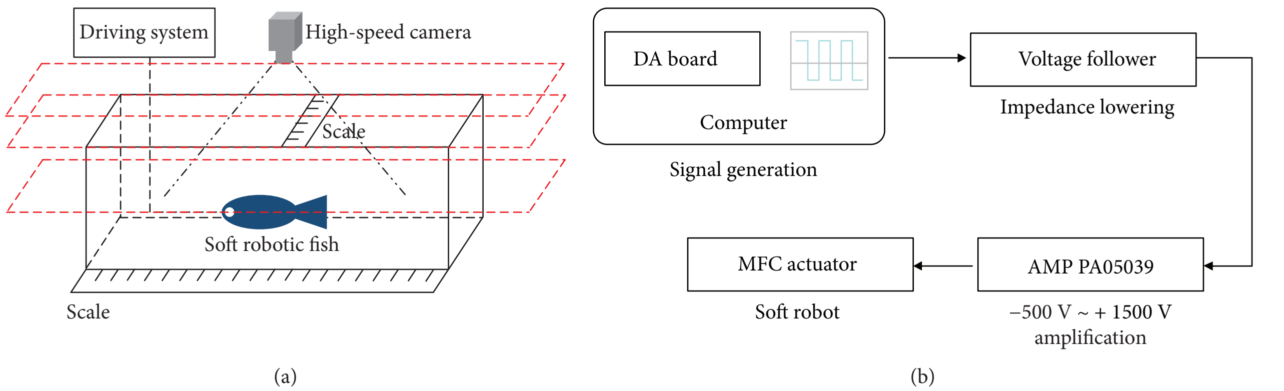

Figure 8: Experiment of robot prototype. (a) Experimental platform. (b) Driving system of the robot prototype.

Table 5: Bending mode frequencies of the new soft robot prototype in the fluid.

Item	1st mode	2nd mode	3rd mode
Frequency (Hz)	2	10	12

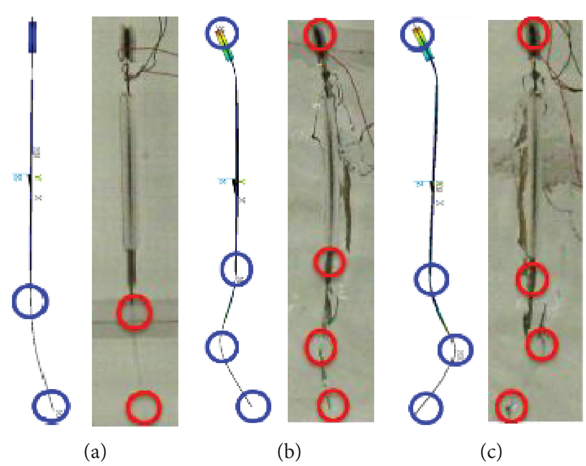

Figure 9: Bending propulsion modes of the new soft robot prototype in simulation and experiment. (a) First bending propulsion modes at 2 Hz. (b) Second bending propulsion modes at 10 Hz. (c) Third bending propulsion modes at 12 Hz.

The corresponding bending propulsion modes are shown in Figure 9 by a high-speed camera. There were very similar bending modes that occurred between the simulation and the experiment at the corresponding mode frequencies. When the frequency was about 2 Hz, the maximum displacement was obtained at the tail end. If the second and third bending modes happened, the maximum deformation generated at different parts of the robot body. The simulation results on bending propulsion modes about frequencies and mode shapes coincided with experimental results well, and fish-like bending propulsion motion was achieved.

The new prototype also could realize the basic swimming motion such as the straight-ahead motion. The swimming velocity is described in Figure 10(a). At 15 Hz, the new prototype obtained the maximum velocity of about 0.6 m/s. In the biomimetics, the swimming number S_w of the fish was widely used to evaluate the swimming performances of the robotic fish [20]. S_w, related to velocity V, frequency f, and body length L, could be expressed by

$$S_w = \frac{V}{fL}. \tag{3}$$

S_w of the fish described the distance fish moved per tail beat. It was generally about 0.6 for high performances with good flexibility and mobility [20]. It meant that there was a representation of the premise of similarity law in the biomimetics. S_w was sufficient to describe the performance related to the swimming motion of the real fish by biomimetic approach [22]. Figure 10(b) presents the S_w of the new soft robot. It was decreasing with the increased frequency in the certain range. Maximum S_w was about 0.75 occurred at 1 Hz. At 2 Hz, S_w was close to 0.6, much closer to the value of real fishes. The new soft robotic fish had better fish-like propulsion performance near the main propulsion mode.

Table 6 presents the comparison of swimming performances among some conventional soft fish robots, considering the maximum velocity and S_w. By comparison, the new soft robot had better fish-like propulsion performances on maximum swimming velocity by using speed (BL/s, body length per second) and S_w. The maximum velocity of the new soft robot was improved by more than one order of magnitude. And S_w was enhanced by at least 3 times. It could be considered that the new soft robotic fish had higher propulsion performance similar to those of real fishes than the conventional soft robotic fish.

By comparison, the new soft robot had better fish-like propulsion performances on maximum swimming velocity by using speed (BL/s, body length per second) and S_w. The maximum velocity of the new soft robot was improved by more than one order of magnitude. And S_w was enhanced by at least 3 times. It could be considered that the new soft robotic fish had higher propulsion performance similar to those of real fishes than the conventional soft robotic fish.

5. Turning Motion Control

By controlling the amplitude of input voltage on soft actuators, the soft robot could obtain the turning motion. The soft

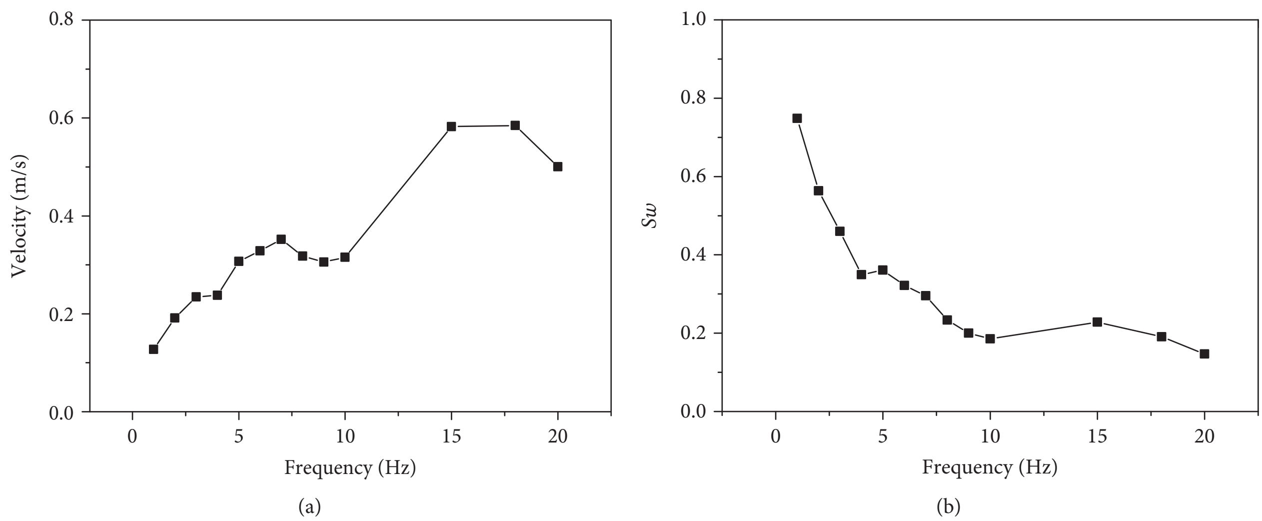

Figure 10: Swimming performance of the new soft robotic fish. (a) Swimming velocity at different frequencies. (b) Swimming number at different frequencies.

Table 6: Comparison of swimming performance of the conventional soft robotic fish.

Soft robotic fish	Soft actuator	Maximum S_w	Maximum speed (BL/s)
Kagawa University	ICPF	0.09	0.16
Polytechnic University of Madrid	SMA	0.2	0.1
Tokyo University	Electrostatic film	0.083	0.14
Michigan State University	IPMC	0.044	0.04848
This study	PFC	0.75	3.5

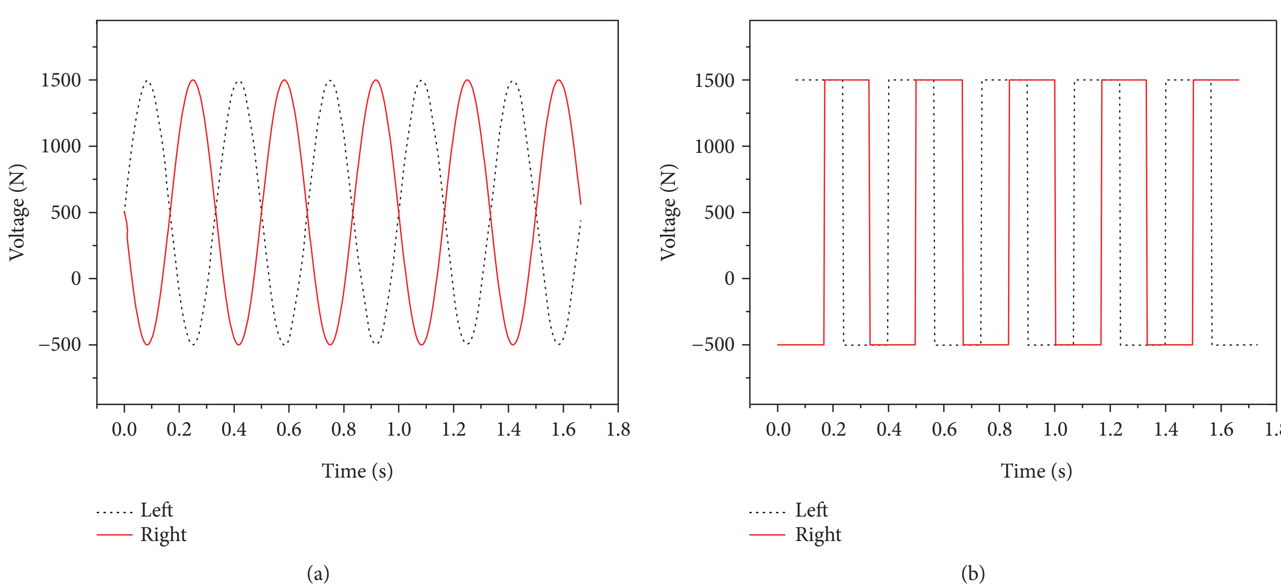

Figure 11: Waveforms on both MFC actuators at 3 Hz in straight-ahead motion. (a) Input voltages in sine waveform. (b) Input voltages in square waveform.

robot in [6] was taken as an example to describe in this part. The input voltage of 3 Hz ranging from −500 V to +1500 V in sine and square waveform was applied on this soft robot.

In the research, the soft robotic fish was composed of two soft actuators for propulsion. When the input voltage signals on both left and right MFC actuators had the same voltage amplitude and were distributed in opposite directions from each other, the straight-ahead motion was realized on the soft robotic fish. Figure 11 describes the input voltages in sine and square waveform on both left and right

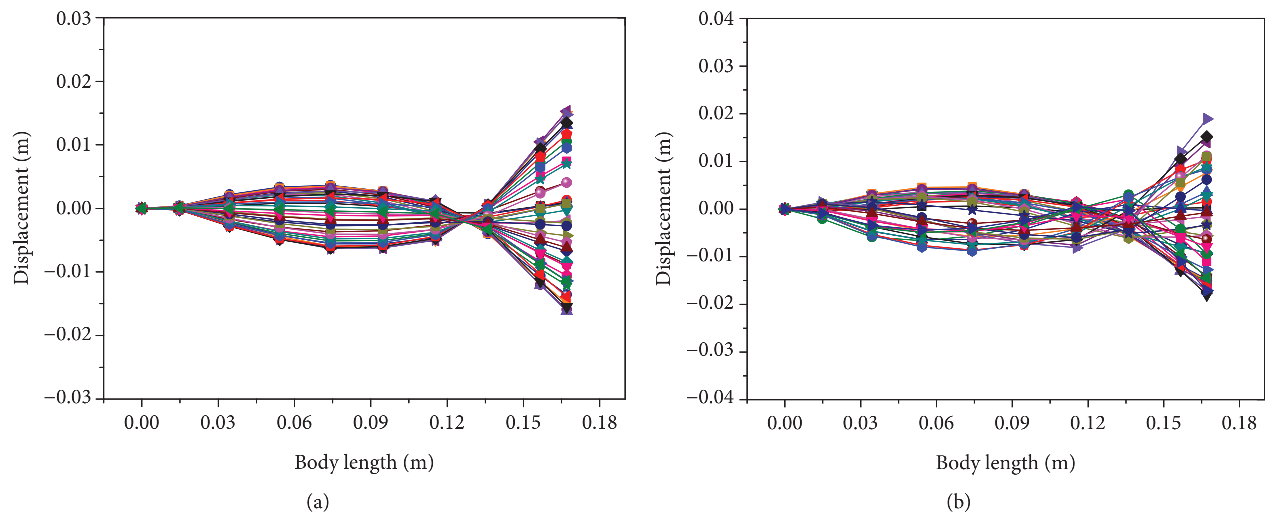

FIGURE 12: Propulsion modes of the soft robotic fish in one cycle at 3 Hz in straight-ahead motion. (a) Results in sine waveform. (b) Results in square waveform.

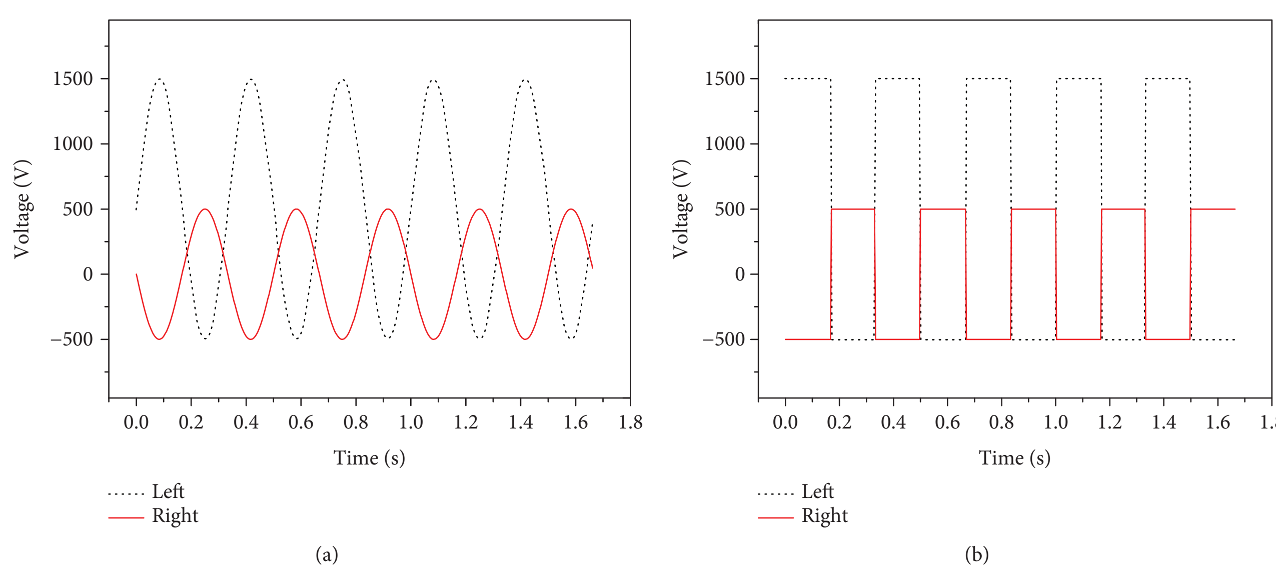

FIGURE 13: Waveforms on both MFC actuators at 3 Hz in the motion of turning right. (a) Input voltages in sine waveform. (b) Input voltages in square waveform.

MFC actuators for straight-ahead motion of the soft robotic fish. The input voltages on both actuators are all in the range of −500 V~+1500 V, and they were applied on the soft robotic fish in the opposite directions.

Based on these input voltage signals on both MFC actuators, the straight-ahead motion of the soft robotic fish was generated and the corresponding propulsion modes are presented in Figure 12. In Figure 12, the positive displacement described the displacement on the left side of the swing. Otherwise, it described the right-side displacement of the swing. The swing of the caudal fin in straight-ahead motion was in symmetrical distribution around the midline of the soft robotic fish in both sine and square waveform. Through characterizing this propulsion mode, the straight-ahead motion was realized. Besides, the swing displacement at the tail end in square waveform was larger. This was because the square waveform not only considered fundamental frequency component but also contained harmonics of fundamental frequency. It was possible that the soft robot had the faster swimming velocity by using the square waveform.

In order to realize the turning motion of the soft robotic fish, the asymmetric signals were applied based on the conditions of the straight-ahead motion. Through controlling input voltage signals for bias voltage between two soft actuators, the turning motion could be obtained due to the asymmetrical output from actuators. When the voltage amplitude on the left actuator was larger, the motion of turning right was obtained. On the contrary, the motion of turning left occurred. Figure 13 presents the input voltages on both actuators in the motion of turning right. The input

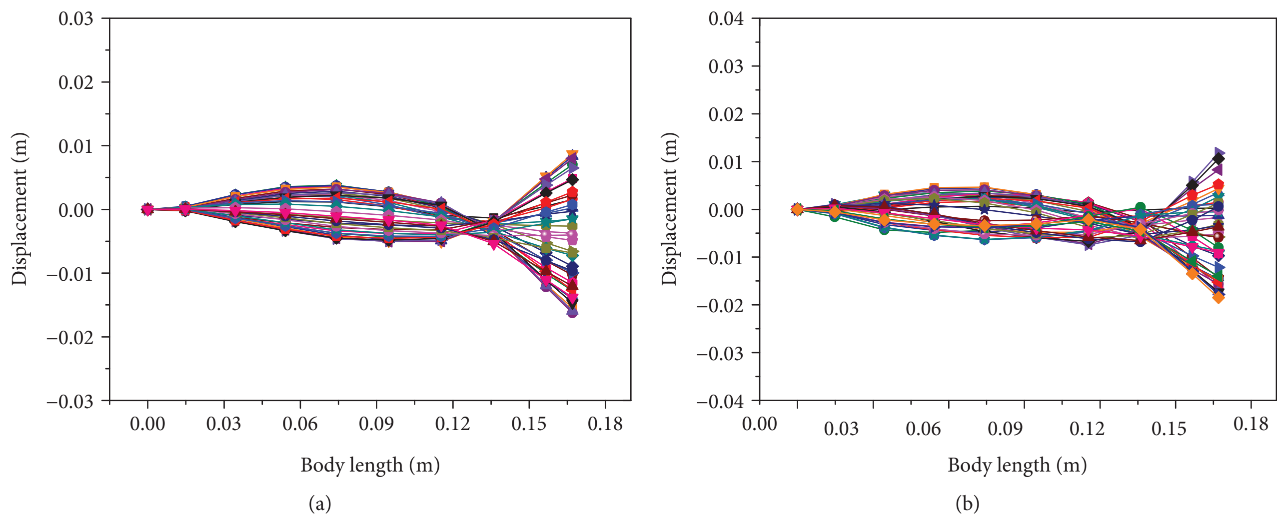

Figure 14: Propulsion modes of soft robotic fish in one cycle at 3 Hz in the motion of turning right. (a) Results in sine waveform. (b) Results in square waveform.

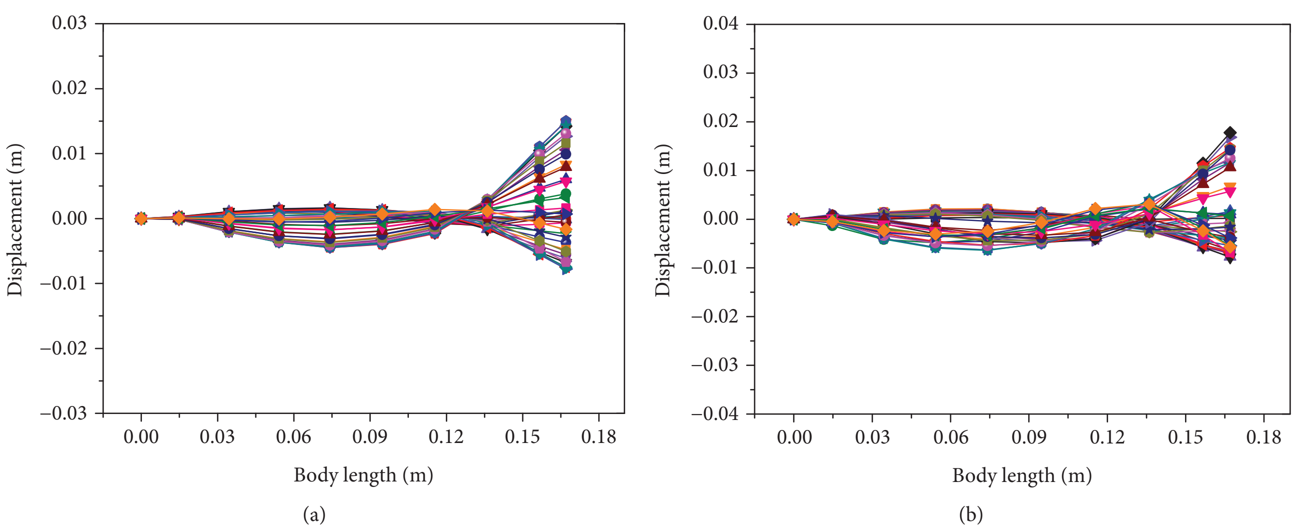

Figure 15: Propulsion modes of soft robotic fish in one cycle at 3 Hz in the motion of turning left. (a) Results in sine waveform. (b) Results in square waveform.

voltage on the left actuator was in the range of −500 V∼+1500 V, larger than the voltage ranged from −500 V to +500 V on the right actuator.

Based on these asymmetrical signals, the motion of turning right was achieved and corresponding propulsion modes are described in Figure 14. The swing of the caudal fin was asymmetrical around the midline of the soft robotic fish in both sine and square waveform. In Figure 14, the positive displacement described the displacement on the left side of the swing. Otherwise, it described the right-side displacement of the swing. The swing of the caudal fin mainly occurred on the right side of the soft robot, and the turning right motion thus generated. Besides, the swing displacement at the tail end in sine waveform was smaller than the results of square waveform due to the representation of only fundamental frequency in sine waveform.

For the motion of turning left, the applied approach of input voltages was contrary to that of turning right motion. The voltage on the left actuator was in the range of −500 V∼+500 V, and the voltage on the right actuator was ranged from −500 V to +1500 V. Based on these asymmetrical input voltages, the turning left motion was achieved and the corresponding propulsion modes are presented in Figure 15. The displacement on the left side of the swing was larger. It could also be found that the displacement at the tail end in sine waveform was smaller.

Based on the controllability of input signals, swimming motions such as turning motion could be achieved. To validate the turning motion control of the soft robot, the corresponding experiments on robot prototype in [10] were performed. The experimental platform on the measurement of the turning motion by a high-speed camera is described

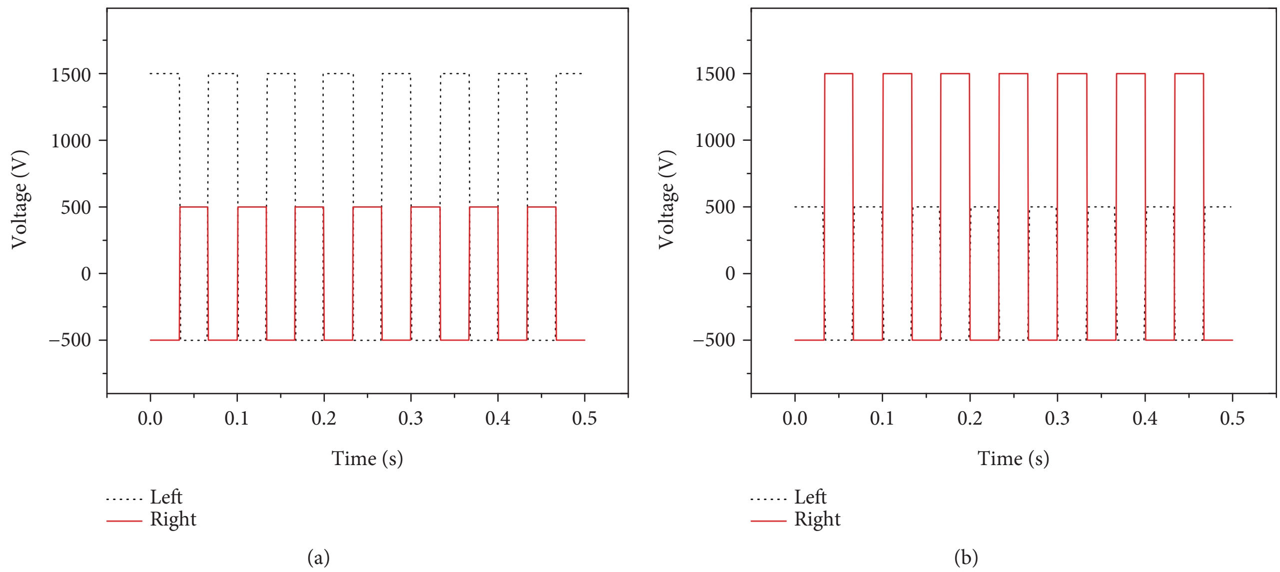

Figure 16: Input voltage signals in square waveform on both MFC actuators at 15 Hz in turning motion. (a) Turning right motion. (b) Turning left motion.

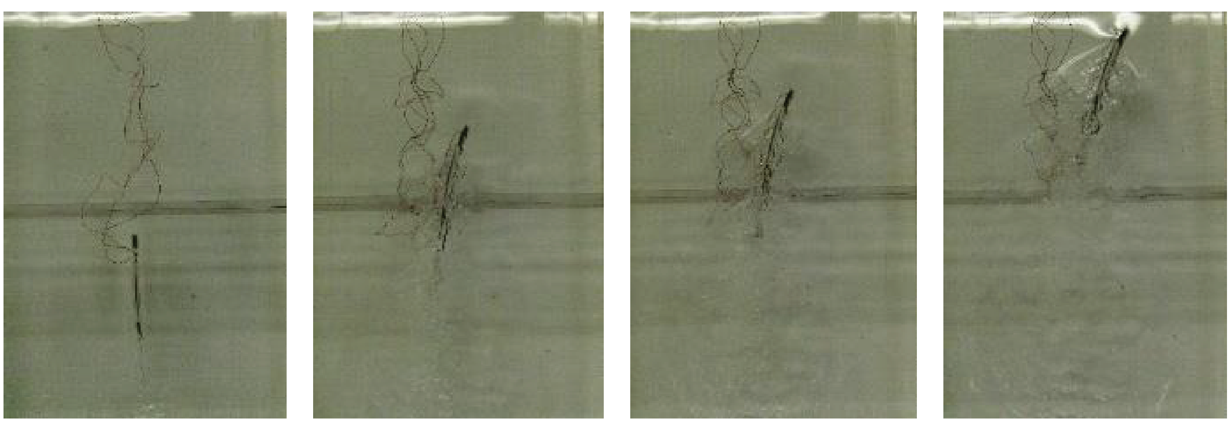

(a) (b) (c) (d)

Figure 17: Turning right motion of new soft robot prototype at 15 Hz. (a) $T = 0$ s. (b) $T = 0.3$ s. (c) $T = 0.4$ s. (d) $T = 0.6$ s.

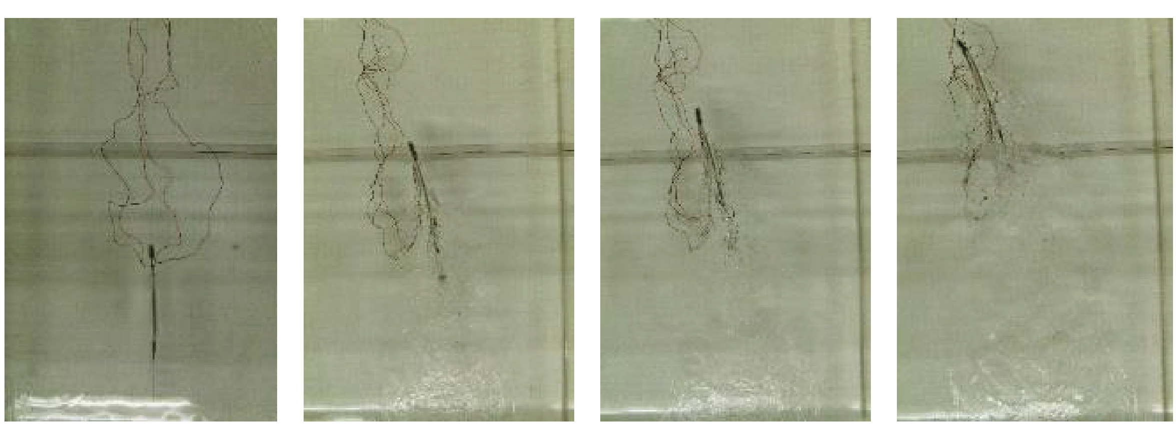

(a) (b) (c) (d)

Figure 18: Turning left motion of new soft robot prototype at 15 Hz. (a) $T = 0$ s. (b) $T = 0.3$ s. (c) $T = 0.4$ s. (d) $T = 0.6$ s.

in Figure 8. The high-speed camera was placed on the top of the fluid tank. The turning velocity of the soft robot could be predicted by photographing the turning motion video. Due to the achievement of larger velocity by using square waveform in robot actuation, the input voltages in square waveform were applied on the prototype to describe the turning motion.

Through applying the asymmetrical signals on both actuators, motions of turning right and turning left were achieved successfully. Based on the trajectory of turning motion and corresponding time, the turning velocity was determined, and the maximum turning velocity was about 27 deg/s by using square waveform.

According to the control method of input voltage signals on both actuators, the turning motion was also achieved on the new soft robot prototype. To describe the turning motion of the new soft robot, the input voltage signals with 15 Hz in square waveform shown in Figure 16 were adopted, where the signals within 0.5 s were used as an example for description. In turning right motion, the input voltage on the right actuator was in the range of −500 V~+500 V, smaller than the voltage ranged from −500 V to +1500 V on the left actuator. For the turning left motion, the applied approach of input voltage signals on both actuators was contrary to that of turning right motion.

Based on these asymmetrical input voltage signals, the turning motions of the new soft robotic fish were achieved. Figures 17 and 18 present the turning right motion and turning left motion of the new soft robot prototype at its maximum swimming velocity by using a high-speed camera, respectively. Based on the trajectory of turning motion and corresponding time, the turning velocity was determined. The turning right motion with about 51.6 deg/s and turning left motion with about 53 deg/s were obtained at 15 Hz. A well-established experiment on a new soft robot prototype also validated the turning motion control.

6. Conclusions

In this paper, a new soft robotic fish using PFC was designed through the fluid-structural coupling analysis based on biomimetic approach. Through the experiment evaluation, it was confirmed that the better fish-like swimming performances were achieved successfully by the new soft robotic fish. The new soft robotic fish with high performance similar to those of real fishes had been developed successfully. In addition, the turning motion control of the soft robotic fish was established by controlling the input signals on both actuators. The turning left motion about 53 deg/s and turning right motion about 51.6 deg/s were achieved through the new soft robotic fish at the place where the maximum swimming velocity occurred.

Data Availability

The data used to support the findings of this study are available from the corresponding author upon request.

Conflicts of Interest

The authors declare that there is no conflict of interest regarding the publication of this paper.

Acknowledgments

The work reported in this paper was supported by the National Natural Science Foundation of China (51605436) and the Natural Science Foundation of Zhejiang Province of China (LQ16E050009).

References

[1] E. J. Kim and Y. Youm, "Design and dynamic analysis of fish robot: Potuna," in *Proceedings of the IEEE Int. Conf. on Robotics and Automation*, pp. 4887–4892, New Orleans, LA, USA, 2004.

[2] J. M. Anderson, "The vorticity control unmanned undersea vehicle-an autonomous robot tuna," in *Proceedings of Association for Unmanned Vehicle System International*, pp. 663–668, Huntsville, AL, USA, 1998.

[3] K. H. Low, C. W. Chong, and C. L. Zhou, "Performance study of a fish robot propelled by a flexible caudal fin," in *2010 IEEE International Conference on Robotics and Automation*, pp. 90–95, Anchorage, AK, USA, 2010.

[4] A. Crespi, A. Badertscher, A. Guignard, and A. J. Ijspeert, "AmphiBot I: an amphibious snake-like robot," *Robotics and Autonomous Systems*, vol. 50, no. 4, pp. 163–175, 2005.

[5] M. Mojarrad and M. Shahinpoor, "Biomimetic robotic propulsion using polymeric artificial muscles," in *Proceedings of International Conference on Robotics and Automation*, pp. 2152–2157, Albuquerque, New Mexico, 1997.

[6] W. Zhao, J. Shintake, A. Ming, and M. Shimojo, "Structural design and dynamic analysis of robotic fish with piezoelectric fiber composite," in *2012 9th France-Japan & 7th Europe-Asia Congress on Mechatronics (MECATRONICS) / 13th Int'l Workshop on Research and Education in Mechatronics (REM)*, pp. 161–168, Paris, France, 2012.

[7] W. Zhao, A. Ming, and M. Shimojo, "Dynamic analysis and optimization of soft robotic fish using fluid-structural coupling method," in *2014 IEEE International Conference on Robotics and Automation (ICRA)*, pp. 1474–1479, Hong Kong, 2014.

[8] D. Trivedi, C. D. Rahn, W. M. Kier, and I. D. Walker, "Soft robotics: biological inspiration, state of the art, and future research," *Applied Bionics and Biomechanics*, vol. 5, no. 3, 117 pages, 2008.

[9] H. Liu, Y. Tang, Q. Zhu, and G. Xie, "Present research situations and future prospects on biomimetic robot fish," *International Journal on Smart Sensing and Intelligent Systems*, vol. 7, no. 2, pp. 458–480, 2014.

[10] A. D. Marchese, C. D. Onal, and D. Rus, "Autonomous soft robotic fish capable of escape maneuvers using fluidic elastomer actuators," *Soft Robotics*, vol. 1, no. 1, pp. 75–87, 2014.

[11] Z. Zhang, N. Yamashita, and M. Gondo, "Electrostatically actuated robotic fish: design and control for high-mobility open-loop swimming," *IEEE Transactions on Robotics*, vol. 24, no. 1, pp. 118–129, 2008.

[12] A. Suleman and C. Crawford, "Design and testing of a biomimetic tuna using shape memory alloy induced propulsion," *Computers & Structures*, vol. 86, no. 3–5, pp. 491–499, 2008.

[13] S. Kim, C. Laschi, and B. Trimmer, "Soft robotics: a bioinspired evolution in robotics," *Trends Biotechnology*, vol. 31, no. 5, pp. 287–294, 2013.

[14] S. Ai and L. Sun, "Fluid-structure coupled analysis of underwater cylindrical shells," *Journal of Marine Science and Application*, vol. 7, no. 2, pp. 77–81, 2008.

[15] S. Sung and D. J. Nefske, "A coupled structural-acoustic finite element model for vehicle interior noise analysis," *Journal of Vibration, Acoustics, Stress, and Reliability in Design*, vol. 106, no. 2, pp. 314–318, 1984.

[16] H. Djojodihardjo and I. Safari, "BEM-FEM acoustic-structure interaction for modeling and analysis of spacecraft structures subject to acoustic excitation," in *2007 3rd International Conference on Recent Advances in Space Technologies*, pp. 165–170, Istanbul, 2007.

[17] R. B. Williams, G. Park, D. J. Inman, and W. K. Wilkie, "An overview of composite actuators with piezoceramic fibers," in *20th International Modal Analysis Conference*, pp. 421–427, Los Angeles, CA, USA, 2002.

[18] R. B. Williams, *Nonlinear mechanical and actuation characterization of piezoceramic fiber composites, [Ph.D. thesis]*, Virginia Polytechnic Institute and State University, USA, 2004.

[19] A. C. Price, C. J. Weadick, J. Shim, and F. H. Rodd, "Pigments, patterns, and fish behavior," *Zebrafish*, vol. 5, no. 4, pp. 297–307, 2008.

[20] A. Azuma, *Encyclopaedia of Creature's Motion*, Asakura Publishing, Asakura, 1997.

[21] H. Kagemoto, D. K. P. Yue, and M. S. Triantafyllou, "Why do fish have the 'fish-like geometry?'," in *Proceedings of the Annual Meeting, Japan Society of Fluid Mechanics*, vol. 29, pp. 395-396, 2010.

[22] I. Tanaka and M. Nagai, *Hydrodynamic of Resistance and Propulsion-Learn from the Fast Swimming Ability of Aquatic Animals*, Ship & Ocean Foundation, 1996.

Hindawi
Applied Bionics and Biomechanics
Volume 2018, Article ID 8203054, 19 pages
https://doi.org/10.1155/2018/8203054

Review Article

Active Impedance Control of Bioinspired Motion Robotic Manipulators: An Overview

Hayder F. N. Al-Shuka,[1] **Steffen Leonhardt**,[2] **Wen-Hong Zhu**,[3] **Rui Song**,[1] **Chao Ding**,[1] **and Yibin Li**[1]

[1]*School of Control Science and Engineering, Shandong University, Jinan, China*
[2]*Philips Chair for Medical Information Technology (MedIT), Helmholtz Institute, RWTH Aachen University, Aachen, Germany*
[3]*Canadian Space Agency, Longueuil, Canada*

Correspondence should be addressed to Rui Song; rsong@sucro.org

Received 6 April 2018; Revised 6 June 2018; Accepted 24 June 2018; Published 18 October 2018

Academic Editor: Dongming Gan

There are two main categories of force control schemes: hybrid position-force control and impedance control. However, the former does not take into account the dynamic interaction between the robot's end effector and the environment. In contrast, impedance control includes regulation and stabilization of robot motion by creating a mathematical relationship between the interaction forces and the reference trajectories. It involves an energetic pair of a flow and an effort, instead of controlling a single position or a force. A mass-spring-damper impedance filter is generally used for safe interaction purposes. Tuning the parameters of the impedance filter is important and, if an unsuitable strategy is used, this can lead to unstable contact. Humans, however, have exceptionally effective control systems with advanced biological actuators. An individual can manipulate muscle stiffness to comply with the interaction forces. Accordingly, the parameters of the impedance filter should be time varying rather than value constant in order to match human behavior during interaction tasks. Therefore, this paper presents an overview of impedance control strategies including standard and extended control schemes. Standard controllers cover impedance and admittance architectures. Extended control schemes include admittance control with force tracking, variable impedance control, and impedance control of flexible joints. The categories of impedance control and their features and limitations are well introduced. Attention is paid to variable impedance control while considering the possible control schemes, the performance, stability, and the integration of constant compliant elements with the host robot.

1. Introduction

When a robot is in contact with the environment via its end effector, some important points should be noted:

(i) Given a specific degree of freedom, it is not possible to independently regulate the position and the contact force. For example, if the task of the target robot is to write something, neglecting control of the interaction force may lead to either loss of contact or hard pressure on the target environment [1]. In general, for rigid or dynamic interaction environments, pure position control schemes are not recommended, especially if the environment is stiff; the contact forces may reach unsafe values [2]

(ii) In addition, the robot loses some degrees of freedom (DoFs) during the contact phase. Consequently, the generalized coordinates of the target robot might be larger than its DoFs due to its constrained motion; this constitutes a closed-chain mechanism with redundant coordinates [3]

(iii) The robot may change its configuration during a transition from an open-chain mechanism to a closed-chain mechanism. In effect, three motion phases can be produced: the free motion phase, the

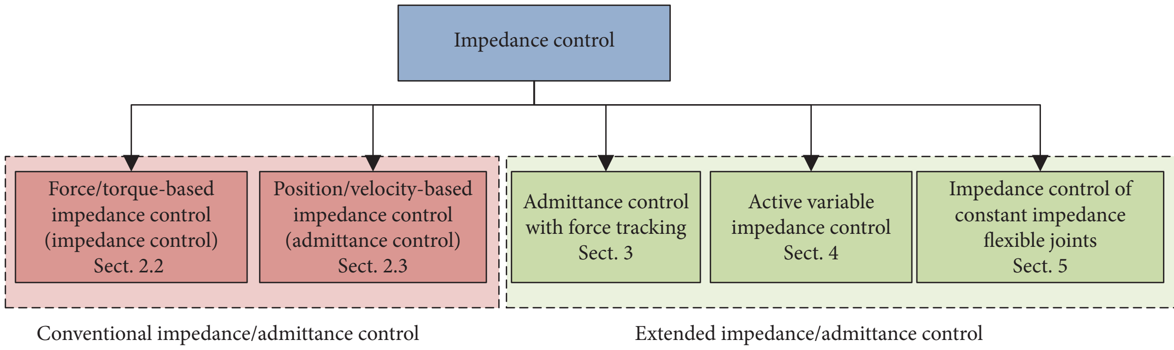

Figure 1: A general classification of the impedance control approaches. The paper is organized according to the depicted classification.

contact motion phase (impact phase), and the constrained motion phase. Each phase can have its own features and control law [3]

One of the solutions to regulate and control the interaction forces is hybrid position/force control proposed by Raibert and Craig [4]. The hybrid force-position control decouples the task space into position-controlled space and force-controlled space. Then the hybrid position/force control law is designed to track the desired position and force references. However, this scheme does not take into consideration the impedance effect between the environment and the robot end effector.

In effect, impedance control plays an important role in any workspace that involves human-robot interactions. The idea behind it is to control the mechanical impedance of a host robot regulating the interaction forces produced by the coupling between the robot and the environment dynamics; mechanical impedance can be defined as the ratio of the output force to the input velocity (motion). For linear systems, mechanical admittance is the inverse of mechanical impedance; it can be defined as the ratio of input velocity (motion) to the output force. In general, the robot can ideally behave as an impedance and the contact environment is an admittance; however, this could not be the case for multibody robotic systems with heavy links and actuators [5, 6]. Impedance control is inspired by the human behavior during contact with different environments. Humans have a considerable amount of adaptability to change muscle impedance (e.g., stiffness) when in contact with an unknown environment. If the environment is stiff, the robot should be soft and vice versa. Rigid robots, however, do not have this capability; in principle, they are stiff. They are well suited for precise free motion space, but problems can occur when moving in an unstructured environment. Excessive interaction forces should be avoided. This can be achieved by making the robots change their stiffness. Therefore, Hogan proposed active impedance control which is based on the biomechanics of human motion in free and constrained spaces [5, 6]. The idea behind impedance control is to design a user-defined dynamic relationship between the reference trajectory of the end effector and the interaction contact force/torque along each axis. However, a trade-off occurs between the tracking of the position and the interaction forces [7]. Hogan proposed two models of impedance control [5, 6]: torque- or force-based impedance control and position-based impedance control. Due to the related limitations of conventional impedance control, Anderson and Spong [8] proposed to use hybrid impedance control. The idea is to exploit the concept of hybrid position/force control and integrate it with impedance control. A robust control version of hybrid impedance control with inner acceleration was proposed by Liu and Goldenberg [9] such that the convergence of position, velocity, and acceleration is proven with bounded force error. Zhu et al. [10] made a link between hybrid control and impedance control using virtual decomposition control for two six-joint industrial robots. Extensions of other schemes were proposed for force tracking impedance control [11–18]. Force tracking impedance control has led researchers towards variable impedance control, which means that the target impedance parameters change adaptively for safe interaction motion with an unknown environment. This behavior is similar to that of humans, who have adaptable flexibility and impedance to deal with interaction tasks. The challenge of variable impedance control may lie in how the analyst can select the impedance time-varying parameters with guaranteed stability. The same problem might be encountered when dealing with fixed impedance parameters [7, 19]. The limitations inherent in active impedance control resulted in the development of new generations of actuator technology, ranging from series elastic actuators to variable impedance actuators [20]. These actuators include constant or variable compliant elements in their design [21, 22]. The idea behind these actuators is to imitate the behavior of human motion during contact with unknown constrained spaces. By controlling the stiffness of the target robot, the robot can adaptively comply with the interaction forces and generate safe contact. However, the way to integrate active impedance control with these passive design-based actuators is important and presents various problems related to control and stability.

In view of the above, this paper is aimed at summarizing the different schemes of impedance control with miscellaneous control modes (see Figure 1). The features and disadvantages of each scheme are described. The problems of stability are discussed, and the applications of impedance control are presented.

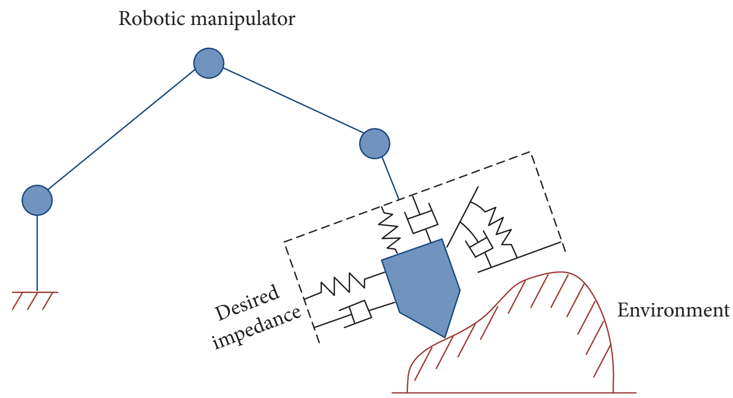

Figure 2: Description of impedance control for a robot in contact with the external environment [1, 32].

The paper is organized as follows: Section 2 introduces the background of the two main modes of conventional impedance control. Section 3 examines force tracking position-/velocity-based impedance control, and Section 4 discusses the scheme of variable impedance control. Section 5 describes impedance control of flexible joints with constant and variable compliance, and Section 6 presents the conclusions.

2. Background

Although the impedance control schemes are referred to as an indirect force method, some of these schemes can include a force tracking loop with the impedance target, e.g., the position-/velocity-based impedance control (admittance control) can be modified to improve the interaction force tracking problems (this is discussed in the following sections). As mentioned, the idea of impedance or admittance control is to generate a dynamic relationship between the interaction force/torque and the position/velocity trajectory of the robot end effector by using the virtual *mass-spring-damper* system; see Figure 2 for a description of the idea of impedance control.

By tuning the parameters of the impedance parameters, a suitable performance can be obtained for the host robot; there is a deviation in robot motion associated with and coupled with the deviation of interaction force. Basically, impedance control may consist of two nested control loops: an outer impedance control loop and an inner position/velocity/force control loop. For more details on the interaction force control schemes, see [23, 24]. Below, we present the modeling of robots with interaction forces and how to obtain a suitable formulation of impedance control for redundant and nonredundant robots. Then the two conventional categories of impedance control are described.

Remark 1. The three related subcategories of impedance control are stiffness control [1], compliance control [25], and damping control [26]; for details, see [1, 25, 26].

2.1. Dynamic Modeling of Robots in Constrained Motion. Target impedance dynamics (outer impedance loop) is preferably expressed in terms of the task coordinate frames, since the task geometry may decide which directions are motion constrained and force sensitive [7]. The task specifications for motion and interaction forces and the force feedback are closely related to the end effector. A description of the dynamic behavior of the end effector and its association with the external environment is essential for high-performance manipulator control [27]. In general, impedance control consists of two control loops: an outer impedance loop regulating the interaction between the end effector and the external environment and an inner control loop which can be a torque control loop or a position/velocity control loop. For an outer impedance loop, representation of the dynamics of the impedance target in terms of task space is necessary. For the inner control loop, there are two possibilities of coordinate representation for the control law. For force-based impedance control, the inner joint space torque control requires a transformation of the commanded forces generated by the outer loop into a commanded torque that should be tracked. Accordingly, this requires calculation of the Jacobian online. For the position-/velocity-based impedance control (admittance control), the inner position/velocity control can be represented in joint space by transformation of the commanded task coordinates into joint coordinates using inverse kinematics [28–30]. However, the inner position/velocity control law can be represented in task coordinates, as presented in [31]. In effect, despite the usefulness of task space formulation for implementation of high-performance control schemes, measurement of the end effector position and orientation (without the use of geometric Jacobian) is not easy; this may require vision technology. On the other hand, implementation of joint space control combined with a Cartesian impedance outer loop may require calculation of Jacobians and inverse kinematic schemes, which could be computationally complex.

Consider an $n-$DoF robot operating in m-dimensional Cartesian coordinates. The kinematics of the host robot can be expressed as

$$x = T(q), \tag{1}$$

$$\dot{x} = J(q)\dot{q},$$
$$J(q) = \frac{\partial T(q)}{\partial q^T}, \tag{2}$$
$$\ddot{x} = J(q)\ddot{q} + \dot{J}(q, \dot{q})\dot{q},$$

where $x \in \mathbb{R}^m$ is the Cartesian position of the end effector, $T(.)$: $\mathbb{R}^n \longrightarrow \mathbb{R}^m$ denotes to the forward kinematics, $q \in \mathbb{R}^n$ is the joint position, and $J(.) \in \mathbb{R}^{m\times n}$ is the manipulator Jacobian matrix. For robots in constrained space, the 2[nd] Lagrangian formulation can be used for modeling. Thus, the dynamic equation of rigid joint fully actuated robots can be expressed in joint space as follows.

$$M(q)\,\ddot{q} + C(q, \dot{q})\dot{q} + g(q) = J(q)^T f_e + \tau_l,$$
$$I_m\ddot{\theta} + \tau_f\left(\dot{\theta}\right) + G\tau_l = \tau_m, \tag{3}$$
$$L\dot{\iota} + R\iota + K_b\dot{\theta} = u,$$

where $M(.) \in \mathbb{R}^{n\times n}$ represents the inertia matrix, $C(.) \in \mathbb{R}^{n\times n}$ is the Coriolis and centripetal matrix, $g(.) \in \mathbb{R}^n$ is the gravity, $f_e \in \mathbb{R}^m$ denotes the external and interactional forces, $\tau_l \in \mathbb{R}^n$ is the output torque on the link side, $I_m \in \mathbb{R}^{n\times n}$ is the equivalent inertia matrix on the motor side, $\theta \in \mathbb{R}^n$ is the motor angular position vector, $\tau_f \in \mathbb{R}^n$ is the friction vector, $G \in \mathbb{R}^{n\times n}$ refers to the diagonal gear ratio matrix, $\tau_m \in \mathbb{R}^n$ is the motor torque that is equal to $K_\tau\iota$, with $K_\tau \in \mathbb{R}^{n\times n}$ being denoted to the torque constant and $\iota \in \mathbb{R}^n$ is the armature current, $L \in \mathbb{R}^{n\times n}$ is the diagonal inductance matrix, $R \in \mathbb{R}^{n\times n}$ is the resistance matrix, $K_b \in \mathbb{R}^{n\times n}$ is the diagonal EMF constant matrix, and $u \in \mathbb{R}^n$ is the input voltage control.

In general, the following points should be noted:

(i) For a robot having $(m = n)$, i.e., the number of the generalized coordinates is equal to the task space coordinates, the robot is nonredundant. Whereas if $n > m$, i.e., the number of the generalized coordinates is higher than the task space coordinates, the robot is called a "kinematically redundant" robot with redundant coordinate $r = n - m$

(ii) In general, there are two possible aspects of redundancy problems, i.e., motion redundancy and torque redundancy [32–34]. For better performance of redundant robots, the null space dynamics should be considered, i.e., dealing only with task space impedance control may not be sufficient. For more details on redundant robots and modified impedance control, see [35–37]

(iii) Equation (3) can be transformed into task space coordinates by using the kinematic relationships of (2). For more details on task space dynamics considering fully actuated, underactuated, and overactuated robotic systems, the reader is referred to [27, 28, 38, 39]

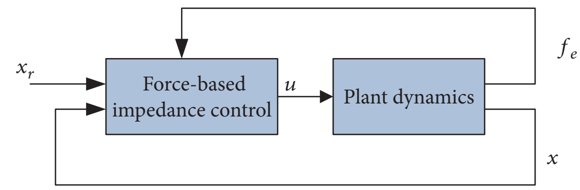

Figure 3: Generic diagram of force-/torque-based impedance control [29, 30]. For the force-/torque-based impedance control, an inner feedback loop for force/torque is optional; see, e.g., (6) that does not use an inner force control loop. For explicit nested loops, the reader is referred to [30].

(iv) Consideration of actuator dynamics is important for a robot with high-velocity movement and highly varying loads. For more details on the effect of neglecting actuator dynamics, the reader is referred to [31]. In addition, Zhu [40] has proposed three motor control modes: the torque control mode, the current control mode, and the voltage control mode. An electric motor can be in the motor torque control mode when the armature current is well controlled by a current servo amplifier and the motor torque/current constant is known. Otherwise, an electric motor should be in the motor current control mode when only the armature current is well controlled but the torque/current constant is unknown. Finally, an electric motor must be in the motor voltage control mode when no current servo control is available

(v) On the other hand, (3) is concerned with electrically driven robots; for dynamic modeling of hydraulic and pneumatic actuators, see [40–42]

(vi) Section 5 will consider the effect of joint flexibility and the associated control problems

2.2. Force-/Torque-Based Impedance Control. The idea behind force-based impedance control (simply called "impedance control" in the literature) is to make the controller react to the motion deviation by generating forces [2, 28]. It consists of two control loops: an outer position loop (target impedance filter) and an optional inner force loop. The controller may attempt to stiffen a soft force source [28]; see Figure 3 for a generic description of force- (torque-) based impedance control.

To motivate the concept of impedance control, consider the following simple second-order system (Figure 4):

$$m\ddot{x} + b\dot{x} + kx = u + f_e, \tag{4}$$

where x refers to the position of the system mass (m), b represents the damping coefficients, k denotes the system stiffness, u is the input control, and f_e is the external force affecting the system (it can be the interaction contact force or any external force).

As stated, impedance control attempts to make a dynamic relationship between the interaction force and position error by assuming a virtual mass-spring-damper

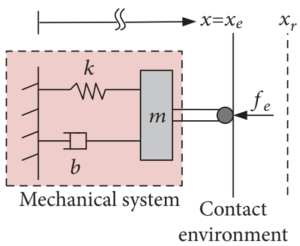

Figure 4: System dynamics in contact with the external environment [62]. The coordinate x_e represents the position of the environment, and the coordinate x_r represents the reference equilibrium trajectory that should slightly be making inside the contact environment to maintain contact. The position error is equal to the difference between the actual position (x) and the reference (x_r); this error should guarantee a compliant contact with the environment.

model with the desired trajectory; accordingly, the target impedance function can be expressed as [1]

$$m_d(\ddot{x}-\ddot{x}_r)+b_d(\dot{x}-\dot{x}_r)+k_d(x-x_r)=f_e, \tag{5}$$

where m_d, b_d, and k_d are the desired target impedance coefficients that govern the performance of the controller.

Changing the structure of the target impedance dynamics or the behavior of the target impedance coefficients leads to different impedance control strategies. Substituting (5) into (4) may lead to the following closed-loop control system

$$\begin{aligned} u = {} & \left(b-mm_d^{-1}b_d\right)\dot{x}+\left(k-mm_d^{-1}k_d\right)x-\left(1-mm_d^{-1}\right)f_e \\ & + mm_d^{-1}\left(b_d\dot{x}_r+k_dx_r\right)+m\ddot{x}_r. \end{aligned} \tag{6}$$

As can be seen, the feedback controller of (6) needs the measurements of interaction force and the state variables of the end effector.

Consider the case $m=m_d$, then (6) can be simplified to

$$u=(b-b_d)\dot{x}+(k-k_d)x+(b_d\dot{x}_r+k_dx_r)+m\ddot{x}_r, \tag{7}$$

which represents classical velocity and position feedback control with a feed-forward term denoted by the desired acceleration. Equation (7) is a special case of (6); however, the impedance implementations are different in terms of stability and transparency. There are several passivity results for the control law (7) including the case of time-varying target impedance (see, e.g., [43] and the references therein). In effect, placing a force sensor at the robot end effector can be difficult in some applications such as robotic surgery, and hence, (7) is preferable.

In effect, there are three possible models for representing the target impedance dynamics that correlate the dynamic relationship between the position and contact forces

$$m_d(\ddot{x}-\ddot{x}_r)+b_d(\dot{x}-\dot{x}_r)+k_d(x-x_r)=f_e, \tag{8}$$

$$m_d(\ddot{x})+b_d(\dot{x}-\dot{x}_r)+k_d(x-x_r)=f_e, \tag{9}$$

$$m_d(\ddot{x})+b_d(\dot{x})+k_d(x-x_r)=f_e. \tag{10}$$

Equations (8), (9), and (10) is essentially the same; only the reference signal has different components. Besides, (8)–(10) makes a compromise between the position and the contact forces such that there could be deviations in the desired position and the force references. Since a control loop based on force error is missing, forces are only indirectly assigned by controlling position. The choice of a specific stiffness in the impedance model along a Cartesian direction results in a trade-off between contact forces and position accuracy in that direction. The effect of virtual impedance parameters on the system response can be investigated by manipulating one of the impedance parameters and fixing the others. Accordingly, larger virtual mass can lead to slow response and vice versa, whereas the virtual stiffness is responsible for the response attenuation. The advantage of damping coefficient b_d is to shape the transient response. See [44] for more details on the parameter tuning. As a rule of thumb, the stiffer the environment is, the softer is the impedance stiffness k_d. The external environment force can be eliminated by substituting (5) into (4) such that the contact force is neglected; however, in this case, the measurement of acceleration is required, which is very noisy.

Seraji and Colbaugh [45] used both (8) and (10) to derive the equations of the steady-state force and position errors, respectively, whereas Yoshikawa [1] used (9) to derive impedance control for both free and constrained spaces. Yoshikawa demonstrated that when there is no contact force, the controller represents position and velocity feedback control. Huang and Chien [31] used regressor-free adaptive backstepping control for flexible joints; they used (8) as the target impedance dynamics. Khan et al. [46] used adaptive impedance control based on the target impedance dynamics of (8) for an upper limb assist exoskeleton. Please see [7, 47, 48] for more details on the characteristics and limitations of this impedance control scheme.

2.3. Position-/Velocity-Based Impedance Control (Admittance Control). In admittance control, the controller aims to soften the stiff position source via reacting to the interaction forces by imposing deviation from the desired motion [2, 28]. Position-/velocity-based impedance control consists of two control loops: an inner position/velocity loop to control the compliant position/velocity references and an outer loop to provide the desired target impedance dynamics that delivers the commanded compliant references (see Figure 5 for a general description).

Below is a simple motivating example that describes the position-based impedance control. However, for the velocity-based impedance control, a similar strategy can be used by replacing the desired and commanded position references with the velocity reference.

For the position-based impedance control of the previous 2nd-order system described in (4), (8)–(10) should be modified to isolate the inner position control loop from the outer impedance control loop. This can be done by introducing a new variable called "the commanded impedance reference trajectory" x_c, for the end effector which results from the desired references of the end effector and measurement of the interaction force wrench (see Figure 6 for details).

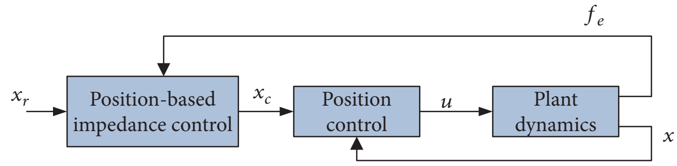

Figure 5: Schematic diagram of position-based impedance control [29, 30].

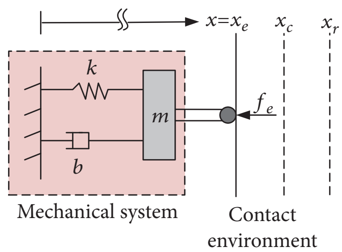

Figure 6: System dynamics in contact with the external environment. The philosophy of impedance target dynamics changes due to adding the commanded impedance trajectory x_c [62].

Accordingly, the outer impedance filter can be expressed as [49–54]

$$m_d(\ddot{x}_c - \ddot{x}_r) + b_d(\dot{x}_c - \dot{x}_r) + k_d(x_c - x_r) = f_e, \tag{11}$$

$$m_d(\ddot{x}_c) + b_d(\dot{x}_c - \dot{x}_r) + k_d(x_c - x_r) = f_e, \tag{12}$$

$$m_d(\ddot{x}_c) + b_d(\dot{x}_c) + k_d(x_c - x_r) = f_e, \tag{13}$$

The inner position control can be implemented using the proportional-integral-derivative (PID) family in our simple example; thus, the control law can be expressed as

$$u = k_p(x_c - x) + k_v(\dot{x}_c - \dot{x}), \tag{14}$$

where k_p and k_v are the feedback gains.

In effect, the well-known nonlinear schemes, e.g., feedback linearization control (computed torque control), passivity-based control, robust sliding mode control, and mode reference adaptive control, can be used for the inner position control loops [31, 49–55].

2.4. Position-Based Impedance Control vs. Force-Based Impedance Control. In effect, force-based impedance control and position-/velocity-based impedance control are based on the assumption of a force-controlled system and a position-controlled system; therefore, their performance and stabilities may differ [48]. Some important points need to be considered when using impedance control [28, 32, 48]:

(i) For the force-/torque-based impedance control, an inner feedback loop for force/torque is optional while for position-based impedance control, the inner position loop is required

(ii) Since most of the industrial electromechanical manipulators are equipped with servo position control loops, position-/velocity-based impedance control might avoid redesigning the inner position loop

(iii) For the desired stiff impedance behavior, force-based impedance control may encounter instability problems due to the amplification of noise. If the environment is soft (compliant), the stiffness of the end effector should be stiffer and vice versa. Accordingly, force-based impedance control might be suitable for interaction with a stiff environment. In contrast, position-based impedance control is more suitable to implement stiff behavior than compliant behavior, i.e., it is suitable for interaction with a compliant environment

(iv) The performance and stability of force-based impedance control may depend on back drivability and the amount of friction for the host system, whereas the performance of position-based impedance control can depend on the performance of inner position control and the quality of the force measurement

For more details on the differences among these categories of impedance control, see [56].

2.5. Position-Based Impedance Control vs. Velocity-Based Impedance Control. Literature proves that an inner velocity control loop can improve the performance and the stability problems associated with impedance control. However, the following points should be considered:

(i) Using a force loop around a position loop seems to be very natural and, therefore, this was exactly the mainstream approach used in the 1980s; see [40, 57–59] for example. Its main problem is the stability in rigid contact. In order to maintain the stability, the small gain theory is employed, leading to a very small gain and a very slow process. In contrast, the velocity-based force control is directly based on passivity theory to ensure the stability (using the Lyapunov-like function) and, therefore, has higher force control bandwidth; see [40, 57, 59] for more details

(ii) Referring to (11), neglecting the stiffness term and assuming a unit step force, the inner position control loop behaves as an integrator. Whereas, the inner velocity control loop under the same conditions can behave as a first-order transfer function (low pass filter) that may not require aggressive tuning [60]. However, the inner velocity/position control can impose a constraint on lower bounds of desired impedance [56, 61]

(iii) In some robotic applications, the desired position trajectory can be unknown, and thereby, the use of an inner velocity control loop is more suitable. Examples of these applications are the unknown final destination of human-robot cooperation [60] and the difficulties associated with determining the desired position trajectory of a low-impact docking mechanism [44]

3. Position-/Velocity-Based Impedance Control with Force Tracking

In humans, the stiffness of muscles plays an important role in dextrous and robust motions. For example, the human arm can control the interaction contact force by modifying its muscle stiffness such that the interaction contact force can be either increased by making the arm stiffer or decreased by reducing the arm's stiffness. In addition, an individual can keep the force tracking error within a specified range in the presence of disturbances and uncertainty [62]. In effect, the target impedance dynamics of (8)–(10) and that of (14) are asymptotically stable in free space, while there are steady-state position and force errors in constrained space.

In general, most robotic systems need to be in contact with the external environment. Regulation of the interaction force is necessary to avoid problems related to instability and safety. Some robot applications include control and stabilization of the constant value interaction force, such as with deburring, welding, and grinding [63]. Nevertheless, human-robot interaction applications require time-variant interaction forces, such as robot-aided cell injection [64, 65] and rehabilitation applications [66, 67]. Accordingly, conventional impedance control may not be suitable for these applications and large deviations of position and forces might be produced; tracking of the time-varying force control combined with impedance behavior is required.

Accordingly, the exact position and force tracking may not occur in conventional impedance control strategies. The main limitation of impedance control is that the interaction forces are controlled indirectly by selecting the desired impedance dynamics. However, this may demand accurate knowledge of environment parameters (e.g., environment location and stiffness) which are difficult to specify in practical applications [45, 68].

To illustrate the importance of knowledge of the environment parameters, consider the following scalar target impedance function

$$m_d(\ddot{x}_r - \ddot{x}_c) + b_d(\dot{x}_r - \dot{x}_c) + k_d(x_r - x_c) = f_r - f_e, \tag{15}$$

replacing the environment contact force by the difference between the required desired force (f_r) and the sensed contact force (f_e). This modification might be necessary for force tracking.

If the desired reference trajectory maintains constant values, their first and second derivatives are equal to zero. Thus, (15) becomes

$$-m_d\ddot{x}_c - b_d\dot{x}_c + k_d(x_r - x_c) = f_r - f_e. \tag{16}$$

Using a simple spring model to represent the deformation of the environment (assuming that environment stiffness dominates its deformation), the interaction force can be expressed as

$$f_e = k_e(x - x_e). \tag{17}$$

Rewriting the above equation to get the end effector position leads to

$$x = \frac{f_e}{k_e} + x_e. \tag{18}$$

Inserting the force error in (18) leads to

$$x = \frac{(f_r - e_f)}{k_e} + x_e, \tag{19}$$

with $e_f = (f_r - f_e)$.

Because the objective of the inner position control loop is to track the commanded compliant impedance references (x_c), a position error can be produced. Accordingly, x_c can be expressed as

$$x_c = \frac{(f_r - e_f)}{k_e} + x_e + e_p, \tag{20}$$

with

$$e_p = x_c - x = x_c - \frac{(f_r - e_f)}{k_e} - x_e. \tag{21}$$

Substituting (20) in (16) produces the following force/position error differential equation (closed loop)

$$\begin{aligned} m_d\ddot{e}_f + b_d\dot{e}_f + (k_d + k_e)e_f &= k_e k_d x_e + m_d\ddot{f}_r + b_d\dot{f}_r + k_d f_r \\ &\quad + k_e\left(m_d\ddot{e}_p + b_d\dot{e}_p + k_d\left(e_p - x_r\right)\right). \end{aligned} \tag{22}$$

If the impedance system reaches the steady-state region assuming that the desired environment force is of constant value, the steady-state force error can be expressed as

$$e_f = \frac{k_d k_e}{k_d + k_e}\left[\frac{f_r}{k_e} + x_e + e_p - x_r\right]. \tag{23}$$

Let $x_r = x_e + (f_r/k_e)$ which *includes adequate knowledge of the environment parameters*; then (23) reduces to the following equation

$$e_f = \frac{k_d k_e}{k_d + k_e} e_p, \tag{24}$$

in which *the position error plays an important role in the steady-state force error*.

Accordingly, the convergence of interaction force tracking could not be ensured in position-based impedance control, especially with uncertain environment stiffness and uncertain modeling of the host robotic system [69]. Three essential techniques are available to attenuate the force tracking error: (i) modification of the reference trajectory combined with estimation of the environment geometry and physics [45], (ii) modification of the target stiffness to carefully control the required interaction force [62], and (iii) modification of both the reference trajectory and the target stiffness [69].

Seraji and Colbaugh [45] proposed two control schemes for position-based impedance control with contact force tracking. The key idea of the schemes is to modify the desired reference trajectory required to compensate for the environment force error considering uncertain environment stiffness and location. The first scheme used the model reference adaptive control (MRAC) to generate the desired position reference online as a function of the environment force error. The second scheme is designed based on the indirect adaptive control such that the environment parameters (stiffness and location) are estimated online and desired position references are generated based on these estimates; further detailed results on indirect adaptive control are described in [70]. Lee and Buss [62] preferred to change the target (virtual) stiffness for environment force tracking because modification of the desired reference trajectory is unintuitive and the small change of x_r may lead to drastic changes in the environment forces. The target stiffness is variable and represents the PD controller of environment force error. Therefore, the impedance model has been designed as

$$m_d(\ddot{x}_r - \ddot{x}_c) + b_d(\dot{x}_r - \dot{x}_c) + k_d(t)(x_r - x_c) = f_e, \tag{25}$$

with

$$k_d(t) = \frac{k_p e_f + k_v \dot{e}_f}{x_r - x_c}, \tag{26}$$

where k_p and k_v are the proportional and derivative control gains, respectively. In effect, the stiffness effect is no longer present and it just becomes a term to correct for errors in the force tracking. Its value could be negative or time varying according to the proposition of the authors.

Kim et al. [69] used position-based impedance control for force tracking of a wall-cleaning unit. The proposed outer impedance filter includes the adaptation of the virtual stiffness accompanied by modification of the desired position references. The target impedance stiffness is variable and represents the PID controller in terms of environment force error and the model-following error. Accordingly, the proposed impedance model can be expressed exactly as (25) with the following desired virtual stiffness

$$k_d(t) = \frac{\left(k_p e_f + k_v \dot{e}_f + k_i \int_0^t e_f(\tau) d(\tau)\right)}{(x_r - x_i)} + k_0, \tag{27}$$

$$x_r = x_r^0 - \gamma(x_r - x_c), \tag{28}$$

where k_p, k_v, and k_i denote the feedback gains, k_0 denotes the initial impedance stiffness, x_r^0 represents the initial desired equilibrium trajectory, and γ is constant. The Routh-Hurwitz stability criterion was used as a basis to verify the stability of the proposed controller.

For more details on force tracking-based admittance control, see [11–18, 68]. In summary, the following points need to be considered:

(i) In effect, making the system stiffness variable imitate human behavior is considered to be variable impedance control (see explanation in the following section)

(ii) The knowledge of environment stiffness and location is necessary for force tracking-based admittance control

(iii) An inner velocity control loop can alternatively be used with features discussed in Section 2.5

(iv) The derivative of the environment force error is required in some schemes, that is, undesirable. The two possible techniques to solve this problem are (i) making a filter for the sensed force signal then differentiating the filtered signal [71] or (i) exploiting the simple spring model for the environment [72]

(v) Most researchers assume that the decoupled outer impedance filter can simplify the control problem such that stability analysis and performance of the proposed force tracking impedance filter may depend on the linear control theory, such as root locus analysis and Routh-Hurwitz stability

(vi) An important observation is that virtual stiffness of impedance behavior can lead to steady-state errors; therefore, cancelling this term may lead to zero steady-state errors [16, 73]

4. Variable Impedance Control

For most biological movements, muscles behave as mechanical actuators with a nonlinear stiffness behavior; according to biological studies, muscle viscosity can be considered constant. The force-velocity relationship includes nonlinear characteristics during contraction and stretching; increasing the applied force may result in an increase in muscle stiffness. It is important to note that the slopes of the impedance curve represent the muscle impedance associated with muscle movement [74, 75] and the references therein. The impedance profiles of the human joint can vary during motion [76]. In effect, humans can grasp objects softly and safely by regulating muscle stiffness. Moreover, it is known that the locomotion of humans consists of miscellaneous motion phases, e.g., a single-support phase, double-support phase, and jumping. Therefore, humans should modify muscle stiffness to attenuate any heterogeneous disturbances or even to track desired interaction forces [77].

There are essential applications that the robot is in contact with the human such as exoskeletons, orthosis, and prostheses. In view of the above statement, using the conventional impedance control with fixed coefficients, e.g., fixed stiffness, cannot achieve the required target impedance for the human-robot interaction. Accordingly, variable stiffness-based impedance control can improve the performance of the desired force tracking and the dexterity of the robotic system. It is a suitable strategy for modulation of the parameters of the impedance behavior such that stability is guaranteed and the performance is improved and safer. This policy of changing stiffness is explained above (Section 3) and is mentioned here due to its correlation with variable impedance control; see also [62, 73, 78].

Mathematically, the target impedance behavior with variable parameters can be expressed as

$$m_d(t)(\ddot{x}_r - \ddot{x}_c) + b_d(t)(\dot{x}_r - \dot{x}_c) + k_d(t)(x_r - x_c) = f_r - f_e, \tag{29}$$

with possibly time-varying $m_d(t)$, $b_d(t)$, and $k_d(t)$.

In view of the above statement, there are two main objectives for equipping the target impedance with variable impedance:

(i) to track interaction force references; please see Section 3

(ii) to increase adaptability and to imitate the biological behavior during contact with different environment stiffness

However, straightforward implementation of impedance control with time-varying virtual impedance parameters can destroy passivity conditions of the system unless a proper impedance model is selected. To prove this, consider the 2$^{\text{nd}}$-order dynamics system combined with the target impedance model described in (4) and (8). Assuming a constant virtual mass with time-varying virtual spring and damper and considering the following positive definite Lyapunov function

$$V = \frac{1}{2} m_d (\dot{x} - \dot{x}_r)^2 + \frac{1}{2} k_d(t)(x - x_r)^2. \tag{30}$$

Taking the derivative of the last equation and substituting (8) into (30) lead to

$$\dot{V} = f_e(\dot{x} - \dot{x}_r) + \left(\frac{1}{2}\dot{k}_d(t)(x - x_r)^2 - b_d(t)(\dot{x} - \dot{x}_r)^2\right). \tag{31}$$

According to the last equation, the time-varying virtual stiffness could violate the passivity condition, whereas the virtual damping term could have a positive effect on the energy dissipation. However, assuming constant-value virtual parameters can ensure the system stability as follows.

$$\dot{V} = f_e(\dot{x} - \dot{x}_r) - b_d(\dot{x} - \dot{x}_r)^2 \le f_e(\dot{x} - \dot{x}_r). \tag{32}$$

Integrating the last equation to get the following satisfied passivity condition gets

$$V(t) - V(0) \le \int_0^t f_e(\tau)\,(\dot{x}(\tau) - \dot{x}_r(\tau))d\tau. \tag{33}$$

See [43] for more details on passivity conditions for variable impedance control.

Remark 2. It is important to keep in mind that the time-varying virtual stiffness parameter can be the critical determinant of the system stability. Literature proves that there are two options for time-varying virtual impedance mass/inertia: (1) it can be of constant value with no effect of Lyapunov stability or (2) it can be of a value equal to the mass/inertia of the robot end effector. The last case can be exploited to design a control law free of contact force feedback; see [43, 73] and the references therein. In addition, the virtual damping parameters can be selected as $d(t) = 2\xi\sqrt{m\,k(t)}$, where $\xi > 0$ is a constant damping ratio.

In effect, four techniques are possible to deal with active variable impedance control:

(i) manipulation of the virtual stiffness term such that it is related to interaction force error via a PID family controller; see the work of [62, 69, 79] described in the last section. However, this strategy assumed time-varying virtual stiffness only with other constant-value impedance parameters

(ii) neglecting the virtual stiffness term of the impedance model and manipulating the virtual mass and damping terms. Tsumugiwa et al. [80] proposed variable impedance control for human-robot cooperative calligraphy with a time-varying virtual damping term only. The idea is to adjust the target-damping coefficient of the robot impedance function proportional to the estimation of the arm stiffness of the human operator. This procedure may avoid instability due to increased stiffness of the operator's arm. Even if the stiffness of the human operator's hand is very high, introducing a low damping coefficient for the target impedance of the robot may lead to stable operation. Ficuciello et al. [73] improved the performance of impedance control of a 7-DoF KUKA LWR4 by exploiting the kinematic redundancy and modulation of impedance parameters (the virtual mass and damping terms) such that they imitate human behavior. The authors found that redundancy may enlarge the stability margins of the impedance parameters. In addition, the virtual variable impedance behavior with convenient modulation of the time-varying parameters might be superior compared to constant coefficient impedance behavior. The variable impedance target may (i) enhance the performance and safety of the interaction tasks with humans and (ii) make a compromise between accuracy and execution time

(iii) augmentation of the impedance model with an energy-storing element whose role is to store the energy dissipated by the controlled system such that the passivity conditions are satisfied. With this scheme, impedance control with time-varying stiffness matrices can be a powerful tool to deal with a compliant environment that requires time-varying interaction forces. This technique has been called energy tank-based impedance control and implemented by [43, 81]. Although the strategy of tank-based impedance control for generating stable interaction forces with variable stiffness is strong [43, 81, 82], it is dependent on the states of the system, which means that it should be applied online

(iv) design of adaptive laws for tracking the virtual damper and spring parameters. However, this technique could impose constraints on the values of the virtual damping and stiffness in order to ensure the system stability; for more details, see the work of [83]. In addition, Kronander and Billard [19] found that the admissible stiffness profile could depend on the states of the robot that can be unknown beforehand. Therefore, they proposed a state-independent scheme to ensure stability of variable impedance control. This means that the time-varying parameters (damping and stiffness) of the target impedance behavior can be applied offline before the performance of the task

However, some works injected the time-varying stiffness directly to the impedance model without considering the overall system stability and the associated passivity conditions, e.g., see [84]. In general, the following points need to be considered:

(i) There are two strategies for imitation of human impedance behavior: variable impedance actuators [20, 85–88] and active impedance control with suitable modulation for the time-varying tuned parameters

(ii) A challenge in the application of variable impedance target with human behavior is how to transfer the impedance characteristics from humans to robots and ensure overall system stability. Various techniques are available for estimation of human impedance: most are based on neurological schemes, such as the human central nervous system [89], learning control strategy [90], and teleimpedance [91]. On the other hand, the Lyapunov theory is a powerful tool to investigate the validity of the proposed impedance model. In addition, a systematic tuning method is proposed in [92]

(iii) In general, if the robot is to be freely driven by the human, robot impedance should be low; zero stiffness is recommended in this case. For fast motion purposes, virtual robot damping should be decreased and vice versa, whereas decreasing virtual inertia may lead to instability problems [73]

(iv) On the other hand, regulation of the virtual stiffness of the host robot is necessary for surgery, rehabilitation applications, and collaborative robots [73, 93]. Most researchers have focused on manipulation of the system's stiffness due to (1) the wide range of adjustability of the system stiffness compared with damping and inertia coefficients, (2) because the stiffness term is the dominant factor for low-velocity motion, and (3) because the stiffness term has a considerable effect on system stability for the steady-state regions. For details on the stiffness of human limbs, see [94–97]. However, the time-varying virtual stiffness should be associated with guaranteed stability

(v) With constant parameter-based impedance control, the passivity property is conserved; however, with arbitrary time-varying parameters for impedance behavior, the passivity property can be lost [19]

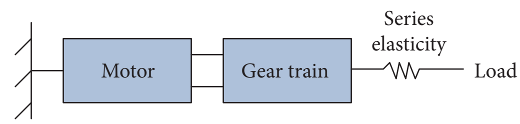

Figure 7: Simplified schematic for series elastic actuators (SEA) [56].

5. Active Impedance Control of Constant Impedance Flexible Joints

In this section, impedance control of robots with flexible elements is discussed. The focus is on constant impedance series elastic actuators (SEAs). The cascade control combined with an outer impedance loop is often proposed for these types of compliant actuators; for more details on cascade control theory, see [98–102]. The general structure of a flexible joint can consist of three components: the actuator, the gear train, and the elastic element that may be in series with the output link [20] (Figure 7).

Accordingly, the actuator is called constant SEA or variable stiffness actuator (VSA) based on the behavior of the designed joint stiffness (constant stiffness or variable). In this category of actuators, the actuator does not control the link directly but will exchange energy with the transmission system that generates the flexible torque that actuates the link. In recent technology, flexible joints are integrated with robots to guarantee safe motion during the contact phase or to attenuate the impact shock of unexpected forces [103, 104]. The classical rigid body formulation for robots may be inadequate for motion in complicated tasks. The flexibility may exist due to the compliance of the gear transmission, belts, and drive shafts. Adding the elastic element in series with the actuator and the output load can have the following characteristics [105–108]:

(i) It serves as an accurate torque source and as a low-cost torque sensor

(ii) The elastic element also serves as a compliant interface between the human and the robot, protecting the user and actuating system from sudden shocks and improving back drivability characteristics. In effect, the contact force can be indirectly regulated and controlled by the passive elements

(iii) The motor is isolated from shock loads, and hence, the dynamic effects of backlash and friction can be filtered by the flexible element

(iv) A drawback is the reduced large torque bandwidth due to motor saturation

The following points need to be considered when designing flexible joints:

(i) The output flexible torque is important in the performance of interaction tasks; the flexible element should be exploited in the control structure rather than dealing with it as a disturbance source

(ii) The flexible element (e.g., spring) acts as a force sensor allowing the actuator output force to be controlled, and hence, the design of the control law could be easy; see [105] for more details

(iii) The behavior of the flexible transmission cannot be known completely for variable impedance actuators, due to the inherent nonlinearity and associated complexity

Recalling (3), the Lagrangian formulation for robots with flexible joints (e.g., simple harmonic drive, SEA, or even VSA) in constrained space can be expressed as [109, 110]

$$\begin{aligned} M(q)\,\ddot{q} + C(q,\dot{q})\dot{q} + g(q) &= J(q)^T f_e + \tau_s, \\ I_m\ddot{\theta} + \tau_f\left(\dot{\theta}\right) + G\tau_s &= \tau_m, \\ \tau_s &= K_s(G\theta - q), \\ Li + R\imath + K_b\dot{\theta} &= u, \end{aligned} \tag{34}$$

where K_s is the spring stiffness matrix and the other nomenclatures are defined previously.

According to (34), some major problems can be produced due to the presence of the joint flexibility, e.g., (i) the degree of freedom of the robotic system increases twofold, (ii) the resulting system is not fully actuated due to the induced joint flexibility, (iii) the joint flexibility results in fast dynamics which may stimulate the vibration problems, and (iv) for motion in constrained space, a small deviation in joint position may lead to excessive contact force on the environment due to the coupling effect [111, 112] (The dynamic model of a flexible joint-actuated robotic system can be considered as a slow-fast system (i.e., a system with different time scales). The modal frequencies associated with the fast dynamics are well separated from the rigid body modes. This assumption is associated with the singular perturbation theory; see [113, 114] for more details).

Different techniques are available to deal with the control of flexible joints: decoupling control schemes [111, 115, 116], backstepping control [117], singular perturbation control [118], and adaptive control [57, 119–121]. Efforts have been performed for controlling arbitrary stiffness flexible-joint robots in free space [122–124] and in constrained space [40, 57, 59, 112]. The joint torque control is essential for vibration damping during the free space motion and soft and safe interaction control during the contact phase [125]. Modifications of (34) to meet the requirements of inner torque control may require calculation of the fourth derivatives of the angular positions and measurement of the derivatives of a torque sensor (which could be rather noisy) [112] (Elastic joints usually avoid torque sensors by measuring the spring displacement. Such solution usually leads to a clean force derivative [125].). In effect, (34) should be modified such that the full dynamics has output variables (q, τ_s) with the input control u. Albu-Schäffer et al. [125] described a passivity-based impedance control framework based on motor position and joint torque signals, as well as their first-order derivatives. It provides a high degree of robustness to unmodeled robot dynamics and in the contact with unknown environments. The proposed control law consists of two terms: (1) the first term is to regulate the joint-level impedance and (2) the second term is a torque feedback loop. Second- and higher-order derivatives of the variable states are not required, which give some preference to other techniques that use third derivatives of the variable states; see [29] for more improvements.

The rest of this section considers specifically the possible problems associated with nested control loops of the SEA. Many researchers used simple force control of SEA-driven robots based on linear control theory. However, the system stability and passivity conditions should be satisfied in order to achieve feasible performance [126, 127]. A comprehensive overview of existing controller passivity is presented in [128]. Pratt et al. [129] have proposed a passive force control architecture including some feedforward terms and one PID-based feedback for tracking the desired interaction force. The authors replaced the integral term of the PID controller by a first-order low pass filter for ensuring passivity but with possible static errors. Yuan and Stepanenko [122] and Lozano and Brogliato [123] proposed to use an inner velocity loop combined with an outer force control to improve the system performance and overcome some undesired effects of the actuator and the transmission element. For robots with SEAs, cascade control is often implemented with an outer impedance loop and inner torque control. In effect,

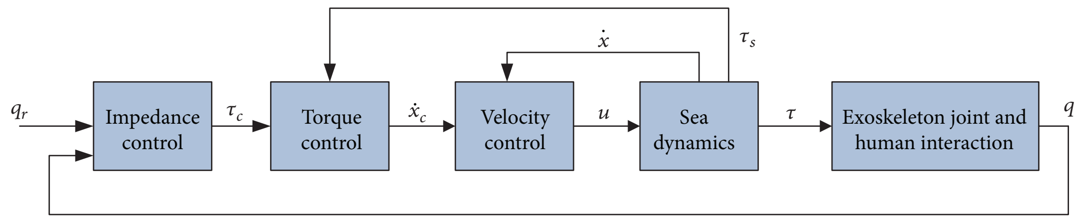

Figure 8: Multilevel control of the LOPES robotic system where the subscript c refers to the commanded signals [107].

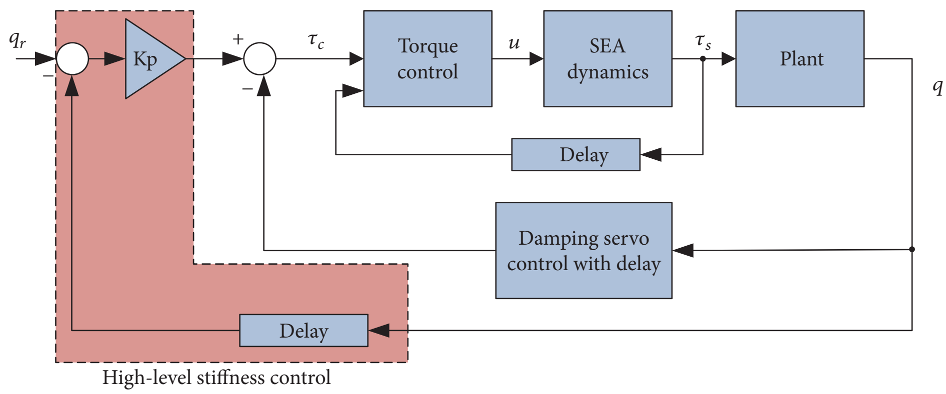

Figure 9: Proposed cascade control with three control loops: high-level stiffness servo loop, inner embedded damping servo loop, and the innermost torque control [131].

there are miscellaneous nested loops coupled with the impedance control (see details below). Currently, torque sensors are widely available; however, using an inner torque loop combined with another control loop can encounter challenges associated with stability problems. For example, the PI-based torque control might be difficult to tune or to provide a high bandwidth if the load side has some damping. In addition, the control feedback might require a torque sensor, which is always noisy [56]. Vallery et al. [126, 127] described cascade control with three nested loops: the outer impedance loop for regulating the relationship between the interaction force and the reference trajectory, an inner torque control, and the innermost velocity loop. The passivity conditions for the rendering of a pure spring are derived, and the control gains are selected. In effect, the same structure for impedance control of SEA has been proposed in [107, 130]; see Figure 8.

Tagliamonte et al. [130] investigated the performance and stability conditions for three multilevel control loops: an outer impedance loop with a virtual spring-damper system, and an inner PI torque control generating a set-point reference for the innermost PI velocity loop. The authors proposed guidelines for tuning the controller gains and the possible ranges of virtual impedance parameters based on the passivity theory, generalizing the results of [126]. Zhao et al. [131] proposed a critically damped fourth-order system gain selection criterion for a cascaded SEA control structure with inner torque and outer impedance feedback loops. Velocity filtering and feedback delays are taken into consideration for stability and impedance performance analysis. The proposed scheme is depicted in Figure 9. The authors focused on maximizing the impedance range of SEA because most studies are concerned with low or near-zero impedance dynamics [132, 133]. The authors show that decreasing the impedance gain may lead to instability problems. This is also confirmed in the literature [128]. However, there is no clear result regarding the increase of the inner torque loop gain and its effect on the system stability [134–136].

Mosadeghzad et al. [56] investigated the passivity and implementation problems associated with different control loops (inner position control, inner torque control, and inner velocity control). The authors made important observations as follows.

(i) The discrete impedance control system may require the lower bounds for the bandwidth of the inner control loop; however, in a continuous time control system, larger values for the inner loop gains can be obtained to ensure the stability and achieve high overall bandwidth

(ii) With the inner torque control loop, the model of the host robot should be known to avoid instability. However, using only an inner torque loop, the system can drift and this is because torque control only stabilizes the torque response of the system but does not provide internal stability. This can be overcome by setting an outer loop with PD control, a zero reference position, and velocity and even setting the P gain to zero but using a nonzero D gain to avoid drift. This still does not control position but avoids drift in the system. The use of an inner position control avoids these problems, but if a controller with integral action is used, then passivity is greatly impaired and there might be interactions with passive environments that cause instability

Li et al. [137, 138] proposed an adaptive MIMO human-robot interaction control for a SEA-actuated robot. An adaptive single controller was proposed to deal with the two motion modes associated with the human-robot interaction: robot-in-charge mode and human-in-charge mode. It is a two-level control architecture: high-level control for designing force region function-based virtually desired joint references and low-level control for tracking control of the desired references for the SEA considering the uncertainty of the system. (The force region function is used to monitor the variation of the interaction force, and hence, based on it, a weight factor is designed. The adjustment of the target impedance can be achieved by manipulating the weight factor.)

In view of the above statement, the following points can be noted:

(i) The control architecture of the SEA can consist of three nested control loops: an innermost velocity loop, an intermediate torque loop, and the outer impedance control loop that renders virtual impedance for safe and comfortable human-robot interactions: see [107, 126, 127, 130, 134]. However, many control schemes do not use the innermost velocity loop [139–145]. In addition, a nested loop using acceleration feedback has been proposed showing excellent results in terms of both performance and stability [105, 146]

(ii) A powerful tool for tuning the gains of cascade control of the SEA and determining the ranges of the virtual impedance target is the passivity theory. Most work has focused on stability/passivity constraints of cascade control for single SEA-actuated joints using linear control theory. Extending the work for MIMO robots considering the nonlinearities, time delay problems, and stability problems associated with the coupling nested loops is not straightforward; see [138] for example. In addition, the control algorithms that regard arbitrary stiffness joint can be exploited for motion stabilization of a SEA-actuated robot

(iii) For pure virtual spring impedance target, the maximum value of the virtual spring impedance can overcome the physical stiffness while retaining passivity [128]

Remark 3.

(1) Most of the standard control schemes of soft robots such as high-gain robust/adaptive control, feedback linearization, and active impedance control attempt to regulate/control the target system at the expense of stiffening it. Therefore, Santina et al. [147] showed that using a feedforward control loop combined with a low-gain feedback gain can achieve better-desired behavior comparing with feedback control schemes

(2) The constant impedance actuators described above may have limitations associated with dealing with the different tasks and motion frequencies; the different tasks need variable stiffness (impedance) actions that could be lost in the SEAs. Therefore, robotic systems with VSAs are capable of rejecting disturbances, storing energy, and controlling the end effector stiffness in contact space [41]; see [20–22, 148] for details on the design, performance, and classification of VSAs

(3) In general, there are three control schemes of VSAs: (i) simultaneous control of position and stiffness control [149], (ii) impedance control with inner torque control [150, 151], and (iii) bioinspired control, e.g., time-based compliance control [152] and coactivation control [153–155]

(4) The proposed control schemes, the performance, and stability have not yet been extensively investigated. The stability of impedance control associated with VSAs requires more research. However, impedance control associated with inner torque control is the easiest control scheme to deal with constant and VSAs. For more details on the control architecture and stability of VSAs, see [149–151, 156–169]

6. Conclusions

This paper is aimed at systematically introducing the features and limitations of the categories of impedance control schemes. Basically, impedance control can be classified as force-based impedance control and position-based impedance control. The conventional impedance control schemes do not consider the force tracking problems in the outer impedance filter, resulting in a deviation of the desired force references. Accordingly, modification of the impedance filter to satisfy the force-tracking problem is a motivating technique of imitation of human behavior. As mentioned, one strategy for force tracking-based impedance control is to change the virtual stiffness. Therefore, a clear connection is required between variable impedance control and force tracking-based impedance control. On the other hand, changing the impedance parameters is not trivial; investigation of the stability problems of variable impedance control requires additional work.

Impedance control of flexible-joint actuated robots remains a challenge. Control of robots with constant impedance joints could be easier than variable impedance joints. In variable impedance actuators, the stiffness is an added variable output that should carefully be controlled. In general, an outer impedance filter integrated with torque control is an effective strategy to solve this category of transmission. In general, a careful control architecture is required to exploit joint flexibility. For example, using the standard feedback control schemes may make the system stiffer, and hence, the system behavior changes. Therefore, bioinspired-based control systems such as feedforward action can work well to exploit the system impedance.

Conflicts of Interest

The authors declare that they have no conflict of interest.

Acknowledgments

This work was funded by the Key Project of the National Natural Science Foundation of China under award no. 61233014, by the National Natural Science Foundation of China Project under award no. U150920072, by the Science and Technology Innovation Major Project of Shandong Province, China, under award no. 2017CXGC0903, and by the Key Research and Development Project of Shandong Province under award no. 2016ZDJS02A07.

References

[1] T. Yoshikawa, *Foundations of Robotics: Analysis and Control*, MIT Press, 2003.

[2] L. Villani, "Force control in robotics," in *Encyclopedia of Systems and Control*, J. Baillieul and T. Samad, Eds., Springer-Verlag, London, 2015.

[3] H. F. N. Al-Shuka, "Adaptive hybrid regressor and approximation control of robotic manipulators in constrained space," *International Journal of Mechanical & Mechatronics Engineering, IJMME-IJENS*, vol. 17, no. 3, pp. 11–19, 2017.

[4] M. H. Raibert and J. J. Craig, "Hybrid position/force control of manipulators," *ASME, Journal of Dynamic Systems, Measurement, and Control*, vol. 102, pp. 126–133, 1981.

[5] N. Hogan, "Impedance control: an approach to manipulation: part I—theory," *Journal of Dynamic Systems, Measurement, and Control*, vol. 107, no. 1, pp. 1–7, 1985.

[6] N. Hogan, "Impedance control: an approach to manipulation: part II—implementation," *Journal of Dynamic Systems, Measurement, and Control*, vol. 107, no. 1, pp. 8–16, 1985.

[7] D. A. Lawrence, "Impedance control stability properties in common implementations," in *Proceedings. 1988 IEEE International Conference on Robotics and Automation*, vol. 2, pp. 1185–1190, Philadelphia, PA, USA, April 1988.

[8] R. Anderson and M. Spong, "Hybrid impedance control of robotic manipulators," in *Proceedings. 1987 IEEE International Conference on Robotics and Automation*, vol. 4, pp. 1073–1080, Raleigh, NC, USA, April 1987.

[9] G. Liu and A. A. Goldenberg, "Robust hybrid impedance control of robot manipulators via a tracking control method," in *Proceedings of IEEE/RSJ International Conference on Intelligent Robots and Systems (IROS'94)*, vol. 3, pp. 1594–1601, Munich, Germany, September 1994.

[10] W.-H. Zhu, J. De Schutter, and Y. Zou, "Experimental verifications of virtual-decomposition-based motion/force control," *IEEE Transactions on Robotics and Automation*, vol. 18, no. 3, pp. 379–386, 2002.

[11] H. Wang, K. H. Low, and M. Y. Wang, "Reference trajectory generation for force tracking impedance control by using neural network-based environment estimation," in *2006 IEEE Conference on Robotics, Automation and Mechatronics*, pp. 1–6, Bangkok, Thailand, June 2006.

[12] W. Xu, "Robotic Time-Varying Force Tracking in Position-Based Impedance Control," *Journal of Dynamic Systems, Measurement, and Control*, vol. 138, no. 9, article 091008, 2016.

[13] L. Roveda, F. Vicentine, N. Pedrocchi, and L. M. Tosatti, "Impedance control based force-tracking algorithm for interaction robotics tasks: an analytically force overshoots-free approach," in *2015 12th International Conference on Informatics in Control, Automation and Robotics (ICINCO)*, vol. 2, pp. 386–391, Colmar, France, July 2015.

[14] L. Roveda, N. Iannacci, F. Vicentini, N. Pedrocchi, F. Braghin, and L. M. Tosatti, "Optimal impedance force-tracking control design with impact formulation for interaction tasks," *IEEE Robotics and Automation Letters*, vol. 1, no. 1, pp. 130–136, 2016.

[15] S. Jung and T. C. Hsia, "Force tracking impedance control of robot manipulators for environment with damping," in *IECON 2007 - 33rd Annual Conference of the IEEE Industrial Electronics Society*, pp. 2742–2747, Taipei, Taiwan, November 2007.

[16] S. Jung and T. C. Hsia, "Stability and convergence analysis of robust adaptive force tracking impedance control of robot manipulators," in *Proceedings 1999 IEEE/RSJ International Conference on Intelligent Robots and Systems. Human and Environment Friendly Robots with High Intelligence and Emotional Quotients (Cat. No.99CH36289)*, vol. 2, pp. 635–640, Kyongju, South Korea, October 1999.

[17] S. Jung and T. C. Hsia, "Reference compensation technique of neural force tracking impedance control for robot manipulators," in *2010 8th World Congress on Intelligent Control and Automation*, pp. 650–655, Jinan, China, July 2010.

[18] B. Komati, C. Clevy, and P. Lutz, "Force tracking impedance control with unknown environment at the microscale," in *2014 IEEE International Conference on Robotics and Automation (ICRA)*, pp. 5203–5208, Hong Kong, China, May-June 2014.

[19] K. Kronander and A. Billard, "Stability considerations for variable impedance control," *IEEE Transactions on Robotics*, vol. 32, no. 5, pp. 1298–1305, 2016.

[20] F. P. Petit, "Analysis and control of variable stiffness robots," PhD Dissertation, Sciences of ETH Zurich, 2014.

[21] B. Vanderborght, A. Albu-Schaeffer, A. Bicchi et al., "Variable impedance actuators: a review," *Robotics and Autonomous Systems*, vol. 61, no. 12, pp. 1601–1614, 2013.

[22] R. van Ham, T. G. Sugar, B. Vanderborght, K. W. Hollander, and D. Lefeber, "Compliant actuator designs," *IEEE Robotics & Automation Magazine*, vol. 16, no. 3, pp. 81–94, 2009.

[23] M. Vukobratovic, D. Surdilovic, Y. Ekalo, and D. Katic, *Dynamics and Robust Control of Robot-Environment Interaction*, World Scientific Publishing Company, 1 edition, 2009.

[24] L. Villani and J. De Schutter, "Force control," in *Springer Handbook of Robotics*, B. Siciliano and O. Khatib, Eds., pp. 161–185, Springer, Berlin, Heidelberg, 2008.

[25] J. K. Salisbury, "Active stiffness control of a manipulator in Cartesian coordinates," in *1980 19th IEEE Conference on Decision and Control including the Symposium on Adaptive Processes*, pp. 95–100, Albuquerque, NM, USA, December 1980.

[26] D. E. Whitney, "Force feedback control of manipulator fine motions," *Journal of Dynamic Systems, Measurement, and Control*, vol. 99, no. 2, pp. 91–97, 1977.

[27] O. Khatib, "A unified approach for motion and force control of robot manipulators: the operational space formulation," *IEEE Journal on Robotics and Automation*, vol. 3, no. 1, pp. 43–53, 1987.

[28] M. Ali, "Impedance control of redundant manipulators," PhD Dissertation, Tampere University of Technology, Finland, 2011.

[29] C. Ott, *Cartesian Impedance Control of Redundant and Flexible-Joint Robots*, Springer Tracts in Advanced Robotics, Springer-verlag, 2008.

[30] A. Dietrich, *Whole-Body Impedance Control of Wheeled Humanoid Robots*, Springer Tracts in Advanced Robotics, Springer-verlag, 2016.

[31] A.-C. Huang and M.-C. Chien, *Adaptive Control of Robot Manipulators: A unified regressor-free approach*, World Scientific Publishing Company, 2010.

[32] Y. Oh, W. K. Chung, Y. Youm, and M. Kim, "Hybrid impedance control of redundant manipulators: an approach to decouple task space and null space motions," *Intelligent Automation & Soft Computing*, vol. 5, no. 2, pp. 149–164, 1999.

[33] O. Khatib, "Motion/force redundancy of manipulators," in *JAPAN-USA. Symposium on flexible automation-A Pacific Rim Conference-ISCIE*, pp. 337–342, Kyoto, Japan, 1990.

[34] O. Khatib, "Inertial properties in robotic manipulation: an object-level framework," *The International Journal of Robotics Research*, vol. 14, no. 1, pp. 19–36, 1995.

[35] C. Pholsiri, D. Rabindran, M. Pryor, and C. Kapoor, "Extended generalized impedance control for redundant manipulators," in *42nd IEEE International Conference on Decision and Control (IEEE Cat. No.03CH37475)*, vol. 4, pp. 3331–3336, Maui, HI, USA, December 2003.

[36] C. Ott, A. Dietrich, and A. Albu-Schäffer, "Prioritized multi-task compliance control of redundant manipulators," *Automatica*, vol. 53, pp. 416–423, 2015.

[37] N. Oda, H. Ohta, T. Murakami, and K. Ohnishi, "A robust impedance control strategy for redundant manipulator," in *Proceedings of IECON '95 - 21st Annual Conference on IEEE Industrial Electronics*, vol. 2, pp. 1254–1259, Orlando, FL, USA, November 1995.

[38] M. Mistry and L. Righetti, "Operational space control of constrained and underactuated systems," in *Proceedings of Robotics: Science and Systems*, H. Durrant-Whyte, N. Roy, and P. Abbeel, Eds., MIT Press, 2011.

[39] W. Shang, S. Cong, and Y. Ge, "Coordination motion control in the task space for parallel manipulators with actuation redundancy," *IEEE Transactions on Automation Science and Engineering*, vol. 10, no. 3, pp. 665–673, 2013.

[40] W.-H. Zhu, *Virtual Decomposition Control: Toward Hyper Degrees of Freedom Robots*, Springer Tracts in Advanced Robotics, Springer-verlag, 2010.

[41] C. M. Best, "Position and stiffness control of inflatable robotic links using rotary pneumatic actuation," MSc dissertation, Brigham Young University, USA, 2016.

[42] T. Boaventura, J. Buchli, C. Semini, and D. G. Caldwell, "Model-based hydraulic impedance control for dynamic robots," *IEEE Transactions on Robotics*, vol. 31, no. 6, pp. 1324–1336, 2015.

[43] F. Ferraguti, C. Secchi, and C. Fantuzzi, "A tank-based approach to impedance control with variable stiffness," in *2013 IEEE International Conference on Robotics and Automation*, pp. 4948–4953, Karlsruhe, Germany, May 2013.

[44] C. Chen, H. Nie, J. Chen, and X. Wang, "A velocity-based impedance control system for a low impact docking mechanism (LIDM)," *Sensors*, vol. 14, no. 12, pp. 22998–23016, 2014.

[45] H. Seraji and R. Colbaugh, "Force tracking in impedance control," in *[1993] Proceedings IEEE International Conference on Robotics and Automation*, vol. 2, pp. 499–506, Atlanta, GA, USA, May 1993.

[46] A. M. Khan, D.-W. Won, M. A. Ali, J. Han, K. Shan, and C. Han, "Adaptive impedance control for upper limb assist exoskeleton," in *2015 IEEE International Conference on Robotics and Automation (ICRA)*, pp. 4359–4366, Seattle, WA, USA, May 2015.

[47] B. Siciliano and L. Villani, *Robot Force Control*, Springer Science+Business Media LLC, New York, 1999.

[48] C. Ott, R. Mukherjee, and Y. Nakamura, "A hybrid system framework for unified impedance and admittance control," *Journal of Intelligent & Robotic Systems*, vol. 78, no. 3-4, pp. 359–375, 2015.

[49] Z. M. Sotirov and R. G. Botev, "A model reference approach to adaptive impedance control of robot manipulators," in *Proceedings of 1993 IEEE/RSJ International Conference on Intelligent Robots and Systems (IROS '93)*, vol. 2, pp. 727–733, Yokohama, Japan, July 1993.

[50] M. Sharifi, S. Behzadipour, and G. Vossoughi, "Nonlinear model reference adaptive impedance control for human–robot interactions," *Control Engineering Practice*, vol. 32, pp. 9–27, 2014.

[51] R. Kamnik, D. Matko, and T. Bajd, "Application of model reference adaptive control to industrial robot impedance control," *Journal of Intelligent and Robotic Systems*, vol. 22, no. 2, pp. 153–163, 1998.

[52] R. Colbaugh and K. Glass, "Adaptive compliant motion control of manipulators without velocity measurements," *Journal of Robotic Systems*, vol. 14, no. 7, pp. 513–527, 1997.

[53] W.-S. Lu and Q.-H. Meng, "Impedance control with adaptation for robotic manipulations," *IEEE Transactions on Robotics and Automation*, vol. 7, no. 3, pp. 408–415, 1991.

[54] B. Alqaudi, H. Modares, I. Ranatunga, S. M. Tousif, F. L. Lewis, and D. O. Popa, "Model reference adaptive impedance control for physical human-robot interaction," *Control Theory and Technology*, vol. 14, no. 1, pp. 68–82, 2016.

[55] R. Kelly, R. Carelli, M. Amestegui, and R. Ortega, "On adaptive impedance control of robot manipulators," in *Proceedings, 1989 International Conference on Robotics and Automation*, vol. 1, pp. 572–577, Scottsdale, AZ, USA, May 1989.

[56] M. Mosadeghzad, G. A. Medrano-Cerda, J. A. Saglia, N. G. Tsagarakis, and D. G. Caldwell, "Comparison of various active impedance control approaches, modeling, implementation, passivity, stability and trade-offs," in *2012 IEEE/ASME International Conference on Advanced Intelligent Mechatronics (AIM)*, pp. 342–348, Kachsiung, Taiwan, July 2012.

[57] W.-H. Zhu and J. De Schutter, "Adaptive control of mixed rigid/flexible joint robot manipulators based on virtual decomposition," *IEEE Transactions on Robotics and Automation*, vol. 15, no. 2, pp. 310–317, 1999.

[58] J. M. Tao, J. Y. S. Luh, and Y. F. Zheng, "Compliant coordination control of two moving industrial robots," *IEEE Transactions on Robotics and Automation*, vol. 6, no. 3, pp. 322–330, 1990.

[59] W.-H. Zhu, Z. Bien, and J. De Schutter, "Adaptive motion/force control of multiple manipulators with joint flexibility based on virtual decomposition," *IEEE Transactions on Automatic Control*, vol. 43, no. 1, pp. 46–60, 1998.

[60] V. Duchaine and C. M. Gosselin, "General model of human-robot cooperation using a novel velocity based variable impedance control," in *Second Joint EuroHaptics Conference and Symposium on Haptic Interfaces for Virtual Environment and Teleoperator Systems (WHC'07)*, pp. 146–451, Tsukaba, Japan, March 2007.

[61] A. Calanca, R. Muradore, and P. Fiorini, "A review of algorithms for compliant control of stiff and fixed-compliance robots," *IEEE/ASME Transactions on Mechatronics*, vol. 21, no. 2, pp. 613–624, 2016.

[62] K. Lee and M. Buss, "Force tracking impedance control with variable target stiffness," *IFAC Proceedings Volumes*, vol. 41, no. 2, pp. 6751–6756, 2008.

[63] W. Xu, C. Cai, and Y. Zou, "Neural-network-based robot time-varying force control with uncertain manipulator–environment system," *Transactions of the Institute of Measurement and Control*, vol. 36, no. 8, pp. 999–1009, 2014.

[64] H. Huang, D. Sun, J. K. Mills, and S. H. Cheng, "Integrated vision and force control in suspended cell injection system: Towards automatic batch biomanipulation," in *2008 IEEE International Conference on Robotics and Automation*, pp. 3413–3418, Pasadena, CA, USA, May 2008.

[65] C. T. Freeman, E. Rogers, A.-M. Hughes, J. H. Burridge, and K. L. Meadmore, "A force control approach to a robot-assisted cell microinjection system," *The International Journal of Robotics Research*, vol. 29, no. 9, pp. 1222–1232, 2010.

[66] Y. Xie, D. Sun, C. Liu, H. Y. Tse, and S. H. Cheng, "Iterative learning control in health care: electrical stimulation and robotic-assisted upper-limb stroke rehabilitation," *IEEE Control Systems Magazine*, vol. 32, no. 1, pp. 18–43, 2012.

[67] B. Várkuti, C. Guan, Y. Pan et al., "Resting state changes in functional connectivity correlate with movement recovery for BCI and robot-assisted upper-extremity training after stroke," *Neurorehabilitation and Neural Repair*, vol. 27, no. 1, pp. 53–62, 2012.

[68] W. Xu, C. Cai, M. Yin, and Y. Zou, "Time-varying force tracking in impedance control," in *2012 IEEE 51st IEEE Conference on Decision and Control (CDC)*, pp. 344–349, Maui, HI, USA, December 2012.

[69] T. Kim, H. S. Kim, and J. Kim, "Position-based impedance control for force tracking of a wall-cleaning unit," *International Journal of Precision Engineering and Manufacturing*, vol. 17, no. 3, pp. 323–329, 2016.

[70] H. Seraji, "Adaptive admittance control: an approach to explicit force control in compliant motion," in *Proceedings of the 1994 IEEE International Conference on Robotics and Automation*, vol. 4, pp. 2705–2712, San Diego, CA, USA, May 1994.

[71] R. A. Volpe, "Real and artificial forces in the control of manipulators: theory and experiments," PhD dissertation, Carnegie Mellon University, USA, 1990.

[72] O. Khatib and J. Burdick, "Motion and force control of robot manipulators," in *Proceedings. 1986 IEEE International Conference on Robotics and Automation*, pp. 1381–1386, San Francisco, CA, USA, April 1986.

[73] F. Ficuciello, L. Villani, and B. Siciliano, "Variable impedance control of redundant manipulators for intuitive human–robot physical interaction," *IEEE Transactions on Robotics*, vol. 31, no. 4, pp. 850–863, 2015.

[74] M. N. Oğuztöreli and R. B. Stein, "The effect of variable mechanical impedance on the control of antagonistic muscles," *Biological Cybernetics*, vol. 66, no. 2, pp. 87–93, 1991.

[75] W. A. Farahat and H. M. Herr, "Optimal workloop energetics of muscle-actuated systems: an impedance matching view," *PLoS Computational Biology*, vol. 6, no. 6, article e1000795, 2010.

[76] Z. Li, Z. Huang, W. He, and C.-Y. Su, "Adaptive impedance control for an upper limb robotic exoskeleton using biological signals," *IEEE Transactions on Industrial Electronics*, vol. 64, no. 2, pp. 1664–1674, 2017.

[77] H. Tomori, S. Nagai, T. Majima, and T. Nakamura, "Variable impedance control with an artificial muscle manipulator using instantaneous force and MR brake," in *2013 IEEE/RSJ International Conference on Intelligent Robots and Systems*, pp. 5396–5403, Tokyo, Japan, November 2013.

[78] D. Heck, D. Kostić, A. Denasi, and H. Nijmeijer, "Internal and external force-based impedance control for cooperative manipulation," in *2013 European Control Conference (ECC)*, pp. 2299–2304, Zurich, Switzerland, July 2013.

[79] J. H. Park and H. C. Cho, "Impedance control with varying stiffness for parallel-link manipulators," in *Proceedings of the 1998 American Control Conference. ACC (IEEE Cat. No.98CH36207)*, vol. 1, pp. 478–482, Philadelphia, PA, USA, June 1998.

[80] T. Tsumugiwa, R. Yokogawa, and K. Hara, "Variable impedance control based on estimation of human arm stiffness for human-robot cooperative calligraphic task," in *Proceedings 2002 IEEE International Conference on Robotics and Automation (Cat. No.02CH37292)*, vol. 1, pp. 644–650, Washington, DC, USA, May 2002.

[81] T. S. Tadele, "Human-friendly robotic manipulators: safety and performance issues in controller design," PhD Dissertation, University of Twente, 2014.

[82] F. Ferraguti, N. Preda, A. Manurung et al., "An energy tank-based interactive control architecture for autonomous and teleoperated robotic surgery," *IEEE Transactions on Robotics*, vol. 31, no. 5, pp. 1073–1088, 2015.

[83] A. Y. Mersha, S. Stramigioli, and R. Carloni, "Variable impedance control for aerial interaction," in *2014 IEEE/RSJ International Conference on Intelligent Robots and Systems*, pp. 3435–3440, Chicago, IL, USA, September 2014.

[84] B. Yuan, M. Sekine, J. Gonzalez, J. Gomez Tames, and W. Yu, "Variable impedance control based on impedance estimation model with EMG signals during extension and flexion tasks for a lower limb rehabilitation robotic system," *Journal of Novel Physiotherapies*, vol. 3, no. 5, p. 178, 2013.

[85] B. Berret, G. Sandini, and F. Nori, "Design principles for muscle-like variable impedance actuators with noise rejection property via co-contraction," in *2012 12th IEEE-RAS International Conference on Humanoid Robots (Humanoids 2012)*, pp. 222–227, Osaka, Japan, November-December 2012.

[86] R. Schiavi, G. Grioli, S. Sen, and A. Bicchi, "VSA-II: a novel prototype of variable stiffness actuator for safe and performing robots interacting with humans," in *2008 IEEE*

International Conference on Robotics and Automation, pp. 2171–2176, Pasadena, CA, USA, May 2008.

[87] A. Jafari, N. G. Tsagarakis, B. Vanderborght, and D. G. Caldwell, "A novel actuator with adjustable stiffness (AwAS)," in *2010 IEEE/RSJ International Conference on Intelligent Robots and Systems*, pp. 4201–4206, Taipei, Taiwan, October 2010.

[88] S. Wolf and G. Hirzinger, "A new variable stiffness design: matching requirements of the next robot generation," in *2008 IEEE International Conference on Robotics and Automation*, pp. 1741–1746, Pasadena, CA, USA, May 2008.

[89] E. Burdet, R. Osu, D. W. Franklin, T. E. Milner, and M. Kawato, "The central nervous system stabilizes unstable dynamics by learning optimal impedance," *Nature*, vol. 414, no. 6862, pp. 446–449, 2001.

[90] M. Howard, D. J. Braun, and S. Vijayakumar, "Transferring human impedance behavior to heterogeneous variable impedance actuators," *IEEE Transactions on Robotics*, vol. 29, no. 4, pp. 847–862, 2013.

[91] A. Ajoudani, N. Tsagarakis, and A. Bicchi, "Tele-impedance: teleoperation with impedance regulation using a body-machine interface," *International Journal of Robotics Research*, vol. 31, no. 13, pp. 1642–1656, 2012.

[92] B. Madonado, M. Mendoza, I. Bonilla, and I. Reyna-Gutiérrez, "Stiffness-based tuning of an adaptive impedance controller for robot-assisted rehabilitation of upper limbs," in *2015 37th Annual International Conference of the IEEE Engineering in Medicine and Biology Society (EMBC)*, pp. 3578–3581, Milan, Italy, August 2015.

[93] H. He, M. Luo, and Q. Zhang, "Dual impedance control with variable object stiffness for the dual-arm cooperative manipulators," in *2016 Asia-Pacific Conference on Intelligent Robot Systems (ACIRS)*, pp. 102–108, Tokyo, Japan, July 2016.

[94] R. J. Butler, H. P. Crowell III, and I. M. C. Davis, "Lower extremity stiffness: implications for performance and injury," *Clinical Biomechanics*, vol. 18, no. 6, pp. 511–517, 2003.

[95] S. Rapoport, J. Mizrahi, E. Kimmel, O. Verbitsky, and E. Isakov, "Constant and variable stiffness and damping of the leg joints in human hopping," *Journal of Biomechanical Engineering*, vol. 125, no. 4, pp. 507–514, 2003.

[96] M. Plocharski and P. Plocharski, "Ankle joint stiffness during phases of human walking," MSc dissertation, Department of Health Science & technology, Aalborg University, 2013.

[97] F. Ficuciello, L. Villani, and B. Siciliano, "Impedance control of redundant manipulators for safe human-robot collaboration," *Acta Polytechnica Hungarica*, vol. 13, no. 1, pp. 223–238, 2016.

[98] S. Song, W. Cai, and Y.-G. Wang, "Auto-tuning of cascade control systems," *ISA Transactions*, vol. 42, no. 1, pp. 63–72, 2003.

[99] T. Liu and F. Gao, "Chapter 9: cascade control. system," in *Industrial Process Identification and Control Design: Step-Test and Relay-Experiment-Based Methods*, Advances in industrial control, Springer-verlag, 2014.

[100] R. Ghorbani, "On controllable stiffness bipedal walking," PhD Dissertation, Department of Mechanical and Manufacturing Engineering, The University of Manitoba, Canada, 2008.

[101] K. Aström and T. Hagglund, *PID Controllers: Theory, Design, and Tuning*, ISA, 2nd edition, 1995.

[102] S. Skogestad and I. Postlethwaite, *Multivariable Feedback Control: Analysis and Design*, Wiley-Blackwell, 2nd edition, 2007.

[103] M. Zinn, B. Roth, O. Khatib, and J. K. Salisbury, "A new actuation approach for human friendly robot design," *The International Journal of Robotics Research*, vol. 23, no. 4-5, pp. 379–398, 2004.

[104] A. Bicchi, G. Tonietti, M. Bavaro, and M. Piccigallo, "Variable stiffness actuators for fast and safe motion control," in *Robotics Research. The Eleventh International Symposium*, P. Dario and R. Chatila, Eds., vol. 15 of Springer Tracts in Advanced Robotics, Springer, Berlin, Heidelberg, 2005.

[105] G. Pratt and M. Williamson, "Series elastic actuators," in *IEEE/RSJ International Conference on Intelligent Robots and Systems*, vol. 1, pp. 399–406, Pittsburgh, PA, USA, 1995.

[106] B.-S. Kim and J.-B. Song, "Object grasping using a 1 DoF variable stiffness gripper actuated by a hybrid variable stiffness actuator," in *2011 IEEE International Conference on Robotics and Automation*, pp. 4620–4625, Shanghai, China, May 2011.

[107] C. Lagoda, A. C. Schouten, A. H. A. Stienen, E. E. G. Hekman, and H. van der Kooij, "Design of an electric series elastic actuated joint for robotic gait rehabilitation training," in *2010 3rd IEEE RAS & EMBS International Conference on Biomedical Robotics and Biomechatronics*, pp. 21–26, Tokyo, Japan, September 2010.

[108] J. Pratt, B. Krupp, and C. Morse, "Series elastic actuators for high fidelity force control," *Industrial Robot: An International Journal*, vol. 29, no. 3, pp. 234–241, 2002.

[109] M. W. Spong, "Modeling and control of elastic joint robots," *Journal of Dynamic Systems, Measurement, and Control*, vol. 109, no. 4, pp. 310–318, 1987.

[110] M. M. Bridges, D. M. Dawson, Zhihua Qu, and S. C. Martindale, "Robust control of rigid-link flexible-joint robots with redundant joint actuators," *IEEE Transactions on Systems, Man, and Cybernetics*, vol. 24, no. 7, pp. 961–970, 1994.

[111] T. Lin and A. A. Goldenberg, "Robust adaptive control of flexible joint robots with joint torque feedback," in *Proceedings of 1995 IEEE International Conference on Robotics and Automation*, vol. 1, pp. 1229–1234, Nagoya, Japan, May 1995.

[112] T. Lin, "Adaptive and robust control of flexible joint robots with joint torque feedback," PhD Dissertation, Department of Electrical and Computer Engineering University of Toronto, Canada, 1995.

[113] M. C. Readman and P. R. Belanger, "Analysis and control of a flexible joint robot," in *29th IEEE Conference on Decision and Control*, vol. 4, pp. 2551–2559, Honolulu, HI, USA, December 1990.

[114] G. Ellis and Z. Gao, "Cures for low-frequency mechanical resonance in industrial servo systems," in *Conference Record of the 2001 IEEE Industry Applications Conference. 36th IAS Annual Meeting (Cat. No.01CH37248)*, vol. 1, pp. 252–258, Chicago, IL, USA, September-October 2001.

[115] R. M. Berger and H. A. ElMaraghy, "Feedback linearization control of flexible joint robots," *Robotics and Computer-Integrated Manufacturing*, vol. 9, no. 3, pp. 239–246, 1992.

[116] A. DeLuca and P. Lucibello, "A general algorithm for dynamic feedback linearization of robots with elastic joints, IEEE International Conference on Robotics and Automation, Leuven," *Belgium*, vol. 1, pp. 504–510, 1998.

[117] C.-M. Ou and J.-S. Lin, "Nonlinear adaptive backstepping control design of flexible-joint robotic manipulators," in *2011 8th Asian Control Conference (ASCC)*, pp. 1352–1357, Kaohsiung, Taiwan, May 2011.

[118] M. W. Spong, J. Y. Hung, S. A. Bortoff, and F. Ghorbel, "A comparison of feedback linearization and singular perturbation techniques for the control of flexible joint robots," in *1989 American Control Conference*, pp. 25–30, Pittsburgh, PA, USA, June 1989.

[119] M. W. Spong, "Adaptive control of flexible joint manipulators," *Systems & Control Letters*, vol. 13, no. 1, pp. 15–21, 1989.

[120] S. Nicosia and P. Tomei, "A method to design adaptive controllers for flexible joint robots," in *Proceedings 1992 IEEE International Conference on Robotics and Automation*, vol. 1, pp. 701–706, Nice, France, May 1992.

[121] C. Ott, A. Albu-Schäffer, and G. Hirzinger, "Comparison of adaptive and nonadaptive tracking control laws for a flexible joint manipulator," in *IEEE/RSJ International Conference on Intelligent Robots and Systems*, vol. 2, pp. 2018–2024, Lausanne, Switzerland, September-October 2002.

[122] J. Yuan and Y. Stepanenko, "Adaptive control of flexible joint robots with arbitrary stiffness," *IFAC Proceedings Volumes*, vol. 26, no. 2, Part 3, pp. 903–906, 1993.

[123] R. Lozano and B. Brogliato, "Adaptive control of robot manipulators with flexible joints," *IEEE Transactions on Automatic Control*, vol. 37, no. 2, pp. 174–181, 1992.

[124] B. Brogliato, R. Ortega, and R. Lozano, "Global tracking controllers for flexible-joint manipulators: a comparative study," *Automatica*, vol. 31, no. 7, pp. 941–956, 1995.

[125] A. Albu-Schäffer, C. Ott, and G. Hirzinger, "A unified passivity-based control framework for position, torque and impedance control of flexible joint robots," *The International Journal of Robotics Research*, vol. 26, no. 1, pp. 23–39, 2007.

[126] H. Vallery, R. Ekkelenkamp, H. van der Kooij, and M. Buss, "Passive and accurate torque control of series elastic actuators," in *2017 International Conference on Rehabilitation Robotics (ICORR)*, pp. 3534–3538, San Diego, CA, USA, October-November 2007.

[127] H. Vallery, J. Veneman, E. van Asseldonk, R. Ekkelenkamp, M. Buss, and H. van der Kooij, "Compliant actuation of rehabilitation robots," *IEEE Robotics & Automation Magazine*, vol. 15, no. 3, pp. 60–69, 2008.

[128] A. Calanca, R. Muradore, and P. Fiorini, "Impedance control of series elastic actuators: passivity and acceleration-based control," *Mechatronics*, vol. 47, pp. 37–48, 2017.

[129] G. A. Pratt, M. W. Williamson, P. Dillworth, J. Pratt, K. Ulland, and A. Wright, "Stiffness isn't everything," in *Proceedings of the Fourth International Symposium on Experimental Robotics (ISER '95)*, Stanford, California, 1995.

[130] N. L. Tagliamonte, D. Accoto, and E. Guglielmelli, "Rendering viscoelasticity with series elastic actuators using cascade control," in *2014 IEEE International Conference on Robotics and Automation (ICRA)*, pp. 2424–2429, Hong Kong, China, May-June 2014.

[131] Y. Zhao, N. Paine, and L. Sentis, "Feedback parameter selection for impedance control of series elastic actuators," in *2014 IEEE-RAS International Conference on Humanoid Robots*, pp. 999–1006, Madrid, Spain, November 2014.

[132] G. A. Pratt, P. Willisson, C. Bolton, and A. Hofman, "Late motor processing in low-impedance robots: impedance control of series-elastic actuators," in *Proceedings of the 2004 American Control Conference*, vol. 4, pp. 3245–3251, Boston, MA, USA, June-July 2004.

[133] K. Kong, J. Bae, and M. Tomizuka, "Control of rotary series elastic actuator for ideal force-mode actuation in human–robot interaction applications," *IEEE/ASME Transactions on Mechatronics*, vol. 14, no. 1, pp. 105–118, 2009.

[134] N. L. Tagliamonte and D. Accoto, "Passivity constraints for the impedance control of series elastic actuators," *Proceedings of the Institution of Mechanical Engineers, Part I: Journal of Systems and Control Engineering*, vol. 228, no. 3, pp. 138–153, 2013.

[135] T. Boaventura, G. Medrano-Cerda, C. Semini, J. Buchli, and D. Caldwell, "Stability and performance of the compliance controller of the quadruped robot HYQ," in *2013 IEEE/RSJ International Conference on Intelligent Robots and Systems*, pp. 1458–1464, Tokyo, Japan, November 2013.

[136] A. Calanca and P. Fiorini, "Impedance control of series elastic actuators based on well-defined force dynamics," *Robotics and Autonomous Systems*, vol. 96, pp. 81–92, 2017.

[137] X. Li, Y. Pan, G. Chen, and H. Yu, "Multi-modal control scheme for rehabilitation robotic exoskeletons," *The International Journal of Robotics Research*, vol. 36, no. 5–7, pp. 759–777, 2017.

[138] X. Li, Y. Pan, G. Chen, and H. Yu, "Adaptive human–robot interaction control for robots driven by series elastic actuators," *IEEE Transactions on Robotics*, vol. 33, no. 1, pp. 169–182, 2017.

[139] M. Wang, L. Sun, W. Yin, S. Dong, and J. Liu, "A novel sliding mode control for series elastic actuator torque tracking with an extended disturbance observer," in *2015 IEEE International Conference on Robotics and Biomimetics (ROBIO)*, pp. 2407–2412, Zhuhai, China, December 2015.

[140] H. Yu, S. Huang, G. Chen, Y. Pan, and Z. Guo, "Human-robot interaction control of rehabilitation robots with series elastic actuators," *IEEE Transactions on Robotics*, vol. 31, no. 5, pp. 1089–1100, 2015.

[141] A. Calanca and P. Fiorini, "Human-adaptive control of series elastic actuators," *Robotica*, vol. 32, no. 8, pp. 1301–1316, 2014.

[142] A. Calanca and P. Fiorini, "Understanding environment-adaptive force control of series elastic actuators," *IEEE/ASME Transactions on Mechatronics*, vol. 23, no. 1, pp. 413–423, 2018.

[143] S. Oh and K. Kong, "High-precision robust force control of a series elastic actuator," *IEEE/ASME Transactions on Mechatronics*, vol. 22, no. 1, pp. 71–80, 2017.

[144] N. Paine, J. S. Mehling, J. Holley et al., "Actuator control for the NASA-JSC Valkyrie humanoid robot: a decoupled dynamics approach for torque control of series elastic robots," *Journal of Field Robotics*, vol. 32, no. 3, pp. 378–396, 2015.

[145] W. Roozing, J. Malzahn, D. G. Caldwell, and N. G. Tsagarakis, "Comparison of open-loop and closed-loop disturbance observers for series elastic actuators," in *2016 IEEE/RSJ International Conference on Intelligent Robots and Systems (IROS)*, pp. 3842–3847, Daejeon, South Korea, October 2016.

[146] A. Calanca and P. Fiorini, "A rationale for acceleration feedback in force control of series elastic actuators," *IEEE Transactions on Robotics*, vol. 34, no. 1, pp. 48–61, 2018.

[147] C. Della Santina, M. Bianchi, G. Grioli et al., "Controlling soft robots: balancing feedback and feedforward elements," *IEEE Robotics & Automation Magazine*, vol. 24, no. 3, pp. 75–83, 2017.

[148] F. Flacco, "Modeling and control of robots with compliant actuation," Dipartimento di Ingegneria Informatica, Automatica e Gestionale, SAPIENZA Universit'a di Roma, PhD Dissertation, 2012.

[149] A. Albu-Schäffer, S. Wolf, O. Eiberger, S. Haddadin, F. Petit, and M. Chalon, "Dynamic modelling and control of variable stiffness actuators," in *2010 IEEE International Conference on Robotics and Automation*, pp. 2155–2162, Anchorage, AK, USA, May 2010.

[150] T. Wimböck, C. Ott, A. Albu-Schäffer, A. Kugi, and G. Hirzinger, "Impedance control for variable stiffness mechanisms with nonlinear joint coupling," in *2008 IEEE/RSJ International Conference on Intelligent Robots and Systems*, pp. 3796–3803, Nice, France, September 2008.

[151] L. Liu, S. Leonhardt, and B. J. E. Misgeld, "Design and control of a mechanical rotary variable impedance actuator," *Mechatronics*, vol. 39, pp. 226–236, 2016.

[152] D. Formica, L. Zollo, and E. Guglielmelli, "Torque-dependent compliance control in the joint space for robot-mediated motor therapy," *Journal of Dynamic Systems, Measurement, and Control*, vol. 128, no. 1, pp. 152–185, 2006.

[153] L. Zollo, B. Siciliano, E. Guglielmelli, and P. Dario, "A bio-inspired approach for regulating visco-elastic properties of a robot arm," in *2003 IEEE International Conference on Robotics and Automation (Cat. No.03CH37422)*, vol. 3, pp. 3576–3581, Taipei, Taiwan, September 2003.

[154] L. Zollo, L. Dipietro, B. Siciliano, E. Guglielmelli, and P. Dario, "A bio-inspired approach for regulating and measuring visco-elastic properties of a robot arm," *Journal of Robotic Systems*, vol. 22, no. 8, pp. 397–419, 2005.

[155] H. Gomi and R. Osu, "Task-dependent viscoelasticity of human multijoint arm and its spatial characteristics for interaction with environments," *The Journal of Neuroscience*, vol. 18, no. 21, pp. 8965–8978, 1998.

[156] G. Tonietti, R. Schiavi, and A. Bicchi, "Design and control of a variable stiffness actuator for safe and fast physical human/robot interaction," in *Proceedings of the 2005 IEEE International Conference on Robotics and Automation*, pp. 526–531, Barcelona, Spain, April 2005.

[157] G. Palli, C. Melchiorri, T. Wimbock, M. Grebenstein, and G. Hirzinger, "Feedback linearization and simultaneous stiffness-position control of robots with antagonistic actuated joints," in *Proceedings 2007 IEEE International Conference on Robotics and Automation*, pp. 4367–4372, Roma, Italy, April 2007.

[158] J. Nakanishi, K. Rawlik, and S. Vijayakumar, "Stiffness and temporal optimization in periodic movements: an optimal control approach," in *2011 IEEE/RSJ International Conference on Intelligent Robots and Systems*, pp. 718–724, San Francisco, CA, USA, September 2011.

[159] I. Sardellitti, G. Medrano-Cerda, N. G. Tsagarakis, A. Jafari, and D. G. Caldwell, "A position and stiffness control strategy for variable stiffness actuators," in *2012 IEEE International Conference on Robotics and Automation*, pp. 2785–2791, Saint Paul, MN, USA, May 2012.

[160] G. Buondonno and A. De Luca, "Efficient computation of inverse dynamics and feedback linearization for VSA-based robots," *IEEE Robotics and Automation Letters*, vol. 1, no. 2, pp. 908–915, 2016.

[161] T. R. Kerkhof, "Control strategy for variable stiffness actuators in bilateral teleimpedance interaction tasks," EEMCS/Electrical Engineering, MSc Report, 2013.

[162] P. Erler, P. Beckerle, B. Strah, and S. Rinderknecht, "Experimental comparison of nonlinear motion control methods for a variable stiffness actuator," in *5th IEEE RAS/EMBS International Conference on Biomedical Robotics and Biomechatronics*, pp. 1045–1050, Sao Paulo, Brazil, August 2014.

[163] M. Lendermann, B. R. P. Singh, F. Stuhlenmiller, P. Beckerle, S. Rinderknecht, and P. V. Manivannan, "Comparison of passivity based impedance controllers without torque-feedback for variable stiffness actuators," in *2015 IEEE International Conference on Advanced Intelligent Mechatronics (AIM)*, pp. 1126–1131, Busan, South Korea, July 2015.

[164] F. Petit and A. Albu-Schäffer, "Cartesian impedance control for a variable stiffness robot arm," in *2011 IEEE/RSJ International Conference on Intelligent Robots and Systems*, pp. 4180–4186, San Francisco, CA, USA, September 2011.

[165] F. Flacco, A. De Luca, I. Sardellitti, and N. G. Tsagarakis, "On-line estimation of variable stiffness in flexible robot joints," *The International Journal of Robotics Research*, vol. 31, no. 13, pp. 1556–1577, 2012.

[166] A. Serio, G. Grioli, I. Sardellitti, N. G. Tsagarakis, and A. Bicchi, "A decoupled impedance observer for a variable stiffness robot," in *2011 IEEE International Conference on Robotics and Automation*, pp. 5548–5553, Shanghai, China, May 2011.

[167] T. Ménard, G. Grioli, and A. Bicchi, "A stiffness estimator for agonistic-antagonistic variable-stiffness-actuator devices," *IEEE Transactions on Robotics*, vol. 30, no. 5, pp. 1269–1278, 2014.

[168] N. Kashiri, G. A. Medrano-Cerda, N. G. Tsagarakis, M. Laffranchi, and D. Caldwell, "Damping control of variable damping compliant actuators," in *2015 IEEE International Conference on Robotics and Automation (ICRA)*, pp. 850–856, Seattle, WA, USA, May 2015.

[169] L. Visser, "Variable stiffness actuator: modeling, control, and application to compliant bipedal walking," PhD Dissertation, Universiteit Twente, The Netherlands, 2013.

Hindawi
Applied Bionics and Biomechanics
Volume 2018, Article ID 1391032, 6 pages
https://doi.org/10.1155/2018/1391032

Research Article

Real-Time Evaluation of the Signal Processing of sEMG Used in Limb Exoskeleton Rehabilitation System

Baofeng Gao,[1] Chao Wei,[1] Hongdao Ma,[1] Shu Yang,[1] Xu Ma,[2] and Songyuan Zhang[3]

[1]*Key Laboratory of Convergence Medical Engineering System and Healthcare Technology, The Ministry of Industry and Information Technology, School of Life Science, Beijing Institute of Technology, No. 5, Zhongguancun South Street, Haidian District, Beijing 100081, China*
[2]*Tianjin Key Laboratory for Control Theory & Applications in Complicated System, The School of Electrical and Electronics Engineering, Tianjin University of Technology, Tianjin, China*
[3]*State Key Laboratory of Robotics and System, Harbin Institute of Technology, Harbin, China*

Correspondence should be addressed to Baofeng Gao; gaobaofeng@bit.edu.cn, Xu Ma; maxu2015@aliyun.com, and Songyuan Zhang; zhangsy@hit.edu.cn

Received 3 May 2018; Accepted 31 July 2018; Published 14 October 2018

Academic Editor: Dongming Gan

As an important branch of medical robotics, a rehabilitation training robot for the hemiplegic upper limbs is a research hotspot of rehabilitation training. Based on the motion relearning program, rehabilitation technology, human anatomy, mechanics, computer science, robotics, and other fields of technology are covered. Based on an sEMG real-time training system for rehabilitation, the exoskeleton robot still has some problems that need to be solved in this field. Most of the existing rehabilitation exoskeleton robotic systems are heavy, and it is difficult to ensure the accuracy and real-time performance of sEMG signals. In this paper, we design a real-time training system for the upper limb exoskeleton robot based on the EMG signal. It has four main characteristics: light weight, portability, high precision, and low delay. This work includes the structure of the rehabilitation robotic system and the method of signal processing of the sEMG. An experiment on the accuracy and time delay of the sEMG signal processing has been done. In the experimental results, the recognition accuracy of the sEMG is 94%, and the average delay time is 300 ms, which meets the accuracy and real-time requirements.

1. Introduction

Stroke, also known as cerebrovascular accident (CVA), is a disease caused by acute cerebrovascular injury. Sequelae are often seen as loss of hemiplegia, facial paralysis, visual impairment, and language impairment. Hemiplegia is the most common symptom of a stroke [1]. According to the statistics of the Ministry of Health, cerebrovascular disease is the second cause of death in the population, and the surviving patients are left with various degrees of sequelae of hemiplegia, which brings a heavy burden to families and the society. Therefore, the treatment and rehabilitation of hemiplegic patients following cerebrovascular disease are particularly important and urgent, and the scholars in the related disciplines are also studying how to improve the rehabilitation effect. The rehabilitation therapy for hemiplegia after stroke which is proved to be an effective method has become a focal point of modern rehabilitation medicine and rehabilitation projects.

Functional compensation and reorganization of the human cerebral cortex are of great importance in the treatment of hemiplegic patients. However, this functional reorganization is also influenced by external environmental stimuli [2]. Clinical practice shows that external functional recovery can play an important role in all stages of neurological impairment. Through continuous movement and relearning, the plasticity of the nervous system has been strengthened and consolidated. Exercise relearning is a popular method in hemiplegic rehabilitation [3]. This method is based on neurophysiology, sports science, biomechanics, and behavioral science. It emphasizes the importance of the subjective participation and cognition of the patients. It also regards the recovery training of the motor function after the central nervous system injury as a process of exercise relearning. Thus, the rehabilitation therapy for hemiplegia after stroke which is proved to be an effective method has become a focal point of modern rehabilitation medicine and rehabilitation projects [4].

The development of an upper limb rehabilitation training robot started earlier, and its development in western countries has relatively matured. In 1991, researchers from MIT in the United States developed the world's first upper limb rehabilitation training robotic system, called MIT-MANUS. The robot adopted a connecting rod mechanism, through a handle at the end of the patient's hand. It can complete the motion in a two-dimensional plane, and the robot is connected to a computer. It can provide real-time visual feedback for the patient. In the process of sports training, parameters are collected and evaluated according to the parameter and evaluation system. In 2005, researchers at the University of Zurich developed a rehabilitation robot called ARMin, which has the characteristics of low inertia, low friction, and directional driving. It has four kinds of moving patterns, mainly in the four modes of rehabilitation training for patients. In the course of training, it can record the basic information of its movement track and then evaluate the whole training [5–8].

In the field of sEMG signal processing, the researchers have also made a lot of achievement. A. M. Simon and other scholars have identified more than ten kinds of action types of the upper limb and wrist. In this method, they select four time domain features to construct the feature space and use the LDA (linear discriminant analysis) method to identify the moving pattern, a method which finally achieved an accuracy of 86%–96%. In addition, in view of the nonstationarity of the sEMG signals, the scientific research team of Kazakhstan extracted the AR model parameters of an EMG signal to construct the feature space, then they used the method of principal component analysis (PCA) to reduce the dimension of the feature space, and lastly, they used the Back Propagation Neural Networks (BPNN) as the classification method [9, 10].

From the existing studies, we can see that the research trend for an upper limb exoskeleton robot is to make it portable, lightweight, and intelligentized. In this paper, we developed a system for an upper limb exoskeleton rehabilitation robot with 3 DOFs and where the control of robot motion is based on pattern recognition of the sEMG. In the signal processing of the sEMG, we extract the characteristics of the time and frequency signal to construct the feature space, and use random forest as the classifier for pattern recognition. In the final system test, we tested the classification accuracy of this classification result.

In this paper, some domestic and foreign researches about upper limb rehabilitation robots are introduced. Then, an upper limb exoskeleton rehabilitation robotic system is presented, and the experiments are carried out for the accuracy of its pattern recognition based on sEMG. The results are then discussed.

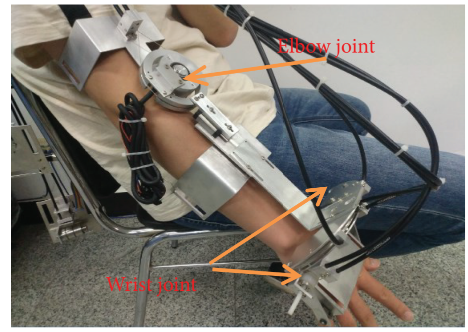

Figure 1: The structure of the upper limb exoskeleton.

2. System Structure Design

2.1. Upper Limb Exoskeleton Design. Three key requirements should be considered. First of all, in order for patients to wear it, it should be flexible and light weight, and it should have high accuracy. Secondly, it should have the ability to apply enough power for combinatorial actions of the patients. Thirdly, the movement space must conform to the physiological structure [11].

To achieve the goal of our design, the device should provide enough torque to train the upper limb. The actuator should have high power to drive the device and move the upper limbs. The material of the device should have high strength to prevent the device from performing poorly in sports.

For most patients, the length or width of the upper limb has many dimensions and should be carefully considered. Therefore, when we design flexible, wearable, and adjustable concepts for most patients, the adjustable design is much better.

In addition, combined exercise is more beneficial to the rehabilitation process of patients'. Our devices should be free to carry out combined movements without interference. We designed a rehabilitation robot with three DOFs. Compared to the previous device, this design can overcome some shortcomings which makes it flexible, portable, light weight, highly accurate, and easy to wear [12].

The robot is shown in Figure 1. It has the following characteristics:

(1) The stability of the wear. The upper limb rehabilitation robot has fixed grooves on the upper back, forearm, and upper arm of the human body, respectively, and is fixed with bandages in these places. These fixed places can guarantee the normal movement of 3 degrees of freedom.

(2) Low weight. The common exoskeleton device is to put the motor on the axis of the arm movement, but the robot uses a rope driven method to remove the motor from the exoskeleton robot, greatly reducing its weight and reducing the burden of the patient [12].

(3) Taking into account the size and range of motion of each person's upper limbs, many adaptive passive

Table 1: Range of three degrees of freedom.

3 DOFs of a joint	Elbow joint Flexion/ extension	Wrist joint Flexion/ extension	Pronation/ supination
Limit angle	0°–150°	0°–150°	−90°–90°
Motion range	0°–120°	0°–120°	−60°–90°

adjustment devices have been added to the robot to adapt to its changes. This also improves the comfort of the patient.

This robot has 3 parts, one for elbow joint and two for the wrist. The elbow joint of the human body has only one DOF, flexion and extension. The wrist has three DOFs, but we only designed for two DOFs, namely flexion and extension, as well as pronation and supination. The range of each motion is shown in Table 1 [13, 14].

2.2. Collection and Processing of sEMG. The exoskeleton robotic system has real-time recognition of sEMG signals and signal processing; therefore, the acquisition device uses real-time acquisition of EMG chips. As shown in Figure 2. The sEMG acquisition instrument can collect the original myoelectric signal and rectify and integrate on the basis of the original electromyographic signal, which is carried out in the chip. The output of the chip can be a rectified integral sEMG signal, and the most original surface EMG signal can also be the output. When electromyography is used to collect myoelectric signals, the position of the electrode sticking is very important. The sEMG acquisition instrument has two channels, and each channel has 2 electrode posts that are attached at the middle and ends of the measured muscles, respectively. There is also a muscle free part attached to the electrode.

The collected signal is sent as output to the digital multimeter, and the digital multimeters function as an AD conversion device. Then, the signal collected by the digital multimeter is connected to the computer and sent as output to the computer under the pretext of USB. We then use Matlab software to process signals and pattern recognition.

3. System Evaluation

3.1. Experimental Design and Data Collection. In the evaluation of the robot, we collect and process the EMG signals to get information, and then we control the movement of the robot in real time. Therefore, the purpose of the experimental design is to evaluate real-time and accurate acquisition and processing of electromyographic signals in the robotic system. In this process, EMG signal feature extraction and classifier design are two core issues.

In this experiment, we have designed the action mode of a BFNND elbow with four action modes: 0 degrees, 30 degrees, 60 degrees, and 90 degrees. We then collected the electromyographic signals of these four angles. The surface electromyographic signals of biceps brachii and triceps brachii muscle were collected by using a dual channel

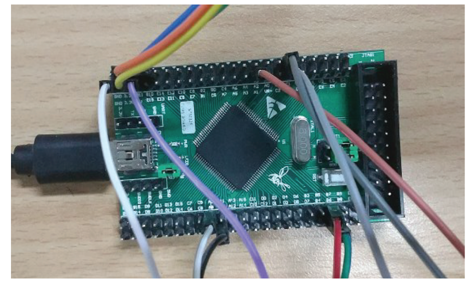

Figure 2: The sEMG acquisition instrument.

electromyographic acquisition device. 100 sets of data were collected and the duration of each group was 1 second. The frequency of EMG acquisition is 1000 Hz, so there are 1000 points in each group. In this way, 100 sets of dual channel data points were obtained.

Figure 3 shows the time domain information of 1 set of dual channel signals at the degree of 0. This is the original signal collected from the electromyographic acquisition instrument. After that, signal processing and pattern recognition will also be done.

3.2. Signal Preprocessing. According to the low frequency, weak, and nonlinear characteristics of the sEMG signal, we first carry on the band through an aluminum foil for the signal, and the bandpass bandwidth of the bandpass filter is 0–150 Hz. The following Butterworth amplitude square function is used:

$$|H(\omega)|^2 = \frac{1}{1+(\omega/\omega_c)^{2n}} = \frac{1}{1+\varepsilon^2(\omega/\omega_p)^{2n}}. \quad (1)$$

In (1), n is the order of the filter, and ω_c is the cutoff frequency; that is, the frequency of the amplitude falling to 3 dB. ω_p is the band edge frequency [15].

Then, we use the EEMD method to filter. EEMD is based on EMD, adding the white noise-aided analysis method. The EEMD method considers that the real signal and white noise superposition form the original signal. Each original signal can be obtained by means of EMD to get the IMF component. However, the IMF obtained by EMD alone still contains the effect of white noise. The IMF component directly obtained by the EMD method is a true signal.

$$x_i'(t) = \frac{1}{N}\sum_{j=1}^{N} x_{ij}(t). \quad (2)$$

In (2), x_{ij} is the original 1 IMF component with white noise, and N is the number of EMD execution times. The white noise per IMF is different, but when the number of EMD executions is sufficient, that is, when the number of IMF is enough, the average of all IMF will be considered to be close to the real result. With more and more tests, the additional noise is considered completely eliminated and only the signal is stable.

Figure 4 shows the filtered sEMG signal at a degree of 0. We can see that after the signal preprocessing, the high-

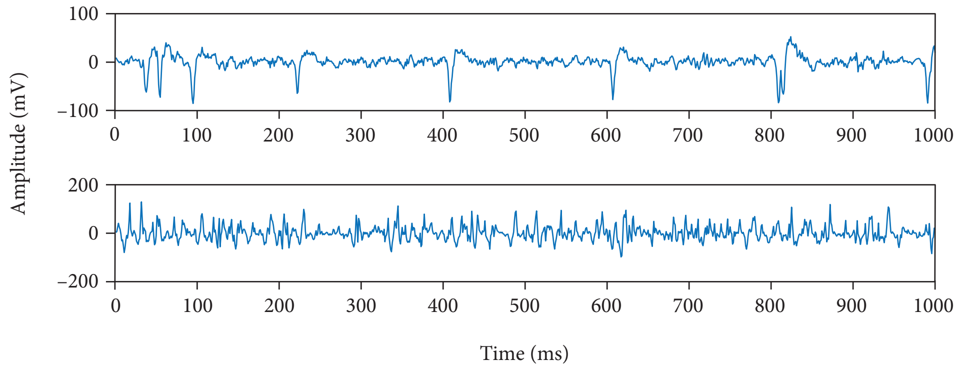

Figure 3: Time domain at a degree of 0.

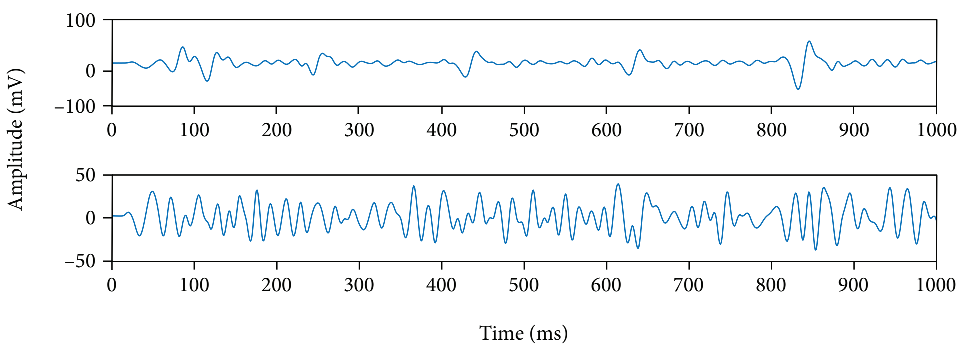

Figure 4: Filtered sEMG signal at a degree of 0.

frequency component of the sEMG signal is obviously less than the original signal, and the signal is smoother. This is because signal preprocessing has filtered out the high-frequency signal. In this experiment, four modes of electromyography are taken, respectively, but in this paper, only 0 degree signals are cited as examples. After signal preprocessing, feature extraction is needed [16].

3.3. Feature Extraction. Wavelet transform (WT) is derived from the localization of short-time Fourier transform, which improves the defect that the frequency cannot change in the transformation process and the size of the window is unchanged from the beginning to the end. It can make the time accuracy change with the frequency. It is an ideal tool for time frequency analysis and processing of the signal. Wavelet transform can highlight the characteristics of the problem, which greatly improves the precision of the frequency time analysis. With the expansion and translation operation wavelet function, the original signal is gradually refined; the time subdivision at high frequency and the frequency subdivision at low frequency are used to solve the problem of Fourier transform and become a new and useful transformation method for signal processing. Therefore, the wavelet energy feature is used as part of the feature space in the design.

Wavelet packet can be considered as a family of functions, where the signal is decomposed in the feature space at a finer level, and the corresponding frequency band is selected for the decomposed signal, which makes each decomposition signal match the original signal spectrum; that is, it has better analysis in time and frequency. Compared with wavelet transform, wavelet packet transform performs better in the decomposition of high frequency, and it is more accurate and does not lose the composition of the original signal. The decomposition diagram is shown in Table 2:

In this method, the highest level (zeroth layer) contains all the frequency band signals, the first layer has 21 nodes, the frequency segment is divided into 21 parts, the N layer is divided into $2N$ parts, and there are $2N$ nodes, with each node signal in this node signal band being a signal within the node. Each layer has the maximum amplitude of the node signal, which is the most effective signal in the same layer, which can be considered as representing the effectiveness of the signal on this layer to the maximum extent [17].

The method of wavelet analysis has opened up a new way for the weak signal detection technology, but the key to the feature extraction of the weak signal in the wavelet transform is to determine the threshold of the wavelet coefficients. On the basis of the soft threshold, the concept of wavelet, which reflects the energy distribution characteristic of the signal, has a different wavelet entropy on different decomposition scales, and the threshold of the high-frequency coefficient can be determined adaptively.

Wavelet entropy can accurately locate weak signals in a strong noise environment and achieve effective extraction of the energy's passing signals. Therefore, in the feature

Table 2: Wavelet packet multilayer decomposition.

U_0^0							
U_1^0						U_1^1	
U_2^0			U_2^1		U_2^2		U_2^3
U_3^0	U_3^1	U_3^2	U_3^3	U_3^4	U_3^5	U_3^6	U_3^7

space, wavelet entropy is selected as one of the characteristics. Finally, we get a multidimensional feature space.

Finally, the feature space is composed of wavelet energy features and wavelet entropy features.

3.4. Pattern Recognition. In the pattern recognition of electromyography, we have made some attempts to classify commonly used algorithms. Finally, through the analysis of results, the random forest can get a good classification effect in the classification algorithm. So in this experiment, the random forest classifier is used to classify. Here are some introductions to the random forest classifier.

In the method of RT, k samples are randomly selected from the original training sample set N to generate a new set of training samples, and then a random forest is formed by generating K classification trees based on the self-help sample set. The classification results of new data are determined by the number of votes cast by the classification tree. The essence is an improvement of the decision tree algorithm, which combines multiple decision trees together. The establishment of each tree depends on an independent sample. Each tree in the forest has the same distribution. The classification error depends on the classification ability of each tree and the correlation between them. Feature selection uses a stochastic method to separate each node, and then compares the errors produced in different situations. The inherent estimation error, classification ability, and correlation can be detected to determine the number of selection features. The classification ability of a single tree may be very small, but after a large number of decision trees are produced randomly, a test sample can choose the most likely classification by the statistics of each tree [18].

3.5. Classification Results. We completed the processing, training, and testing of all the EMG signals. The ratio of training samples to test samples is 9 : 1. The random forest classifier is applied to pattern recognition. We have done 10 experiments in all, and the results are shown in Figure 5.

Experimental results show that the classification accuracy of the classifier is about 94%. In the setup of this experiment, we used a 9 : 1 ratio and randomized collected experimental data to classify. This sample includes 0 modes of four actions: 30 degrees, 30 degrees, 60 degrees, and 90 degrees. The model trained by these samples will be used in the classification of the rehabilitation exoskeleton robot. In the actual system operation, we should also take into account the delay time. In some data, the maximum time delay of the patient is 200 ms–400 ms, and the robotic system shows that the average delay is about 300 ms, which is in line with the time delay [19].

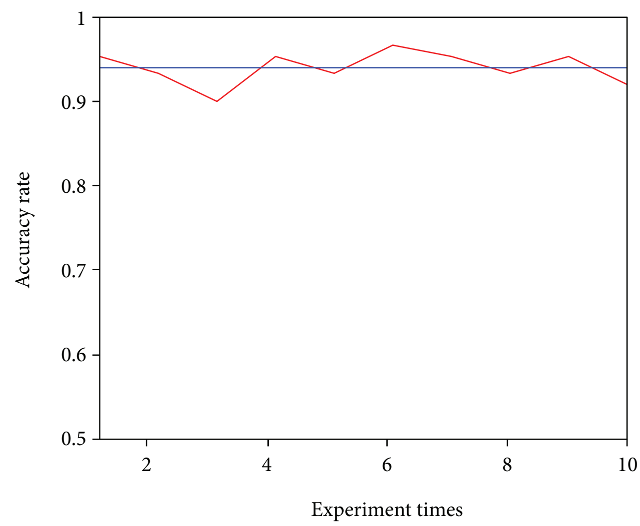

Figure 5: Wavelet packet multilayer decomposition.

4. Conclusion

Robot assisted rehabilitation training for hemiplegic patients is a new research hotspot which has attracted more and more attention.

The main structure of the robot is first introduced. The exoskeleton robot overcomes the heavy features of the existing mechanical device. Then, the design for acquiring and processing electromyographic signals for the robotic system is introduced. In this experiment, we use the four action modes of the elbow to recognize the pattern. In the process of signal processing, we take into account the weak and high noise characteristics of the signal, and use EEMD and other methods to preprocess the signal. The feature space of this experiment is composed of wavelet energy features and wavelet entropy features.

The final classification method is based on the random forest method. From the final results, the experiment has achieved good results. In the field of designing rehabilitation robots, one requires its classification accuracy. On the other hand, it also has high requirements for the time delay performance of the algorithm. In the experiment, the average time delay is in line with the actual requirements. Based on the above conclusions, it can be concluded that the robotic system can achieve the actual application requirements in general.

Data Availability

The data used to support the findings of this study are available from the corresponding author upon request.

Conflicts of Interest

The authors declare that there is no conflict of interest regarding the publication of this paper.

Acknowledgments

This research is partly supported by the National High Tech. Research and Development Program of China (No. 2015AA043202), the National Key Research and Development Program of China (2017YFB1304401), and the Natural Science Foundation of Tianjin (14JCYBJC42700).

References

[1] R. Merletti, "Electromyography physiology, engineering and on invasive applications," IEEE Press, John Wiley & Sons Inc., 2004.

[2] H. I. Krebs, B. T. Volpe, M. L. Aisen, and N. Hogan, "Increasing productivity and quality of care: robot-aided neuro-rehabilitation," *Journal of Rehabilitation Research and Development*, vol. 37, no. 6, pp. 639–652, 2000.

[3] Z. Song, S. Guo, and Y. Fu, "Development of an upper extremity motor function rehabilitation system and an assessment system," *International Journal of Mechatronics and Automation*, vol. 1, no. 1, p. 19, 2011.

[4] M. Hallett, B. T. Shahani, and R. R. Young, "EMG analysis of stereotyped voluntary movements in man," *Journal of Neurology, Neurosurgery, and Psychiatry*, vol. 38, no. 12, pp. 1154–1162, 1975.

[5] P. Shenoy, K. J. Miller, B. Crawford, and R. P. N. Rao, "Online electromyographic control of a robotic prosthesis," *IEEE Transactions on Biomedical Engineering*, vol. 55, no. 3, pp. 1128–1135, 2008.

[6] S. S. Rautaray and A. Agrawal, "Real time multiple hand gesture recognition system for human computer interaction," *International Journal of Intelligent Systems and Applications*, vol. 4, no. 5, pp. 56–64, 2012.

[7] K. R. Wheeler, M. H. Chang, and K. H. Knuth, "Gesture based control and EMG decomposition," *IEEE Transactions on Systems, Man, and Cybernetics*, vol. 36, no. 4, pp. 503–514, 2006.

[8] H. I. Krebs, N. Hogan, B. T. Volpe, M. L. Aisen, L. Edelstein, and C. Diels, "Overview of clinical trials with MIT-MANUS: a robot-aided neuro-rehabilitation facility," *Technology and Health Care*, vol. 7, no. 6, pp. 419–423, 1999.

[9] A. M. Simon, L. J. Hargrove, B. A. Lock, and T. A. Kuiken, "The target achievement control test: evaluating real-time myoelectric pattern recognition control of a multifunctional upper-limb prosthesis," *Journal of Rehabilitation Research & Development*, vol. 48, no. 6, pp. 619–627, 2011.

[10] G. R. Naik, H. Weghorn, D. K. Kumar, V. P. Singh, and M. Palaniswami, "Real-time hand gesture identification for human computer interaction based on ICA of surface electromyogram," in *International Conference Interfaces and Human Computer Interaction*, pp. 83–90, Czech Republic, 2007.

[11] X. Chen, X. Zhang, Z.-Y. Zhao, J.-H. Yang, V. Lantz, and K.-Q. Wang, "Hand gesture recognition research based on surface EMG sensors and 2D-accelerometers," in *2007 11th IEEE International Symposium on Wearable Computers*, pp. 11–14, Boston, MA, USA, October 2007.

[12] B. Gao, H. Ma, S. Guo, H. Xu, and S. Yang, "Design and evaluation of a 3-degree-of-freedom upper limb rehabilitation exoskeleton robot," in *2017 IEEE International Conference on Mechatronics and Automation (ICMA)*, pp. 938–942, Takamatsu, Japan, August 2017.

[13] K. Veer and T. Sharma, "A novel feature extraction for robust EMG pattern recognition," *Journal of Medical Engineering & Technology*, vol. 40, no. 4, pp. 149–154, 2016.

[14] M. Jiang, R. Wang, J. Wang, and D. W. Jin, "A method of recognizing finger motion using wavelet transform of surface EMG signal," in *2005 IEEE Engineering in Medicine and Biology 27th Annual Conference*, pp. 2672–2674, Shanghai, China, January 2006.

[15] H. Yu and Y. Choi, "Real time tracking algorithm of sEMG-based human arm motion," in *2007 IEEE/RSJ International Conference on Intelligent Robots and Systems*, pp. 3416–3421, San Diego, CA, USA, November 2007.

[16] J. Jiang, Z. Zhang, Z. Wang, and J. Qian, "Study on real-time control of exoskeleton knee using electromyographic signal," in *Life System Modeling and Intelligent Computing*, vol. 63, no. 30pp. 75–83, Springer, Berlin, Heidelberg, 2012.

[17] D. Moshou and H. Ramon, "Wavelets and self-organizing maps in financial time-series analysis. Neural network world," *International Journal on Neural and Mass-Parallel Computing and Information Systems*, vol. 10, no. 1, pp. 231–238, 2000.

[18] A. B. Ajiboye and R. F. H. Weir, "A heuristic fuzzy logic approach to EMG pattern recognition for multi-functional prosthesis control," *IEEE Transactions on Neural Systems and Rehabilitation Engineering*, vol. 13, no. 3, pp. 280–291, 2005.

[19] A. Subasi, "Application of adaptive neuro-fuzzy inference system for epileptic seizure detection using wavelet feature extraction," *Computers in Biology and Medicine*, vol. 37, no. 2, pp. 227–244, 2007.

Hindawi
Applied Bionics and Biomechanics
Volume 2018, Article ID 9289505, 7 pages
https://doi.org/10.1155/2018/9289505

Research Article

Design and Evaluation of a Wearable Powered Foot Orthosis with Metatarsophalangeal Joint

Yixiang Liu ,[1,2,3] Xizhe Zang ,[1] Niansong Zhang,[2,3,4] and Ming Wu [2,3]

[1]*State Key Laboratory of Robotics and System, Harbin Institute of Technology, Harbin 150080, China*
[2]*Legs and Walking Lab, Shirley Ryan AbilityLab Formerly the Rehabilitation Institute of Chicago, Chicago, IL 60611, USA*
[3]*Department of Physical Medicine and Rehabilitation, Northwestern University, Chicago, IL 60611, USA*
[4]*School of Mechanical Engineering, Nanjing University of Science and Technology, Nanjing 210016, China*

Correspondence should be addressed to Xizhe Zang; zangxizhe@hit.edu.cn

Received 3 February 2018; Accepted 16 August 2018; Published 19 September 2018

Academic Editor: Nan Xiao

The metatarsophalangeal (MTP) joints play critical roles in human locomotion. Functional restriction or loss of MTP joints will lead to lower walking speed, poorer walking balance, and more consumed metabolic energy cost compared with normal walking. However, existing foot orthoses are focused on maintaining the movement of the ankle joint, without assisting the MTP joints. In this paper, in order to improve the walking performance of people with lower limb impairments, a wearable powered foot orthosis (WPFO) which has actuated MTP joint is designed and constructed. Preliminary experiments on three nondisabled subjects demonstrated functionality and capabilities of the WPFO to provide correctly timed dorsiflexion and plantar flexion assistance at the MTP joint during walking. These results also suggest that the WPFO could offer promise in certain rehabilitation applications and clinical treatment.

1. Introduction

Ankle-foot orthoses and prostheses have been studied widely over the past few decades for patients with walking disabilities caused by injuries or neurological and muscular pathologies such as trauma, stroke, cerebral palsy, spinal cord injuries, and muscular dystrophies. They are intended to enhance the basic walking function of patients by maintaining the range of motion of the ankle and foot [1] and providing stability during stance [2]. According to system actuation, these devices can be roughly divided into two categories, that is, passive devices and powered devices. Passive devices, as the name implies, do not have any active power sources and are not able to supply nonconservative positive work [3]. To improve their ankle push-off properties, the so-called energy storing and returning (ESR) mechanisms are proposed by the researchers [4]. Specifically, mechanical elements with elastic and damping characteristics are equipped on passive devices to harvest energy during loading and release it during push-off [5–7]. Contrary to passive devices, powered devices have onboard power sources and actuators that can provide positive and negative work to assist the users in the stance phase. They are usually actuated by electric motors [8–10], artificial pneumatic muscles [11, 12], linear or rotary pneumatic actuators [13–15], and hydraulic cylinders [16]. In these two categories of ankle-foot orthoses and prostheses, passive devices are relatively more popular in daily use due to their simplicity, compactness, durability, and comfort but have not been shown to sufficiently improve patients' biomechanics and energetic cost [17]. Nevertheless, some research has demonstrated that powered devices, although mostly at the research level, exert promise for improving the locomotor performance of patients, for instance, reducing walking metabolic energy [18] and achieving more natural gait [19].

One important issue existing in the research of powered ankle-foot orthoses and prostheses is that active assistance is applied only to the ankle joint. The metatarsophalangeal (MTP) joints are usually incorporated into the devices passively using an arc-shaped carbon-composite forefoot or a

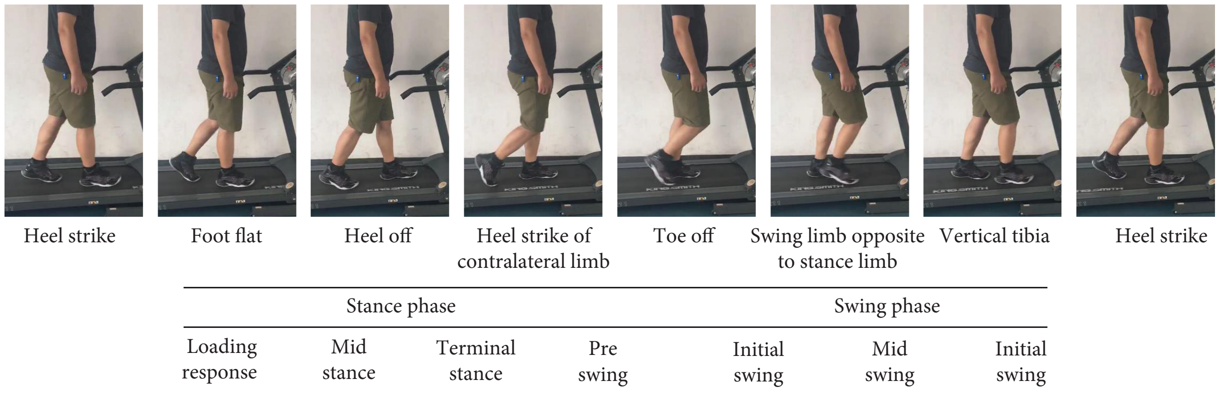

Figure 1: A gait cycle of human walking.

passive rotary joint [20–23] to mimic the rocker-like function of the forefoot [24]. This is mainly because the ankle joint produces substantially more work than other joints of the lower limb, in a burst late in the push-off phase [25]. However, the MTP joints actually have the largest range of motion among the other joints of the foot except for the ankle joint [26] and play important roles in human locomotion. Functional restriction or loss of MTP joints leads to lower walking speed, smaller step length, and more consumed metabolic energy compared with normal walking [27]. These facts indicate that to further improve the walking function of patients, it is necessary and will be beneficial to add actuated MTP joints into ankle-foot orthoses and prostheses and restore the normal range of motion of the MTP joints.

Therefore, in this paper, we propose a wearable powered foot orthosis (WPFO) that consists of an actuated MTP joint. The powered MTP joint is intended to provide assistance in dorsiflexion and plantar flexion when the foot pushes off the ground during walking. In order to verify the functionality and performance of the WPFO, preliminary experiments on three nondisabled subjects are carried out.

The rest of this paper is organized as follows. Section 2 introduces the fundamentals of human walking gait and the MTP joints. Section 3 presents the design of the WPFO device including mechanical structure and control system. The experiment procedure, data analysis, and results are presented in Section 4. Finally, the discussion and conclusion are given in Section 5 and Section 6, respectively.

2. Fundamentals of Human Gait and the MTP Joints

2.1. Human Gait. Human walking is the repetition of consecutive gait cycles in which the body is alternately supported by the right and left leg. A normal gait cycle presented in Figure 1 starts at the heel strike of one foot and ends at the next heel strike of the same foot. According to the contact of one leg and the ground in walking, a gait cycle can be divided into two phases, i.e., stance phase where the foot is in contact with the ground and swing phase where the foot is in the air. The stance phase ensures body progression while maintaining an upright posture, whereas the swing phase advances the leg to prepare for the next step [28]. Duration is about 60% of the gait cycle for the stance phase and the remaining 40% for the swing phase. The stance phase and swing phase can be further divided into multiple subphases including loading response, midstance, terminal stance, preswing, initial swing, midswing, and terminal swing. Each subphase with corresponding kinematic events and temporal distribution is defined according to the convention, as presented schematically.

2.2. The MTP Joints. During walking, the movement of MTP joints mainly occurs in the sagittal plane. In the terminal stance subphase, the heel lifts up from the ground and the body rotates relative to the toes around the MTP joints; in other words, the MTP joints are dorsiflexed. After reaching the maximum dorsiflexion angle of about 30° in the middle of preswing subphase, the MTP joints are rapidly plantar flexed towards the neural position, as having been shown in Figure 1 [29]. Although the MTP joints generate only a small amount of energy during walking, their movement especially dorsiflexion plays important roles in helping the ankle-foot complex to bear body weight and generate necessary propulsion force for forward walking. In our previous study [30, 31], we investigated the kinetic responses of human bodies when unilateral MTP joints were constrained during walking. Gait analyses of 12 healthy subjects were performed in terms of joint kinetics in two conditions, that is, walking normally and walking with the MTP joints of unilateral foot constrained. Based on the results, it was found that the constraints of the MTP joints had the most significant effects on the ankle joint. In more detail, the vertical and anterior/posterior (A/P) GRF, corresponding support and propulsion impulses, and moment and power of the ankle joint of the constrained leg significantly decreased. And it was more obvious when walking at a fast speed. This was perhaps owing to the protective mechanism of the human body. The constrained foot, of which the rotation around the MTP joint was affected by the constraints, was unsuitable for load bearing and propulsion.

3. Design of the WPFO

3.1. Mechanical Structure. The virtual model and prototype of the WPFO device are shown in Figures 2 and 3,

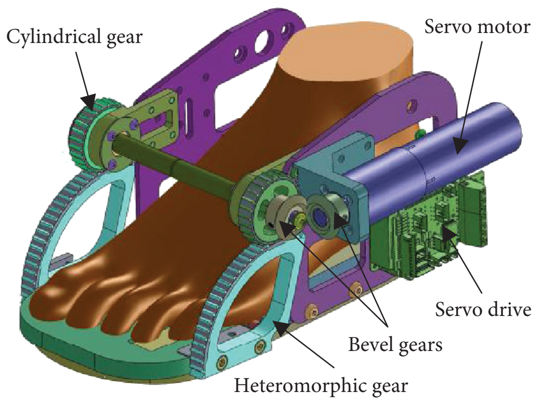

FIGURE 2: The virtual model of the WPFO.

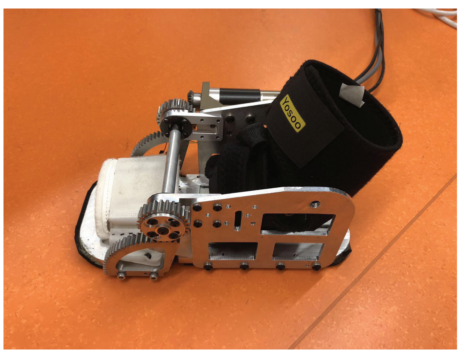

FIGURE 3: The prototype of the WPFO.

respectively. The sole of the WPFO consists of two parts, namely, the forefoot plate and the heel plate, which are hinged through a pivot shaft. The heteromorphic gears are connected with the forefoot plate, while the cylindrical gears engaged with the heteromorphic gears are connected with the heel plate. The servo motor (Maxon Motor AG, Sachseln, Switzerland) and servo drive (Elmo Motion Control Ltd., Petah Tikva, Israel) are mounted on the side plate which is connected to the heel plate. The cylindrical gear is actuated by the servo motor through a pair of engaged bevel gears. A layer of soft material is attached beneath the sole to soften the impact as the WPFO makes contact with the ground. The WPFO can be tied to the wearer's foot and shank through the braces. The total length of the WPFO is 270 mm, with distribution between the forefoot plate and heel plate in a similar ratio with the human foot. And its gross weight is about 1.2 kg. It should be noted that the weight can be reduced if locating the motor at a higher position, for example, on the leg or waist, and transmitting the actuation through some methods like rope dive. However, in this study, the motor is mounted on the foot to simplify the mechanical structure of the WPFO.

3.2. Control System. The control system hardware of the WPFO is composed of a controller, a servo drive, and two contact switches. For the sake of simplicity, a personal computer instead of a single-board microcontroller is adopted

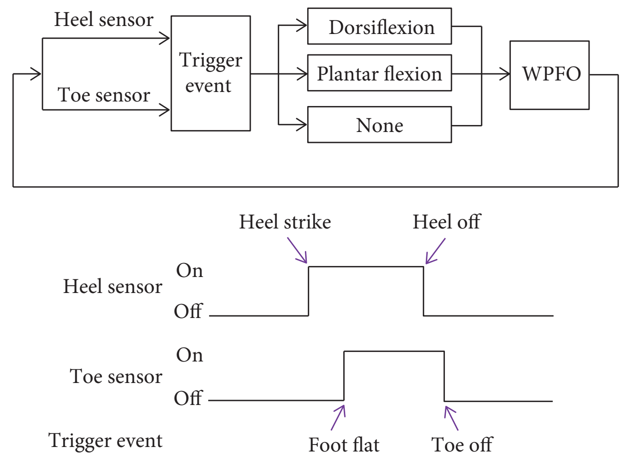

FIGURE 4: Working mechanism of the control system of the WPFO.

as the controller. One of the two contact switches is installed at the back of the heel plate, and the other one is installed on the forefoot plate near the pivot shaft. The signals of the contact switches are fed to the servo drive. The controller receives the feedback from the servo drive and sends commands to the drive based on the sensor status. The controller communicates with the drive via RS-232 protocol.

The control scheme of the WPFO is based on finite-state machine control, as illustrated in Figure 4. Gait events are detected when the switches make contact or lose contact with the ground. Specifically, when the heel lifts off from the ground (the heel sensor changes from on to off), the WPFO is triggered to provide assistive dorsiflexion torque until the toe starts to lift up; and when the toe lifts off from the ground (the toe sensor changes from on to off), the WPFO is triggered to provide assistive plantar flexion torque until the toe is fully off the ground. The lower-level motor controller is based on position tracking control. The reference trajectory of the MTP joint presented in Figure 5 is generated by a polynomial fit of human MTP joint kinematic data. At the start and the end of the trajectory, there are an accelerating segment and a decelerating segment, respectively, which are used to smooth the whole trajectory.

4. Experiments

4.1. Experiment Procedure. Three nondisabled subjects (mean ± standard deviation age 27 ± 3 yr, height 172 ± 8 cm, and weight 65 ± 12 kg) were recruited from Northwestern University to participate in the experiments. These subjects were experienced treadmill walkers and had no walking-related injuries such as muscle strains, joint sprains, or back injuries at the time of testing. And they all wore size 8-9 shoes in order to fit with the WPFO. All the subjects received written and verbal information about the experiment procedure and gave written informed consent prior to participation. The experiments were carried out in the Legs and Walking Lab of Shirley Ryan AbilityLab after the approval was obtained from the Institutional Review Board of Northwestern University.

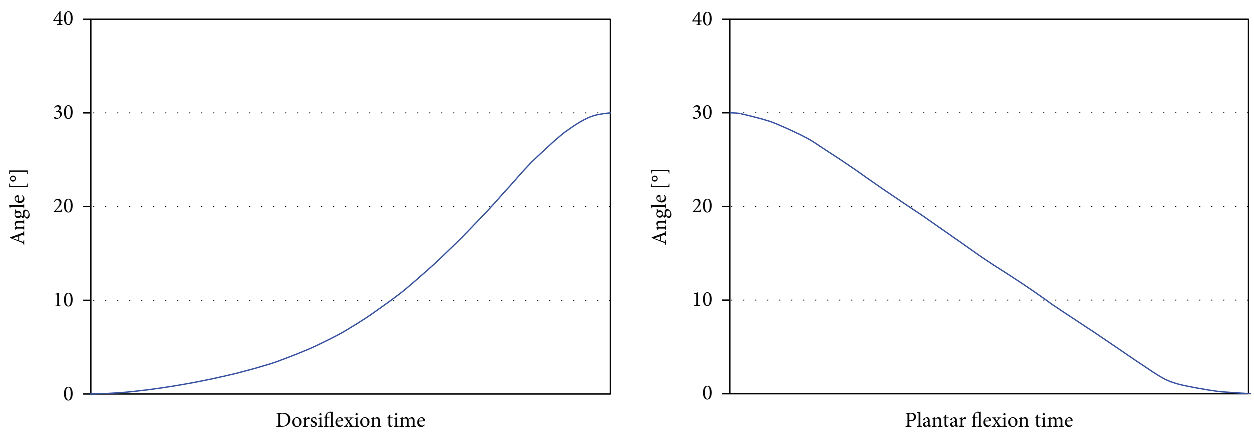

Figure 5: Reference trajectory of the MTP joint of the WPFO.

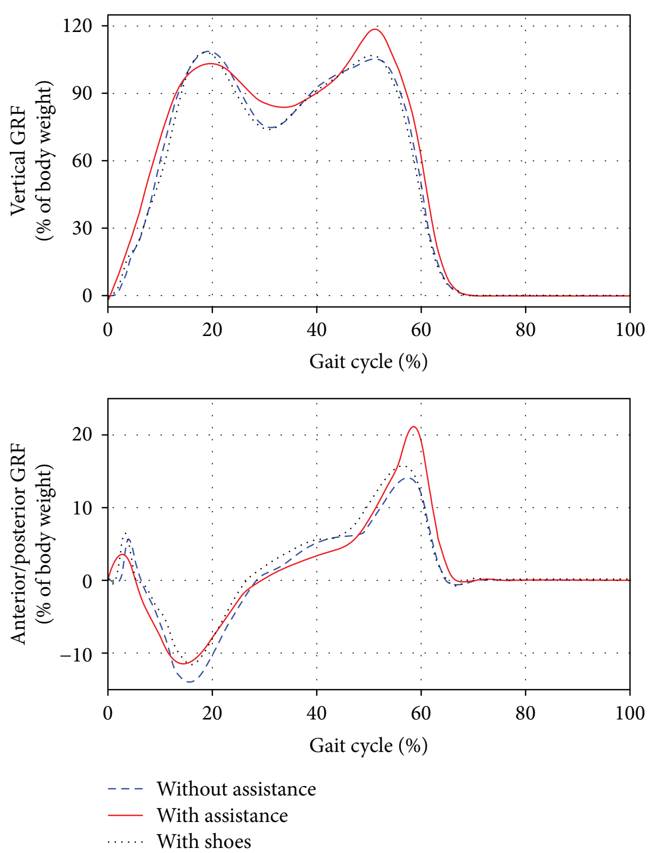

Figure 6: Averaged vertical GRF and anterior/posterior GRF during treadmill walking under the two conditions.

In order to verify the functionality of the WPFO, subjects walked on a split-belt treadmill with embedded force plates (Fully Instrumented Treadmill, Bertec Corporation, Columbus, OH, USA) wearing the WPFO on the right foot. All subjects were instructed to walk at their self-selected speed under two conditions, that is, (1) without assistance torque and (2) with assistance torque. The order of experimental conditions was randomized across subjects. Under each condition, subjects completed 3 walking trials and walked for 2 minutes in each trial with a 2 min standing break inserted between two trials to avoid fatigue effect. Before the start of formal experiments, multiple practice trials were performed for subjects to acclimate to the devices.

4.2. Data Acquisition and Analysis. During the walking trials, ground reaction forces (GRF) on the right foot were collected by the force plates at 1000 Hz. And three-dimensional motion of the lower limbs was captured by an 8-camera motion capture system (NaturalPoint Inc., Corvallis, OR, USA) at 100 Hz. To make them available for analysis and comparison, the collected data were processed using custom programs written in MATLAB (The Mathworks, Natick, MA, USA) in the following method. GRF and marker position data were first low-pass filtered using a fourth-order Butterworth filter with cutoff frequencies of 20 Hz and 6 Hz, respectively [32], then were segmented into step cycles from heel strike to the next heel strike of the same foot. Because of the variability in the duration of each step cycle, the data were interpolated and resampled and then averaged across the last consecutive 20 strides to create a mean pattern [33]. After that, the obtained mean GRF of each subject were normalized to the corresponding body weight. In the end, the parameters of each subject were averaged across the 3 trials and further averaged across all subjects.

Based on the introduction in Section 2.2, the data including GRF, corresponding support and propulsion impulse, and ankle joint moment and power of the constrained leg were analyzed to evaluate whether the WPFO could restore the natural walking pattern. The support impulse was quantified as the time integral of vertical GRF during stance, and propulsion impulse was quantified as the time integral of A/P GRF when the force was directed forward [34]. Inverse dynamic analyses were performed in the sagittal plane to compute the ankle joint moment [35]. The joint power was then calculated by multiplying joint moments with joint angular velocities. Positive power occurs when the joint moment is in the same direction with the resultant angular velocity, while negative power occurs in the opposite direction.

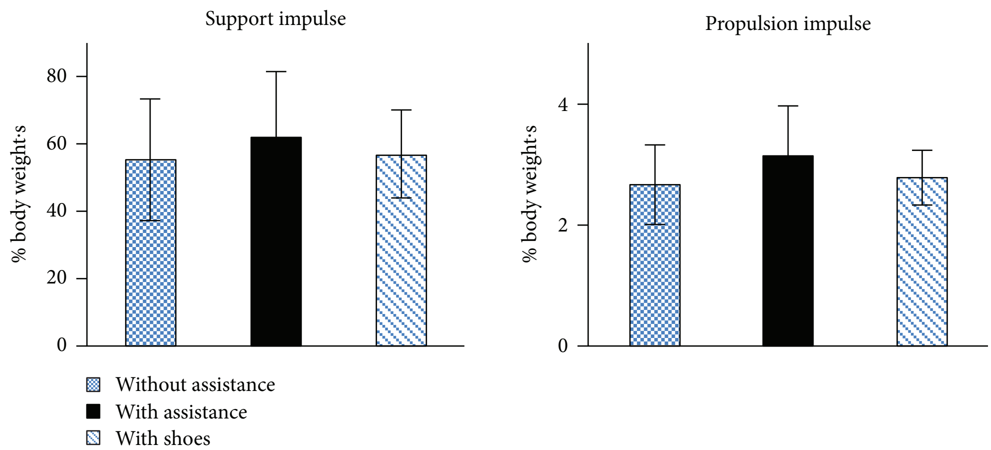

FIGURE 7: The support impulse and propulsion impulse during treadmill walking under the two conditions.

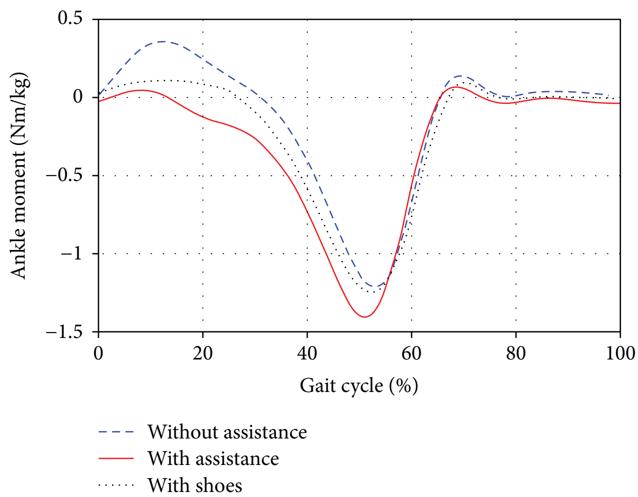

FIGURE 8: The right ankle moment over one complete stride for walking under the two conditions.

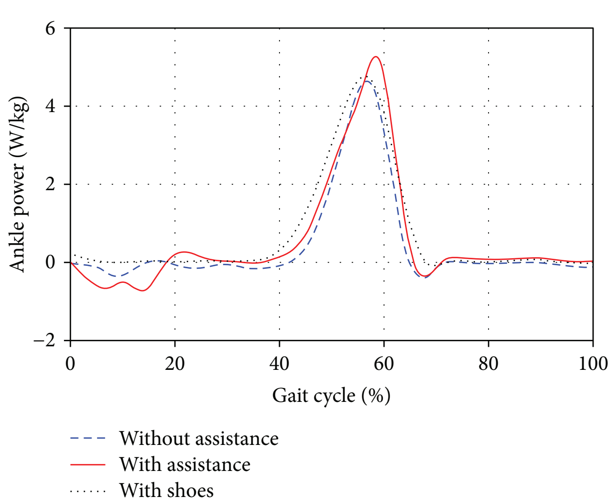

FIGURE 9: The right ankle power over one complete stride for walking under the two conditions.

4.3. Experiment Results. Figure 6 illustrates the averaged vertical GRF and A/P GRF acted on the right foot during treadmill walking under the two conditions. During the propulsive phase of walking, the peak value of support force (positive vertical GRF) increased by about 12% of the body weight, while the peak value of forward propulsive force (positive A/P GRF) increased by about 8% of the body weight.

The support impulse and propulsion impulse incorporating both the magnitude and duration of vertical GRF and A/P GRF were analyzed and presented in Figure 7. Obviously, when walking with assistance torque, both the support impulse and propulsion impulse increased.

Figures 8 and 9 present the moment and power of the right ankle over one complete stride of treadmill walking under the two conditions, respectively. The ankle moment for walking with assistance was larger than that without assistance. And increased peak power was generated by subjects at the push-off phase with the assistance of WPFO.

In the above figures from Figures 6 to 9, the data of subjects walking with shoes are also presented. By comparing the data of walking without assistance and with shoes, it can be found that the WPFO without assistance had some small effects on normal gait patterns. Specifically, the GRF, impulse, and ankle joint moment and power slightly decreased. In addition, the comparison between the data of walking with assistance and without assistance showed that the WPFO with assistance allowed the gait pattern to return to a more normative behavior.

5. Discussion

The objective of this study was to design a novel wearable foot orthosis which had an actuated MTP joint to help patients to achieve dorsiflexion and plantar flexion of the MTP joint. From the experiments, we found that sufficient torque could be provided by a 200-watt electric servo motor that transmitted the power through a reducing mechanism. Pilot data collected from nondisabled subjects were used to demonstrate the function of the WPFO device. It was verified that the WPFO was able to provide both dorsiflexion and plantar flexion assistance during walking. The assistive capabilities of the proposed WPFO were most clearly illustrated by the vertical GRF and A/P GRF data during the walking trials with assistance torque. The increased second peak value of the vertical GRF and the increased peak of positive A/P GRF were indicative of larger push-off force that was provided by the WPFO for forward propulsion during the late stance phase. What is more, the timing of the GRF data and the moment and power of ankle joint showed small differences between the durations of stance phase in the two experimental cases, indicating that the WPFO could provide quick response and appropriately timed functional assistance.

Nowadays, plenty of people are suffering from lower limb disabilities caused by stroke, cerebral palsy, spinal cord injuries, or muscular dystrophies. The disabilities have severely affected their quality of life. Consequently, there is a growing demand for technological advances in orthotic and prosthetic systems, especially portable and powered devices. On the basis of our previous researches on the effects of the MTP joints on human walking performances, we proposed and constructed the novel WPFO that has a powered MTP joint. The WPFO provided a potentially new modality for applications in in-home assistive walking training and clinical rehabilitation or treatment. And hopefully, it may contribute to the improvement of the functional outcomes of daily training and treatment.

Although encouraging results are obtained from this study, there are still some important limitations to consider. Firstly, the WPFO device is a little bit heavy. To reduce the weight, the actuator and control system can be relocated on the leg or waist. Metal materials can also be replaced by composite materials with high strength and rigidity but low density. Secondly, the actuator adopted in this study is rigid. It will be better if compliant actuators like series elastic actuators or pneumatic artificial muscles are used, because inherent compliance is essential for human-machine interaction. Thirdly, the two contact switches can only detect the contact status between the ground and the two specific points on the sole. More force-sensitive resistors distributed beneath the sole can offer more reliable gait event detection during walking. Last but not the least, we only tested the WPFO on nondisabled subjects. More experiments have to be performed on patients with impairments to the MTP joints to further demonstrate the functionality of the device.

6. Conclusion

In this paper, the design and evaluation of a novel WPFO device with an actuated MTP joint are presented. The WPFO is proposed to help improve walking performance of patients with MTP joint impairments. The pilot data from three nondisabled subjects demonstrated the capabilities of the WPFO to provide functional assistance at the MTP joint during walking, which suggests that the WPFO could be potentially utilized in certain rehabilitation applications and clinical treatment. In the future, our research will be focused on the improvements to hardware structure and control scheme of the WPFO device.

Data Availability

The data used to support the findings of this study are available from the corresponding author upon request.

Conflicts of Interest

The authors declare that they have no conflicts of interest.

Acknowledgments

This research is funded and supported by the National Institutes of Health (NIH) under Grant R01HD082216 to author M. Wu, the China Scholarship Council (CSC) under Grant 201606120094 to author Y. Liu, and the National Key Research and Development Plan of China under Grant 2017YFC0806501 to author X. Zang.

References

[1] L. Deberg, M. Taheri Andani, M. Hosseinipour, and M. Elahinia, "An SMA passive ankle foot orthosis: design, modeling, and experimental evaluation," *Smart Materials Research*, vol. 2014, Article ID 572094, 11 pages, 2014.

[2] S. J. Mulroy, V. J. Eberly, J. K. Gronely, W. Weiss, and C. J. Newsam, "Effect of AFO design on walking after stroke: impact of ankle plantar flexion contracture," *Prosthetics and Orthotics International*, vol. 34, no. 3, pp. 277–292, 2010.

[3] H. Masum, S. Bhaumik, and R. Ray, "Conceptual design of a powered ankle-foot prosthesis for walking with inversion and eversion," *Procedia Technology*, vol. 14, pp. 228–235, 2014.

[4] B. J. Hafner, J. E. Sanders, J. M. Czerniecki, and J. Fergason, "Transtibial energy-storage-and-return prosthetic devices: a review of energy concepts and a proposed nomenclature," *Journal of Rehabilitation Research and Development*, vol. 39, no. 1, pp. 1–11, 2002.

[5] B. Brackx, M. van Damme, A. Matthys, B. Vanderborght, and D. Lefeber, "Passive ankle-foot prosthesis prototype with extended push-off," *International Journal of Advanced Robotic Systems*, vol. 10, no. 2, p. 101, 2017.

[6] S. H. Collins and A. D. Kuo, "Recycling energy to restore impaired ankle function during human walking," *PLoS One*, vol. 5, no. 2, article e9307, 2010.

[7] P. Cherelle, A. Matthys, V. Grosu, B. Vanderborght, and D. Lefeber, "The AMP-foot 2.0: mimicking intact ankle behavior with a powered transtibial prosthesis," in *2012 4th IEEE RAS & EMBS International Conference on Biomedical Robotics and Biomechatronics (BioRob)*, pp. 544–549, Roma, Italy, June 2012.

[8] S. Au, M. Berniker, and H. Herr, "Powered ankle-foot prosthesis to assist level-ground and stair-descent gaits," *Neural Networks*, vol. 21, no. 4, pp. 654–666, 2008.

[9] H. M. Herr and A. M. Grabowski, "Bionic ankle-foot prosthesis normalizes walking gait for persons with leg amputation," *Proceedings of the Royal Society B: Biological Sciences*, vol. 279, no. 1728, pp. 457–464, 2011.

[10] Y. Bai, X. Gao, J. Zhao, F. Jin, F. Dai, and Y. Lv, "A portable ankle-foot rehabilitation orthosis powered by electric motor," *The Open Mechanical Engineering Journal*, vol. 9, no. 1, pp. 982–991, 2015.

[11] R. Versluys, A. Desomer, G. Lenaerts et al., “A pneumatically powered below-knee prosthesis: design specifications and first experiments with an amputee,” in *2008 2nd IEEE RAS & EMBS International Conference on Biomedical Robotics and Biomechatronics*, pp. 372–377, Scottsdale, AZ, USA, October 2008.

[12] R. Versluys, A. Desomer, G. Lenaerts et al., “A biomechatronical transtibial prosthesis powered by pleated pneumatic artificial muscles,” *International Journal of Modelling, Identification and Control*, vol. 4, no. 4, pp. 394–405, 2008.

[13] K. A. Shorter, Y. Li, E. A. Morris, G. F. Kogler, and E. T. Hsiao-Wecksler, “Experimental evaluation of a portable powered ankle-foot orthosis,” in *2011 Annual International Conference of the IEEE Engineering in Medicine and Biology Society*, pp. 624–627, Boston, Massachusetts USA, August 2011.

[14] K. A. Shorter, G. F. Kogler, E. Loth, W. K. Durfee, and E. T. Hsiao-Wecksler, “A portable powered ankle-foot orthosis for rehabilitation,” *The Journal of Rehabilitation Research and Development*, vol. 48, no. 4, pp. 459–472, 2011.

[15] H. Zheng and X. Shen, “Design and control of a pneumatically actuated transtibial prosthesis,” *Journal of Bionic Engineering*, vol. 12, no. 2, pp. 217–226, 2015.

[16] A. Gmerek, N. Meskin, E. S. Tehrani, and R. Kearney, “Design of a hydraulic ankle-foot orthosis,” in *2016 6th IEEE International Conference on Biomedical Robotics and Biomechatronics (BioRob)*, pp. 1041–1048, UTown, Singapore, June 2016.

[17] A. D. Segal, K. E. Zelik, G. K. Klute et al., “The effects of a controlled energy storage and return prototype prosthetic foot on transtibial amputee ambulation,” *Human Movement Science*, vol. 31, no. 4, pp. 918–931, 2012.

[18] S. K. Au, J. Weber, and H. Herr, “Powered ankle–foot prosthesis improves walking metabolic economy,” *IEEE Transactions on Robotics*, vol. 25, no. 1, pp. 51–66, 2009.

[19] R. C. Martinez, R. L. Avitia, M. E. Bravo, and M. A. Reyna, “A low cost design of powered ankle-knee prosthesis for lower limb amputees-preliminary results,” in *Proceedings of the International Conference on Biomedical Electronics and Devices*, pp. 253–258, Angers, Loire Valley, France, March 2014.

[20] J. M. Caputo and S. H. Collins, “A universal ankle-foot prosthesis emulator for human locomotion experiments,” *Journal of Biomechanical Engineering*, vol. 136, no. 3, article 035002, 2014.

[21] R. Jiménez-Fabián and O. Verlinden, “Review of control algorithms for robotic ankle systems in lower-limb orthoses, prostheses, and exoskeletons,” *Medical Engineering & Physics*, vol. 34, no. 4, pp. 397–408, 2012.

[22] J. Zhu, Q. Wang, Y. Huang, and L. Wang, “Adding compliant joints and segmented foot to bio-inspired below-knee exoskeleton,” in *2011 IEEE International Conference on Robotics and Automation*, pp. 605–610, Shanghai, China, May 2011.

[23] J. Zhu, Q. Wang, and L. Wang, “On the design of a powered transtibial prosthesis with stiffness adaptable ankle and toe joints,” *IEEE Transactions on Industrial Electronics*, vol. 61, no. 9, pp. 4797–4807, 2014.

[24] A. H. Hansen, D. S. Childress, and E. H. Knox, “Roll-over shapes of human locomotor systems: effects of walking speed,” *Clinical biomechanics*, vol. 19, no. 4, pp. 407–414, 2004.

[25] T. P. Huang, K. A. Shorter, P. G. Adamczyk, and A. D. Kuo, “Mechanical and energetic consequences of reduced ankle plantar-flexion in human walking,” *Journal of Experimental Biology*, vol. 218, no. 22, pp. 3541–3550, 2015.

[26] T. L. Nguyen, S. J. Allen, and S. J. Phee, “Exploiting 3D printing technology to develop robotic running foot for footwear testing,” *Virtual and Physical Prototyping*, vol. 8, no. 4, pp. 259–269, 2013.

[27] J. Zhang, Y. Si, Y. Zhang, and Y. Liu, “The effects of restricting the flexion-extension motion of the first metatarsophalangeal joint on human walking gait,” *Bio-medical Materials and Engineering*, vol. 24, no. 6, pp. 2577–2584, 2014.

[28] D. Torricelli, J. Gonzalez, M. Weckx et al., “Human-like compliant locomotion: state of the art of robotic implementations,” *Bioinspiration & Biomimetics*, vol. 11, no. 5, article 051002, 2016.

[29] Y. Kim, S. Kim, J. Son, and B. Jeong, “Kinetic role of the metatarsophalangeal joint in normal walking: joint moment and power,” *International Journal of Precision Engineering and Manufacturing*, vol. 13, no. 8, pp. 1481–1485, 2012.

[30] Y. Liu, X. Zang, N. Zhang, and Y. Liu, “Kinetic responses to unilateral constraint of the metatarsophalangeal joints during bipedal walking,” *International Journal of Humanoid Robotics*, article 1850018, 2018.

[31] Y. Liu, X. Zang, N. Zhang, and M. Wu, “Gait symmetry can reduce dependence on the intact limb during walking with constraint of unilateral metatarsophalangeal joints,” in *Proceedings of the 40th International Conference of IEEE Engineering in Medicine and Biology Society*, Honolulu, Hawaii, July 2018.

[32] C. L. Peterson, S. A. Kautz, and R. R. Neptune, “Braking and propulsive impulses increase with speed during accelerated and decelerated walking,” *Gait & Posture*, vol. 33, no. 4, pp. 562–567, 2011.

[33] C.-J. Hsu, J. Kim, R. Tang, E. J. Roth, W. Z. Rymer, and M. Wu, “Applying a pelvic corrective force induces forced use of the paretic leg and improves paretic leg EMG activities of individuals post-stroke during treadmill walking,” *Clinical Neurophysiology*, vol. 128, no. 10, pp. 1915–1922, 2017.

[34] J. Rice and M. K. Seeley, “An investigation of lower-extremity functional asymmetry for non-preferred able-bodied walking speeds,” *International Journal of Exercise Science*, vol. 3, no. 4, pp. 182–188, 2010.

[35] H. Salehi, L. Ren, and D. Howard, “A fast inverse dynamics model of walking for use in optimisation studies,” *Computer Methods in Biomechanics and Biomedical Engineering*, vol. 19, no. 11, pp. 1201–1209, 2016.

Hindawi
Applied Bionics and Biomechanics
Volume 2018, Article ID 8610458, 9 pages
https://doi.org/10.1155/2018/8610458

Research Article

Design and Performance Evaluation of a Wearable Sensing System for Lower-Limb Exoskeleton

Chunfeng Yue,[1,2] Xichuan Lin,[1,2] Ximing Zhang,[1] Jing Qiu ,[1,2] and Hong Cheng [1,2]

[1]*The School of Automation Engineering, University of Electronic Science and Technology of China, China*
[2]*Center for Robotics, University of Electronic Science and Technology of China, China*

Correspondence should be addressed to Hong Cheng; hcheng@uestc.edu.cn

Received 12 February 2018; Revised 27 April 2018; Accepted 13 June 2018; Published 18 September 2018

Academic Editor: Dongming Gan

Because the target users of the assistive-type lower extremity exoskeletons (ASLEEs) are those who suffer from lower limb disabilities, customized gait is adopted for the control of ASLEEs. However, the customized gait is unable to provide stable motion for variable terrain, for example, flat, uphill, downhill, and soft ground. The purpose of this paper is to realize gait detection and environment feature recognition for AIDER by developing a novel wearable sensing system. The wearable sensing system employs 7 force sensors as a sensing matrix to achieve high accuracy of ground reaction force detection. There is one more IMU sensor that is integrated into the structure to detect the angular velocity. By fusing force and angular velocity data, four typical terrain features can be recognized successfully, and the recognition rate can reach up to 93%.

1. Introduction

Lower limb exoskeleton (LLE) robotic technology has been developed rapidly for the past 20 years. Three implementation fields, that is, augmentation, rehabilitation, and living support are explored. First, the human augmentation type LLE (AULLE) was developed for the military and aims at improving a soldier's weight loading ability. The fields of application extend to disaster relief and industrial transport assistance. Kazerooni et al. developed the typical first generation AULLE which is named BLEEX [1, 2]. Then, the third generation AULLE which is named HULC was developed for carrying a load of about 90 kg. Second, the rehabilitation type LLE (RELLE) was developed for patients whose lower limbs are inconvenienced [3–5]. Typical patients include those with foot drop, spinal cord injuries, and strokes. The most famous RELLE is Lokomat, which is developed by the Hocoma Company [6]. The assistive-type LLE (ASLLE) is used to assist patients with lower limb disabilities but whose upper limbs are normal. The ASLLEs assist patients to return to their normal life. They do not only assist in walking motion on flat ground, climbing on stairs, or sitting down and standing, but they also rebuild their confidence in daily life. There are three typical commercial products that have been developed: ReWalk 6.0 [7], Ekso GT [8], and HAL-5 [9]. They each have a weight of about 20 kg. Besides these, lightweight ASLLEs have also been developed to assist spinal cord injury patients, such as Phoenix 3.0 [10] and INDEGO [11]. The researchers are also trying to prove their benefit to patients who have used the ASLLEs [12, 13].

In our previous research, we focused on the human augmentation exoskeleton [14–16] and an ASLLE named the AIDER [17, 18] for individuals. An illustration of a prototype of AIDER with a SCI patient is shown in Figure 1. Based on AIDER and two crutches, the patient can form a stable area to keep balance. Four DC motors are installed on the hip and knee joints respectively. The patient controls the AIDER by two controllers which are installed on the grab handles of the crutches. A battery and control circuit placed in the backpack are the core part for controlling the DC motors. This paper is an extension for my previous work [19].

Avoiding harm to the patient when piloting an exoskeleton is a critical issue. Table 1 shows the influence of three kinds of LLEs on the interaction between human, machine,

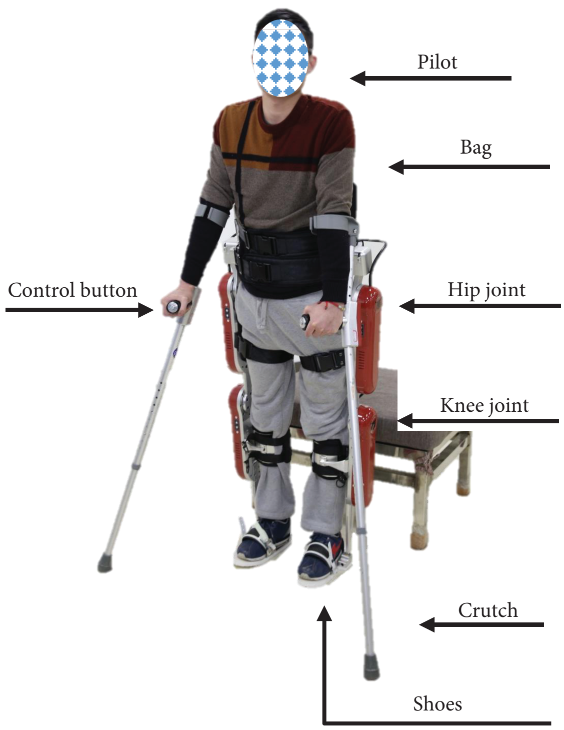

Figure 1: The prototype of AIDER with a SCI patient.

Table 1: The influence for three kinds of exoskeletons on the human-machine-environment.

Factors	AULLE	RELLE	ASLLE
Human	Health	Weak	Weak
Machine	Low	High	High
Environment	Daily life/unsafe	Hospital/safe	Daily life/unsafe

and the environment. For an AULLE, the mechanical parts follow the pilot's motion and support the weight of the load. The pilot takes the initiative in the human-machine-environment system. For a RELLE, the machine controls the human motion because of the lower-limb paralysis of SCI patients. The working environment of a RELLE is very safe because the pilot is always protected by fixed support. For an ASLLE, although the potential pilots are the same as those of a RELLE, the working environment for an ASLLE is complex daily life. The safety for the pilot of an ASLLE relies on the exoskeleton's stability. Besides, patients with complete injury have lost their sensory ability. They cannot keep their balance when wearing the exoskeleton. Therefore, the ASLLE should be able to sense the human-machine state and adjust the gait trajectory for the pilot to avoid a dangerous situation.

Based on the analysis for the safety of a human-machine system, a sensing system is necessary to improve the stability of ASLLEs. The shoes are suitable components for installing sensors. In related works, researchers have used foot-sensing systems to detect gait information. Footscan is a typical commercial product which was developed by the RSscan Company. Based on this product, the relationship between the gait characteristics and foot pressure for overweight children was analyzed [20]. Besides, researchers also designed a number of wearable sensing systems to meet their research requirements. In [21], the researchers designed sensing shoes to estimate the CoM displacement continuously using an ambulatory measurement system which contains 2 IMUs and 2 6DOF force/moment sensors. Although the precision of the sensor is really high, the large size influences gait analysis resulting from normal walking. Even high precision data can be collected easily. The large size of the IMU and pressure sensor gives the pilot poor wearing experience. Liu et al. have worked on gait analysis for serval years. They developed smart shoes for human gait analysis [22, 23]. The novel point of the smart shoes is that they contain three 6-axis force sensors with 1 cm thickness. The sensors are mounted on the heel, arch, and forefoot respectively to subdivide the phase of human walking and get high accuracy gait data. Bamberg et al. developed a multiple sensing system and integrated it with shoes. The sensing system contains 6 kinds of sensors including an accelerometer, gyroscope, force sensitive resistor, bend sensor, polyvinylidene fluoride strip, and electric field sensor [24]. The multiple sensors provide redundancy gait data to ensure stability. Due to the complex environment as shown in Table 1, we intend to develop a wearable sensing system for AIDER which can not only detect human body motion but also detect the state of the environment, such as the features of the ground.

2. Motivation

2.1. User and Application Environment for AIDER. AIDER is intended for users with SCI with injury levels from T9 to T12 caused by traumatic injuries (e.g., vehicular crashing or falling from buildings) or disease (e.g., myelitis) [25, 26]. The AIDER is aimed at extending the range of activities to advance their rehabilitation programs for SCIs. Besides, walking upright makes the patients feel more confident because they can make a conversation with friends at eye level and walk like normal persons.

As illustrated in the Introduction, the target environments for the application of AIDER are daily life and clinic rehabilitation. Compared with the clinical environment, the daily life environment is more complex. Therefore, in this research, we pay more attention in analyzing the main features of the daily life environment, especially the ground. Generally, two main features of the ground influence the gait for normal walking, that is, hardness and terrain. Figure 2 shows the relationship between these two features and the common implementation environment. The typical materials in daily life have two relative features: for example, the typical features of marble ground are flat and hard.

2.2. Gait Analysis and Environment Detection for the AIDER. For healthy people, the gait is changed adaptively when they cross from one terrain to another. For instance, the gait will change when someone crosses from hard ground to sand. However, the AIDER works on a customized gait to realize the walking motion for SCI patients [15]. It would cause a

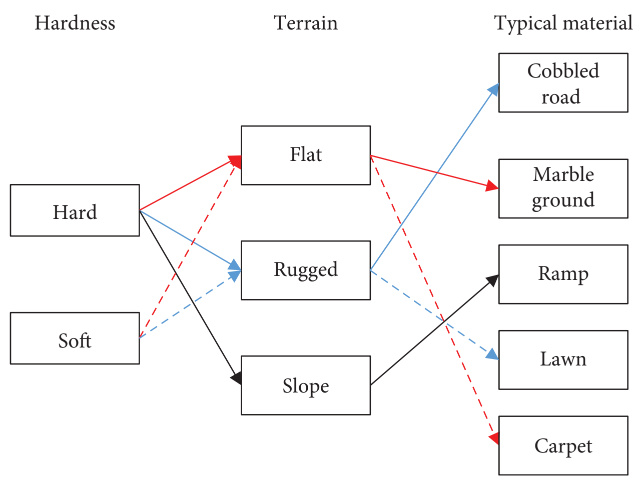

Figure 2: The common application environment for users of AIDER. The solid line and dotted line stand for hard and soft features, respectively; red, blue, and black denote flat, rugged, and slope features, respectively.

potential safety hazard because it cannot adapt to the change of terrains adaptively in a social environment.

Gait analysis mainly focuses on two parameters which are ground reaction force (GRF) and body posture. These two parameters can be utilized to confirm whether the system state is suitable for the next motion. For the stability control of biped robots, findings from [27] indicated that, comparing with a hard ground, step height tends to increase for avoiding collision between a robot's feet and soft ground. Besides, terrain features are also the essential factors for gait adjustment. For AIDER, the control strategy of stability not only depends on the system controller but also the environmental features. Typical environments for AIDER are shown in Figure 2. Therefore, we intend to design a wearable sensing system for AIDER which can be used to detect and recognize environmental features and CoP of the feet in this paper.

3. Method and Materials

3.1. Design Requirement of a Wearable Sensing System. Section 1 shows the benefit of a wearable sensing system for gait analysis and the safety of a human-machine system. Therefore, a wearable sensing system for the feet is proposed to realize gait analysis and environment detection. The following design requirements are proposed according to the features of a SCI patient:

(a) To make the user comfortable, the thickness of sole should be less than 20 mm.

(b) To ensure convenience, people should be able to put on the shoe using one hand.

(c) To ensure the accuracy for gait analysis, the magnitude of output force from the sensors should be obtained.

(d) To avoid the force from exceeding the acceptable range, the force measurement range of the wearable sensing system should be from 0 to at least 120 kg.

(e) To cut the cost, the hardware cost of the wearable sensing system should be less than ¥2000.

(f) To provide enough data for control strategies, the wearable sensing system should be designed to be able to detect and recognize ground features.

(g) Finally, the wearable sensing system needs to realize attitude measurement and gait analysis.

3.2. Design of the Wearable Sensing System. As proposed in Section 3.1, 7 design requirements should be met. The mechanical design of the wearable sensing system is shown in Figure 3. In Figure 3(a), there are 3 layers that form the sensing part for force detection. The bottom layer is constructed of wear-resistant rubber which is used to ensure that the pilot's foot does not slip. A hook and loop tape is used to fasten the foot. The middle layer is a holder for the force sensor. The total thickness of the 3 layers is 18 mm which can meet the conditions of requirement (a). Seven strain gauge force sensors are employed to sense the center of force in the z-axis. The top layer is used to install the 7 force sensors which are made of aluminum alloy. It is necessary to recognize the force for the heel and forefoot [27, 28]. Therefore, the top layer is made of two separated aluminum alloys. Three force sensors on the forefoot form a stable plane. The other 4 force sensors form a trapezoid to keep stable. The accuracy of each force sensor is about 0.1%. All the seven force sensors together are capable of high accuracy measurement. Because the range of a force sensor is about 25 kgf, the measured range of the wearable sensing system is about 175 kgf. The IMU sensors and control circuit are used to collect attitude data which is installed in the circuit box as shown in Figure 3(a). The connection rod is designed to link the wearable sensing system and the shanks of AIDER. To meet requirement (e), the cost of the wearable sensing system is listed in Table 2.

3.3. Force Measurement Experiment. To test the performance of our force sensing system in terms of accuracy and dynamic stability, a force measurement experiment was conducted. In this experiment, we used the force platforms to verify and calibrate the accuracy of the wearable sensing system. Figure 4 describes the setup of the force measurement experiment, where the pilot stands astraddle on two force platforms. During the experiment, the pilot shifts the support foot at the center of his body weight from the left to the right and then shifts back again to the left. The motion frequency is about 2 seconds. Finally, we used a wireless module to translate the data of the wearable sensing system to a PC for sensing system analysis. The experimental results are indicated in Figure 5. The red line indicates the output of the force plates and the blue line indicates the output of the wearable sensing system. This figure shows that the data from the shoes follow the data from the force plate with high

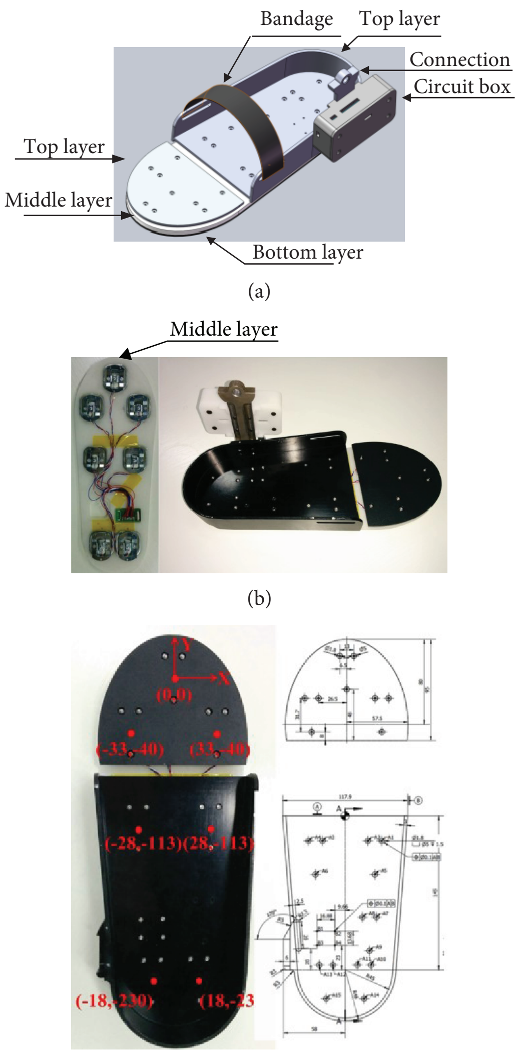

Figure 3: The mechanical structure of the wearable sensing system for AIDER. (a) The structure of the wearable sensing system. (b) The prototype of the wearable sensing system. (c) The coordinate system for the left foot.

Table 2: The cost of wearable sensing system.

Name	Unit cost	Unit	quantity	Total price/¥
IMU	25	piece	2	50
Force sensor	15	piece	14	210
Mechanical parts	500	Set	2	1000
Circuit board	100	Piece	4	400
Hook and loop tape	10	piece	2	20
Sum				1680

precision. With a shaking motion, the wearable system detected the body shaking accurately.

3.4. Center of Pressure (CoP). For biped locomotion control, ZMP (zero moment point) and CoP are two important criteria. CoP coincides with ZMP when the system is under a quasistatic state. Di et al. developed a cane robot to realize human fall detection by estimating the CoP [29]. In our research, CoP is also involved in AIDER for stability estimation of the human-machine system. To estimate the CoP of the human-machine system, the first step is to calculate the ground reaction force (GRF) and the CoP of the feet. According to [30], the CoP can be estimated by

$$\begin{aligned} X_{\text{CoP}} &= \frac{\int x \cdot F(x)dx}{\int F(x)dx}, \\ Y_{\text{CoP}} &= \frac{\int y \cdot F(y)dy}{\int F(y)dy}. \end{aligned} \tag{1}$$

Based on the mechanical design of the force sensory system, after being dispersed (1), the CoP of the foot is obtained by

$$\begin{aligned} X_{\text{CoP}} &= \frac{\sum x_i \cdot f_{ni}}{\sum f_{ni}}, \\ Y_{\text{CoP}} &= \frac{\sum y_i \cdot f_{ni}}{\sum f_{ni}}, \end{aligned} \tag{2}$$

where $P_i(x_i, y_i)$, $(i = 1, 2, \dots, 7)$ denotes the coordinate for each force sensor. f_{ni} denotes the force that is obtained by each force sensor. n is the mark for recognizing the left and right foot. Based on mechanical design, the coordinate of each sensor can be obtained by Figure 3(c).

A verification experiment is designed to prove the performance of a wearable sensing system for CoP detection. The experimental setup is similar to that in Figure 4. The difference is that the pilot is walking in a daily life state but on a force platform. Figure 6 showed the experimental results from the point when the heel touches the ground up to the point when the toe lifts from the ground. In this experiment, the trajectory transforms from the heel to the big toe as shown in Figure 6(a). Figure 6(b) shows the magnitude of the total force in the z-axis. The trajectory of CoP in the X-Y plane is shown in Figure 6(c). Based on [31], the trajectory of CoP agrees with human habit because of a similar curve.

4. Ground Characteristic Analysis and Recognition

4.1. Ground Characteristic Analysis. Based on Section 2, the main features of the application environment contain hardness and terrain. More specifically, soft/hard and flat/slope are two pairs of critical factors for a control strategy. After considering the environment in daily life, carpet, ramp, and marble ground are selected as the recognized subjects. For the ramp, uphill and downhill is the difference. For a flat ground, soft and hard is the main difference feature. Therefore, the main purpose of the wearable sensing system is to recognize the following combined features which are flat/hard (F/H), flat/soft (F/S), uphill/hard (U/H), and downhill/hard (D/H).

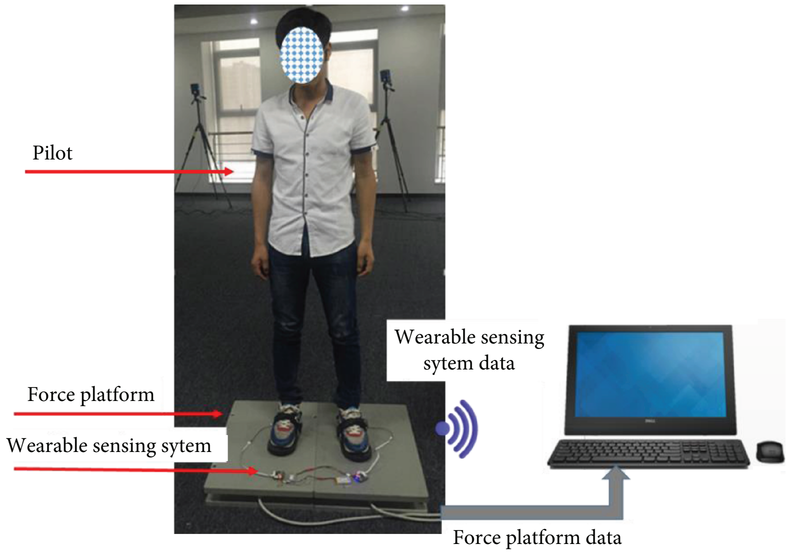

FIGURE 4: The setup of the stability test for a force measurement experiment.

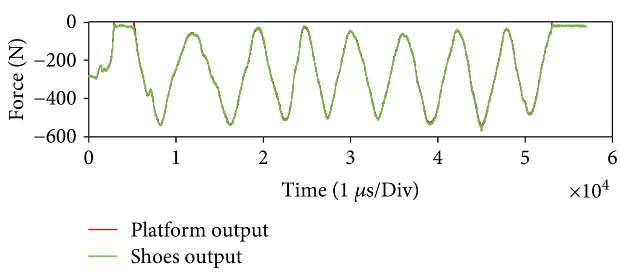

FIGURE 5: Results for the accuracy verification of a wearable sensing system.

To recognize these features, the data from the IMU and force sensor are necessary. Generally, a walking motion can be divided into 8 phases, that is, initial contact (IC), loading response (LR), midstance (MS), preswing (PS), initial swing (IS), midswing (MS), and terminal swing (TS) [24]. For a ramp, 3 force sensors are used in [32] to recognize the slope by adjusting the sequence of the force sensor output. The IC and LR phases contain impact information caused by the hardness of the ground. Therefore, the sensor data from the IC and LR phases are collected by the data window for feature recognition.

A total of 7 force sensors and one IMU is used to sense the ground features. The force of each sensor is f_{ni} ($i = 1, 2, \ldots, 7$). The output of the IMU sensor is angular velocity $\omega = \left[\omega_x \quad \omega_y \quad \omega_z\right]^T$ and acceleration $a = \left[a_x \quad a_y \quad a_z\right]^T$. To get a credible result, the gravitational acceleration is removed and the resultant force of the 7 sensors is normalized. To keep the data in the same magnitude, the force is multiplied with a scale factor. The drastic vibration makes the IC and LR phases easy to detect and the force output also increases. Therefore, according to the output of the force sensors, the data window for feature recognition is obtained as shown in Figure 7.

4.2. Principal Component Analysis (PCA) for the Four Ground Feature Extraction. PCA is a data analysis method that uses an orthogonal transformation to obtain principal components which are used to present the original data feature by a low-dimensional variable. As a popular pattern recognition method, PCA is widely used in face recognition [33]. This method is aimed at reducing the dimension for the eigenvector. In our research, the dimension of the eigenvector for an environmental feature extraction is 30 which contains the sum, mean, and variance of the 7 normalized force sensor output and 3-axis motion acceleration. After analyzing the data by PCA, the variance that explains principal components are obtained.

According to the result of Figures 8–11, the variance that explained the first three principal components is more than 85%. Therefore, the first three principal components are enough to distinguish the four ground features. Figures 8 and 9 particularly show that the uphill and downhill motions are easy to describe using the first 2 principal components. In Figures 9 and 10, the variance explained on the third principal component is more than 10%. The results indicate that the soft and hard features are relatively complex. Finally, the ground features are described by the first three and two principal components in Figures 12 and 13, respectively.

Due to the four ground features, it is easy to classify the minimum-distance classifier [34] which is employed to classify the four features.

4.3. Experiments. To verify the performance of the recognition method, 5 experimental subjects wore the wearable sensing system and walked on carpet, ramp (uphill and downhill), and flat ground surface in a normal gait, and about 2000 steps were obtained. After preprocessing, half of data are used as training data. The left part is used for testing the training model, and the experimental results are obtained as shown in Figure 14. The black circles indicate the points that are not classified in features on the right.

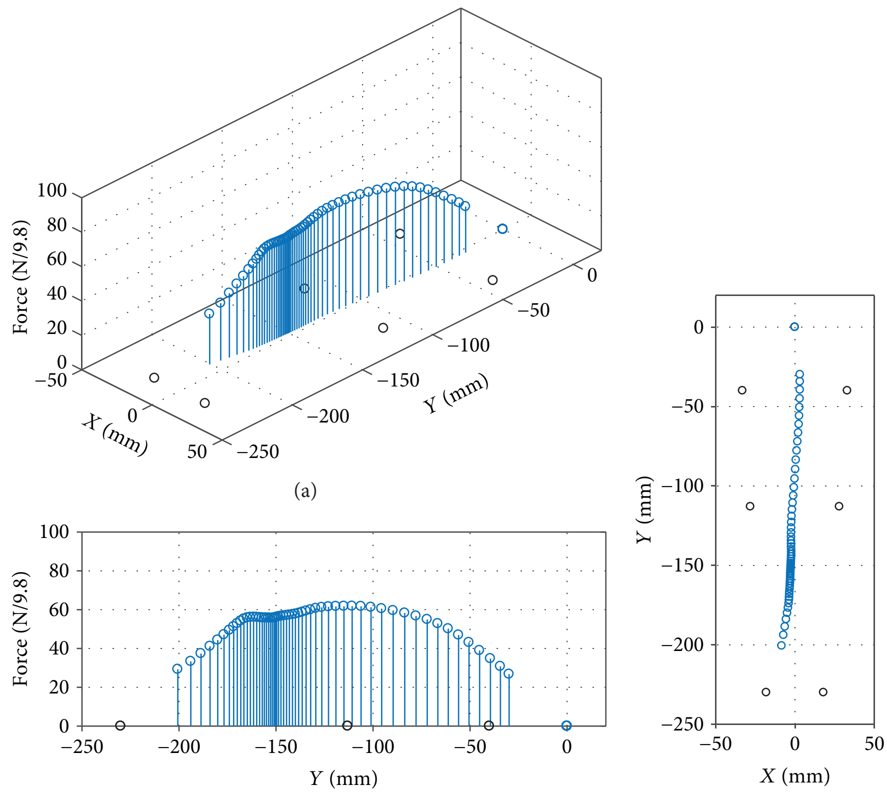

Figure 6: The CoP for the left foot; the black circle denotes the pressure-bearing point. (a) The trajectory of the CoP. (b) The magnitude of the total force during contact of the left foot to the ground. (c) The trajectory of CoP when the heel touches the ground up to point when the toe lifts from the ground.

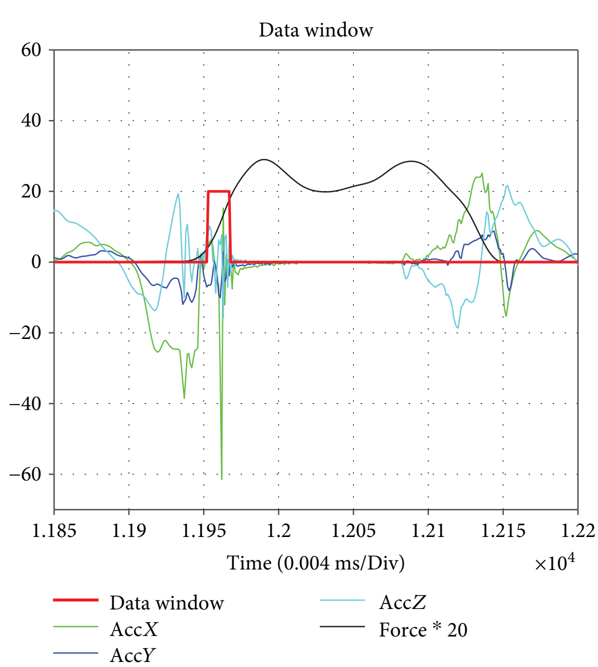

Figure 7: Data window for the feature extraction. The force multiplied by 20 is the aim for analyzing in the same magnitude.

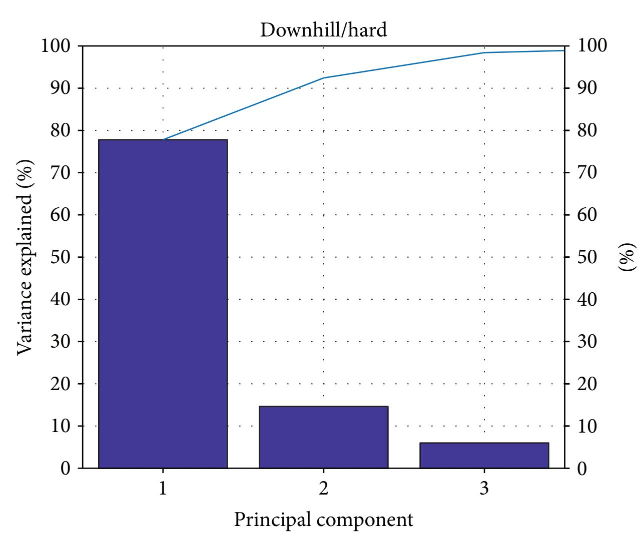

Figure 8: The relationship between the principal component and the variance explained for D/H.

Finally, the recognition rate for 4 ground features is listed in Table 3. The recognition rate of hard/flat ground and downhill/hard ground is more than 95%. This result shows that the eigenvector which is extracted by PCA and the minimum-distance classifier is suitable for the ground feature recognition.

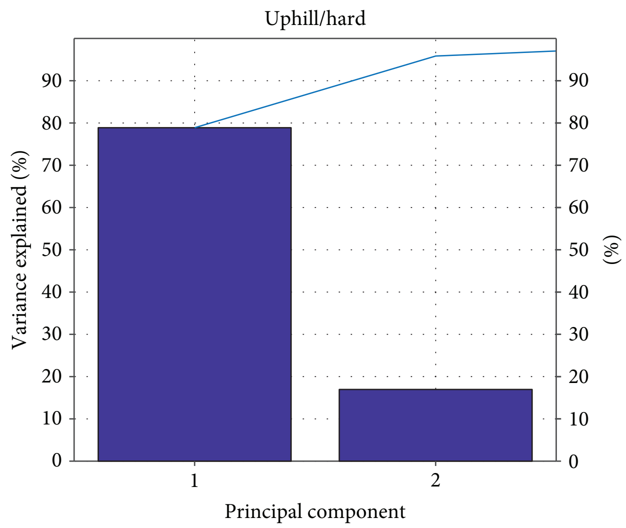

Figure 9: The relationship between the principal component and the variance explained for U/H.

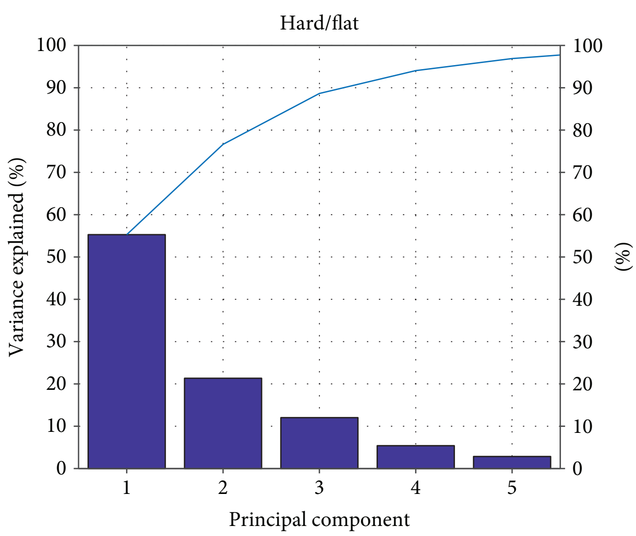

Figure 10: The relationship between the principal component and the variance explained for H/F.

5. Discussion

A mechanical design has been proposed in Section 3.2 that meets design requirements (a), (b), (d), and (e). To meet design requirement (c), 7 force sensors were used to form a force measurement plate. The force sensor can bear the weight of a pilot. The main contribution of this research is that ground feature detection and recognition were realized which is mentioned in requirements (f) and (g). Attitude and force data were combined to get the data window which is used to analyze the ground features. Besides, the main work of the IMU is to obtain the attitude data for the shoes. The detection result is also the effect of the properties of the material used in the bottom layer. The rubber layer can absorb the noise from the motion of touching the ground.

PCA and the minimum-distance classifier are involved in realizing the ground feature recognition. Four classical

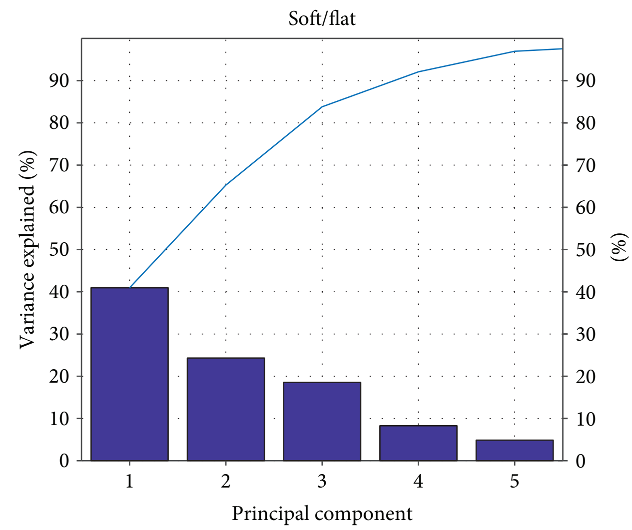

Figure 11: The relationship between the principal component and the variance explained for S/F.

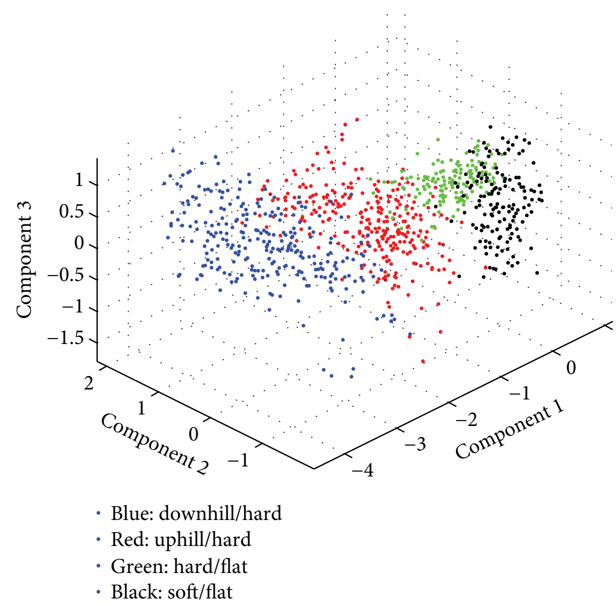

Figure 12: The four ground features are described by the first three principal components.

terrains are involved in this paper. However, the daily life environment is more complex than an experiment. The data in Table 3 indicates the accuracy of the ground feature recognition. The maximum error is about 5.3% which occurred on soft and hard ground feature detection. An error of about 4.4% occurred in the up and down features.

6. Conclusions and Future Work

In this work, we introduced the application environment for AULLE, RELLE, and ASLLE respectively. As an ASLEE, AIDER is used to help SCI patients return to a normal life. We proposed a wearable sensing system that is able to improve the flexibility and safety of the pilot by detecting gait

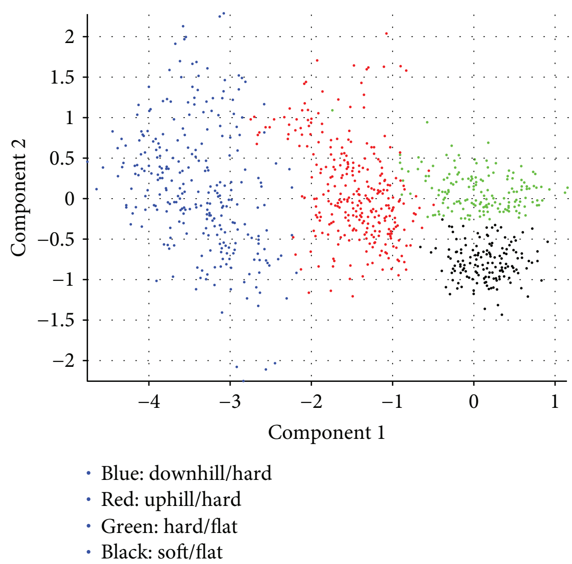

Figure 13: The four ground features are described by the first two principal components.

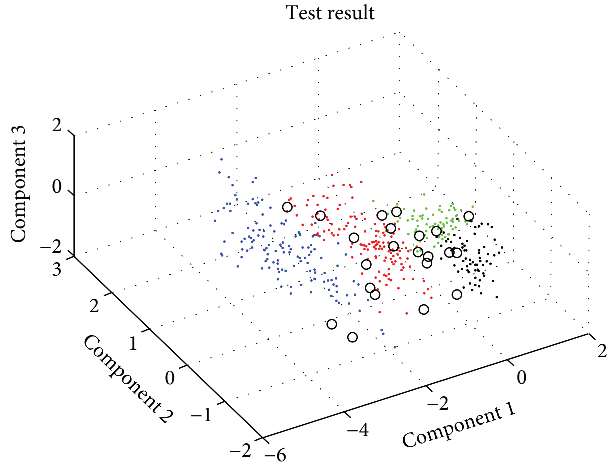

Figure 14: The recognition results for the 4 ground features.

Table 3: The recognition rate for the 4 features.

	D/H	U/H	H/F	S/F
D/H	95.620%	4.380%	0	0
U/H	0.680%	93.878%	2.721%	2.721%
H/F	0	3.448%	96.552%	0
S/F	0	0	5.333%	94.667%

and GRF. The mechanical design of the wearable sensing shoes is proposed to fulfill the design requirements. Seven force sensors are used to form two rigid planes to detect the GRF that showed a good performance on force and CoP detection. The IMU sensor was installed on the wearable sensing system to sense the attitude and acceleration data which were calculated for ground feature recognition. A verification experiment of the wearable sensing system was executed to test the performance for CoP detection. The results indicated that the wearable sensing system is able to realize human gait trajectory detection, and the trajectory trend of CoP agrees with the normal human trajectory. PCA is involved in ground feature recognition because of the large dimension of the eigenvector. The analysis result showed that the first three principal components are enough for the uphill/hard, downhill/hard, hard/flat, and soft/flat ground feature extraction. Finally, a test was carried out to verify the recognition performance, and the results showed that the recognition rate is more than 93%.

In the future, more environmental situations should be considered into the recognition experiment to verify the performance of the wearable sensing system, for example, a road made of sand and cobblestones. Until now, the recognition algorithm is still executed on a PC, which is not convenient for real time work.

Data Availability

The data used to support the findings of this study are available from the corresponding author upon request.

Conflicts of Interest

The authors declare that there is no conflict of interests regarding the publication of this paper.

Acknowledgments

This research project is supported by the National Key Research and Development Plan (2017YFB1302300) and the National Natural Science Foundation of China (nos. U1613223 and 61503060).

References

[1] A. B. Zoss, H. Kazerooni, and A. Chu, "Biomechanical design of the Berkeley lower extremity exoskeleton (BLEEX)," *IEEE/ASME Transactions on Mechatronics*, vol. 11, no. 2, pp. 128–138, 2006.

[2] R. Steger, S. H. Kim, and H. Kazerooni, "Control scheme and networked control architecture for the Berkeley lower extremity exoskeleton (BLEEX)," in *Proceedings 2006 IEEE International Conference on Robotics and Automation, 2006. ICRA 2006*, pp. 3469–3476, Orlando, FL, USA, May 2006.

[3] C. Teng, Z. Wong, W. Ten, and Y. Chong, "Design and development of inexpensive pneumatically-powered assisted knee-ankle-foot orthosis for gait rehabilitation-preliminary finding," in *2012 International Conference on Biomedical Engineering (ICoBE)*, Penang, Malaysia, February 2012.

[4] Y. Eguchi, H. Kadone, and K. Suzuki, "Standing mobility device with passive lower limb exoskeleton for upright locomotion," *IEEE/ASME Transactions on Mechatronics*, vol. 23, no. 4, pp. 1608–1618, 2018.

[5] T. Vouga, K. Z. Zhuang, J. Olivier et al., "EXiO—A brain-controlled lower limb exoskeleton for rhesus macaques," *IEEE Transactions on Neural Systems and Rehabilitation Engineering*, vol. 25, no. 2, pp. 131–141, 2017.

[6] M. Munera, A. Marroquin, L. Jimenez et al., "Lokomat therapy in Colombia: current state and cognitive aspects," in *2017*

International Conference on Rehabilitation Robotics (ICORR), pp. 394–399, London, UK, July 2017.

[7] M. Talaty, A. Esquenazi, and J. E. Briceño, "Differentiating ability in users of the ReWalk™ powered exoskeleton," in *2013 IEEE 13th International Conference on Rehabilitation Robotics (ICORR)*, pp. 1–5, Seattle, WA, USA, June 2013.

[8] P. N. Gad, Y. P. Gerasimenko, S. Zdunowski et al., "Iron 'ElectriRx' man: overground stepping in an exoskeleton combined with noninvasive spinal cord stimulation after paralysis," in *2015 37th Annual International Conference of the IEEE Engineering in Medicine and Biology Society (EMBC)*, pp. 1124–1127, Milan, Italy, August 2015.

[9] Y. Sankai, "Hal: hybrid assistive limb based on cybernics," in *Robotics Research. Springer Tracts in Advanced Robotics, vol 66*, M. Kaneko and Y. Nakamura, Eds., pp. 25–34, Springer, Berlin, Heidelberg, 2010.

[10] http://www.suitx.com.

[11] A. D. Gardner, J. Potgieter, and F. K. Noble, "A review of commercially available exoskeletons' capabilities," in *2017 24th International Conference on Mechatronics and Machine Vision in Practice (M2VIP)*, Auckland, New Zealand, November 2017.

[12] P. Asselin, S. Knezevic, S. Kornfeld et al., "Heart rate and oxygen demand of powered exoskeleton-assisted walking in persons with paraplegia," *Journal of Rehabilitation Research and Development*, vol. 52, no. 2, pp. 147–158, 2015.

[13] L. A. Rapp, V. Huang, S. Firpi, L. Tovar, J. M. Zanca, and J. Baeza-Dager, "The age of the bionic man has arrived: the use of Ekso exoskeleton in acute paraplegia," *The Journal of Spinal Cord Medicine*, vol. 36, no. 5, pp. 504–523, 2013.

[14] M. K. Duong, H. Cheng, H. T. Tran, and Q. Jing, "Minimizing human-exoskeleton interaction force using compensation for dynamic uncertainty error with adaptive RBF network," *Journal of Intelligent & Robotic Systems*, vol. 82, no. 3-4, pp. 413–433, 2016.

[15] R. Huang, H. Cheng, Q. Chen, H.-T. Tran, and X. Lin, "Interactive learning for sensitivity factors of a human-powered augmentation lower exoskeleton," in *2015 IEEE/RSJ International Conference on Intelligent Robots and Systems (IROS)*, pp. 6409–6415, Hamburg, Germany, September-October 2015.

[16] R. Huang, H. Cheng, H. Guo, Q. Chen, and X. Lin, "Hierarchical interactive learning for a human-powered augmentation lower exoskeleton," in *2016 IEEE International Conference on Robotics and Automation (ICRA)*, pp. 257–263, Stockholm, Sweden, May 2016.

[17] X. Shu, H. Cheng, and X. Lin, "Adaptive stair-ascending and stair-descending strategies for powered lower limb exoskeleton," in *2017 IEEE International Conference on Mechatronics and Automation (ICMA)*, pp. 1579–1584, Takamatsu, Japan, August 2017.

[18] Q. Chen, H. Cheng, C. Zou, R. Huang, and H. Guo, "Intention recognition for exoskeleton," in *2017 2nd International Conference on Advanced Robotics and Mechatronics (ICARM)*, pp. 535–539, Hefei, China, August 2017.

[19] C. Yue, H. Cheng, Y. Chen, Q. Deng, and X. Lin, "Design of a wearable sensing system for a lower extremity exoskeleton," in *2017 IEEE International Conference on Mechatronics and Automation (ICMA)*, pp. 464–468, Takamatsu, Japan, August 2017.

[20] S. Yan, W. Ren, X. Liang, and K. Zhang, "Gait characteristics of overweight and obese children with different ages," in *2014 7th International Conference on Biomedical Engineering and Informatics*, pp. 184–188, Dalian, China, October 2014.

[21] H. M. Schepers, E. van Asseldonk, J. H. Buurke, and P. H. Veltink, "Ambulatory estimation of center of mass displacement during walking," *IEEE Transactions on Biomedical Engineering*, vol. 56, no. 4, pp. 1189–1195, 2009.

[22] G. Li, T. Liu, J. Yi, H. Wang, J. Li, and Y. Inoue, "The lower limbs kinematics analysis by wearable sensor shoes," *IEEE Sensors Journal*, vol. 16, no. 8, pp. 2627–2638, 2016.

[23] T. Liu, Y. Inoue, K. Shibata, and K. Shiojima, "Three-dimensional lower limb kinematic and kinetic analysis based on a wireless sensor system," in *2011 IEEE International Conference on Robotics and Automation*, pp. 842–847, Shanghai, China, May 2011.

[24] S. J. M. Bamberg, A. Y. Benbasat, D. M. Scarborough, D. E. Krebs, and J. A. Paradiso, "Gait analysis using a shoe-integrated wireless sensor system," *IEEE Transactions on Information Technology in Biomedicine*, vol. 12, no. 4, pp. 413–423, 2008.

[25] M. Pazzaglia and M. Molinari, "The embodiment of assistive devices-from wheelchair to exoskeleton," *Physics of Life Reviews*, vol. 16, pp. 163–175, 2016.

[26] P. J. O'Connor, "Trends in spinal cord injury," *Accident Analysis & Prevention*, vol. 38, no. 1, pp. 71–77, 2006.

[27] K. Hashimoto, H. Kang, M. Nakamura et al., "Realization of biped walking on soft ground with stabilization control based on gait analysis," in *2012 IEEE/RSJ International Conference on Intelligent Robots and Systems*, pp. 2064–2069, Vilamoura, Portugal, October 2012.

[28] M. K. Shepherd and E. J. Rouse, "The VSPA foot: a quasi-passive ankle-foot prosthesis with continuously variable stiffness," *IEEE Transactions on Neural Systems and Rehabilitation Engineering*, vol. 25, no. 12, pp. 2375–2386, 2017.

[29] P. Di, J. Huang, S. Nakagawa, K. Sekiyama, and T. Fukuda, "Fall detection for elderly by using an intelligent cane robot based on center of pressure (COP) stability theory," in *2014 International Symposium on Micro-NanoMechatronics and Human Science (MHS)*, pp. 1–4, Nagoya, Japan, November 2014.

[30] T. T. Pham, S. T. Moore, S. J. G. Lewis et al., "Freezing of gait detection in Parkinson's disease: a subject-independent detector using anomaly scores," *IEEE Transactions on Biomedical Engineering*, vol. 64, no. 11, pp. 2719–2728, 2017.

[31] A. De Cock, J. Vanrenterghem, T. Willems, E. Witvrouw, and D. De Clercq, "The trajectory of the centre of pressure during barefoot running as a potential measure for foot function," *Gait & Posture*, vol. 27, no. 4, pp. 669–675, 2008.

[32] K. Suwanratchatamanee, M. Matsumoto, and S. Hashimoto, "Haptic sensing foot system for humanoid robot and ground recognition with one-leg balance," *IEEE Transactions on Industrial Electronics*, vol. 58, no. 8, pp. 3174–3186, 2011.

[33] W. Xueyun and Z. Wei, "Application of kernel PCA for foetal ECG estimation," *Electronics Letters*, vol. 54, no. 6, pp. 340–342, 2018.

[34] S. Bag and G. Sanyal, "An efficient face recognition approach using PCA and minimum distance classifier," in *2011 International Conference on Image Information Processing*, pp. 1–6, Shimla, India, November 2011.

Hindawi
Applied Bionics and Biomechanics
Volume 2018, Article ID 9737418, 10 pages
https://doi.org/10.1155/2018/9737418

Research Article

Muscle Coordination Control for an Asymmetrically Antagonistic-Driven Musculoskeletal Robot Using Attractor Selection

Shoichiro Ide[1] and Atsushi Nishikawa[2,3]

[1]*Interdisciplinary Graduate School of Science and Technology, Shinshu University, Ueda 386-8567, Japan*
[2]*Faculty of Textile Science and Technology, Shinshu University, Ueda 386-8567, Japan*
[3]*Division of Biological and Medical Fibers, Institute for Fiber Engineering (IFES), Interdisciplinary Cluster for Cutting Edge Research (ICCER), Shinshu University, Ueda 386-8567, Japan*

Correspondence should be addressed to Atsushi Nishikawa; nishikawa@shinshu-u.ac.jp

Received 31 March 2018; Revised 21 June 2018; Accepted 5 July 2018; Published 12 September 2018

Academic Editor: Dongming Gan

Recently, numerous musculoskeletal robots have been developed to realize the flexibility and dexterity analogous to human beings and animals. However, because the arrangement of many actuators is complex, the design of the control system for the robot is difficult and challenging. We believe that control methods inspired by living things are important in the development of the control systems for musculoskeletal robots. In this study, we propose a muscle coordination control method using attractor selection, a biologically inspired search method, for an antagonistic-driven musculoskeletal robot in which various muscles (monoarticular muscles and a polyarticular muscle) are arranged asymmetrically. First, muscle coordination control models for the musculoskeletal robot are built using virtual antagonistic muscle structures with a virtually symmetric muscle arrangement. Next, the attractor selection is applied to the control model and subsequently applied to the previous control model without muscle coordination to compare the control model's performance. Finally, position control experiments are conducted, and the effectiveness of the proposed muscle coordination control and the virtual antagonistic muscle structure is evaluated.

1. Introduction

Human beings and animals move flexibly and dexterously by controlling their musculoskeletal system with the brain. To understand and imitate the flexible and dexterous motion of human beings and animals, several musculoskeletal robots have recently been developed. The primary driving mechanism in musculoskeletal robots is a tendon-driven assembly using motors [1, 2] or pneumatic artificial muscles (PAMs). In particular, using PAMs as actuators enables flexible movement of the musculoskeletal robot compared with conventional robots that use motors because the compressibility and low viscosity of air provide compliance and rapid contraction. The extremely high power-to-weight ratio of the PAM is also good for flexible and dynamic motion.

The musculoskeletal robot comprises antagonistic-driven systems. An antagonistic-driven system includes two or more actuators for joint movement. The actuators are antagonistically arranged around one link, and their output characteristics and arrangements are, for the most part, symmetrical.

Many studies have proposed the musculoskeletal robots comprising this simple antagonistic system, and various control methods (e.g., PID control, neural network, and fuzzy logic) have also been proposed for musculoskeletal robots [3–8]. However, the drive system of our musculoskeletal robot [9] differs from a simple antagonistic-driven system because the output characteristics and the arrangements of the actuators of the robot are not symmetrical.

This robot has two kinds of PAM actuators, a monoarticular muscle that drives one joint and a polyarticular muscle that drives multiple joints consecutively. Therefore, the mechanism that drives each joint is not symmetrical. Furthermore, the actuators are not arranged symmetrically, although each actuator is antagonistically arranged around each link. Since each actuator is not arranged symmetrically and the sensors for measuring each joint angle are not arranged, design of the control system for the robot is more difficult and challenging.

Honda et al. [9, 10] proposed a biologically inspired control method using muscle coordination for the robot. They hypothesized that human beings use the synergies between antagonistic muscle pairs when joints move, and they defined two parameters, the antagonistic muscle ratio and the antagonistic muscle activity, as the key parameters in human muscle coordination. The parameters are computed by a PID controller [10] and are implemented to control the angle of the robot's joints.

Although good control performance was obtained for one joint, the controller did not work well for multiple joints of the robot [9]. An adaptive method that dynamically and adaptively searches the parameters for muscle coordination was required because PAMs have time variance, compliance, high hysteresis, and nonlinearity. In general, this search problem can be formulated as a combinatorial optimization problem of minimizing an object function subject to the search variables, which requires a precise model (object function) in advance, but system identification against an asymmetrically antagonistic-driven PAM system having nonlinear dynamics is difficult.

As an alternative to such a model-based theoretical approach, we believe that heuristic control methods inspired from living things are important for the control of the musculoskeletal robot. The musculoskeletal structures of human beings and animals are antagonistic-driven systems. They are also asymmetrically antagonistic-driven systems because monoarticular muscles and polyarticular muscles are arranged around various joints. Human beings and animals move flexibly by controlling their various muscles dexterously.

Recent research about the mechanisms of living things indicates that a biological system behaves flexibly using noise [11]. *Escherichia coli* (*E. coli*) cells usually prefer to switch to an adaptive attractor using noise to survive better in a new external environment after the environmental conditions have been changed. This adaptive behavior of the *E. coli* cells is known as attractor selection [12]. The novel control method based on the attractor selection has been proposed and applied to a signal-control method for traffic networks [13], network management [14, 15], android motion generation [16], robot navigation and locomotion [17–19], robotic arm control [20–22], and endoscopic surgery [23].

The control method was described by a stochastic differential equation, input variables for the network systems or robots were computed by solving the equation, and the systems accomplished the tasks without the dynamics and model of the systems and environments. Since the attractor selection is conducted adaptively using noise in the systems or environments, the control method is robust for changes of tasks and environments. Attractor selection was applied to an asymmetrically antagonistic-driven musculoskeletal robot (Figure 1) with muscles arranged asymmetrically [24]. From the control experiment, the position of the tip of the robot was moved to the desired position by searching pressure for four PAMs individually using the attractor selection. The control time had to be more than 100 s to accomplish tasks. Therefore, modification of the control method is required to accomplish tasks quickly.

In this study, we propose a novel muscle coordination control method for the asymmetrically antagonistic-driven musculoskeletal robot using the attractor selection. The primary difference between the previous method [24] and the proposed one is that the proposed method introduced a virtual antagonistic muscle structure as a muscle coordination control model. Instead of individually and directly searching the PAM pressure in the actual asymmetric antagonistic muscle structure, the new method indirectly searches pressure for actual PAMs via a virtual symmetric antagonistic muscle structure.

First, muscle coordination control models of the musculoskeletal robot were built using virtual antagonistic muscle structures with a virtually symmetric arrangement of muscles. Next, the attractor selection was applied to the control model and also applied to the previous control model without the muscle coordination to compare control performance. Finally, position control experiments were conducted, and the effectiveness of the proposed muscle coordination control applied attractor selection and the virtual antagonistic muscle structure was evaluated.

2. Materials and Methods

2.1. Purpose: Control of the Position of an Asymmetrically Antagonistic-Driven Musculoskeletal Robot. In this study, a five-fingered robot hand (Figure 1(a)) inspired by the right hand of a human being was used, and the position of the tip of the index finger of the robot hand was controlled as a musculoskeletal robot. Figure 1(b) shows the structure of the index finger. It has a three-degrees-of-freedom mechanism that is formed by four links (a distal phalange, an intermediate phalange, a proximal phalange, and a metacarpal) and three joints (distal interphalangeal (DIP), proximal interphalangeal (PIP), and metacarpophalangeal (MP)). Four PAMs are used: one actuator on the intermediate phalange, one on the proximal phalange, and two on the metacarpal for flexion and extension. The actuator for extension (referred to as the "extensor") is a polyarticular muscle in which wire covers all joints. Therefore, the number of actuators for flexion and extension is not symmetrical.

Let P_{e}, P_{MPf}, P_{PIPf}, and P_{DIPf} be the pressure supplied to the muscles A, B, C, and D, respectively, in Figure 1. The subscript "e" indicates the extensor, "MPf" indicates the flexor (the actuator for flexion) for driving the MP joint, "PIPf" indicates the flexor for driving the PIP joint, and "DIPf" indicates the flexor for driving the DIP joint, and they are calculated as follows:

$$P_{\mathrm{e}} = P_{\max} \cdot x_{\mathrm{e}}, \quad (1)$$

$$P_{\mathrm{MPf}} = P_{\max} \cdot x_{\mathrm{MPf}}, \quad (2)$$

$$P_{\mathrm{PIPf}} = P_{\max} \cdot x_{\mathrm{PIPf}}, \quad (3)$$

$$P_{\mathrm{DIPf}} = P_{\max} \cdot x_{\mathrm{DIPf}}, \quad (4)$$

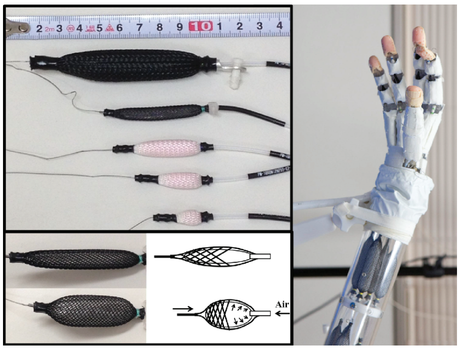

(a)

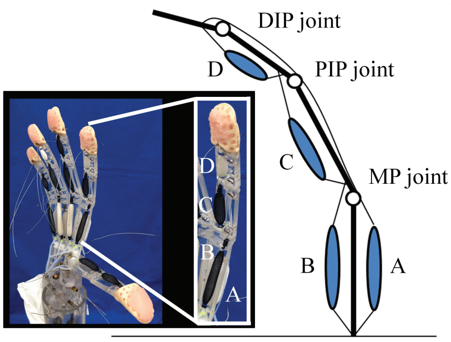

(b)

Figure 1: Control target and purpose. (a) Our five-fingered robot hand (right photograph) and pneumatic artificial muscles (PAMs) (left photographs) used as the actuator of the robot hand. These muscles are the McKibben actuator made in SQUSE Inc. and are driven by supplied compressed air (bottom-left pictures). (b) The structure of the index finger of the robot hand (the image and the closed photograph in the inset). The position of the tip of the index finger is controlled as a musculoskeletal robot. Various muscle lengths shown in (a) are arranged on the links of the index finger (they are also arranged for other fingers). The muscles A and B are of the same length. The muscle C is shorter than muscle A or B, and the muscle D is the shortest of all muscles on the finger. Each joint is driven from 0 deg (maximum extended state) to 90 deg (maximum flexed state).

where $x_{\mathrm{e}}(\in[0,1])$, $x_{\mathrm{MPf}}(\in[0,1])$, $x_{\mathrm{PIPf}}(\in[0,1])$, and x_{DIPf} $(\in[0,1])$ are the normalized search variables and $P_{\max}$ is the maximum pressure supplied to the actuator. Since the actuators of the robot hand break if a pressure of more than 0.2 MPa is supplied, the value of $P_{\max}$ is set to 0.19 MPa.

2.2. Muscle Coordination Hypothesis. Honda et al. suggested the hypothesis that muscle coordination of human beings is a coordination of antagonistic muscles (the extensor and flexor) [9, 10]. They express the ratio of the coordination using two parameters, the antagonistic muscle ratio (Ar) and antagonistic muscle activity (Ac). The Ar is the value that regulates the ratio of pressure (P_{e} and P_{f}) between the antagonistic muscle e (the extensor) and f (the flexor). Ar is calculated between 0 and 1 and is defined as follows:

$$\mathrm{Ar}=\frac{P_{\mathrm{e}}}{P_{\mathrm{e}}+P_{\mathrm{f}}}. \tag{5}$$

Ac is the sum of pressure for the extensor e and the flexor f and is calculated by

$$\mathrm{Ac}=P_{\mathrm{e}}+P_{\mathrm{f}}. \tag{6}$$

In this study, Ac is always set to the maximum pressure for driving joints sufficiently. That is,

$$\mathrm{Ac}=P_{\max}. \tag{7}$$

Pressures P_{e} and P_{f} are calculated from (5), (6), and (7).

$$P_{\mathrm{e}}=P_{\max}\cdot\mathrm{Ar}, \tag{8}$$

$$P_{\mathrm{f}}=P_{\max}\cdot(1-\mathrm{Ar}). \tag{9}$$

Equations (8) and (9) show that the pressures of the extensor and the flexor are determined by searching for the normalized variable $\mathrm{Ar}\in[0,1]$. Figure 2(a) shows the principle of muscle coordination using the antagonistic muscle ratio Ar and antagonistic muscle activity Ac.

2.3. Two Types of Virtual Antagonistic Muscle Structures. Four actuators were used in the musculoskeletal robot: the polyarticular muscle was used as the extensor and three monoarticular muscles were used as the flexor (Figure 1(b)). To calculate the pressure for each actuator based on the muscle coordination hypothesis, two methods that make the total number of extensors and flexors match virtually are proposed.

The first method is composed as follows. The virtual antagonistic muscle structure (Figure 2(b)) is composed so that the number of extensors is increased from one to three extensors. Next, Ar is applied to each antagonistic muscle to drive each joint. Hence, Ar is described as $\mathrm{Ar}_{\mathrm{MP}}$, $\mathrm{Ar}_{\mathrm{PIP}}$, and $\mathrm{Ar}_{\mathrm{DIP}}$, and the pressures for the extensor and the flexor at each antagonistic muscle for driving each joint are denoted as P_{MPe}, P_{MPf}, P_{PIPe}, P_{PIPf}, P_{DIPe}, and P_{DIPf}. The pressures are calculated as follows:

$$P_{\mathrm{MPe}}=P_{\max}\cdot\mathrm{Ar}_{\mathrm{MP}}, \tag{10}$$

$$P_{\mathrm{PIPe}}=P_{\max}\cdot\mathrm{Ar}_{\mathrm{PIP}}, \tag{11}$$

$$P_{\mathrm{DIPe}}=P_{\max}\cdot\mathrm{Ar}_{\mathrm{DIP}}, \tag{12}$$

$$P_{\mathrm{MPf}}=P_{\max}\cdot(1-\mathrm{Ar}_{\mathrm{MP}}), \tag{13}$$

$$P_{\mathrm{PIPf}}=P_{\max}\cdot(1-\mathrm{Ar}_{\mathrm{PIP}}), \tag{14}$$

$$P_{\mathrm{DIPf}}=P_{\max}\cdot(1-\mathrm{Ar}_{\mathrm{DIP}}). \tag{15}$$

Finally, P_{e} that applies to the real extensor on the real form (Figure 2(d)) is calculated using

$$P_{\mathrm{e}}=\frac{1}{3}(P_{\mathrm{MPe}}+P_{\mathrm{PIPe}}+P_{\mathrm{DIPe}}). \tag{16}$$

The second method is distinguishable in the following ways. First, the other virtual antagonistic muscle structure (Figure 2(c)) reduces the number of flexors to one. Next, Ar is applied to the virtual antagonistic muscle structure, and the pressures P_{e} for the virtual extensor and P_{f} for the virtual flexor are calculated using (8) and (9). Here, P_{f} is the total

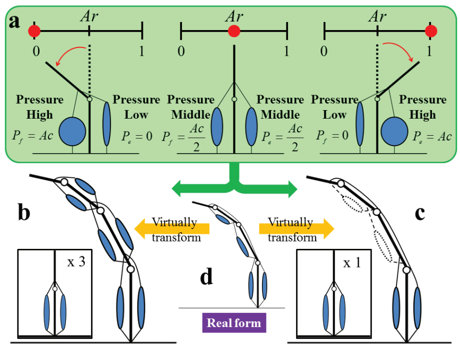

Figure 2: Muscle coordination and two types of virtual antagonistic muscle structures. (a) Principle of the muscle coordination using the antagonistic muscle ratio Ar and the antagonistic muscle activity Ac. When Ar is 0 (left picture), the pressure for the flexor is high ($P_{\mathrm{f}} = \mathrm{Ac}$) and the extensor is low ($P_{\mathrm{e}} = 0$). When Ar is 0.5 (middle picture), the pressure for the flexor and the extensor is identical ($P_{\mathrm{f}} = P_{\mathrm{e}} = \mathrm{Ac}/2$). When Ar is 1 (right picture), the pressure for the flexor is low ($P_{\mathrm{f}} = 0$) and the extensor is high ($P_{\mathrm{e}} = \mathrm{Ac}$). Therefore, the pressures of the extensor and the flexor are determined by searching for the normalized variable $\mathrm{Ar} \in [0, 1]$. (b) One of the virtual antagonistic structures. Two muscles are added virtually to the musculoskeletal system (shown in (d)) to form a symmetrically antagonistic arrangement on the intermediate phalange and the proximal phalange. Therefore, the virtual antagonistic structure has three simple antagonistic muscle structures (inset picture in (b)). (c) The other virtual antagonistic muscle structure. Two muscles on the intermediate phalange and the proximal phalange are decreased virtually from the musculoskeletal robot (shown in (d)), and the muscles are symmetrically arranged on the metacarpal. Therefore, the virtual antagonistic structure has one simple antagonistic muscle structure (inset picture in (c)). (d) The real form of the musculoskeletal robot that is controlled. The value of Ar (shown in (a)) is applied to the virtual antagonistic structure (shown in (b) or (c)) virtually transformed from the musculoskeletal robot (shown in (d)).

pressure for the three real flexors (P_{MPf}, P_{PIPf}, and P_{DIPf}) and is defined as $P_{\mathrm{f}} \le P_{\max}$. Finally, P_{f} is distributed to the three real flexors on the real form (Figure 2(d)). Two distribution ratios ($\mathrm{Dr}_{\mathrm{MP}}$ and $\mathrm{Dr}_{\mathrm{PIP}}$) are used, and the pressure for the three real flexors is calculated by

$$P_{\mathrm{MPf}} = P_{\mathrm{f}} \cdot \mathrm{Dr}_{\mathrm{MP}}, \tag{17}$$

$$P_{\mathrm{PIPf}} = \left(P_{\mathrm{f}} - P_{\mathrm{MPf}}\right) \cdot \mathrm{Dr}_{\mathrm{PIP}}, \tag{18}$$

$$P_{\mathrm{DIPf}} = P_{\mathrm{f}} - \left(P_{\mathrm{MPf}} + P_{\mathrm{PIPf}}\right). \tag{19}$$

Pressure for the real extensor is the same as that for the virtual extensor and is calculated using (8).

2.4. Attractor Selection Model. Let us consider the combinatorial optimization problem of minimizing an object function $U(x)$ subject to the search variable $x \in \{X_1, X_2, \ldots, X_N\}$, where X_i is a feasible solution (an attractor) and N means the number of attractors. Rather than seek an optimal solution, we try to quickly find good approximate solutions. To accomplish this, our study uses the revised attractor selection model, which has been generalized as a stochastic differential equation [24]:

$$\frac{d}{dt}x(t) = f(x(t)) \cdot \mathrm{Activity}(t) + (1 - \mathrm{Activity}(t)) \cdot \eta(t), \tag{20}$$

where t is time, x is the search variable or state ($\in [0, 1]$ for our case), the value Activity ($\in [0, 1]$) is the degree of accomplishment of the task, η is assumed as noise, and $f(x)$ is the function that makes x converge to a suitable attractor. Typically, the function f can be represented as $f(x) = -\partial U(x)/\partial x$ if the objective function $U(x)$ is known precisely in advance.

This model searches for a solution (the attractor) that successfully accomplishes the task using noise, and the Acti vity makes the behavior of the total system change. Notice that as Activity increases, the term $f(x) \cdot \mathrm{Activity}$ becomes more dominant in (20) and the state transition becomes more deterministic. Consequently, state x tends to be entrained into a suitable attractor, where it remains despite the persistent noise. By contrast, decreasing the Activity increases the dominance of the noise η, thereby flattening the potential landscape. In this scenario, the transition becomes more probabilistic, like a random walk, and x is driven away from the attractor.

The function $f(x)$ can be designed freely, even if the objective function $U(x)$ is unknown or not precisely described. Two elements are required. The value of x must converge to the attractors, and the x must remain at a suitable attractor. To satisfy these elements, $f(x)$is defined as follows:

$$f(x) \equiv \sum_{i=0}^{N-1} \frac{k_d^2}{\left(X_i - x\right)^2 + k_w^2} \cdot \frac{X_i - x}{\left\|X_i - x\right\|}, \tag{21}$$

where X_i is the ith attractor, N is the number of attractors, k_d is the power that attracts x, and k_w is the range in which the attractor's power k_d is effective.

2.5. Employing the Attractor Selection to Determine the Pressure Supplied to Each Actuator. The selection of the attractor is employed to determine the pressure supplied to each actuator. The three methods used to determine the pressure using attractor selection are presented as follows.

The first method uses the real musculoskeletal structure (Figure 2(d)) and directly calculates the four pressures by searching for the four variables (x_{e}, x_{MPf}, x_{PIPf}, and x_{DIPf}) using the attractor selection. We refer to this as a pressure search-type controller. The pressure supplied to each actuator is calculated by (1), (2), (3), and (4). This method is the same as reported in our previous method in [24].

The second method uses the first virtual antagonistic muscle structure (Figure 2(b)). It searches for the three ratios ($\mathrm{Ar}_{\mathrm{MP}}$, $\mathrm{Ar}_{\mathrm{PIP}}$, and $\mathrm{Ar}_{\mathrm{DIP}}$) using the attractor selection and supplies the pressure to each actuator using (10), (11), (12), (13), (14), (15), and (16). We refer to this as an Ar search-type controller.

The third method uses the second virtual antagonistic muscle structure (Figure 2(c)). It searches for the Ar value and the two distribution ratios ($\mathrm{Dr}_{\mathrm{MP}}$ and $\mathrm{Dr}_{\mathrm{PIP}}$) using the attractor selection and then supplies the pressure to each actuator using (8), (9), (17), (18), and (19). This is referred to as an Ar and Dr search-type controller.

Notice that the search space for all the variables (x_e, x_{MPf}, x_{PIPf}, and x_{DIPf}; Ar_{MP}, Ar_{PIP}, and Ar_{DIP}; and Ar, Dr_{MP}, and Dr_{PIP}) ranges from 0 to 1.

3. Experimental Procedures

A control experiment that makes the tip of the index finger of the musculoskeletal robot (see the bottom-right inset in Figure 3) move to the desired position was conducted using the above three controllers. Figure 3 depicts the experiment setup, which comprises the musculoskeletal robot (SQUSE hand G type, SQUSE Inc.), the control PC (MDV ADVANCE ST 6300B (MouseComputer Co. Ltd.), Windows XP, and an Intel Core i7 920 (2.67 GHz)), an A/D converter (AI-1664L-LPE, CONTEC Co. Ltd.), two D/A converters (AO-1616L-LPE, CONTEC Co. Ltd.), a digital output board (RRY-32-PE, CONTEC Co. Ltd.), a motion capture system (Nobby Tech. Ltd.), regulators (ITV0030, SMC Corporation), solenoid valves (S070-5DCO-32, SMC Corporation), and an air compressor (DPP-AYAD, Koganei Corporation). The sampling frequency was set at 100 Hz. The input signals were voltages generated by the control PC and were converted to pressures by the regulators. The output signals were the coordinates of the tip position [E_X, E_Y, E_Z] sensed by the motion capture system. The Euclidean norm (the distance between the desired position [E_{Xd}, E_{Yd}, E_{Zd}] and the tip position) was used as the evaluation index of the controller. The Euclidean norm is described by l and computed using

$$l = \sqrt{(E_{Xd} - E_X)^2 + (E_{Yd} - E_Y)^2 + (E_{Zd} - E_Z)^2}. \tag{22}$$

And Activity of the attractor selection model is calculated from 0 to 1 using

$$\text{Activity} = -\frac{l}{l_{\max}} + 1. \tag{23}$$

Here, $l_{\max}$ is the maximum value of a norm computed from the desired position and the tip position on either the maximum flexion, which is a steady state in which maximum pressure (0.19 MPa) is supplied to all flexors, or the maximum extension, which is a steady state in which maximum pressure is supplied to only the extensor of the robot.

Each norm was obtained in advance, and the larger norm was selected as $l_{\max}$. Two tasks were conducted in the experiment. The flexion task involved making the robot flex to a desired position from an extended state, the extension task involved extending the robot to a desired position from a flexed state, and the tasks were changed after a constant time. First, the flexion task was conducted. After a constant time, the desired position was changed and the extension task was conducted. The control time was set at 60 s, and the task was changed 30 s after the control was started. The first position and the desired position were defined when the robot was in a steady state after constant pressure was applied to each actuator. Each position was captured in advance.

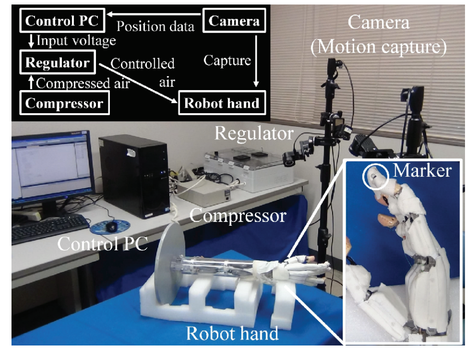

Figure 3: System overview. Two insets show the system flow (top-left) and the position of the marker captured by the cameras in an enlarged view of the robot hand (bottom-right). The marker is set to the tip of the musculoskeletal robot (the index finger). The input voltage from the control PC is converted to the controlled pressures by the regulators, and the musculoskeletal robot is driven by the pressures supplied to each muscle of the robot. The position of the tip is measured using the marker captured by the cameras and is saved to the PC.

In this experiment, the pressure value, represented by P_e, P_{MPf}, P_{PIPf}, and P_{DIPf} (0.05, 0.15, 0.05, and 0.05, resp.), was applied to each actuator to determine the desired position for the flexion task, and 0.15, 0.05, 0.05, and 0.05, respectively, were applied to each actuator to determine the desired position for the extension task. The initial values of x_e, x_{MPf}, x_{PIPf}, and x_{DIPf}; Ar_{MP}, Ar_{PIP}, and Ar_{DIP}; and Ar, Dr_{MP}, and Dr_{PIP} were set to 0.9, 0.1, 0.1, and 0.1; 0.9, 1.0, and 0.0; and 0.9, 1.0, and 0.0, respectively, and the noise η was generated between −10 and 10. The parameter values in (21) were set as follows: $N = 11$, $k_d = 0.01$, $k_w = 0.01$, and $X_i = 0.1 \times i$.

4. Results and Discussion

Figures 4–6 show the results using the pressure search-type controller, the Ar search-type controller, and the Ar and Dr search-type controller, respectively. The transition of the search variables, the pressures supplied to each actuator, the tip position captured by the motion capture, and Activity of the attractor selection model were then plotted. In Figure 4, Activity increased from 3 s and became constant at 0.96. Therefore, the flexion task was almost accomplished, and the search variables converged to an attractor. However, the extension task was not completed. Activity increased from 33 s to 35 s and remained at nearly 0.8, but it decreased from 39 s and did not reach a high value. The difference in the accomplishment ratio of the task is caused by the relationship of pressure between the extensor and the flexor. When Activity increased and became constant in the flexion task, the pressure on the extensor (P_e) decreased and the pressure on the flexor responsible for driving the MP joint (P_{MPf}) increased. Therefore, the power for the flexion became large, and the robot flexed toward the desired position. In the extension task, pressures for the extensor (P_e) and pressure for the flexor for driving the MP joint (P_{MPf}) increased from 33 s to 35 s. Therefore, the power for the extension did not increase dramatically,

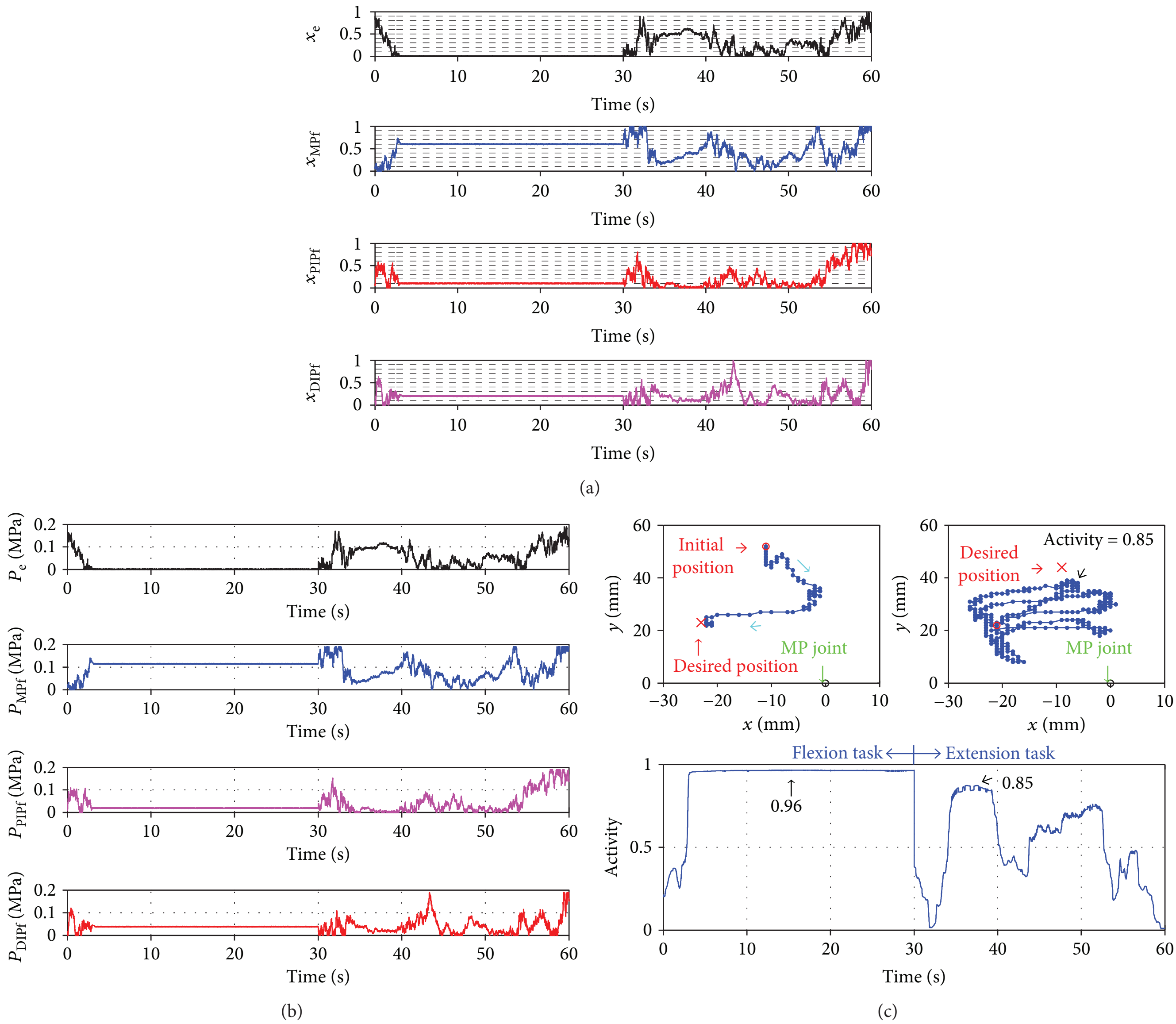

FIGURE 4: Results using the pressure search-type controller. (a) Plots of the transition of the search variables (x_e, x_{MPf}, x_{PIPf}, and x_{DIPf}) and the attractors (dashed lines). (b) Plots of the transition of the input pressures (P_e, P_{MPf}, P_{PIPf}, and P_{DIPf}). (c) Plots of the trajectory of the tip of the robot for the flexion task (top-left) and the extension task (top-right) and the transition of the Activity (bottom). Cyan arrows, green arrows, and black arrows show the direction of the movement, the MP joint position, and the value of Activity, respectively.

and the robot did not accomplish the extension task. The difference between the pressure for the extensor and the flexor is important for achieving the task efficiently.

In Figure 5, Activity increased after 10 s and reached a constant value of 0.91 at 17 s. The flexion task was close to being accomplished, but compared with the pressure search-type controller, the accomplishment ratio was 5% lower and the control time for accomplishment of the task was 13 s longer. Therefore, the control was not as good as that of the pressure search-type controller. In the extension task, Activity did not attain a high value. Therefore, the extension task was not accomplished. As a result, the controller did not work well for the extension task. To efficiently accomplish the task, it was necessary that the differences between the pressures for the extensor and the flexors be easily calculated by the controller because the differences can decrease power which prevents accomplishment of tasks and can make the tip position of the robot move quickly to the desired position, but this controller cannot calculate the differences between the pressures as well as the pressure search-type controller. This controller searches for three Ar values independently. Therefore, each Ar takes on a different value, and the pressure for the flexor does not decrease satisfactorily. Thus, the power for flexion does not decrease sufficiently, and the extension task is not accomplished.

In Figure 6, Activity increased greatly and became constant at 0.95 for the flexion task. On the extension task, Activity increased gradually right after the change of the task and became constant at 0.97. Therefore, the flexion task and the extension task were accomplished. The Ar and Dr search-

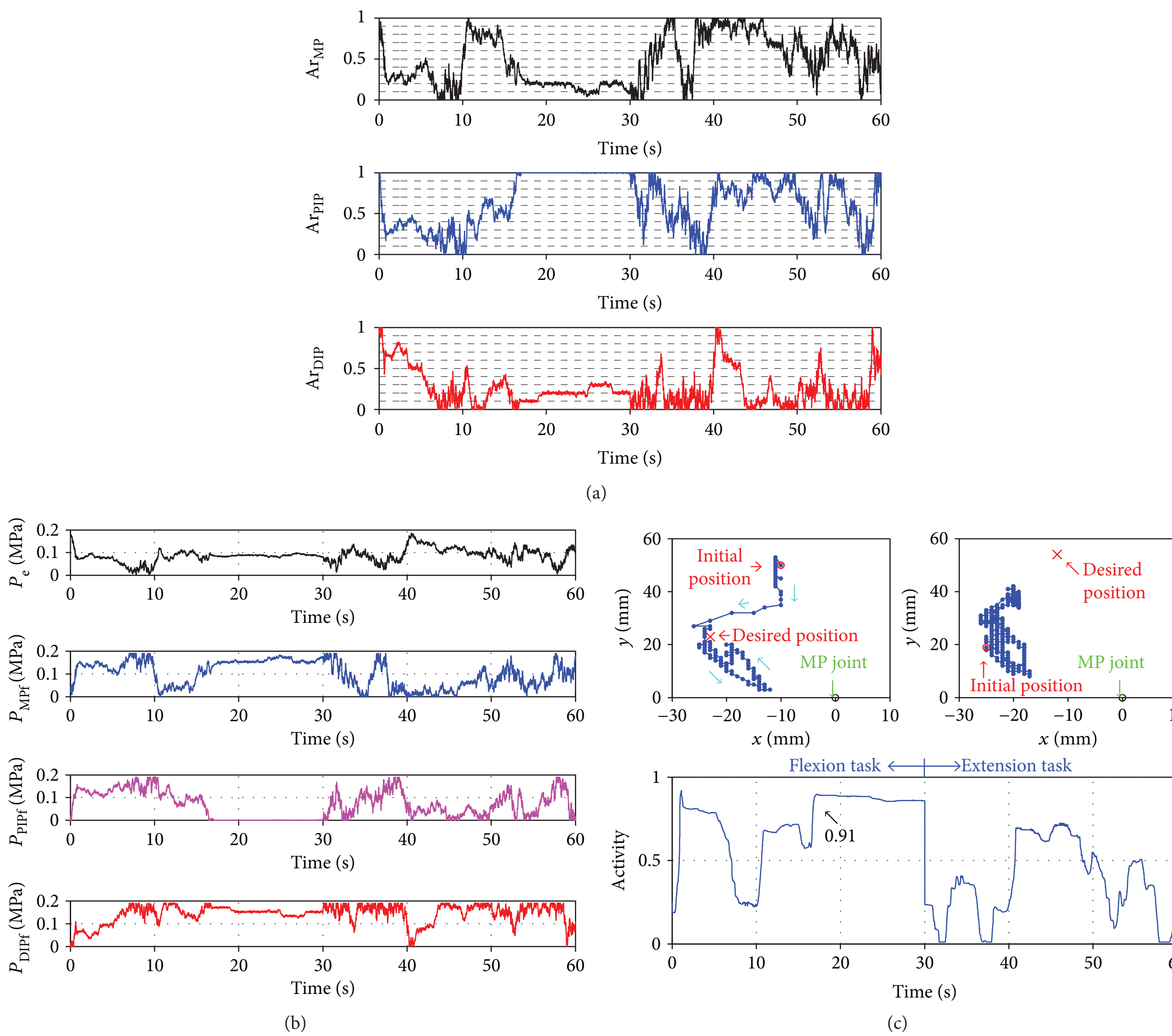

Figure 5: Results using the Ar search-type controller. (a) Plots of the transition of the search variable (Ar_{MP}, Ar_{PIP}, and Ar_{DIP}) and the attractors (dashed lines). (b) Plots of the transition of the input pressures (P_e, P_{MPf}, P_{PIPf}, and P_{DIPf}). (c) Plots of the trajectory of the tip of the robot on the flexion task (top-left) and the extension task (top-right) and the transition of the Activity (bottom). Cyan arrows, green arrows, and black arrows show the direction of the movement, the MP joint position, and the value of Activity, respectively.

type controller is, thus, more highly adaptive for tasks than the pressure search-type controller and the Ar search-type controller. Especially, the effectiveness of the Ar and Dr search-type controller for the extension task was shown. The robot has four actuators arranged asymmetrically on the extension side and the flexion side. One actuator is installed on the extension side, and three actuators are installed on the flexion side. Therefore, the power for flexion easily becomes large compared with the power for extension. To make this robot extend sufficiently, the power for flexion must become small.

In the Ar and Dr search-type controller, the difference between the power in the flexion and in the extension is determined easily because the difference between the pressures for the flexor and the extensor is calculated by searching only one Ar. Therefore, the power for flexion becomes small, and the robot can sufficiently extend. We also conducted the different task for the Ar and Dr search-type controller to show the adaptability of the controller. Figure 7 shows the results of the experiment. We set four tasks, two flexion tasks and two extension tasks, which were conducted alternately. The desired position for each flexion task was different, and each desired position for each extension task was different. Each task was changed at the following constant times: 30 s, 60 s, and 90 s after the control is started. Experimental results show that Activity became the high value for each task. Therefore, the Ar and Dr search-type controller displayed good adaptability for the tasks in the experiments. Thus, it was shown that the proposed muscle coordination control of the Ar and Dr search-type controller using the attractor selection facilitated easy control of an asymmetrically antagonistic-driven musculoskeletal robot with a polyarticular muscle.

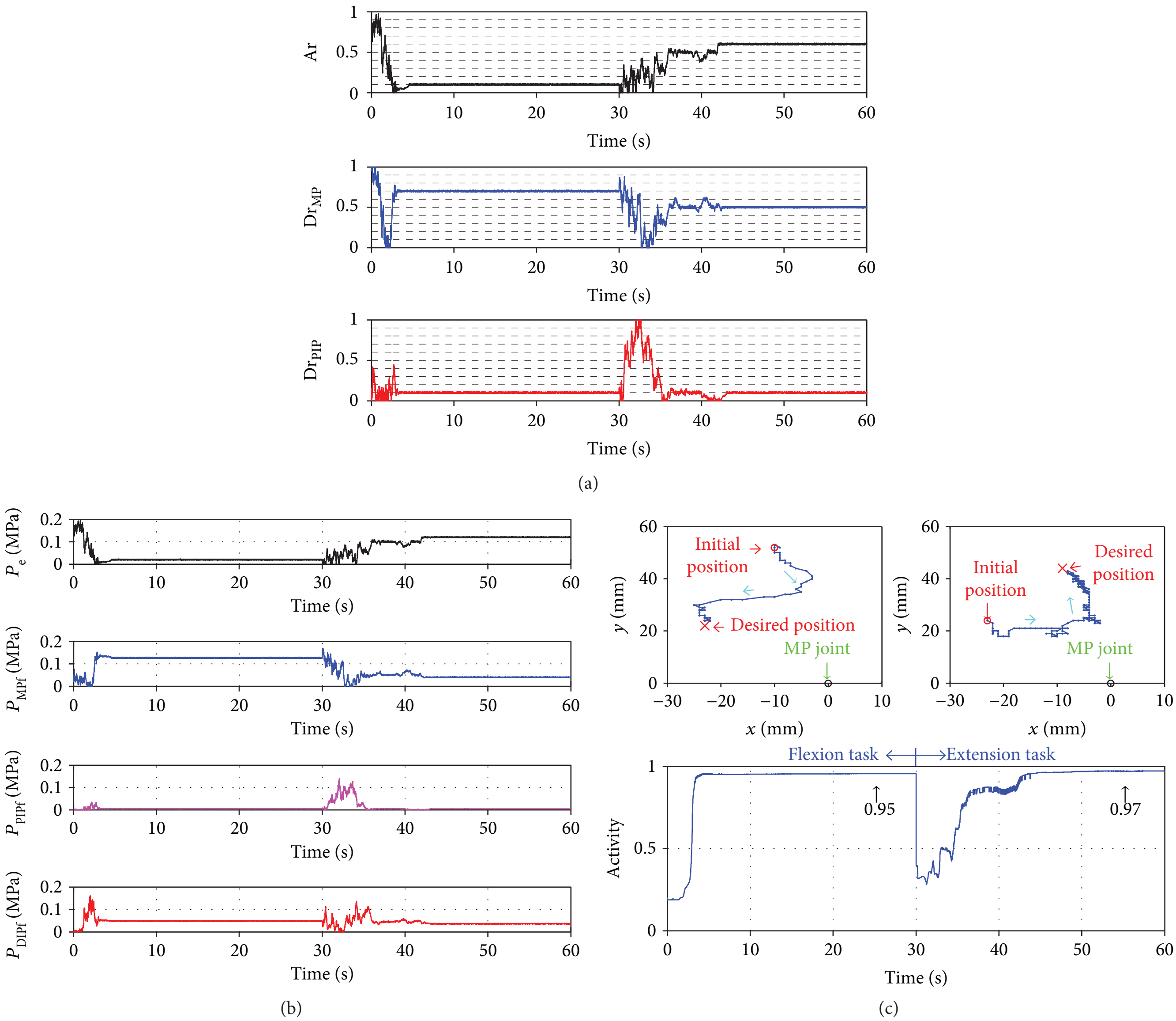

FIGURE 6: Results using the Ar and Dr search-type controller. (a) Plots of the transition of the search variable (Ar, $\mathrm{Dr}_{\mathrm{MPf}}$, and $\mathrm{Dr}_{\mathrm{PIPf}}$) and the attractors (dashed lines). (b) Plots of the transition of the input pressures (P_{e}, P_{MPf}, P_{PIPf}, and P_{DIPf}). (c) Plots of the trajectory of the tip of the robot on the flexion task (top-left) and the extension task (top-right) and the transition of the Activity (bottom). Cyan arrows, green arrows, and black arrows show the direction of the movement, the MP joint position, and the value of Activity, respectively.

5. Conclusions

This work demonstrated a muscle coordination control of an asymmetrically antagonistic-driven musculoskeletal robot using attractor selection which is a biologically inspired search method.

First, muscle coordination control models of the musculoskeletal robot were built using virtual antagonistic muscle structures with a virtually symmetric arrangement of muscles, and the calculation methods of the input pressure for PAMs of the musculoskeletal robot with and without muscle coordination were shown. Next, the attractor selection was applied to both the muscle coordination control model and to another control model without the muscle coordination to compare the control performance. Finally, position control experiments were conducted, the effectiveness of the proposed muscle coordination control applied to the attractor selection was demonstrated, and it was also shown to be faster and more robust to accomplish the task by generating control commands virtually assuming a symmetrical and simpler metastructure rather than providing a control command according to the actual complex (asymmetric) antagonistic muscle structure.

Based on the virtual antagonistic muscle structure proposed in this research, we may be able to build a musculoskeletal robot that achieves a more complicated task faster by devising how to give noise [25] and adaptively updating the attractor structure [21]. In future work, the muscle coordination control method, using the attractor selection, will be applied to the multifingered robot hand formed by increasing the number of musculoskeletal robots (i.e., robot fingers).

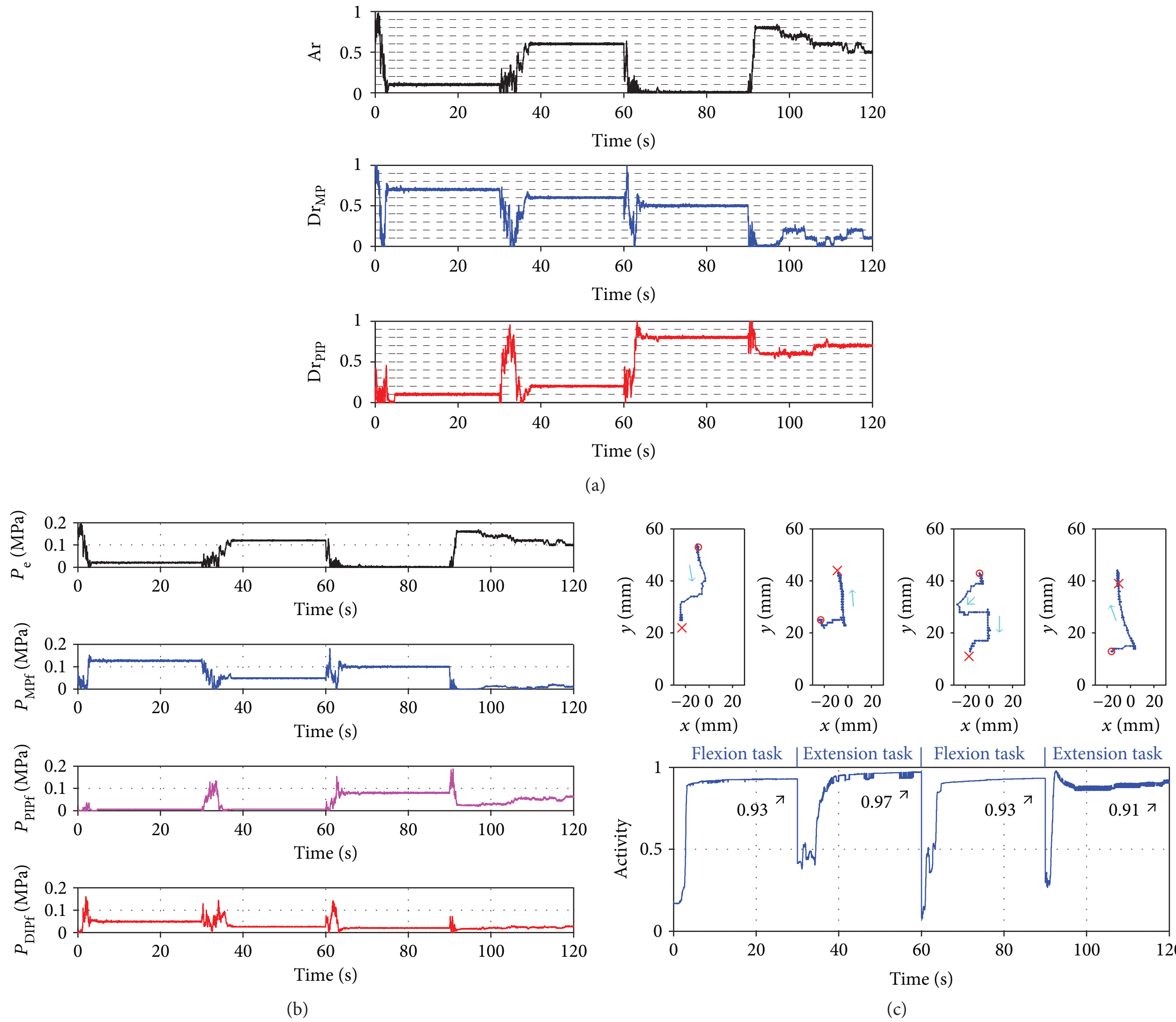

FIGURE 7: Results using the Ar and Dr search-type controller at four desired positions. (a) Plots of the transition of the search variable (Ar, Dr_{MPf}, and Dr_{PIPf}). (b) Plots of the transition of the input pressures (P_e, P_{MPf}, P_{PIPf}, and P_{DIPf}). In (c), the top images plot the trajectory of the tip of the robot: the first flexion task, the first extension task, the second flexion task, and the second extension task from the left image, whereas the bottom image plots the transition of the Activity. Cyan arrows and black arrows show the direction of the movement and the value of Activity, respectively.

Furthermore, the effectiveness of the control method will be investigated for asymmetrically antagonistic-driven musculoskeletal robots, which have entirely different arrangements of muscles compared with our musculoskeletal robot.

The muscle coordination control method using attractor selection can be applied not only to musculoskeletal robots but also to human hands. Therefore, the control method will be applied to rehabilitation using functional electrical stimulations (FESs) [26, 27] as a novel approach to controlling human hands.

Data Availability

The raw data for Figures 4–7 are available from the corresponding author upon request.

Conflicts of Interest

The authors declare that there is no conflict of interest regarding the publication of this paper.

Acknowledgments

This work was supported by JSPS KAKENHI Grant nos. JP23560524, JP26420196, and JP17K06259.

References

[1] I. Mizuuchi, T. Yoshikai, Y. Sodeyama et al., “Development of musculoskeletal humanoid Kotaro,” in *Proceedings 2006 IEEE*

International Conference on Robotics and Automation, 2006. ICRA 2006, pp. 82–87, Orlando, FL, USA, May 2006.

[2] H. G. Marques, M. Jantsch, S. Wittmeier et al., "ECCE1: the first of a series of anthropomimetic musculoskeletal upper torsos," in *2010 10th IEEE-RAS International Conference on Humanoid Robots*, vol. 6-8, pp. 391–396, Nashville, TN, USA, December 2010.

[3] N. C. Park and H. S. Yang, "Control of a flexible manipulator with artificial muscle-type pneumatic actuators, using μ-synthesis," *Journal of Vibration and Control*, vol. 4, no. 4, pp. 481–502, 1998.

[4] T. V. Minh, B. Kamers, T. Tjahjowidodo, H. Ramon, and H. Van Brussel, "Modeling torque-angle hysteresis in a pneumatic muscle manipulator," in *2010 IEEE/ASME International Conference on Advanced Intelligent Mechatronics*, pp. 1122–1127, Montreal, ON, Canada, July 2010.

[5] T. D. C. Th;anh and K. K. Ahn, "Nonlinear PID control to improve the control performance of 2 axes pneumatic artificial muscle manipulator using neural network," *Mechatronics*, vol. 16, no. 9, pp. 577–587, 2005.

[6] B. Verrelst, R. V. Ham, B. Vanderborght, F. Daerden, D. Lefeber, and J. Vermeulen, "The pneumatic biped "Lucy" actuated with pleated pneumatic artificial muscles," *Autonomous Robots*, vol. 18, no. 2, pp. 201–213, 2005.

[7] A. Rezoug, S. Boudoua, and F. Hamerlain, "Fuzzy logic control for manipulator robot actuated by pneumatic artificial muscles," *Journal of Electrical Systems*, vol. 1, pp. 1–6, 2009.

[8] K. K. Ahn and H. T. C. Nguyen, "Intelligent switching control of a pneumatic muscle robot arm using learning vector quantization neural network," *Mechatronics*, vol. 17, no. 4-5, pp. 255–262, 2007.

[9] Y. Honda, F. Miyazaki, and A. Nishikawa, "Control of pneumatic five-fingered robot hand using antagonistic muscle ratio and antagonistic muscle activity," in *2010 3rd IEEE RAS & EMBS International Conference on Biomedical Robotics and Biomechatronics*, pp. 337–342, Tokyo, Japan, September 2010.

[10] Y. Honda, F. Miyazaki, and A. Nishikawa, "Angle control of pneumatically-driven musculoskeletal model using antagonistic muscle ratio and antagonistic muscle activity," in *2010 IEEE International Conference on Robotics and Biomimetics*, pp. 1722–1727, Tianjin, China, December 2010.

[11] T. Yanagida, M. Ueda, T. Murata, S. Esaki, and Y. Ishii, "Brownian motion, fluctuation and life," *Biosystems*, vol. 88, no. 3, pp. 228–242, 2007.

[12] A. Kashiwagi, I. Urabe, K. Kaneko, and T. Yomo, "Adaptive response of a gene network to environmental changes by fitness-induced attractor selection," *PLoS One*, vol. 1, no. 1, article e49, 2006.

[13] D. Tian, J. Zhou, Z. Sheng, Y. Wang, and J. Ma, "From cellular attractor selection to adaptive signal control for traffic networks," *Scientific Reports*, vol. 6, no. 1, article 23048, 2016.

[14] G. Motoyoshi, K. Leibnitz, and M. Murata, "Proposal and evaluation of a future mobile network management mechanism with attractor selection," *EURASIP Journal on Wireless Communications and Networking*, vol. 2012, no. 1, 2012.

[15] D. Tian, J. Zhou, H. Qi et al., "A bio-inspired QoS-oriented handover model in heterogeneous wireless networks," *Journal of Applied Mathematics*, vol. 2014, Article ID 920123, 13 pages, 2014.

[16] T. Chikaraishi, T. Minato, and H. Ishiguro, "Development of an android system integrated with sensor networks," *Journal of Information Processing Society of Japan*, vol. 49, no. 12, pp. 3821–3834, 2008.

[17] S. G. Nurzaman, Y. Matsumoto, Y. Nakamura, S. Koizumi, and H. Ishiguro, "Attractor selection based biologically inspired navigation system," in *In Proceedings of the 39nd ISR(International Symposium on Robotics)*, pp. 837–842, Seoul, Korea, October 2008.

[18] S. G. Nurzaman, X. Yu, Y. Kim, and F. Iida, "Guided self-organization in a dynamic embodied system based on attractor selection mechanism," *Entropy*, vol. 16, no. 5, pp. 2592–2610, 2014.

[19] Y. Kim, S. G. Nurzaman, F. Iida, and E. F. Fukushima, "A self organization approach to goal-directed multimodal locomotion based on attractor selection mechanism," in *2015 IEEE International Conference on Robotics and Automation (ICRA)*, pp. 5061–5066, Seattle, WA, USA, May 2015.

[20] I. Fukuyori, Y. Nakamura, Y. Matsumoto, and H. Ishiguro, "Flexible control mechanism for multi-DOF robotic arm based on biological fluctuation," in *SAB '08 Proceedings of the 10th international conference on Simulation of Adaptive Behavior: From Animals to Animats*, pp. 22–31, Osaka, Japan, July 2008.

[21] A. Sugahara, Y. Nakamura, I. Fukuyori, Y. Matsumoto, and H. Ishiguro, "Generating circular motion of a human-like robotic arm using attractor selection model," *Journal of Robotics and Mechatronics*, vol. 22, no. 3, pp. 315–321, 2010.

[22] A. De Rengerve, S. Boucenna, P. Andry, and P. Gaussier, "Emergent imitative behavior on a robotic arm based on visuo-motor associative memories," in *2010 IEEE/RSJ International Conference on Intelligent Robots and Systems*, pp. 1754–1759, Taipei, Taiwan, October 2010.

[23] A. Nishikawa, K. Taniguchi, M. Sekimoto et al., "Design and control of a compact laparoscope manipulator: a biologically inspired approach," in *Advanced Strategies for Robot Manipulators*, S. Ehsan Shafiei, Ed., pp. 365–380, Intech Open, 2010.

[24] S. Ide and A. Nishikawa, "Bio-inspired control of a multi-fingered robot hand with musculoskeletal system," in *Smart Textiles and Their Applications*, V. Koncar, Ed., pp. 185–195, Elsevier, 2016.

[25] S. G. Nurzaman, Y. Matsumoto, Y. Nakamura, K. Shirai, S. Koizumi, and H. Ishiguro, "From Lévy to Brownian: a computational model based on biological fluctuation," *PLoS One*, vol. 6, no. 2, article e16168, 2011.

[26] K. Matsui, Y. Hishii, K. Maegaki et al., "Equilibrium-point control of human elbow-joint movement under isometric environment by using multichannel functional electrical stimulation," *Frontiers in Neuroscience*, vol. 8, p. 164, 2014.

[27] K. Takemura, M. Kurosawa, K. Atsuumi, K. Matsui, F. Miyazaki, and A. Nishikawa, "Frequency domain system identification of human finger dynamics using functional electrical stimulation based on an agonist-antagonist concept," in *Proceedings of the 2017 Annual Conference of the International Functional Electrical Stimulation Society*, p. 114, London, UK, July 2017.

Hindawi
Applied Bionics and Biomechanics
Volume 2018, Article ID 5651315, 9 pages
https://doi.org/10.1155/2018/5651315

Research Article

Development of a Novel Micro Photoionization Detector for Rapid Volatile Organic Compounds Measurement

Qi Zhou,[1] **Sixiang Zhang**,[1] **Xu Zhang**,[2] **Xu Ma**,[3] **and Wei Zhou**[1]

[1]*School of Mechanical Engineering, Hebei University of Technology, Tianjin 300130, China*
[2]*School of Mechanical Engineering, Tianjin University of Technology and Education, Tianjin 300130, China*
[3]*School of Electrical and Electronic Engineering, Tianjin University of Technology, Tianjin 300130, China*

Correspondence should be addressed to Sixiang Zhang; 13502063552@163.com and Xu Ma; maxu2015@aliyun.com

Received 12 April 2018; Accepted 22 July 2018; Published 5 September 2018

Academic Editor: Liwei Shi

The simulation of the gas flow field and electrostatic field in the photoionization detector by COMSOL was conducted based on principle investigation in the present study. Under the guidance of simulation results, structural optimization was carried out to significantly reduce the dead volume of the ionization chamber, and finally, the relationship between offset voltage and collection efficiency was obtained which led to a remarkable increase in the collection efficiency of charged ions in the photoionization detector. Then an ionization chamber with low interference and fast response was developed. Then experiment was performed with toluene as a VOCs gas under the condition of optimal gas flow rate of 50 ml, UV lamp ionization energy of 10.86 eV. The results showed that the ion collection efficiency reached 91% at a bias voltage of 150 V. Moreover, a preferred linearity of 99.99% was obtained, and a ppb level of LOD can be achieved. The determination results well-fitted the relationship between offset voltage and the response value obtained in the simulation.

1. Introduction

Volatile organic compounds (VOCs) is the general term of volatile organicity even at room temperature, which not only can influence our daily life but also can threaten human being's health [1]. By comparing the performance of different detectors, finding the appropriate VOCs detector, and comparing the working principle and performance characteristics of different detectors, the characteristics of different detectors are introduced in Table 1.

By comparing the performance of different detectors, it can be concluded that different types of detectors have different types of gases. The difference between the types of detectable gases is called the selectivity of the detector. The gas detectors with strong selectivity are limited by their own characteristics and are difficult to be widely used. Therefore, the detector used for VOCs detection should be a universal detector, the detection accuracy should be high, and the volume should be small, which is conducive to system integration and miniaturization design. In the detectors described above, the detection accuracy of FID is very high, but FID requires hydrogen as the combustion gas. The application range of ECD and ion migration spectrum detector is narrow, and it is not suitable for use as a VOCs detector. TCD has strong universality, but its low detection accuracy cannot achieve trace detection. Considering the characteristics of the above detectors, the photoionization detector is used as the terminal detector of the VOCs detection system [5].

In the early stage of the study, the UV light source and the ionization chamber were in the same space, which limits the sensitivity and accuracy of the detector. Later, as the research progressed, the scientists separated the two and made the detector more accurate. In practical work, the sensitivity of the photoionization detector is greatly influenced by the performance of the ionization chamber. After the introduction

Table 1: Performance comparison table of odor detectors.

Name	Abbr.	Applicable substance	Selectivity	Carrier gas	Linear range	LOD	Temperature upper limit
Thermal conductivity detector	TCD	All compounds	Nonselective	H_2, He, N_2	10^5	10^{-7}–10^{-9}	450
Flame ionization detector	FID	Organic compound	No reaction to permanent gases or formic acid	H_2, He, N_2	5×10^6–5×10^7	10^{-11}–10^{-14}	450 [2]
Photoionization detector	PID	A compound below the maximum ionization energy	Most organic compounds	H_2, He, N_2, air	10^7–10^8	10^{-13}	250 [3]
Electronic capture detector	ECD	Compounds containing oxygen or halogen	Good response to electronegative compounds	Ar, $N_2 + CH_4$	10^2–10^4	10^{-13}–10^{-14}	400
Ion migration spectrum detector	IMS	Organic matter and toxic substances [4]	Most organic compounds	He, N_2	10^4–10^5	10^{-10}	300

of the commercialized PID by HNU in 1976, companies such as RAE and Ion Science also introduced the PID detection devices [6]. However, these devices are complex in structure, lack scale production, are not competitive in the market, and cannot meet the requirements of trace detection. Recently, gas pollution is ubiquitous, and the research on PID is at a high level at home and abroad. The existing sensors still have the characteristics of large size, large power consumption, low efficiency, and high cost, and cannot meet the requirements for efficient portable detection [7].

The photoionization detector is a versatile, selective detector that responds to most organic compounds and acts as a nondestructive detector. This detector can be combined well with mass spectrometers or infrared detectors [8]. In practical work, the sensitivity of the photoionization detector was mainly determined by ionization chamber performance [9], and the detection level of PID was generally determined by the quantity of electron flow produced in the ionization chamber. Therefore, the design of the ionization chamber should be the key to PID design.

We have developed a microfluidic PID that can be used in a GC (μGC) system for rapid and highly sensitive VOCs detection. The photoionization detector has been integrated into the GC (μGC) system [10].

2. Method

As shown in Figure 1, the main reason for PID is that the charged ions are generated by the ultraviolet lamp through ionization of the gas between the electrodes. The main principle of PID is that the gas between the electrodes is ionized by ultraviolet light excited by the UV lamp to produce charged ions which can form a current when driven by a high voltage electric field. The current value is proportional to the concentration of charged ions generated between the electrodes. In combination with the separation of the chromatographic column, the qualitative or quantitative detection of the sample compound can be achieved based on the change in the current intensity between the electrodes over time [11].

The photoionization current was defined as the quantity of an ion pair generated by ionization per unit time and can be showed as

$$\frac{dN_i}{dt} = 2\sigma i\phi\left[1 - e^{-\sigma_i N(t)l}\right], \tag{1}$$

with N_i denoting the quantity of the ion pair, σ_i denoting the absorption coefficient of photoionization, ϕ denoting the quantity of photons injected into the ionization chamber per unit time, σ_0 denoting the absorption coefficient caused by other reasons, $\sigma_t = \sigma_i + \sigma_0$ was the total absorption coefficient, $N(t)$ was the amount of gas molecule to be determined, namely, the gas concentration to be determined, and l denoting the optical path length.

It can be seen from (1) that the quantity of the ion pair produced in the ionization chamber by excitation of gas molecules per unit time dN_i/dt exhibited exponential relationship with VOCs concentration in the sample; (1) can be converted to

$$\frac{dN_i}{dt} = 2\sigma_i\varphi\sigma_t N(t)\cdot l, \tag{2}$$

within $\sigma_i N(t)l \leq 1$.

Then dN_i/dt was in proportion to $N(t)$, namely, as the value of l, the optical path of ultraviolet light, in the ionization chamber was short enough and the concentration of gas to be determined was relatively low, then the rough linear relationship of ionization current with gas concentration in the sample and ϕ, the quantity of photons injected into the ionization chamber per unit time, can be obtained [12]. Therefore, both the gas concentration of the sample and intensity of UV light may affect the strength of ionization current; hence, the ionization current will increase with both the value of gas concentration and UV light intensity.

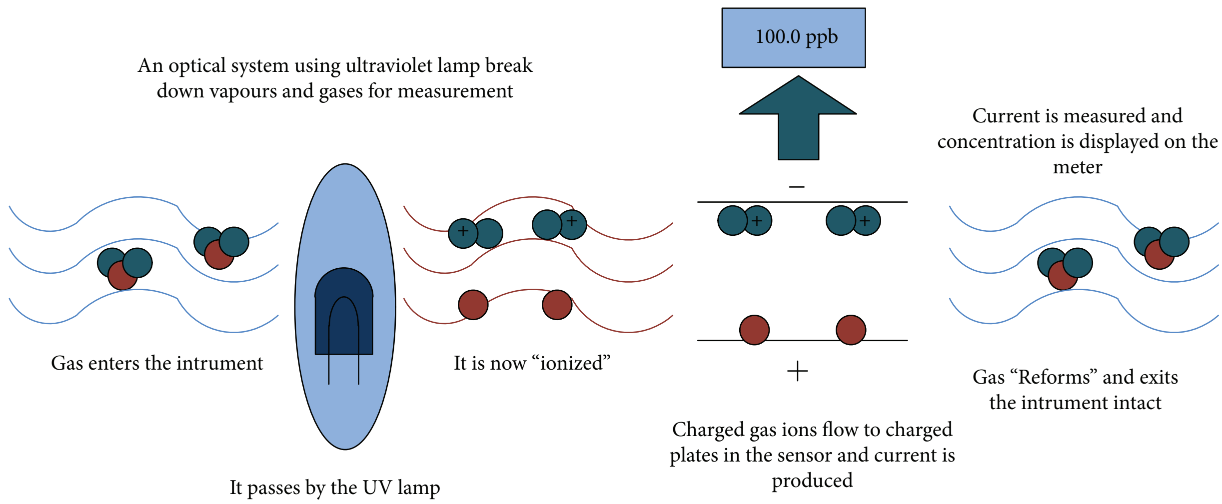

Figure 1: The working principle of PID.

In 1982, Freedman proposed the use of photoionization detector for gas detection, then the actual ionization current (i) was written as

$$i = I_0 F\eta\sigma NL[AB], \tag{3}$$

with I_0 as the intensity of light radiation, F as the Faraday constant, N as the Avogadro constant, η as the absorption cross section of components, σ as the ionization efficiency of excited-state molecule, L as the thickness of light absorption layer, and $[AB]$ as the gas component concentration to be determined [13].

In the parameters mentioned above, the values of I_0 and L were associated with a PID structure, both values would be constant with a certain PID structure, the R value, namely, mole-basis response, was only determined by η and σ, and the relationship can be written as $R = i/[AB] = K\eta\sigma$. Among them, the product of η and σ was defined as the photoionization section, which was highly dependent on the ionization potential (IP) of gas molecules; hence, (3) can be written as

$$i = I_0 FNL[AB](IP), \tag{4}$$

in which (IP) was a key factor that may affect the ionization response of PID.

According to the principle of photoionization, there are three main factors that affect the performance of photoionization: background noise, ionization chamber volume, and electron and ion collection efficiency. Among these three factors, background noise is impossible to avoid, which can cause the detection limit and baseline drift. So, minimizing the impact of background noise is the key element of optimization. The background noise is caused by the interference between the collector plates, which can be solved by optimizing the structure. Chamber volume of detection limit and the response speed is an important factor to ensure the volume as small as possible, so that it can get a lower detection limit and faster response speed and get a larger linear response area. Meanwhile, the detection limit and response speed can be improved by increasing the collection efficiency of electron and ion. The factors mentioned above can be improved by enhancing the sealing performance of the overall structure, reducing the ionization chamber volume, and increasing the bias voltage. According to the above analysis, we design the PID detector.

3. Description of the Model Equations

3.1. The Relationship between Electrode Offset Voltage and the Collection Intensity of Ionization Gas. The collection efficiency of the collecting electrode is of great significance to the overall sensitivity and stability of the detector. The finite element method was used to analyze the electrostatic field model to simulate the electrostatic field distribution in PID. In addition, based on the electrostatic field model, the particle tracking model in the software is further used to study the effect of the collecting electrode size on the collection efficiency of the charged particle, by which providing guidance for the structure design [14].

For the electric field distribution within PID was actually an electrostatic field issue, thus the Poisson equation shown in (5) can be used for simulation

$$\nabla^2\varphi = \frac{-\rho}{\varepsilon}, \tag{5}$$

in which, φ was the electric potential, ρ was intensity of free charge, and ε was the dielectric constant of electrolyte. For no free charge distribution in the solution space, hence $\rho = 0$, then the Poisson equation can be further simplified as a Laplace equation shown in

$$\nabla^2 = 0. \tag{6}$$

The finite element method electrostatic field model was used to simulate the simplified model of electrostatic field distribution in PID [15]. Based on the proposed electrostatic

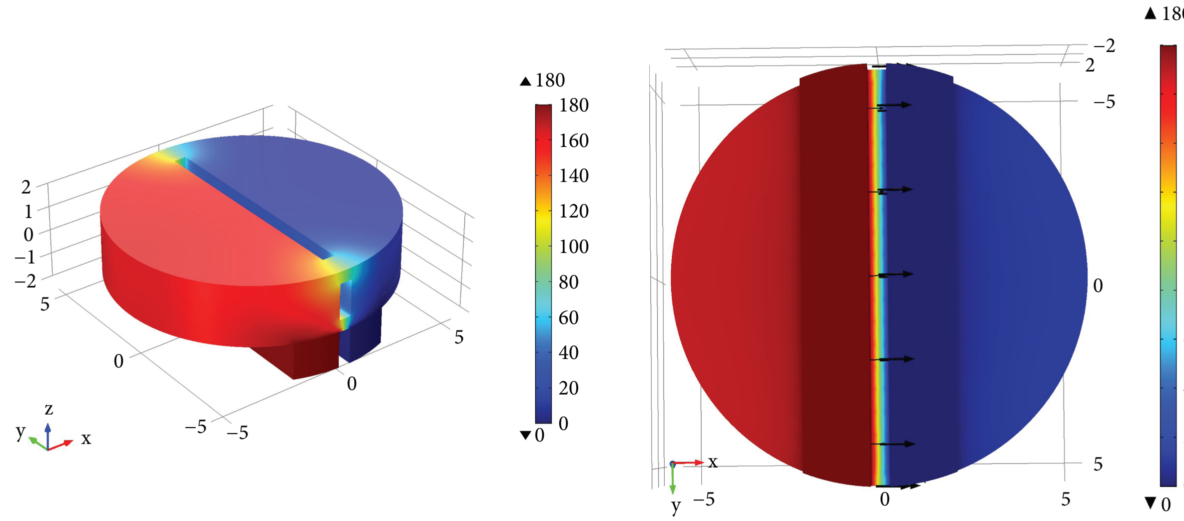

Figure 2: The distribution of collecting electrode potential and electric field lines.

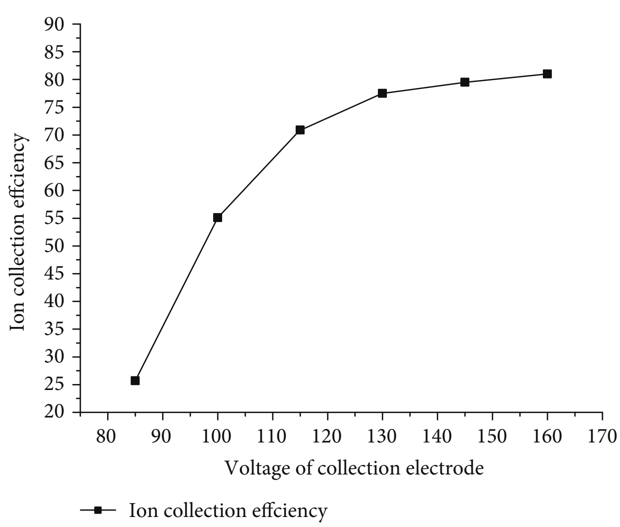

Figure 3: Effect of plate voltage of the collecting electrode on the charged ion collection efficiency.

field model, the particle trajectory model was used to simulate the trajectories of charged ions in the PID to study the effect of collecting electrode size on the collection efficiency of charged particles.

As shown in Figure 2, the potential gradually decreases from the polarizing electrode to the collecting electrode. The electric potential line was convex to the collecting electrode. Between the biasing electrode and the collecting electrode, the electric field line is emitted from the top of the biasing electrode and converges on the inner surface of the collecting electrode. Which revealed that, with the effect of electric field force towards the collecting electrode, the positively charged particles formed on top of the polarization electrode would move towards the inner surface of the collecting electrode, while the negatively charged particles move towards the collecting electrode.

As shown in Figure 3, most positively charged particles formed on top of the polarization electrode may rapidly move to the inner surface of the collecting electrode by the force of the electric field. Formula (7) can be employed to demonstrate the particle collection efficiency of PID, where the ratios of quantity of particles captured by the collecting electrode to the total quantity of particles emitted were employed to represent the particle collection efficiency of PID.

Through simulation, the collection voltage of the bias electrode under designed conditions can be obtained; meanwhile, the particle collection efficiency of PID can be obtained as

$$f(x) = 0.0001492x^3 - 0.06939x^2 + 10.82x - 485. \tag{7}$$

3.2. The Relationship between the Length and Plate Distance of Collecting Electrodes and Ionization Gas Collection Efficiency. Given the even distribution of the electric field, then the period t for ions moved from one electrode to another can be deduced by the following equation:

$$t = \sqrt{\frac{2m}{eV}} \cdot L, \tag{8}$$

in which m and e were the mass and charge of the ions, respectively, V was the offset voltage, and L was the polar plate distance. From which, for constant gas composition, the plate distance L may directly affect the sensor response speed. However, if the distance between the plates is too small, the gas cannot enter between the plates at a high gas flow rate so the ultraviolet light cannot be received for sufficient ionization. Therefore, under these two parameters, the design of the plate with the length of 7~11 mm guarantees the response speed of the sensor and the complete ionization of the gas after entering the plate [16].

Another parameter that can greatly affect the response speed was the polar plate distance of the collecting electrode, which can be obtained by the Gauss Law as follows:

$$\int \overrightarrow{D} \cdot d\overrightarrow{S} = \sum q = \int \rho(s) \cdot d\overrightarrow{S}. \tag{9}$$

The $\rho(s)$ in (9) was the surface density of charges, and the following equation can be obtained in the direction of the electric field when rectangular and parallel plates were employed:

$$\overrightarrow{D} = \rho = \frac{q}{S}, \tag{10}$$

in which $\overrightarrow{D}$ was the electric displacement vector; the relationship between $\overrightarrow{D}$ and the electric field intensity $\overrightarrow{E}$ was as follows:

$$\overrightarrow{D} = \varepsilon \cdot \overrightarrow{E}. \tag{11}$$

The electric field intensity of parallel plates was

$$\overrightarrow{E} = \frac{U}{d}. \tag{12}$$

The relationship in the direction of the electric field can be derived by (11) and (12):

$$\overrightarrow{D} = \varepsilon \cdot \overrightarrow{E} = \varepsilon \cdot \frac{U}{d}. \tag{13}$$

It can be seen from (13) that D was constant for a fixed electric field intensity and polar plate distance. Therefore, it can be revealed that the quantity of charge between the polar plates q was associated with the ion collection plate area S, and both the quantity of charges and ion current increased with the value of S, and hence, the sensitivity of PID would improve. Moreover, the ion collection efficiency of the ionization chamber can be obtained according to the Boag theory as

$$f = \left(1 + \frac{\xi^2}{6}\right)^{-1}, \tag{14}$$

within $\xi = m \cdot d^2 \cdot q^{0.5}/V$, d was the polar plate distance, V was the voltage difference between the plates, q was the charge density of the air per unit time, and m was the correction factor for environmental effect. It can be concluded from (13) that the collection efficiency of the ionization chamber was associated with polar plate distance and polar voltage. For constant environment conditions, the higher ion collection efficiency can be obtained with smaller polar plate distance in the ionization chamber and more polar voltage difference [17].

Therefore, according to the gas flow rate requirements, an improved gas flow model is used to simulate the gas flow field. The channel width is 1 mm, the boundary condition of two carrier gas inlets on the top was set as constant with the gage pressure of 0.05 MPa, the outlet boundary condition was set as laminar flow with the value of $2e-7\,\mathrm{m}^3/\mathrm{s}$, and the inlet boundary condition was also set as laminar flow with the value of $2e-8\,\mathrm{m}^3/\mathrm{s}$ [18].

According to the variability of liquid density with external conditions, the fluid can be classified into incompressible fluid and compressible fluid. The gas was usually regarded as compressible fluid, but when the gas flow rate is low, for example, when the Mach number Ma is less than 0.1 while the pressure change is small, the gas can be considered as an incompressible fluid. Therefore, with the gas flow rate of 50 ml/min, the Mach number of carrier gas can be obtained by

$$\mathrm{Ma} = \frac{V}{a}, \tag{15}$$

in which V was the fluid flow rate with the unit of m/s and a was the local sonic speed with the unit of m/s. By which, the Mach number of gas can be obtained as $1.95e-4$, which well-satisfied the conditions for incompressible gas flow.

The flow mode of fluid in the pipe can be divided into laminar flow and turbulent flow. As for laminar flow, the flow style of flow-cell within the fluid was stratified flow, and there was no mixture of radial flow and interlayer fluid; as for the turbulent flow, both radial flow and interlayer fluid within the fluid existed for the flow-cells, and the intense mixing among the flow-cells could be obtained. And the flow style of fluid can be distinguished by the Reynolds number (Re), in which the Reynolds number can be calculated by the following equation:

$$\mathrm{Re} = \frac{\rho V L}{\mu}, \tag{16}$$

in which ρ was the fluid density with the unit of $\mathrm{kg/m^3}$, V was the fluid flow rate, with the unit of m/s, L was the characteristic length, with the unit of m, and μ was the dynamic viscosity, with the unit of Pa·s. The flow state of fluid can be determined by the comparison of the calculated Reynolds number with the critical Reynolds number. The flow state was laminar flow when $\mathrm{Re} \le \mathrm{Re}_c$ and was turbulent flow when $\mathrm{Re} \ge \mathrm{Re}_c$. In the present study, for the calculated Reynolds number was $\mathrm{Re} = 17.49$, which was far less than Re_c, thus the corresponding flow state was viscous laminar flow [19].

In brief, the carrier gas flow in the circuit can be regarded as incompressible viscous flow, and the mathematical model can be proposed based on the Navier-Stokes equations:

$$\rho\left(\frac{\partial v}{\partial t} + v\nabla v\right) + \nabla P - \mu \Delta v = 0, \tag{17}$$

where $\nabla v = 0$.

In which the flow rate v and pressure P were unknown variables, ρ was fluid density, with the unit of $\mathrm{kg/m^3}$, and μ was dynamic viscosity, with the unit of Pa·s.

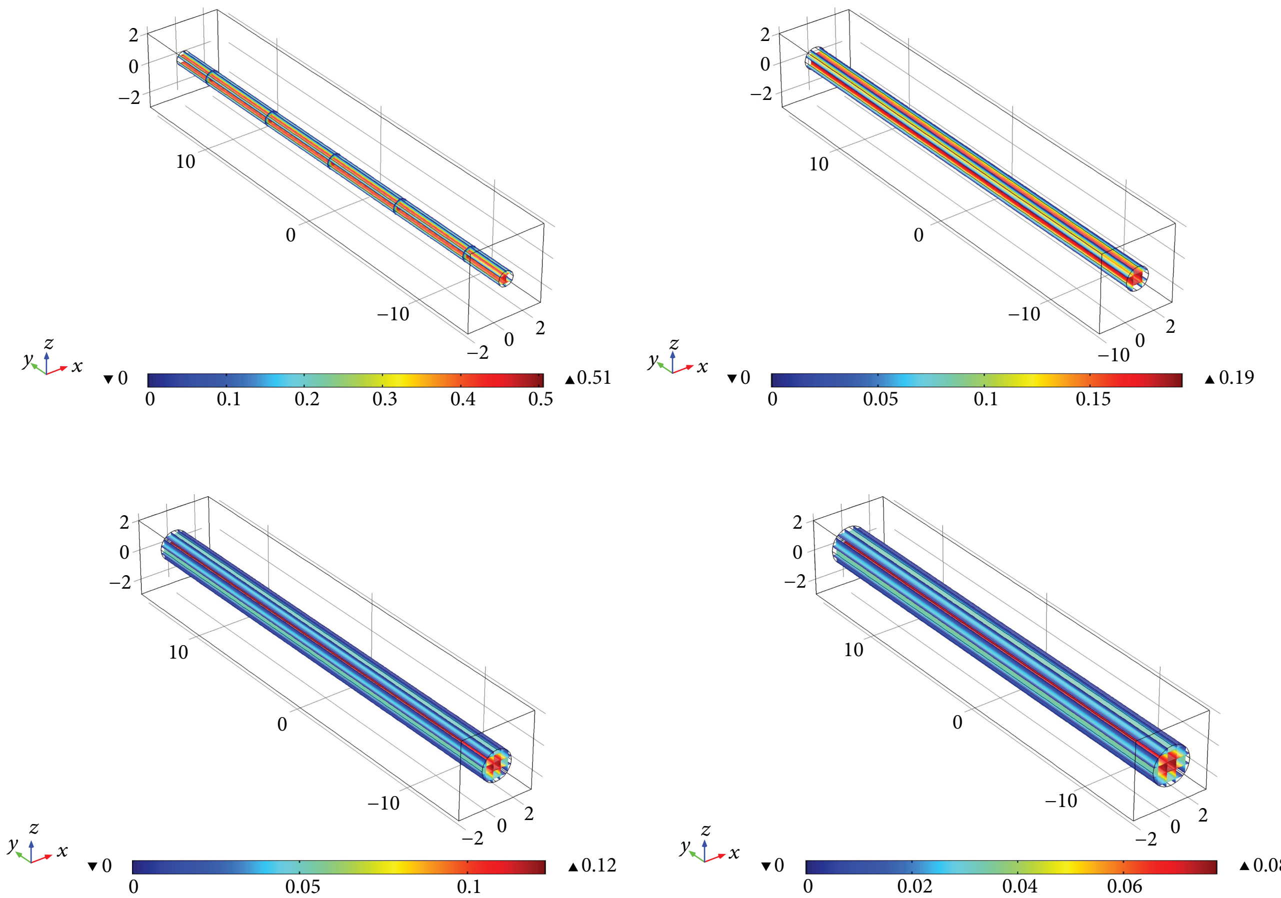

Figure 4: Simulation of the gas flow rate in the gas circuit.

The CFD module in COMSOL Multiphysics simulation software is used to simulate the gas flow field formed by the carrier gas flow in the gas path, and the results were shown in Figure 4.

Significant differences between the airflow pattern near the central area of the carrier gas inlet and the airflow pattern in other areas of the ionization chamber can be clearly observed. Among them, for an extremely small pipe diameter, a dead volume in an annular flow pattern may be formed due to a constant flow of 50 ml. And the presence of a relatively large dead volume can lead to a series of problems, such as widening of the chromatographic peaks, retention of the sample in the ionization chamber, and contamination of subsequent samples to be detected. Thus, it was necessary to reduce such areas during the design of the ionization chamber. Therefore, the diameter of the gas pipeline was designed to be 1.2 mm according to the diameter of the chromatographic column [20].

4. Experimental Section

4.1. System Characterization and Optimization. As shown in Figure 5, using borosilicate glass as the ionization chamber and electrode shell of the photoionization detector, the electrode is integrated into the etched channel using MEMS technology. By this way, the problem of the compact structure of the collector plates is solved. The ultraviolet lamp is mounted together with the electrode, and the sealing is guaranteed by the bonding process. Chromatographic columns are used as input and output channels, and weak signals are processed by the amplifier circuit.

The miniature photoionization detector consists of a lamp, an upper sealing layer, an air chamber, an electrode, and a lower sealing layer. The lamp body uses the baseline line vacuum ultraviolet lamp (IP/N 043-257), the ionization energy is 10.6 eV, and the internal filling gas is krypton. The upper end sealing layer of the lamp is selected with a glass wafer of 0.5 mm, a 20 mm × 20 mm rectangle is cut through the laser etching method, and the opening is processed in the center area with a diameter of 8 mm. The lower sealing layer of the lamp also uses the glass wafer of BF33 with a thickness of 1 mm. Laser technology is used to etch the rectangular area of 30 mm × 30 mm, the air inlet, the air outlet, the electrode installation groove, and the conduit groove. The electrode with high conductivity is used as the collector of ion and electron, and the sealing layer is sealed by the anode bonding process. The inlet and outlet are connected by chromatographic column, and the two ends are sealed with UV curing adhesive. The opening and the ultraviolet lamp window of the upper sealing layer are sealed with UV curing adhesive. The miniature photoionization detector is shown in Figure 6.

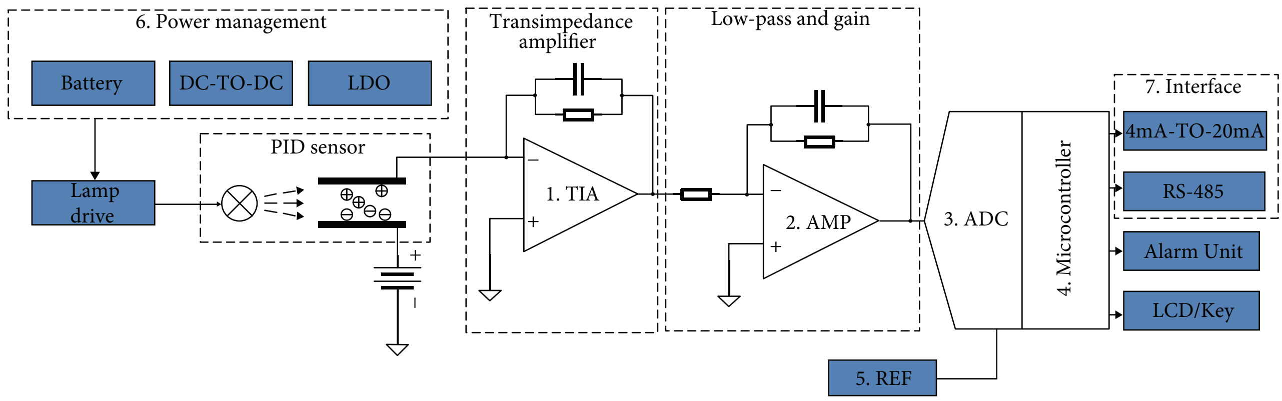

Figure 5: Schematic diagram of the miniature PID.

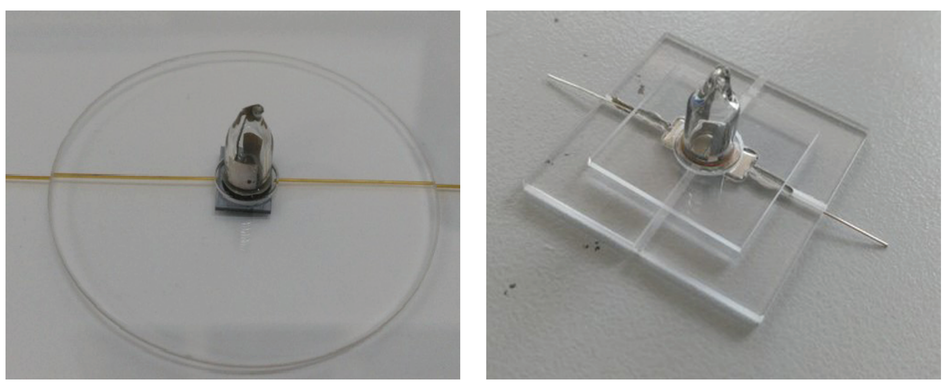

(a) Conductive silicon electrode detector

(b) Silver electrode detector

Figure 6: Miniature photoionization detector.

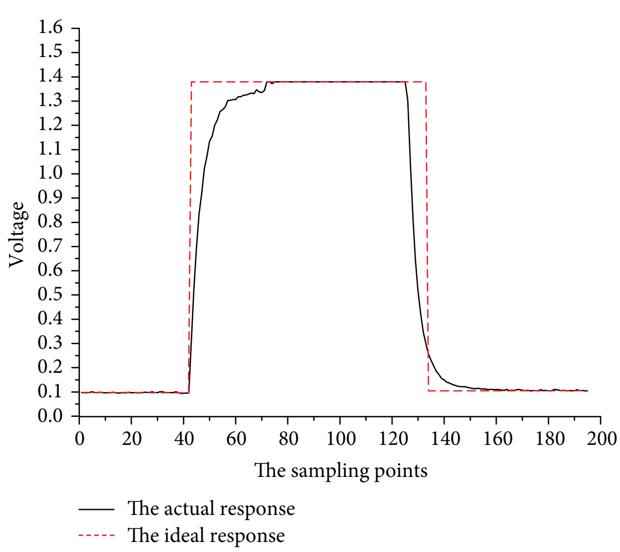

Figure 7: The sensor response process of the PID.

The UV lamp is surrounded by two symmetrical copper sheets and activated by high voltage (100 kHz). This excitation method is similar to RF excitation and has the advantages of good reliability, uniform radiation intensity, and so on, but needs lower frequency. It can effectively reduce the electromagnetic interference to the rest of the circuit.

The determination process can be simplified as shown in Figure 7. The sample was introduced at time $t = 60$ and ended when it was stable. And the injection process is equivalent to the rectangular step shown in Figure 7:

$$x(t) = A[u(t) - u(t - t_x)], \quad 0 \leq t < t_y, \tag{18}$$

in which A was the steady value of the sensor responding to gas components. The sensor response value was associated with the gas flow rate and surrounding conditions. When the gas flow rate and surrounding conditions were constant, the sensor response value may only depend on the concentration and species of gas to be determined, and the steady value A may exhibit certain functional relationship with the gas concentration [21].

4.2. The Effect of Offset Voltage of the Paranoid Electrode on the Sensor Response. The suction flow rate of the diaphragm pump was maintained at 50 ml/min using the MFC (mass flow controller). The bias voltage is continuously increased from 85 V to 165 V for a certain voltage test point. Three sample injections (5 ppm toluene) were performed for each flow rate when both the system and background gases were

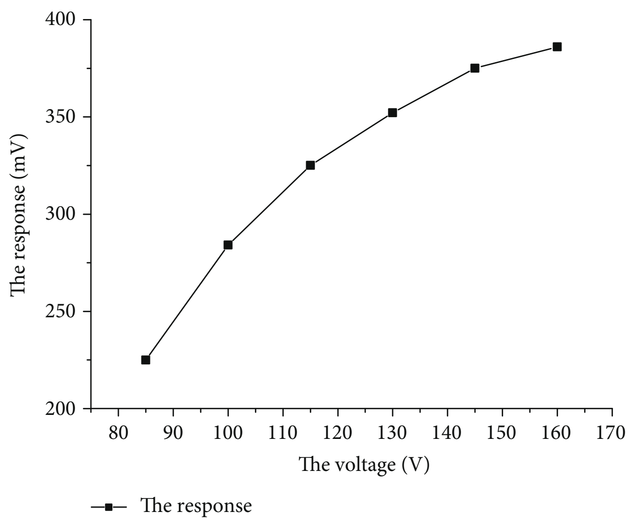

Figure 8: The effect of offset voltage on sensor response of the PID.

steady, acquiring the response using a micro current amplifier, and the results were shown in Figure 8.

Polynomial fitting of the experimental data obtained was performed by the MATLAB software, where the x-axis indicated the offset voltage strength and the y-axis indicated the value of response, and then the following equation can be derived:

$$f(x) = 0.0001402 * x^3 - 0.07638 * x^2 + 14.54x - 539.2. \quad (19)$$

As can be seen from Figure 8, the response value of toluene at 5 ppm gradually increases with the increase of the voltage, but the response value grows more slowly with the voltage. After reaching a certain voltage, the response voltage reaches a maximum value, and the response tends to stabilize as the voltage value continues to rise.

4.3. Linear Calibration of the Sensor. The gas with different toluene concentrations of 0.5 ppm, 1 ppm, 1.7 ppm, 2.5 ppm, and 5.1 ppm produced by a gas generator was employed in the present study, with nitrogen as the ambient gases, and 3 times of sample introduction for each concentration was conducted; the results were shown in Table 2.

By the linear polynomial fitting of the experimental data shown in the table above, the following equation can be derived:

$$p = 0.00394 * C + 0.2563, \quad (20)$$

in which p was the response value, with the unit of mV, and C was the concentration, with the unit of ppm. The result was shown in Figure 9.

5. Conclusions

According to the analysis of experimental results, with toluene as the gas component to be determined, the relationship between the gas flow rate and response value of the PID sensor can well-satisfy the mechanisms of the photoionization sensor. The optimal working flow rate was in the range of 50 ml/min–70 ml/min. The finite element method was used to simulate the photoionization rate. The simulation results show that the structure of the photoionization detector is optimized. Ion collection efficiency reaches 91% with bias voltage of 150 V. Moreover, a preferable linearity of 99.99% of the photoionization detector was obtained and the LOD can reach ppb. The experimental results indicated that, in the range of 0 ppm–5 ppm, clear linear relationship of gas concentration with PID response value was obtained. The experiment proved that the micro photoionization detector can be widely applied to online detection of VOCs.

Table 2: Experimental results of concentration-response.

	0.5 ppm	1 ppm	1.7 ppm	2.5 ppm	5.1 ppm
	60	176	320	487	1288
Voltage value	62	173	317	478	1284
	60	175	319	479	1279
Average value	61	174.6	318.7	481.3	1283.7
Variance	1	1.52	1.53	4.93	4.51

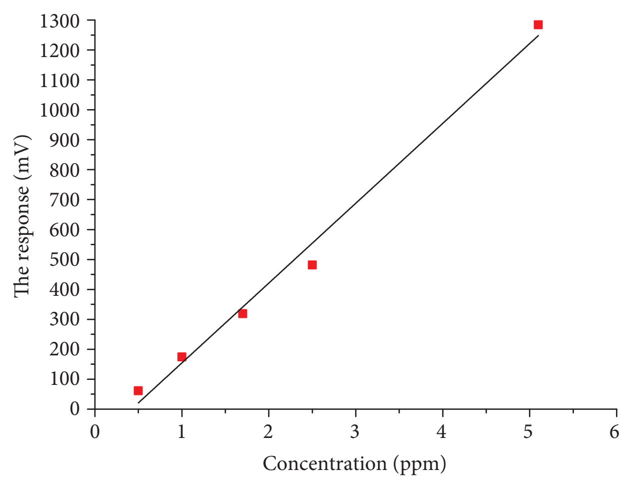

Figure 9: The effect of gas concentration on response value.

Data Availability

No data were used to support this study.

Conflicts of Interest

We do not have any competing interest.

Acknowledgments

This research is supported by Natural Science Foundation of Tianjin (14JCYBJC42700) and the National Key Scientific Instrument and Equipment Development Project (2012YQ060165).

References

[1] L. Fernandez, S. Guney, A. Gutierrez-Galvez, and S. Marco, "Calibration transfer in temperature modulated gas sensor arrays," *Sensors and Actuators B: Chemical*, vol. 231, pp. 276–284, 2016.

[2] G. P. P. Kamatou and A. M. Viljoen, "Comparison of fatty acid methyl esters of palm and palmist oils determined by GCxGC–ToF–MS and GC–MS/FID," *South African Journal of Botany*, vol. 112, pp. 483–488, 2017.

[3] A. Bellili, M. Schwell, Y. Bénilan et al., "VUV photoionization and dissociative photoionization spectroscopy of the interstellar molecule aminoacetonitrile: theory and experiment," *Journal of Molecular Spectroscopy*, vol. 315, pp. 196–205, 2015.

[4] T. T. Fernandez, M. Sakakura, S. M. Eaton et al., "Bespoke photonic devices using ultrafast laser driven ion migration in glasses," *Progress in Materials Science*, vol. 94, pp. 68–113, 2018.

[5] C. Oberhüttinger, A. Habauzit, A. Hackner, and G. Müller, "A rate equation approach towards surface ionisation gas detection," *Sensors and Actuators B: Chemical*, vol. 160, no. 1, pp. 981–990, 2011.

[6] L. Lorenzelli, A. Benvenuto, A. Adami et al., "Development of a gas chromatography silicon-based microsystem in clinical diagnostics," *Biosensors & Bioelectronics*, vol. 20, no. 10, pp. 1968–1976, 2005.

[7] G. Ferri, E. Caselli, V. Mattoli, A. Mondini, B. Mazzolai, and P. Dario, "SPIRAL: a novel biologically-inspired algorithm for gas/odor source localization in an indoor environment with no strong airflow," *Robotics and Autonomous Systems*, vol. 57, no. 4, pp. 393–402, 2009.

[8] J. N. Gavgani, A. Hasani, M. Nouri, M. Mahyari, and A. Salehi, "Highly sensitive and flexible ammonia sensor based on S and N co-doped graphene quantum dots/polyaniline hybrid at room temperature," *Sensors and Actuators B: Chemical*, vol. 229, pp. 239–248, 2016.

[9] T. Jamshaid, E. T. T. Neto, M. M. Eissa et al., "Magnetic particles: from preparation to lab-on-a-chip, biosensors, microsystems and microfluidics applications," *TrAC Trends in Analytical Chemistry*, vol. 79, pp. 344–362, 2016.

[10] H. Zhu, R. Nidetz, M. Zhou et al., "Flow-through microfluidic photoionization detectors for rapid and highly sensitive vapor detection," *Lab on a Chip*, vol. 15, no. 14, pp. 3021–3029, 2015.

[11] A. Heptner, T. Reinecke, N. Angerstein, and S. Zimmermann, "A novel ion selective gas sensor based on pulsed atmospheric pressure chemical ionization and ion-ion-recombination," *Sensors and Actuators B: Chemical*, vol. 246, pp. 252–257, 2017.

[12] B. Wang, E. C. Sivret, G. Parcsi, and R. M. Stuetz, "Determination of VOSCs in sewer headspace air using TD–GC–SCD," *Talanta*, vol. 137, pp. 71–79, 2015.

[13] A. Abdelhalim, M. Winkler, F. Loghin, C. Zeiser, P. Lugli, and A. Abdellah, "Highly sensitive and selective carbon nanotube-based gas sensor arrays functionalized with different metallic nanoparticles," *Sensors and Actuators B: Chemical*, vol. 220, pp. 1288–1296, 2015.

[14] J. Sun, F. Guan, D. Cui, X. Chen, L. Zhang, and J. Chen, "An improved photoionization detector with a micro gas chromatography column for portable rapid gas chromatography system," *Sensors and Actuators B: Chemical*, vol. 188, pp. 513–518, 2013.

[15] M. Suresh, N. J. Vasa, V. Agarwal, and J. Chandapillai, "UV photo-ionization based asymmetric field differential ion mobility sensor for trace gas detection," *Sensors and Actuators B: Chemical*, vol. 195, pp. 44–51, 2014.

[16] J. Liu, J. H. Seo, Y. Li, D. Chen, K. Kurabayashi, and X. Fan, "Smart multi-channel two-dimensional micro-gas chromatography for rapid workplace hazardous volatile organic compounds measurement," *Lab on a Chip*, vol. 13, no. 5, pp. 818–825, 2013.

[17] R. Zimmermann, W. Welthagen, and T. Groger, "Photo-ionisation mass spectrometry as detection method for gas chromatography. Optical selectivity and multidimensional comprehensive separations," *Journal of Chromatography. A*, vol. 1184, no. 1-2, pp. 296–308, 2008.

[18] J. Liu, M. K. Khaing Oo, K. Reddy et al., "Adaptive two-dimensional microgas chromatography," *Analytical Chemistry*, vol. 84, no. 9, pp. 4214–4220, 2012.

[19] L.-S. Zhai, P. Bian, Z.-K. Gao, and N.-D. Jin, "The measurement of local flow parameters for gas–liquid two-phase bubbly flows using a dual-sensor probe array," *Chemical Engineering Science*, vol. 144, pp. 346–363, 2016.

[20] C. Gnodtke, U. Saalmann, and J.-M. Rost, "Slow and fast multi-photon ionization of clusters in strong XUV and X-ray pulses," *Chemical Physics*, vol. 414, pp. 65–68, 2013.

[21] W. R. Collin, K. W. Scholten, X. Fan, D. Paul, K. Kurabayashi, and E. T. Zellers, "Polymer-coated micro-optofluidic ring resonator detector for a comprehensive two-dimensional gas chromatographic microsystem: μGC × μGC–μOFRR," *The Analyst*, vol. 141, no. 1, pp. 261–269, 2016.

Hindawi
Applied Bionics and Biomechanics
Volume 2018, Article ID 4357602, 13 pages
https://doi.org/10.1155/2018/4357602

Research Article

Mechanical Design and Assessment of a Low-Cost 7-DOF Prosthetic Arm for Shoulder Disarticulation

José-Alfredo Leal-Naranjo,[1] **Christopher-René Torres-San Miguel**,[2] **Marco Ceccarelli**,[3] **and Horacio Rostro-Gonzalez**[1]

[1]*Departamento de Electrónica, DICIS, Universidad de Guanajuato, 36885 Salamanca, GTO, Mexico*
[2]*Instituto Politécnico Nacional, Sección de Estudios de Posgrado e Investigación, Unidad Profesional "Adolfo López Mateos", Escuela Superior de Ingeniería Mecánica y Eléctrica Zacatenco, Edificio 5, 2° Piso Col. Lindavista, 07738 México City, Mexico*
[3]*Laboratory of Robotics and Mechatronics (LARM), DiCEM, University of Cassino and Southern Lazio, 03043 Cassino, Italy*

Correspondence should be addressed to José-Alfredo Leal-Naranjo; lealnaranjo@gmail.com

Received 12 April 2018; Revised 28 June 2018; Accepted 25 July 2018; Published 3 September 2018

Academic Editor: Dongming Gan

This work presents the design of a low-cost prosthetic device for shoulder disarticulation. A proper design of the mechanisms has been addressed to obtain a prototype that presents 7 degrees of freedom. Shoulder movement is achieved by means of a spherical parallel manipulator, elbow movement is performed by a six-bar mechanism, and the wrist movement is implemented by a spherical parallel manipulator. A set of dynamic simulations was performed in order to assess the functionality of the design. The prototype was built using 3D printing techniques and implementing low-cost actuators. An experimental evaluation was carried out to characterize this device. The result of this work is a prototype that weighs 1350 g that is able to perform movements related to activities of daily living.

1. Introduction

One of the main issues related to the design of prosthetic devices is to mimic as close as possible the human motion. It has been demonstrated that the reduced dexterity of prosthetic arms yields to compensatory movements that could cause injuries in the long-term use [1]. Furthermore, the low functionality of the device causes overuse syndrome in people with upper limb deficiency [2]. Besides, the more proximal the amputation, the higher is the rate of abandonment of prosthetic arms [3]; this is mainly due to a low functionality and comfort. Shoulder disarticulation shows the lowest rate of incidence, so there is low incentive to develop solutions for people with this disability, and therefore, few prosthetic devices have been designed [4]. The amputation of the shoulder involves the necessity of more DOFs in the prosthetic device, and consequently, the complexity of the system increases.

Currently, some commercial solutions exist for different levels of arm amputation; among these, the most advanced prosthetic upper limbs available in the market are the *i-limb Ultra*, the *bebionic® v2 hand*, the *Contineo Multi-Grasp®*, and the *Michelangelo®* [5]. The patients with above-elbow amputation and shoulder disarticulation are the most difficult cases to approach; this is because more functional segments are needed in the prosthetic device and the difficulty of its design increases.

To the best of our knowledge, very few research works have been developed related to the design of a total upper limb. A design sponsored by the Defense Advanced Research Projects Agency (DARPA) of the USA is presented in [6]. This is a 4.8 kg device with different configurations and consists of a two-DOF actuated shoulder, a humeral rotator, an elbow, and a battery, which has been characterized by 26 DOFs (including the hand). The complexity of this device makes it unaffordable for most people.

The DEKA arm is one of the most advanced upper limb prostheses [7]. Patients with different amputation levels can use this device. It is the result of a project sponsored by DARPA. It shows a modular configuration that can be adapted to different amputation levels. The configuration for shoulder disarticulation has 10 DOFs that are distributed with six DOFs in the arm and four in the hand with a weight of 4.5 kg. This prosthesis can be controlled by different signals like switches and myoelectric signals and even with targeted reinnervation [8].

A 7-DOF prosthetic upper limb is presented in [9]. This prototype includes an underactuated hand with 15 DOFs. This device is based on differential mechanisms, where the load is shared between two motors, allowing the use of smaller actuators. The total weight of this system is 4.45 kg, which makes it heavy for use for a long time.

A survey on the current prosthetic arms shows that these solutions have been generally designed with fewer DOFs than the required ones. These designs present the limitations of low functionality and high weight. Furthermore, the most sophisticated prosthetic arms are unaffordable for most of the population and have been designed by long-term projects sponsored by the US Army.

Considering the previously outlined, in this work, we propose a light and easy-to-afford upper limb prosthesis for people with shoulder disarticulation that allows mimicking the movement of an arm through a set of prescribed trajectories.

2. Design of a Prosthetic Arm

The open issues referring to the upper limb prosthesis are the lack of functionality and discomfort due to high weight and that most of the devices are unaffordable.

The necessity of more functional segments presented in devices for shoulder disarticulation makes the mechanical design of the prosthetic arm an important topic. The prototype developed in this work has seven degrees of freedom achieved by a 3-DOF shoulder, a 1-DOF elbow, and a 3-DOF wrist. A preliminary design where the feasibility of the mechanism is shown is presented in [10].

3. Shoulder Design

The available space to allocate the shoulder mechanism makes the design of the shoulder a challenging task if an anthropomorphic shape is required. The prosthetic shoulder supports the entire structure of the device; therefore, the largest joint loads are developed in the shoulder.

The shoulder mechanism is modeled as a 3-RRR-type spherical parallel manipulator (Figure 1). The dimensional synthesis of this manipulator was carried out using a multi-objective optimization based on genetic algorithms [11].

After the dimensional synthesis, from the inverse kinematics of the manipulator, it was observed that the links of the manipulator only perform rotations of an amplitude smaller than 90°. Considering this, it was proposed to include a mechanism in order to increase the torque that the motors exert to the links of the spherical manipulator.

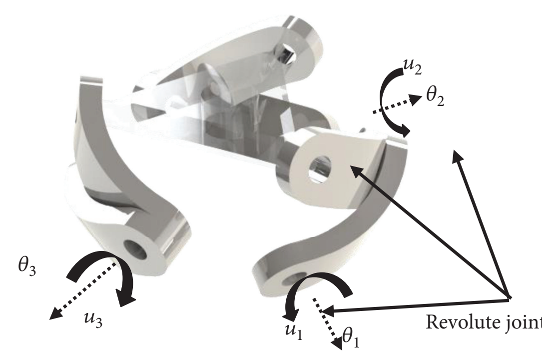

Figure 1: 3-RRR parallel manipulator.

The proposed mechanism to achieve a mechanical advantage is a four-bar mechanism that is installed before the designed solution. A single-objective optimization procedure was carried out to define the link lengths. The objective function was the minimization of the maximum torque exerted by the motor. A static analysis of the four-bar mechanism was performed as shown in Figure 2.

From the free body diagram in Figure 2, an equation can be found to evaluate the torque of the motor (τ_{in}) as a function of the parameters of the mechanism and the torque that requires the manipulator (τ_{out}) for a defined task. This can be established as

$$\mathbf{A}x = b, \tag{1}$$

where $\mathbf{A}$ is the coefficient matrix that depends on the link lengths and the position of the mechanism, $x = [F1_x, F1_y, F2_x, F2_y, F3_x, F3_y, F4_x, F4_y, \tau_{in}]$, and $b = [0, 0, 0, 0, 0, 0, 0, 0, \tau_{out}]$.

From previous dynamic simulations [11], τ_{out} and θ_3 are known values. An optimization based on GA was carried out using the algorithm in Figure 3. The chosen parameters were the link lengths (L_1, L_2, L_3, and L_4). An initial population of 200 elements was set in order to have a wide diversity of elements, and the maximum number of iterations was set to 100.

The initial population was created in a random way with link lengths ranging from 1 to 10 cm. Figure 4 shows the evolution of the link lengths during the optimization process (left y-axis). It can be seen that convergence is reached approximately at iteration 70. Figure 4 shows the evolution of the torque during the optimization process (right y-axis). This procedure was repeated for the three limbs of the parallel manipulator; thus, three different four-bar mechanisms were obtained. A four-bar mechanism attached to the parallel manipulator can be seen in Figure 5.

4. Elbow Design

The flexion-extension of the elbow and the pronation-supination of the forearm can be modeled as two perpendicular revolute joints in series, but in this design, the pronation-supination is left as a movement of the wrist.

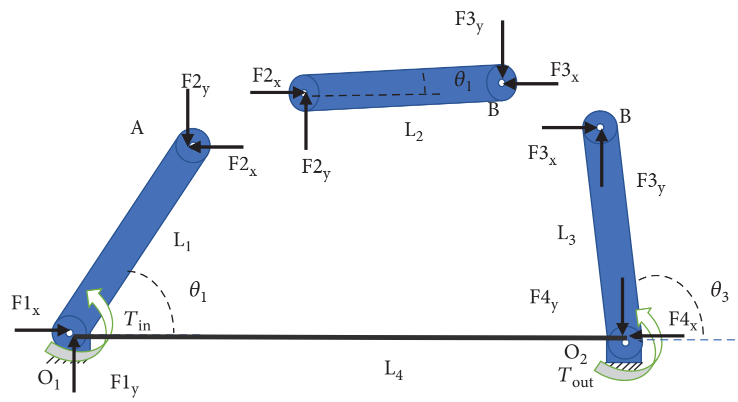

FIGURE 2: Free body diagram of the four-bar mechanism that joins the actuator and the base link of the parallel manipulator.

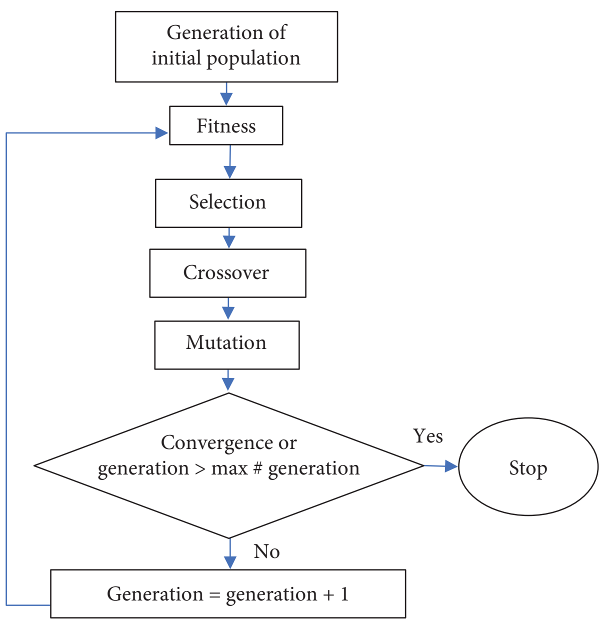

FIGURE 3: A flowchart of a genetic algorithm optimization.

The flexion-extension is performed using a six-bar mechanism that can be analyzed as two four-bar mechanisms. In the first part of the mechanism, links a and c have the same length as well as links b and d (Figure 6(a)). In this mechanism, the rotation of link c is the same as the rotation of link a. Link b is designed with a curvature in order to avoid collision with the external part of the prosthesis. The first four-bar mechanism is driven by a second one (Figure 6(b)). This mechanism is a singularity-based four-bar mechanism as suggested in [12]. As the input mechanism approaches a singularity, the output torque increases. The first link is attached to the actuator, and the third link is part of link a. The links of the second mechanism were designed in such a way that the range of motion of the third link is 90°; this is done to be able to complete the elbow flexion-extension motion. A graphical linkage synthesis was applied [13]. This design allows placing the actuator near to the shoulder, and in this way, the reduction of the moment of inertia is achieved.

5. Wrist Design

The forearm pronation-supination, wrist flexion-extension, and wrist ulnar-radial deviation are achieved by means of a spherical manipulator that is placed at the wrist. This mechanism is used because the load is distributed into small motors that can be fitted inside the forearm structure (Figure 7).

To simplify, the design was considered a symmetrical architecture for the parallel mechanism. This means that the upper and lower pyramid of the manipulator are regular pyramids and are defined by the angles γ and β and were defined as suggested in [14]. As a symmetrical mechanism, the three legs are equal and there are only two parameters to define. Such parameters are the angles of the two links of each leg, α_1 and α_2. The dexterity and torque were calculated for different values of α_1 and α_2 ranging from 50° to 80, and it was concluded that the most suitable values for the size of the links were $\alpha_1 = 60^\circ$ and $\alpha_2 = 80^\circ$.

Three servomotors were placed inside the forearm. Each servo drives a bevel gear. There is a timing belt at the output side of the gear. A second timing belt is attached to the driving link of the parallel manipulator of the wrist (Figure 8).

According to [15], the required wrist range of motion (ROM) to perform different activities of daily living is 40° for wrist flexion and extension (each) and 40° of combined radial-ulnar deviation. This ROM is achieved with the selected parameters of the wrist mechanism.

6. Overall Design of the Prosthetic Arm

The proposed mechanisms were assembled together in a serial configuration to make a human-like upper limb prosthesis as shown in Figure 9, including a prosthetic hand design in a previous work [16]. The shoulder presents the three-DOF spherical manipulator with its actuators. The spherical mechanism allows the three movements of the shoulder using small motors. The end effector of the manipulator is attached to the forearm structure by means of a plate. The actuator that drives the elbow is placed at the proximal part of the forearm. With the described design, the prosthetic device can be constructed with a human-like size.

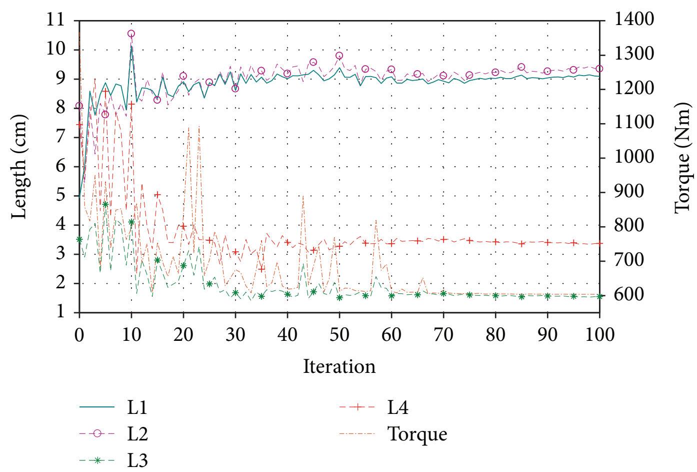

FIGURE 4: Evolution of the length links (left y-axis) and torque (right y-axis) during the optimization procedure.

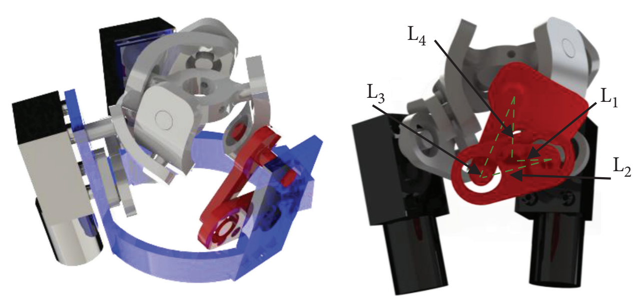

(a) (b)

FIGURE 5: A CAD design of the final parallel manipulator with the four-bar mechanisms: (a) isometric view; (b) frontal view.

Inside the prosthetic arm, there is enough space to place the batteries and control system.

7. Numerical Evaluation

Using the software MSC.ADAMS®, a set of dynamic simulations was performed in order to assess the relationship between the actuators and forces acting on the mechanism and the resulting acceleration, velocity, and motion trajectories. ABS with a density of 1020 kg/m^3 was considered for the elements of the prosthetic arm. The weights of the actuators inside the arm were taken into account. At the joints of the shoulder mechanism of the prototype, deep groove ball bearings are located, so the friction coefficient was considered as 0.0015 [SKF, 2017]. In the remaining joints, the assembly was done using bolts, so the friction coefficient was considered as 0.1.

To evaluate the prototype, the simulations were defined as follows: Test I, a humeral flexion from −20° to 90° with the elbow extended and with a load of 5 N at hand (Figure 10(a)); Test II, an elbow flexion from 0° to 90° with the arm in vertical position and a load of 5 N at hand (Figure 10(b)); and Test III, a flexion from −40° to 40° of the wrist with the elbow flexed at 90° (Figure 10(c)).

Test I was performed in two different cases. In the first case, the experiment was carried out using the proposed four-bar mechanism attached to the parallel manipulator and with a duration of 2 s, and in the second case, it was performed actuating directly the parallel manipulator. Both cases were compared to show the performance of the implementation for the four-bar mechanism.

For the first case in Test I, the shoulder motor torques required to perform the humeral flexion were computed (Figure 11(a)). It can be seen from the plot that the maximum torque is nearly 1.25 Nm. When the arm is crossing the vertical, the torques reach their minimum value. As the movement continues, the torques increase smoothly until they reached the maximum and then fall by the end of the motion. The angular displacement, the angular velocity, and the angular acceleration of the actuators were evaluated (Figures 11(b)–11(d)). It can be seen that the motors show a smooth movement. The range of the motion of the first and third motors is approximately 200°, and the second motor rotates 160°. There is an instant where motor 2 is stopped and then changes the direction of rotation. Along the entire movement, the angular acceleration is low until the last phase of the motion where motor 2 exhibits a significant acceleration. The mechanical power was calculated as the product of the torque and the angular velocity (Figure 11(e)). It can be seen that the maximum power is developed by motor 2 near the end of the motion with a value of 4 W. Regarding the elbow joint, despite no movement of this joint in this test, the torque required to maintain the elbow extended changes along the task ranging from 0 to almost 0.25 Nm (Figure 11(f)).

For the second case in Test I, when the parallel manipulator is actuated directly, the torque required is increased and the maximum torque is approximately 2.1 Nm, which is roughly 60% more than the highest torque of case a (Figure 12(a)). For this case, the maximum power is developed by motor 2 as in case a. The maximum value is 2.9 W (Figure 12(b)). This value is smaller than that in the first case; this could be explained due to the friction in the four-bar mechanism considered in case a.

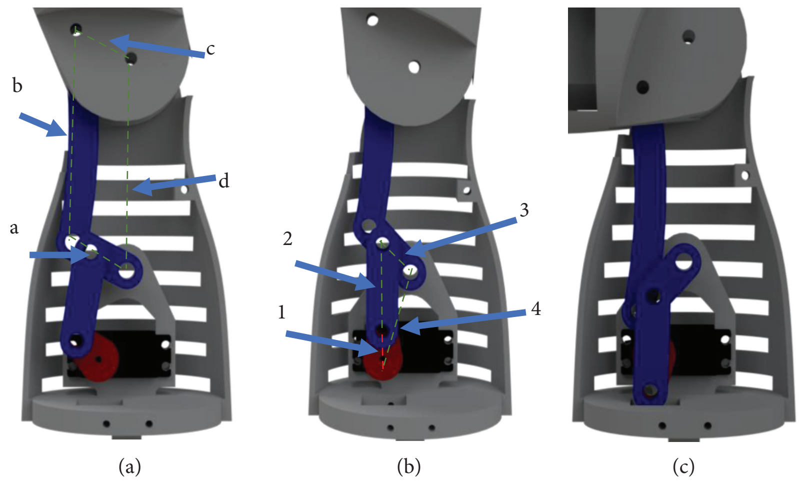

Figure 6: Mechanism design for the elbow flexion-extension: (a) the first four-bar mechanism; (b) the second four-bar mechanism in a singular position; (c) second singular position of the mechanism.

Figure 7: A CAD design of the parallel manipulator of the wrist.

Figure 9: A CAD design of the prosthetic upper limb.

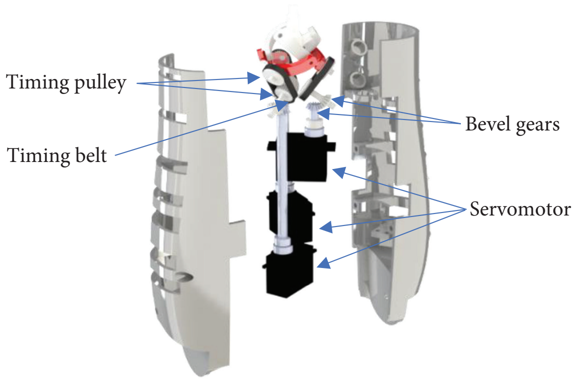

Figure 8: A CAD design of the transmission system of the wrist mechanism.

In Test II, we evaluate the required torque for the elbow actuator to perform the flexion while the arm is in a vertical position. While the motion of the elbow continues, the torque increases until it reaches its maximum value of 1.5 Nm; then this value decreases as the four-bar mechanism of the elbow reaches its singular position (Figure 13(a), left y-axis). The power has a maximum value of 3.1 W (Figure 13(a), right y-axis). At the beginning and at the end of the movement, the power is low since the required torque is also low. The angular velocity (left y-axis) and angular acceleration (right y-axis) of the elbow actuator during this movement follow a sinusoidal wave (Figure 13(b)).

The functionality of the wrist is evaluated during Test III. In this test, as the load reaches the midpoint of the movement, where the lever arm of the wrist is maximum, the torques increase to their maximum value of 0.45 Nm; then it is reduced as the final position is reached (Figure 14(a)). The

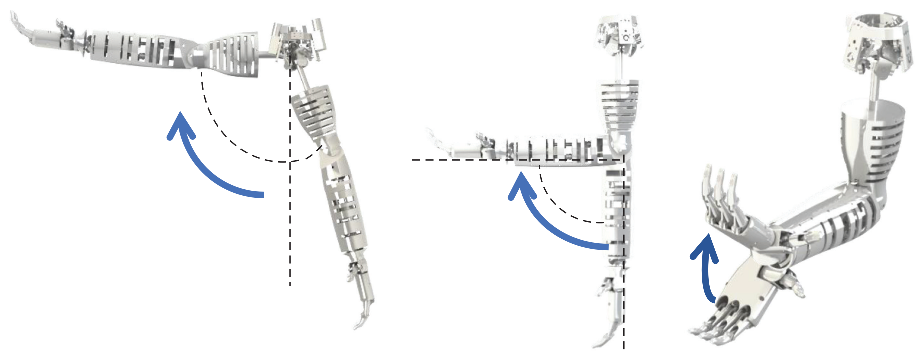

Figure 10: Simulation modes for the prototype: (a) humeral flexion with the elbow extended; (b) elbow flexion in a vertical position; (c) wrist flexion.

angular displacements, angular velocity, and angular acceleration of the motors present a smooth behavior, and the maximum range is approximately 70° (Figures 14(b)–14(d)). The power developed by the wrist motors during Test III has a maximum value of 0.42 W and is produced by motor 1 (Figure 14(e)). At the beginning and at the end of the movement, the power is close to 0.

8. Prototype Construction and Experimental Validation

A lab prototype of the prosthetic arm was built using a 3D printer Stratasys® Dimension 1200. The material used was ABS. For the parallel manipulator of the shoulder, three gear motors were used. This kind of motor works at 12 V, and the rated torque of the gearbox is 20 kg cm. At the joints of the shoulder mechanism, ball bearing 688zz was used ($8 \times 16 \times 5$ mm). The elbow was actuated with a servomotor model PDI-6221MG. This is a digital servomotor with a stall torque of 20 kg cm. Three MG996R servomotors were used to drive the wrist. These servomotors have a stall torque of 10 kg cm. Table 1 summarizes the cost of the components of the prototype.

The elbow motor was attached to the proximal part of the forearm (Figure 15(a)). Due to its reduced size, it can be easily fitted inside the arm, including the four-bar mechanism (Figure 15(b)). The wrist motors are fitted inside the forearm (Figure 15(c)) and actuate the wrist using bevel gears.

The previous elements and a prosthetic hand were assembled together to form the prosthetic arm (Figure 16).

The weight of the set arm-forearm-hand is 960 g, and the weight of the shoulder is 700 g. Therefore, the total weight of the device is 1660 g, which is lighter than that of a real arm. A comparison of the characteristics between the present design and the state-of-the-art solutions is found in Table 2.

Two movements of the prototype were experimentally assessed. The first movement was the flexion of the elbow, and the second movement was the humeral flexion.

To characterize the movements, the electric current of the motor using an ACS712 current sensor was measured. This sensor, based on a linear Hall sensor, is capable of measuring from 0 to 5 amperes. Its low offset makes it possible to use it without previous calibration and only using the gain of the output (185 mV/A). A GY-87 IMU sensor was used to measure the angular velocity and orientation of the forearm during the elbow flexion and the orientation of the arm during the humeral flexion. The IMU was attached to the forearm section of the prototype. The calibration of the gyroscope was performed measuring the reading offset in each axis while the IMU is not moving. The accelerometer was calibrated using the procedure that is reported in [17]. After calibration, the angular velocity is measured using the gain of the sensor and the orientation was calculated by performing a sensor fusion with a Kalman filter [18]. The data were acquired by using an Arduino Mega at a frequency of 50 Hz.

Considering that the servo tries to reach its final position as fast as possible, a subroutine was programed in order to send intermedium positions to the servomotor, and in this way, the speed is reduced to a proper level. This was performed to have a speed approximately equivalent to the 10% and 50% of the maximum operational speed (0.16 s/60°), namely, speed A and speed B, respectively, and speed C as the maximum speed.

9. Experiment Results

Elbow flexion was performed at three different speeds. The first experiment was at speed A, the second at speed B, and the third experiment at 100% of the speed of the motor. The motor was supplied with 6 V during the experiments. It can be seen that the forearm does not reach a horizontal position (Figure 17). This could be originated by the reduced stiffness of the links of the four-bar mechanism.

The results of the first experiment at speed A show that at the beginning of the movement, there is a peak of power consumption with a current of 2 A (Figure 18(a)). As the movement continues, the current is reduced to an average value of 0.7 A. The sudden decrease of the current could be originated as a result of the singular position of the mechanism at the beginning of the movement; then the current consumption rises as the lever arm increases while

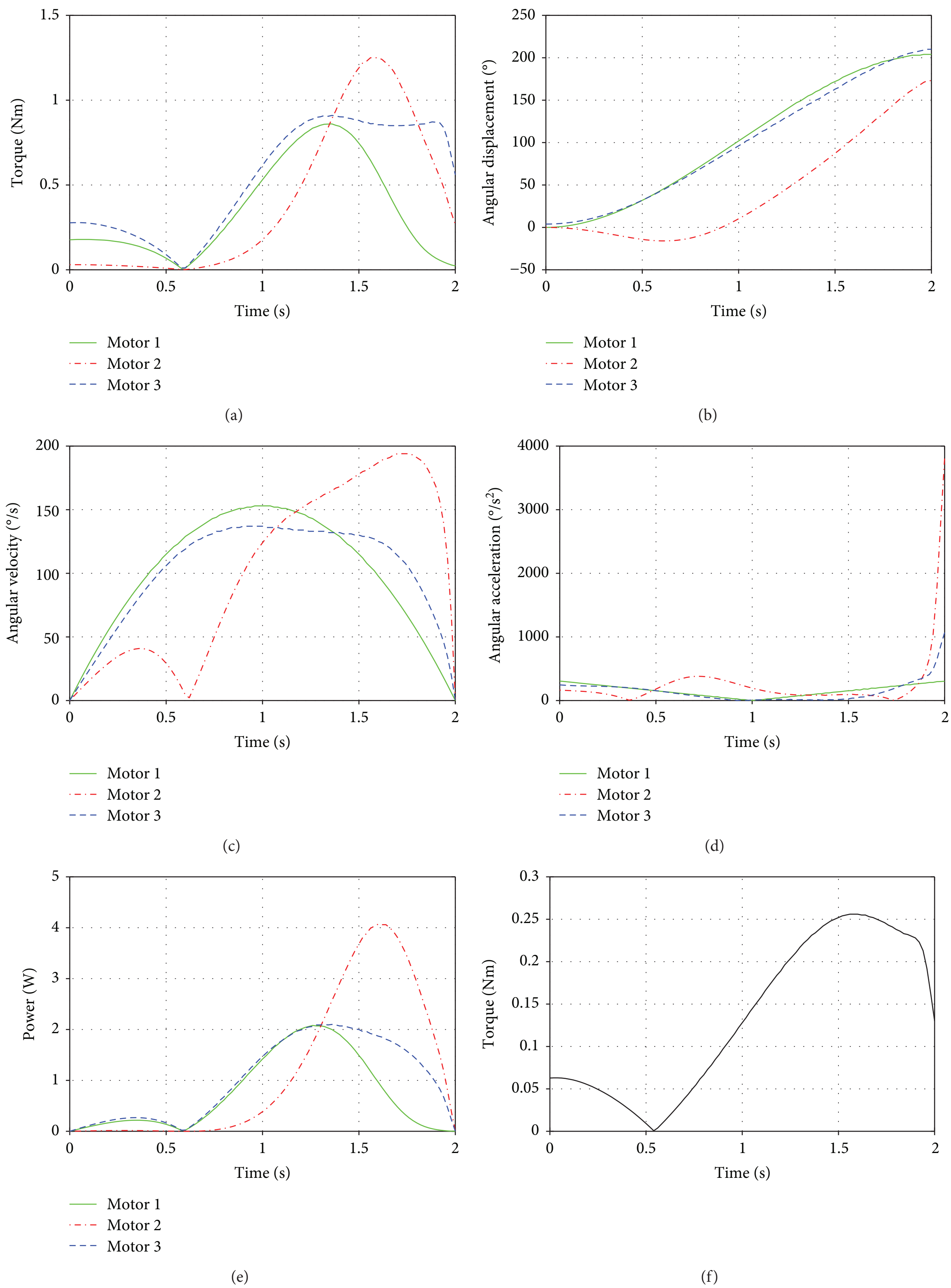

FIGURE 11: Results of Test I case a: (a) torques of the shoulder motors; (b) angular displacement; (c) angular velocity; (d) angular acceleration; (e) power of the motors of the shoulder; (f) torque of the elbow actuator.

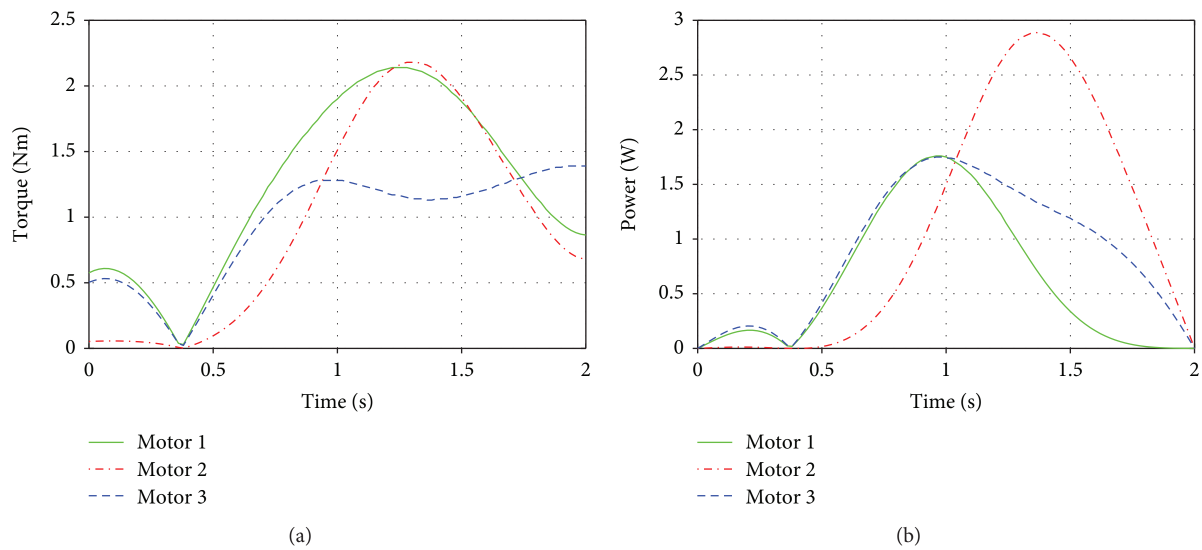

FIGURE 12: Results of Test I case b: (a) torques of the shoulder actuators and (b) power of the motors of the shoulder.

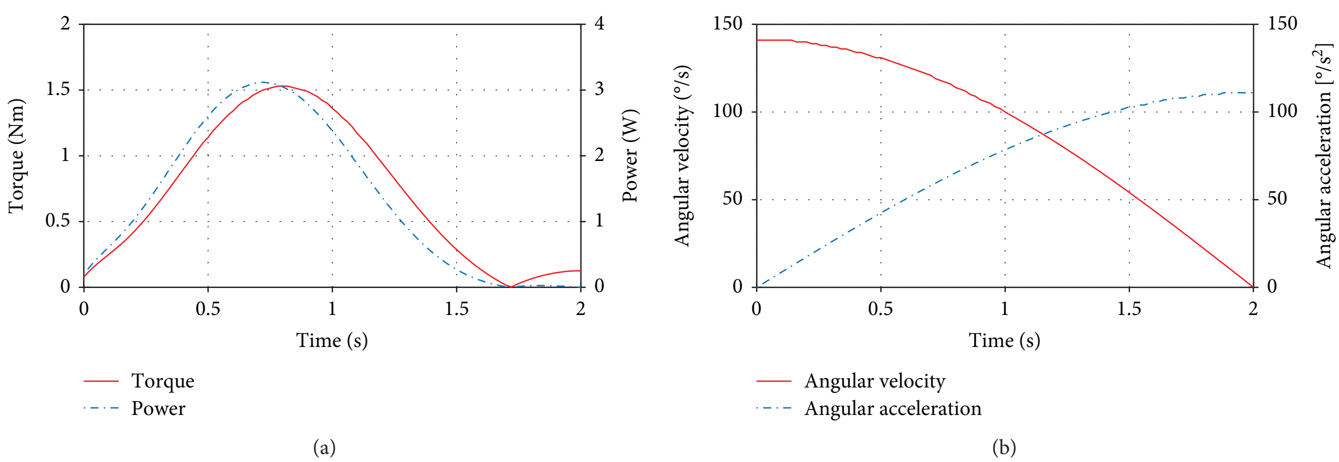

FIGURE 13: Results from Test II: (a) torque of the elbow actuator and mechanical power; (b) angular velocity and angular acceleration of the actuator.

the movement continues. The lever arm reaches its maximum in the middle of the movement and then decreases as the current does. Considering that the voltage supplied was 6 V, the power consumption was calculated. The maximum angular velocity was 20°/s, and the duration of the movement was approximately 3.6 s that is too long to represent a natural movement of the elbow (Figure 18(b)). From Figure 18(c), it can be seen that the movement of the forearm follows a linear function. The range of the motion was approximately 65°; therefore, the entire elbow flexion is not completed.

When the speed of the experiment is set at speed B, the average current is increased to 1.5 A (Figure 18(a)). This represents almost 220% of the current at a velocity of 10%. It can be seen that after the initial peak, there is a drastic drop in the current, again because of the singularity of the mechanism. When the velocity is increased, there is an evident rise in the power consumption, showing a maximum consumption of 9 W. The maximum angular velocity developed during the movement is 85°/s, and it is reached at the midpoint of motion (Figure 18(b)). From Figure 18(d), it can be seen that the final position is reached at 1.6 s; this represents a reduction of the time in more than 100% compared with the previous experiment. This duration is acceptable for an elbow task.

When the speed is set at 100%, the average current is approximately 1.6 A (Figure 18(a)). Knowing that the voltage supply to the motor is 6 V, the power consumption, in this case, is around 9.5 W. In this case, the maximum angular velocity is 110°/s (Figure 18(b)). It can be seen that the duration is shorter than 1.1 s.

After the evaluation of the elbow mechanism, the shoulder flexion with the prototype was performed (Figure 19).

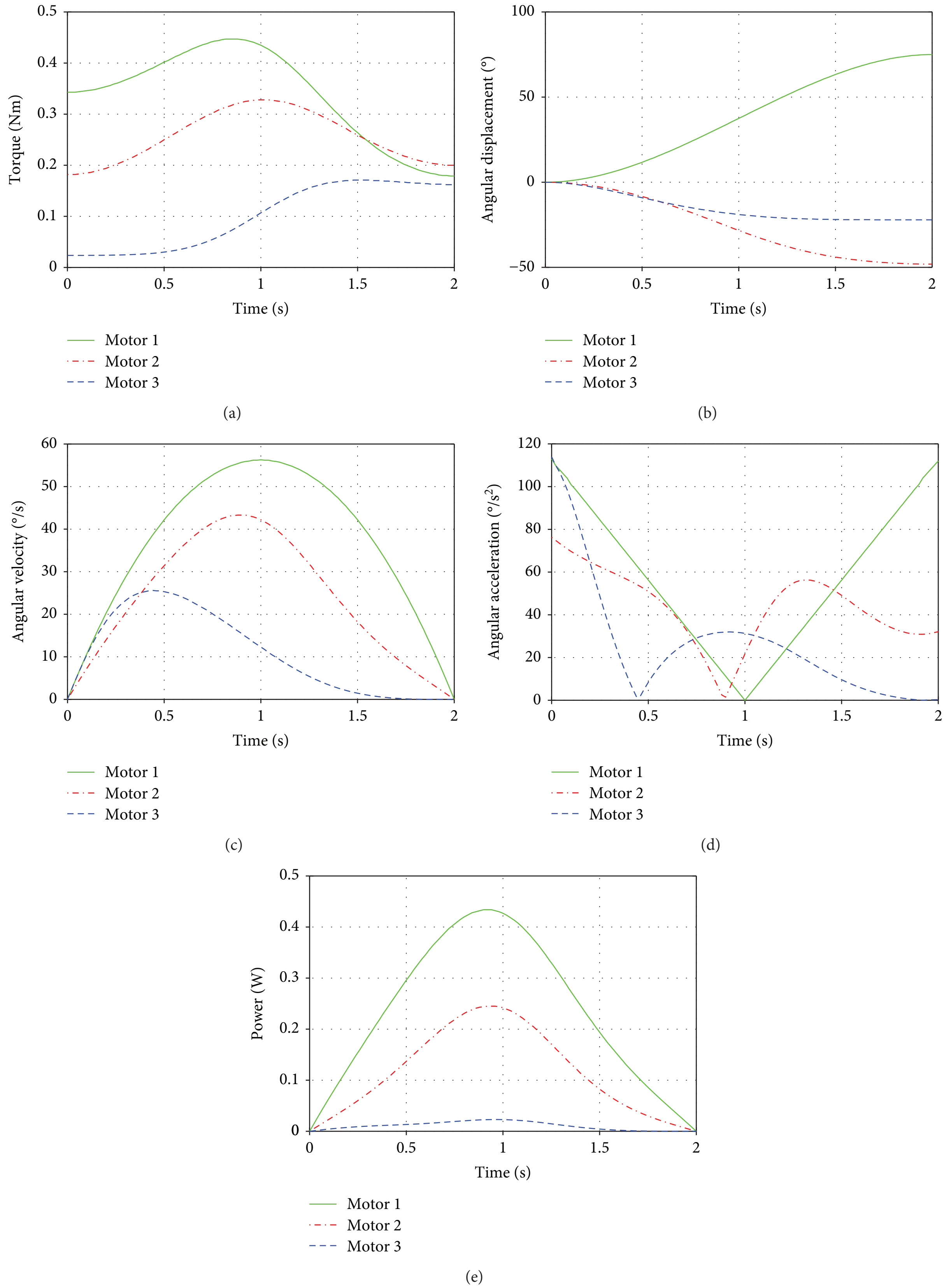

Figure 14: Results of torques of the wrist actuators during Test III: (a) wrist actuator torques; (b) angular displacement; (c) angular velocity; (d) angular acceleration; (e) mechanical power.

Table 1: Cost of the components used to build the prototype.

Component	Total price (USD)
3 gear motors	42
1 servomotor PDI-6221MG	13
3 servomotor MG966R	14
Bearings	6
3D-printed parts	215
Total	290

(a) (b) (c)

Figure 15: Different structures of the prototype: (a) actuator and the four-bar mechanism of the elbow, (b) arm structure, and (c) forearm structure.

(a) (b) (c)

Figure 16: Prototype of the prosthetic arm: (a) frontal view; (b) lateral view; (c) hand attached to the prosthetic arm.

It can be seen that in this case, the arm does not reach a horizontal position but the range of motion is about 90°.

During this experiment, the angular velocity was slow, having a mean value of 10°/s and the duration of the motion of 8.5 s (Figure 20(a)). It can be seen that at the beginning of the movement, there is a peak in the current that is higher in motor 2 (Figure 20(b)). The maximum average current required for this motion was 0.3 A.

Table 2: Main characteristics of the proposed design and the state-of-the-art devices.

Author reference	DOF	Weight	Payload
[6]	7	4.8 kg	55 N
[7]	6	4.5 kg	—
[9]	7	4.45 kg	—
Present work	7	1.66 kg (included hand)	5 N

Figure 17: Snapchat of the elbow flexion experiment.

The experimental validation shows that the proposed prototype is able to perform the movements with a reduced power consumption, but some elements of the device must be made of a different material in order to have enough strength to withstand the loads and not affect the operation of the mechanism.

10. Conclusions

In this work, a new human-like low-cost prosthetic arm has been designed. This device is formed by a three-DOF parallel manipulator at the shoulder, a six-bar mechanism of one DOF at the elbow, and a three-DOF spherical manipulator at the wrist, which are connected in a serial architecture. The spherical manipulator at the shoulder allows sharing the load, and therefore, the required torque and the power consumption of the motors are lower than those in other solutions. The use of small motors has the benefit that its weight is low and it is possible to create a design with a reduced cost and easier to afford than existing solutions. The shoulder mechanism makes it possible to place the actuator of the elbow close to the shoulder, and in this way, the inertial effects are reduced, in comparison to common solutions where the elbow is actuated with big motors placed at the elbow. The synthesis of this mechanism allows locking the elbow when it is fully extended or flexed; then the consumption of the elbow actuator can be reduced in these common positions. The wrist mechanism has a suitable range of

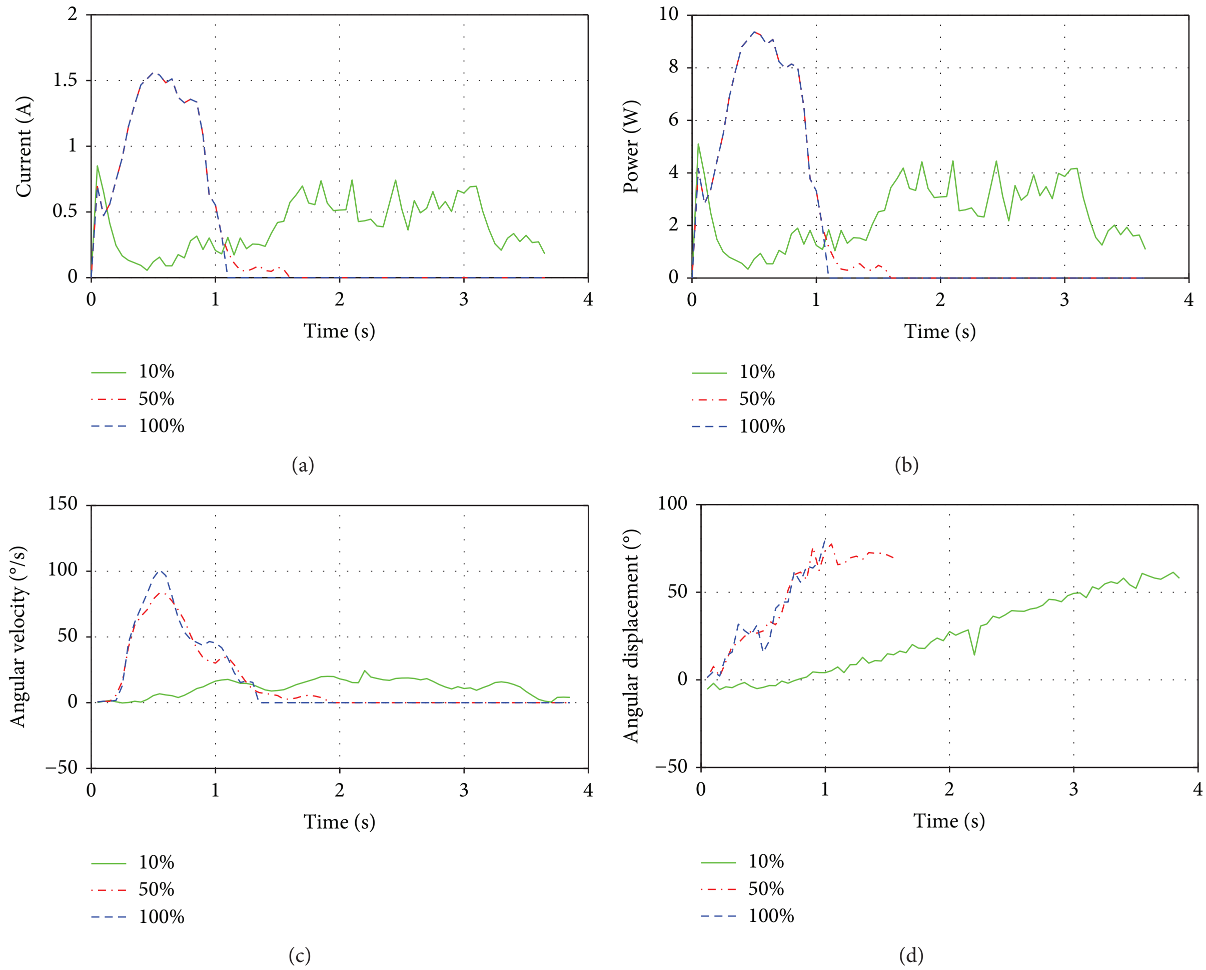

Figure 18: Results from experimental elbow flexion at speeds A, B, and C: (a) electrical current of the elbow motor; (b) electric power; (c) angular velocity; (d) angular displacement.

Figure 19: Sequence of the shoulder performing a humeral flexion movement.

motion to perform ADLs using small actuators. The selection of the mechanism makes it possible to have a prototype with a total weight of 1350 g, not including the hand. This weight is lower than the average weight of a human arm that is approximately 5 kg. The numerical and experimental evaluations show that the prototype can perform natural movements of the human arm.

Despite the feasibility of this device being demonstrated, further work needs to be done: this includes performing structural analysis in order to determinate the most suitable materials and dimensions of the main elements of the prosthesis aiming to assure its structural integrity, the implementation of compliant joints must be addressed to increase the safety for the user, and the

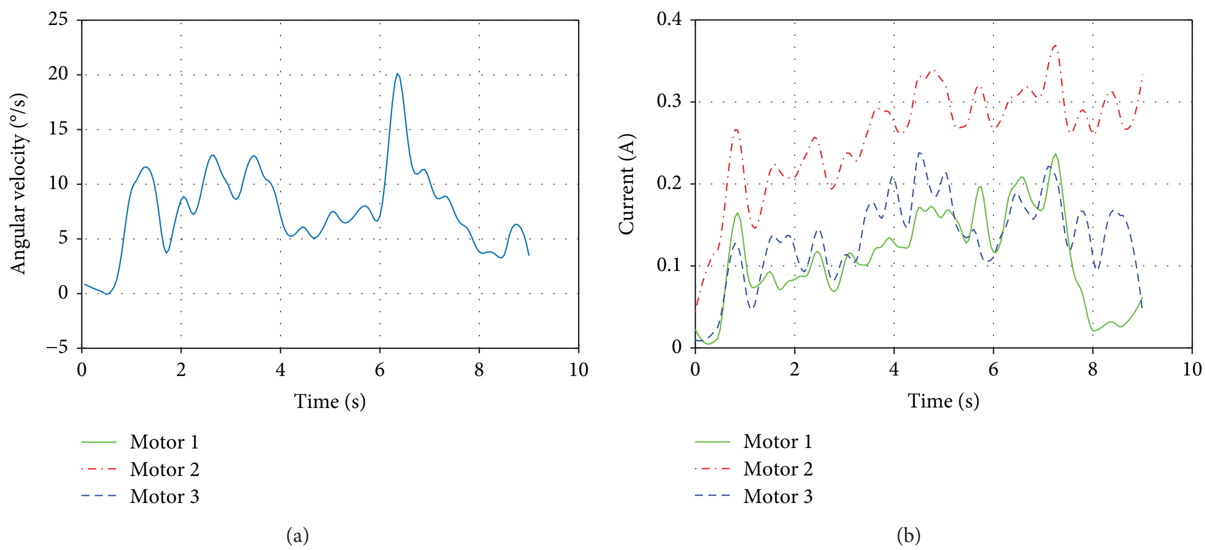

FIGURE 20: Results of the experimental shoulder flexion: (a) angular velocity of the arm and (b) electric current of the shoulder actuators.

establishment of an appropriate control scheme for this device is required.

Data Availability

The data used to support the findings of this study are available from the corresponding author upon request.

Conflicts of Interest

The authors declare that there is no conflict of interest regarding the publication of this paper.

Acknowledgments

This research has been supported by the CONACYT Project FC2016-1961 "Neurociencia Computacional: de la teoría al desarrollo de sistemas neuromórficos."

References

[1] A. J. Metzger, A. W. Dromerick, R. J. Holley, and P. S. Lum, "Characterization of compensatory trunk movements during prosthetic upper limb reaching tasks," *Archives of Physical Medicine and Rehabilitation*, vol. 93, no. 11, pp. 2029–2034, 2012.

[2] H. Burger and G. Vidmar, "A survey of overuse problems in patients with acquired or congenital upper limb deficiency," *Prosthetics and Orthotics International*, vol. 40, no. 4, pp. 497–502, 2016.

[3] K. Østlie, I. M. Lesjø, R. J. Franklin, B. Garfelt, O. H. Skjeldal, and P. Magnus, "Prosthesis rejection in acquired major upper-limb amputees: a population-based survey," *Disability and Rehabilitation. Assistive Technology*, vol. 7, no. 4, pp. 294–303, 2012.

[4] T. R. Dillingham, L. E. Pezzin, and E. J. MacKenzie, "Limb amputation and limb deficiency : epidemiology and recent trends in the United States," *Southern Medical Journal*, vol. 95, no. 8, pp. 875–883, 2002.

[5] D. A. Zlotolow and S. H. Kozin, "Advances in upper extremity prosthetics," *Hand Clinics*, vol. 28, no. 4, pp. 587–593, 2012.

[6] M. S. Johannes, J. D. Bigelow, J. M. Burck, S. D. Harshbarger, M. V. Kozlowski, and T. Van Doren, "An overview of the developmental process for the modular prosthetic limb," *Johns Hopkins APL Technical Digest*, vol. 30, no. 3, pp. 207–216, 2011.

[7] L. Resnik, F. Acluche, S. Lieberman Klinger, and M. Borgia, "Does the DEKA Arm substitute for or supplement conventional prostheses," *Prosthetics and Orthotics International*, 2017.

[8] L. Resnik, S. L. Klinger, and K. Etter, "The DEKA Arm: its features, functionality, and evolution during the Veterans Affairs study to optimize the DEKA Arm," *Prosthetics and Orthotics International*, vol. 38, no. 6, pp. 492–504, 2014.

[9] L. He, C. Xiong, and K. Zhang, "Mechatronic design of an upper limb prosthesis with a hand," in *Intelligent Robotics and Applications. ICIRA 2014*, X. Zhang, H. Liu, Z. Chen, and N. Wang, Eds., vol. 8917 of Lecture Notes in Computer Science, Springer, Cham, Switzerland, 2014.

[10] J. A. Leal-Naranjo, M. Ceccarelli, and C. R. T. S. Miguel, "Mechanical design of a prosthetic human arm and its dynamic simulation," in *Advances in Intelligent Systems and Computing*, Springer, Cham, 2017.

[11] J.-A. Leal-Naranjo, M. Ceccarelli, C.-R. Torres-San-Miguel, L.-A. Aguilar-Perez, G. Urriolagoitia-Sosa, and G. Urriolagoitia-Calderón, "Multi-objective optimization of a parallel manipulator for the design of a prosthetic arm using genetic algorithms," *Latin American Journal of Solids and Structures*, vol. 15, no. 3, 2018.

[12] T. Mashimo, T. Urakubo, and T. Kanade, "Singularity-based four-bar linkage mechanism for impulsive torque with high energy efficiency," *Journal of Mechanisms and Robotics*, vol. 7, no. 3, article 031002, 2015.

[13] R. L. Norton, *Machine Design: an Integrated Approach*, vol. 4, Pearson Prentice Hall Publishers, USA, 2006.

[14] C. Gosselin and J. Angeles, "The optimum kinematic design of a spherical three-degree-of-freedom parallel manipulator,"

Journal of Mechanisms Transmissions and Automation in Design, vol. 111, no. 2, p. 202, 1989.

[15] J. Ryu, W. P. Cooney III, L. J. Askew, K.-N. An, and E. Y. S. Chao, "Functional ranges of motion of the wrist joint," *The Journal of Hand Surgery*, vol. 16, no. 3, pp. 409–419, 1991.

[16] J. A. Lealndash, C. R. Torres-San Miguel, M. F. Carbajalndash, and L. Martinez-Saez, "Structural numerical analysis of a three fingers prosthetic hand prototype," *International Journal of Physical Sciences*, vol. 8, no. 13, pp. 526–536, 2013.

[17] S. P. Won and F. Golnaraghi, "A triaxial accelerometer calibration method using a mathematical model," *IEEE Transactions on Instrumentation and Measurement*, vol. 59, no. 8, pp. 2144–2153, 2010.

[18] S. Zihajehzadeh, D. Loh, M. Lee, R. Hoskinson, and E. J. Park, "A cascaded two-step Kalman filter for estimation of human body segment orientation using MEMS-IMU," in *2014 36th Annual International Conference of the IEEE Engineering in Medicine and Biology Society*, pp. 6270–6273, Chicago, IL, USA, August 2014.

Hindawi
Applied Bionics and Biomechanics
Volume 2018, Article ID 4250541, 7 pages
https://doi.org/10.1155/2018/4250541

Research Article

Magnetostrictive Bioinspired Whisker Sensor Based on Galfenol Composite Cantilever Beam Realizing Bidirectional Tactile Perception

Ran Zhao,[1,2] **Qan-guo Lu**,[1] **and Qinghua Cao**[1]

[1]*Jiangxi Province Key Laboratory of Precision Drive & Control, Nanchang Institute of Technology, Nanchang, China*
[2]*School of Electrical Engineering, Hebei University of Technology, Tianjin, China*

Correspondence should be addressed to Ran Zhao; zhaoran@nit.edu.cn

Received 10 April 2018; Revised 27 June 2018; Accepted 3 July 2018; Published 24 July 2018

Academic Editor: Dongming Gan

A magnetostrictive bioinspired whisker sensor based on a galfenol/beryllium-bronze/galfenol composite cantilever beam was developed in this work. According to the new design concept, the proposed whisker can output positive and negative voltages under different bending directions. Besides, the proposed whisker sensor can realize the bidirectional distance and microforce perception. Using the classical beam theory, a theoretical model was used to predict the output performance of the whisker. An experimental system was established to test the whisker's output performance. In the experiment, the designed whisker, compared with a traditional unimorph whisker, displayed an output voltage range of −240 to 240 mV. The parameters were as follows: the distance was 0–22 mm, with the microforce sensing range of 9.8–2744 mN, the average distance was 10.90 mm/mV, and the force sensitivity was 11.4 mN/mV. At last, obstacle perception was applied. The experiment showed that the proposed whisker sensor can realize the bidirection tactile perception in one-dimensional space. The work expands the function of the magnetostrictive bioinspired whisker, acquiring the multi-information for single-sensor system.

1. Introduction

Recently, with the development of robot technology, the bioinspired whisker has attracted the attention of researchers. As a "nonvisual" perception method, it is installed on bionic robots and automatic vehicles, to realize tactile perception, hydrodynamic measurement, and shape sensing [1–5]. Due to the excellent environmental adaptability, the bioinspired whisker, by providing an artificial "tactile," can collect more ambient information to make up for the lack of machine vision.

Until now, the reported bioinspired whiskers include capacitive whisker, piezoelectric whisker, elastic whisker, and magnetostrictive whisker [6–11]. Wherein, magnetostrictive whisker shows the advantages of working under static or low-frequency conditions [12, 13], comparing to piezoelectric and capacitive whiskers.

However, for traditional magnetostrictive whisker, its structure and principle (the position of magnetism sensor and the measuring method) determine that in the following condition—when bending to different directions, the output signals are asymmetrical. Thus, it is insensitive to the directions of stress and vibration, which limits its application.

Due to this, we developed a magnetostrictive whisker sensor, which is basing on a composite cantilever beam with sandwich structure. The operation principle was analyzed, compared to that of traditional magnetostrictive whisker. We used two Hall sensors to generate a differential output, thus realizing the detection of bidirectional bending. The experimental system was built to test the proposed whisker.

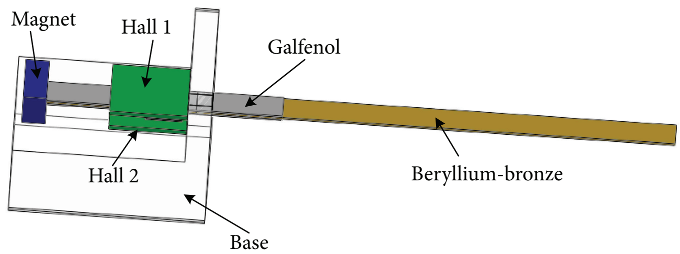

(a)

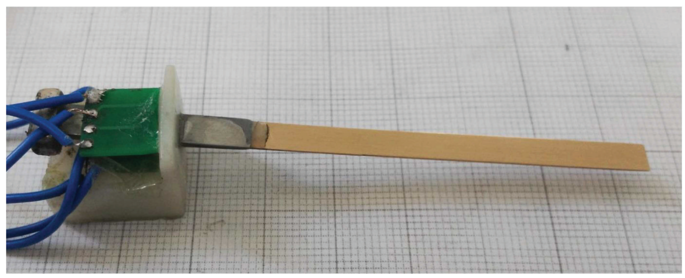

(b)

Figure 1: Magnetostrictive whisker sensor: (a) 3-D model and (b) photography.

Table 1: Physical parameters of the whisker.

Material	Parameter	Value (unit)
Galfenol	Magnetostrictive coefficient	220 ppm
	Young's modulus	70 GPa
	Poisson's ratio	0.35
Beryllium-bronze	Young's modulus	128 GPa
	Poisson's ratio	0.42
Bias magnet	Bias magnetic field	190 mT
Hall	Measurable range	±150 Gauss

Table 2: Geometric parameters of the whisker.

Component	Material/type	Dimensions (mm)
Composite beam	Galfenol	$30 \times 4 \times 0.2$
	Beryllium-bronze	$80 \times 4 \times 0.3$
Bias magnet	NdFeB	$8 \times 4 \times 3$
Base	PVC	$20 \times 25 \times 20$
Hall	WH202	—

2. Design

2.1. Structure. Figure 1 gives the structure of the whisker, consisting of a galfenol/beryllium-bronze/galfenol composite cantilever beam, a magnet, two Hall sensors, and a base. The magnet uses a bias magnetic field to magnetize two galfenol sheets. When a stress is applied, the flux linkage change induced by the bending beam is measured by the two Halls. The composite beam is fixed by the base with an optimal distance between the magnet and the clamped point [12], enabling the Hall to detect the maximum change flux.

The composite cantilever beam was fabricated by a long beryllium-bronze beam as substrate, with two short galfenol beams bonding on it. The beryllium-bronze substrate provides excellent elasticity, making the composite beam bear larger stress and higher vibration frequency than the single beam. Tables 1 and 2 show the physical and geometry parameters of the proposed whisker, respectively.

2.2. Principle. Figure 2 shows the working principle of traditional, newly designed magnetostrictive whiskers. It can find the way to realize the bidirection detection. Figure 2(a) shows a conventional structure of magnetostrictive whisker developed by Flatua; there is only one Hall sensor used to detect the linkage flux. Thus, we can know how the magnetic domains rotate with the application of a stress (observed by Raghunat et al. by using Kerr microscope [14]).

Figures 2(b) and 2(c) (named "mode I" and "mode II") show that these rotations are different for magnetic domains distributed on both sides of the natural center line. Using a unipolar Hall to detect the linkage flux (see Figure 2(d)), the output signal is asymmetric. Furthermore, the output signal of mode I is larger than that of mode II (see Figure 2(e)). It is the reason why the traditional magnetostrictive whisker cannot identify the directions of loading stress.

Defining the output of Hall as U_{h} and the reference voltage (when magnetic flux is zero) as U_{ref} (see Figure 2(a)), we can obtain the final output signal with a different operation.

$$U_{\mathrm{uni}} = U_{\mathrm{h}} - U_{\mathrm{ref}}. \tag{1}$$

For the given whisker, a composite beam is used instead of the original single beam. Figure 2(f) shows the natural center line is in the middle of the beryllium-bronze beam. It makes the rotation of the bending magnetic domains consistent in each galfenol beam.

Moreover, the changes of linkage flux for each galfenol beam are measured by different Hall sensors (see Figures 2(g) and 2(h)). Two bipolar Halls are used to realize

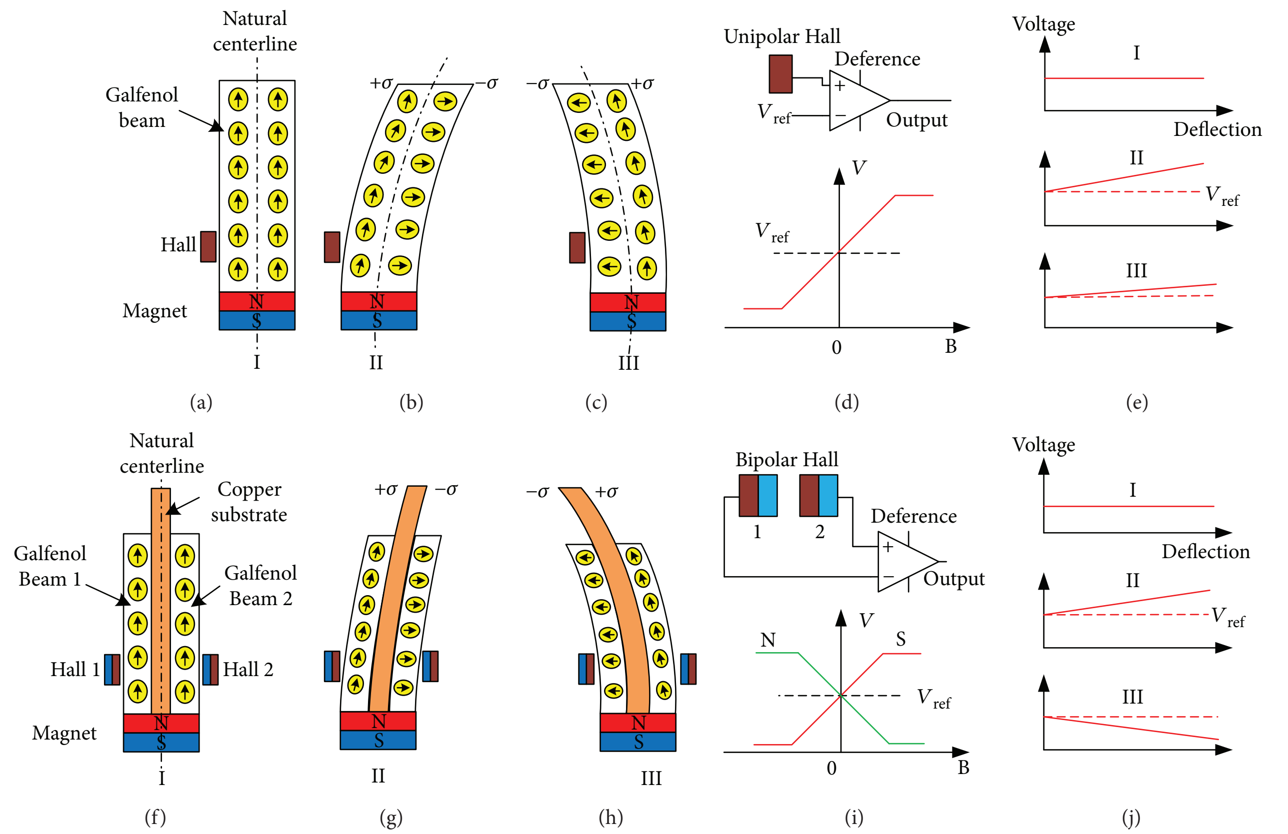

Figure 2: Principle of the traditional and proposed magnetostrictive bioinspired whisker: structure, operation mode, measurement method, and output signal.

the magnetic field detection. Figure 2(i) shows that bipolar Hall has two different outputs of north pole and south pole (abbreviated *N* and *S*), which are used to implement differential output. Supposing *N* output of Hall 1 as U_{h1} and *S* output of Hall 2 as U_{h2}, the final output signal is

$$U = U_{h1} - U_{h2} - U_{ref}. \tag{2}$$

The new measuring circuit is used to obtain a signal with positive and negative symmetry (see Figure 2(j)), which makes the proposed whisker sensor identify the force directions.

3. Model

Figure 3 shows a simplified bending model of the galfenol/beryllium-bronze/galfenol composite beam. Figure 3(a) shows that the proposed model is different from the conventional beam model—there is a clamper to limit the starting location of the bending beam (with the origin of coordinate changing from O to O$'$).

Based on the 2-dimensional coordinate of the beam (shown in Figure 3(a)), l is the total length of the substrate beam; h_s is the thickness; l_0 is the length of galfenol beam; and h_t is the thickness: $l = l_0 + l_1$.

Figure 3(b) shows how the beam bends when a force is applied at the beam's free end. It is assumed that F is the loading force and w is the deflection. At the coordinate point O', σ_x is the tensile stress along the x-direction of the beam and ε_x is the strain of galfenol beam under the tensile stress.

According to the Euler-Bernoulli beam theory, the equivalent tensile stress of the bending beam at O$'$ can be expressed as [15]

$$\sigma_x = zE_s I \frac{d^2 w}{dx^2} = z\frac{F(L_1 - x)}{I}, \tag{3}$$

where z is the distance between the position to the natural center line of the composite beam along z-direction; x is the position at x-axis; E_s is the Young's modulus of the substrate beam; and I is the second moment of area of the beam's cross section.

The relation of loading force and deflection is expressed as

$$w = \frac{F}{3E_s I} L_1^3. \tag{4}$$

Figure 2(a) shows that there is a composite cantilever beam with sandwich structure from O to O'. The effective Young's modulus of the composite beam can be obtained by

$$E_e = \frac{2E_t h_t + E_s h_s}{2h_t + h_s}, \tag{5}$$

where E_t is the Young's modulus of galfenol beam.

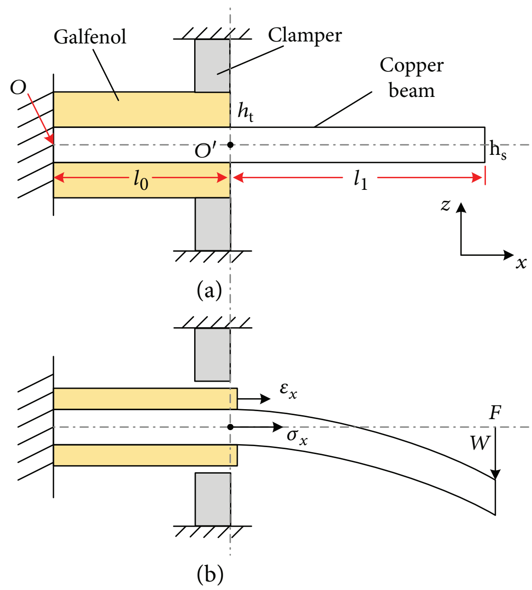

Figure 3: Bending model of the composite cantilever beam.

The elastic relation can be expressed by Hook's law, $\sigma = E \cdot \varepsilon$, and there is

$$\varepsilon_x = \frac{\sigma_x}{E_e} = \frac{2h_t + h_s}{2E_t h_t + E_s h_s}\sigma_x. \quad (6)$$

Using the piezomagnetic equation, Downey and Flatau and Datta and Flatau derived the expression of magnetic flux [16, 17], that is,

$$B = d_{33}^* E_t \varepsilon_x - d_{33} d_{33}^* E_t H_0 + \mu_0 \mu_r H_0, \quad (7)$$

where d_{33} is the piezomagnetic coefficient; d_{33}^* is the inverse piezomagnetic coefficient; H_0 is the bias magnetic field; μ_0 is the permeability of vacuum; and μ_r is the relative permeability of galfenol.

Substituting (7) into (2), we can obtain

$$U = 2s_H B = 2s_H d_{33}^* E_t \varepsilon_x, \quad (8)$$

where s_H is the sensitivity of Hall sensor.

According to (3), (4), (5), and (6), we derive the expressions of output voltage in different loading conditions as follows:

$$U_\sigma = 2s_H d_{33}^* \frac{E_t(2h_t + h_s)}{2E_t h_t + E_s h_s}\frac{zL_1}{I}F, \quad (9)$$

$$U_d = 2s_H d_{33}^* \frac{3E_t E_s(2h_t + h_s)}{2E_t h_t + E_s h_s}\frac{z}{L_1^3}w. \quad (10)$$

4. Experiment

The work studied the static performances of the proposed sensor. An experimental system was established to test the relations between deflection-voltage and force-voltage, thus investigating the tactile perception of the whisker sensor. Additionally, a dynamic contact experiment was performed to investigate its obstacle identification.

Figure 4 shows the experimental system. The deflection was measured when the beam bends, with the output signal recorded by an oscilloscope (see Figure 4(a)). The largest deflection was limited to 22 mm, thus preventing the beam from damage. With a traditional load-bearing experiment method (hanging standard weights), the microforce sensing performance of the whisker sensor was studied, and the weights changed from 1 to 280 g. The sensor's distance (deflection) and force sensitivity were obtained by the two experiments.

Figure 4(b) shows the experimental system of dynamic contact; the whisker was fixed on a motion stage, with a simulated obstacle placed on its motion path. The deflection was measured by a laser displacement sensor (Lts-250). Besides, the voltage was recorded by an oscilloscope. This experiment shows how the sensor works when a dynamic contact occurs. It can simulate not only the active exploration for the unknown obstacle (such as a whisker system installed on a robot rat [2]) but also the passive perception for external contact force changes. Both refers to a bionic tactile.

5. Results and Discussion

Firstly, we compared the performance of the magnetostrictive whisker with traditional structure and newly designed structure. In Figure 5, for the traditional one (see Figure 5(a)), the maximum output voltage is 640 mV at a deflection of 22 mm, when the beam bends to the left. When it bends to another direction, the output voltage is positive, but smaller than the former. From Section 2, it can be found that the asymmetry of the curve is caused by the

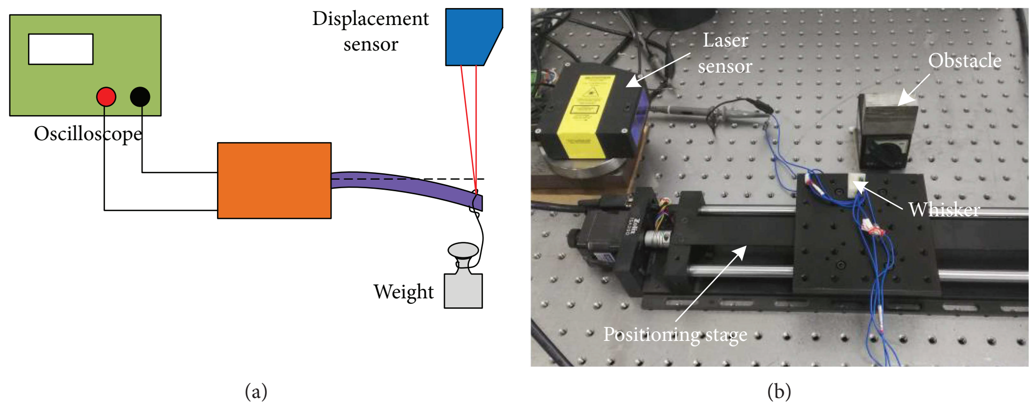

Figure 4: Experimental system for (a) deflection and force test and (b) contact test.

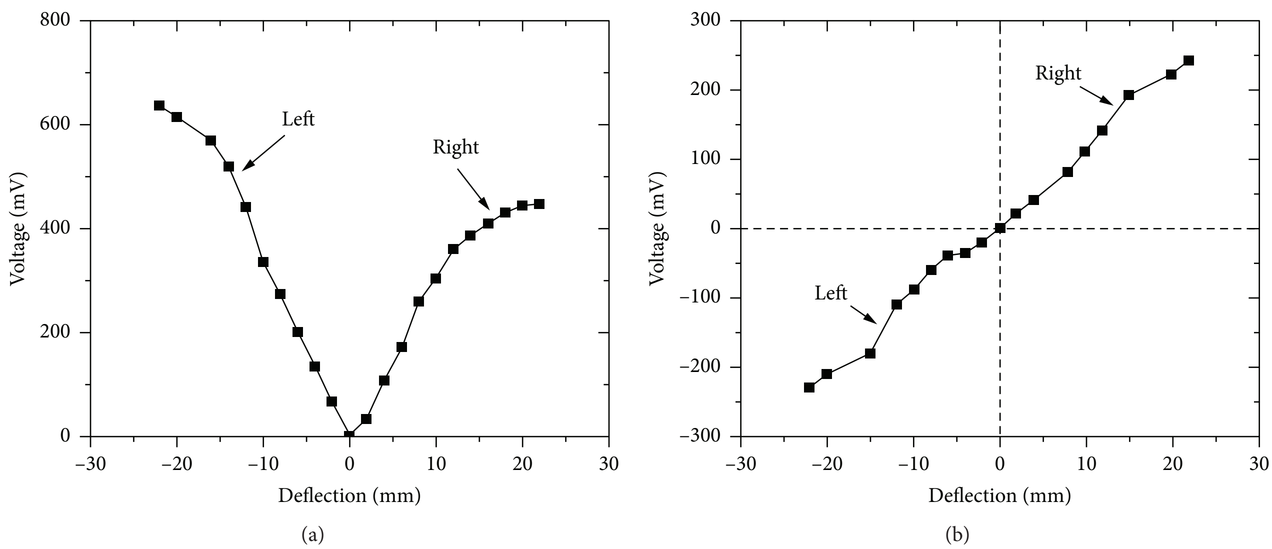

Figure 5: Deflection-voltage curve of (a) traditional and (b) newly designed magnetostrictive whisker sensor.

inhomogeneity of magnetic domain rotation and the position of the Hall sensor.

The deflection-voltage curve shows a nearly linear relationship and changes from negative to positive with the changed bending direction (see Figure 5(b)). The maximum output voltage is 240 mV at a deflection of 22 mm. The average deflection sensitivity of the proposed whisker sensor is 10.9 mV/mm.

In Figure 6, we compared the experimental and theoretical result for distance and microforce sensing. As shown in Figure 6(a), the theoretical calculation is closed to the experimental result; however, there is an error between them in Figure 6(b). As in the distance sensing experiment, the whisker sensor is working at its linear region. For force sensing test, the whisker sensor reaches its saturated region. Equations (9) and (10) provide a linear description. In fact, in these two equations, the inverse piezomagnetic coefficient is not a constant, which depends on the value of the magnetic field and stress. Therefore, the prediction will be more accurate if we replace the constant with a function of d_{33}^{*}.

Figure 6 shows the microforce sensing performance of the whisker sensor. The proposed whisker is tested when the load changes from 9.8 to 2744 mN. When the applied force is 2744 mN, the output voltage is 240 mV. The average force sensitivity is 11.42 mN/mV, and the proposed sensor has a resolution of 9.8 mN/2 mV.

Figure 7 shows the obstacle perception of the proposed whisker sensor. The whisker sensor is fixed on the motion stage and moves at a constant speed. The dynamic contact process can be divided into three stages: (a) at stage 1 ($0{\sim}t_1$), there was no contact between the sensor and obstacle; (b) at stage 2 ($t_1{\sim}t_2$), the beam contacted the obstacle and begun to bend; and (c) at stage 3 (after t_2), when the control unit has detected the raising voltage, the moving process was stopped immediately. In this test, we focused on the response time of the whisker sensor in the contact process.

There is a delay time (t_{d}) between the deflection and sensing voltage. The delay time can be calculated by $w_{\min}/v$, where $w_{\min}$ is the minimum deflection of the cantilever beam measured by Hall sensor and v is the relative vocasity

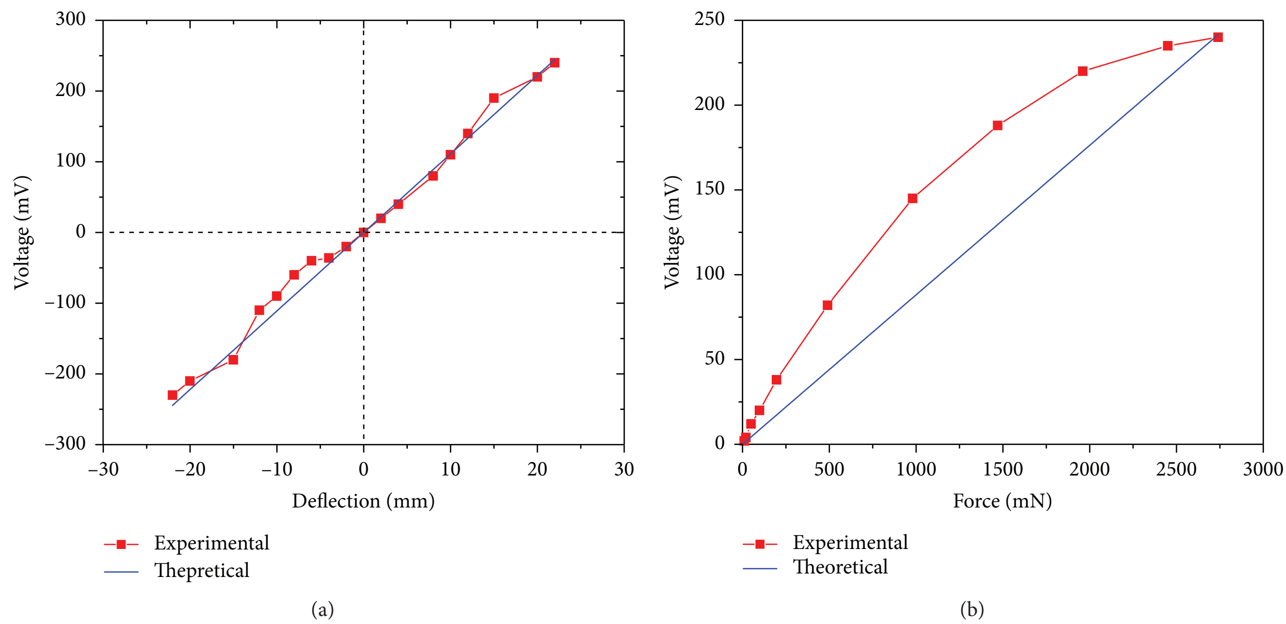

Figure 6: Comparison of the experimental and theoretical sensing performance for (a) distance and (b) force sensing.

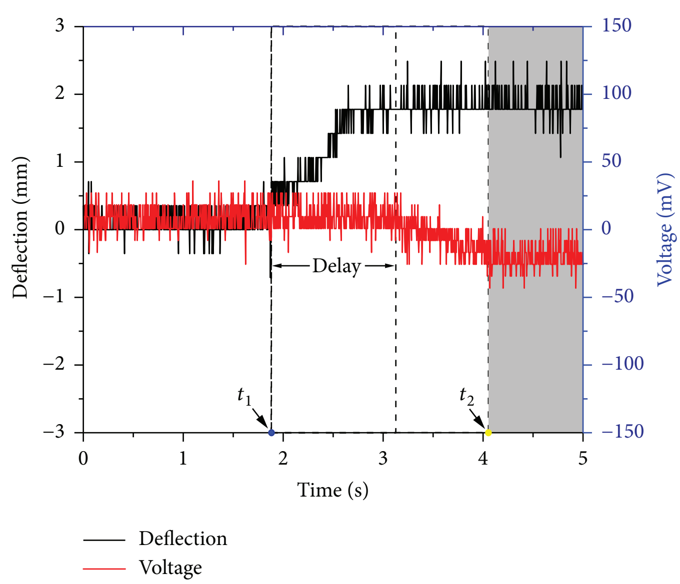

Figure 7: Obstacle perception process of the proposed whisker sensor.

between the whisker sensor and obstacle. After that, the sensing voltage increases, and an addition time (t_p) is needed for the measuring circuit to test the voltage changing from zero (which is usually very short and can be ignored). As a result, we can define the total perception time as

$$t_{tot} = t_d + t_p \approx \frac{w_{min}}{v}. \tag{11}$$

Equation (11) indicates that the total perception time t_{tot} is mainly due to the relative speed v. This experiment indicates that the proposed whisker can detect the obstacles.

6. Conclusions

In this work, a bioinspired magnetostrictive whisker was proposed. Based on the new structure composite cantilever beam and differential measurement method, the proposed whisker realized the perception of bidirectional tactile. To testify the operation principle, an experimental system was established. Furthermore, the static performances of the proposed whisker sensor were tested. The designed whisker has properties as follows:

(i) The distance measurement range is 2–22 mm, with sensitivity of 10.9 mV/mm.

(ii) The microforce sensing range is 9.8–2744 mN, with force sensitivity of 11.4 mN/mV and resolution of 9.8 mN (at 2 mV).

(iii) It has bidirectional perception.

Our research expands the function of magnetostrictive bioinspired whisker. Applied to dynamic measurement, the given sensor can detect more information than existing whisker sensors. The "multi-information sensing technique" based on bioinspired magnetostrictive whisker will be deeply studied.

Data Availability

The data used to support the findings of this study are included within the article.

Conflicts of Interest

The authors declare that there are no conflicts of interest.

Acknowledgments

This work was supported by the Science & Technology Project of Jiangxi Province Education Department of China (Grant nos. GJJ161105 and GJJ161102).

References

[1] S. N'Guyen, P. Pirim, and J. Meyer, "Texture discrimination with artificial whiskers in the robot-rat Psikharpax," in *Biomedical Engineering Systems and Technologies. BIOSTEC 2010*, A. Fred, J. Filipe, and H. Gamboa, Eds., vol. 127 of Communications in Computer and Information Science, pp. 252–265, Springer, Berlin, Heidelberg, 2011.

[2] C. Tuna, J. H. Solomon, D. L. Jones, and M. J. Z. Hartmann, "Object shape recognition with artificial whiskers using tomographic reconstruction," in *2012 IEEE International Conference on Acoustics, Speech and Signal Processing (ICASSP)*, vol. 22no. 10, pp. 2537–2540, Kyoto, Japan, March 2012.

[3] H. Beem, M. Hildner, and M. Triantafyllou, "Calibration and validation of a harbor seal whisker-inspired flow sensor," *Smart Material and Structures*, vol. 22, no. 1, article 014012, 2013.

[4] C. Lucarotti, A. Sadeghi, M. Totaro, A. Mondini, L. Beccai, and B. Mazzolai, "Soft tactile sensing for bioinspired robotic roots," in *IEEE International Conference on Robotics & Automation*, pp. 1-2, Seattle, WA, USA, May 2015.

[5] M. Kaneko and T. Tsuji, "A whisker tracing sensor for manufacturing application," *IFAC Proceedings Volumes*, vol. 33, no. 26, pp. 383–388, 2000.

[6] W. C. Eberhardt, Y. A. Shakhsheer, B. H. Calhoun, J. R. Paulus, and M. Appleby, "A bio-inspired artificial whisker for fluid motion sensing with increased sensitivity and reliability," in *SENSORS, 2011 IEEE*, pp. 982–985, Limerick, Ireland, October 2011.

[7] M. I. Tiwana, M. I. Tiwana, S. J. Redmond, N. H. Lovell, and J. Iqbal, "Bio-inspired PVDF-based, mouse whisker mimicking, tactile sensor," *Applied Sciences*, vol. 6, no. 10, p. 297, 2016.

[8] F. Ju and S. F. Ling, "Sensing fluid viscosity and density through mechanical impedance measurement using a whisker transducer," *Measurement Science and Technology*, vol. 24, no. 5, article 055105, 2013.

[9] P. V. Alvarado, V. Subramaniam, and M. Triantafyllou, "Performance analysis and characterization of bio-inspired whisker sensors for underwater applications," in *2013 IEEE/RSJ International Conference on Intelligent Robots and Systems*, pp. 5956–5961, Tokyo, Japan, November 2013.

[10] M. Kaneko and T. Tsuji, "A whisker tracing sensor with 5 μm sensitivity," in *Proceedings 2000 ICRA. Millennium Conference. IEEE International Conference on Robotics and Automation. Symposia Proceedings (Cat. No.00CH37065)*, vol. 4, pp. 3907–3912, San Francisco, CA, USA, April 2000.

[11] G. Raghunath, A. Flatau, S. Na, and B. Barkley, "Development of a bio-inspired tactile Magnetostrictive whisker sensor using alfenol," in *ASME 2014 Conference on Smart Materials, Adaptive Structures and Intelligent Systems*, pp. 1–15, Newport, RI, USA, September 2014.

[12] S. M. Na, M. Rice, G. Raghunath, and V. Klimchenko, "Magnetostrictive alfenol whisker sensor performance and sensitivity to whisker thickness," *IEEE Transaction on Magnetics*, vol. 50, no. 11, pp. 1–4, 2014.

[13] R. Zhao, Q. Yuan, J. Yan, and Q. Lu, "The static and dynamic sensitivity of magnetostrictive bioinspired whisker sensor," *Journal of Nanotechnology*, vol. 2018, Article ID 2591080, 6 pages, 2018.

[14] G. Raghunath, M. Marana, S. Na, and A. Flatau, "Kerr microscopy studies of the effects of bending stress on galfenol," *Journal of Applied Physics*, vol. 115, no. 17, article 17E310, 2014.

[15] Q. Cao, D. F. Chen, Q. Lu et al., "Sensor performance of cantilevered magnetostrictive beam," *International Journal on Smart Sensing and Intelligent Systems*, vol. 7, no. 3, pp. 1221–1238, 2014.

[16] P. R. Downey and A. B. Flatau, "Bending behavior of iron-gallium (galfenol) alloys for sensor applications," in *Smart Structures and Materials 2005: Smart Structures and Integrated Systems*, vol. 5764, San Diego, CA, USA, May 2005.

[17] S. Datta and A. B. Flatau, "Application of iron-gallium alloy as magnetostrictive sensors," in *Smart Structures and Materials 2005: Smart Structures and Integrated Systems*, vol. 5764, San Diego, CA, USA, May 2005.

Hindawi
Applied Bionics and Biomechanics
Volume 2018, Article ID 1925694, 9 pages
https://doi.org/10.1155/2018/1925694

Research Article

Design on the Bowden Cable-Driven Upper Limb Soft Exoskeleton

Wei Wei ,[1] Zhicheng Qu ,[1] Wei Wang,[1] Pengcheng Zhang,[1] and Fuchun Hao[2]

[1]*College of Physics, Optoeletronics and Energy and Collaborative Innovation, Soochow University, Suzhou 215000, China*
[2]*College of Rehabilitation Therapeutic Specialty, Tianjin Medical College, Tianjin 300000, China*

Correspondence should be addressed to Wei Wei; weiwei0728@suda.edu.cn

Received 30 March 2018; Revised 25 May 2018; Accepted 10 June 2018; Published 17 July 2018

Academic Editor: Liwei Shi

To assist hemiplegic patients with the activities of daily life, many upper limb soft exoskeletons have been developed. In this paper, we propose the structure of upper limb soft exoskeleton for rehabilitation training based on human biomechanics. The soft driving structure based on Bowden cable is devised. Man-machine interaction force must be considered because it can damage on the joint and lead to arm discomfort. We focus on structural optimization to minimize man-machine interaction force. Human arm model is established to perform motion simulation in ADAMS. To summarize optimality conditions, the movements of elbow are simulated in ADAMS when the number and location of force bearing points are changed. This paper describes the movement of the shoulder skeletal system through a mathematical model based on the Bowden cable transmission and utilizes man-machine contact force sensor to detect human interaction forces for analysis of experimental data. The experimental results show that man-machine interaction force can be reduced when the number of bearing force points is increased and bearing force point is away from the elbow.

1. Introduction

In recent years, many wearable exoskeletons were developed rapidly in the field of assistance and rehabilitation [1]. Exoskeletons have been applied to provide biological joint assistive torques to strengthen the sport ability of human body or assist the person with disability [2]. These wearable exoskeletons are usually made up of rigid links that run in parallel with the biological limb [3]. Rigid structure is substituted by soft structure to overcome discomfort resulting in rigid exoskeleton. The pneumatic artificial muscle actuator is used to replace the traditional motor and hydraulic drive [4]. Even if rigid structures are made of aluminum and clad metal, the entire weight of exoskeleton with pneumatic artificial muscles can be reduced greatly. However, the discomfort and joint injury aroused by mechanical impedance and kinematic constraints have not been well solved [5].

In order to eliminate these limitations, concept of soft exoskeleton was put forward. Firstly, a novel soft cable-driven exosuit which can apply forces to the body to assist walking was proposed [6]. The binding structure consisted of textile fabric without rigid connections and hinges. Human body is connected to soft exoskeleton through the quasioptimal compliant interface. To solve the limitations of stretch elongation for the pneumatic actuator, a new type of actuator based on Bowden cable for soft wearable exoskeletons was put forward [7]. This actuation structure allows the motor to be placed on better-loaded parts away from the motion joint. The extremity of Bowden cable sheath is connected to pulley cover, another extremity is connected to the anchor point. Soft exoskeleton transmits driving force through inner Bowden cable, and the pulling force of Bowden cable is converted to joint torque [8]. The force transfer effect of the Bowden cable is good. Hence, the actuation structure based on Bowden cable transmission is becoming the first choice of design.

At present, the number of stroke patients in China is over 2 million each year. About 75% of stroke survivors have different degrees of disability. Apoplectic hemiplegia is one of the common sequelae. Targeted treatments for apoplectic hemiplegic patients include the functional recovery of shoulder, elbow, hip, and knee [9]. While the stroke hemiplegia patient with upper limb soft exoskeleton performs rehabilitation training, man-machine interaction force can inflict

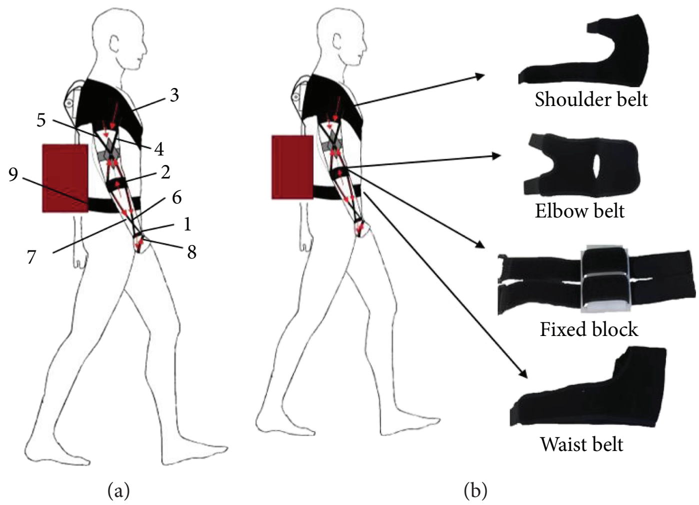

FIGURE 1: Overall structure of upper limb soft exoskeleton.

damage on human body. The chief solution is to reduce the man-machine interaction force in the supporting process by optimizing control strategies. Hierarchical cascade controller was proposed to improve control strategy for upper limb soft exoskeleton. The high-level controller performs assistance level estimation, midlevel controller performs adaptive gap compensation, and low-level controller performs adaptive friction compensation and position control [10]. In this paper, the structural optimization is mainly studied to reduce man-machine interaction force. The selection of the fixed anchor position between the Bowden cable and the surface textiles of the human body has a great influence on the comfort and compliance. The number of Bowden cables also has an impact on man-machine interaction force.

This paper primarily introduces three parts. Firstly, on the basis of the existing research on soft exoskeleton, a structure of upper extremity soft exoskeleton for the rehabilitation training is proposed. Then, the influence factors of human-machine interaction force are discussed and some methods of structural optimization are put forward. Finally, the subject with upper limb soft exoskeleton performs flexion movements of elbow to verify the conclusions presented in simulation experiments. The man-machine interaction force can be decreased when force bearing points are added and away from the center of elbow in a certain range.

2. Structure Design

2.1. Design Overview. Based on the analysis of the human upper limb biomechanics, textile materials constitute the basic structure of soft exoskeleton [11]. Force transfer of soft exoskeleton is shown in Figure 1. The numbers mentioned in this article are labels in the figure. The upper limb soft exoskeleton attaches around the shoulder (3), below the elbow (2) and around the waist (9). Force is transmitted through the straps (4–8). The extremity of Bowden cable sheath is attached to a fixed point of the webbing strap (3) around the shoulder. The inner Bowden cable extends from the extremity of Bowden cable sheath down to the fixed point of the webbing strap (2) below the elbow. When extension movements of elbow are performed with assistance delivered by soft exoskeleton, the distance between fixed points on the straps (2) and (3) is pulled closer. Strap (2) transfers the downward force to strap (1) when flexion movements of elbow are performed. At the same time, strap (2) transmits the upward force to strap (3).

The upper limb soft exoskeleton produces torque at the elbow through Bowden cable transmission system. The operation principle of muscle tendon can be simulated by Bowden cable transmission system. Further, man-machine coupling coefficient of flexible structure is high. Part of the driving force is generated passively by the human body, and the other is provided by the exoskeleton. Referring to Figure 1, when flexion movements of elbow are performed, the strap (2) gradually tightens. The strap (2) generates impedance torque while the elbow is flexed to the maximum extent. When extension movements of elbow are performed, the strap (2) releases the stored energy and assists the elbow movement.

The webbing belts are mode of pump-effect materials to enhance breathability and comfort. The waist belt is constructed to be a single piece to be secured in the front with Velcro. The Velcro on the waist belt can fit waist sizes within a 10 cm range. It is more convenient to don and stretches less due to Velcro than buckle form. The shoulder belt is made into “I”-shape and has two independently adjustable Velcro-covered tabs along its height, enabling it to be secured to the subject’s shoulder in a comfortable manner. A layer of fabric sewn on the shoulder belt is utilized to fix the Bowden cable sheath, and the interior is filled with sponge to reduce pressure.

The elbow belt is constructed to be a single piece and has two independently adjustable Velcro at the end of belt to fit elbow sizes within a 8 cm range. The belt which is utilized for force transmission between shoulder belt and elbow belt is sewn up, and the width of belt is 3 cm.

There are two fixed blocks made of ABS plastic to fix the Bowden cable between the upper arm and forearm. Each fixed block has two independently adjustable Velcro, and the Velcro can fit upper arm and forearm sizes within a 5 cm range. The weight of the entire upper limb soft exoskeleton structure is less than 800 g. Suitable length of Bowden cable is selected to prevent excessive bending and acts as a mechanical limit to protect the subject.

2.2. Design Principles. The role of upper limb soft exoskeleton is to assist hemiplegic stroke patients for rehabilitation training. In order to avoid the damage resulting in displacement of webbing straps, overall stiffness should be improved. It is less possible to lead to damage when the overall stiffness is higher. Therefore, a few principles should be followed when designing the upper limb soft exoskeleton for patients. Certain areas of the human body are more load bearing, and this feature needs to be fully taken into account. These areas are defined as key anchors such as shoulders, buttocks, and soles. These typical areas are mainly composed of bones which can withstand normal or near-normal reaction forces. The primary structure of soft exoskeleton is located on the shoulder. During the driving stage, the skin has less displacement relative to the bone. Webbing strap (3) provides the humerus upward tension to prevent downward and lateral movement of the humerus. So, the shoulder with soft exoskeleton can remain relative stable.

Most of the load is transferred to the pelvis to ensure relative movement of the bone and skin as normal as possible when the body is loaded. Shearing forces can result in damage to the human body if it exceeds the friction force of the skin. It is impossible to completely avoid the shearing force between the soft exoskeleton and human body. A little displacement can occur in skin and bone under low shearing force. For example, when flexion movements of the elbow are performed, a few displacement at the elbow cannot give rise to damage to human body. In the binding structure of soft exoskeleton, the displacement under the normal force hardly results in harm to the human body.

The wide webbing strap can be utilized to reduce the pressure between soft exoskeleton and human body. The body can withstand some degree of pressure before discomfort. The estimated maximum comfort pressure is usually around 0.5 N/cm. When contact area of webbing strap is increased, the displacement of webbing strap can be reduced to increase the overall stiffness. In addition to the increase in the width of webbing strap, pressure can be reduced when the tension on the webbing straps is balanced. If the patient with soft exoskeleton carries out rehabilitation training, the comfort of the patients can be improved by adjusting the balance tension of the webbing straps (4–7). Due to the particularity of hemiplegia stroke patients, the Bowden cable sheath is connected to the fixed position through a pulley mounted on the back to avoid harm to body.

2.3. Structure of Actuator. Considering that the upper limb soft exoskeleton is used for rehabilitation training, the maximum torque generated by DC motor must help the patients to lift the forearm passively. The maximum torque delivered by actuation system can be defined as follows:

$$\tau_{\mathrm{m}} = W \times L, \tag{1}$$

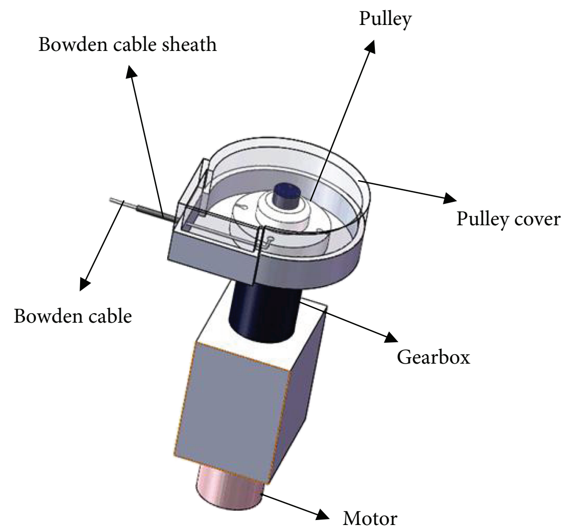

Figure 2: A 3-D model of the actuator system.

where τ_{m} is maximum torque provided by DC motor, W is the weight of forearm, and L is the distance from the centroid of the forearm to the center of elbow [12].

As shown in Figure 2, it is an actuation system of upper limb soft exoskeleton. The actuation system is composed of a Maxon EC 45 251601 Flat brushless DC motor and a 5 : 1 planetary gearbox connected to the DC motor. Bowden cable sheath is wrapped outside the Bowden cable to prevent damage resulting in Bowden cable during transmission. The extremity of the Bowden cable sheath is connected to the outer frame of the pulley cover. Another extremity is connected to the bottom of the rear arm by means of a pulley mounted on the back. The extremity of the Bowden cable is connected to the pulley, and the other is connected to the fixed anchor of the forearm [13]. The Bowden cable is pulled tight, and torque is generated at the elbow during driving stage. This actuator primarily delivers torque generated by the motor to the soft exoskeleton through the Bowden cable. Hence, the actuator can be installed in a position away from the elbow. The patient with upper limb soft exoskeleton is subjected to a smaller load and improves comfort during rehabilitation training.

2.4. Selection and Calibration of Sensors. The flex sensor 4.5″ (SparkFun, USA) acts like a variable resistor whose output voltage is changed by flexing it. We utilize a simple magnified voltage divider to convert a variation in resistance into a variation in voltage. The relationship between the output voltage and the bending angle is assumed to be linear [14]. The flex sensor needs to be calibrated to obtain the mapped relationship between the output voltage and the bending angle before experiment to render the measurement. A film pressure sensor DF9-40@10 kg (LEANSTAR, China) is a sensor for measuring the degree of pressure. When the external pressure acts on the film pressure sensor, the resistance value of the sensor is changed. The change in external pressure is converted into the change in voltage by a voltage divider. According to the manual of data, the film pressure sensor is

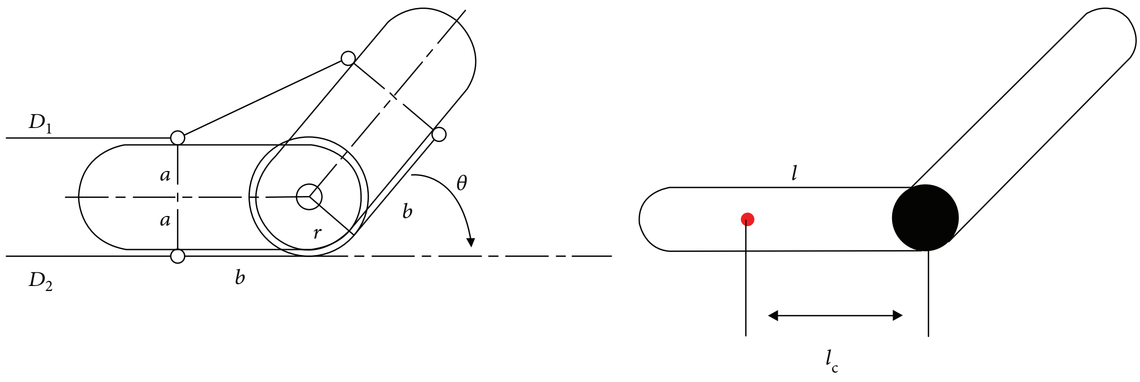

FIGURE 3: (a) The soft exoskeleton with Bowden-cable transmission worn by the subject. (b) Human arm model.

calibrated to establish the linear mapped relationship between the output voltage and the pressure value. Due to the interference of environment and other factors, the Butterworth filter is utilized to filter the noise when the sensor is connected to the circuit.

3. Structural Optimization

3.1. Dynamic Analysis of Upper Limb Soft Exoskeleton. Due to the different motion abilities of patients, the torque provided by soft exoskeleton changes with the patients' condition. The relationship among force on Bowden cable, body torque, and the motion angle is obtained by establishing a mathematical model based on the Bowden cable transmission [15].

The human arm model based on the Bowden cable transmission is shown in Figure 3(a). The objective function $D_1(\theta)$ of the flexible Bowden cable is defined as

$$D_1(\theta) = 2\sqrt{a^2 + b^2}\cos\left(\tan^{-1}\left(\frac{a}{b}\right) + \frac{\theta}{2}\right) - 2b. \tag{2}$$

The objective function $D_2(\theta)$ of the extensor Bowden cable is defined as

$$D_2(\theta) = r\theta, \tag{3}$$

where a is half of the width of arm, b is the distance from the center of the elbow to the fixed point, r is the radius of the elbow, and θ is the angle of the flexion/extension movements. Matrix $\mathbf{J}$ is defined as

$$\begin{gathered}\mathbf{J}(\theta) = \frac{\partial D^{\mathrm{T}}}{\partial \theta}(\theta),\\ D = [D_1(\theta)\ \ D_2(\theta)]^{\mathrm{T}}.\end{gathered} \tag{4}$$

Assistance torque of Bowden cable is defined as

$$\begin{gathered}\tau = J(\theta) f,\\ f = [f_1\ \ f_2]^{\mathrm{T}},\end{gathered} \tag{5}$$

where f is the tension of Bowden cable detected by the load cell. The human arm dynamics can be established by the Lagrange formula [16]. The kinetic energy and potential energy of the arm are defined as follows:

$$\begin{gathered}T = \frac{1}{3} m l^2 \dot{\phi}_{\mathrm{b}}^2,\\ V = m g l_{\mathrm{c}} - m g l_{\mathrm{c}} \cos\phi_{\mathrm{b}},\end{gathered} \tag{6}$$

where m is the quality of the human arm, l is the length of human arm, and l_c is the distance from the center of gravity of the forearm to the center of the elbow. By defining the Lagrange function $L = T - V$ and Lagrange formula, a dynamic model of the human arm is established as

$$\tau_{\mathrm{h}} = \tau_{\mathrm{t}} - \tau_{\mathrm{a}} = \frac{2}{3} m l^2 \ddot{\phi}_{\mathrm{b}} + m g l_{\mathrm{c}} \sin\phi_{\mathrm{b}} - J(\theta)[f_1 f_2], \tag{7}$$

where τ_t is the total moment of the human arm and exoskeleton, τ_a is the estimated moment of exoskeleton, and τ_h is the moment of the human arm.

The upper limb soft exoskeleton system detects man-machine interaction force in real time through the flex sensor and feeds back to control system, so that the exoskeleton system can work stably and accurately. The soft binding structure enables high degree of man-machine coupling and maintains the stability of exoskeleton system to a certain extent without professional protect.

3.2. Motion Simulation. The impact of man-machine interaction force on wearers needs to be taken into account because the subject of upper limb soft exoskeleton is hemiplegic patients. Considering the interaction forces between the upper limb soft exoskeleton and human being, two factors need to be considered: pressure distribution and pressure size. The former reflects the comfort of the wearer, and the latter is related to the safety of the patient [17]. In general, there are two main ways to reduce the man-machine interaction force. The method is that greater pressure is exerted on a place with greater resistance. Another method is that the pressure is dispersed in as large as a range as possible to reduce the pressure on the skin. Some parts of the body are not suitable for man-machine interaction force. The following points should be paid attention to. In order to ensure the freedom of movement for joint, it is not possible to

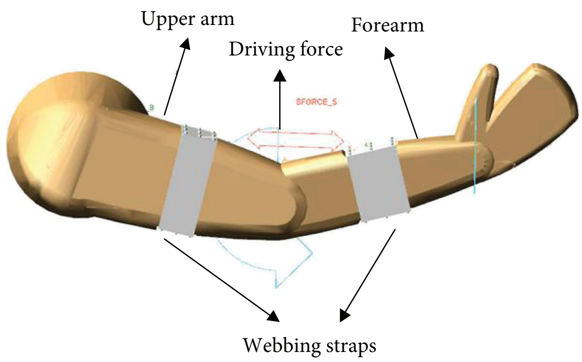

Figure 4: Human arm model built in ADAMS.

choose the contact point around the active joint. Nerve intensive areas should be evaded to avoid unnecessary damage [18]. Due to the diversity of patients' body and athletic ability, we need to find a universal optimization structure which can improve the comfort of patients. The upper limb soft exoskeleton transfers the driving force through the Bowden cable connected to the webbing strap of body. On the one hand, we should take into account the influence of number of Bowden cables on man-machine interaction force; on the other hand, we should consider the influence of fixed position between the Bowden cable and the webbing strap on man-machine interaction force.

As is shown in Figure 4, a human arm model with soft exoskeleton is established in ADAMS. The rotation angle of the human elbow model is 60 degrees [19]. The flexion movements of elbow with assistance provided by soft exoskeleton are simulated under different conditions to study the variation curve of man-machine interaction force.

Firstly, the influence of the size of driving force on the man-machine interaction force is analyzed. Results of simulation experiments comparing the man-machine interaction force with different driving forces are depicted in Figure 5, showing that the man-machine interaction force is enhanced with the increase of driving force. The spread of pressure in a larger range is often proved to be a good way to eliminate the pain and the resulting damage [20]. The transmission of man-machine interaction force between human and soft exoskeleton is affected by the soft tissues of the human body.

The relationship between man-machine interaction force and the deformation of human skin soft tissue is established. Soft tissue models are usually divided into uniaxial and multiaxis models, and each model can be divided into nonlinear elastic and viscoelastic elements. In the nonlinear model, the relationships between stress T and strain ε are expressed as

$$\begin{aligned} \varepsilon^2 &= aT^2 + bT, \\ T &= \frac{F}{S_0}, \\ \varepsilon &= \frac{(L - L_0)}{L_0}. \end{aligned} \tag{8}$$

In elastic fibers, the relationship between stress and strain is expressed as $\varepsilon^2 = a(1 - e^{bT})$. The elastic model of the skin is expressed as $T = a\varepsilon^b$. The linear viscoelastic characteristics of the soft tissue are described by the Maxwell element and the Voight element. The equation of Maxwell element is expressed as follows:

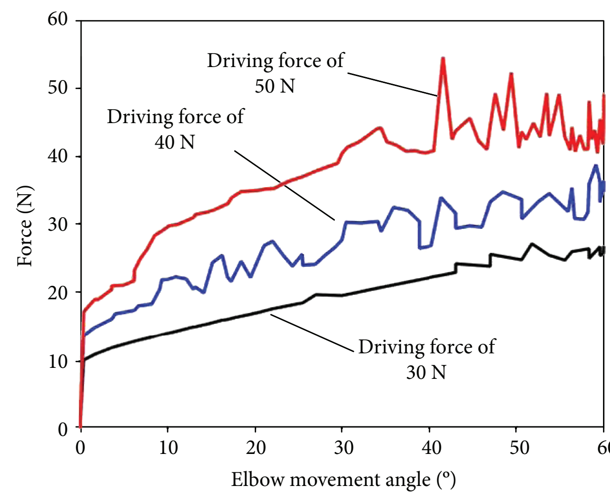

Figure 5: Man-machine interaction force at different tensions.

$$\begin{aligned} k(t) &= k_i e^{-(t/\lambda_i)}, \\ \lambda_i &= \frac{B_i}{k_i}, \end{aligned} \tag{9}$$

where k is the stiffness coefficient and B is the damping coefficient. The equation of Voight element is expressed as follows:

$$\begin{aligned} J(t) &= J_i e^{-(t/\lambda_i)}, \\ J_i &= \frac{1}{k_i}. \end{aligned} \tag{10}$$

The man-machine interaction force is studied when the number of Bowden cables connected to the fixed point on the webbing strap of forearm is changed. According to the spatial integration theory, as the pressure contact area increases, the number of surface pressure sensors also increases and human comfort will deteriorate. Therefore, the maximum number of Bowden cables is set to three. Results of simulation experiments comparing the man-machine interaction force with different numbers of Bowden cables are depicted in Figure 6, showing that interaction force is decreased with the increase of the number of Bowden cables. As the number of Bowden cables is increased, force bearing points on webbing strap are added and force exerted by a single connection point is decreased.

The man-machine interaction force is studied based on different force bearing points on the webbing strap of forearm. The center of the forearm is defined as the middle position. The position which extends three meters from the middle position to the wrist is defined as the position away from the elbow. The position which extends in the opposite direction is defined as the position close to the elbow. Results of simulation experiments comparing the man-machine interaction force with different force bearing points are

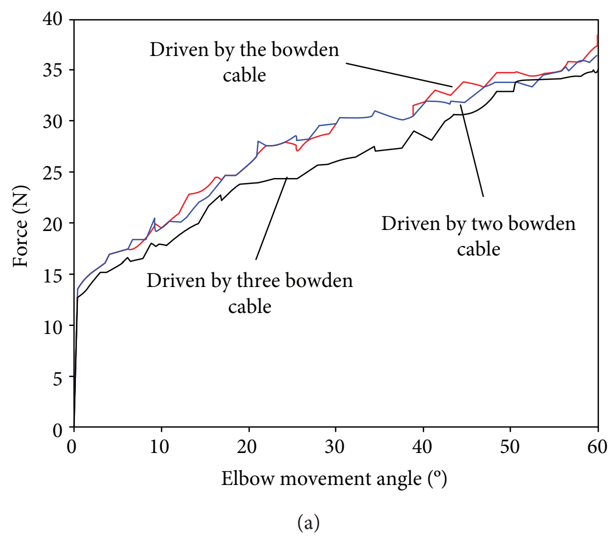

Figure 6: Man-machine interaction force at different numbers of Bowden cables. (a) The flexion movement of elbow under the driving force of 40 N. (b) The flexion movement of elbow under the driving force of 50 N.

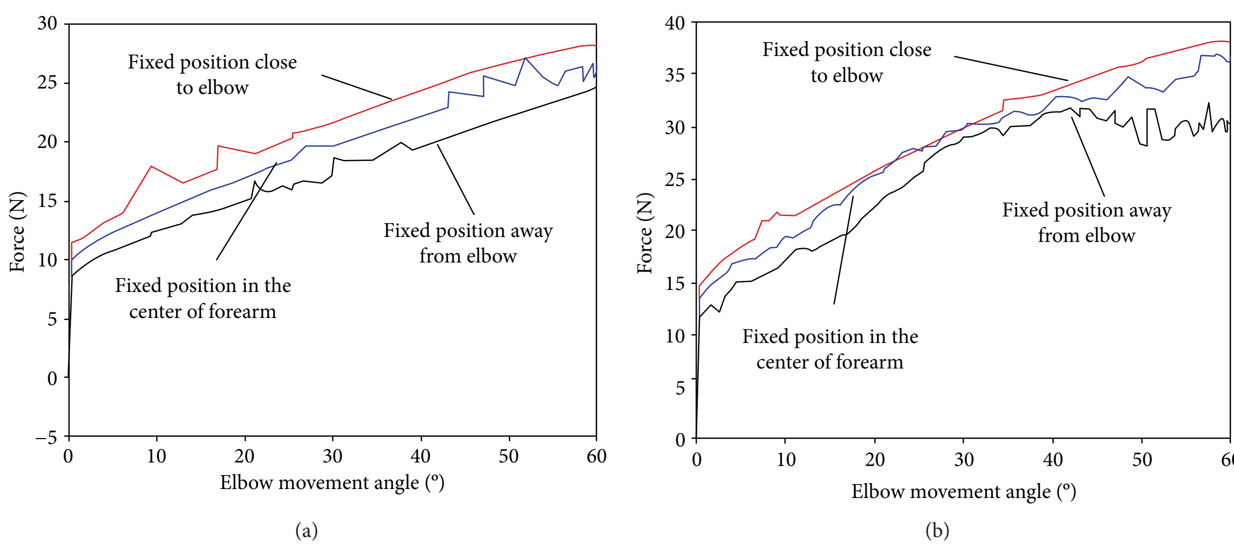

Figure 7: Man-machine interaction force at different force bearing points. (a) The flexion movement of elbow under the driving force of 30 N. (b) The flexion movement of elbow under the driving force of 40 N.

depicted in Figure 7. Based on webbing strap of forearm built in ADAMS, the farther the force bearing point is from the center of elbow, the smaller the man-machine interaction force is.

From the simulation results, it is concluded that the man-machine interaction force between the human body and the exoskeleton can be reduced by changing the number of Bowden cables and connection point on the webbing strap of forearm.

4. Experimental Evaluation

4.1. Experimental Scheme. The purpose of the experiment is to demonstrate that the proposed upper extremity soft exoskeleton structure optimization is effective. The human subject experiments were carried out on a 70 kg male subject. As is shown in Figure 8, a subject performs flexion and extension movements with upper limb soft exoskeleton. When wearing the upper limb soft exoskeleton, the subject can adjust the binding position through the Velcro to make sure fix binding belts in the right place accurately. The structural optimization described in the previous section is validated during these tests. During the experiment, the subject is instructed to perform multiple repetitive flexion movements with complete assistance provided by the soft exoskeleton. The center of the forearm is defined as the middle position. The position which extends three meters from the middle position to the wrist is defined as the position away from the elbow. The position which extends in the opposite direction is defined as the position close to the elbow. Two experiments are carried out separately.

FIGURE 8: Subject with upper limb soft exoskeleton.

(1) Based on the fixed position of the connecting point between the soft exoskeleton and the arm, multiple repetitive flexion movements of the elbow are performed with complete assistance delivered by the exoskeleton when the number of the Bowden cables is changed.

(2) On the basis of a fixed number of Bowden cable, multiple flexion movements of the elbow are performed with complete assistance offered by the exoskeleton when the connection position between the exoskeleton and the arm is changed.

A film pressure sensor mounted between the body and the soft exoskeleton detects the pressure on the surface of the human body F. The flex sensor fixed on the elbow detects the motion for elbow ϕ_e. Pressure F and angle ϕ_e are fitted through MATLAB to get the curves of pressure and motion angle.

4.2. Experimental Results. Results of the first experiment comparing the different numbers of the Bowden cables are depicted in Figure 9(a), showing that the pressure on the human body surface is reduced in pace with the increase of number of Bowden cables. As shown in Figure 9(a), man-machine interaction forces are almost same until flexion angle of elbow is 18 degrees. Afterwards, the man-machine interaction force is reduced with the increase of number of Bowden cables. The experimental results verify the conclusion with regard to the number of Bowden cables in the simulation experiment. The man-machine interaction force can be reduced when the number of force bearing points is increased in a certain range to spread the pressure over the wider range. Therefore, the safety and comfort of the exoskeleton system can be improved by increasing the number of Bowden cables. The results of the second experiment comparing the different connection positions between Bowden cable and the webbing strap are depicted in Figure 9(b), showing that the man-machine interaction force is reduced when force bearing point is away from the elbow. As shown in Figure 9(b), man-machine interaction forces are almost the same until flexion angle of elbow is 10 degrees. Afterwards, the man-machine interaction force is decreased when the force bearing point is away from the center of elbow. The experimental results verify the conclusion about the fixed position in the simulation experiment. Man-machine interaction force can be reduced when then connection point between Bowden cable and webbing strap is away from the center of elbow in a certain range.

5. Conclusions and Future Work

We propose the design of the mechanical structure and actuator for upper limb soft exoskeleton based on Bowden cable. Methods of structural optimization are proposed to reduce the man-machine interaction force. Human arm model with upper limb soft exoskeleton is established in ADAMS. Through simulation experiments, the influence of the number of force bearing points and the fixed position of force bearing point on man-machine interaction force in a certain range is summarized. A pilot evaluation demonstrates conclusions of simulation experiments. The subject with upper limb soft exoskeleton performs flexion movements of the elbow with assistance provided by soft exoskeleton under the condition of different numbers of Bowden cables and different connection points between Bowden cable and webbing strap. The following conclusions are obtained.

(1) The man-machine interaction force can be reduced when the number of Bowden cables is increased to distribute pressure in a wider range within measure.

(2) The man-machine interaction force can be reduced when the connection position is changed to make force bearing point away from the center of the elbow.

Based on the optimized structure proposed in the paper, the upper limb soft exoskeleton is suitable for the recovery training of stroke patients. This optimized structure can reduce the man-machine interaction force by 10%–15% and avoid the damage to patients.

The soft exoskeleton is extremely light and hardly causes scratch. This soft exoskeleton also does not limit motion freedom basically and allows the wearer to move through their full range of motion.

There are many areas for future improvement of the exoskeleton system. At present, a simple actuation is built to facilitate the structure optimization. In the future, the motor and gearbox need to be systematically selected and the structure of actuation should be further optimized to improve the transmission and reduce the friction of the Bowden cable transmission system. Friction is temporarily neglected in the design of the control system. In the actual situation, the control system needs to be improved and

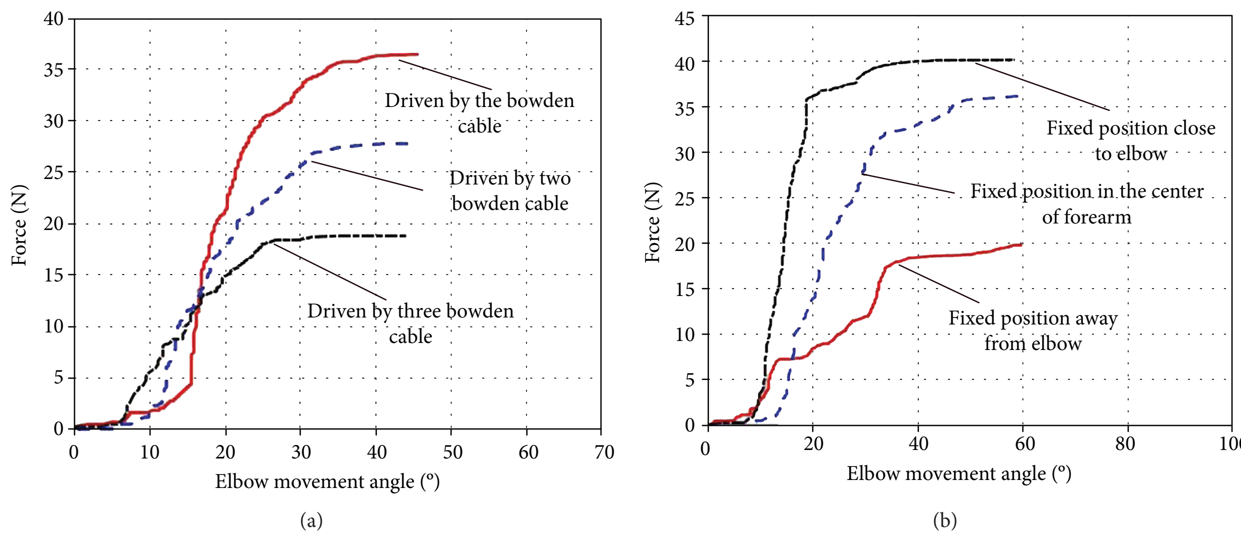

Figure 9: (a) Pressure comparison on different numbers of Bowden cable with exoskeleton's assistance. (b) Pressure comparison on different fixed positions with exoskeleton's assistance.

friction factor needs to be considered. In the future, patients with apoplectic hemiplegia will participate in the experiment to verify the accuracy of the hierarchical control system and evaluate the effect of the exoskeleton.

Data Availability

All the data supporting the results were shown in the paper and can be available from the corresponding author.

Conflicts of Interest

The authors declare that there is no conflict of interest regarding the publication of this paper.

Acknowledgments

This research is partly supported by the Natural Science Foundation of Tianjin (14JCYBJC42700) and partly by the Natural Science Research General Program of Higher Education of Jiangsu Province (16KJB510040).

References

[1] H. S. Lo and S. Q. Xie, "Exoskeleton robots for upper-limb rehabilitation: state of the art and future prospects," *Medical Engineering & Physics*, vol. 34, no. 3, pp. 261–268, 2012.

[2] W. van Dijk, H. van der Kooij, and E. Hekman, "A passive exoskeleton with artificial tendons: design and experimental evaluation," in *2011 IEEE International Conference on Rehabilitation Robotics*, pp. 1–6, Zurich, Switzerland, 2011.

[3] M. Wehner, D. Rempel, and H. Kazerooni, "Lower extremity exoskeleton reduces back forces in lifting," in *ASME 2009 Dynamic Systems and Control Conference*, vol. 2, pp. 49–56, Hollywood, CA, USA, 2009.

[4] M. Wehner, B. Quinlivan, P. M. Aubin et al., "A lightweight soft exosuit for gait assistance," in *2013 IEEE International Conference on Robotics and Automation*, pp. 3362–3369, Karlsrube, Germany, 2013.

[5] P. Heo, G. M. Gu, S. J. Lee, K. Rhee, and J. Kim, "Current hand exoskeleton technologies for rehabilitation and assistive engineering," *International Journal of Precision Engineering and Manufacturing*, vol. 13, no. 5, pp. 807–824, 2012.

[6] A. T. Asbeck, R. J. Dyer, A. F. Larusson, and C. J. Walsh, "Biologically-inspired soft exosuit," in *2013 IEEE 13th International Conference on Rehabilitation Robotics (ICORR)*, pp. 1–8, Seattle, WA, USA, 2013.

[7] L. Cappello, D. K. Binh, S. C. Yen, and L. Masia, "Design and preliminary characterization of a soft wearable exoskeleton for upper limb," in *2016 6th IEEE International Conference on Biomedical Robotics and Biomechatronics (BioRob)*, pp. 623–630, Singapore, 2016.

[8] Y. Ding, I. Galiana, A. Asbeck, B. Quinlivan, S. M. M. De Rossi, and C. Walsh, "Multi-joint actuation platform for lower extremity soft exosuits," in *2014 IEEE International Conference on Robotics and Automation (ICRA)*, pp. 1327–1334, Hong Kong, 2014.

[9] S. Barreca, S. L. Wolf, S. Fasoli, and R. Bohannon, "Treatment interventions for the paretic upper limb of stroke survivors: a critical review," *Neurorehabilitation and Neural Repair*, vol. 17, no. 4, pp. 220–226, 2003.

[10] B. K. Dinh, M. Xiloyannis, C. W. Antuvan, L. Cappello, and L. Masia, "Hierarchical cascade controller for assistance modulation in a soft wearable arm exoskeleton," *IEEE Robotics and Automation Letters*, vol. 2, no. 3, pp. 1786–1793, 2017.

[11] A. T. Asbeck, S. M. M. De Rossi, K. G. Holt, and C. J. Walsh, "A biologically inspired soft exosuit for walking assistance," *The International Journal of Robotics Research*, vol. 34, no. 6, pp. 744–762, 2015.

[12] W. T. Dempster and G. R. L. Gaughran, "Properties of body segments based on size and weight," *American Journal of Anatomy*, vol. 120, no. 1, pp. 33–54, 1967.

[13] S. Lee, S. Crea, P. Malcolm, I. Galiana, A. Asbeck, and C. Walsh, "Controlling negative and positive power at the ankle with a soft exosuit," in *2016 IEEE International Conference on*

Robotics and Automation (ICRA), pp. 3509–3515, Stockholm, Sweden, 2016.

[14] G. Saggio, F. Riillo, L. Sbernini, and L. R. Quitadamo, "Resistive flex sensors: a survey," *Smart Materials and Structures*, vol. 25, no. 1, article 013001, 2016.

[15] R. M. Murray, Z. Li, and S. S. Sastry, *A Mathematical Introduction to Robotic Manipulation*, CRC Press Inc., 1994.

[16] K. Kong and M. Tomizuka, "Control of exoskeletons inspired by fictitious gain in human model," *IEEE/ASME Transactions on Mechatronics*, vol. 14, no. 6, pp. 689–698, 2009.

[17] Y. Mao and S. K. Agrawal, "Wearable cable-driven upper arm exoskeleton - motion with transmitted joint force and moment minimization," in *2010 IEEE International Conference on Robotics and Automation*, pp. 4334–4339, Anchorage, AK, USA, 2010.

[18] L. Y. He, Z. Q. Zhang, and B. L. Zheng, "Biomechanics design and strength analysis of exoskeleton frame," *Journal of Medical Biomechanics*, vol. 29, no. 6, pp. 504–510, 2014.

[19] C. Liao, J. Zhang, W. Chen, and M. Lv, "Union simulation on lower limbs rehabilitation robot based on MATLAB and ADAMS," in *2015 IEEE 10th Conference on Industrial Electronics and Applications (ICIEA)*, pp. 557–562, Auckland, New Zealand, 2015.

[20] T. A. Krouskop, R. Williams, M. Krebs, I. Herszkowicz, and S. Garber, "Effectiveness of mattress overlays in reducing interface pressures during recumbency," *Journal of Rehabilitation Research and Development*, vol. 22, no. 3, pp. 7–10, 1985.

Hindawi
Applied Bionics and Biomechanics
Volume 2018, Article ID 7435746, 11 pages
https://doi.org/10.1155/2018/7435746

Research Article

Feasibility of Neurorehabilitation Using a Hybrid Assistive Limb for Patients Who Underwent Spine Surgery

Aya Yatsugi,[1,2] Takashi Morishita ,[1] Hiroyuki Fukuda,[1,2] Naoya Kotani,[2] Kenji Yagi,[1] Hiroshi Abe,[1] Etsuji Shiota,[2] and Tooru Inoue[1]

[1]*Department of Neurological Surgery, Fukuoka University Faculty of Medicine, Fukuoka, Japan*
[2]*Department of Rehabilitation Medicine, Fukuoka University Hospital, Fukuoka, Japan*

Correspondence should be addressed to Takashi Morishita; tmorishita@fukuoka-u.ac.jp

Received 17 February 2018; Revised 21 May 2018; Accepted 19 June 2018; Published 10 July 2018

Academic Editor: Liwei Shi

Recent studies of robotic rehabilitation have demonstrated its efficacy for neurological disorders. However, few studies have used the Hybrid Assistive Limb (HAL) during the early postoperative stage of spine disorders. We aimed to evaluate the safety and efficacy of HAL treatment during the early postoperative period for spine disorder patients. We retrospectively identified patients who underwent spine surgery and who could complete HAL treatment. We evaluated the 10-m walking test (10MWT), the modified Gait Abnormality Rating Scale (GARS-M), Barthel Index (BI), and the walking index for spinal cord injury II (WISCI II) score results before and after robotic rehabilitation. Clinical outcomes were compared after treatment. We included nine patients with various spine problems. After HAL treatment, the speed during the 10MWT significantly improved from 64.1 ± 16.0 to 74.8 ± 10.8 m/min, and the walking cadence decreased from 102.7 ± 17.6 to 92.7 ± 10.9 steps/min. The BI score also improved from 83.3 ± 16.0 to 95.6 ± 5.8, and the WISCI II score improved from 19.7 ± 0.5 to 20.0 ± 0.0. Furthermore, the total GARS-M score improved from 6.0 ± 5.7 to 2.3 ± 3.3. The maximum angles of the trunk swing were improved from 2.2 ± 1.9 to 1.2 ± 0.9 degrees. Neurorehabilitation therapy using HAL for spinal surgery patients was considered feasible following spine surgery.

1. Introduction

Robotic technologies have been increasingly gaining attention in the field of neurorehabilitation. The Hybrid Assistive Limb (HAL) (Cyberdyne Inc., Ibaraki, Japan) is a unique exoskeleton robot for neurorehabilitation that was developed by Sankai and colleagues based on the interactive biofeedback (iBF) theory [1, 2]. HAL has a hybrid system that allows both voluntary and autonomous modes of action to support training, and it supports voluntary muscle movement by detecting bioelectrical signals (BES). For walking training, movements of the joints are accurately adjusted by the pressure sensor in the foot bottom and joint angle sensors of the frame. Based on the input information, four actuators of the hip and knee joint are controlled independently [3]. Movements of the affected limbs supported by the HAL system generate sensory feedback to the brain (i.e., iBF) and accelerate motor learning in the process of functional recovery.

Recent studies have shown the safety and efficacy of rehabilitation using HAL robotics for various disorders, including stroke [3–7], spinal cord injury (SCI) [8–14], and quadriceps arthrogenic muscle inhibition [15]. Another recent study demonstrated neuroplasticity induced by HAL treatment [16, 17]. However, five case reports have focused on the efficacy of HAL therapy for postoperative thoracic ossification of the posterior longitudinal ligament (OPLL) [18–22]. These reports indicated that HAL was used as a last resort for gait recovery during the almost chronic phase of the postoperative state [21, 22], and the authors recommended starting HAL-assisted training during the early stage following surgery. Neurorehabilitation during the postoperative state is essential for returning to social activities and preventing disuse syndrome. Based on the findings indicated by these five case reports [18–22], in addition to the reports demonstrating the efficacy of HAL training for SCI cases [8–14], we hypothesized that using HAL may facilitate early recovery after spine surgery. Therefore, we aimed to evaluate the safety and efficacy of HAL-assisted rehabilitation for spine disorder patients during the early postoperative period.

2. Materials and Methods

2.1. Patient Selection and Study Design. We performed a retrospective chart review of patients with spine disorders treated at our neurosurgical department from October 2011 to February 2016. To evaluate the effects of HAL treatment for improvements in gait, we included patients who could complete HAL treatment at least three times. Additionally, because voluntary muscle contractions are required to gain assistance from the HAL system, we excluded patients with complete or nearly complete paralysis. The protocol of the present study was approved by our institutional review board (IRB), and HAL treatment was performed after receiving written informed consent from each patient.

HAL treatment was performed for 31 patients with spine disorders; however, 22 patients did not meet the inclusion criteria of the current study (Figure 1). Among those 22 patients, 13 did not undergo surgery.

We investigated the remaining nine patients (six male patients and three female patients) with the following characteristics: severe impairment resulting in the inability to use HAL ($n = 5$) and less than three sessions of HAL treatment ($n = 4$). The mean age of the cohort was 53.6 years (SD, ±16.1). Diagnoses were dural arteriovenous fistula (AVF) ($n = 2$), cervical ossification of the posterior longitudinal ligament (OPLL) ($n = 1$), spinal lipoma ($n = 1$), arachnoid cyst ($n = 1$), spinal ependymoma ($n = 3$), and cervical spondylosis ($n = 1$). Spine lesion levels are summarized in Table 1.

2.2. Rehabilitation Program. We performed conventional physical therapy in addition to HAL treatment. Conventional physical therapy started within 2 days after surgery. Depending on the patient's condition, the programs included manual leg stretching, muscular workouts, and basic movement training such as standing, walking, and going up and down stairs. When patients felt fatigue during the HAL treatment, they were allowed to rest. Each session lasted approximately 50 minutes, including time necessary for robotic attachment, and was performed two or three times per week.

HAL treatment started when the patients were able to sit stably. On average, intervention with therapists and HAL treatment began 14.2 ± 8.1 days (range 7–29 days) after surgery. The mean number of HAL treatment sessions was 5.0 ± 2.6 (range 3–12). Rehabilitation periods comprised 13.6 ± 9.1 days (range 4–35 days) during hospitalization at our institution (Table 1).

A bilateral leg version of HAL was used for patients involved in this study (HAL for Living Support–Lower Limb; Cyberdyne Inc.). Training started with the Cybernic Voluntary Control mode, which measures BES from the extensor and flexor muscles of the hip and knee. HAL treatment was

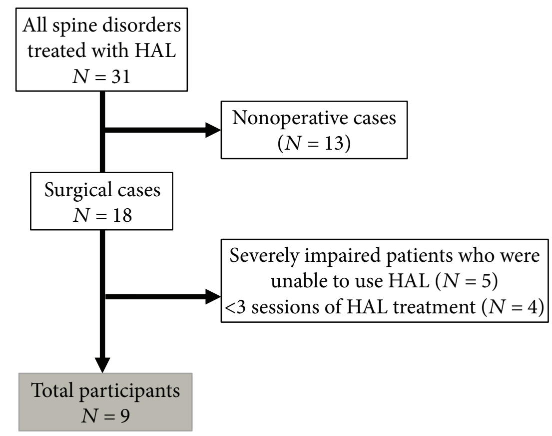

Figure 1: Patient selection flowchart.

performed by one or two physiotherapists and a medical doctor who were trained to use the HAL system. During gait training, the physiotherapist checked the BES and adjusted the HAL assist level.

During HAL treatment, several sets of a knee extension movement were performed (10 times with the left leg and 10 times with the right leg). The standing movement was performed 10 times. Balance training was performed for several seconds with open eyes or closed eyes so that the center of gravity would be in the middle. Finally, walking training was performed on a flat ground or a treadmill. During balance training and gait training, we used a monitor displayed in front of the patient to provide visual feedback regarding the center of gravity, posture, and balance (Figure 2).

We focused on walking training. We used a walk aid called All-In-One Walking Trainer (Ropox A/S, Naestved, Denmark) to secure the safety of patients when walking on a flat floor. It is able to support body weight and enables safe HAL treatment with the use of a harness. We did not use body weight support. After the patient became accustomed to walking on the ground, we began treadmill walking. Patients performed several sets of 5 minutes of walking at a speed that was comfortable with HAL. If patients wanted to continue and were not fatigued, then we increased the speed or increased the walking time. When there was deflection of the center of gravity (it does not take weight to walk on tiptoes), we instructed the patient to move the weight from the heel to the tiptoes.

2.3. Outcome Measures. All patients were video-recorded during rehabilitation. The speed and steps during the 10-m walking test (10MWT) as an evaluation of motor function at the time of treatment immediately before wearing HAL and during the last training session after excluding HAL were used to evaluate HAL treatment times. We used the modified Gait Abnormality Rating Scale (GARS-M) [23], the Barthel Index (BI), and the walking index for spinal cord injury II (WISCI II) to evaluate walking appearance, activities of daily living (ADL), and the patients' ambulatory walking capacity on the basis of the need for physical assistance and assistive devices, respectively [24]. The GARS-M includes variables that provide a description of gait associated with an increased

Table 1: Patient characteristics.

Patient	Age (years)	Sex	Diagnosis	Lesion level	Surgery-HAL interval (days)	Number of HAL sessions	Rehabilitation period (days)
1	48	Male	Arachnoid cyst	C5–Th1	7	3	7
2	65	Male	Dural AVF	Th6-7	13	12	35
3	56	Male	Dural AVF	Th6-7	10	3	4
4	70	Male	Cervical OPLL	C2–Th1	14	5	9
5	67	Male	Spinal lipoma	L2–5	21	5	7
6	72	Male	Cervical spondylosis	C4–5	11	5	10
7	29	Female	Spinal ependymoma	C6	29	4	18
8	36	Female	Spinal ependymoma	C2-3	14	3	21
9	39	Female	Spinal ependymoma	Medulla oblongata to Th1	19	5	11
Mean ± SD	53.6 ± 16.1				14.2 ± 8.1	5.0 ± 2.6	13.6 ± 9.1

AVF = arteriovenous fistula; OPLL = ossification of the posterior longitudinal ligament; SD = standard deviation.

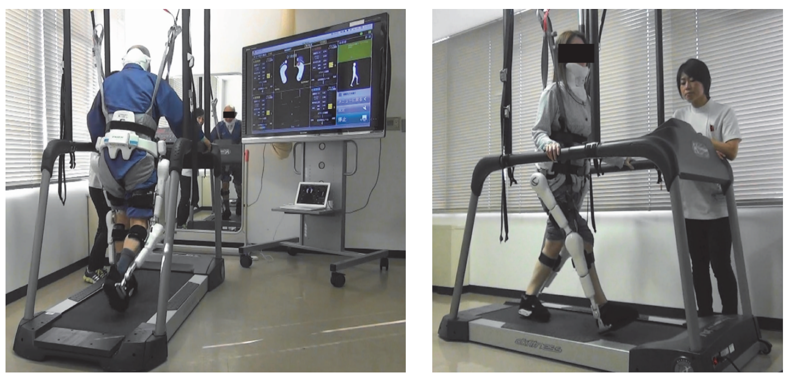

(a) (b)

Figure 2: (a, b) Hybrid Assistive Limb (HAL) treatment. Gait training on a treadmill in front of a large monitor.

risk of falling. The GARS-M considered the following seven items: (1) variability, (2) guardedness, (3) staggering, (4) foot contact, (5) hip range of motion (ROM), (6) shoulder extension, and (7) arm–heel strike synchrony. Each item of the GARS-M is rated from 0 to 3, with a maximum of 21 points; a score of 21 points indicates the worst state. We measured the maximum angle of the trunk swing during the 10MWT before and after treatment using the Total Motion Coordinate System version 3.28 (Toso System Inc., Tokyo, Japan) motion analysis device.

2.4. Statistical Analysis. We performed a paired t-test to compare the clinical outcomes and baseline. We used SPSS version 21.0 (IBM Corp., Armonk, NY, USA) for the analyses. The mean ± SD values are described.

3. Results

After HAL treatment, the speed during the 10MWT significantly improved from 64.1 ± 16.0 to 74.8 ± 10.8 m/min ($P = 0.031$), and the cadence decreased from 102.7 ± 17.6 to 92.7 ± 10.9 steps/min ($P = 0.046$). The BI score also improved from 83.3 ± 16.0 to 95.6 ± 5.8 ($P = 0.043$). Furthermore, the total GARS-M score improved from 6.0 ± 5.7 to 2.3 ± 3.3 ($P = 0.005$). The maximum angles of the trunk swing were improved from 2.2 ± 1.9 to 1.2 ± 0.9 degrees ($P = 0.033$). The WISCI II score also improved from 19.7 ± 0.5 to 20.0 ± 0.0 ($P = 0.081$). These scores are summarized in Figure 3. There were no adverse events due to HAL treatment such as pain and/or falling.

It is noteworthy that almost all subjects had improved gait posture. After reviewing each item before and after HAL treatment, it became clear that the subscores of guardedness (item 2), staggering (item 3), and shoulder extension (item 6) showed the most dramatic improvements. Momentum and the ability to move the legs forward were improved. Collapse of balance toward the side was decreased. The movement range of the shoulder toward the backside was expanded.

3.1. Representative Case (Case 2). A 65-year-old man was diagnosed with dural AVF at the level of Th6-7 and underwent laminectomy for ligation of the draining vein. Preoperatively, he had urinary continence and was wheelchair-bound. A few days after surgery, conventional physical therapy was started and his walking ability gradually improved so that he could walk with an aid on postoperative day 9. However, his gait posture had involved sweeping out his lower limbs at the cost of laterally bending the trunk to the opposite side (Figure 4). He also had difficulty in kicking the ground with the toes.

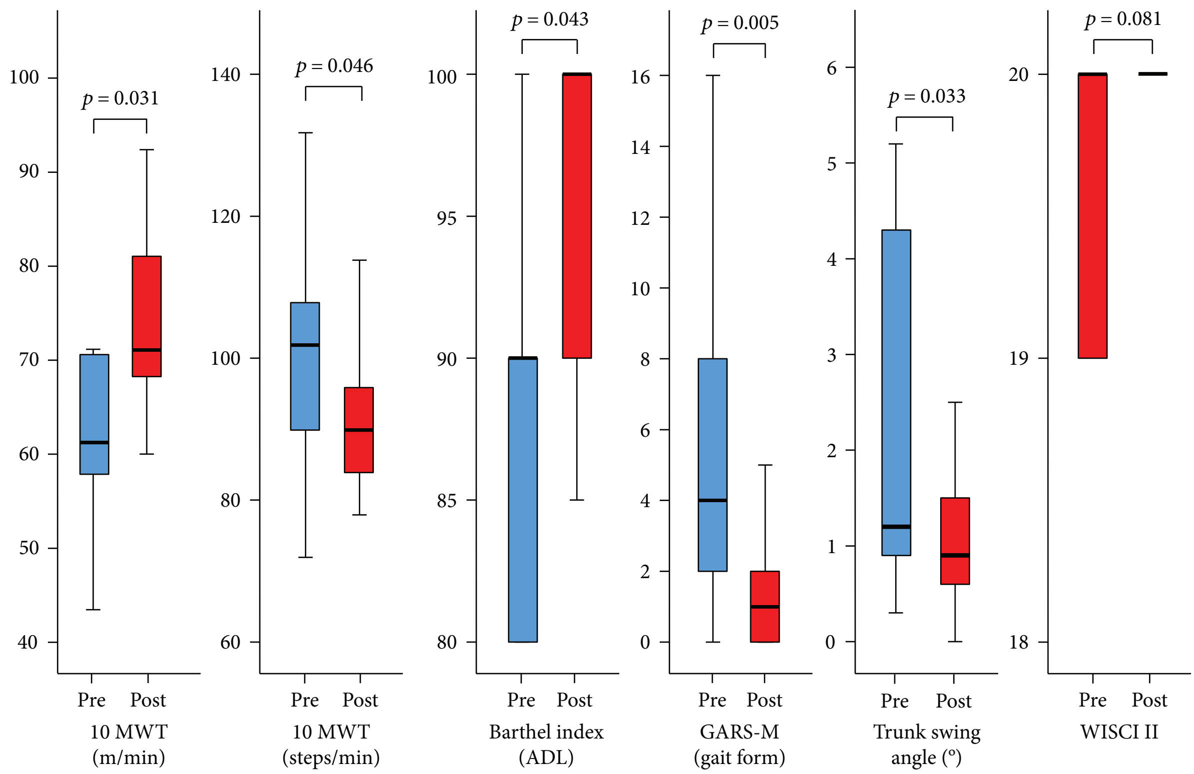

Figure 3: Graph showing functional outcomes evaluated by the 10-m walking test (10MWT): speed (m/min), cadence (steps/min), the Barthel Index, modified Gait Abnormality Rating Scale (GARS-M), trunk swing angle before and after Hybrid Assistive Limb (HAL) treatment, and the walking index for spinal cord injury II (WISCI II) score. Whiskers represent the standard deviation. Pre: before treatment; Post: after treatment.

We started using HAL on postoperative day 13. At this point, his WISCI II score was 19. At first, he performed knee extension movements and standing training. Next, he started balance training and gait training with a walking device (All-In-One Walking Trainer; Ropox A/S). Later, walking training on a treadmill was initiated.

Before HAL treatment, his trunk was bending forward and he required walking support. After 12 sessions of HAL treatment, the trunk lifted while walking and posture improved. He could constantly set the position of his foot and the step width. He became able to kick the ground on tip-toes and swing out his lower limbs without side bending of the trunk. The angle of his trunk swing during 10MWT decreased from 4.6 to 1.4 degrees (Figure 4). His 10MWT speed improved from 43.4 to 65.7 m/min, and the walking cadence decreased from 132 to 96 steps/min. The total GARS-M score improved from 16 to 10. Similarly, the BI and WISCI II score improved from 55 to 100 and from 19 to 20, respectively.

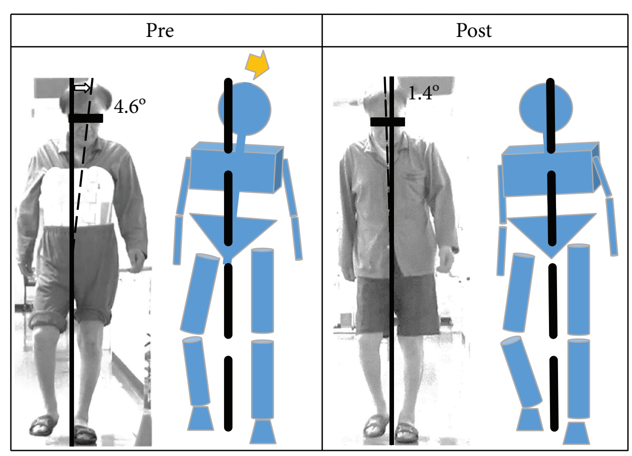

Figure 4: Representative case showing improvements in walking appearance. Prior to Hybrid Assistive Limb (HAL) treatment, the trunk leaned toward the left when standing with the left leg. Furthermore, the trunk was leaned 4.6° to the left. After 12 sessions of HAL treatment, the upper body was stabilized. Pre: before training; Post: after training.

4. Discussion

The HAL was invented based on the iBF theory [1, 2] that movements of the affected limbs supported by the HAL system generate sensory feedback to the brain (i.e., iBF) and accelerate motor learning in the process of functional recovery. HAL therapy may address spasticity due to central nervous system (CNS) lesions. A CNS lesion above the level of the central pattern generator (CPG) results in a loss of supraspinal drive and spasticity. The consequences are hyperexcitability of short-latency reflexes, loss of long-latency reflexes, and changes in muscle properties [25]. According to the iBF theory, sensory input is sent back to the CNS to activate the impaired neuronal networks

TABLE 2: Review of reports of several postoperative spinal diseases.

Diagnosis	Author, year	Sample size, *n* (sex)	Age (years) (mean)	Follow-up (mean)	Outcome measures	Presenting symptoms	Rehabilitation program	Long-term results after surgical treatment
Arachnoid cyst	Bond et al., 2012 [31]	31 (M 14; F 17)	1–17 (8.1)	13 days to 12.6 years (4.4 years)	Categorized as complete remission, improvement, stable, or worse	Pain: 13 cases Lower extremity weakness: 12 cases Gait instability: 10 cases Spasticity: 6 cases Sensory loss: 3 cases Bladder dysfunction: 2 cases	N/A	21 patients had complete remission of symptoms 6 patients had symptom improvement 3 patients were stable 1 patient had worsened symptoms
Dural AVF	Behrens and Thron, 1999 [30]	21 (M 18; F 3)	33–75 (57.0)	5 months to 11 years (50 months)	Muscle strength	Flaccid: 9 patients Spastic: 12 patients	N/A	Improved: 67%; unchanged: 19%; deteriorated: 14%
					Walking distance	Wheelchair: 7 patients	N/A	Improved: 57%; unchanged: 29%; deteriorated: 14%
					Sensory loss	Sensory disturbance: 18 patients	N/A	Improved: 38%; unchanged: 62%
					Pain	No patient	N/A	Improved: 5%; unchanged: 71%; deteriorated: 24%
	Van Dijk et al., 2002 [32]	49 (M 39; F 10)	28–78 (63)	12 days to 9.9 years (32.9 months)	BI (score)	70.5 ± 20.43 (range 20–95)	N/A	85.75 ± 13.81 (range 50–100)
					Aminoff score of disability*	The median gait score was 3 The median bladder score was 3	N/A	The median gait score was 2 The median gait score was 2
Cervical OPLL	Onari et al., 2001 [33]	30 (M 22; F 8)	34–61 (51.3)	10–23 years (14.7 years)	Okamoto's classification for the degree of walking disability**	Grade a: no patient Grade b: 9 patients Grade c: 18 patients Grade d: 3 patients	N/A	Improvement: 2 grades in 16 patients Improvement: 1 grade in 8 patients Ambulatory deterioration in 6 patients
	Iwasaki et al., 2002 [34]	64 (M 43; F 21)	42–78 (56)	10–16 years (12.2 years)	JOA scoring system for cervical myelopathy***	The mean preoperative total JOA score was 8.9 UE motor score: 2.5 ± 1.0 LE motor score: 2.2 ± 0.9 Sensory score: 2.2 ± 1.7 Bladder score: 2.2 ± 0.8	N/A	The mean last follow-up total JOA score was 13.8 UE motor score: 3.5 ± 0.8 LE motor score: 2.9 ± 1.1 Sensory score: 4.6 ± 1.4 Bladder score: 2.7 ± 0.5
Spinal lipoma	Lee et al., 1995 [35]	6 (M 3; F 3)	8–45 (27)	12–96 months (53.8 months)	Clinical and functional classification scheme****	Grade I: no patient Grade II: 3 patients Grade III: 3 patients Grade IV: no patient	N/A	Grade I: 1 patient Grade II: 2 patients Grade III: 2 patients Grade IV: 1 patient

Table 2: Continued.

Diagnosis	Author, year	Sample size, n (sex)	Age (years) (mean)	Follow-up (mean)	Outcome measures	Presenting symptoms	Rehabilitation program	Long-term results after surgical treatment
Cervical spondylosis	Wang et al., 2004 [36]	204 (M 145; F 59)	36–92 (63)	16 months	Nurick score for myelopathy*****	Score 0: 6 patients Score 1: 56 patients Score 2: 71 patients Score 3: 28 patients Score 4: 24 patients Score 5: 19 patients	N/A	Score 0: 64 patients Score 1: 72 patients Score 2: 31 patients Score 3: 10 patients Score 4: 19 patients Score 5: 8 patients
	Singh et al., 2009 [37]	50 (M 36; F 14)	56.7 ± 13.7	3 years	30-m walking test (sec)	53.6 ± 10.3	N/A	38.6 ± 6.9
	Kadaňka et al., 2011 [38]	64 (M, 46; F, 18)		12 years	10-m walking test (sec)		N/A	
		Without surgery: $n = 32$	Without surgery: 47–65 (54.5)	12 years	10-m walking test (sec)	7.0 (5.3; 10.7)******	N/A	7.1 (5.1; 12.5)
		With surgery: $n = 32$	With surgery: 41–65 (51.0)	12 years	10-m walking test (sec)	8.0 (5.0; 29.8)	N/A	7.3 (5.1; 25.7)
Spinal ependymoma	Li et al., 2013 [39]	38 (M 19; F 19)	11–60 (35.3)	1 year	Modified McCormick classification*******	Grade I: 18 patients Grade II: 11 patients Grade III: 9 patients Grade IV: 0 patient	N/A	Grade I: 15 patients Grade II: 14 patients Grade III: 7 patients Grade IV: 2 patients
	Kaner et al., 2010 [40]	21 (M, 13; F, 8)	17–57 (34)	12–168 months (54 months)	Modified McCormick classification	Grade I: 11 patients Grade II: 5 patients Grade III: 3 patients Grade IV: 2 patients	They performed rehabilitation from an early postoperative day, but the content and method were not described at all	Grade I: 20 patients Grade II: 1 patient Grade III: 0 patient Grade IV: 0 patient

M = male; F = female; N/A = not available; AVF = arteriovenous fistula; BI = Barthel Index; OPLL = ossification of the posterior longitudinal ligament; JOA = Japanese Orthopaedic Association; UE = upper extremity; LE = lower extremity; the mean ± the standard deviation. *Aminoff score of disability (classification of gait disturbance: grade 1: leg weakness or abnormal gait and no restricted activity; grade 2: grade 1 with restricted activity; grade 3: requiring 1 stick or similar support for walking; grade 4: requiring 2 sticks or crutches for walking; and grade 5: unable to stand and confined to bed or wheelchair. Classification of micturition: grade 1: hesitance, urgency, or frequency; grade 2: occasional urinary incontinence or retention; and grade 3: total urinary incontinence or retention). **Okamoto's classification for the degree of walking disability (a: impossible to walk; b: walk with aids; c: independent walk with spasm; d: walk with difficulty, with or without spasm; e: walk easily but difficult to walk continuously; and f: normal or almost normal walking). ***JOA scoring system for cervical myelopathy (motor function of fingers, shoulder and elbow, and lower extremity; sensory function of upper extremity, trunk, and lower extremity; and bladder function. Total score for a healthy patient = 17. Normal score of UE motor: 4, LE motor: 4, sensory: 6, and bladder: 3). ****Clinical and functional classification scheme (grade I: neurologically normal, grade II: sensorimotor deficit affecting the function of the involved limb, grade III: more severe neurological deficit, and grade IV: severe deficit). *****Nurick score for myelopathy (0: root involvement but no evidence of spinal cord disease; 1: spinal cord disease but no difficulty in walking; 2: slight difficulty in walking, but still employable; 3: difficulty in walking preventing full-time work or housework but independent ambulation; 4: able to walk with assistance or a walker; and 5: chair-bound or bedridden). ******Median (5th–95th percentile range). *******Modified McCormick classification (grade I: neurologically normal, normal ambulation and professional activity, and minimal dysesthesia; grade II: mild motor and sensory deficit, independent function, and ambulation maintained; grade III: moderate sensorimotor deficit, restriction of function, and independent with an external aid; grade IV: severe sensorimotor deficit, restricted function, and dependent; and grade V: paraplegia and quadriplegia and even/flickering movement).

Table 3: Review of HAL treatment for spinal disease.

Author, year	Age (years), sex	Diagnosis	Time when starting HAL	Number of HAL sessions	10MWT Speed (m/min)		10MWT Cadence (steps/min)		BI		WISCI II	
					Pre	Post	Pre	Post	Pre	Post	Pre	Post
Our result	53.6 ± 16.1, M 6; F 3	Table 1	POD 14.2 (7–29 days)	2-3 times/ week, 5.0 ± 2.6	64.1 ± 16.0	74.8 ± 10.8	102.7 ± 17.6	92.7 ± 10.9	83.3 ± 16.0	95.6 ± 5.8	19.7 ± 0.5	20.0 ± 0.0
Sakakima et al., 2013 [18]	60, F	T2–8 OPLL, T9–10 OLF	POD 49 (after bed rest) to 15 weeks	6 times/ week, 48	N/A	N/A	N/A	N/A	N/A	N/A	0	8
Kubota et al., 2016 [19]	43, M	T8–11, L1–3 OPLL	POD 14–44	2-3 times/ week, 10	Approximately 20*	Approximately 50*	Approximately 42*	Approximately 85*	60	85	13	16
Fujii et al., 2017 [20]	63, F	T3–7 OPLL	POD 44 (after bed rest) to POD 73	2-3 times/ week, 10	15.9	31.8	43.8	77.9	N/A	N/A	8	16
Kubota et al., 2017 [21]	66, F	C5-6 OPLL	14 years after surgery	Once/2 weeks, 10	22.5	46.7	61.9	81.6	N/A	N/A	16	16
Shimizu et al., 2017 [41]	48, M	T12–L1 SDAVF	6 months after surgery	2 times/ week, 10	Approximately 13*	Approximately 29*	Approximately 39*	Approximately 62*	N/A	N/A	7	12
Taketomi et al., 2018 [22]	70, M	T9–12, L2/3, L5 OLF, C3–7 OPLL	1 year after his third surgery	2 times/ week, 10	49.8	58.2	109.8	120	N/A	N/A	N/A	N/A
Puentes et al., 2018 [26]	59.6 ± 13.9, M 2; F 3 (acute group)	OPLL	POD 24.4 (15–32 days)	2 times/ week, 10	Approximately 28*	Approximately 54*	N/A	N/A	Approximately 63*	Approximately 83*	N/A	N/A
	70.1 ± 6.9, M 7 (chronic group)		POD 1151.4 (287–3655 days)		Approximately 48*	Approximately 56*	N/A	N/A	Approximately 100*	Approximately 100*	N/A	N/A
Aach et al., 2014 [9]	48 ± 9.4, M 6; F 2	T8–L2 SCI	8.1 (1–19) years posttrauma—90 days	5 times/ week, 51.75 ± 5.6	0.28 ± 0.28 (m/sec)	0.5 ± 0.34	N/A	N/A	N/A	N/A	10 ± 4.3	11.1 ± 3.7

Table 3: Continued.

Author, year	Age (years), sex	Diagnosis	Time when starting HAL	Number of HAL sessions	10MWT Speed (m/min)		10MWT Cadence (steps/min)		BI		WISCI II	
					Pre	Post	Pre	Post	Pre	Post	Pre	Post
Cruciger et al., 2016 [10]	52, M	L3 SCI	10 years posttrauma—12 weeks	5 times/ week, mean 54.5	85.6 ± 56.9 (sec)	44.3 ± 34.6	N/A	N/A	N/A	N/A	N/A	N/A
	40, F	L1 SCI	19 years posttrauma—12 weeks									
Sczesny-Kaiser et al, 2015 [11]	46.9 ± 2.7, M 7; F 4	T8–L2 SCI	8.8 (0.7–17) years postinjury—12 weeks	5 times/ week, 60	0.25 ± 0.05 (m/sec)	0.5 ± 0.07	N/A	N/A	N/A	N/A	N/A	N/A
Watanabe et al., 2017 [12]	62, M	T12–L1 SCI	7 days post onset	3-4 times/ week, 7-8	21.6	39.6	62	99.5	35	60	5	18
	61, F	T8–10 SCI	14 days post onset	3-4 times/ week, 7-8	21.6	60.7	52	97.3	60	80	4	13
Grasmücke et al., 2017 [8]	44.3 ± 13.9, M 43; F 12	C2–L4 SCI	6.9 (1–22) years posttrauma—12 weeks	5 times/ week, 60	70.45 ± 61.5 (sec)	35.22 ± 30.8	N/A	N/A	N/A	N/A	9.35 ± 5.12	11.04 ± 4.52
Jansen et al., 2017 [13]	48 ± 9.4, M 6; F 2	T8–L2 SCI	8.1 (1–19) years posttrauma—12 weeks	5 times/ week, 51.75 ± 5.6	0.28 ± 0.10 (m/sec)	0.5 ± 0.12	41.85 ± 9.45	56.7 ± 9.9	N/A	N/A	10 ± 1.5	11.13 ± 1.3
	Subgroup 1: $n = 4$	T8–L2 SCI	Plus 40 weeks (at 52 weeks)	3–5 times/ week, 126.8 ± 7.9	28.61 ± 6.9 (sec)	21.22 ± 6.6	49.71 ± 8.8	72.16 ± 6.9	N/A	N/A	No patient improved or worsened	
	Subgroup 2: $n = 4$	T8–L2 SCI	Plus 40 weeks (at 52 weeks)	Once/ week, 32.3 ± 3.3	34.28 ± 18.2 (sec)	34.61 ± 17.3	63.65 ± 18.7	62 ± 18.8	N/A	N/A	No patient improved or worsened	
Jansen et al., 2018 [14]	44.8 ± 13.8, M 15; F 6	C4–L3 SCI	6.5 (1–19) years posttrauma—12 weeks	5 times/ week, 60	61.17 ± 44.27 (sec)	32.18 ± 25.53	30.9 ± 8.71 (number of steps)	20.7 ± 5.51	N/A	N/A	10.7 ± 4.95	11.7 ± 4.5

M = male; F = female; 10MWT = 10-m walking test; BI = Barthel Index; WISCI II = the walking index for spinal cord injury; POD = postoperative day; Pre = before training; Post = after training; N/A = not available; OPLL = ossification of the posterior longitudinal ligament; OLF = ossification of ligamentum flavum; SDAVF = spinal dural arteriovenous fistula; SCI = spinal cord injury. *Estimated from the presented figure in the paper.

(biofeedback); in turn, the activated CNS enhances its descending signals [2]. Therefore, the spasticity could be ameliorated by HAL therapy. Furthermore, a previous study showed that HAL was effective for treating spastic hemiplegia due to stroke [16], and two studies have shown that HAL treatment for stroke patients facilitated cortical activities in the damaged brain [16, 17].

In this study, significant improvements were seen in gait ability following robotic rehabilitation. The results showed improvements in a series of clinical scales such as 10MWT, BI, GARS-M, and WISCI II. All participants showed improvements in gait ability that were similar to those of previous reports concerning the use of HAL for spine disorders such as SCI [8–14], SDAVF [41], and OPLL [18–22, 26]. It is noteworthy that participants in our study underwent surgery for various reasons such as spinal cord tumor, vascular disease, and bone degenerative disease. Additionally, clinical manifestations of vascular disease and tumors in the spine are similar [27, 28], and rehabilitation outcomes following vascular-related and traumatic SCI were reportedly not significantly different [29]. These facts may indicate that HAL therapy may be applied for a variety of disorders with spinal cord origins.

This study also showed the usefulness of HAL for postoperative rehabilitation. There have been only five case reports of HAL-assisted rehabilitation for a patient who underwent surgery for thoracic OPLL [18–22]. It is advantageous that HAL does not interfere with the skin incision and can be used for patients with a corset. In our experience, HAL was considered to facilitate early recovery after spine surgery.

In this study, HAL treatment was performed for patients with rare spinal diseases. In previous studies, the diagnosis and surgical management were emphasized rather than the rehabilitation programs, even though it has been considered that improvement after surgery depends on the length of time and initiation of neurological rehabilitation [30]. However, outcome measures have not been standardized. Previous reports showing the clinical outcomes of treatment for the same spine disorders are summarized in Table 2 [30–40].

We also reviewed clinical studies of gait training using HAL for spine disorders. A systematic search of the literature was conducted using the PubMed database. Search terms were "HAL" OR "Hybrid Assistive Limb" AND "Spinal Cord Injury" OR "OPLL." We searched Google Scholar, and only one work [19] was included from that search. Studies only reporting HAL for gait training were included. Of 20 literatures, six were excluded due to the difference in the type of HAL robot. Overall, 14 studies met the inclusion criteria and were subject to critical review (Table 3) [8–14, 18–22, 26, 41].

Results of the systematic review revealed that HAL treatment was performed mainly for spinal cord injury and degenerative disease at various stages of disorders. Overall, these previous reports [12, 13, 19–22, 41] showed that both the speed and cadence were increased compared with our results. We considered the difference in the change in the gait speed. Previous reports [12, 13, 19–22, 41] indicated that more steps increased the cadence, whereas our results indicated that long steps decreased the cadence. Although natural recovery in the acute state following injury or surgical intervention has to be taken into account, it was thought that the functional recovery rate could be facilitated by HAL treatment from an early stage [18–20, 26].

Even though our study showed a significant improvement with HAL treatment, it had several limitations. We investigated a relatively small number of patients with heterogeneous characteristics. Our patients underwent HAL treatment during the early postoperative state, but our cohort did not have a control group. Therefore, it is possible that spontaneous recovery following surgery may have contributed to the postoperative course. However, it should also be noted that our patients experienced earlier recovery than those described in previous reports [18–20, 26] because our patients started HAL therapy during relatively early postoperative periods.

5. Conclusions

We showed the feasibility and safety of HAL treatment and determined that it could potentially facilitate functional recovery, even for postoperative patients. Further studies involving more patients and a control group are warranted to verify our findings.

Data Availability

The data used to support the findings of this study are available from the corresponding author upon request.

Conflicts of Interest

The authors declare that they have no conflicts of interest.

Acknowledgments

This study was partly supported by the Japan Society for the Promotion of Science grant-in-aid for young scientists ((B) 15 K19984); Takeda Science Foundation, Uehara Memorial Foundation; and Central Research Institute, Fukuoka University (Grant no. 161042). The authors appreciate the help of Ms. Asuka Ikezaki, who assisted with the statistical analysis.

References

[1] K. Suzuki, G. Mito, H. Kawamoto, Y. Hasegawa, and Y. Sankai, "Intention-based walking support for paraplegia patients with robot suit HAL," *Advanced Robotics*, vol. 21, no. 12, pp. 1441–1469, 2007.

[2] T. Morishita and T. Inoue, "Interactive bio-feedback therapy using hybrid assistive limbs for motor recovery after stroke: current practice and future perspectives," *Neurologia Medico-Chirurgica*, vol. 56, no. 10, pp. 605–612, 2016.

[3] H. Kawamoto, S. Taal, H. Niniss et al., "Voluntary motion support control of robot suit HAL triggered by bioelectrical signal for hemiplegia," in *2010 Annual International Conference of the IEEE Engineering in Medicine and Biology*, pp. 462–466, Buenos Aires, Argentina, 2010.

[4] T. Ueba, O. Hamada, T. Ogata, T. Inoue, E. Shiota, and Y. Sankai, “Feasibility and safety of acute phase rehabilitation after stroke using the Hybrid Assistive Limb robot suit,” *Neurologia Medico-Chirurgica*, vol. 53, no. 5, pp. 287–290, 2013.

[5] H. Fukuda, T. Morishita, T. Ogata et al., “Tailor-made rehabilitation approach using multiple types of Hybrid Assistive Limb robots for acute stroke patients: a pilot study,” *Assistive Technology*, vol. 28, no. 1, pp. 53–56, 2016.

[6] H. Fukuda, K. Samura, O. Hamada et al., “Effectiveness of acute phase Hybrid Assistive Limb rehabilitation in stroke patients classified by paralysis severity,” *Neurologia Medico-Chirurgica*, vol. 55, no. 6, pp. 487–492, 2015.

[7] T. Ogata, H. Abe, K. Samura et al., “Hybrid Assistive Limb (HAL) rehabilitation in patients with acute hemorrhagic stroke,” *Neurologia Medico-Chirurgica*, vol. 55, no. 12, pp. 901–906, 2015.

[8] D. Grasmücke, A. Zieriacks, O. Jansen et al., “Against the odds: what to expect in rehabilitation of chronic spinal cord injury with a neurologically controlled Hybrid Assistive Limb exoskeleton. A subgroup analysis of 55 patients according to age and lesion level,” *Neurosurgical Focus*, vol. 42, no. 5, p. E15, 2017.

[9] M. Aach, O. Cruciger, M. Sczesny-Kaiser et al., “Voluntary driven exoskeleton as a new tool for rehabilitation in chronic spinal cord injury: a pilot study,” *The Spine Journal*, vol. 14, no. 12, pp. 2847–2853, 2014.

[10] O. Cruciger, T. A. Schildhauer, R. C. Meindl et al., “Impact of locomotion training with a neurologic controlled Hybrid Assistive Limb (HAL) exoskeleton on neuropathic pain and health related quality of life (HRQoL) in chronic SCI: a case study,” *Disability and Rehabilitation. Assistive Technology*, vol. 11, no. 6, pp. 529–534, 2016.

[11] M. Sczesny-Kaiser, O. Hoffken, M. Aach et al., “HAL® exoskeleton training improves walking parameters and normalizes cortical excitability in primary somatosensory cortex in spinal cord injury patients,” *Journal of Neuroengineering and Rehabilitation*, vol. 12, no. 1, p. 68, 2015.

[12] H. Watanabe, A. Marushima, H. Kawamoto et al., “Intensive gait treatment using a robot suit Hybrid Assistive Limb in acute spinal cord infarction: report of two cases,” *The Journal of Spinal Cord Medicine*, pp. 1–7, 2017.

[13] O. Jansen, T. A. Schildhauer, R. C. Meindl et al., “Functional outcome of neurologic-controlled HAL-exoskeletal neurorehabilitation in chronic spinal cord injury: a pilot with one year treatment and variable treatment frequency,” *Global Spine Journal*, vol. 7, no. 8, pp. 735–743, 2017.

[14] O. Jansen, D. Grasmuecke, R. C. Meindl et al., “Hybrid Assistive Limb exoskeleton HAL in the rehabilitation of chronic spinal cord injury: proof of concept; the results in 21 patients,” *World Neurosurgery*, vol. 110, pp. e73–e78, 2018.

[15] K. Goto, T. Morishita, S. Kamada et al., “Feasibility of rehabilitation using the single-joint Hybrid Assistive Limb to facilitate early recovery following total knee arthroplasty: a pilot study,” *Assistive Technology*, vol. 29, no. 4, pp. 197–201, 2016.

[16] K. Saita, T. Morishita, K. Hyakutake et al., “Combined therapy using botulinum toxin A and single-joint Hybrid Assistive Limb for upper-limb disability due to spastic hemiplegia,” *Journal of the Neurological Sciences*, vol. 373, pp. 182–187, 2017.

[17] K. Saita, T. Morishita, H. Arima et al., “Biofeedback effect of Hybrid Assistive Limb in stroke rehabilitation: a proof of concept study using functional near infrared spectroscopy,” *PLoS One*, vol. 13, no. 1, article e0191361, 2018.

[18] H. Sakakima, K. Ijiri, F. Matsuda et al., “A newly developed robot suit Hybrid Assistive Limb facilitated walking rehabilitation after spinal surgery for thoracic ossification of the posterior longitudinal ligament: a case report,” *Case Reports in Orthopedics*, vol. 2013, Article ID 621405, 4 pages, 2013.

[19] S. Kubota, T. Abe, K. Fujii et al., “Improvement of walking ability using Hybrid Assistive Limb training in a patient with severe thoracic myelopathy caused by ossification of the posterior longitudinal ligament - a case report,” *Journal of Spine*, vol. 1, Supplement 7, 2016.

[20] K. Fujii, T. Abe, S. Kubota et al., “The voluntary driven exoskeleton Hybrid Assistive Limb (HAL) for postoperative training of thoracic ossification of the posterior longitudinal ligament: a case report,” *The Journal of Spinal Cord Medicine*, vol. 40, no. 3, pp. 361–367, 2017.

[21] S. Kubota, T. Abe, H. Kadone et al., “Walking ability following Hybrid Assistive Limb treatment for a patient with chronic myelopathy after surgery for cervical ossification of the posterior longitudinal ligament,” *The Journal of Spinal Cord Medicine*, pp. 1–9, 2017.

[22] M. Taketomi, Y. Shimizu, H. Kadone et al., “Hybrid Assistive Limb intervention in a patient with late neurological deterioration after thoracic myelopathy surgery due to ossification of the ligamentum flavum,” *Case Reports in Orthopedics*, vol. 2018, Article ID 6171760, 10 pages, 2018.

[23] J. M. VanSwearingen, K. A. Paschal, P. Bonino, and J. F. Yang, “The modified Gait Abnormality Rating Scale for recognizing the risk of recurrent falls in community-dwelling elderly adults,” *Physical Therapy*, vol. 76, no. 9, pp. 994–1002, 1996.

[24] P. L. Dittuno and J. F. Dittuno Jr, “Walking index for spinal cord injury (WISCI II): scale revision,” *Spinal Cord*, vol. 39, no. 12, pp. 654–656, 2001.

[25] V. Dietz, “Proprioception and locomotor disorders,” *Nature Reviews Neuroscience*, vol. 3, no. 10, pp. 781–790, 2002.

[26] S. Puentes, H. Kadone, S. Kubota et al., “Reshaping of gait coordination by robotic intervention in myelopathy patients after surgery,” *Frontiers in Neuroscience*, vol. 12, p. 99, 2018.

[27] K. Jellema, C. C. Tijssen, and J. van Gijn, “Spinal dural arteriovenous fistulas: a congestive myelopathy that initially mimics a peripheral nerve disorder,” *Brain*, vol. 129, no. 12, pp. 3150–3164, 2006.

[28] F. J. Rodriguez, B. A. Crum, W. E. Krauss, B. W. Scheithauer, and C. Giannini, “Venous congestive myelopathy: a mimic of neoplasia,” *Modern Pathology*, vol. 18, no. 5, pp. 710–718, 2005.

[29] W. McKinley, A. Sinha, J. Ketchum, and X. Deng, “Comparison of rehabilitation outcomes following vascular-related and traumatic spinal cord injury,” *The Journal of Spinal Cord Medicine*, vol. 34, no. 4, pp. 410–415, 2011.

[30] S. Behrens and A. Thron, “Long-term follow-up and outcome in patients treated for spinal dural arteriovenous fistula,” *Journal of Neurology*, vol. 246, no. 3, pp. 181–185, 1999.

[31] A. E. Bond, G. Zada, I. Bowen, J. G. McComb, and M. D. Krieger, “Spinal arachnoid cysts in the pediatric population: report of 31 cases and a review of the literature,” *Journal of Neurosurgery. Pediatrics*, vol. 9, no. 4, pp. 432–441, 2012.

[32] J. M. C. Van Dijk, K. G. TerBrugge, R. A. Willinsky, R. I. Farb, and M. C. Wallace, “Multidisciplinary management of spinal dural arteriovenous fistulas: clinical presentation and long-

term follow-up in 49 patients," *Stroke*, vol. 33, no. 6, pp. 1578–1583, 2002.

[33] K. Onari, N. Akiyama, S. Kondo, A. Toguchi, H. Mihara, and T. Tsuchiya, "Long-term follow-up results of anterior interbody fusion applied for cervical myelopathy due to ossification of the posterior longitudinal ligament," *Spine*, vol. 26, no. 5, pp. 488–493, 2001.

[34] M. Iwasaki, Y. Kawaguchi, T. Kimura, and K. Yonenobu, "Long-term results of expansive laminoplasty for ossification of the posterior longitudinal ligament of the cervical spine: more than 10 years follow up," *Journal of Neurosurgery: Spine*, vol. 96, no. 2, pp. 180–189, 2002.

[35] M. Lee, A. R. Rezai, R. Abbott, D. H. Coelho, and F. J. Epstein, "Intramedullary spinal cord lipomas," *Journal of Neurosurgery*, vol. 82, no. 3, pp. 394–400, 1995.

[36] M. Y. Wang, S. Shah, and B. A. Green, "Clinical outcomes following cervical laminoplasty for 204 patients with cervical spondylotic myelopathy," *Surgical Neurology*, vol. 62, no. 6, pp. 487–492, 2004.

[37] A. Singh, D. Choi, and A. Crockard, "Use of walking data in assessing operative results for cervical spondylotic myelopathy: long-term follow-up and comparison with controls," *Spine*, vol. 34, no. 12, pp. 1296–1300, 2009.

[38] Z. Kadaňka, J. Bednarik, O. Novotny, I. Urbanek, and L. Dusek, "Cervical spondylotic myelopathy: conservative versus surgical treatment after 10 years," *European Spine Journal*, vol. 20, no. 9, pp. 1533–1538, 2011.

[39] D. Li, S. Y. Hao, Z. Wu, G. J. Jia, L. W. Zhang, and J. T. Zhang, "Intramedullary medullocervical ependymoma–surgical treatment, functional recovery, and long-term outcome," *Neurologia Medico-Chirurgica*, vol. 53, no. 10, pp. 663–675, 2013.

[40] T. Kaner, M. Sasani, T. Oktenoglu, B. Solmaz, A. C. Sarloglu, and A. F. Ozer, "Clinical analysis of 21 cases of spinal cord ependymoma: positive clinical results of gross total resection," *Journal of Korean Neurosurgical Association*, vol. 47, no. 2, pp. 102–106, 2010.

[41] Y. Shimizu, K. Nakai, H. Kadone et al., "The Hybrid Assistive Limb® intervention for a postoperative patient with spinal dural arteriovenous fistula and chronic spinal cord injury: a case study," *The Journal of Spinal Cord Medicine*, pp. 1–8, 2017.

Hindawi
Applied Bionics and Biomechanics
Volume 2018, Article ID 9573951, 8 pages
https://doi.org/10.1155/2018/9573951

Research Article

Influence of a Soft Robotic Suit on Metabolic Cost in Long-Distance Level and Inclined Walking

Shanhai Jin ,[1] Shijie Guo ,[2] Hashimoto Kazunobu,[3] Xiaogang Xiong ,[4] and Motoji Yamamoto [5]

[1]*School of Engineering, Yanbian University, Yanji 133002, China*
[2]*School of Mechanical Engineering, Hebei University of Technology, Tianjin 300130, China*
[3]*Ningbo Institute of Intelligent Manufacturing Industry, Ningbo 315400, China*
[4]*School of Mechanical Engineering and Automation, Harbin Institute of Technology Shenzhen Graduate School, Shenzhen 518055, China*
[5]*Faculty of Engineering, Kyushu University, Fukuoka 819-0395, Japan*

Correspondence should be addressed to Motoji Yamamoto; yama@mech.kyushu-u.ac.jp

Received 31 January 2018; Revised 17 April 2018; Accepted 10 May 2018; Published 5 July 2018

Academic Editor: Liwei Shi

Metabolic cost during walking is positively linked to exercise intensity. For a walking assistive device, one of the major aims should be the maximization of wearers' metabolic benefits for different walking situations. Toward this goal, this paper experimentally evaluates the influence of an authors' soft robotic suit, which has been developed to assist hip flexion for energy-efficient walking of elderly persons in daily life activities, on metabolic cost reduction in the long-distance level and inclined walking. Experiment results show that, for a 79-year-old healthy male subject, the robotic suit significantly reduced metabolic cost in the condition of the robotic suit worn and powered on compared with the condition of worn but powered off.

1. Introduction

The proportion of the elderly population is steadily increasing, and the number is estimated to reach almost 22% of the global population in 2050 [1–3]. Many elderly persons suffer walking difficulties because of lower limb skeletal muscle decline caused by aging. As a result, they perform shorter and fewer walking activity, which is positively related to the quality of elderly life, compared with young ones [4]. Such reduced walking activity may result in many psychosocial problems, for example, social isolation, unhappiness, or depression. On the other hand, reduced walking activity, in turn, causes further lower limb skeletal muscle decline. Finally, they may experience a vicious cycle of physical activity reduction and skeletal muscle decline.

To prevent the abovementioned vicious cycle, lower limb exoskeletons have been studied. For example, an exoskeleton for rehabilitating walking function has been produced by Cyberdyne Inc. [5, 6]. As another example, a semiexoskeleton for improving walking ability has been presented by Honda Motor Co. Ltd. [7–9]. Besides these, various lower limb exoskeletons are designed, for example, [10–16]. One major advantage of lower limb exoskeletons is that they are capable of providing sufficiently large assistive force, which may reach several times larger than that produced by human joints [17, 18]. In addition, they can support the full amount or a significant portion of body weight of wearers through rigid frames [19, 20].

However, some challenging problems must be overcome in designing and implementing exoskeletons. (1) Uncomfortable resistive force may be generated between exoskeleton and wearer in the case of axial joint misalignment [21], and thus leading to increased metabolic cost. (2) The motion range of the lower limbs is constrained by rigid frames of the exoskeletons, while conducting daily life activities requires a large motion range [18]. (3) A massive power supply system is required for producing a large assistive force. In addition, the mass attaches an additional payload

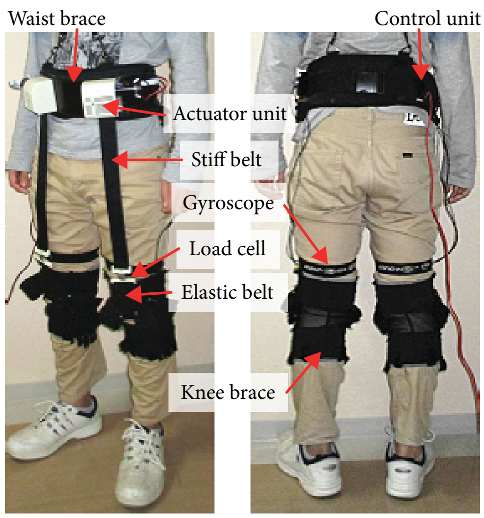

Figure 1: Overall structure of a soft wearable robotic suit.

to the wearer. (4) The procedures of mounting and removing an exoskeleton are complicated. Such problems cannot be ignored in the use of an exoskeleton in daily life activities.

To avoid the drawbacks of exoskeletons, some researchers have researched soft walking assistive devices [22–32]. One of the major advantages of soft robotic suits is that exact matching of device's joints to those of wearer is not required. Besides that, owing to the use of soft materials, they are almost free from kinematic constraints. Additionally, the strength of the provided assistive force is usually less than that of exoskeletons, and thus, the power supply system can be built with smaller size and lighter weight. Moreover, they can realize compatible and safe interactions with wearers [33].

Specifically, the authors' group has developed a soft robotic suit for energy-efficient walking for elderly persons in daily life activities [29–32], as shown in Figure 1. The robotic suit provides a small but effective assistive force for hip flexion via winding belts that contain elastic elements. Moreover, it is lightweight and it almost does not restrict the motion range of the lower limbs. It is reported [29] that, in the case of 6-minute level walking, the use of the robotic suit in the worn and powered on (PON) condition significantly reduced metabolic cost and significantly improved gait characteristics compared with the condition of worn but powered off (POFF).

One of our final goals is to develop a soft robotic suit that reduces metabolic cost as much as possible for elderly persons during walking in daily life, so that they can conduct more physical activities, for example, shopping, taking a walk, and visiting friends living far, for preventing health care. Toward this goal, this paper experimentally evaluates the influence of the soft robotic suit on metabolic cost of walking in an environment that demonstrates the potential use of the robotic suit in real-life situation.

The rest of this paper is organized as follows. Section 2 gives an overview of the authors' soft robotic suit. Section 3 experimentally evaluates the influence of the soft robotic suit on metabolic cost in long-distance level and inclined walking.

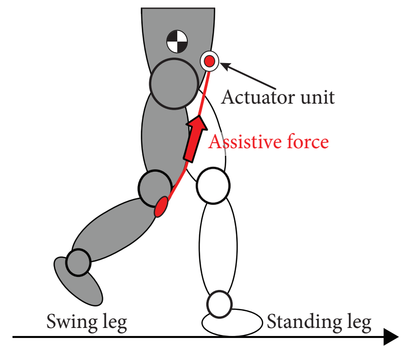

Figure 2: Assistance motion for the swing phase.

Section 4 discusses the experimental results. Section 5 covers conclusions and future work.

2. Overview of a Soft Wearable Robotic Suit

The authors' group has presented a soft wearable robotic suit for energy-efficient walking for elderly persons in daily life activities. Figure 1 illustrates the overall structure of the robotic suit. For each leg, it is composed of one actuator, one control unit, one knee brace, one stiff upper, and one elastic lower belt that are attached to the actuator unit and the knee brace, respectively, one load cell that connects the two belts, and one gyroscope. Here, it should be mentioned that the actuator and the control units, which contain most of the system mass, are mounted to the front and the back of a waist brace, respectively. This is due to the fact that mounting a 4 kg mass to the waist does not significantly increase the metabolic cost, while adding a 4 kg mass to the thigh, shank, or foot expends more metabolic cost compared with the case of waist [34]. The total weight of the robotic suit, excluding the power supply system, is 2.7 kg (the power of the device is externally provided by a DC power source through a cable).

In the robotic suit, undesirable forces generated by disturbances or significant control errors can be absorbed by the elastic elements. Moreover, the robotic suit almost does not restrict the motion range of the lower limbs, and thus wearers can perform a risk-avoiding action in the cases of emergencies. Furthermore, owing to its simple structures, wearers can easily take the robotic suit on and off by themselves.

The soft robotic suit provides a small but effective assistive force for hip flexion in the sagittal plane of walking. Specifically, as illustrated in Figure 2, during the swing phase, the actuator unit winds up the stiff and elastic belts, and the correspondingly produced tension force on the belt is transmitted to the wearer's joints for assisting hip flexion. On the other hand, during the standing phase, the tension force is maintained in a small but sufficient value (0.6 N) that allows the belts "creeping" along the thigh without influencing the extension of the hip.

Figure 3 shows the block diagram of the control system of the soft robotic suit. Hip angular velocity during walking is measured by the gyroscope. Then, it is converted to hip angle by applying numerical integration. It is known that

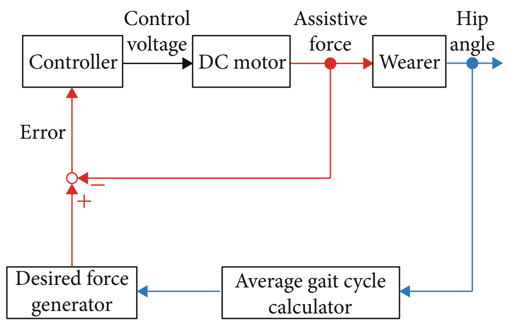

FIGURE 3: Block diagram of a tension force control scheme.

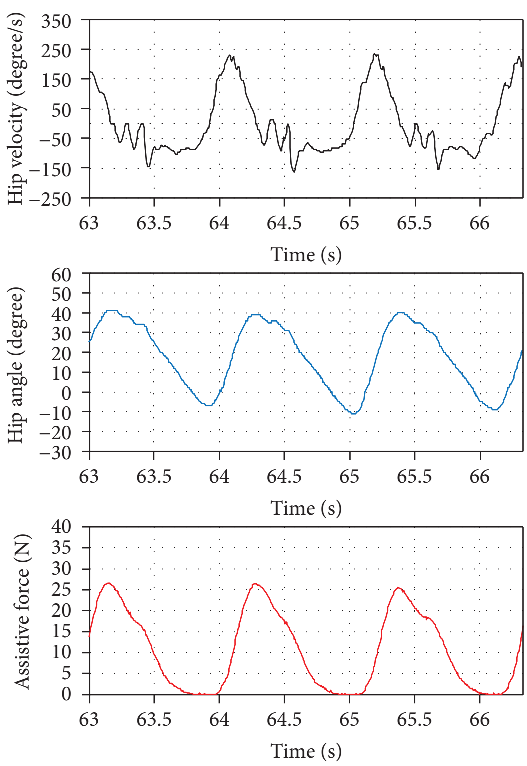

FIGURE 4: Typical data of hip angular velocity, hip angle, and assistive force.

numerical integration of gyroscope velocity signal introduces in angular drift. Toward this problem, a 0-degree angular offset compensation is performed. The timings of minimum hip angle, maximum hip angle and heel contact, and the average gait period are estimated in an average gait cycle calculator, and they are used for generating the desired assistive force profile. A proxy-based sliding mode controller [35], which realizes smooth and safe response [36, 37], is implemented for tracking the desired one with the sampling interval $T = 0.001$ s. Figure 4 shows typical data of measured hip angular velocity, hip angle, and generated assistive force.

3. Experiment

This section experimentally evaluates the influence of the robotic suit on metabolic cost in long-distance level and

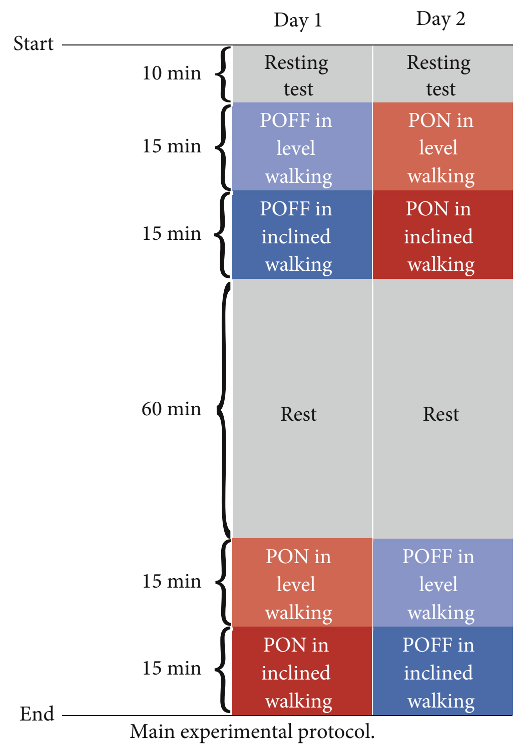

FIGURE 5: Main experimental protocol.

inclined walking. The experiment was approved by the Experiment Ethics Committee of the Faculty of Engineering, Kyushu University.

3.1. Subject. One healthy male elderly subject (age = 79 years, weight = 61.6 kg, and height = 157 cm) participated in the experiment.

3.2. Protocol. Before the main experiment, a preliminary exercise was performed for the subject. First, the subject was instructed to familiarize himself with treadmill walking. Then, his preferred walking speed (2.2 km/h) was evaluated by applying the procedure reported in [38]. After that, the subject practiced the treadmill walking in the PON condition with the maximum assistive force (MAF) 25.3 N that he felt comfortable at the preferred walking speed for getting used to the robotic suit.

The experiment was performed in two days. Figure 5 shows the main experimental protocol. A 30-minute treadmill walking trial at the preferred speed with the POFF condition versus the PON condition constituted one set of the comparative experiment. On each experimental day, one set of comparison was performed. For each trial, firstly the subject conducted a level walking for 15 minutes. After that, the treadmill was inclined to 2% slope by the experimenter, and the subject performed an inclined walking for the left 15 minutes. Specifically, in the case of the PON condition, the same assistive force profile, as illustrated in Figure 4, was applied for both level and inclined walking. A 10-minute resting test was performed for determining the resting metabolic cost. In addition, a 60-minute rest period was provided after trial 1 for both recovering metabolic activity and

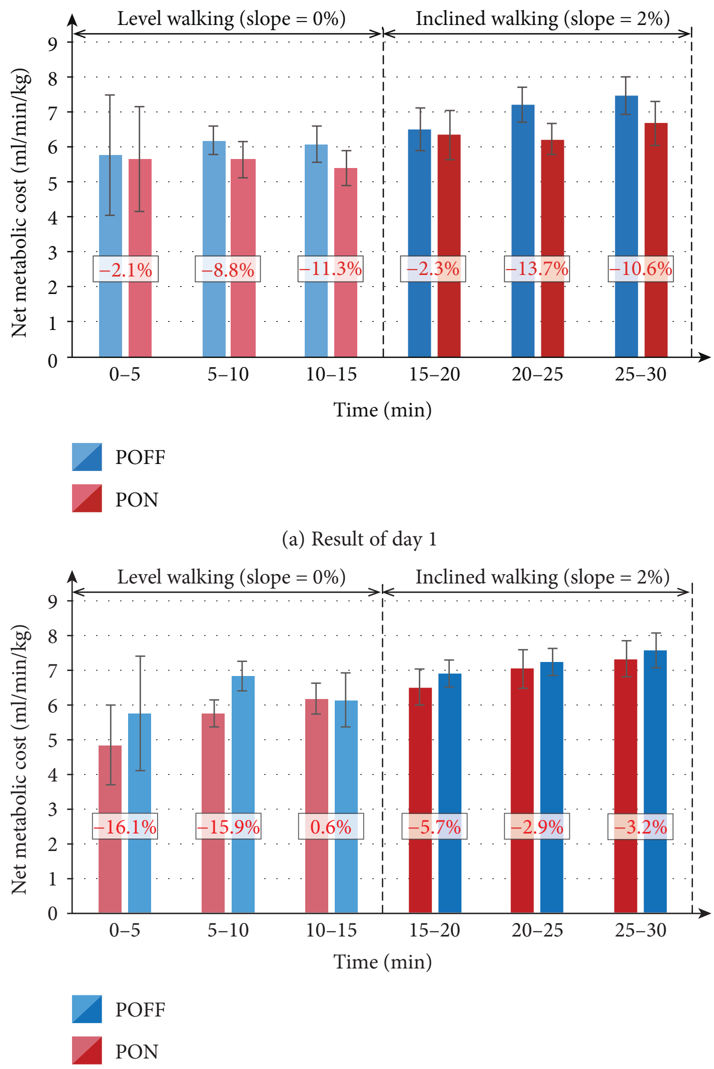

(b) Result of day 2

Figure 6: Comparison of metabolic cost between the POFF condition and the PON condition for 5-minute intervals. On each bar chart, the error bar denotes standard deviation. In addition, the number expressed in percentage represents the difference of the PON condition compared with the POFF condition.

separating of the two trials. To exclude the influence of metabolic and biomechanical variations and measurement errors, reversed orders of the POFF condition and PON condition were used on different days. Here, it should be mentioned that, because the purpose of the experimental protocol was to validate the effectiveness of walking assistance strategy, that is, assistance for hip flexion via winding belts, during long-distance level and inclined walking, and since the actuator unit was not optimized for weight, only the comparison between the POFF condition and the PON condition was considered, excluding the condition of the robotic suit not worn.

Expired gas was collected continuously by a gas analyzer (AT-1100, Anima, Co., Japan) for the entire 30-minute walking.

3.3. Data Analysis. For each day, average values of resting metabolic cost $\dot{V}_{\mathrm{O2(rest)}}$ (ml/min) during the last 5-minute interval of resting test were calculated for determining the resting metabolic level. In addition, for all trials, average values of gross walking metabolic cost $\dot{V}_{\mathrm{O2(gross)}}$ (ml/min) in both 15-minute level walking and 15-minute inclined walking were computed. Moreover, average values of $\dot{V}_{\mathrm{O2(gross)}}$ over the entire 30-minute interval were calculated. Besides that, for each trial, in order to examine the transition of metabolic cost, average values of $\dot{V}_{\mathrm{O2(gross)}}$ per 5-minute interval were computed. Then, average values of net metabolic cost $\dot{V}_{\mathrm{O2(net)}}$ (ml/min) were obtained by subtracting corresponding $\dot{V}_{\mathrm{O2(rest)}}$ from the abovementioned each $\dot{V}_{\mathrm{O2(gross)}}$. After that, $\dot{V}_{\mathrm{O2(net)}}$ was normalized by body weight (kg). The averages of all the trials in each measure were used for the analysis.

3.4. Statistical Analysis. Paired t-tests were performed to identify the significant differences between the POFF

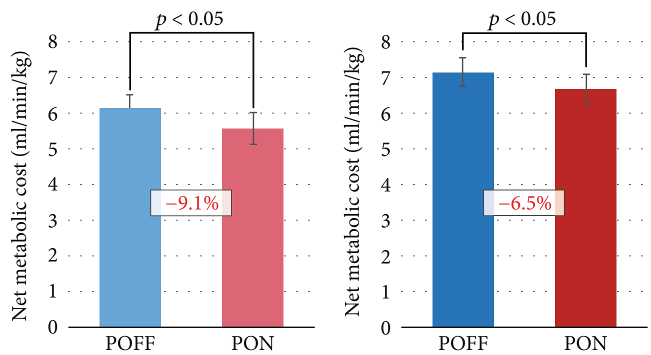

(a) Result of level walking (slope = 0%)

(b) Result of inclined walking (slope = 2%)

FIGURE 7: Comparisons of two-day average value of metabolic cost between the POFF condition and the PON condition for 15-minute level walking and 15-minute inclined walking. On each bar chart, the error bar denotes standard deviation. In addition, the number expressed in percentage represents the difference of the PON condition compared with the POFF condition.

condition and the PON condition in averaged $\dot{V}_{O2(net)}$ of 15-minute level walking, 15-minute inclined walking, and entire 30-minute walking. In addition, standard deviations were computed for each averaged $\dot{V}_{O2(net)}$.

4. Results

Figure 6 shows the metabolic costs achieved in the POFF condition and the PON condition for each 5-minute intervals. Metabolic cost was reduced in the PON condition in eleven of twelve intervals compared with the POFF condition, with a maximum reduction of 16.1%.

Figure 7 compares the two-day average value of metabolic cost between the two conditions in terms of level walking and inclined walking. One can observe that, for both cases, statistically significant differences were found between the two conditions, with averaged 9.1% and 6.5% reductions in the PON condition.

Two-day average value of metabolic cost of entire 30-minute walking was compared in Figure 8. It is shown that the use of the robotic suit significantly reduced metabolic cost by an average of 7.7%.

5. Discussion

One of the final aims of the robotic suit is to reduce metabolic cost as much as possible for elderly persons in daily life activities. As illustrated by the results, metabolic cost of level walking was reduced in the PON condition compared with the POFF condition for almost every 5-minute intervals, with a maximum reduction of 16.1% and an average reduction of 9.1%. This result is consistent with our previous result [29] showing that the use of the robotic suit reduced metabolic cost with an average of 5.9% during 6-minute level walking. However, it is known that metabolic stress of walking increases as walking duration increases [39–42]. Thus, it should be highlighted that, compared with the previous result of 6-minute walking that might be too short for imposing significant metabolic stress

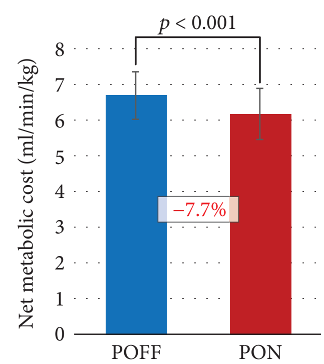

FIGURE 8: Comparison of two-day average value of metabolic cost between the POFF condition and the PON condition for entire 30-minute walking. On each bar chart, the error bar denotes standard deviation. In addition, the number expressed in percentage represents the difference of the PON condition compared with the POFF condition.

on the subject, the reduction of metabolic cost during the 15-minute walking was achieved under the condition of longer continuous accumulation of metabolic stress. The major underlying cause of this reduction was probably owing to the continuous energy injection of the robotic suit for assisting the hip flexion, that is, metabolic cost reduction obtained by mechanical energy injection.

In the case of inclined walking, metabolic cost was higher than the case of level walking for both conditions. This is primarily due to the fact that, in the case of inclined walking, the human body has to be raised against gravity by increasing hip flexion as gradient increases [43–45]. Thus, additional mechanical power might be consumed in the hip joint for increasing the gravitational potential energy of the body's center of mass (COM) compared with the level walking [43, 46, 47]. Besides that, the metabolic stress accumulated through the previous 15-minute level walking was also probably linked to the increased metabolic cost of the inclined walking. However, by comparing the results of the two conditions, one can found that metabolic cost of the PON condition was lower than that of the POFF condition, with a maximum reduction of 13.7% and an average reduction of 6.5%. Toward such a reduction, we assume that the provided hip flexion assistance contributed to the hip flexion strength by compensating the metabolic burden of the hip joint during the inclined walking and consequently led to the reduced metabolic cost of the PON condition.

Interestingly, it should be observed that the metabolic reduction rate of inclined walking was less than that of level walking. From this result, we suppose that, under the same injected power, that is, the same assistive force profile parameters, the injected power during inclined walking was not sufficient for compensating the increased mechanical power required to accelerate COM upward, achieving a similar metabolic reduction as the case of level walking. This finding suggests that, in order to maximize the effectiveness of the robotic suit, optimized assistive force profile parameters, for example, shape, MAF, and timings of start, MAF, and end, should be explored by getting a better understanding of complex human-machine interaction.

As a whole, since metabolic cost is positively related to exercise intensity [48], we argue that the subject probably walked more easily and comfortably in the PON condition with the less metabolic cost during the 30-minute level and inclined walking. Thus, it can be concluded that the robotic suit is effective not only in short-distance level walking as reported in the previous work [29], but also in long-distance level and inclined walking.

6. Conclusions and Future Work

This paper has experimentally evaluated the influence of the authors' soft robotic suit on metabolic cost in 30-minute level and inclined walking. Experimental results show that metabolic cost reduced with a maximum reduction of 16.1% in the PON condition compared with the POFF condition for eleven of twelve 5-minute intervals. In addition, significant metabolic cost reductions of 9.1% and 6.5% were found in the PON condition for level walking and inclined walking, respectively. Moreover, for the entire 30-minute walking, the robotic suit significantly reduced metabolic cost by an average of 7.7%.

One limitation of this study is that, by considering the 2.7 kg mass of the robotic suit additionally imposed to the wearer, the effectiveness of the robotic suit was only compared between the POFF condition and the PON condition. Future study includes optimizations of mechanical structure (including weight reduction), assistive force profile parameters (including shape, MAF, and timings of start, MAF, and end), and design of adaptive control scheme for specific populations and walking environments with the aim of achieving greater metabolic cost reduction and compliant human-machine interaction.

Conflicts of Interest

The authors declare that they have no conflicts of interest.

Acknowledgments

This work was supported by the following grants: Grant-in-Aid for the Adaptable & Seamless Technology Transfer program through Target driven R&D (Grant no. AS2415010K) from Japan Science and Technology Agency (JST), Science & Technology Development Foundation of Jilin Province (Grant no. 20180520019JH), Science & Technology Research Foundation of the Education Department of Jilin Province (Grant no. JJKH20180883KJ), and Shenzhen Peacock Technical Innovation Funding (Grant no. KQJSCX20170726103546683).

References

[1] M. Khazaee-pool, R. Sadeghi, F. Majlessi, and A. Rahimi Foroushani, "Effects of physical exercise programme on happiness among older people," *Journal of Psychiatric and Mental Health Nursing*, vol. 22, no. 1, pp. 47–57, 2015.

[2] United Nations Population Fund, "Aging," 2015, http://www.unfpa.org/ageing.

[3] M. Herrmann, J. M. Guzman, S. Juran, and D. Schensul, "Population dynamics in the least developed countries: challenges and opportunities for development and poverty reduction," 2011, http://www.unfpa.org/publications/populationdynamics-ldcs.

[4] Transportation Research Board National Research Council (US), *Transportation in an Aging Society: Improving Mobility and Safety for Older Persons*, The National Academies Press, Washington, DC, USA, 1988.

[5] H. Kawamoto, T. Hayashi, T. Sakurai, K. Eguchi, and Y. Sankai, "Development of single leg version of HAL for hemiplegia," in *Proceedings of the 31st Annual International Conference of the IEEE Engineering in Medicine and Biology Society*, pp. 5038–5043, Minneapolis, MN, USA, September 2009.

[6] A. Tsukahara, Y. Hasegawa, and Y. Sankai, "Gait support for complete spinal cord injury patient by synchronized leg-swing with HAL," in *Proceedings of 2011 IEEE/RSJ International Conference on Intelligent Robots and Systems*, pp. 1737–1742, San Francisco, CA, USA, September 2011.

[7] K. Yasuhara, K. Shimada, T. Koyama, T. Ido, K. Kikuchi, and Y. Endo, "Walking assist device with stride management assist," *Honda R&D Technical Review*, vol. 21, no. 2, pp. 54–62, 2009.

[8] H. Shimada, T. Hirata, Y. Kimura et al., "Effects of a robotic walking exercise on walking performance in community-dwelling elderly adults," *Geriatrics and Gerontology International*, vol. 9, no. 4, pp. 372–381, 2009.

[9] H. Shimada, T. Suzuki, Y. Kimura et al., "Effects of an automated stride assistance system on walking parameters and muscular glucose metabolism in elderly adults," *British Journal of Sports Medicine*, vol. 42, no. 11, pp. 622–629, 2008.

[10] A. K. Raj, P. D. Neuhaus, A. M. Moucheboeuf, J. H. Noorden, and D. V. Lecoutre, "Mina: a sensorimotor robotic orthosis for mobility assistance," *Journal of Robotics*, vol. 2011, Article ID 284352, 8 pages, 2011.

[11] T. J. Yeh, M. J. Wu, T. J. Lu, F. K. Wu, and C. R. Huang, "Control of McKibben pneumatic muscles for a power-assist, lower-limb orthosis," *Mechatronics*, vol. 20, no. 6, pp. 686–697, 2010.

[12] T. Ikehara, E. Tanaka, K. Nagamura et al., “Development of closed-fitting-type walking assistance device for legs with self-contained control system,” *Journal of Robotics and Mechatronics*, vol. 22, no. 3, pp. 380–390, 2010.

[13] Q. Wu, X. Wang, F. Du, and X. Zhang, “Design and control of a powered hip exoskeleton for walking assistance,” *International Journal of Advanced Robotic Systems*, vol. 12, no. 3, p. 18, 2015.

[14] K. Kong and D. Jeon, “Design and control of an exoskeleton for the elderly and patients,” *IEEE/ASME Transactions on Mechatronics*, vol. 11, no. 4, pp. 428–432, 2006.

[15] S. Hyon, J. Morimoto, T. Matsubara, T. Noda, and M. Kawato, “XoR: hybrid drive exoskeleton robot that can balance,” in *Proceedings of 2011 IEEE/RSJ International Conference on Intelligent Robots and Systems*, pp. 3975–3981, San Francisco, CA, USA, September 2011.

[16] T. Nakamura, K. Saito, Z. Wang, and K. Kosuge, “Realizing model-based wearable antigravity muscles support with dynamics terms,” in *Proceedings of 2005 IEEE/RSJ International Conference on Intelligent Robots and Systems*, pp. 2694–2699, Edmonton, AB, Canada, August 2005.

[17] A. T. Asbeck, S. M. M. de Rossi, I. Galiana, Y. Ding, and C. J. Walsh, “Stronger, smarter, softer: next-generation wearable robots,” *IEEE Robotics & Automation Magazine*, vol. 21, no. 4, pp. 22–33, 2014.

[18] M. Cenciarini and A. Dollar, “Biomechanical considerations in the design of lower limb exoskeletons,” in *Proceedings of IEEE International Conference on Rehabilitation Robotics*, pp. 1–6, Zurich, Switzerland, 2011.

[19] R. Bogue, “Exoskeletons and robotic prosthetics: a review of recent developments,” *Industrial Robot: An International Journal*, vol. 36, no. 5, pp. 421–427, 2009.

[20] K. Low, “Robot-assisted gait rehabilitation: from exoskeletons to gait systems,” in *Proceedings of 2011 Defense Science Research Conference and Expo*, pp. 1–10, Singapore, Singapore, August 2011.

[21] A. Schiele, “Ergonomics of exoskeletons: subjective performance metrics,” in *Proceedings of 2009 IEEE/RSJ International Conference on Intelligent Robots and Systems*, pp. 480–485, St. Louis, MO, USA, October 2009.

[22] Y. Park, B. Chen, D. Young et al., “Bio-inspired active soft orthotic device for ankle foot pathologies,” in *Proceedings of 2011 IEEE/RSJ International Conference on Intelligent Robots and Systems*, pp. 4488–4495, San Francisco, CA, USA, September 2011.

[23] Y. L. Park, B. R. Chen, N. O. Pérez-Arancibia et al., “Design and control of a bio-inspired soft wearable robotic device for ankle-foot rehabilitation,” *Bioinspiration & Biomimetics*, vol. 9, no. 1, article 016007, 2014.

[24] L. Stirling, C. H. Yu, J. Miller et al., “Applicability of shape memory alloy wire for an active, soft orthotic,” *Journal of Materials Engineering and Performance*, vol. 20, no. 4-5, pp. 658–662, 2011.

[25] A. T. Asbeck, S. M. M. de Rossi, K. G. Holt, and C. J. Walsh, “A biologically inspired soft exosuit for walking assistance,” *The International Journal of Robotics Research*, vol. 34, no. 6, pp. 744–762, 2015.

[26] A. Asbeck, K. Schmidt, I. Galiana, D. Wagner, and C. Walsh, “Multi-joint soft exosuit for gait assistance,” in *Proceedings of 2015 IEEE International Conference on Robotics and Automation*, pp. 6197–6204, Seattle, WA, USA, May 2015.

[27] Y. Ding, I. Galiana, A. T. Asbeck et al., “Biomechanical and physiological evaluation of multi-joint assistance with soft exosuits,” *IEEE Transactions on Neural Systems and Rehabilitation Engineering*, vol. 25, no. 2, pp. 119–130, 2017.

[28] Y. Li and M. Hashimoto, “PVC gel soft actuator-based wearable assist wear for hip joint support during walking,” *Smart Materials and Structures*, vol. 26, no. 12, article 125003, 2017.

[29] S. Jin, N. Iwamoto, K. Hashimoto, and M. Yamamoto, “Experimental evaluation of energy efficiency for a soft wearable robotic suit,” *IEEE Transactions on Neural Systems and Rehabilitation Engineering*, vol. 25, no. 8, pp. 1192–1201, 2017.

[30] S. Jin, S. Guo, K. Hashimoto, and M. Yamamoto, “Effects of a soft wearable robotic suit on metabolic cost and gait characteristics in healthy young subjects,” in *Proceedings of the 17th International Conference on Control, Automation and Systems*, pp. 680–684, Jeju, South Korea, October 2017.

[31] S. Jin, S. Guo, K. Hashimoto, and M. Yamamoto, “Evaluation of long-term effect on gait improvement for a soft robotic suit,” in *Proceedings of 2017 IEEE International Conference on Robotics and Biomimetics*, pp. 1654–1658, Macau, China, December 2017.

[32] S. Jin, S. Guo, K. Hashimoto, and M. Yamamoto, “Influence of maximum assistive force of a soft wearable robotic suit on metabolic cost reduction,” in *Proceedings of the 8th IEEE International Conference on Cybernetics and Intelligent Systems and the 8th IEEE International Conference on Robotics, Automation and Mechatronics*, pp. 146–150, Ningbo, China, November 2017.

[33] C. Majidi, “Soft robotics: a perspective–current trends and prospects for the future,” *Soft Robotics*, vol. 1, no. 1, pp. 5–11, 2014.

[34] R. C. Browning, J. R. Modica, R. Kram, and A. Goswami, “The effects of adding mass to the legs on the energetics and biomechanics of walking,” *Medicine & Science in Sports & Exercise*, vol. 39, no. 3, pp. 515–525, 2007.

[35] R. Kikuuwe, S. Yasukouchi, H. Fujimoto, and M. Yamamoto, “Proxy-based sliding mode control: a safer extension of PID position control,” *IEEE Transactions on Robotics*, vol. 26, no. 4, pp. 670–683, 2010.

[36] K. Knaepen, P. Beyl, S. Duerinck, F. Hagman, D. Lefeber, and R. Meeusen, “Human-robot interaction: kinematics and muscle activity inside a powered compliant knee exoskeleton,” *IEEE Transactions on Neural Systems and Rehabilitation Engineering*, vol. 22, no. 6, pp. 1128–1137, 2014.

[37] G. Chen, Z. Zhou, B. Vanderborght, N. Wang, and Q. Wang, “Proxy-based sliding mode control of a robotic ankle-foot system for post-stroke rehabilitation,” *Advanced Robotics*, vol. 30, no. 15, article 9921003, pp. 992–1003, 2016.

[38] K. G. Holt, J. Hamill, and R. O. Andres, “Predicting the minimal energy costs of human walking,” *Medicine & Science in Sports & Exercise*, vol. 23, no. 4, article 491498, 1991.

[39] N. Felsing, J. Brasel, and D. Cooper, “Effect of low and high intensity exercise on circulating growth hormone in men,” *The Journal of Clinical Endocrinology & Metabolism*, vol. 75, no. 1, pp. 157–162, 1992.

[40] F. Grego, J. M. Vallier, M. Collardeau et al., “Effects of long duration exercise on cognitive function, blood glucose, and counterregulatory hormones in male cyclists,” *Neuroscience Letters*, vol. 364, no. 2, pp. 76–80, 2004.

[41] J. Brisswalter, B. Fougeron, and P. Legros, "Effect of three hours race walk on energy cost, cardiorespiratory parameters and stride duration in elite race walkers," *International Journal of Sports Medicine*, vol. 17, no. 03, pp. 182–186, 1996.

[42] A. M. Swartz, L. Squires, and S. J. Strath, "Energy expenditure of interruptions to sedentary behavior," *International Journal of Behavioral Nutrition and Physical Activity*, vol. 8, no. 1, p. 69, 2011.

[43] G. S. Sawicki and D. P. Ferris, "Mechanics and energetics of incline walking with robotic ankle exoskeletons," *Journal of Experimental Biology*, vol. 212, no. 1, pp. 32–41, 2008.

[44] A. Leroux, J. Fung, and H. Barbeau, "Adaptation of the walking pattern to uphill walking in normal and spinal-cord injured subjects," *Experimental Brain Research*, vol. 126, no. 3, pp. 359–368, 1999.

[45] S. D. Prentice, E. N. Hasler, J. J. Groves, and J. S. Frank, "Locomotor adaptations for changes in the slope of the walking surface," *Gait & Posture*, vol. 20, no. 3, pp. 255–265, 2004.

[46] R. Margaria, "Positive and negative work performances and their efficiencies in human locomotion," *Internationale Zeitschrift für angewandte Physiologie einschließlich Arbeitsphysiologie*, vol. 25, no. 4, pp. 339–351, 1968.

[47] A. N. Lay, C. J. Hass, T. Richard Nichols, and R. J. Gregor, "The effects of sloped surfaces on locomotion: an electromyographic analysis," *Journal of Biomechanics*, vol. 40, no. 6, pp. 1276–1285, 2007.

[48] T. Roberts, J. Weber, H. Hoppeler, E. Weibel, and C. Taylor, "Design of the oxygen and substrate pathways. II. Defining the upper limits of carbohydrate and fat oxidation," *The Journal of Experimental Biology*, vol. 199, no. 8, pp. 1651–1658, 1996.

Hindawi
Applied Bionics and Biomechanics
Volume 2018, Article ID 3158439, 13 pages
https://doi.org/10.1155/2018/3158439

Research Article

Pathological Voice Source Analysis System Using a Flow Waveform-Matched Biomechanical Model

Xiaojun Zhang,[1,2] Lingling Gu,[2] Wei Wei,[2] Di Wu,[2] Zhi Tao,[1,2] and Heming Zhao[1]

[1]*School of Electronic and Information Engineering, Soochow University, Suzhou 215000, China*
[2]*College of Physics, Optoelectronics and Energy, Soochow University, Suzhou 215000, China*

Correspondence should be addressed to Wei Wei; weiwei0728@suda.edu.cn and Zhi Tao; taoz@suda.edu.cn

Received 30 March 2018; Accepted 24 May 2018; Published 2 July 2018

Academic Editor: Liwei Shi

Voice production occurs through vocal cord and vibration coupled to glottal airflow. Vocal cord lesions affect the vocal system and lead to voice disorders. In this paper, a pathological voice source analysis system is designed. This study integrates nonlinear dynamics with an optimized asymmetric two-mass model to explore nonlinear characteristics of vocal cord vibration, and changes in acoustic parameters, such as fundamental frequency, caused by distinct subglottal pressure and varying degrees of vocal cord paralysis are analyzed. Various samples of sustained vowel /a/ of normal and pathological voices were extracted from MEEI (Massachusetts Eye and Ear Infirmary) database. A fitting procedure combining genetic particle swarm optimization and a quasi-Newton method was developed to optimize the biomechanical model parameters and match the targeted voice source. Experimental results validate the applicability of the proposed model to reproduce vocal cord vibration with high accuracy, and show that paralyzed vocal cord increases the model coupling stiffness.

1. Introduction

Vocal cord vibration interrupts the straight airflow expelled by the lungs into a series of pulses that act as the excitation source for voice and sound. Denervation or organic diseases of vocal cords, such as paralysis and polyps, can cause irregular vibration with consequential changes, manifested as breathy or hoarse voice. These diseases generally affect one side of vocal structure, causing significant imbalance in bilateral vocal cord tension [1, 2]. Irregular vibration of the vocal cords corresponding to a variety of voice disorders can be observed with electronic laryngoscope to assist diagnosing vocal cord disease. However, laryngoscopy examination is invasive, and the outcomes are relatively subjective. Acoustic analysis can complement and in some cases replace the other invasive methods, which based on direct vocal fold observation [3, 4].

Clinical diagnosis and pathological voice classification using objective methods is an important issue in medical evaluation. Previous studies have mainly combined acoustic parameters with pattern recognition algorithms to assist diagnosis of pathological voice [5, 6]. However, the selected voice signal parameters are not directly linked with the actual physical structure, and vocal structural changes that cause vocal voice disorders require further study.

Nonlinear dynamics theory has provided a new avenue for dynamical system related research, for example, methods combining nonlinear theory with spectral analysis have been successfully applied to EEG and ECG signal analysis. It has also been extended to study voice signals [7, 8].

Nonlinearity inherent in the vocal system can cause irregular voice behavior, as indicated by harmonics, bifurcation, and low-dimensional chaos in high-speed recording of vocal cord vibration signals [9, 10]. The degree of pathological vocal fold is closely related to the nonlinear vibration of the vocal cords. [11]. Therefore, traditional analysis of acoustic parameters may not be accurate, but nonlinear dynamics theory has been shown to have good applicability in characterizing such signals [12]. Time frequency shape analysis based on embedding phase space plots and nonlinear dynamics methods can be used to evaluate the vocal fold dynamics during phonation [13]. Nonlinear models can also simulate various vocal sound phenomena and have been used for dynamic prediction of disordered speech associated with larynx pathology [14–16]. Many physical modeling methods for glottal excitation have been proposed, and the corresponding model parameters have been utilized to study various voice disorders. The two-mass (IF) model is the most well-known classical physical model of the vocal cords, first proposed by Ishizaka and Flanagan and simplified by Steinecke and Herzel (SH model), to study vibration characteristics of the vocal cords. Xue combined the work of Steinecke and Herzel with Navier-Stokes equations and analyzed irregular vibrations caused by tension imbalance in bilateral vocal cord, as well as sound effects [17]. Recently, Sommer modified the asymmetric vocal contact force of the SH model based on Newton's third law [18]. However, a comprehensive nonlinear analysis for the modified SH model remains incomplete.

Although physical modeling has enormous potential in speech synthesis and voice analysis, the large number of model parameters and the complexity of model optimization to match observational data have prevented its practical application [19]. Döllinger used the Nelder–Mead algorithm to minimize the error between experimental curves obtained from high-speed glottography sequences and curves generated with the two-mass model (2MM) [20]. However, this is an invasive method because an endoscope is required to record vocal cord vibrations during phonation. Gómez computed biomechanical parameters based on the power spectral density of the glottal source to improve detection of voice pathology [21].

Other researchers have used genetic algorithms to optimize model parameters to match recorded glottal area, trajectory, and glottal volume wave and have shown the possibility of model inversion [22, 23]. Tao extracted the physiologically relevant parameters of the vocal fold model from high-speed video image series [24].

The complex optimization process and large number of parameters mean the matching result can be unstable. Thus, finding the important tuning parameters and selecting appropriate optimization algorithms are still important issues to be resolved for physical modeling applications, and simulations for asymmetric vocal cords also require further study.

This paper designed a pathological voice source analysis system using an optimized model to study the dynamics of asymmetric vocal cords. Incorporating spectral analysis, and bifurcation and phase diagrams, this paper investigates the impact of structural change of the vocal cord on its vibration and fundamental frequency. Sound effects due to lung pressure are also studied. An optimized SH model combined with particle swarm and quasi-Newton methods (GPSO-QN) is proposed to determine biomechanical model parameters. Parameter adjustments and changing the oscillation mode of the model allow normal and paralyzed voice sources to be simulated. Differences between optimized model parameters are analyzed to assist in identifying the source of vocal paralysis.

2. Method

2.1. Symmetric Vocal Model. Vocal cords are two symmetrical membranous anatomical structures located in the throat. Airflow out of the trachea and lungs continuously impacts the vocal cords and causes vibration. The vibration behavior modulates the airflow to generate glottal pulses [25]. Based on the elastic and dynamic properties of the vocal cords, each fold is represented by two coupled oscillators with two masses, three springs, and two dampers, where the quality of the mass and spring constants denote vocal quality and tension, respectively. Figure 1 shows the simplified two-mass (SH) model, which can be expressed as

$$\begin{aligned}
\dot{x}_{1\alpha} &= v_{1\alpha},\\
\dot{v}_{1\alpha} &= -\frac{1}{m_{1\alpha}}\left(F_{1\alpha} + I_{1\alpha} - r_{1\alpha}v_{1\alpha} - k_{1\alpha}x_{1\alpha} - k_{c\alpha}(x_{1\alpha} - x_{2\alpha})\right),\\
\dot{x}_{2\alpha} &= v_{2\alpha},\\
\dot{v}_{2\alpha} &= -\frac{1}{m_{2\alpha}}\left(I_{2\alpha} - r_{2\alpha}v_{2\alpha} - k_{2\alpha}x_{2\alpha} - k_{2\alpha}(x_{2\alpha} - x_{1\alpha})\right),
\end{aligned} \tag{1}$$

where

$$\begin{aligned}
F_{1\alpha} &= \frac{LdP_1}{m_{1\alpha}},\\
I_{i\alpha} &= -\Theta(-a_i)\frac{c_{i\alpha}}{m_{i\alpha}}\frac{a_i}{2L},\\
\Theta(x) &= \begin{cases} 1, x > 0 \\ 0, x < 0, \end{cases}\\
a_i &= a_{0i} + L(x_{il} + x_{ir}),\\
a_{\min} &= \min\left(a_1, a_2\right),
\end{aligned} \tag{2}$$

index $i = 1, 2$ denotes the upper and lower mass, respectively; $\alpha = l, r$ denotes the left and right parts, respectively; P_s is the subglottal pressure; $x_{i\alpha}$ and $v_{i\alpha}$ are the displacement and corresponding velocity of the masses, respectively; $m_{i\alpha}$, $k_{i\alpha}$, $k_{c\alpha}$, and $r_{i\alpha}$ represent the mass, spring constant, coupling constant, and damping constant, respectively; L, d, and a_{0i} represent the vocal cord length, thickness of mass $m_{1\alpha}$, and rest area, respectively; $c_{ia} = 3k_{ia}$ is an additional spring constant for handling collision; a_i is the glottal area; F_{1a} and I_{ia} are the Bernoulli force and restoring force due to vocal cord collision, respectively; and P_1 is the pressure on the lower masses.

Using aerodynamic analysis, pressure drops at the glottal entrance and viscous loss within the glottis is ignored.

In contrast to the IF model, Bernoulli flow exists below the narrowest glottis gap only, with a jet region above the contraction where pressure is considered to be constant [26]. From Bernoulli's equation,

$$P_s = P_1 + \frac{\rho}{2}\left(\frac{U_g}{a_1}\right)^2 = P_0 + \frac{\rho}{2}\left(\frac{U_g}{a_{\min}}\right)^2, \tag{3}$$

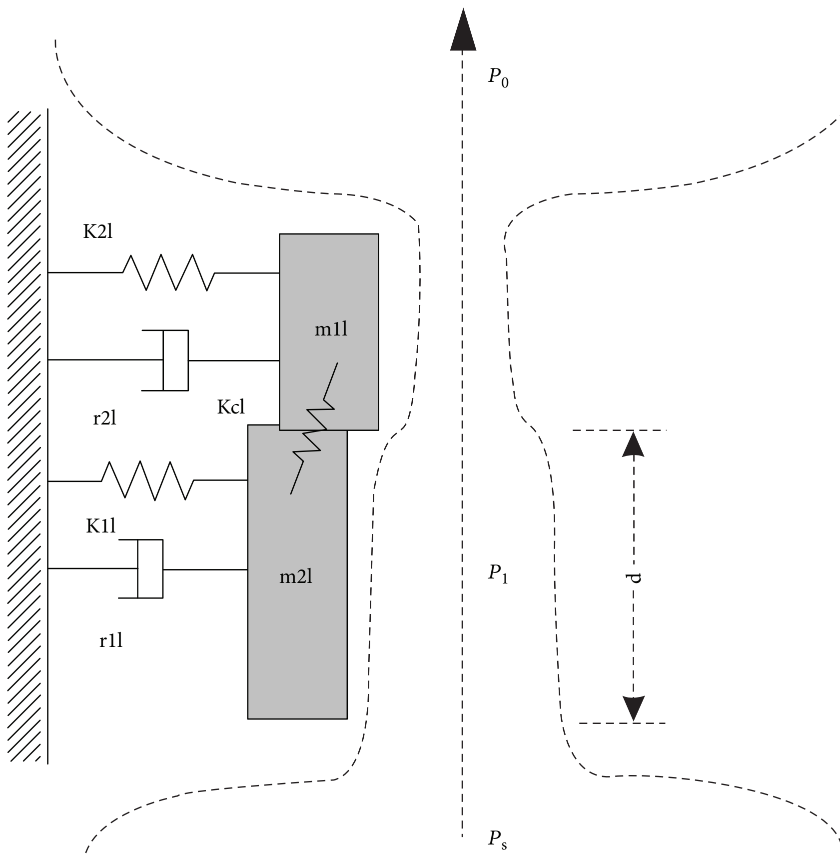

Figure 1: Schematic of the Herzel and Steinecke model.

where P_0 is the supraglottal pressure, U_g is volume flow velocity (glottal waveform), and ρ is air density. We ignore channel coupling, that is, $P_0 = 0$, and consider that Bernoulli pressure exists only when the glottis is open. Therefore,

$$P_1 = P_s\left[1 - \Omega(a_{\min})\left(\frac{a_{\min}}{a_1}\right)^2\right]\Omega(a_1), \quad (4)$$

$$U_g = \sqrt{2P_s/\rho}\,a_{\min}\Theta(a_{\min}), \quad (5)$$

where

$$\Omega(x) = \begin{cases} \tanh\left[50(x/x_0)\right], & x > 0 \\ 0, & x < 0, \end{cases} \quad (6)$$

with the units centimeters, grams, and milliseconds, respectively.

The standard parameters of this model are $m_{1\alpha} = 0.125$, $m_{2\alpha} = 0.025$, $k_{1\alpha} = 0.08$, $k_{2\alpha} = 0.008$, $k_{c\alpha} = 0.025$, $r_{1\alpha} = r_{2\alpha} = 0.02$, $Ps = 0.008$, $d = 0.25$, $a_{01} = a_{02} = 0.05$, and $L = 1.4$. These parameters are used by the symmetric model to simulate vocal cord vibration, solving the differential equations using the standard fourth order Runge-Kutta method with initial conditions $x_{1\alpha}(0) = 0.01$, $x_{2\alpha}(0) = 0.01$, $v_{1\alpha}(0) = 0$, and $v_{2\alpha}(0) = 0$, as shown in Figure 2. Displacement of upper and lower masses and glottal airflow waveforms are cyclical, and a fixed phase difference exists for the displacement waveform (see Figure 2(a)).

2.2. Asymmetric Vocal Cord Model. Vocal polyps and paralysis often occur in one side of the vocal cords. Asymmetric vocal cords cause tension imbalance, and overcritical imbalance may cause irregular vibration. Without loss of generality, we assume the left vocal cord is normal, that is, unchanged parameters, and lesions occur only on the right vocal cord. This imbalance is represented by an asymmetry parameter $\beta (0.4 < \beta \le 1)$, and right vocal parameters can be expressed as

$$\begin{aligned} \tilde{m}_{ir} &= \frac{m_{ir}}{\beta}, \\ \tilde{k}_{ir} &= \beta k_{ir}, \\ \tilde{k}_{cr} &= \beta k_{cr}, \\ \tilde{c}_{ir} &= \beta c_{ir}. \end{aligned} \quad (7)$$

Small β means a high degree of asymmetry and leads to more complex vocal cord vibration. Consequently, subharmonic performance is enhanced and chaos occurs. Bifurcation diagrams and phase portraits can be used to describe the impact of β changes on the vocal system.

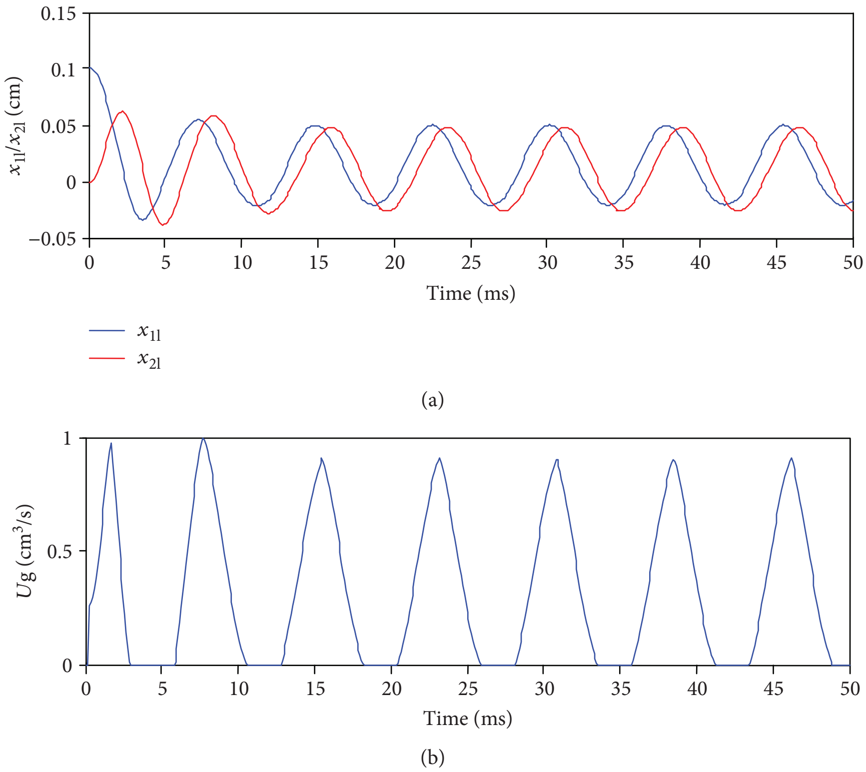

Figure 2: Simulation of the standard symmetric model showing oscillation of (a) left lower and upper masses (x_{1l} and x_{2l}, resp.), and (b) glottal volume flow velocity U_g.

When the vocal cords are asymmetric, contact forces are modified as

$$I_{ir} = -\Theta(-a_i)\frac{c_{ir}}{m_{ir}}\frac{a_i}{L}\left(\frac{1}{\beta+1}\right),$$
$$I_{il} = -\Theta(-a_i)\frac{c_{il}}{m_{il}}\frac{a_i}{L}\left(\frac{\beta}{\beta+1}\right). \tag{8}$$

2.3. Analysis of Vocal Vibration. Vibration characteristics of the asymmetric two-mass model were analyzed with respect to time, frequency, and phase. The vocal mechanism of clinical pathological voice was also investigated with respect to physical simulation. As discussed above, we assumed the left vocal cord was normal, and lesions occurred only in the right vocal cord. Clinical observation of vocal cord physiological characteristics suggested $0.4 < \beta \leq 1$ was an appropriate range and subglottal pressure was fixed at 0.8 kPa.

Figure 3 shows displacement of the lower bilateral mass for $\beta = 0.45$, 0.53, 0.6, 0.8, and 1. Vocal cords on both sides were structurally symmetrical for normal voice, and the vibrational waveforms on both sides coincided completely. Duration of the vocal opening and closing once is defined as one pitch period, and there exists one maximum value of x_{ir} in such a period.

Asymmetric vocal cord vibrations are significantly more complex. When the degree of asymmetry was relatively small ($\beta = 0.8$), right vocal amplitude was slightly larger than the left side, and the phase was relatively advanced. As the degree of asymmetry increases, right vocal amplitude also increases with left amplitude remaining essentially unchanged. Consequently, phase difference increases, and the extrema ratio of both sides is no longer 1 : 1. Figure 3(d) shows the extrema ratio changes to 1 : 3, and quasiperiodic or irregular oscillations appear, leading to irregular airflow velocity.

Before and after bifurcation, evolution of the dynamical systems in phase space can be described with phase diagrams of the displacement of bilateral vocal cord vibration in the $x_{1\mathrm{l}} - x_{1\mathrm{r}}$ plane. Figure 4 shows that when $\beta = 0.8$, no bifurcation occurs, and the phase trajectory is a limit cycle. As β reduces to 0.53, asymmetry increases, bifurcation appears, and the phase trajectory becomes a complicated period doubling limit cycle. However, when $\beta = 0.45$, the phase trajectory geometry simplifies, which is consistent with the results in the time domain.

Considering the cases with fixed subglottal pressure (0.8 kPa) and $\beta = 0.45$, 0.53, 0.6, 0.8, and 1, we compared Fourier spectra corresponding to $x_{1\mathrm{l}}$, $x_{1\mathrm{r}}$, U_g, and the natural frequencies obtained from an eigenvalue analysis of the system. Figures 5(a)–(e) show two vertical dashed lines that represent the two natural frequencies of the left vocal cord, and dash-dotted lines represent those of the right vocal cord.

When $\beta = 1$ (Figure 5(a)), the healthy phonation case and the bilateral folds have the same natural frequency. This phonation frequency is approximately 145 Hz, located between the two eigenfrequencies of the left (or right) side.

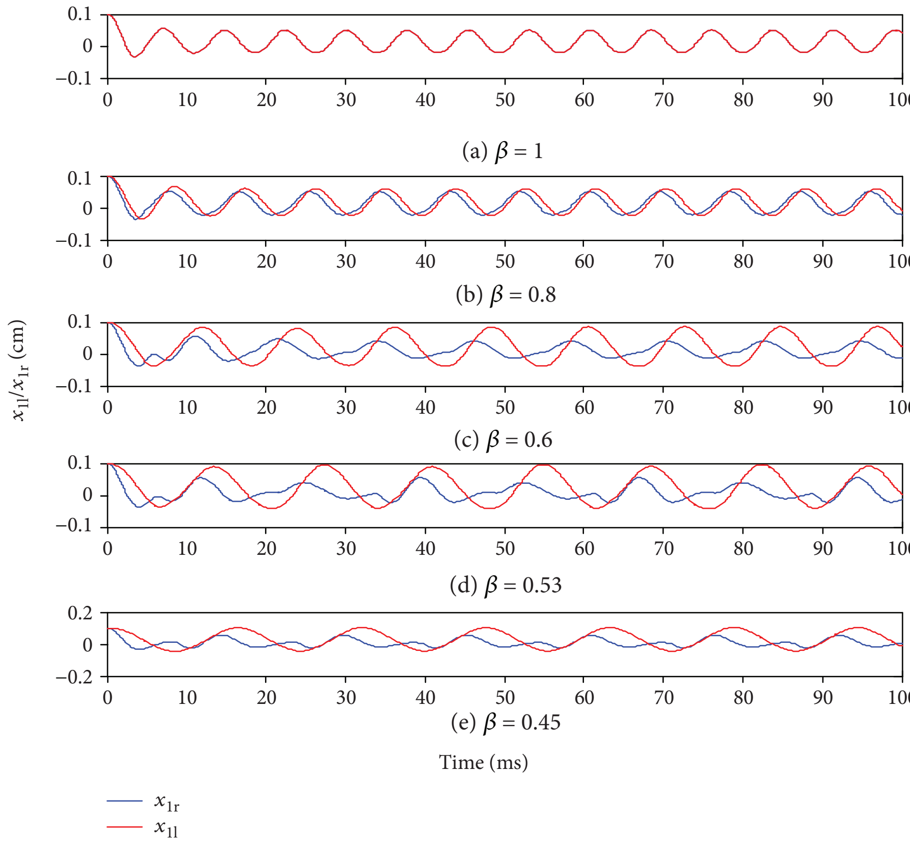

Figure 3: Mass displacements of the lower left and right sides.

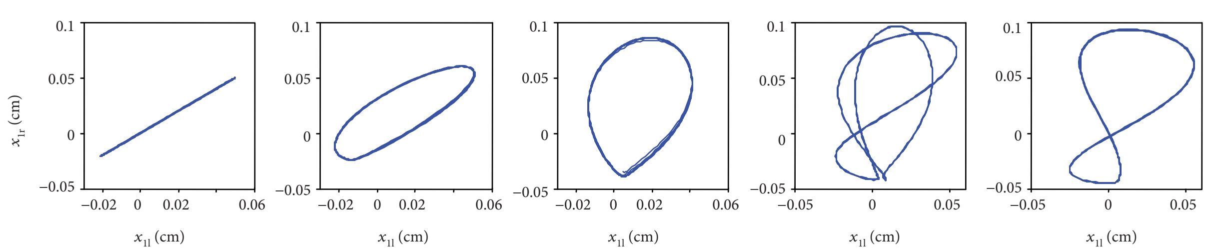

(a) $\beta = 1$ (b) $\beta = 0.8$ (c) $\beta = 0.6$ (d) $\beta = 0.53$ (e) $\beta = 0.45$

Figure 4: Phase space portrait in the $x_{1l} - x_{1r}$ plane.

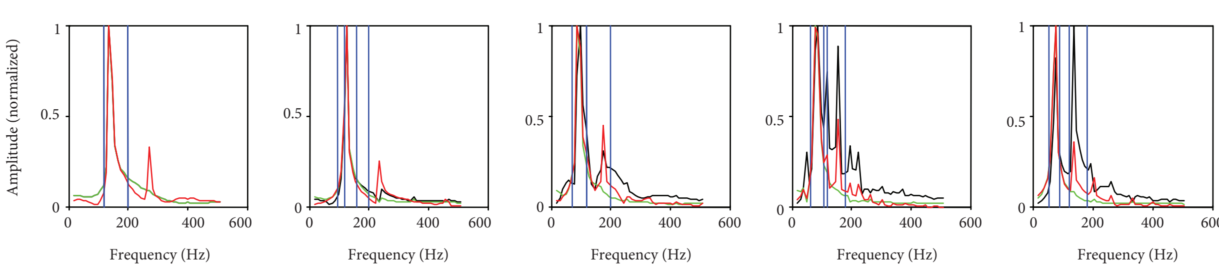

(a) $\beta = 1$ (b) $\beta = 0.8$ (c) $\beta = 0.6$ (d) $\beta = 0.53$ (e) $\beta = 0.45$

Figure 5: Fourier spectra corresponding to displacement of the two lower masses and the normalized glottal volume flow rate with $Ps = 0.8$ kPa. Volume flow rate and left and right mass displacement are represented by the red, black, and green lines, respectively. Vertical dash lines represent the two left vocal cord natural frequencies, and the dash-dot lines represent those of the right vocal cord.

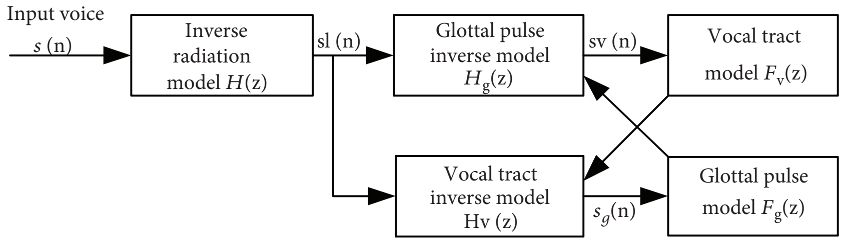

Figure 6: Estimation of the glottal pulse $s_g(\mathrm{n})$ by iterative filtering.

As β reduces, the eigenfrequencies do not coincide again and more complex vibratory behaviors are observed. Figure 5(b) shows that for less asymmetry, $\beta = 0.8$, although the intrinsic frequency changes, there is relatively little effect on the frequency spectrum. Figure 5(c) shows that when $\beta = 0.6$, a frequency approximately 190 Hz with relatively small amplitude appears between the two eigenfrequencies of the left normal folds. Figure 5(d) shows that when $\beta = 0.53$, the overlapped frequencies of the preexisting overtone separate and a small overtone frequency appears between them at 110 Hz. Figure 5(e) shows that when $\beta = 0.45$, the overtone between the second eigenfrequency of the right fold and the first left fold disappears. However, the amplitude of the overtone frequency between the eigenfrequencies of the left normal folds becomes nearly as large as the pitch frequency.

Thus, the fundamental frequency is mainly dependent on the pathological vocal cords, while the normal folds mainly influence the overtone.

3. Model Parameter Optimization

We propose an optimization process to find appropriate parameters for the biomechanical model that can accurately simulate normal and paralyzed voice sources. First, inverse filtering is implemented to reduce the channel effect on the speech signal, and glottal flow is extracted. Glottal flow is separately parameterized in time and frequency domains to reduce computational complexity. Then, an optimization algorithm is employed to optimize SH model parameters to obtain a simulated glottal flow. Finally, minimizing error between the parameters of the simulated and extracted glottal flows allows the model to accurately reproduce the particular voice source, and corresponding vocal parameters can also be obtained.

3.1. Estimation of the Glottal Source. Reconstruction of the glottal source is based on the adaptive version of iterative inverse filtering developed by Alku [27]. The voice trace, s, may be considered as the output of a generation model, f_g, excited by a train pulse, δ, whose output is modeled by the vocal tract transfer function, f_v to, yield voice at the lips, s_l, which is radiated as s, where r is the radiation model, that is, * means convolution of signals,

$$s = \left(\left(\delta * f_g\right) * f_v\right) * r = \left(f_g * f_v\right) * r) = s_l * r \qquad (9)$$

Figure 6 shows the inverse filtering procedure. The radiation effect is first removed by $H(\mathrm{z})$, and the resulting radiation compensated voice, $s_l(\mathrm{n})$, is filtered by $H_g(\mathrm{z})$ to reconstruct the deglottalized voice, $s_v(\mathrm{n})$, from which the estimate of $F_v(\mathrm{z})$ may be derived. The vocal tract inverse model fed with the $F_v(\mathrm{z})$ filter parameters was used to remove the influence of the vocal tract from $s_l(\mathrm{n})$, producing a first estimate of the glottal pulse, $s_g(\mathrm{n})$. Another iteration was started with the new estimated $H_g(\mathrm{z})$ loaded by $F_g(\mathrm{z})$, and the cycle repeated 2 or 3 times to obtain a good estimation of the glottal source.

The glottal flow will be defined as

$$u_g(n) = s_g(n)\text{-}\bar{s}_g(n). \qquad (10)$$

An example of the glottal flow estimation from inverse filtering is shown in Figure 7.

3.2. Objective Function Vocal Cord. Since the asymmetric SH model influences oscillations in both time and frequency domains, the glottal flow, u_g, and simulated waveforms, Ug, were also parameterized within those domains for comparison frequency, F_0, and time quotients based on the Lijiencrants-Frant model were calculated, including speed quotient (*SQ*), the ratio of the glottal opening to closing time open quotient (*OQ*), the ratio of the open time to the fundamental period; closing quotient (*CIQ*), the closing time divided by the fundamental period; and normalized amplitude quotients (*NAQ*), the ratio of amplitude quotients (maximum amplitude divided by corresponding maximum negative peak of its first derivative) to the fundamental period.

To describe the error between normal target glottal flow and simulated waveforms, the objective function, *FY*, was defined as

$$FY = \omega_1 \left(\frac{|OQ - OQ'|}{OQ} + \frac{|SQ - SQ'|}{SQ} + \frac{|CIQ - CIQ'|}{CIQ} + \frac{|NAQ - NAQ'|}{NAQ} \right) + \omega_2 \frac{|F_0 - F_0{}'|}{F_0}, \qquad (11)$$

where "′" means the parameters are derived from the simulation waveform.

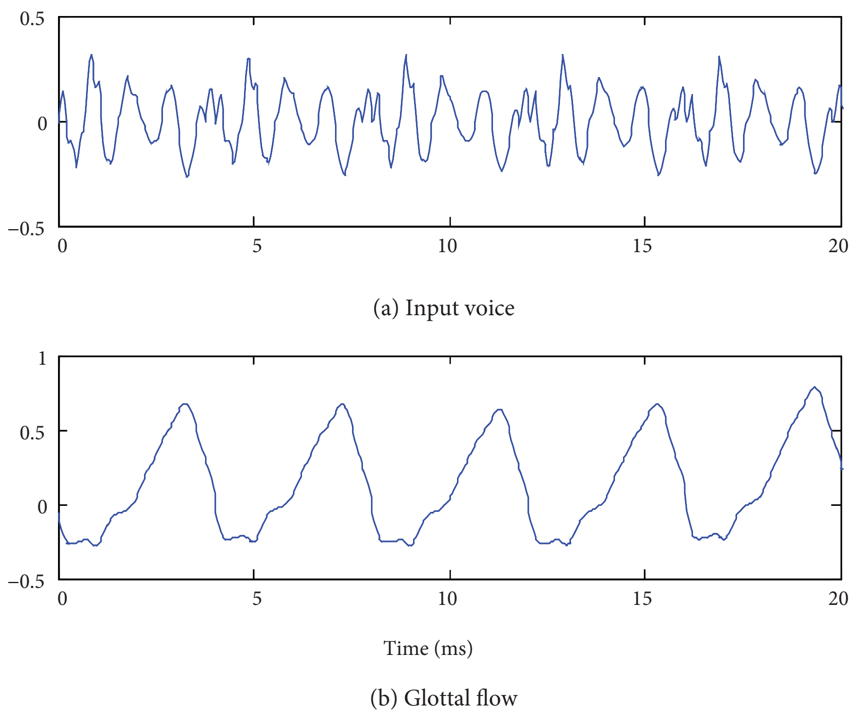

Figure 7: Example from vovel /a/ for a normal speaker.

Traditional perturbation analyses have shown instability of pathological vocal sound. The resultant objective function is defined as:

$$FY_p = \omega_3 FY + \omega_4 \left(\frac{|J_{OQ} - J_{OQ}'|}{J_{OQ}} + \frac{|J_{SQ} - J_{SQ}'|}{J_{SQ}} + \frac{|J_{CIQ} - J_{CIQ}'|}{J_{CIQ}} + \frac{|J_{NAQ} - J_{NAQ}'|}{J_{NAQ}} + \frac{|J_{F0} - J_{F0}'|}{J_{F0}} \right), \quad (12)$$

where variables with superscript denote parameters of the simulated glottal flow.

If the time-based quotients are equally weighted, the effect of frequency and time parameters on F are the same, and their differential impact on F_p is equivalent to the original parameters, that is, $\omega_1 = 0.125$ and $\omega_2 = \omega_3 = \omega_4 = 0.5$. When F or F_p reaches a global minimum, the corresponding model can accurately reproduce the target glottal waveform.

3.3. Optimization Algorithm. Gradient techniques have proven to be inadequate, since the objective function is nonconvex and contains many local minima. The evolutionary algorithm has high robustness, and broad applicability for global optimization can deal with complex problems that traditional optimization algorithms cannot solve. Particle swarm optimization (PSO) and genetic algorithm (GA) are similar but have various strengths in dealing with different problems [28].

Therefore, we combined their advantages. PSO is an evolutionary computation technique based on swarm intelligence and is a community-based optimization tool. The PSO algorithm first initializes a group of random particles with random solutions and then all individuals and the best individuals of groups breed. The optimal solution is found through an iterative process. We added selection and crossover processes similar to GA into PSO, generating a GPSO algorithm.

In contrast, the quasi-Newton method is commonly used for solving nonlinear optimization problems, where the gradient of the objective function at each iteration step is obtained. An objective function can be constructed from the measured gradient to produce superlinear convergence. However, this method is somewhat sensitive to the initial point, and results are mostly local optima. Therefore, we combined the GPSO and quasi-Newton algorithm (GPSO-QN) to optimize the biomechanical model parameters to match the target voice sources.

The masses, spring constants, coupling coefficients, damping constants, and subglottal pressure all need optimization, which can be expressed as a vector $\Phi = [m_{i\alpha}, k_{i\alpha}, k_{c\alpha}, r_{i\alpha}, P_s]$. With optimized Φ the model should simulate Ug in good agreement with u_g.

Previous analysis has shown that asymmetric pathological vocal cords are the leading cause of irregular vibration. Consequently, we took Φ and β as matching parameters with the search interval $[m_{i\alpha}, k_{i\alpha}, k_{c\alpha}, r_{i\alpha}] \in [0.001, 0.5]$, $\beta \in [0.4, 1]$, and $P_s \in [0.001, 0.05]$. Then suitable matching parameters

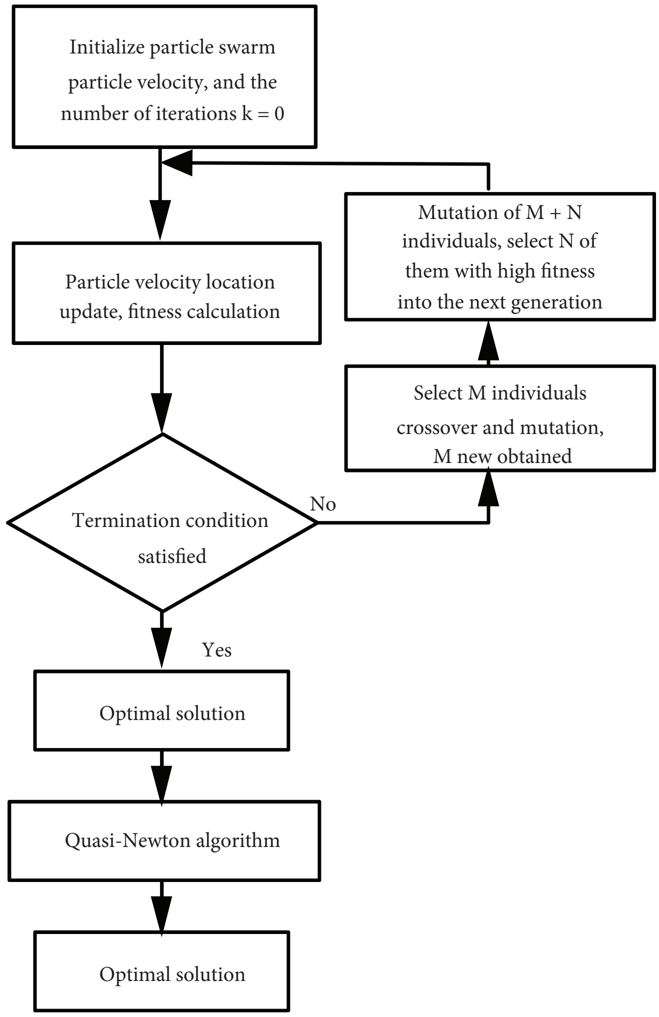

Figure 8: Proposed GPSO-QN algorithm structure.

can be obtained using the proposed GPSO-QN algorithm to ensure the optimized model accurately reproduces the glottal waveform.

To avoid obtaining local minima in a nonconvex search space by direct application of the gradient method, the GPSO algorithm is first applied to provide a rough approximation, and then the QN method is applied to locally optimize the approximate solution, providing the globally optimal result.

Figure 8 shows the parameter optimization process. Selection and crossover process utilizes the Monte Carlo selection rule to choose M individuals. The termination condition is that the obtained maximum fitness value exceeds a preset threshold or the preset number of iterations is reached.

4. Result and Discussion

4.1. Experimental Parameters. This paper selected sustained vowel /a/ from the MEEI database [29], numbering the samples 1–8 (4 normal and 4 paralysis voices). Sampling frequency was 25 kHz, and the proposed GPSO-QN algorithm was used to optimize the model parameters with the number of particles for the initial population set as 30 and the number of generations limited to 400. Learning factors c_1 and c_2 were set = 2, and the range of weight coefficient ω was set = [0.5, 0.9].

4.2. Normal Voice Source Matching. Figure 9 shows the excitation sources (red dashed lines) extracted from the four normal voice samples using the optimized model were accurately simulated. Using sample 3 as an example, Figure 10 shows that the simulated and actual spectra also have good consistency.

4.3. Paralysis Voice Source Matching. Figure 11 shows that the model simulated waveforms for paralyzed voice samples (red dashed lines) have significant errors to actual samples, particularly for samples 7 and 8. However, the spectra show good consistency with only magnitude bias, as shown in Figure 12.

4.4. Difference Analysis of Matching Results. To investigate the differences between normal and paralysis voice sources, we matched 9 consecutive frames of samples 1–8, and Figure 13 shows the statistical distribution of the optimized

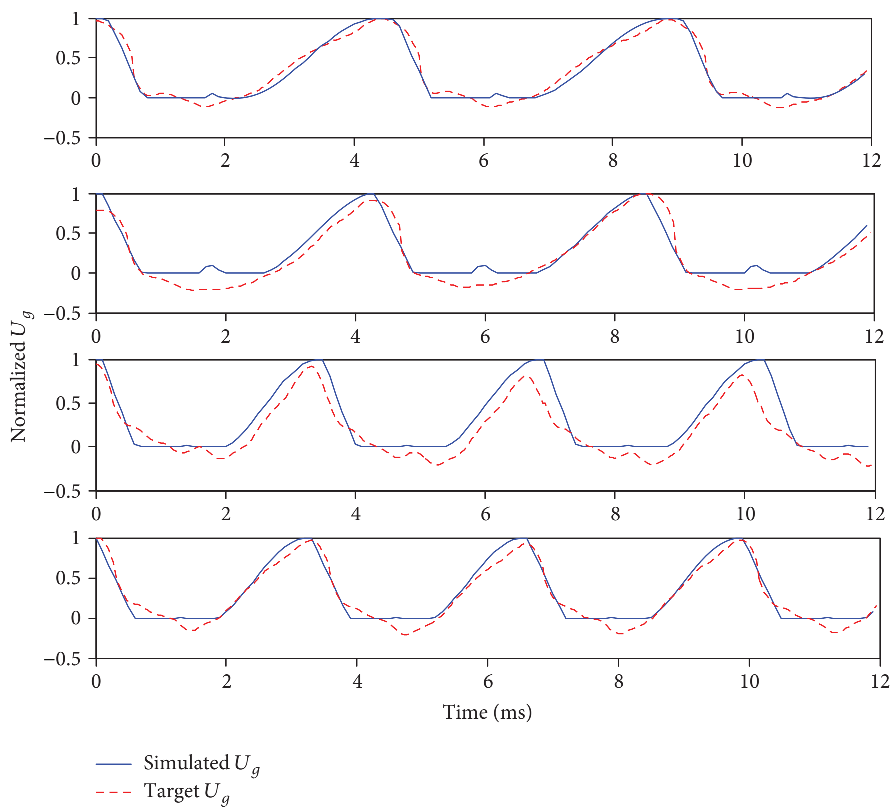

Figure 9: Matching result of normal voice source in the time domain.

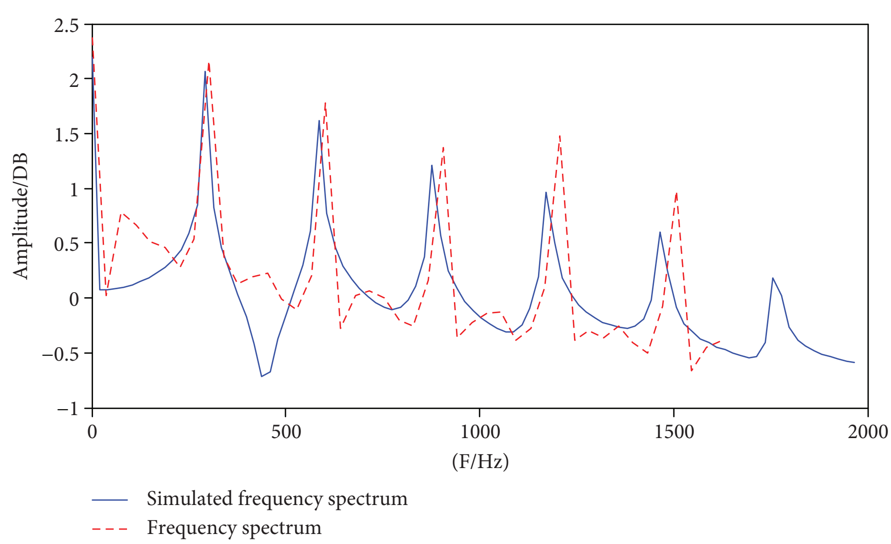

Figure 10: Matching result of sample 3 voice source in the frequency domain.

parameters. There were no significant differences between stiffness, quality, and damping of normal and paralysis models. However, the coupling stiffness of paralyzed vocal voice sources is greater than that of normal sources, and significant asymmetry in the paralyzed vocal cords was observed, as shown in the last two rows of Figure 13(b).

Therefore, coupling stiffness and the asymmetry parameter, β, could be used as a basis for classifying normal and paralyzed vocal sources. Figure 14 shows the pathological voice source analysis system. It is designed and programmed by MATLAB.

5. Conclusion

This study analyzed nonlinear characteristics of asymmetric vocal cord motion using an optimized biomechanical model to design a pathological voice source analysis system. A proposed algorithm was employed to optimize the

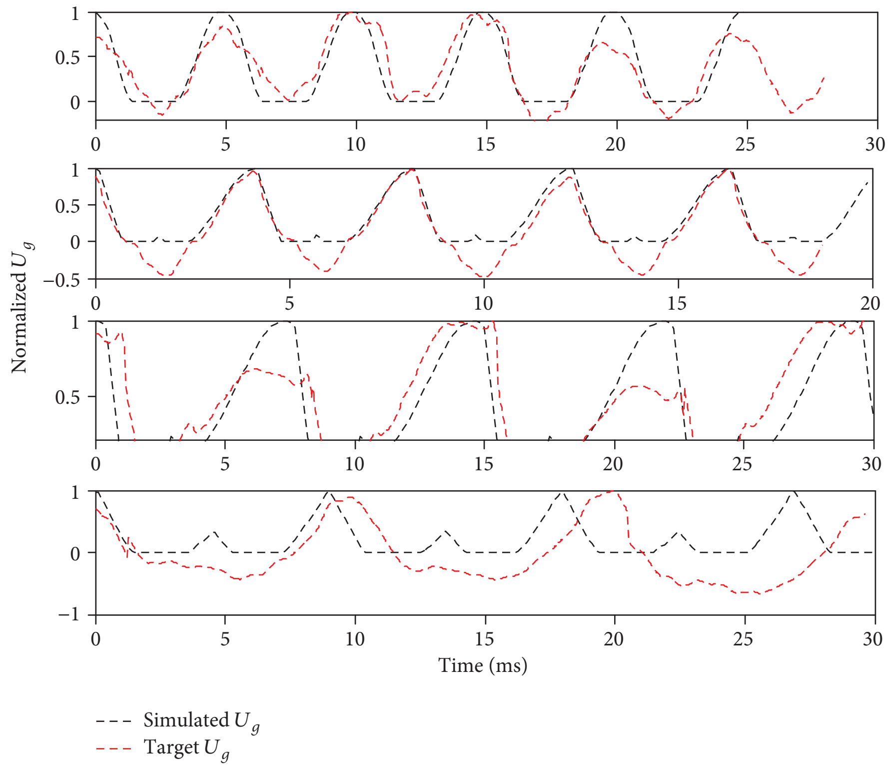

Figure 11: Matching result of paralysis voice source in the time domain.

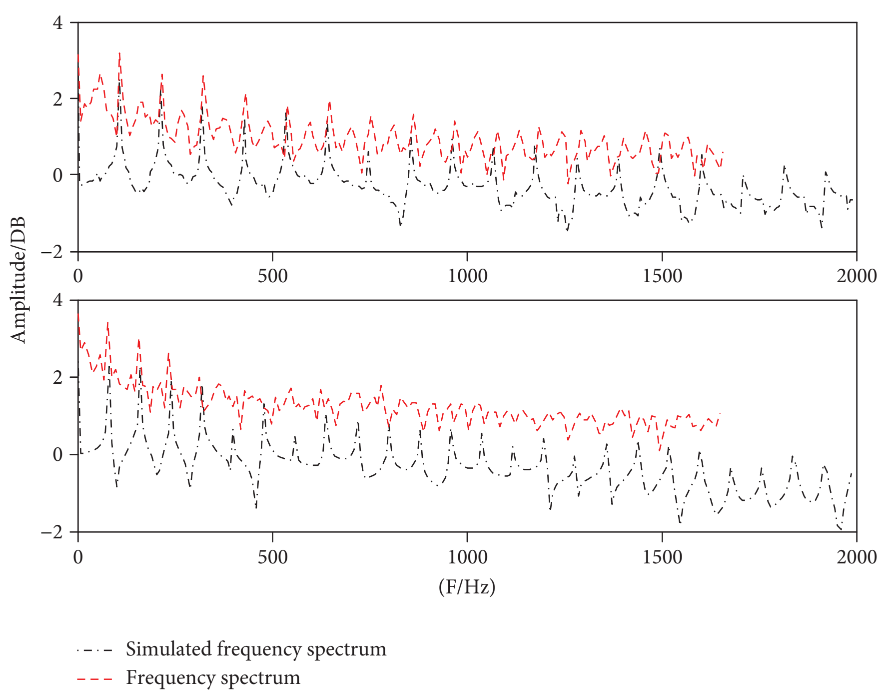

Figure 12: Matching results of samples 7 and 8 in the frequency domain.

masses, spring constants, coupling coefficient, damping constants, asymmetry parameter, and subglottal pressure of the mass model.

The proposed biomechanical model accurately simulated irregular vibration caused by unbalanced vocal tension. Period doubling bifurcation and frequency entrainment were observed in the bifurcation and phase diagrams, and spectrograms.

Vibration system complexity and asymmetry do not have a simple proportional relationship. This study shows that

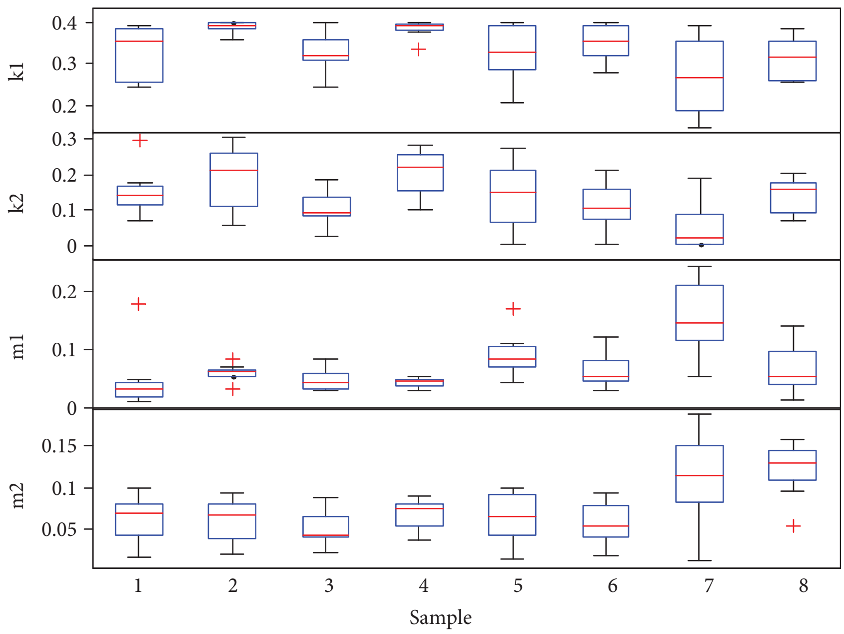

FIGURE 13: Statistical distribution of normal (1–4) and paralyzed samples (5–8).

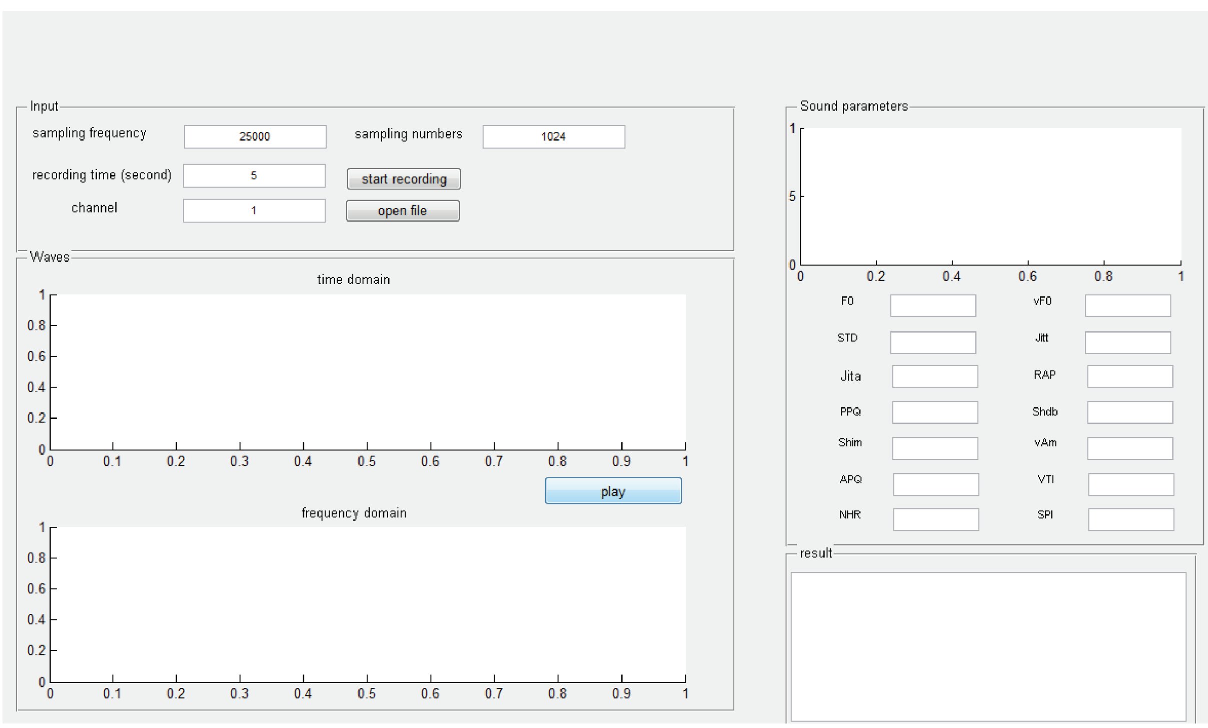

FIGURE 14: Pathological voice source analysis system.

pitch frequency is mainly affected by the asymmetric structure of the vocal cord, whereas the impact of subglottal pressure is relatively small.

The optimal biomechanical model can accurately reproduce the voice source stream modulated by asymmetric vocal cords. Although the physiological parameters of voice sources were different, the asymmetry and coupling stiffness parameters helped determine paralysis voice sources.

Optimized model simulations will be of great value for understanding clinical hoarse voices corresponding to asymmetric vocal structure and predicting the effect on unilateral vocal disease treatment.

Future work will establish rational sound models for vocal cord polyps and other organic diseases to match real voice sources, assisting in classification of vocal cord diseases.

Data Availability

The data used to support the findings of this study are available from the corresponding author upon request.

Conflicts of Interest

The authors declare that there are no conflicts of interest regarding the publication of this paper.

Acknowledgments

This project was funded by National Natural Science Foundation of China under Grant no. 61372146 and no. 61271359. The authors are thankful for the support from Collaborative Innovation Centre of Suzhou Nano Science and Technology and Key Joint Laboratory of Jiemei Biomedical Engineering, Soochow University.

References

[1] Q. Xue, R. Mittal, X. Zheng, and S. Bielamowicz, "Computational modeling of phonatory dynamics in a tubular three-dimensional model of the human larynx," *The Journal of the Acoustical Society of America*, vol. 132, no. 3, pp. 1602–1613, 2012.

[2] A. Granados, M. K. Misztal, J. Brunskog, V. Visseq, and K. Erleben, "A numerical strategy for finite element modeling of frictionless asymmetric vocal fold collision," *International Journal for Numerical Methods in Biomedical Engineering*, vol. 33, no. 2, 2017.

[3] J. Lohscheller, J. G. Švec, and M. Döllinger, "Vocal fold vibration amplitude, open quotient, speed quotient and their variability along glottal length: kymographic data from normal subjects," *Logopedics Phoniatrics Vocology*, vol. 38, no. 4, pp. 182–192, 2013.

[4] L. Verde, G. De Pietro, and G. Sannino, "A methodology for voice classification based on the personalized fundamental frequency estimation," *Biomedical Signal Processing and Control*, vol. 42, pp. 134–144, 2018.

[5] N. Huang, Y. Zhang, W. Calawerts, and J. J. Jiang, "Optimized nonlinear dynamic analysis of pathologic voices with laryngeal paralysis based on the minimum embedding dimension," *Journal of Voice*, vol. 31, no. 2, pp. 249.e1–249.e7, 2017.

[6] E. Cataldo and C. Soize, "Voice signals produced with jitter through a stochastic one-mass mechanical model," *Journal of Voice*, vol. 31, no. 1, pp. 111.e9–111.e18, 2017.

[7] P. S. Deshpande and M. S. Manikandan, "Effective glottal instant detection and electroglottographic parameter extraction for automated voice pathology assessment," *IEEE Journal of Biomedical and Health Informatics*, vol. 22, no. 2, pp. 398–408, 2018.

[8] J. J. Jiang, Y. Zhang, and C. McGilligan, "Chaos in voice, from modeling to measurement," *Journal of Voice*, vol. 20, no. 1, pp. 2–17, 2006.

[9] L. Lancia, D. Voigt, and G. Krasovitskiy, "Characterization of laryngealization as irregular vocal fold vibration and interaction with prosodic prominence," *Journal of Phonetics*, vol. 54, no. 9, pp. 80–97, 2016.

[10] M. Zañartu, D. D. Mehta, J. C. Ho, G. R. Wodicka, and R. E. Hillman, "Observation and analysis of in vivo vocal fold tissue instabilities produced by nonlinear source-filter coupling: a case study," *The Journal of the Acoustical Society of America*, vol. 129, no. 1, pp. 326–339, 2011.

[11] N. Wan, D. D. Peng, M. Sun, and D. Zhang, "Nonlinear oscillation of pathological vocal folds during vocalization," *Science China Physics, Mechanics and Astronomy*, vol. 56, no. 7, pp. 1324–1328, 2013.

[12] A. P. Pinheiro and G. Kerschen, "Vibrational dynamics of vocal folds using nonlinear normal modes," *Medical Engineering & Physics*, vol. 35, no. 8, pp. 1079–1088, 2013.

[13] A. P. Pinheiro, D. E. Stewart, C. D. Maciel, J. C. Pereira, and S. Oliveira, "Analysis of nonlinear dynamics of vocal folds using high-speed video observation and biomechanical modeling," *Digital Signal Processing*, vol. 22, no. 2, pp. 304–313, 2012.

[14] Y. Zhang, A. J. Sprecher, Z. X. Zhao, and J. J. Jiang, "Nonlinear detection of disordered voice productions from short time series based on a Volterra–Wiener–Korenberg model," *Chaos, Solitons & Fractals*, vol. 44, no. 9, pp. 751–758, 2011.

[15] Y. Zhang and J. J. Jiang, "Chaotic vibrations of a vocal fold model with a unilateral polyp," *The Journal of the Acoustical Society of America*, vol. 115, no. 3, pp. 1266–1269, 2004.

[16] S. H. Choi, Y. Zhang, J. J. Jiang, D. M. Bless, and N. V. Welham, "Nonlinear dynamic-based analysis of severe dysphonia in patients with vocal fold scar and sulcus vocalis," *Journal of Voice*, vol. 26, no. 5, pp. 566–576, 2012.

[17] Q. Xue, R. Mittal, X. Zheng, and S. Bielamowicz, "A computational study of the effect of vocal-fold asymmetry on phonation," *The Journal of the Acoustical Society of America*, vol. 128, no. 2, pp. 818–827, 2010.

[18] D. E. Sommer, B. D. Erath, M. Zañartu, and S. D. Peterson, "Corrected contact dynamics for the Steinecke and Herzel asymmetric two-mass model of the vocal folds," *The Journal of the Acoustical Society of America*, vol. 132, no. 4, pp. EL271–EL276, 2012.

[19] S. Panchapagesan and A. Alwan, "A study of acoustic-to-articulatory inversion of speech by analysis-by-synthesis using chain matrices and the Maeda articulatory model," *The Journal of the Acoustical Society of America*, vol. 129, no. 4, pp. 2144–2162, 2011.

[20] M. Dollinger, U. Hoppe, F. Hettlich, J. Lohscheller, S. Schuberth, and U. Eysholdt, "Vibration parameter extraction from endoscopic image series of the vocal folds," *IEEE Transactions on Biomedical Engineering*, vol. 49, no. 8, pp. 773–781, 2002.

[21] P. Gómez-Vilda, R. Fernández-Baillo, V. Rodellar-Biarge et al., "Glottal source biometrical signature for voice pathology detection," *Speech Communication*, vol. 51, no. 9, pp. 759–781, 2009.

[22] P. J. Hadwin, G. E. Galindo, K. J. Daun et al., "Non-stationary Bayesian estimation of parameters from a body cover model of the vocal folds," *The Journal of the Acoustical Society of America*, vol. 139, no. 5, pp. 2683–2696, 2016.

[23] X. L. Zeng, X. J. Zhang, D. Wu et al., "Parameter inversion method of vocal fold dynamic model in pathological voice classification," *Acta Acustica*, vol. 43, no. 1, pp. 91–100, 2018.

[24] C. Tao, Y. Zhang, and J. J. Jiang, "Extracting physiologically relevant parameters of vocal folds from high-speed video image series," *IEEE Transactions on Biomedical Engineering*, vol. 54, no. 5, pp. 794–801, 2007.

[25] T. Riede, Z. Li, I. T. Tokuda, and C. G. Farmer, "Functional morphology of the Alligator mississippiensis larynx with implications for vocal production," *The Journal of Experimental Biology*, vol. 218, no. 7, pp. 991–998, 2015.

[26] Z. Zhang, J. Kreiman, B. R. Gerratt, and M. Garellek, "Acoustic and perceptual effects of changes in body layer stiffness in symmetric and asymmetric vocal fold models," *The Journal of the Acoustical Society of America*, vol. 133, no. 1, pp. 453–462, 2013.

[27] P. Alku, "Parameterisation methods of the glottal flow estimated by inverse filtering," in *In ISCA Tutorial and Research Workshop on Voice Quality: Functions, Analysis and Synthesis*, pp. 81–87, International Speech Communication Association, 2003.

[28] X. H. Shi, Y. C. Liang, H. P. Lee, C. Lu, and L. M. Wang, "An improved GA and a novel PSO-GA-based hybrid algorithm," *Information Processing Letters*, vol. 93, no. 5, pp. 255–261, 2005.

[29] Massachusetts Eye and Ear Infirmary, *Voice Disorders Database (Version 1.03)*, Kay Elemetrics Corp, Lincoln Park, NJ, 1994.

Hindawi
Applied Bionics and Biomechanics
Volume 2018, Article ID 7847014, 10 pages
https://doi.org/10.1155/2018/7847014

Research Article

Dynamic Balance Gait for Walking Assistance Exoskeleton

Qiming Chen, Hong Cheng, Chunfeng Yue, Rui Huang, and Hongliang Guo

Center for Robotics, School of Automation Engineering, University of Electronic Science and Technology of China, Chengdu, China

Correspondence should be addressed to Qiming Chen; kipochen@163.com

Received 22 January 2018; Accepted 23 May 2018; Published 2 July 2018

Academic Editor: Dongming Gan

Purpose. Powered lower-limb exoskeleton has gained considerable interests, since it can help patients with spinal cord injury(SCI) to stand and walk again. Providing walking assistance with SCI patients, most exoskeletons are designed to follow predefined gait trajectories, which makes the patient walk unnaturally and feels uncomfortable. Furthermore, exoskeletons with predefined gait trajectories cannot always maintain balance walking especially when encountering disturbances. *Design/Methodology/Approach*. This paper proposed a novel gait planning approach, which aims to provide reliable and balance gait during walking assistance. In this approach, we model the exoskeleton and patient together as a linear inverted pendulum (LIP) and obtain the patients intention through orbital energy diagram. To achieve dynamic gait planning of exoskeleton, the dynamic movement primitive (DMP) is utilized to model the gait trajectory. Meanwhile, the parameters of DMP are updated dynamically during one step, which aims to improve the ability of counteracting external disturbance. *Findings*. The proposed approach is validated in a human-exoskeleton simulation platform, and the experimental results show the effectiveness and advantages of the proposed approach. *Originality/Value*. We decomposed the issue of obtain dynamic balance gait into three parts: (1) based on the sensory information of exoskeleton, the intention estimator is designed to estimate the intention of taking a step; (2) at the beginning of each step, the discrete gait planner utilized the obtained gait parameters such as step length S and step duration T and generate the trajectory of swing foot based on (S, T); (3) during walking process, continuous gait regulator is utilized to adjust the gait generated by discrete gait planner to counteract disturbance.

1. Introduction

SCI is a temporary or permanent damage to the spinal cord that changes its function and might cause loss of muscle function and sensation. According to the survey of the World Health Organization [1], between 250,000 and 500,000 people are suffering from SCI every year around the world. SCI patients who are forced to be bedridden and wheelchair bound are susceptible to developing decubitus, loss of bone density, articular contracture of the lower limbs, and deep-vein thrombosis [2]. Gait support using an exoskeleton robot may be an effective way to address the abovementioned problems because a patient wearing the robot moves their legs actively and the ground reaction force stimulates the sensory and musculoskeletal system. Furthermore, the gait support has a particularly meaningful role in the regaining of walking function in several SCI patients. Therefore, lower-limb exoskeletons are designed to provide movement assistance for people suffering SCI and have attracted increasing interest from both academic researchers and industrial entrepreneurs [3–5].

On the development of lower-limb exoskeletons for walking assistance, comfort and safety are two essential features. Many efforts are made on the development of lower exoskeletons for walking assistance. Yan et al.[6] suggest that most of the exoskeletons for assistance still employ predefined trajectories based on off-line simulations or captured human gait data. The generated reference patterns are generally tracked by position controllers of powered joints. It forces patients to move with exoskeletons and lead uncomfortable experience. Moreover, with predefined trajectories, exoskeletons and patients cannot keep balance when encountering a disturbance. Therefore, for obtaining dynamic balance gait, we consider both when to step and how to step.

For when to step, various human-machine interfaces (HMI) are designed. In [7], electromyography (EMG) signal is utilized to get the intention of patients. However, it is difficult to measure EMG signal for patients with SCI motion features such as tilt of torso [8] and upper arms [9] are utilized to obtain the intention of walking and trigger a step. Center of mass (COM) based approaches are also employed in HAL [10] and MINDWALKER [11, 12]. However, these approaches are only based on observed information and the experience of system designer Thresholds in these approaches must be adjusted manually for different patients and situations.

For how to walk, many dynamic gait planning approaches are proposed. In [10], the exoskeleton changes the speed of swing foot dynamically according to duration of support phase for improving the experience of patients. However, balance of exoskeleton is not considered in this research. In [11, 12], extrapolated center of mass (XCoM) [13] method is proposed to prevent the MINDWALKER exoskeleton from falling sideways by online adjusting the step width (hip ab/adduction). However, disturbance in sagittal plane is not taken in account.

In this paper, we proposed a dynamic balance gait approach to obtain balance gait pattern for lower-limb exoskeleton. We model the human-exoskeleton system with linear inverted pendulum (LIP) and design the intention estimator based on the concept of orbital energy diagram. Discrete gait planner (planning a gait at the beginning of each step) and online gait regulator (online adjust the gait during step taking) are proposed for achieving balance gait. The trajectory of swing foot is modeled with DMPs, which can be adjusted dynamically and smoothly. In discrete gait planner, we utilize an optimization method with targeting orbital energy to obtain parameters of a gait trajectory. In online gait regulator, we adjust DMPs dynamically for counteracting the disturbance during a step.

Hence, our contributions are twofolded: first, our approach enables exoskeleton walk as the intention of patients. Secondly, our approach obtain gait trajectories and adjust it dynamically to stabilize balance during walking. Experimental results in simulation environment show the effectiveness and advantages of the proposed method.

2. Literature Review

Although predefined trajectory approach is utilized in most of exoskeleton for SCI patients, some attention is paid on technologies for obtain balance gait patterns. In this section, we will lay down the related works about technologies and lower limb exoskeleton systems for keeping balance during walking. Some biomechanics researchers reveal several approaches balance recovery of humanoid robots [14]. These approaches can be divided into two categories: internal joint approach and step taking approach. These approaches also have been used for balance control of exoskeletons.

2.1. Internal Joint Approach. Joints of exoskeletons are controlled to serve some crucial features of balance like zero moment point (ZMP) for internal joint approach. In [15], for real-time balance control, variable physical stiffness actuators were implemented to exoskeletons. An abstracted biped model, torsional spring-loaded flywheel, is utilized to capture approximated angular momentum and physical stiffness. The mathematical relation between ZMP and physical stiffness is described with this model. Moreover, ZMP is regarded as conditions of stability. Thus, for keeping balance desired, ZMP is served with the stiffness of joint actuators.

Reference [16] shows that in dynamic balance, the condition for static balance which says the projection of center of mass (CoM) should be within the support polygon is not sufficient and turns out to be instantaneous capture point (ICP) should be within the support polygon. The paper [17] presents a balance control for a powered lower-limb exoskeleton based on the concept ICP and implement it on the exoskeleton named EMY-Balance (CEA-LIST). Joint torques for the specific actuation of EMY-Balance is computed to keep the ICP in support polygon.

In these approaches, ankle joints are needed to be actuated. However, for portability in most of the exoskeletons for SCI patients, ankle joints are not actuated.

2.2. Stepping Approach. Stepping approach is widely utilized in balance control for humanoid robots [18, 19] and exoskeletons [11, 12, 20]. MINDWALKER [11, 12] is a powered lower-limb exoskeleton designed for paraplegics to regain locomotion capability. It has five DOFs at each leg, with hip flexion/extension and adduction/abduction and knee flexion/extension powered by SEAs, while hip rotation and ankle pronation/supination passively sustained with certain stiffness. Finite state machine (FSM) is defined with various states and state transitions can also be triggered when the user manipulates the CoM position of the user-exoskeleton system. A trigger to initiate a step will be generated when the projection of the sagittal and lateral CoM positions on the ground fall in the desired quadrant.

To prevent the user-exoskeleton from falling sideways, MINDWALKER implements online correction of the step width by adapting the amount of hip ab/adduction needed during the swing phase. The required adjustment of hip joints is determined using XCoM [13]. If the user-exoskeleton system falls towards one side due to external perturbations such as being pushed at the shoulder or internal perturbations such as user's upper body motion, the foot placement is adjusted resulting in a wider or a narrower step width to counteract such perturbations. However, this XCoM approach does not take the adaptation of sagittal plane in count.

In [20], gait planning for balance is based on ZMP. 7-links model [21] is utilized to model exoskeleton. Trajectories of hip, knee, and ankle are modeled by parameters. These parameters are obtained by optimal algorithm with targeting ZMP. However, this approach is based on the 7-links model which is too complex for exoskeleton.

3. Dynamic Balance Gait

In this section, we will introduce the dynamic balance gait approach. We first present the framework of this approach followed by the details of subsystems.

3.1. Framework for Dynamic Balance Gait. On the development of lower-limb exoskeletons for SCI patients, most of their ankle joints are passive (without actuators). Therefore, we proposed a novel gait planning approach in this paper which based on the stepping strategy and the LIP model. Figure 1 shows the framework of proposed dynamic balance gait strategy, which decomposed into three parts: intention estimator, discrete gait planner, and continuous gait regulator.

The gait is divided into single-support phase and double-support phase during normal walking. In single-support phase, the upper body of the human-exoskeleton system is controlled by hip joint of stand leg, which should keep torso stay vertical. Therefore, the gait of human-exoskeleton system can be expressed as foot trajectories of swing leg. We model the trajectories of swing foot with DMPs, which can be learned with sample trajectories of healthy people and adjust gait trajectories online smoothly. Based on the LIP model and gait description with DMPs, three fundamental parts in Figure 1 are employed to achieve dynamic balance gait. According to sensory information of exoskeleton, the intention estimator is designed to estimate the intention of taking a step. At the beginning of each step, the discrete gait planner utilized the obtain trajectory of swing foot. With the intention estimation of taking a step, discrete gait planner obtains gait parameters such as step length S and step duration T. DMPs are utilized to regenerate trajectories with these different parameters (S, T). Joints control serve these trajectories to lead exoskeleton and patient move forward. During the process of taking a step, online gait regulator adjusts the parameters (S, T) based on gait planer to counteract disturbance.

3.2. Model of Human and Exoskeleton. In many applications of exoskeletons, patients walk with crutches to keep balance [8, 9, 11, 12]. Thus, quadruped robot model is utilized to express these human-exoskeleton system. With this model, static stable based on CoM is considered during the walking process. Although patients are enabled to walk again with this approach, for stability, they must rely on crutches, and their gait pattern is less fluent and slower than natural gait. Thus, for achieving fast and natural gait, we use LIP in sagittal plane to model the human-exoskeleton system as Figure 2. Linear inverted pendulum (LIP) is widely used in biped robot [18, 22, 23]. In LIP, we model the body with a point mass with position r at the end of a telescoping mechanism (representing the leg), which is in contact with the flat ground. The point mass is kept on a horizontal plane by suitable generalized forces in the mechanism. Most exoskeletons' ankle joints are not actuated and activated [8–10]. Hence, the base of the pendulum can be seen as a point foot, with position r ankle. Foot position changes, which occur when a step is taken, are assumed instantaneous and have no instantaneous effect on the position and velocity of the point mass. Patients can apply external force to CoM with crutches to interact with exoskeleton.

By definition mentioned before, we can obtain motion equation of point mass (external force set to 0) as follows:

$$\begin{aligned} r^2\ddot{\theta} + 2r\dot{r}\dot{\theta} - gr\sin(\theta) &= \frac{\tau}{M}, \\ r^2 - r\dot{\theta}^2 + g\cos(\theta) &= \frac{f}{M}, \end{aligned} \tag{1}$$

where r is the position of point mass (M) and θ is the angle of LIP with ground. f denotes force applied along the LIP. g is gravity constants. With $f = Mg/\cos(\theta)$ and $\tau = 0$, the point mass is kept on a horizontal line as $M\ddot{x} = f\sin(\theta)$. In this situation, motion of point mass can be written as:

$$\ddot{x} = \frac{g}{z}x, \tag{2}$$

where x and z is the position of point mass in XOZ plane. Thus, given initial conditions x_0 and $\dot{x}_0$, we can get the equation motion of CoM as follows:

$$\begin{aligned} x(t) &= x_0\cosh\left(\frac{t}{T_c}\right) + T_c\dot{x}_0\operatorname{sing}\left(\frac{t}{T_c}\right), \\ \dot{x}(t) &= \frac{x_0}{T_c}\sinh\left(\frac{t}{T_c}\right) + \dot{x}_0\cosh\left(\frac{t}{T_c}\right), \end{aligned} \tag{3}$$

where T_c is $\sqrt{g/z}$.

3.3. Intention Estimator for Taking a Step. Walking with exoskeleton is a periodic phenomenon, and a complete walking cycle is composed of two phases: a double-support phase and a single-support phase. The double-support phase begins with the heel of the forward foot touching the ground and ends with the toe of the rear foot leaving the ground. During the double-support phase, both feet are in contact with the ground. During the single-support phase, one foot is stationary on the ground and the other foot swings from the rear to the front. After the end of a step (swing leg touches the ground), human-exoskeleton system enter double support phase.

In this phase, the patient has two choices: stopping to walk and taking a new step. As shown in the left side of Figure 3, the patient moves forward/backward slightly; weight will load on front/behind leg. Thus, we can also use LIP to model this system. With this model, we can design a intention estimator for take a step according to the concept of orbital energy diagram.

The orbital energy E [24] can be obtained with the integration of $\dot{x}(\ddot{x} - (g/z)x) = 0$:

$$\int \dot{x}\ddot{x} - \frac{g}{z}x\dot{x}dt = \frac{1}{2}\dot{x}^2 - \frac{g}{2z}x^2 = E. \tag{4}$$

It is the sum of two terms: dynamic energy and potential energy. It is conserved during a single support phase. Given $E = 0$, LIP moves to straight up position with $\dot{x} = 0$. We can infer that if initial $x > 0$, LIP can move over the straight up position with $E > 0$, otherwise it will move back. Thus, letting $E = 0$, we can obtain a line: $x = \pm\sqrt{g/z}\dot{x}$. With axis $(x, \dot{x})$ and this line. As shown in Figure 3, we separate the motion states of LIP $(x, \dot{x}, E)$ into 8 regions. Thus, we call it orbital diagram. When $x < 0$ we can get results from orbital diagram:

(1) If $E > 0$, $x < 0$ and $\dot{x} > 0$, LIP would cross the straight up position.

(2) If $E < 0$, $x < 0$ and $\dot{x} > 0$, LIP would move back to initial position.

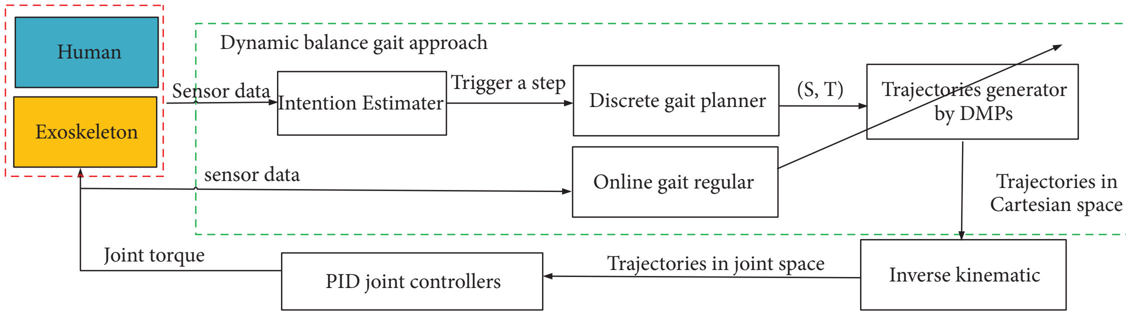

Figure 1: The framework of dynamic balance gait planning.

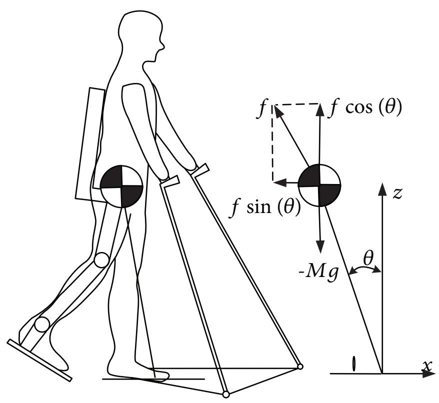

Figure 2: Model of exoskeleton and human based on LIP.

(3) If $E < 0$, $x < 0$ and $\dot{x} < 0$, LIP would move backward.

(4) If $E > 0$, $x < 0$ and $\dot{x} < 0$, LIP would move backpack.

As shown in Figure 3, if stand leg is front leg and the state of system can be described with state 1, 7, and 8, then a step must be taken forward to prevent falling down. Commonly, after the transition of weight, system will come to state 1 before 7 and 8. If stand leg is behind leg and the state of system can be described in state 3, 4, and 5, exoskeleton must take a step backward for preventing falling. Thus, after determining stand leg, we can obtain the intention of patient (step forward or step backward) by the quadrant of orbital energy diagram, the status $(x, \dot{x}, E)$ belong to.

3.4. Gait Description with DMPs. As many studies on gait planning [25–27] have assumed that the double-support phase is instantaneous, we focus the gait of single-support phase. If foot trajectories and the hip trajectory are already known, all joint trajectories of the exoskeleton can be determined by kinematic equations. The walking pattern can therefore be denoted uniquely by foot trajectories and hip trajectories. As most of exoskeleton ankle joints are not actuated, foot of stand leg can be modeled as point. With known initial position and velocity of LIP, trajectories of hip are known. Thus, gait pattern can be modeled by trajectories of ankle joint of swing leg. In [21], gait pattern is formulated by the constraints of a complete foot trajectory and generate the foot trajectory by third spline interpolation. In [10], min-jert method is used to model this trajectory. However, with these approaches, the whole trajectory must be replanned if a single point of motion changed. In our approach, we obtain the foot trajectory from normal person and regenerate it with targeting step length S and duration T. DMP is utilized to regenerate this trajectory to adjust this trajectory online.

DMP has been widely employed in robotic applications, since it can solve flexible modelling problems with coupled terms [28]. It is easy to learn with statistical methods and can be adapted through a few parameters after imitation learning [29, 30]. Moreover, it can quickly be adapted to the inevitable perturbations of a dynamically changing, stochastic environment. Modelling a trajectory with the framework of DMP, a trajectory $x(t)$ is supposed to be the output of a mass spring damper system perturbed by a force term:

$$\begin{aligned} \tau \dot{v} &= K(g - x) - Dv + (g - x_0) f, \\ \tau \dot{x} &= v, \end{aligned} \tag{5}$$

where x and v indicate the position and velocity of the system, respectively. x_0 and g are the start and goal positions. τ is a temporal scaling factor. K and D are the spring and damping factors of the system. Therefore, with a known $x(t)$, $f(t)$ can be calculated through the inverse of the system. Then, f can be learned by combining with Gaussian kernels:

$$f(s) = \frac{\sum_{i=1}^{N} \omega_i \Psi_i(s) s}{\sum_{i=1}^{N} \Psi_i(s)}, \tag{6}$$

where $\psi = \exp\left(-h_i (s - o_i)^2\right)$ are Gaussian basis functions with center o_i and width h_i. w_i are weights which should be learned. The phase variable in the nonlinear function (6) is utilized to avoid f directly dependence off on time. Use first-order dynamics to define the phase variable x:

$$\tau \dot{s} = \alpha s. \tag{7}$$

The goal g is close to the start position x_0, a small change in g may lead to huge accelerations, which may reach the limitation of the exoskeleton system. Therefore, modified system equations introduced in [31] are used:

$$\tau \dot{v} = K(g - x) - Dv + K(g - x_0) s + K f(s), \tag{8}$$

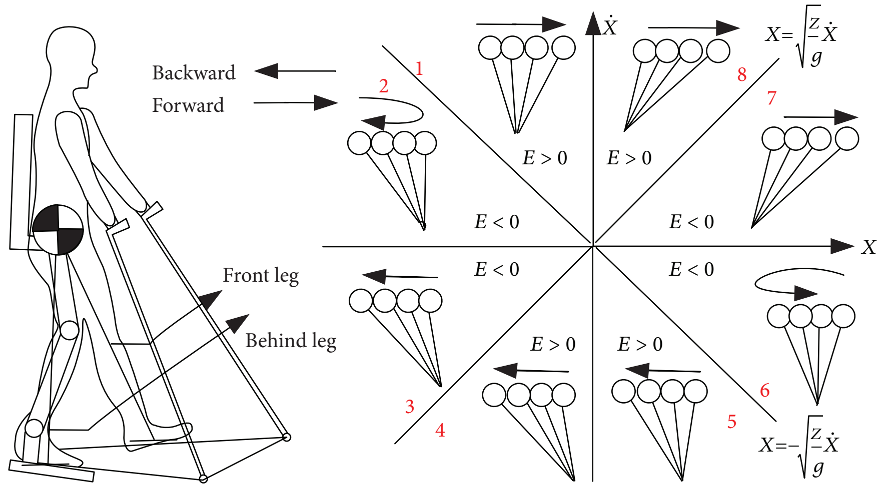

FIGURE 3: In double-support phase, state of human-exoskeleton system and orbital energy can be describe with the diagram with 8 quadrants.

where the third term can avoid jump movements at the beginning of each step. After obtaining the target function:

$$f_{\text{target}}(s) = \frac{\tau\dot{v} + Dv}{K} - (g - x) + (g - x_0)s, \tag{9}$$

the weighted parameters ω_i are able to learn via statistical learning methods. With specified start position x_0 and goal position g, the foot trajectories can be generated through the learn weights ω_i. In our approach, we first imitate trajectories of foot of swing leg in single-support phase $\{x(t), z(\mathrm{t})\}$ with a duration of 1 s. Then, as shown in Figure 4, we regenerate trajectories with different (S, T) by changing τ and g by following equations:

$$\begin{aligned} g_x &= S, \\ g_z &= 0, \\ \tau_{\text{new}} &= T\tau_{\text{original}}, \end{aligned} \tag{10}$$

where τ_{original} is the time constant of DMP learned before.

3.5. Discrete Gait Planner. Aiming to obtain balance gait, we define the concept of balance based on N-step capturability [18, 32]: the ability of a legged system to come to a stop without falling by taking N or fewer steps. As exoskeleton modeled by LIP, "stop" means orbital energy is 0 ($\dot{x} = 0$ when $x = 0$). Thus, the balance of exoskeleton is defined as: the orbital energy can be controlled to 0 with the limitation of swing speed and length of leg. In other words, as shown in Figure 5(a), if E is too large to decrease even extending swing leg with max speed, CoM of LIP will go to the limitation of stand leg and body rotate around the tip of toe as shown. However, walking with exoskeleton, patients can change orbital energy by applying external force with crutches. Thus, for walking easily, they expect to walk several steps continuously and smoothly without applying much force on exoskeleton. Therefore orbital energy needs to keep at a positive value.

To control orbital energy, we consider two steps as shown in Figure 5 and consider that the walking gait begins with

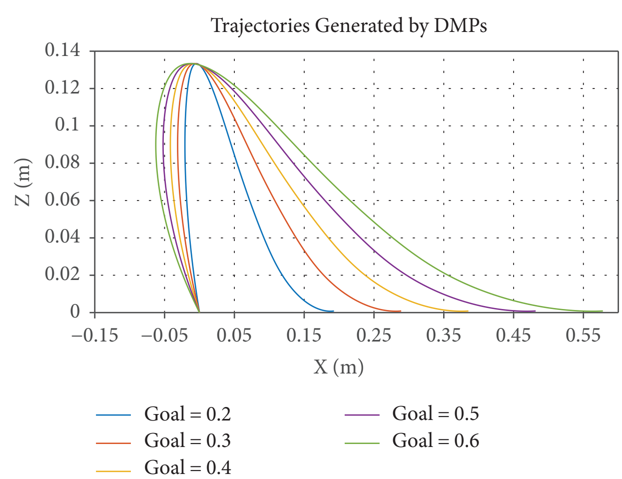

FIGURE 4: DMPs of foot trajectories with different parameters (S, T).

swing leg leaving the ground and end with contacting the ground. T denotes the time cost in this process called gait duration. In the first step, if no external force posed on LIP, we can obtain the $x_1(t)$ and $\dot{x}_1(t)$ and the E_1 with initial the $x_1(0)$ and $\dot{x}_1(0)$. At the moment of leg switching, velocity of CoM does not change ($\dot{x}_1(T) = \dot{x}_2(0)$) [22, 23]. Thus, we obtain orbital energy of second step as the following equation:

$$\frac{1}{2}\dot{x}_1{}^2(T) - \frac{g}{2z}(S - x_1(T))^2 = E_2, \tag{11}$$

where S is step length shown in Figure 5(b). With this equation, orbital energy of second step can be controlled by adjusting (S, T).

Given the aiming orbital energy E_2, the gait planer obtains (S, T) at each beginning of step. This planner is called discrete gait planner (DGP), since it plans the gait at the beginning of each step.

As the $x_1(t)$ and $\dot{x}_1(t)$ is the nonlinear function of t, we cannot solve it directly. Moreover, for a given targeting E_2, the mount of solutions is infinite. As we learn the trajectory

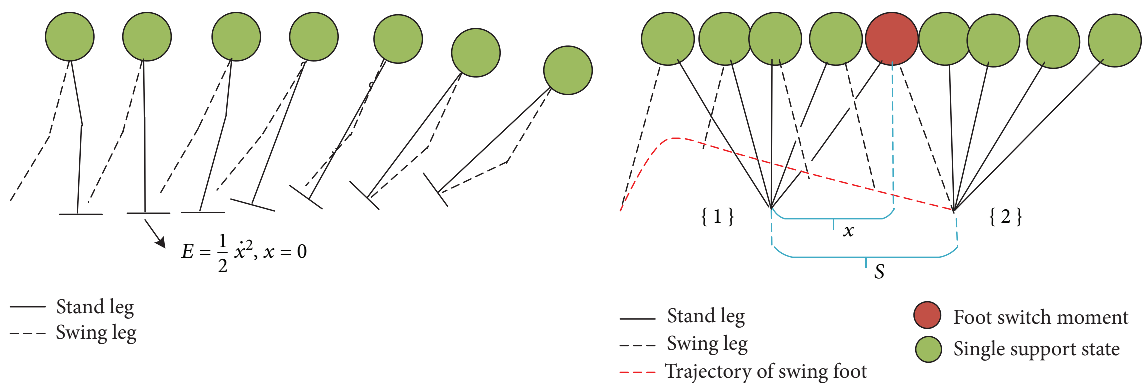

(a) When orbital energy is too large to decrease, LIP model falls down (b) Control orbital energy by changing step length S

Figure 5: Definition of balance with orbital energy.

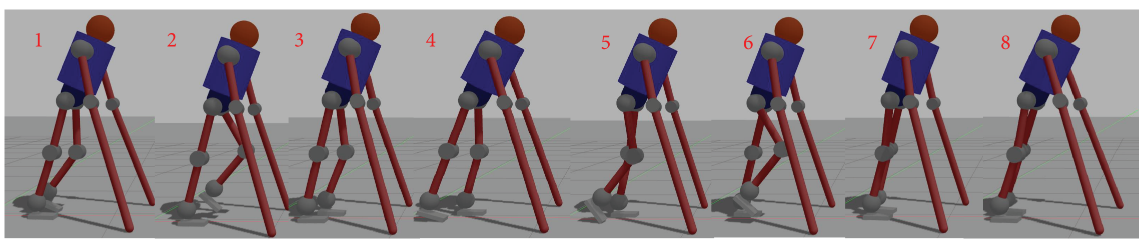

Figure 6: Snapshot of simulation during walking.

$(\widehat{S}, \widehat{T})$ recorded from healthy person, we expect that the trajectory regenerated by our approach is similar to the original one. Thus, we formulate this problem as optimization problem as follows.

$$\underset{S,T}{\operatorname{argmin}} \; J(S,T) = \alpha\left(\widehat{E} - E(T)\right)^2 + \beta\left(\widehat{S} - S\right)^2 + \gamma\left(\widehat{T} - T\right)^2$$
$$\text{s.t.}: \frac{S}{T} < v_{\max}, \quad S < S_{\max}, \quad T > T_{\min}, \tag{12}$$

where $\widehat{E}$, $\widehat{S}$, and $\widehat{T}$ are target values of orbital energy, step length, and duration of gait. α, β, and γ are weighted parameters. Gradient descent method is utilized to solve this optimization problem with gradient as follows:

$$P_i = P_{i-1} - \lambda \nabla J(S,T), \tag{13}$$

where $P_i = (S_i, T_i)^2$ and $\nabla J(s,t)$ is shown as follows:

$$\begin{pmatrix} \dfrac{\partial J}{\partial S} \\ \dfrac{\partial J}{\partial T} \end{pmatrix} = \begin{pmatrix} 2\beta\left(S - \widehat{S}\right) + \dfrac{2\alpha g}{z}\left(E(T) - \widehat{E}\right)\left(x(T) - S\right) \\ 2\alpha\left(E(T) - \widehat{E}\right)\dfrac{\dot{x}g}{z}(x+1) + \gamma\left(\widehat{T} - T\right) \end{pmatrix}. \tag{14}$$

Iterations of optimization ends with $\nabla J(S,T) = 0$ or numbers of iterations reach the limitation. If $\nabla J(S,T)$ is to 0 after iterations, we obtain the solution (S,T) closer to the targeting $\widehat{E}$ at this step. And E will be more closer to target $\widehat{E}$ step by step.

3.6. Continuous Gait Regulator. As we mentioned, DGP plans a gait at beginning of the step and adjust the orbital energy of the next step. After gait planning, trajectory of foot is fixed during a step. While, if a disturbance occurs during single-support phase, the gait cannot change until leg switching moment. Thus, we design a continuous gait regulator (CGR) to adjust the gait continuously during swing phase.

CGR adjusts gait by changing the parameters (S,T) obtained from discrete gait planner. It improve the DGP's ability of keeping balance. In each sample time i, we can obtain the $\dot{x}(i)$ and $x(i)$. We calculate (S_i, T_i) with the same optimal approach of DGP and update remain time T_{remain} of original trajectory generated by DGP. Then, we change the parameter of the DMPs with $g = S_i$ and $\tau = T_{\text{remain}}/T_i$.

4. Experiments on Simulation

In this section, we first lay down on the performance metrics definition and evaluate this approach in simulation platform.

4.1. Performance Metrics Definition. Evaluating the performance of proposed approach is to evaluate the ability of keeping balance especially when a disturbance occurs. As we mentioned before, balance of system is depended on the controllable ability of orbital energy. Thus, in our evaluation, we exert disturbance and compare orbital energy of different approaches during the whole process.

4.2. Simulator Introduction. We build a simulator to evaluate the performance of our approach in a desktop-computing platform with CPU:i7 4790 k and 8 G RAM with Gazebo robotics simulation software as shown in Figure 6. As the

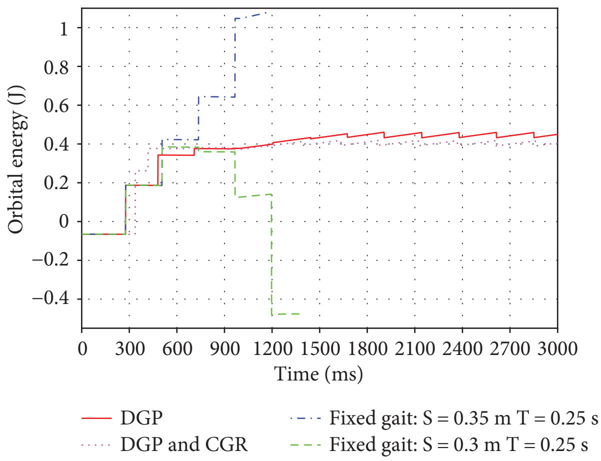

(a) Orbital energy of different gait patterns with external force 5 N

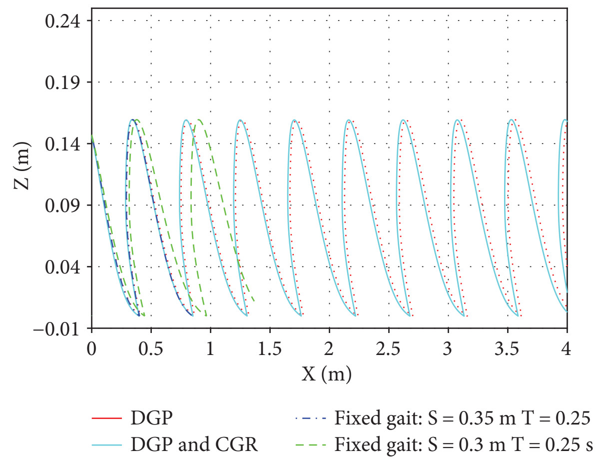

(b) Foot trajectories of different gait patterns with external force 5 N

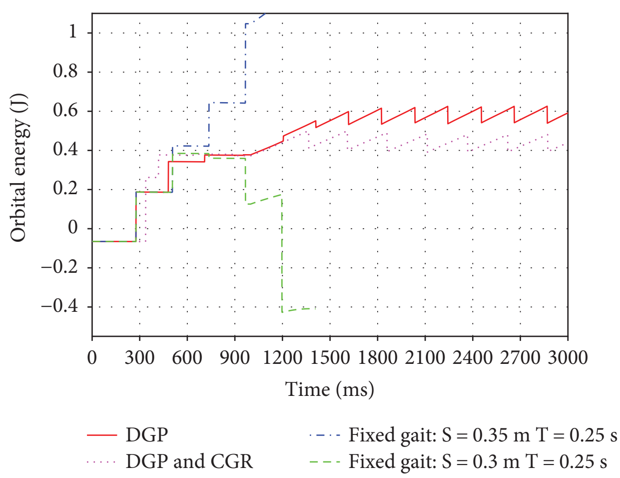

(c) Orbital energy of different gait patterns with external force 15 N

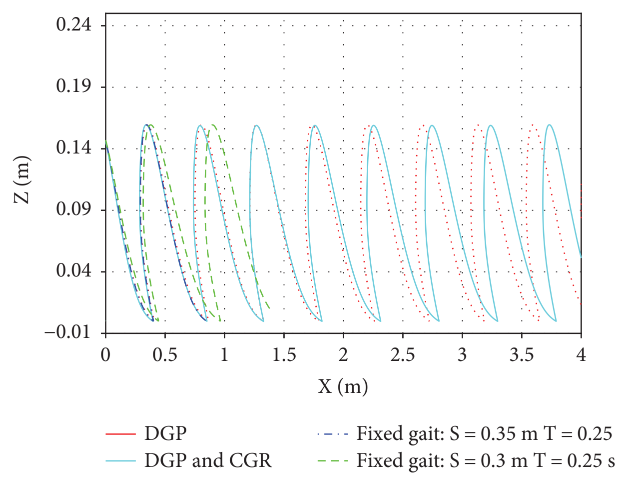

(d) Foot trajectories of different gait patterns with external force 15 N

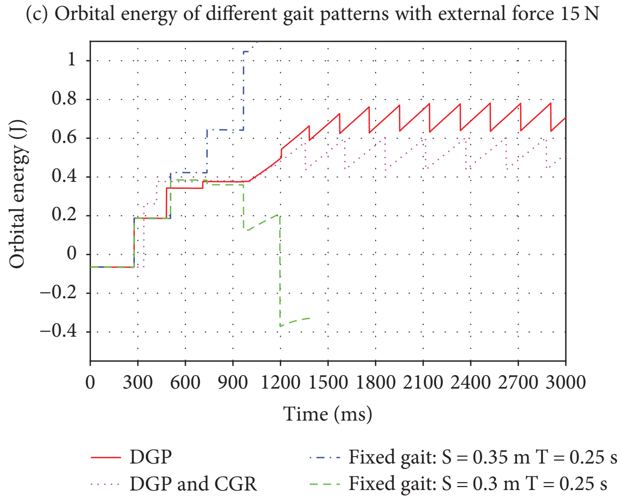

(e) Orbital energy of different gait patterns with external force 25 N

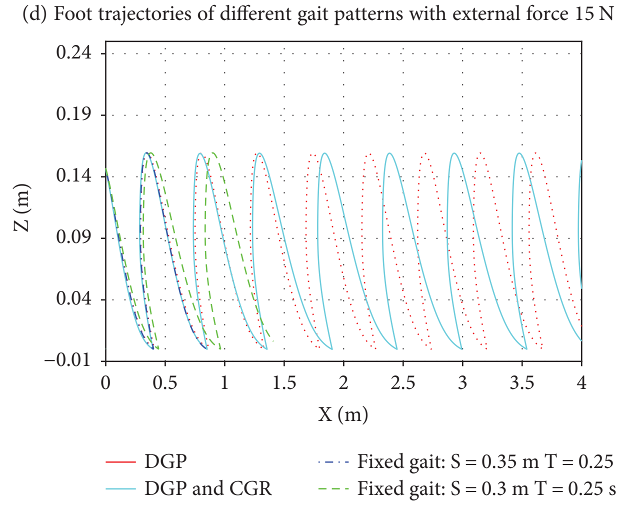

(f) Foot trajectories of different gait patterns with external force 25 N

Figure 7: Experimental results of different gait patterns with external force (5 N, 15 N, 25 N).

patient holds crutches to preserve falling sideways during normal walking, we model this coupled system as model shown in Figure 6 and constrain the motion in sagittal plane. In this model, hip joint (flexion/extension) and knee joint (flexion/extension) are actuated just like most of exoskeletons. PID controllers with 1000 Hz sample frequency are used in each joint with limitation of output torque 200 N.M. At each joint, joint encoders are embedded to obtain motion state of joints. We simulate 3000 ms in each trail with initial state of LIP: $x_{\text{init}} = 0.1$ m, $\dot{x}_{\text{init}} = 0.1$ m/s, $z = 0.7$ m. The

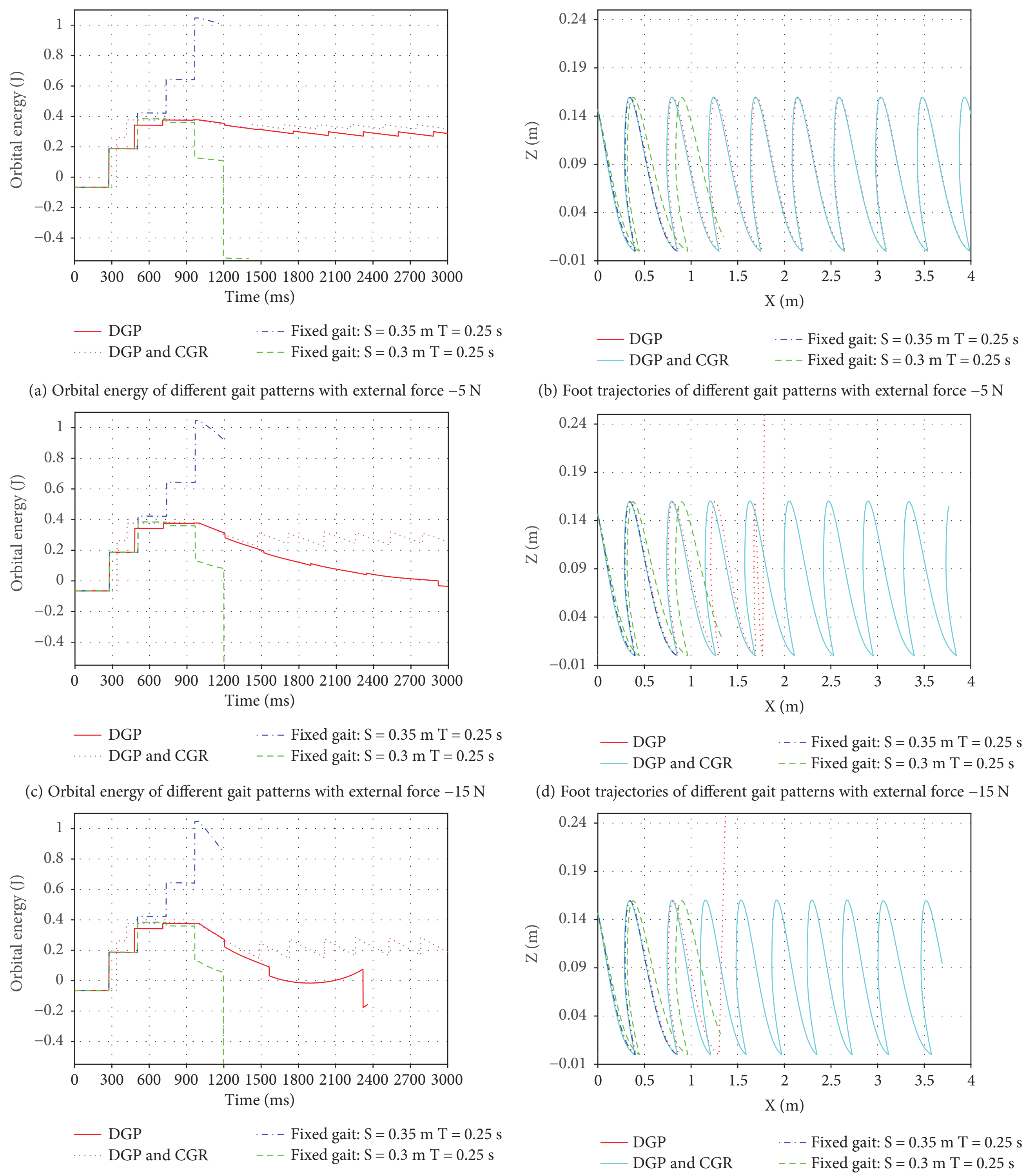

(a) Orbital energy of different gait patterns with external force −5 N

(b) Foot trajectories of different gait patterns with external force −5 N

(c) Orbital energy of different gait patterns with external force −15 N

(d) Foot trajectories of different gait patterns with external force −15 N

(e) Orbital energy of different gait patterns with external force −25 N

(f) Foot trajectories of different gait patterns with external force −25 N

Figure 8: Experimental results of different gait patterns with external force (−5 N, −15 N, and −25 N).

targeting orbital energy is set to be 0.4 J. Four gait patterns are compared in our experiment:

Gait with fixed parameters: $(S = 0.35, T = 0.25)$.

Gait with fixed parameters: $(S = 0.3, T = 0.25)$.

Gait generated by DGP.

Gait generated by DGP combined with CGR.

Different disturbance: −5 N, −15 N, −25 N, 5 N, 15 N, and 25 N in sagittal plane is posed on LIP from 500 ms to 2000 ms. A trail ends if the model falls down during walking. Orbital energy and foot transition of different gait patterns are recorded for evaluating the ability to keep balance.

4.3. Experiment Results. Figure 7 illustrates the simulation results of different gait patterns with positive external force as disturbance: 5 N, 15 N, and 25 N. With fixed gait pattern, the model of human-exoskeleton in simulation falls down forward after 5 steps. Patients have to control body with stick to keep balance with fixed gait. Both DGP and DGP combining with CGR can keep balance with disturbance from 5 N to 15 N. As disturbance increases, the error orbital energy of DGP increases significantly. With DGP alone, orbital energy of system cannot get back to given target after step taking. As shown in Figure 7(f), trajectory of swing foot trajectory generated by DGP combined with CGR adjusts the step length after encountering a disturbance. Thus, DGP combined with CGR achieves better performance than DGP in orbital energy control.

Simulation results with native external force as disturbance is shown in Figure 8. Walking with fixed gait model, the patient falls down without providing force to keep balance. With external force −5 N, gait generated by both DGP and DGP with CGR can achieve balance during the whole process. However, as shown in Figure 8(d) and 8(f), model will fall down with the external force increasing to −15 N. Compared to DGP, DGP with OGR can still achieve balance with disturbance (−25 N) and control the orbital energy close given value.

5. Conclusions and Future Works

In this paper, we proposed a novel approach to obtain dynamic balance gait. We model exoskeleton-human system with LIP and express gait trajectory with DMP. Three subsystems intention estimator, discrete gait planner, and continuous gait regulator, are designed. Intention estimator is designed based on the orbital energy diagram to get the intention to step forward or backward. With the intention of patient, discrete gait planner obtain the gait parameters (S, T) to keep balance. To improve the ability to counteract disturbance, continuous gait regulator is designed to change gait in time. Experiments on both simulation and real system with different environment demonstrate the efficiency of this approach.

In the future, we will firstly extend this approach to different environments. For example, external force would let the system lose balance during walking process, which is unacceptable. LIP should be modified with the changing height of model for upstairs walking situation. Then the ankle joints of exoskeletons for SCI patients are always passively actuated. Thus, LIP model with point foot is used to model exoskeleton-human system. However, spring damping system are employed in exoskeletons which should be taken into account.

Data Availability

Readers can access the data supporting this study by the clone git of this program: "https://gitee.com/kipochen_uestc/LIP_python.git" or from the corresponding author upon request.

Conflicts of Interest

The authors declare that there is no conflict of interests regarding the publication of this paper.

Acknowledgments

This research was supported by the National Natural Science Foundation of China (no. 61503060, 6157021026). This research was supported by the Fundamental Research Funds for the Central Universities (ZYGX2014Z009).

References

[1] World Health Organization, *Spinal Cord Injury*, July 2017, http://www.who.int/mediacentre/factsheets/fs384/en/.

[2] R. W. Teasell, J. T. Hsieh, J. A. Aubut, J. J. Eng, A. Krassioukov, and L. Tu, "Venous thromboembolism after spinal cord injury," *Archives of Physical Medicine and Rehabilitation*, vol. 90, no. 2, pp. 232–245, 2009.

[3] J. Cao, S. Q. Xie, R. Das, and G. L. Zhu, "Control strategies for effective robot assisted gait rehabilitation: the state of art and future prospects," *Medical Engineering and Physics*, vol. 36, no. 12, pp. 1555–1566, 2014.

[4] A. M. Dollar and H. Herr, "Lower extremity exoskeletons and active orthoses: challenges and state-of-the-art," *IEEE Transactions on Robotics*, vol. 24, no. 1, pp. 144–158, 2008.

[5] D. X. Liu, X. Wu, W. Du, C. Wang, C. Chen, and T. Xu, "Deep spatial-temporal model for rehabilitation gait: optimal trajectory generation for knee joint of lower-limb exoskeleton," *Assembly Automation*, vol. 37, no. 3, pp. 369–378, 2017.

[6] T. Yan, M. Cempini, C. M. Oddo, and N. Vitiello, "Review of assistive strategies in powered lower-limb orthoses and exoskeletons," *Robotics and Autonomous Systems*, vol. 64, pp. 120–136, 2015.

[7] X. Sun, Z. Li, H. Cheng, and H. Guo, "Compliant training control of ankle joint by exoskeleton with human emg-torque interface," *Assembly Automation*, vol. 37, no. 3, pp. 349–355, 2017.

[8] M. Talaty, A. Esquenazi, and J. E. Briceno, "Differentiating ability in users of the rewalk(tm) powered exoskeleton: an analysis of walking kinematics," in *2013 IEEE 13th International Conference on Rehabilitation Robotics (ICORR)*, pp. 1–5, Seattle, WA, USA, June 2013.

[9] K. A. Strausser and H. Kazerooni, "The development and testing of a human machine interface for a mobile medical exoskeleton," in *2011 IEEE/RSJ International Conference on Intelligent Robots and Systems*, pp. 4911–4916, San Francisco, CA, USA, September 2011.

[10] A. Tsukahara, Y. Hasegawa, K. Eguchi, and Y. Sankai, "Restoration of gait for spinal cord injury patients using hal with intention estimator for preferable swing speed," *IEEE Transactions on Neural Systems and Rehabilitation Engineering*, vol. 23, no. 2, pp. 308–318, 2015.

[11] L. Wang, S. Wang, E. H. F. V. Asseldonk, and H. V. D. Kooij, "Actively controlled lateral gait assistance in a lower limb exoskeleton," in *2013 IEEE/RSJ International Conference on Intelligent Robots and Systems*, pp. 965–970, Tokyo, Japan, November 2013.

[12] S. Wang, L. Wang, C. Meijneke et al., "Design and control of the mindwalker exoskeleton," *IEEE Transactions on Neural*

Systems and Rehabilitation Engineering, vol. 23, no. 2, pp. 277–286, 2015.

[13] A. L. Hof, "The 'extrapolated center of mass' concept suggests a simple control of balance in walking," *Human Movement Science*, vol. 27, no. 1, pp. 112–125, 2008.

[14] B. Stephens, "Humanoid push recovery," in *2007 7th IEEE-RAS International Conference on Humanoid Robots*, pp. 589–595, Pittsburgh, PA, USA, December 2007.

[15] B. Ugurlu, C. Doppmann, M. Hamaya et al., "Variable ankle stiffness improves balance control: experiments on a bipedal exoskeleton," *IEEE/ASME Transactions on Mechatronics*, vol. 21, no. 1, pp. 1–87, 2016.

[16] A. L. Hof, M. G. Gazendam, and W. E. Sinke, "The condition for dynamic stability," *Journal of Biomechanics*, vol. 38, no. 1, pp. 1–8, 2005.

[17] V. Huynh, C. Bidard, and C. Chevallereau, "Balance control for an underactuated leg exoskeleton based on capture point concept and human balance strategies," in *2016 IEEE-RAS 16th International Conference on Humanoid Robots (Humanoids)*, pp. 483–488, Cancun, Mexico, November 2016.

[18] J. Pratt, T. Koolen, T. D. Boer et al., "Capturability-based analysis and control of legged locomotion, part 2: application to m2v2, a lower-body humanoid," *The International Journal of Robotics Research*, vol. 31, no. 10, pp. 1117–1133, 2012.

[19] J. Pratt, J. Carff, S. Drakunov, and A. Goswami, "Capture point: a step toward humanoid push recovery," in *2006 6th IEEE-RAS International Conference on Humanoid Robots*, pp. 200–207, Genova, Italy, December 2006.

[20] M. A. Gomes, G. L. M. Silveira, and A. A. G. Siqueira, "Gait-pattern adaptation algorithms based on neural network for lower limbs active orthoses," in *IEEE/RSJ International Conference on Intelligent Robots and Systems*, pp. 4475–4480, St. Louis, MO, USA, October 2009.

[21] Q. Huang, K. Yokoi, S. Kajita, and K. Kaneko, "Planning walking patterns for a biped robot," *IEEE Transactions on Robotics and Automation*, vol. 17, no. 3, pp. 280–289, 2002.

[22] S. Kajita, F. Kanehiro, K. Kaneko, and K. Fujiwara, "A realtime pattern generator for biped walking," in *Proceedings 2002 IEEE International Conference on Robotics and Automation (Cat. No.02CH37292)*, vol. 1, pp. 31–37, Washington, DC, USA, May 2002.

[23] S. Kajita, F. Kanehiro, K. Kaneko, K. Yokoi, and H. Hirukawa, "The 3d linear inverted pendulum mode: a simple modeling for a biped walking pattern generation," in *Proceedings 2001 IEEE/RSJ International Conference on Intelligent Robots and Systems. Expanding the Societal Role of Robotics in the the Next Millennium (Cat. No.01CH37180)*, vol. 1, pp. 239–246, Maui, HI, USA, November 2001.

[24] S. Kajita and K. Tani, "Study of dynamic biped locomotion on rugged terrain-derivation and application of the linear inverted pendulum mode," in *Proceedings. 1991 IEEE International Conference on Robotics and Automation*, vol. 2, pp. 1405–1411, Sacramento, CA, USA, April 1991.

[25] P. H. Channon, S. H. Hopkins, and D. T. Pham, "Derivation of optimal walking motions for a bipedal walking robot," *Robotica*, vol. 10, no. 2, pp. 165–172, 1992.

[26] M. Rostami and G. Bessonnet, "Impactless sagittal gait of a biped robot during the single support phase," in *Proceedings. 1998 IEEE International Conference on Robotics and Automation (Cat. No.98CH36146)*, vol. 2, pp. 1385–1391, Leuven, Belgium, May 1998.

[27] L. Roussel, C. Canudas-De-Wit, and A. Goswami, "Generation of energy optimal complete gait cycles for biped robots," in *Proceedings. 1998 IEEE International Conference on Robotics and Automation (Cat. No.98CH36146)*, vol. 3, pp. 2036–2041, Leuven, Belgium, May 1998.

[28] S. Schaal, "Dynamic movement primitives -a framework for motor control in humans and humanoid robotics," in *Adaptive Motion of Animals and Machines*, H. Kimura, K. Tsuchiya, A. Ishiguro, and H. Witte, Eds., Springer, Tokyo, 2006.

[29] A. J. Ijspeert, J. Nakanishi, S. Schaal, S. Becker, S. Thrun, and K. Obermayer, "Learning attractor landscapes for learning motor primitives," *Advances in Neural Information Processing Systems*, vol. 15, pp. 1547–1554, 2002.

[30] A. J. Ijspeert, J. Nakanishi, and S. Schaal, "Trajectory formation for imitation with nonlinear dynamical systems," in *Proceedings 2001 IEEE/RSJ International Conference on Intelligent Robots and Systems. Expanding the Societal Role of Robotics in the the Next Millennium (Cat. No.01CH37180)*, vol. 2, pp. 752–757, Maui, HI, USA, November 2001.

[31] P. Pastor, H. Hoffmann, T. Asfour, and S. Schaal, "Learning and generalization of motor skills by learning from demonstration," in *2009 IEEE International Conference on Robotics and Automation*, pp. 763–768, Kobe, Japan, May 2009.

[32] T. Koolen, T. D. Boer, J. Rebula, A. Goswami, and J. Pratt, "Capturability-based analysis and control of legged locomotion, part 1: theory and application to three simple gait models," *The International Journal of Robotics Research*, vol. 31, no. 9, pp. 1094–1113, 2012.

Hindawi
Applied Bionics and Biomechanics
Volume 2018, Article ID 2719631, 15 pages
https://doi.org/10.1155/2018/2719631

Research Article

A New Skeleton Model and the Motion Rhythm Analysis for Human Shoulder Complex Oriented to Rehabilitation Robotics

Song Zhibin , Ma Tianyu, Nie Chao, and Niu Yijun

Key Laboratory of Mechanism Theory and Equipment Design of Ministry of Education, Tianjin University, Tianjin 300072, China

Correspondence should be addressed to Song Zhibin; songzhibin@tju.edu.cn

Received 28 November 2017; Revised 23 February 2018; Accepted 13 March 2018; Published 3 June 2018

Academic Editor: Dongming Gan

Rehabilitation robotics has become a widely accepted method to deal with the training of people with motor dysfunction. In robotics medium training, shoulder repeated exercise training has been proven beneficial for improving motion ability of human limbs. An important and difficult paradigm for motor function rehabilitation training is the movement rhythm on the shoulder, which is not a single joint but complex and ingenious combination of bones, muscles, ligaments, and tendons. The most robots for rehabilitation were designed previously considering simplified biomechanical models only, which led to misalignment between robots and human shoulder. Current biomechanical models were merely developed for rehabilitation robotics design. This paper proposes a new hybrid spatial model based on joint geometry constraints to describe the movement of the shoulder skeletal system and establish the position analysis equation of the model by a homogeneous coordinate transformation matrix and vector method, which can be used to calculate the kinematics of human-robot integrated system. The shoulder rhythm, the most remarkable particularity in shoulder complex kinematics and important reference for shoulder training strategy using robotics, is described and analyzed via the proposed skeleton model by three independent variables in this paper. This method greatly simplifies the complexity of the shoulder movement description and provides an important reference for the training strategy making of upper limb rehabilitation via robotics.

1. Introduction

Rehabilitation robots have received increasing interest to provide rehabilitative therapy following neurological injuries such as stroke and spinal cord injury [1]. The shoulder is one of the most complex motor function areas of the human body, which has a direct impact on the recovery of upper limb motor function. When a shoulder has motor dysfunction caused by injury or disease, it often needs reasonable rehabilitation suitable for the specific conditions of the patient. For this situation, some studies have shown that a rehabilitation strategy based on task orientation that fuses high intensity repetitive exercise training will be very conducive to the improvement of athletic ability, which is one of the most effective rehabilitation methods [2–7], while the upper limb rehabilitation robot is a universally acknowledged effective way to carry out the rehabilitation strategy.

There are lots of robotics proposed currently for lower limb and upper limb rehabilitation. Most of them got fruitful achievement even though accurate motion information of bones and muscles was not considered thoroughly. There have been many attempts in robotics which evolved from a simplified 3-degrees of freedom (DoF) ball and socket, such as Carignan and Liszka [8] who have defined the shoulder as a 3-DoF ball-and-socket joint. However, it is not effective for a shoulder rehabilitation using exoskeleton robotics which has three orthogonal axes intersecting at one point to assume shoulder as a ball-and-socket joint, because the shoulder cannot be regarded as a single joint but complex and ingenious combination of bones, muscles, ligaments, and tendons. The remarkable characteristic of the shoulder complex is the movement rhythm involving the motion of the scapula, clavicle, and humerus. The rhythm analysis is important and necessary for shoulder complex rehabilitation training.

Biomedical researchers have done a lot of analysis on musculoskeletal models for shoulder training. In 1965, Dempster [9] established a simple two-dimensional series link model to describe the relative motion characteristics among bones of the shoulder; however, the model only has existing qualitative description, lacking the description with definition and quantitative analysis of the joint type. Engin and Chen [10] established a three-dimensional 6-DoF rigid-body model of the humerus relative to the human torso in 1986. Furthermore, Engin and Tumer increased the degrees of freedom of the shoulder complex model to 9 in 1989. Although Engin and Chen established a three-dimensional model of shoulder bones to analyze their kinematic characteristics, the series connection of the shoulder, without exception, simplified the scapula into two connecting rods that are connected to the clavicle and humerus.

There are complicated models in the shoulder joint. Garner and Pandy [11] established a 13-DoF human upper limb skeleton model in 1999. The model does not define the geometric constraints of the scapulothoracic articulation joint (ST) nor analyze the motion of the model. Based on the concept of this model, Maurel and Thalmann and Maurel et al. [12, 13] treat the ST joint as a single point contacting with the surface with 5 DoFs, but the study lacks systemic analysis. Tondu [14] proposed a similar shoulder mechanism model in 2005, which defines the ST joint as a planar subordinate on the basis of the Maurel model and ignores the rotational freedom of the sternoclavicular joint (SC) along the direction of the clavicle axis, modeling the shoulder girdle as a 2-DoF spatial parallel mechanism. This model simplifies the difficulty of analyzing shoulder girdles. In order to make the shoulder get a larger workspace and more activity, Lenarcic and Stanisic [15] in 2006 proposed a shoulder girdle skeleton system using a six-legged six-joint parallel mechanism to deal with the simulation, but it is difficult to determine the position of each joint and the length of the parallel bars corresponding to the actual shoulder girdle. It is also difficult to correspond to the movement of a single individual bone.

The current rehabilitation robots were designed with a simplified skeleton model and set the degrees of freedom such as the robotic-arm exoskeleton proposed by Klein et al. [16]. Therefore, this paper provides a suitable model that describes the shoulder complex motion via a model of a spatial hybrid mechanism with four rods and four joints and verifies the accuracy of the model through real data for rehabilitation robots in the shoulder joint. Among them, SC joint, acromioclavicular (AC) joint, and glenohumeral (GH) joint are all defined as spherical hinge joints, and the thorax is approximated as an ellipsoid. The constraint of the ST joint is defined as the two fixed points on the suprascapular connected to the thorax ellipsoid in a point contact constraint, and the rotation of the SC joint around the clavicular axis is considered to be an extra DoF.

2. Modeling and Analysis

In the model of the shoulder musculoskeletal dynamics, the posture analysis of the bones constituting the shoulder is the basis for shoulder motion analysis, muscle drive characteristics, muscle strength, and joint force analysis. Due to the complexity of the shoulder skeletal system, it is difficult to obtain the people's posture of the shoulder bone quickly by using the commonly used real-time skeleton marking method. Based on results provided by Garner and Pandy [11, 17] for the anatomical results of human shoulder geometry, the human shoulder skeleton system is simplified as a hybrid spatial mechanism model to simulate and analyze the movement of the shoulder bone. The motions of each joint and bone are described by defining the local coordinate systems fixed on the corresponding bones, and the position inverse analysis of the mechanism is completed by the homogeneous coordinate transfer matrix and vector method, which simplified the analysis and prediction of the shoulder skeleton configuration. Finally, this chapter verifies the rationality of the model through the experiment of the actual human shoulder.

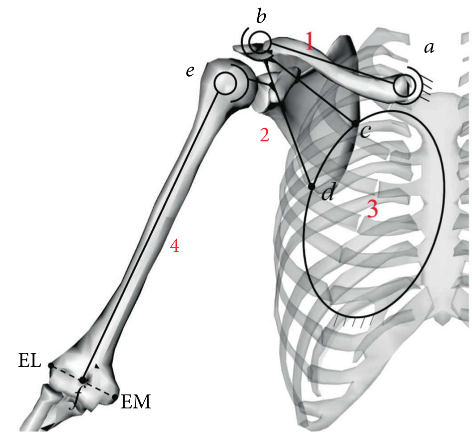

Figure 1: Schematic diagram of the shoulder mechanism.

2.1. A Proposed Model of Shoulder Skeleton System. The kinematics of the shoulder of the human body mainly depends on the skeleton system composed of the shoulder girdle and humerus compared with the muscle system and the tendon system, so in this paper, the skeleton system for the shoulder is mainly discussed. It can be considered a closed-loop rigid system composed of the thorax, clavicle, and scapula. Joints involved in shoulder movement involve the AC joint, the SC joint, the ST joint, and the GH joint.

In this paper, a hybrid spatial mechanism model is used to simulate the shoulder skeletal system, as shown in Figure 1. In this model, the SC joint, the AC joint, and the GH joint are denoted as a, b, and e, respectively, and are treated as the ideal 3-DoF ball-and-socket joint. The scapula achieves two-point contact with the thoracic ellipsoid surface through its medial lateral edge c and d, which may be equivalent to cylindrical-planar pairs with 4 DoFs. Among them, components 1, 2, 3, and 4 represent the clavicle, the scapula, the thoracic surface, and the humerus of the upper arm, respectively. The long axis of the humerus represents component 4, that is, the direction of connecting the center of the GH joint e and the center of the elbow f, where the elbow joint f is defined as the midpoint of the outer lateral ankle EL and the inside ankle EM.

2.2. Kinematics Analysis of the Proposed Model. In the above mechanism model, components 1, 2, 3, and 4 constitute a hybrid spatial mechanism containing a closed chain and an open chain, where components 1, 2, and 3 form a closed-loop chain.

2.2.1. To Calculate DoFs of the Proposed Mechanism. To obtain the kinematics of the mechanism, we should first analyze its DoFs. For the closed loop of the shoulder girdle, the DoF of the mechanism (M) is obtained by the Kutzbach-Grubler formula [18].

$$M = 6(n - g - 1) + \sum_{i=1}^{g} f_i, \tag{1}$$

where n is the number of mechanism components, g is the number of joints, and f_i is the relative freedom of the *ith* motion pair. The closed-loop part has three components and three motion pairs. Both SC and AC are ball-and-socket joints with 3 DoF. The ST joint is a cylinder-plane pair with 4 DoF. So a closed chain with 4 DoF in the shoulder joint system can be obtained. Considering the humerus movement, the total degree of freedom of the shoulder is up to 7. However, in the process of activity of the shoulder, the rotation of the clavicle around its axis is very small and it has an internal DoF that does not change the whole posture of link 4 [19–21]. Therefore, for joint a, the rotation in the direction of the winding of component 2 is an extra freedom. If the rotation angle is known, the motion posture of the shoulder girdle can be obtained by inputting three joint variables.

2.2.2. To Establish Shoulder Global Coordinate and Local Coordinates Fixed to a Single Bone. In order to describe and analyze the kinematics of the skeleton model of the shoulder complex, every bone is fixed to one coordinate system, as shown in Figure 2. The origin point of the global coordinate system $S_o = \{a - x_0 y_0 z_0\}$ is the SC joint at point a, and axes x_0, y_0, and z_0 are, respectively, parallel to three intersections of the human anatomical coronal plane, the sagittal plane, and the transverse plane. For the clavicle system $S_1 = \{a - x_1 y_1 z_1\}$, the origin is located on the SC joint at point a. The z_1 axis is in the direction of the clavicle axis, and the x_1 axis is defined on the horizontal plane and perpendicular to z_1. For the scapular system $S_2 = \{b - x_2 y_2 z_2\}$, its origin point is located at the point of the AC joint at b, where the z_2 axis is in the direction from b to the medial margin of the scapula c and the direction of x_2 is perpendicular to the plane determined by points b, c, and d. S_3 is parallel to S_0. For the humeral coordinate system $S_4 = \{e - x_4 y_4 z_4\}$, the origin point is located at the center e of the glenoid joint, where the z_4 axis is in the direction from f to e; the y_4 axis is perpendicular to the plane determined by point e, EL, and EM; and the x_4 axis is determined by the right-hand rule.

2.2.3. Kinematics Analysis of the Joints in the Shoulder. In the shoulder girdle, the thorax, the clavicle, and the scapula are interconnected with each other through the joints SC, AC, and ST, thus forming a closed-loop mechanism. For the closed-chain mechanism, position analysis can be attributed to determine the remaining joint variables and skeletal posture using the known mechanism geometric parameters and at least three joint variables as inputs. In this paper, the purpose of inverse analysis is to verify the accuracy of the actual shoulder movement predicted by the model.

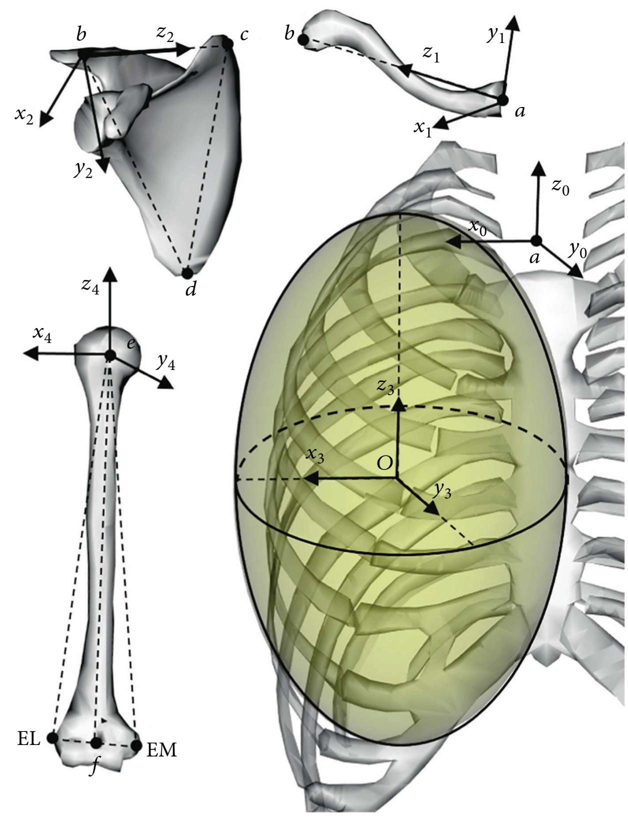

Figure 2: Shoulder bony segments and related reference frames.

In order to describe the matrix conveniently, the distance between joint a and joint b is set as l_1, the distance between the center of joint b and point c is l_2, the distance between b and point d is l_3, and the length of the humerus is l_4.

According to the above definition for the coordinate system, transition from the system $S_o = \{a - x_0 y_0 z_0\}$ to $S_1 = \{a - x_1 y_1 z_1\}$, namely, the motion of the thorax relative to the thorax, can be expressed via the following matrix:

$$\begin{aligned} {}^{0}_{1}\mathbf{T} &= \mathrm{Rot}(z, \theta_1)\mathrm{Rot}(y, \theta_2)\mathrm{Rot}(z, \theta_3) \\ &= \begin{bmatrix} c\theta_1 c\theta_3 - s\theta_1 c\theta_2 s\theta_3 & -c\theta_1 s\theta_3 - s\theta_1 c\theta_2 c\theta_3 & s\theta_1 s\theta_2 & 0 \\ s\theta_1 c\theta_3 + c\theta_1 c\theta_2 s\theta_3 & -s\theta_1 s\theta_3 + c\theta_1 c\theta_2 c\theta_3 & -c\theta_1 s\theta_2 & 0 \\ s\theta_2 s\theta_3 & s\theta_2 c\theta_3 & c\theta_2 & 0 \\ 0 & 0 & 0 & 1 \end{bmatrix}, \end{aligned} \tag{2}$$

where s and c denote sine and cosine, respectively.

The conversion from system S_1 to system S_2 can be assumed to have moved l_1 along the z-axis firstly and rotated

θ_4 around the y-axis, then rotated θ_5 around the x-axis, and finally rotated θ_5 around the y-axis. The conversion matrix is

$$
{}_2^1\mathbf{T} = \mathrm{Trans}(z, l_1)\mathrm{Rot}(y, \theta_4)\mathrm{Rot}(x, \theta_5)\mathrm{Rot}(y, \theta_6)
= \begin{bmatrix} c\theta_4 c\theta_6 - s\theta_4 c\theta_5 s\theta_6 & s\theta_4 s\theta_5 & c\theta_4 s\theta_6 + s\theta_4 c\theta_5 c\theta_6 & 0 \\ s\theta_5 s\theta_6 & c\theta_5 & -s\theta_5 c\theta_6 & 0 \\ -s\theta_4 c\theta_6 - c\theta_4 c\theta_5 s\theta_6 & c\theta_4 s\theta_5 & -s\theta_4 s\theta_6 + c\theta_4 c\theta_5 c\theta_6 & l_1 \\ 0 & 0 & 0 & 1 \end{bmatrix}. \tag{3}
$$

The position and scale of the thoracic ellipsoid are known. Assuming that the position of the ellipsoid center point O in the fixed system S_0 is ${}^0P_O = [x_0, y_0, z_0, 1]^T$, the transfer matrix of ellipsoid S_3 relative to fixed system S_0 is

$$
{}_3^0\mathbf{T} = \begin{bmatrix} 1 & 0 & 0 & x_0 \\ 0 & 1 & 0 & y_0 \\ 0 & 0 & 1 & z_0 \\ 0 & 0 & 0 & 1 \end{bmatrix}. \tag{4}
$$

If the semilong axes of the ellipsoid are, respectively, m, n, and p and point c and point d are located in the thoracic ellipsoid table surface, the position coordinates can be represented by the parametric equation of the ellipsoid:

$$
{}^3P_c = [\, m \sin\varphi_c \cos\varphi_c \quad n \sin\varphi_c \cos\varphi_c \quad p \cos\varphi_c \quad 1\,]^T, \tag{5}
$$

$$
{}^3P_d = [\, m \sin\varphi_d \cos\varphi_d \quad n \sin\varphi_d \cos\varphi_d \quad p \cos\varphi_d \quad 1\,]^T, \tag{6}
$$

where φ_c, ϕ_c, φ_d, and ϕ_d in the formula, respectively, describes the position parameters of point c and point d. Point c and point d are also located on the shoulder blade, as shown in Figure 3. The position coordinates of c and d in the scapula system are

$$
\begin{aligned} {}^2P_c &= [\,0 \quad 0 \quad l_2 \quad 1\,]^T, \\ {}^2P_d &= [\,0 \quad l_3 \sin\gamma \quad l_3 \cos\gamma \quad 1\,]^T, \end{aligned} \tag{7}
$$

where γ in the formula is the included angle of $\overrightarrow{bc}$ and $\overrightarrow{bd}$, because points b, c, and d are all on the scapula, and l_2, l_3, and γ are constant. In summary, using the location transform relationship of c and d, the establishment of displacement constraint equation is as follows:

$$
\begin{aligned} {}^0P_c &= {}_1^0T_2^1T^2p_c = {}_3^0T^3p_c, \\ {}^0P_d &= {}_1^0T_2^1T^2p_d = {}_3^0T^3p_d. \end{aligned} \tag{8}
$$

Formula (8) above can be expressed as follows:

$$
\begin{aligned} {}_1^0T_2^1T^2p_c - {}_3^0T^3p_c &= 0, \\ {}_1^0T_2^1T^2p_d - {}_3^0T^3p_d &= 0. \end{aligned} \tag{9}
$$

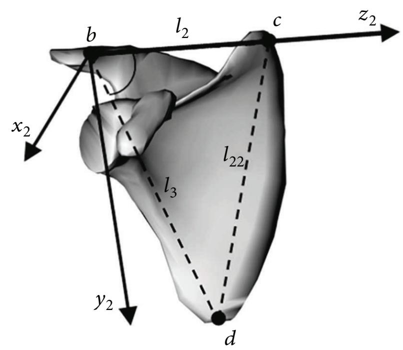

Figure 3: Points c and d located on the scapula.

Equation (9) is the joint position solution constraint equation of the girdle mechanism. Let each component be zero; the equations can be transformed into 6 constraint equations which contain a total of $\theta_1 \sim \theta_6, \varphi_c, \phi_c, \varphi_d, \phi_d$ 10 joint variables. Clavicle rotation around its own axis z_1 is an extra degree of freedom, and if θ_3 is zero, just any three rotational variables can be used as inputs to solve the remaining variables.

The kinematic analysis of the shoulder girdle is completed, while the humerus is connected to the shoulder complex through the GH joint as the end of execution. The motion posture of the upper arm is usually studied in the global reference system, using the ISB standard recommended by Wu and Cavanagh [22, 23] to describe the posture of the humerus. The rotation matrix applied to convert the global system S_0 into the humerus system S_4 is

$$
{}_4^0\mathbf{R} = \mathrm{Rot}(y, \theta_7)\mathrm{Rot}(x, \theta_8)\mathrm{Rot}(z, \theta_9)
= \begin{bmatrix} c\theta_7 c\theta_9 - s\theta_7 c\theta_8 s\theta_9 & s\theta_7 s\theta_8 & c\theta_7 c\theta_9 + s\theta_7 c\theta_8 s\theta_9 & 0 \\ s\theta_8 s\theta_9 & c\theta_8 & -s\theta_8 c\theta_9 & 0 \\ -s\theta_7 c\theta_9 - c\theta_7 c\theta_8 s\theta_6 & c\theta_7 s\theta_8 & -s\theta_7 c\theta_9 + c\theta_7 c\theta_8 s\theta_9 & 0 \\ 0 & 0 & 0 & 1 \end{bmatrix}. \tag{10}
$$

If the position of the GH center coordinates ${}^0P_e = [\,x_e \quad y_e \quad z_e \quad 1\,]^T$ is given, the conversion matrix for the translation from the humeral system S_0 to the global system S_4 is

$$
\begin{bmatrix} c\theta_7 c\theta_9 - s\theta_7 c\theta_8 s\theta_9 & s\theta_7 s\theta_8 & c\theta_7 c\theta_9 + s\theta_7 c\theta_8 s\theta_9 & x_e \\ s\theta_8 s\theta_9 & c\theta_8 & -s\theta_8 c\theta_9 & y_e \\ -s\theta_7 c\theta_9 - c\theta_7 c\theta_8 s\theta_6 & c\theta_7 s\theta_8 & -s\theta_7 c\theta_9 + c\theta_7 c\theta_8 s\theta_9 & z_e \\ 0 & 0 & 0 & 1 \end{bmatrix}. \tag{11}
$$

2.3. Verification for Shoulder Skeletal Motion Based on Reference Data. In this paper, the size of shoulder bones

Table 1: The size parameters of each link of mechanism model.

l_1	l_2	l_3	l_{22}	l_4	γ
154.17 mm	120.71 mm	187.21 mm	109.83 mm	301.56 mm	33.8°

refers to the anatomical data of human upper arm bones and joints obtained by Garner and Pandy [11, 17, 24]. Shoulder Database V1.1, published by Bolsterlee et al. [21] in 2014, is used as a reference source of shoulder motion data. Then, through the joint displacement constraint equations obtained above, the movement of the mechanism is analyzed by using Matlab.

2.3.1. Shoulder Mechanism Geometry. In this paper, the size of the mechanism is based on the anatomy of human bones and joints obtained by Garner and Pandy; the size of each component shown in Figure 1 is as shown in Table 1 below. The semimajor axis of the thorax ellipsoid and the center point of its ellipsoid are shown in Table 2. The coordinates of the center point are in the fixed system S_0.

The position of GH joint center in the scapular S_2 is ${}^2p_e = [-0.29 \quad 43.71 \quad 3.41 \quad 1]^T$.

2.3.2. Description of Shoulder Joint Movement. The local coordinate system of each skeleton in Figure 2 is defined to be calculated conveniently. The ISB standards recommended by Wu and Cavanagh and Wu et al. [22, 23] are widely used in biomedical engineering to describe the human upper body bones and joints in the movement. In the ISB standard, the local coordinate system of the shoulder bones and the bony landmark are shown in Figure 4.

In this paper, the shoulder skeletal configuration analysis results and experimental measurements which are unified according to the ISB standard will be compared; therefore, it is necessary to figure out the corresponding relationship between the calculation of the coordinate system and the ISB coordinate system. Klein Breteler et al. [25] obtained a more favorable shoulder morphological datasets by dissecting the body of a 57-year-old male and establishing a universal dataset of human shoulder bones. Table 3 shows the relevant parameters of bone markers and the size of the thorax of the general model and the experimental subjects in this article. All the coordinates are converted corresponding to the thorax system; the length unit is mm.

Through the definition of each local coordinate system and the characteristic sizes of each marked point of the shoulder skeleton in Tables 2 and 3, the relationship between the coordinate systems S_0, S_1, S_2, and S_4 used in the above calculation and each coordinate system S_t, S_c, S_s, and S_h recommended in ISB standard can be described by the following rotation transformation matrix:

$$ {}^t_0\mathbf{R} = \begin{bmatrix} 0 & 1 & 0 \\ 0 & 0 & 1 \\ 1 & 0 & 0 \end{bmatrix}, \tag{12} $$

Table 2: The size parameters of thorax ellipsoid (mm).

m	n	p	${}^0p_o$
76.85	97.17	217.44	$[28.12 \quad -43.90 \quad -164.51 \quad 1]^T$

$$ {}^c_1\mathbf{R} = \begin{bmatrix} 1 & 0 & 0 \\ 0 & 1 & 0 \\ 0 & 0 & 1 \end{bmatrix}, \tag{13} $$

$$ {}^s_2\mathbf{R} = \begin{bmatrix} 0.9599 & 0.0373 & -0.2778 \\ -0.0131 & -0.9841 & -0.1773 \\ -0.2800 & -0.1738 & -0.9441 \end{bmatrix}, \tag{14} $$

$$ {}^h_4\mathbf{R} = \begin{bmatrix} 0 & 1 & 0 \\ 0 & 0 & 1 \\ 1 & 0 & 0 \end{bmatrix}. \tag{15} $$

2.3.3. Definition of Shoulder Experimental Motion. Shoulder Database (Shoulder Database V1.1) published by Bolsterlee et al. in 2014 provides data of shoulder motion which has been used in the analysis [21, 26]. The experiment collected data from five healthy adult males. This article selects one of the objects S_1 (age 29, height 186 cm, and weight 109 kg) from the database. The experiment used a set of motion detection system (Optotrak System, Northern Digital Inc., Waterloo, Ontario, Canada) to detect the spatial positions of six marker groups fixed to the thorax, scapula, humerus, forearm, and palm shown in Figure 5. The locations of the bone markers are arranged according to ISB standard, and the series of the position of the markers are collected at a frequency of 100 Hz.

In order to get accurate shoulder movement data, during the experiment, the subject was asked to complete the range of motion (ROM) tasks including shoulder abduction (ABD), flexion (FLEX), and scapular plane movement (SCAP) which contain all the basic movement of the shoulder shown in Table 4. With processing, the data of the movement posture of each bone in the shoulder can be uniformly converted into the value in S_t.

2.3.4. The Solution and Verification for Posture and Position of Each Bone. Through the processing of the spatial coordinates of each marker measured in the experiment, the joint variables $\theta_1, \theta_2, \phi_d$ are obtained, and the three independent joint displacements are used as input, and then the remaining six joint variables $\theta_4, \theta_5, \theta_6, \varphi_d, \phi_c, \varphi_c$ are obtained, as well as the shoulder girdle movement gesture, which is finally compared with the experimental measurement results.

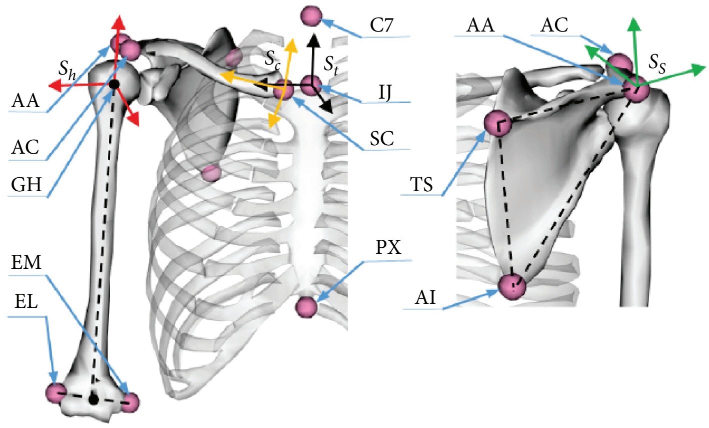

FIGURE 4: The bony landmarks and local coordinate systems defined in ISB.

TABLE 3: The skeletal feature size parameters of the experimental subjects (mm).

Bone markers	Common parameters	Test subject
IJ	(0, 0, 0)	(0, 0, 0)
PX	(31.9, −132.7, −9.8)	(56.0, −163.0, −2.4)
C7	(−124.2, 54.1, 0.0)	(−123.1, 80.7, −4.7)
T8	(−156.61, −171.5, 0.0)	(−179.1, −133.2, 11.2)
AA	(−105.6, 7.5, 182.6)	(−73.5, 9.3, 205.1)
TS	(−156.0, −11.7, 75.0)	(−136.3, 5.1, 121.8)
AI	(−156.7, −126.2, 101.9)	(−141.6, −126.5, 116.2)
AC	(−71.8, 26.6, 165.1)	(−37.0, 40.4, 167.2)
SC	(−2.8, −15.2, 1.4)	(15.3, −31.0, −6.6)
Ellipsoid center	(−62.1, −152.1, 0.0)	(−61.6, −148.1, 0.0)
Ellipsoidal semimajor axis	(95.6, 211.7, 144.6)	(114.4, 222.7, 164.8)
Zoom factor		(1.20, 1.05, 1.14)

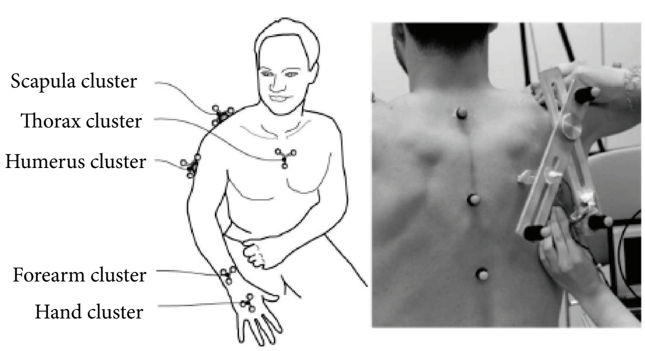

FIGURE 5: Placement of clusters of Optotrak markers.

Figure 6 shows the thorax movement gesture of the experimental subject S_1 in the ABD exercise test, and the posture of the humerus under YXY rotation sequence is described by three corresponding Euler angles HumY_1, HumX, and HumY_2. Figure 7 shows the measured posture of the clavicle relative to the thorax, and according to ISB standard, the posture of the clavicle is described under YXZ rotation sequence. The three Euler angles formed that depended on them are ClavY, ClavX, and ClavZ, respectively.

Thus, at any time, the posture matrix of the clavicle relative to the thorax can be obtained:

$$ {}_{c}^{t}\mathbf{R} = \mathrm{Rot}(y, \mathrm{ClavY})\mathrm{Rot}(x, \mathrm{ClavX})\mathrm{Rot}(z, \mathrm{ClavZ}). \tag{16}$$

Suppose that

$$ {}_{c}^{t}\mathbf{R} = \begin{bmatrix} u_{tcx} & v_{tcx} & w_{tcx} \\ u_{tcy} & v_{tcy} & w_{tcy} \\ u_{tcz} & v_{tcz} & w_{tcz} \end{bmatrix}. \tag{17}$$

Substitute (17) into (12) and (13):

$$ {}_{1}^{0}R = \left({}_{0}^{t}R\right)^{-1} {}_{c}^{t}R_{1}^{c}R = \begin{bmatrix} u_z & v_z & w_z \\ u_x & v_x & w_x \\ u_y & v_y & w_y \end{bmatrix}. \tag{18}$$

Let the third column of (18) and (2) be the same, and the following three constraint equations can be obtained:

$$\begin{aligned} s\theta_1 s\theta_2 &= w_z, \\ -c\theta_1 s\theta_2 &= w_x, \\ c\theta_2 &= w_y, \end{aligned} \tag{19}$$

then

$$\begin{aligned} \theta_1 &= \tan^{-1}\left(-\frac{w_z}{w_x}\right), \\ \theta_2 &= \tan^{-1}\left(\frac{w_z}{w_y s\theta_1}\right). \end{aligned} \tag{20}$$

Figure 8 is the result of the input joint variables θ_1 and θ_2.

Assuming that the object S_1 is at a certain moment of ABD movement, the position vector of the sternoclavicular joint marking point SC is ${}^{t}\mathbf{p}_{sc}$, and the conversion

Table 4: Range of motion (ROM) tasks.

Shoulder movement	Motion description
ABD (shoulder abduction)	Motion in the frontal plane. Initially, the arm relaxes and hangs down and then moves in the frontal plane, until the humerus rises up to the extreme position, and then moves back to the initial location. Keep the palm facing the body and upper limb unbent during exercises.
FLEX (shoulder anteflexion)	Flexion movement in the sagittal plane. Initially, the arm relaxes and hangs down and then flexes in the sagittal plane, until the humerus rises up to the extreme position, and then moves back to the initial location.
SCAP (shoulder scaption)	Movement in the scapular plane. Initially, the arm relaxes and hangs down and then raises the scapular plane (at about 45° to the frontal plane) until the humerus rises up to the extreme position and then back to the initial position.

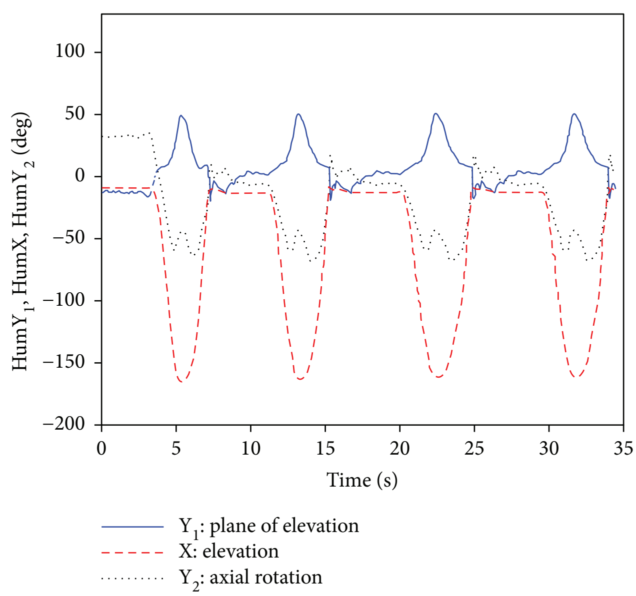

Figure 6: Movement posture of the humerus (ABD).

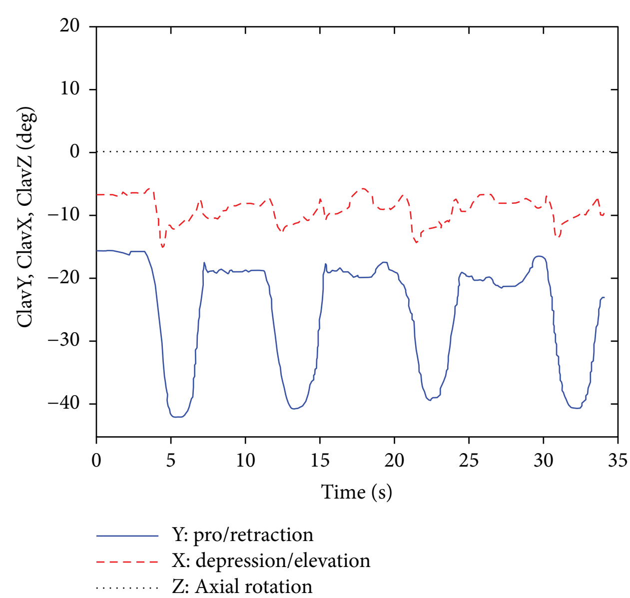

Figure 7: The posture of the clavicle that is adopted to be input parameters (ABD).

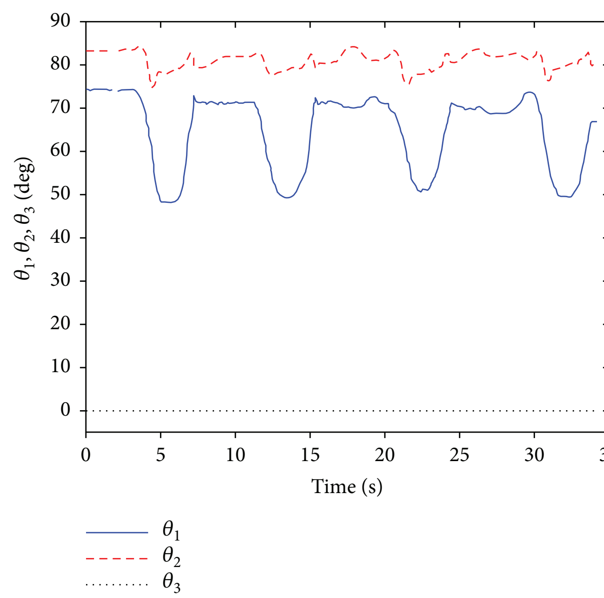

Figure 8: The joint angles θ_1 and θ_2 that are adopted to be input parameters (ABD).

relationship between S_t and S_0 can be expressed as the following transfer matrix:

$$
{}_0^t\mathbf{T} = \begin{bmatrix} \left[{}_0^tR\right]_{3\times 3} & \left[{}^tp_{sc}\right]_{4\times 1} \\ 0 \quad 0 \quad 0 & \end{bmatrix}. \tag{21}
$$

Thus, the position vector of the lower scapular AI in the ellipsoidal system S_3 can be obtained:

$$
{}^3\mathbf{p}_{AI} = \left({}_3^tT\right)^{-1} {}^tp_{AI} = \begin{bmatrix} x_{AI,3} & y_{AI,3} & z_{AI,3} & 1 \end{bmatrix}^T. \tag{22}
$$

Combining formulas (4) and (12) and Table 3 on the thorax data, we can have the following formula:

$$
{}_3^tT = {}_0^tT {}_3^0T = \begin{bmatrix} 0 & 1 & 0 & -61.6 \\ 0 & 0 & 1 & -148.1 \\ 1 & 0 & 0 & 0 \\ 0 & 0 & 0 & 1 \end{bmatrix}. \tag{23}
$$

In the ABD exercise of the experimental subject S_1, the position of the lower scapular angle AI in the ellipsoid S_3 is shown in Figure 9.

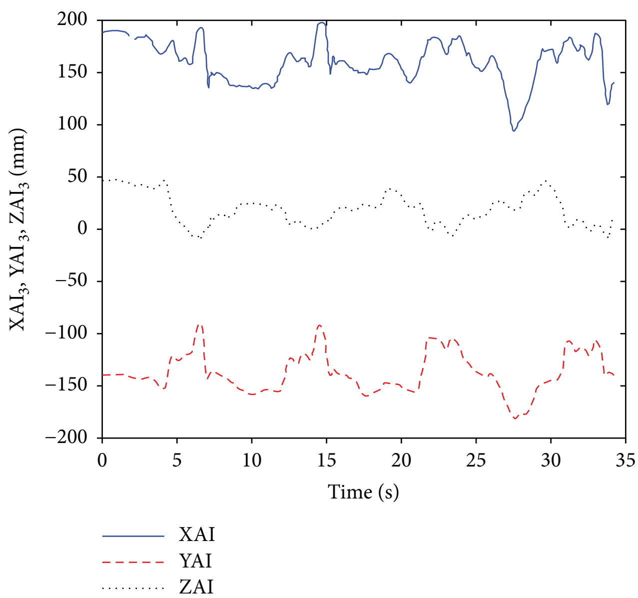

Figure 9: The position vector of AI described in ellipsoid frame S_3.

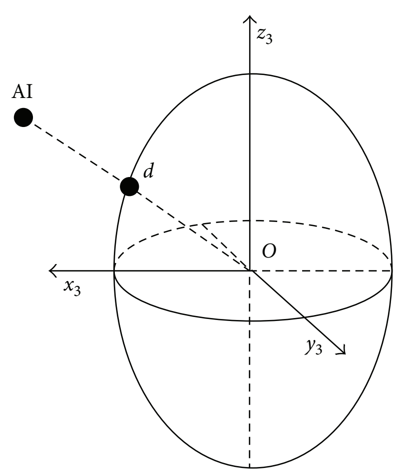

Figure 10: Point AI projects on the elliptical surface.

However, the fact is that the AI point is located on the shoulder blade but not always on the surface of the ellipsoid, which means it does not exactly coincide with point d in the model. In this paper, the projection point of the subscapular AI along the centerline of the ellipsoid is regarded as the equivalent point d. As shown in Figure 10, the connection between AI and ellipsoid center O intersects at d on the ellipsoid surface, and the position and size of the chest ellipsoid of the experimental subject S_1 refer to Table 3.

It can be obtained that $\overrightarrow{Od} \| \overrightarrow{OAI}$. Substitute (6) and (22), then there is

$$\frac{b \sin \varphi_d \sin \phi_d}{a \sin \varphi_d \cos \phi_d} = \frac{y_{AI,3}}{x_{AI,3}}. \tag{24}$$

Another input joint variable can be found:

$$\phi_d = \tan^{-1}\left(\frac{a}{b}\frac{y_{AI,3}}{x_{AI,3}}\right). \tag{25}$$

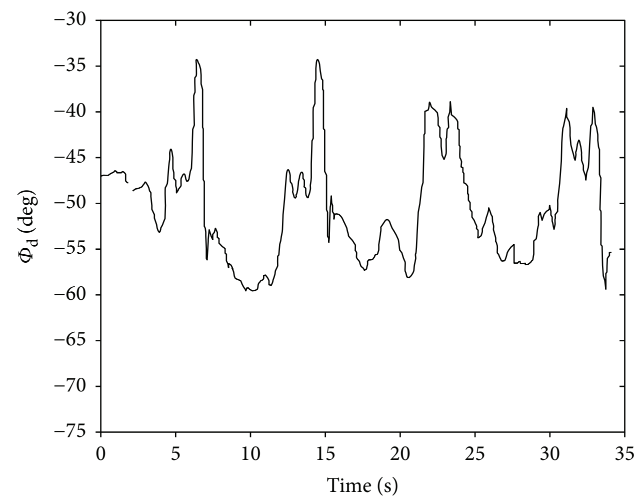

Figure 11: The joint angle ϕ_d that adopted to be the input parameter (ABD).

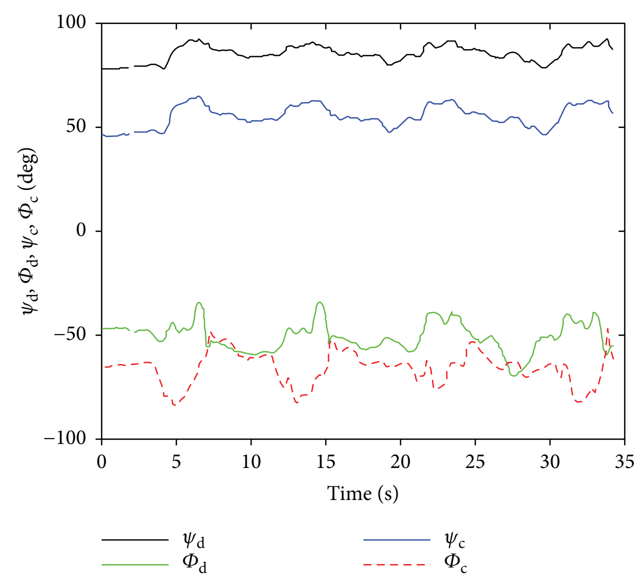

Figure 12: The joint angle φ_d, φ_c, ϕ_c (ABD).

For the summary, for the object S_1 in the ABD motion experiment, the input joint variable ϕ_d for the position analysis of the mechanism is shown in Figure 11.

Then, entering the joint variables $\theta_1, \theta_2, \phi_d$ into closed solution equations, the joint variables $\varphi_d, \varphi_c, \phi_c$ and $\theta_4, \theta_5, \theta_6$ are obtained as shown in Figures 12 and 13.

Thus, the shoulder girdle mechanism position analysis is finished, and the results in the calculated coordinate system of the bone or joint movement posture can be obtained and then converted corresponding to the ISB standard system, so the agency model for shoulder skeletal motion prediction results can be obtained and compared with the experimental measurement results. Figure 14 shows the scapula relative to the thorax motion posture analysis results (ST joint). Figures 15, 16, and 17 are the results of the components of

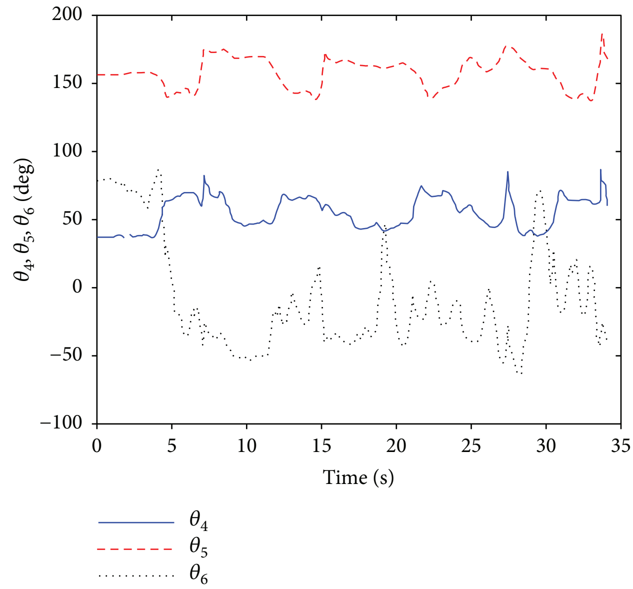

FIGURE 13: The curve of joint angle $\theta_4, \theta_5, \theta_6$ (ABD).

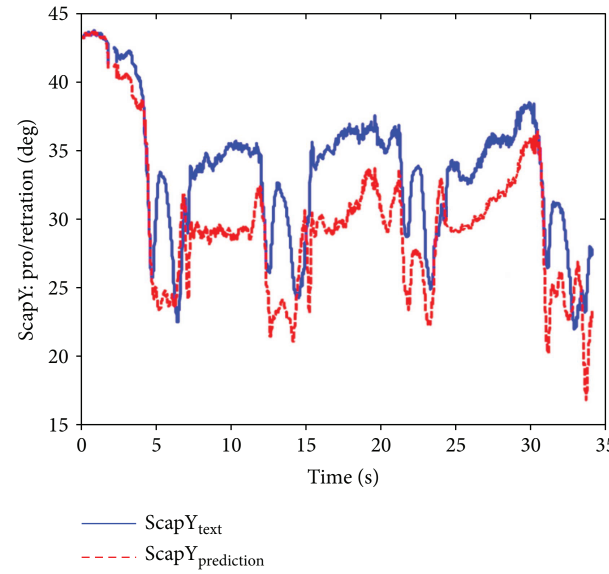

FIGURE 15: Comparison of protraction obtained by prediction and measurement (ABD).

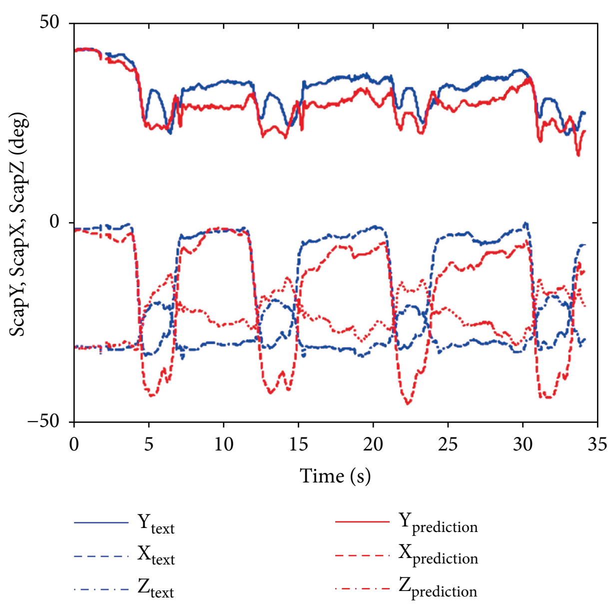

FIGURE 14: The movement of the scapula with respect to the thorax (ABD).

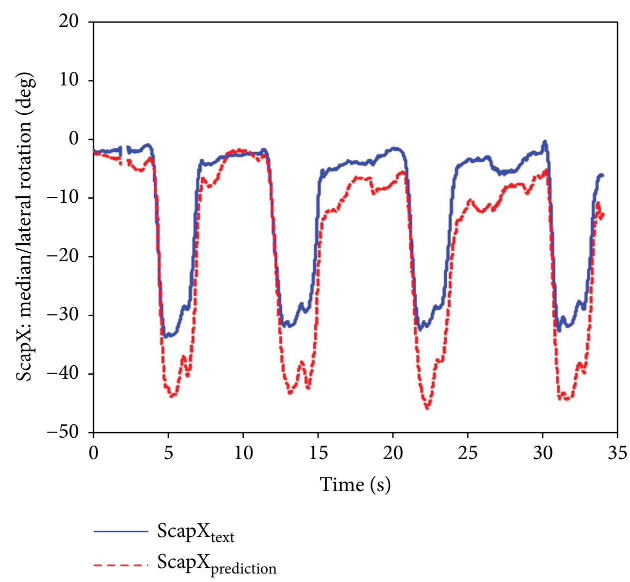

FIGURE 16: Comparison of lateral rotation obtained by prediction and measurement (ABD).

the scapula posture matrix after the decomposition of YXZ rotation sequence according to the ISB standard. Thanks to the fruitful achievement in biological research, the detail and accurate experimental data on shoulder motion can be provided, and in this paper, we selected a set of representative data to verify that the kinematic description of the skeleton model and experimental measurements are consistent.

Using the same method, the exercise experiments of FLEX and SCAP can be analyzed, and the agency model shoulder motion configuration prediction and experimental measurement results are basically consistent.

3. Shoulder Rhythm Model

From the view of the mechanistic model, the three rotational degrees of freedom of the humerus are independent from the three degrees of freedom of movement of the shoulder girdle mechanism. However, a great number of studies have shown that when the shoulders do some basic movements in the natural state (such as abduction, adduction, external rotation, pronation, flexion, and anteversion), there is a significant correlation and repeatability of shoulder girdle and humeral motion, following the law of the rhythm of the shoulder joint.

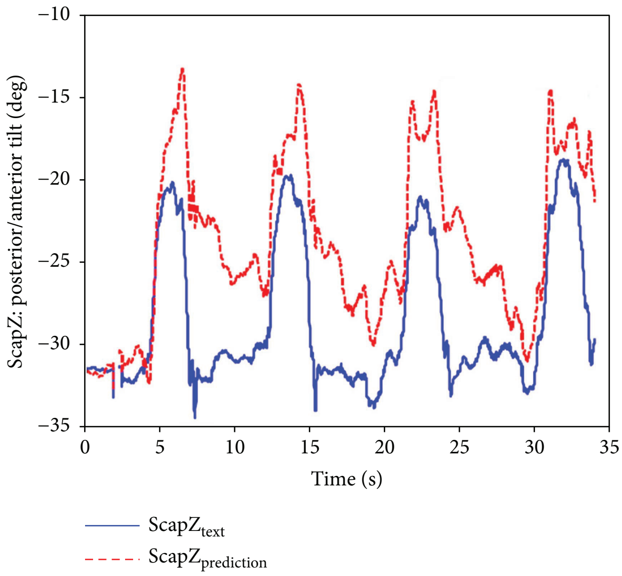

FIGURE 17: Comparison of anterior tilt obtained by prediction and measurement.

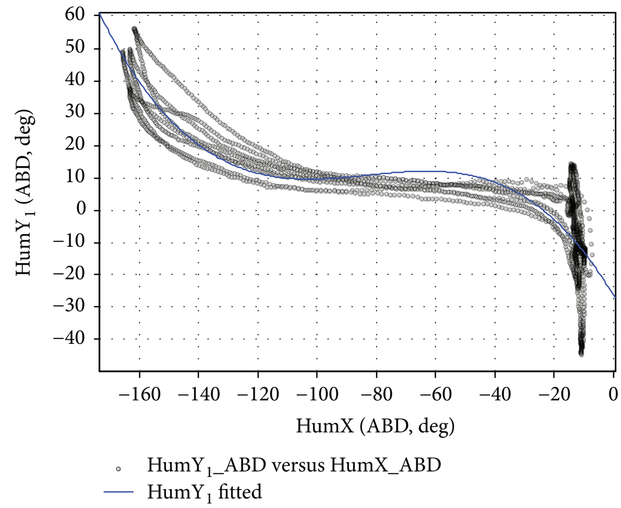

FIGURE 18: The relation between plane of elevation angle and elevation angle (ABD).

This article simplifies shoulder joint rhythm analysis to the problem of establishing the relationship between the humeral posture and the three independent input joint variables of the shoulder girdle mechanism.

3.1. Rhythm Analysis of Three Kinds of Exercise Task Experiment. The shoulder rhythm of an individual is highly repeatable and less affected by the size of the load when shoulders are in the condition of lighter load [27, 28], but there exist individual differences [29]. Therefore, this paper extends the traditional shoulder joint rhythm and describes the relationship between the scapula and the clavicle posture and the posture of the humerus individually via the proposed model with three independent joint variables $(\theta_1, \theta_2, \phi_d)$. Through the constraints in the proposed model considering the individual size of shoulder complex, three independent joint variables can be further used to determine the corresponding relationship between the entire shoulder girdle posture and the humeral posture. This method reduces the number of variables involved in rhythms and increases the impact of individual differences.

Studies of shoulder rhythms by the literature [17, 25–28] showed that the elevation plane ($HumY_1$) and the elevation (HumX) are relatively independent in shoulder bone movement, while the shoulder girdle posture with two joint variables has a strong regularity. When modeling the shoulder rhythms, this research also uses planes of elevation and elevation as independent variables for rhythm functions.

3.1.1. ABD Sports Rhythm. During the ABD exercise, five actions of lifting and dropping humerus are finished, as shown in Figure 6. Although the subject was asked to do abduction in the frontal plane, the actual elevation of the plane mainly focuses in the scoped of −10° to 20°, as shown in Figure 18. Although when the shoulder moved, the joint variable of elevation plane and the joint variable of elevation are considered independent from each other, the strong regularity and reflexivity are shown in Figure 18, because it represents the physical coordination of the experimental subjects in a certain motion like ABD exercise, and the coupling phenomenon will disappear in arbitrary motion. The relationship between the elevation plane and the elevation in Figure 8 is not universal, so this article will use the plane of elevation and the elevation as two independent variables of the law function.

Figure 19 shows the variation of various dependent variables with the humerus elevation angle when the subject does ABD exercise. $\theta_1, \theta_2, \phi_d$ is used to determine the rhythm of the shoulder girdle, while Figure 19(d) is used to determine the rhythm of humerus rotation around its shaft ($HumY_2$, internal/external rotation). Cubic polynomial fitting is adopted, and shoulder rhythm function can be obtained:

$$\begin{bmatrix} \theta_1 \\ \theta_2 \\ \phi_d \\ \mathrm{HumY}_2 \end{bmatrix} = \begin{bmatrix} [P_{\theta_1}]_{1\times4} \\ [P_{\theta_2}]_{1\times4} \\ [P_{\phi_d}]_{1\times4} \\ [P_{\mathrm{HumY}_2}]_{1\times4} \end{bmatrix} \begin{bmatrix} (\mathrm{HumX})^3 \\ (\mathrm{HumX})^2 \\ (\mathrm{HumX}) \\ 1 \end{bmatrix}, \tag{26}$$

where $[P]_{1\times4} = [p_1 \quad p_2 \quad p_3 \quad p_4]$ denotes the polynomial fitting coefficients to the corresponding joint variables. For simplifying the calculation, the rhythm function corresponding to the ABD motion is expressed as follows:

$$f_{\mathrm{ABD}}(\mathrm{HumX}) = p_1(\mathrm{HumX})^3 + p_2(\mathrm{HumX})^2 + p_3(\mathrm{HumX}) + 1. \tag{27}$$

Table 5 shows the fitting results of the dependent variables, and the accuracy and goodness of the fitting curve

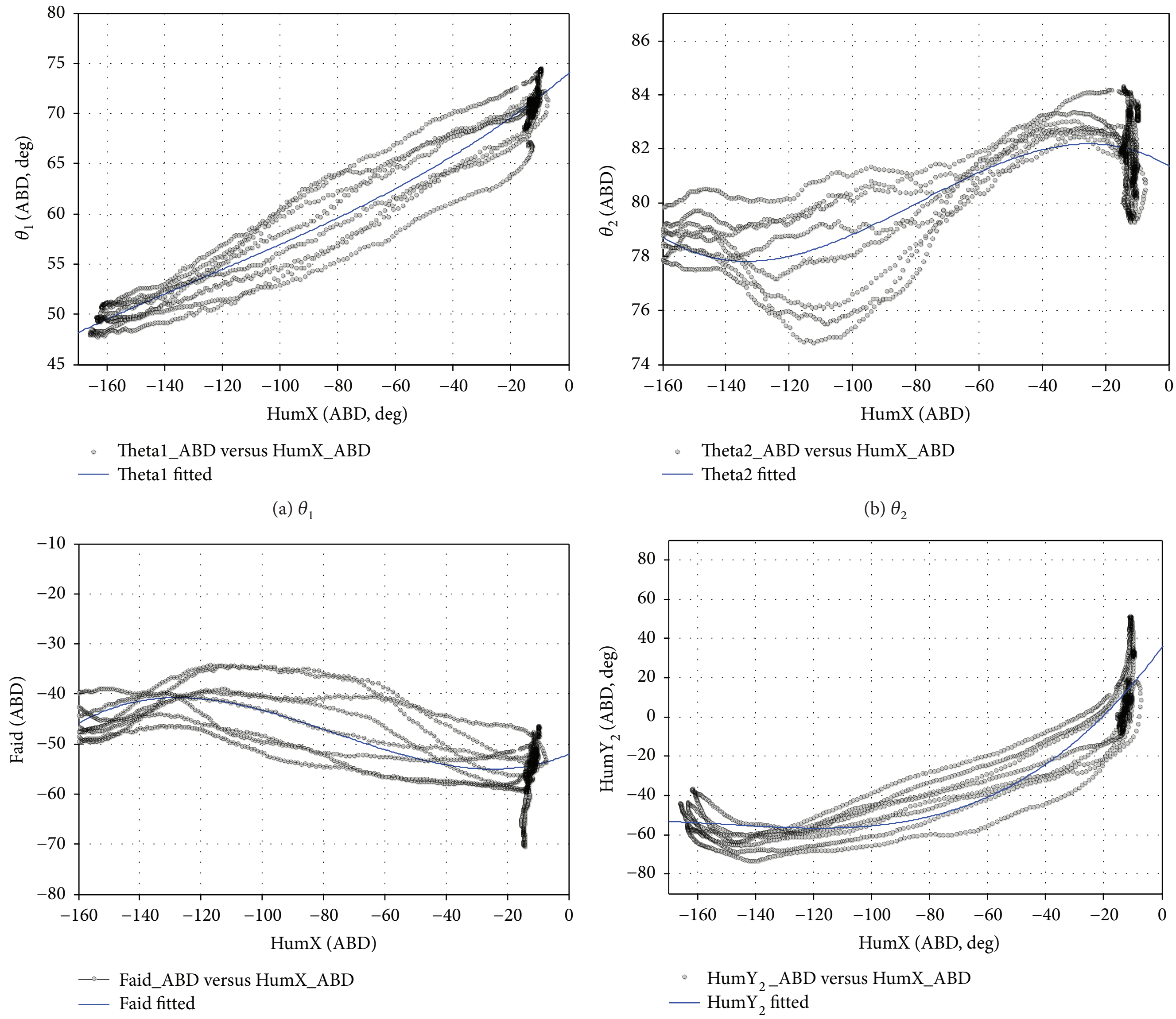

(a) θ_1 (b) θ_2 (c) ϕ_d (d) HumY_2

Figure 19: The joint angles are fit using a third-order polynomial (ABD).

Table 5: Third-order polynomial fit parameters of the rhythm function (ABD).

Dependent variable joint angle	Polynomial coefficients p_1	p_2	p_3	p_4	R-square R^2	Deg RMSE
θ_1	$2.483e-06$	0.0009501	0.2419	74.07	0.9581	1.811
θ_2	$-6.441e-06$	−0.001558	−0.06742	81.4	0.6004	1.271
ϕ_d	$2.822e-05$	0.006688	0.3163	−50.89	0.5203	4.848
HumY_2	$2.443e-05$	0.01201	1.833	32.07	0.8376	13.76

are, respectively, measured by root mean square error (RMSE) and coefficient of determination (R^2).

3.1.2. SCAP Sports Rhythm. During the entire SCAP exercise, lifting and dropping actions in the humerus were completed 4 times. To analyze the ABD motor rhythm, a rhythm function is constructed.

$$f_{\text{SCAP}}(\text{HumX}) = p_1(\text{HumX})^3 + p_2(\text{HumX})^2 + p_3(\text{HumX}) + 1. \tag{28}$$

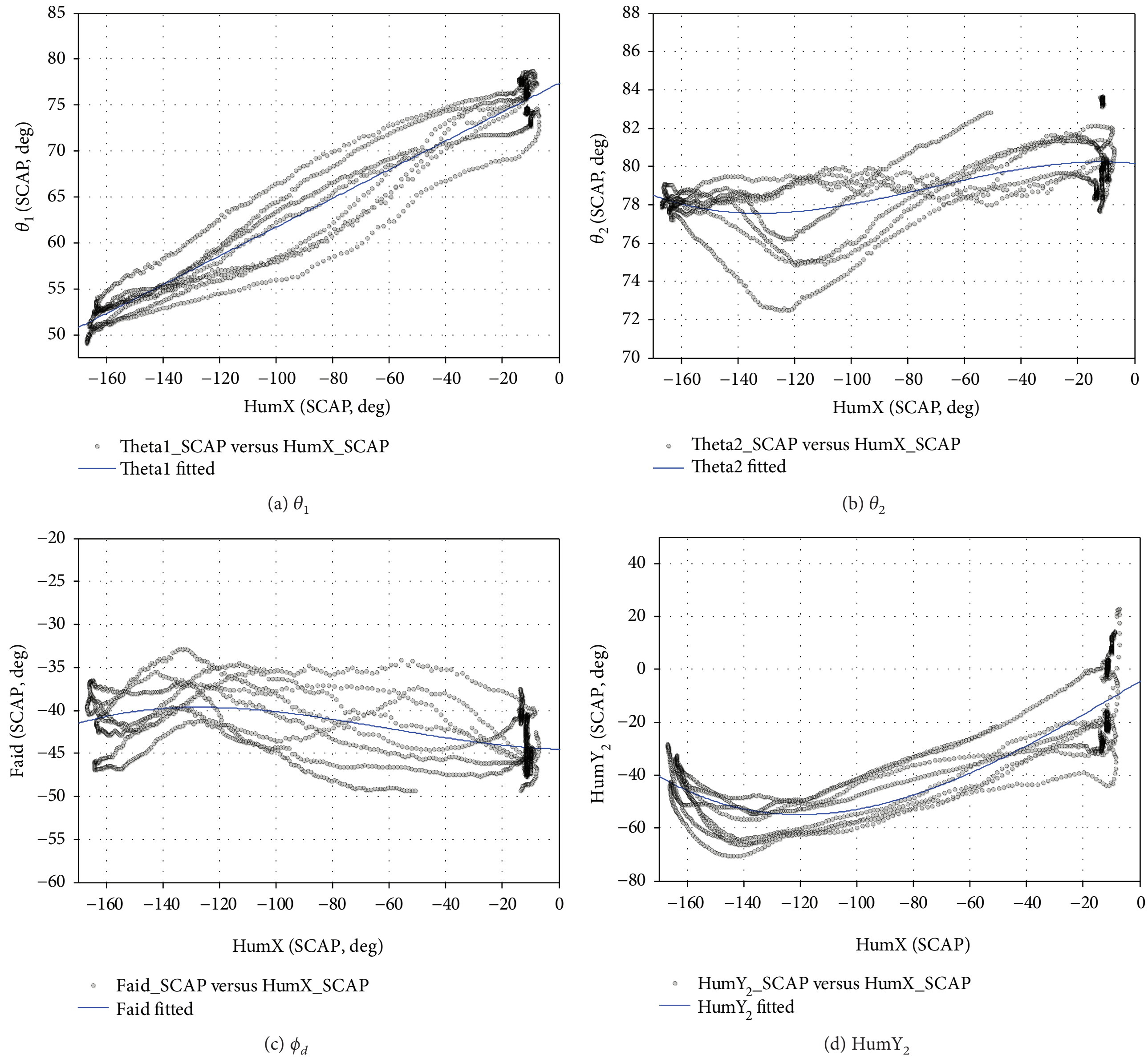

FIGURE 20: The joint angles are fit using a third-order polynomial (SCAP).

TABLE 6: Third-order polynomial fit parameters of the rhythm function (SCAP).

Dependent variable joint angle	Polynomial coefficients				R-square	Deg
	p_1	p_2	p_3	p_4	R^2	RMSE
θ_1	$-6.283e-06$	-0.001732	0.03207	76.14	0.9574	1.922
θ_2	$-2.328e-07$	$-3.272e-06$	0.01831	80.13	0.9161	0.6043
ϕ_d	$4.478e-06$	0.0008388	-0.002783	-44.38	0.3585	2.969
HumY_2	$-1.417e-05$	$8.118e-05$	0.6336	4.591	0.6418	12.61

Figure 20 shows the fitting result curve, and Table 6 shows the polynomial rhythm function coefficients, RSME, and coefficients of determination.

3.1.3. FLEX Sports Rhythm. During the entire FLEX exercise, lifting and dropping actions in the humerus were completed 4 times. The same as the ABD motor rhythm analysis, a rhythm function is constructed.

$$f_{\text{FLEX}}(\text{HumX}) = p_1(\text{HumX})^3 + p_2(\text{HumX})^2 + p_3(\text{HumX}) + 1. \tag{29}$$

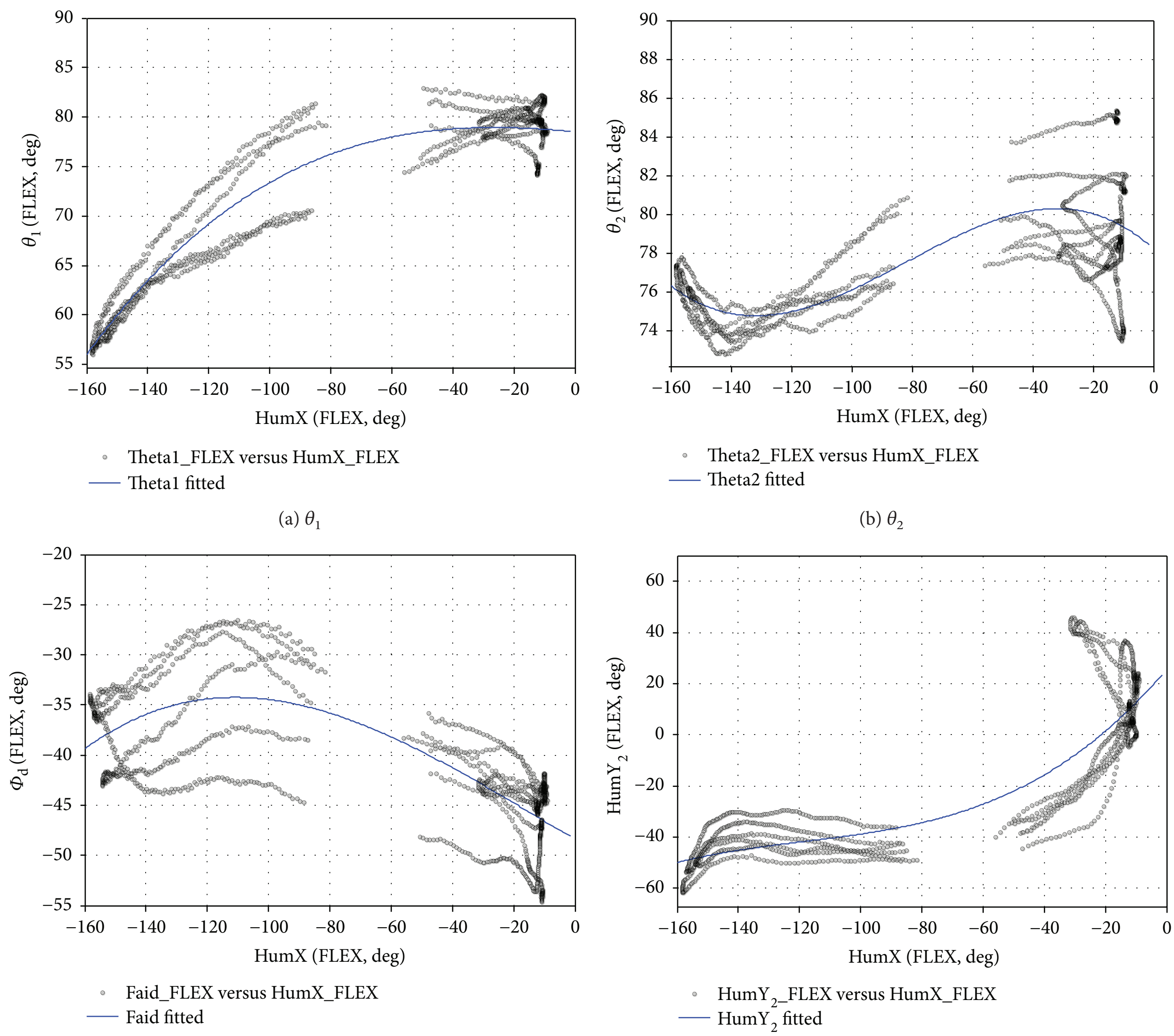

(a) θ_1 (b) θ_2 (c) ϕ_d (d) $HumY_2$

Figure 21: The joint angles are fit using a third-order polynomial (FLEX).

Table 7: Third-order polynomial fit parameters of the rhythm function (FLEX).

Dependent variable joint angle	Polynomial coefficients				R-square	Deg
	p_1	p_2	p_3	p_4	R^2	RMSE
θ_1	$3.587e-06$	−0.000406	−0.01044	79.29	0.9963	0.475
θ_2	$-1.058e-05$	−0.002583	−0.1365	77.43	0.3921	2.833
ϕ_d	$6.167e-06$	0.0002202	−0.179	−48.39	0.5784	3.951
$HumY_2$	$3.011e-05$	0.01069	1.412	25.64	0.7932	12.75

Figure 21 shows the fitting result curve, and Table 7 shows the polynomial rhythm function coefficient, RSME, and coefficient of determination.

3.2. Shoulder Rhythm Expansion. The lifting plane is not uniquely fixed during ABD, SCAP, and FLEX movements. In the ABD, SCAP, and FLEX, the humerus lifting plane angle $HumY_1$ changes as shown in Figures 16 and 22. It can be seen that the main movement range of the plane of elevation during these three movements is as shown in Table 8.

Theoretically, the variables of the shoulder joint rhythm function are $HumY_1$ and HumX in the whole range of activity, and the relationship between the movement of the

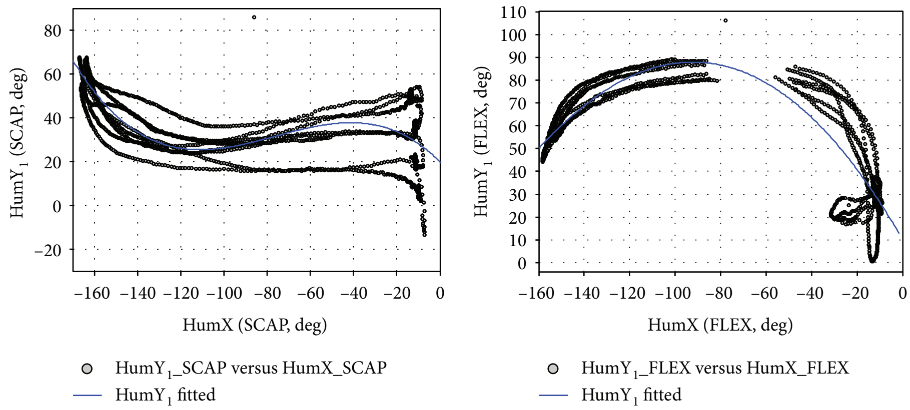

Figure 22: The ranges of plane of elevation when the movement of SCAP and FLEX is exerted.

Table 8: The ranges of plane of elevation.

Type of exercise	ABD	SCAP	FLEX
Range of plane of elevation	-10°~20°	20°~50°	50°~90°

shoulder bones and the axial rotation angle HumY_2 of the humerus is not significant. At the same time, axial rotation angles HumY_2 and HumX are related. Therefore, in this research, the shoulder joint rhythms corresponding to ABD, SCAP, and FLEX are extended to the motion space $-10^\circ \le \mathrm{HumY}_1 \le 90^\circ$ and $0^\circ \le \mathrm{HumX} \le 165^\circ$, and the rhythm can be expressed as follows:

$$f(\mathrm{HumX}) = \begin{cases} f_{\mathrm{ABD}}(\mathrm{HumX}), & -10^\circ \le \mathrm{HumY}_1 \le 20^\circ, \\ f_{\mathrm{SCAP}}(\mathrm{HumX}), & 20^\circ \le \mathrm{HumY}_1 \le 50^\circ, 0^\circ \le \mathrm{HumX} \le 165^\circ, \\ f_{\mathrm{FLEX}}(\mathrm{HumX}), & 50^\circ \le \mathrm{HumY}_1 \le 90^\circ. \end{cases} \quad (30)$$

4. Conclusion

In this paper, a new shoulder complex skeletal model based on joint geometric constraints is proposed using a spatial hybrid mechanism to describe the movement of human shoulder complex, which is developed for the rehabilitation robots. The effectiveness and viability of the proposed model have been verified via the experimental data of shoulder skeletal motion. Based on this model, through the analysis of the angle and change rule of each joint in the shoulder complex during the movement, the shoulder rhythm was obtained by means of polynomial fitting with HumY_1 and HumX as independent variables to make it suitable to guide the training strategy for shoulder rehabilitation via robotics.

Conflicts of Interest

The authors declare that they have no conflicts of interest.

Acknowledgments

This work was supported by the Natural Science Foundation of China (Project nos. 51475322, 51535008, 51775367, and 51721003), Tianjin Municipal Science and Technology Department Program (Grant no. 17JCZDJC30300), and the Programme of Introducing Talents of Discipline to Universities ("111 Program") under Grant no. B16034.

References

[1] D. K. Zondervan, L. Palafox, J. Hernandez, and D. J. Reinkensmeyer, "The resonating arm xerciser: design and pilot testing of a mechanically passive rehabilitation device that mimics robotic active assistance," *Journal of Neuroengineering and Rehabilitation*, vol. 10, p. 39, 2013.

[2] S. Barreca, S. L. Wolf, S. Fasoli, and R. Bohannon, "Treatment interventions for the paretic upper limb of stroke survivors: a critical review," *Neurorehabilitation and Neural Repair*, vol. 17, no. 4, pp. 220–226, 2003.

[3] H. M. Feys, W. J. de Weerdt, B. E. Selz et al., "Effect of a therapeutic intervention for the hemiplegic upper limb in the acute phase after stroke : a single-blind, randomized, controlled multicenter trial," *Stroke*, vol. 29, no. 4, pp. 785–792, 1998.

[4] R. Colombo, F. Pisano, S. Micera et al., "Robotic techniques for upper limb evaluation and rehabilitation of stroke patients," *IEEE Transactions on Neural Systems and Rehabilitation Engineering*, vol. 13, no. 3, pp. 311–324, 2005.

[5] P. S. Lum, C. G. Burgar, P. C. Shor, M. Majmundar, and M. van der Loos, "Robot-assisted movement training compared with conventional therapy techniques for the rehabilitation of upper-limb motor function after stroke," *Archives of Physical Medicine and Rehabilitation*, vol. 83, no. 7, pp. 952–959, 2002.

[6] D. J. Reinkensmeyer, J. L. Emken, and S. C. Cramer, "Robotics, motor learning, and neurologic recovery," *Annual Review of Biomedical Engineering*, vol. 6, no. 1, pp. 497–525, 2004.

[7] R. Riener, T. Nef, and G. Colombo, "Robot-aided neurorehabilitation of the upper extremities," *Medical and Biological Engineering and Computing*, vol. 43, no. 1, pp. 2–10, 2005.

[8] C. Carignan and M. Liszka, "Design of an arm exoskeleton with scapula motion for shoulder rehabilitation," in *2005. ICAR '05. Proceedings., 12th International Conference on Advanced Robotics*, pp. 524–531, Seattle, WA, USA, July 2005.

[9] W. T. Dempster, "Mechanisms of shoulder movement," *Archives of Physical Medicine and Rehabilitation*, vol. 46, pp. 49–70, 1965.

[10] A. E. Engin and S. M. Chen, "Statistical data base for the biomechanical properties of the human shoulder complex—I: kinematics of the shoulder complex," *Journal of Biomechanical Engineering*, vol. 108, no. 3, pp. 215–221, 1986.

[11] B. A. Garner and M. G. Pandy, "Musculoskeletal model of the upper limb based on the visible human male dataset," *Computer Methods in Biomechanics and Biomedical Engineering*, vol. 4, no. 2, pp. 93–126, 2001.

[12] W. Maurel and D. Thalmann, "Human shoulder modeling including scapulo-thoracic constraint and joint sinus cones," *Computers & Graphics*, vol. 24, no. 2, pp. 203–218, 2000.

[13] W. Maurel, D. Thalmann, P. Hoffmeyer et al., "A biomechanical musculoskeletal model of human upper limb for dynamic simulation," in *Computer Animation and Simulation '96. Eurographics*, R. Boulic and G. Hégron, Eds., pp. 121–136, Springer, Vienna, 1996.

[14] B. Tondu, "Modelling of the shoulder complex and application the design of upper extremities for humanoid robots," in *2005 5th IEEE-RAS International Conference on Humanoid Robots*, pp. 313–320, Tsukuba, Japan, December 2005.

[15] J. Lenarcic and M. Stanisic, "A humanoid shoulder complex and the humeral pointing kinematics," *IEEE Transactions on Robotics & Automation*, vol. 19, no. 3, pp. 499–506, 2003.

[16] J. Klein, S. Spencer, J. Allington, J. E. Bobrow, and D. J. Reinkensmeyer, "Optimization of a parallel shoulder mechanism to achieve a high-force, low-mass, robotic-arm exoskeleton," *IEEE Transactions on Robotics*, vol. 26, no. 4, pp. 710–715, 2010.

[17] B. A. Garner and M. G. Pandy, "A kinematic model of the upper limb based on the visible human project (VHP) image dataset," *Computer Methods in Biomechanics and Biomedical Engineering*, vol. 2, no. 2, pp. 107–124, 1999.

[18] H. Zhen, Z. Yongsheng, and Z. Tieshi, *Institution of Higher Space*, Higher Education Press, Beijing, 2014.

[19] C. G. M. Meskers, H. M. Vermeulen, J. H. de Groot, F. C. T. van der Helm, and P. M. Rozing, "3D shoulder position measurements using a six-degree-of-freedom electromagnetic tracking device," *Clinical Biomechanics*, vol. 13, no. 4-5, pp. 280–292, 1998.

[20] F. C. T. van der Helm and G. M. Pronk, "Three-dimensional recording and description of motions of the shoulder mechanism," *Journal of Biomechanical Engineering*, vol. 117, no. 1, pp. 27–40, 1995.

[21] B. Bolsterlee, H. E. J. Veeger, and F. C. T. van der Helm, "Modelling clavicular and scapular kinematics: from measurement to simulation," *Medical & Biological Engineering & Computing*, vol. 52, no. 3, pp. 283–291, 2014.

[22] G. Wu and P. R. Cavanagh, "ISB recommendations for standardization in the reporting of kinematic data," *Journal of Biomechanics*, vol. 28, no. 10, pp. 1257–1261, 1995.

[23] G. Wu, F. van der Helm, H. E. Veeger et al., "ISB recommendation on definitions of joint coordinate systems of various joints for the reporting of human joint motion—part II: shoulder, elbow, wrist and hand," *Journal of Biomechanics*, vol. 38, no. 5, pp. 981–992, 2005.

[24] B. A. Garner and M. G. Pandy, "The obstacle-set method for representing muscle paths in musculoskeletal models," *Computer Methods in Biomechanics and Biomedical Engineering*, vol. 3, no. 1, pp. 1–30, 2000.

[25] M. D. Klein Breteler, C. W. Spoor, and F. C. T. van der Helm, "Measuring muscle and joint geometry parameters of a shoulder for modeling purposes," *Journal of Biomechanics*, vol. 32, no. 11, pp. 1191–1197, 1999.

[26] A. A. Nikooyan, H. E. J. Veeger, P. Westerhoff et al., "An EMG-driven musculoskeletal model of the shoulder," *Human Movement Science*, vol. 31, no. 2, pp. 429–447, 2012.

[27] C. Högfors, B. Peterson, G. Sigholm, and P. Herberts, "Biomechanical model of the human shoulder joint—II. The shoulder rhythm," *Journal of Biomechanics*, vol. 24, no. 8, pp. 699–709, 1991.

[28] P. W. McClure, L. A. Michener, B. J. Sennett, and A. R. Karduna, "Direct 3-dimensional measurement of scapular kinematics during dynamic movements in vivo," *Journal of Shoulder and Elbow Surgery*, vol. 10, no. 3, pp. 269–277, 2001.

[29] M. B. Warner, P. H. Chappell, and M. J. Stokes, "Measurement of dynamic scapular kinematics using an acromion marker cluster to minimize skin movement artifact," *Journal of Visualized Experiments Jove*, vol. 96, no. 96, article e51717, 2015.

Hindawi
Applied Bionics and Biomechanics
Volume 2018, Article ID 4613230, 9 pages
https://doi.org/10.1155/2018/4613230

Research Article

Kinematic Decoupling Analysis and Design of a Biomimetic Robotic Elbow Joint

Bingyan Cui,[1,2,3] **Liwen Chen**,[1] **Yongtao Xie**,[1] **and Zhijun Wang**[1]

[1]*College of Mechanical Engineering, North China University of Science and Technology, Tangshan 063009, China*
[2]*Yanshan University, Qinhuangdao 066009, China*
[3]*Widex Sanitary Co. Ltd., Tangshan 063000, China*

Correspondence should be addressed to Bingyan Cui; mj_cby@126.com

Received 27 November 2017; Revised 30 March 2018; Accepted 15 April 2018; Published 9 May 2018

Academic Editor: Liwei Shi

The research of a biomimetic robotic manipulator is based on the flexible characteristics of the human upper limb joint, and a biomimetic robotic elbow joint plays a very significant role in the kinematic control of the biomimetic robotic manipulator. Most robotic elbow joints encountered today have a common disadvantage of bad neutrality, low rotational capability, and poor biomimetics. To overcome some difficulties, this paper presents a novel biomimetic robotic elbow joint. The structural model of the elbow joint is described, and the position equation is solved. Secondly, the kinematic equation of the elbow joint is established, the kinematic decoupling performance evaluation index of the elbow joint is defined, the kinematic decoupling characteristics of the elbow joint are analyzed, and the kinematic decoupling performance map in the workspace is drawn. Thirdly, using the spatial model theory, the structural parameters of the elbow joint are optimized, the structural parameters are selected by the Monte Carlo method, and the novel biomimetic robotic elbow joint is designed. The analysis results showing the kinematic decoupling performance of the elbow joint are symmetrical and the kinematic decoupling performance decreases with the increase of the angle, and there is a good kinematic decoupling in the workspace of about 35% in the vicinity of the initial position. When the structural parameters of the elbow joint are $R_{e1} = 90$ mm, $R_{e2} = 70$ mm, and $R_{e3} = 30$ mm, the elbow joint has a very good kinematic decoupling. This paper can lay a foundation for further analysis and research of the biomimetic robotic elbow joint.

1. Introduction

Biomimetic robotics is a new branch in the field of robot researches, which have integrated the biomimetic principle into the design and control of the robot and could imitate structure and movement characteristics of animals or humans. The motion behavior and some functions of natural organism have provided a great deal of thinking sources for robot scientists to design and realize flexible control [1–3]. With flexible operation and movement features, biomimetic robotics based on various types of bionic joints has highlighted good application prospects in the fields of rehabilitation medicine, space exploration, rescue, and so on [4–6].

The research of a biomimetic robotic manipulator is based on the flexible characteristics of the human upper limb joint and dexterous hands, and the human upper limbs are composed of the shoulder joint, elbow joint, wrist joint, and finger joint to complete the complex work and reflect the flexibility of the whole limb movement. The more flexible the upper limb joint, the more flexible the upper limb movement can be controlled [7]. Li et al. [8] designed a novel 3-DOF shoulder joint, established the error performance index, and plotted the error map. Li et al. [9] proposed a bionic eye based on a 3-DOF spherical parallel mechanism, and the structure parameters of the bionic eye were optimized. Klein et al. [10] designed a 3-DOF exoskeleton shoulder joint, and the torque capacity character curve is obtained. Zhang and Jin [11] made an in-depth study of theory on the driving characteristics, obtained dynamic characteristics, and optimized size of a 3-DOF shoulder joint. Sun et al. [12]

proposed a wrist joint based on a spherical 3-DOF parallel decoupling mechanism, and the position of the wrist joint was analyzed.

Cui and Jin [13] presented a 2-DOF elbow joint, defined the static performance index, and obtained the static performance curve. In 2015, a novel hip joint is designed and its dynamic characters and structural parameters have studied [14]. Xu et al. [15] designed an elbow joint based on large deceleration ratio traction motor direct drive structure and analyzed the force character, and the elbow provided effective flexion and extension movement based on the double-screw-pair transmission and the elbow joint developed and completed flexion and extension movement [16]. Hwang et al. [17] proposed a novel elbow based on a slider-crank mechanism and obtained the force transmission property curve. Stanišić and Goehler [18] proposed a hybrid shoulder mechanism for copying the grasping movement, and a mechanism capable of reproducing voluntary human reaching motions is introduced along with the procedural method of implementing the coupled motions. Lovasz et al. [19] designed an elbow module, carried on remote control for a haptic arm exoskeleton, and proposed several design solutions and a control strategy. A biomimetic robotic elbow joint plays a very significant role in the motion control of a biomimetic robotic manipulator. The kinematic decoupling is an important index which affects the overall motion and the control of the biomimetic robotic elbow joint. The kinematic decoupling of the mechanism [20] can determine its kinematic characteristics and provide the basis for the robot control and trajectory planning.

The problem of decoupling is closely related to the Jacobian matrix of the biomimetic robotic joint. Researchers have studied less in this field. Gong et al. [21] proposed the decoupling of the moving coordinates in the absolute coordinates and verified the decoupling theory by the corresponding examples. Shen et al. [22] analyzed the kinematic decoupling of a 6-DOF parallel mechanism. Xu et al. [23] studied the 2R1T parallel mechanism on the principle of its motion decoupling based on the positional relationship between the actuation force and the rotational axis. Essomba and Nguyen Vu [24] presented a novel spherical decoupled mechanism and proved the decoupling motion by its kinematic and velocity models.

Based on the analysis of the literature, the existing robotic elbow joint is usually able to achieve flexion and extension. The structure of elbow joint design adopts a series structure; the series structure lacks good centering ability. From the analysis of the performance of elbow joints, there are many literatures on the bearing capacity of elbow joints, and the literature of the kinematic decoupling has not been seen yet. On this basis, this paper proposes a biomimetic robotic elbow joint. The biomimetic robotic elbow joint adopts a 2-DOF spherical parallel mechanism as a prototype which has advantages of good structural characteristics, large range of motion, and high bearing capacity and was compared with the 3-DOF parallel mechanism in the 863 project. From the analysis of the degree of freedom of the mechanism, the 3-DOF spherical parallel mechanism has three degrees of freedom in accordance with the requirements of the prosthetic prototype of the shoulder joint, and the human elbow joint structure has two degrees of freedom of movement characteristics, so the elbow joint mechanism has very good bionic structure. From the analysis of the installation of the mechanism, the rotation center of the 3-DOF spherical parallel mechanism is located in the middle of the moving platform and the static platform. The neutrality requirements for the rods during installation are very high and difficult to install. The rotation center of each rod of the biomimetic robotic elbow joint presents 90 degrees, which is convenient to install and has good neutrality.

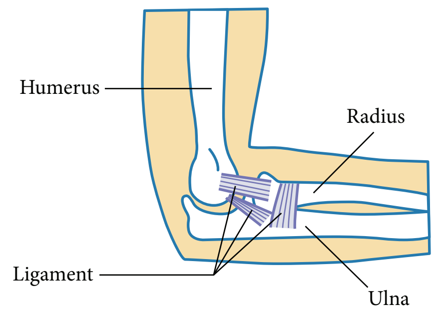

Figure 1: Schematic diagram of the human elbow joint.

In this paper, the kinematic equation of the biomimetic robotic elbow joint is established, the Jacobian matrix is derived, the kinematic decoupling performance evaluation index of the biomimetic robotic elbow joint is defined, the kinematic decoupling performance evaluation index map is drawn in the workspace, and the global kinematic decoupling performance index is established based on the kinematic decoupling analysis. Based on the space model theory, the structural parameters of the elbow joint are optimized and selected by the Monte Carlo method, and the biomimetic robotic elbow joint is designed. The purpose of the decoupling analysis of the elbow joint is to make the control of the elbow joint mechanism more convenient and easier.

2. The Model and Position Analysis

2.1. The Structural Description. The biomimetic robotic elbow joint is an important joint of the biomimetic hand. On the base of the knowledge of bionics, the human elbow joint is composed of the humerus, radius, ulna, and ligament. The human elbow joint is limited to the connection between the three bones and the ligament, which can only rotate about two axes and can realize movement of internal rotation and external rotation and flexion and extension, as shown in Figure 1.

The structure design of the biomimetic robotic elbow joint should be able to realize the movement of the anthropomorphic elbow joint. According to the analysis of joint structure and kinematic characteristics of the human elbow joint, this paper proposed a novel biomimetic robotic elbow joint based on a 2-DOF orthogonal spherical parallel mechanism. The elbow joint has two

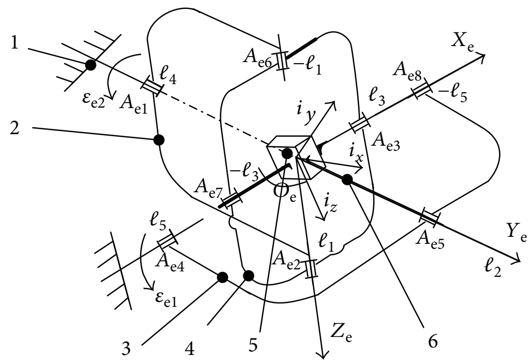

Figure 2: The structure of the biomimetic robotic elbow joint. 1—frame, 2 and 3—connecting rods, 4—annular member, 5—moving platform, and 6—arm connector.

moving branches, the frame and the moving platform, which contain two driving motors, and the driving motor is fixed on the frame. The moving platform of the elbow joint is connected by the arm connector and connected with the ring through the rotating pair. The elbow joint can realize two degrees of freedom of rotation and has advantages of good bionic characteristics, small structure, and little inertial forces. The structure diagram is shown in Figure 2.

Two Cartesian coordinates, the base frame $\{C_e\}$ is fixed and represented by the coordinate $[X_e\, Y_e\, Z_e]$, while the moving platform has a frame, $\{K_e\}$, attached to it with coordinates $[i_x i_y i_z]$. The coordinate center of the two coordinate systems is coincident, and the center point of coordinates is O_e. The plane A_o is composed of O_eA_{e1} and O_eA_{e4} axes. The X_e axis is along O_eA_{e8} the vector direction, the Y_e axis is along O_eA_{e5} the vector direction and passes, and the Z_e axis is vertical to the plane A_o and along O_eA_{e2} the vector direction. $\boldsymbol{\ell}_1$ is the unit vector of O_eA_{e2} axes, $\boldsymbol{\ell}_2$ is the unit vector of O_eA_{e5} axes, $\boldsymbol{\ell}_3$ is the unit vector along O_eA_{e3}, $\boldsymbol{\ell}_4$ is the unit vector of O_eA_{e1} axes, and $\boldsymbol{\ell}_5$ is the unit vector of O_eA_{e4} axes.

Assume that the spherical radius of the reference center of the connection rotation pairs A_{e1} and A_{e4} is R_{e1}, the spherical radius of the reference center of the connection rotation pairs A_{e3} and A_{e5} is R_{e2}, and the spherical radius of the reference center of the connection rotation pairs A_{e2} is R_{e3}. Therefore, the reference centers of the rotation pairs are distributed on concentric spherical surfaces with different radii, $R_{e3} < R_{e2} < R_{e1}$. Thus, the structural parameters of the elbow joint are R_{e1}, R_{e2}, and R_{e3}.

2.2. Derivation of Position Forward Solution. The kinematic equation of the elbow joint is established based on the solution of the inverse position. The attitude angles of the elbow joint moving platform are γ_e and β_e, and the input angles are γ_e and β_e. The moving platform of the elbow joint can rotate around the X axis and the Y axis, and the corresponding transformation matrix of the elbow joint moving platform is introduced and can be written as

$$\mathbf{T}_e = \mathbf{T}(X, \gamma_e)\mathbf{T}(Y, \beta_e) = \begin{bmatrix} \cos\beta_e & 0 & \sin\beta_e \\ \sin\gamma_e \sin\beta_e & \cos\gamma_e & -\sin\gamma_e\cos\beta_e \\ -\cos\gamma_e\sin\beta_e & \sin\gamma_e & \cos\gamma_e\cos\beta_e \end{bmatrix}. \tag{1}$$

In the fixed coordinate system, the unit vector $\boldsymbol{\ell}_2$ can be expressed as

$$\boldsymbol{\ell}_2 = \mathbf{T}_e \begin{pmatrix} 0 \\ 1 \\ 0 \end{pmatrix} = \begin{pmatrix} 0 \\ \cos\gamma_e \\ \sin\gamma_e \end{pmatrix}. \tag{2}$$

According to the mechanism characteristics of the elbow joint, the input angle of the drive motor is ε_{e1} and the unit vector $\boldsymbol{\ell}_2$ can be expressed as the input angle ε_{e1} and is given by

$$\boldsymbol{\ell}_2 = \begin{pmatrix} 1 & 0 & 0 \\ 0 & \cos\varepsilon_{e1} & -\sin\varepsilon_{e1} \\ 0 & \sin\varepsilon_{e1} & \cos\varepsilon_{e1} \end{pmatrix} \begin{pmatrix} 0 \\ 1 \\ 0 \end{pmatrix} = \begin{pmatrix} 0 \\ \cos\varepsilon_{e1} \\ \sin\varepsilon_{e1} \end{pmatrix}. \tag{3}$$

Comparison of (2) and (3) can be obtained as

$$\varepsilon_{e1} = \gamma_e. \tag{4}$$

In the fixed coordinate system, the unit vector $\boldsymbol{\ell}_3$ can be expressed as

$$\boldsymbol{\ell}_3 = \mathbf{T}_e \begin{pmatrix} 1 \\ 0 \\ 0 \end{pmatrix} = \begin{pmatrix} \cos\beta_e \\ \sin\gamma_e\sin\beta_e \\ -\sin\gamma_e\cos\beta_e \end{pmatrix}. \tag{5}$$

In the fixed coordinate system, the unit vector $\boldsymbol{\ell}_1$ is represented by the input angle ε_{e2} and is given by

$$\boldsymbol{\ell}_1 = \begin{bmatrix} \cos\varepsilon_{e2} & 0 & \sin\varepsilon_{e2} \\ 0 & 1 & 0 \\ -\sin\varepsilon_{e2} & 0 & \cos\varepsilon_{e2} \end{bmatrix} \begin{pmatrix} 0 \\ 0 \\ 1 \end{pmatrix} = \begin{pmatrix} \sin\varepsilon_{e2} \\ 0 \\ \cos\varepsilon_{e2} \end{pmatrix}. \tag{6}$$

According to the geometry of the elbow joint, (7) can be obtained.

$$\boldsymbol{\ell}_1 \cdot \boldsymbol{\ell}_3 = 0. \tag{7}$$

Equations (2) and (3) can be written in the form of (7) and can be derived as

$$\varepsilon_{e2} = a\tan 2(\cos\gamma_e \sin\beta_e, \cos\beta_e). \tag{8}$$

The inverse position solution equation of the elbow joint can be written as

$$\begin{aligned} \varepsilon_{e1} &= \gamma_e, \\ \varepsilon_{e2} &= a\tan 2(\cos\gamma_e \sin\beta_e, \cos\beta_e), \end{aligned} \tag{9}$$

The forward positive solution equation of the elbow joint by (9) is deduced as

$$\begin{aligned}\gamma_e &= \varepsilon_{e1},\\ \beta_e &= a\tan 2(\sin\varepsilon_{e2}, \cos\varepsilon_{e1}\cos\varepsilon_{e2}).\end{aligned} \tag{10}$$

3. The Kinematic Decoupling Analysis

3.1. The Derivation of the Kinematic Equation. Differential treatment (10), the kinematic equation is obtained as

$$\dot{\boldsymbol{\phi}}_e = \mathbf{J}_e \dot{\boldsymbol{\varepsilon}}_e, \tag{11}$$

where $\dot{\boldsymbol{\phi}}_e$ is the output angle velocity and is expressed as $\dot{\boldsymbol{\phi}}_e = [\dot{\gamma}_e \dot{\beta}_e]^T$, $\dot{\varepsilon}_e$ is the input angle velocity and is expressed as $\dot{\varepsilon}_e = [\dot{\varepsilon}_{e1}\dot{\varepsilon}_{e1}]^T$, and $\mathbf{J}_e$ is the Jacobian matrix and can be extracted as

$$\mathbf{J}_e = \begin{pmatrix} 1 & 0 \\ \dfrac{\sin\varepsilon_{e1}\sin\varepsilon_{e2}\cos\varepsilon_{e2}}{\sin^2\varepsilon_{e2} + \cos^2\varepsilon_{e1}\cos^2\varepsilon_{e2}} & \dfrac{\cos\varepsilon_{e1}}{\sin^2\varepsilon_{e2} + \cos^2\varepsilon_{e1}\cos^2\varepsilon_{e2}} \end{pmatrix}. \tag{12}$$

The kinematic decoupling analysis of the elbow joint depends on the Jacobian matrix $\mathbf{J}_e$. In order to describe the decoupling characteristic in more detail, the index of kinematic decoupling performance is defined as

$$\wp_e = \frac{\varsigma_{e\max} - \varsigma_{e\min}}{\varsigma_{e\max}}, \tag{13}$$

where the maximum and minimum singular values of the elbow joint Jacobian matrix are $\varsigma_{e\max}$ and $\varsigma_{e\min}$, respectively.

3.2. Analysis of Kinematic Decoupling Performance. The decoupling analysis of the kinematic of the elbow joint is to study the correlation or dependence of the output parameters on the input parameters. If the Jacobian matrix $\mathbf{J}_e$ can be turned into a diagonal matrix, the elbow joint is kinematic decoupling. The kinematic decoupling of the elbow joint under different input conditions is analyzed.

(1) When the input angular velocity of the X_e axis is $\dot{\varepsilon}_{e1}$, the decoupling of the output angular velocity of the elbow joint is analyzed.

The elbow joint has an input angular velocity on the X_e axis, and the input angular velocity on the Y_e axis is $\dot{\varepsilon}_{e2}$ and $\dot{\varepsilon}_{e2} = 0\,\text{rad/s}$. The Jacobian matrix of the elbow joint can be obtained from (12) and can be given by

$$\mathbf{J}_e = \begin{pmatrix} 1 & 0 \\ 0 & 1 \end{pmatrix}. \tag{14}$$

From (14), the Jacobian matrix is a diagonal unit matrix and the evaluation index of the kinematic decoupling performance in the workspace is always zero, so the elbow joint is completely kinematic decoupling and has the highest decoupling performance.

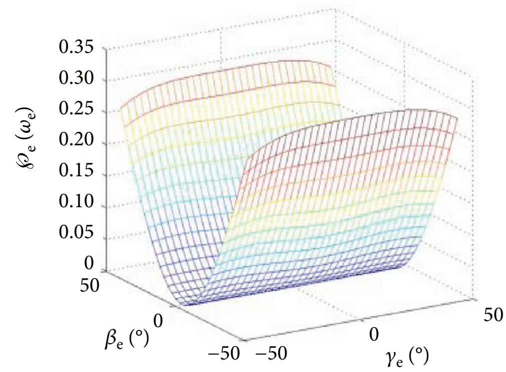

Figure 3: Index of the kinematic decoupling performance of output angle velocity when the input velocity has the X_e axis and Y_e axis.

(2) When the input angular velocities of the X_e axis and Y_e axis are $\dot{\varepsilon}_{e1}$ and $\dot{\varepsilon}_{e2}$, the elbow joint kinematic decoupling is analyzed.

When the elbow joint is driven by two driving motors, (12) expresses the Jacobian matrix. With the decoupling definition of the local motion of the shoulder joint, there is only one nonzero element in the first row of (12), so the elbow joint is locally kinematic decoupling in the whole workspace. According to the kinematic decoupling index of (13), the local kinematic decoupling performance graph of the elbow joint is obtained, as shown in Figure 3.

In Figure 3, the kinematic decoupling index $\wp_e$ changes little with the increase of the γ_e angle. With the increase of the β_e angle, the kinematic decoupling index $\wp_e$ increases gradually, its decoupling becomes smaller, and the coupling gradually increases. The kinematic decoupling of the elbow joint is locally decoupling in the γ_e angle direction, with very good kinematic decoupling in the region of approximately 35% of the initial position.

4. Global Kinematic Decoupling Analysis and Structural Parameter Optimization

The global performance index can better reflect the kinematic decoupling of the elbow joint in the whole posture workspace, and the spatial model theory [25, 26] provides a new idea for the structural parameter optimization of the elbow joint. The structural parameters of the elbow joint are optimized by the theory of the space model, which made the performance evaluation index of kinematic decoupling better. The structure parameters of the elbow joint were selected by the Monte Carlo method.

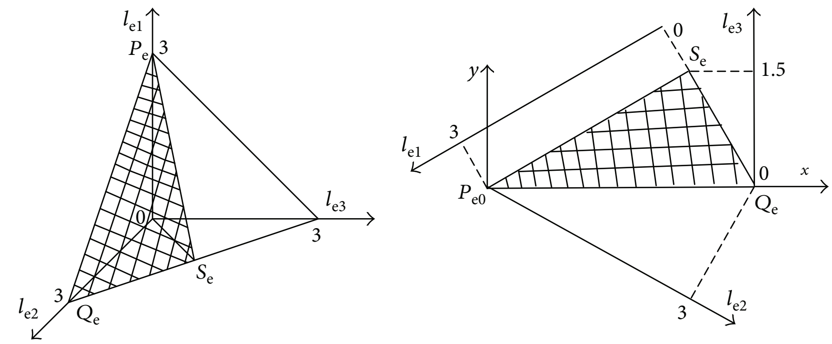

(a) Three-dimensional model of the spatial model

(b) Two-dimensional model of the spatial model

Figure 4: The spatial model of the biomimetic robotic elbow joint.

4.1. Analysis of the Global Kinematic Decoupling Performance. Based on the structural description of the biomimetic robotic elbow joint, the structural parameters are R_{e1}, R_{e2}, and R_{e3}. The spatial model of the structural parameters of the biomimetic robotic elbow joint is established. The structural dimension parameters of the elbow joint are dimensionless and can be given as

$$l_e = \frac{R_{e1} + R_{e2} + R_{e3}}{3}. \tag{15}$$

The dimensionless structural dimensions of the elbow joint are expressed, respectively, as

$$l_{e1} = \frac{R_{e1}}{l_e}, \quad l_{e2} = \frac{R_{e2}}{l_e}, \quad l_{e3} = \frac{R_{e3}}{l_e}. \tag{16}$$

Formula (16) can be obtained as

$$l_{e1} + l_{e2} + l_{e3} = 3. \tag{17}$$

Considering the manufacturing and assembling of the biomimetic robotic elbow joint, the conditions for the structural parameters are satisfied and can be written as

$$0 \le l_{e3} \le l_{e2} \le 3, \quad 0 \le l_{e1} \le 3. \tag{18}$$

The three dimensionless structure parameters are Cartesian axes l_{e1}, l_{e2}, and l_{e3}, respectively. The geometric space model of the biomimetic robotic elbow joint and the triangle $\Delta P_e Q_e S_e$ can be obtained by using (15) and (18), as shown in Figure 4. In order to facilitate drawing, the three-dimensional model is transformed into a two-dimensional model of the space model. The transformation relation of the dimensionless coordinate is generated as

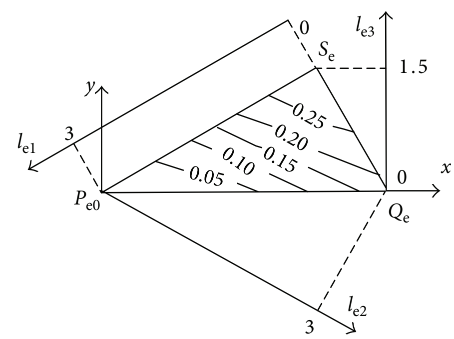

Figure 5: Globe kinematic decoupling performance evaluation index atlases of the elbow joint.

$$x = \frac{\sqrt{3} + (l_{e2} - l_{e1})}{\sqrt{3}}, \quad y = l_{e3}. \tag{19}$$

The global performance index is introduced into the spatial model, and the global kinematic decoupling performance index of the biomimetic robotic elbow joint is defined as

$$\xi_e = \frac{\int_{V_e} \wp_e dV_e}{\int_{V_e} dV_e}, \tag{20}$$

where ξ_e is the global kinematic decoupling performance index and V_e is the workspace of the elbow joint.

Using MATLAB software, the global kinematic decoupling performance map of the elbow joint in the plain geometric space model is drawn according to (1), (2), (3), (4), (5), (6), (7), (8), (9), (10), (11), (12), (13), (14), (15), (16), (17), (18), (19), and (20), as shown in Figure 5. In Figure 5, according to (16), the three coordinates l_{e1}, l_{e2}, and l_{e3} reflect the three structural parameters R_{e1}, R_{e2}, and R_{e3}, respectively.

From Figure 5, the global kinematic decoupling performance of the elbow joint is linearly distributed. With the increase of R_{e3} and R_{e2}, the global kinematic decoupling performance index values increase and the global kinematic

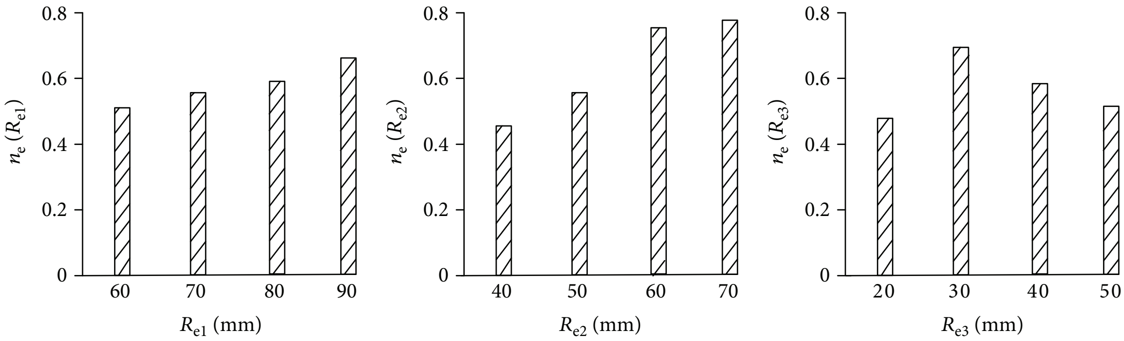

(a) The probability of R_{e1} (b) The probability of R_{e2} (c) The probability of R_{e3}

Figure 6: Probability distribution of the discrete histogram for the structure parameters for the biomimetic robotic elbow joint.

decoupling decreases gradually. With the increase of R_{e1}, the global kinematic decoupling performance index values decrease and the global kinematic decoupling increases.

4.2. The Structural Parameter Optimization. Structural parameters have a direct influence on the kinematic performance of the robot. Stan et al. [27] defined the optimal function based on stiffness and transmission quality. In this paper, the range of structural parameters of the elbow joint is defined. For the optimal design of the elbow joint, reasonable structural parameters should be selected for design and manufacturing. The analysis of global kinematic decoupling performance of the elbow joint based on the spatial model theory has laid the theoretical foundation for the selection of the elbow joint structural parameters. In this paper, based on the Monte Carlo method, the structural parameters of the elbow joint are optimized. The reasonable structural parameters of the elbow joint are obtained by using the probability statistic method.

The value range of the global kinematic decoupling performance index of the elbow joint is the interval [0, 1], which conforms to the rule of rectangle distribution. Combined with the structural features of the elbow joint, the structural parameter ranges of the elbow joint R_{e1}, R_{e2}, and R_{e3} are $R_{e1} \in [60, 90]$ mm, $R_{e2} \in [40, 70]$ mm, and $R_{e3} \in [20, 50]$ mm.

In [28], the structural parameters of the mechanical arm are optimized using the Monte Carlo method, and the intermediate value of the performance index is selected as the structural parameter optimization objective. Therefore, the intermedia value of the global kinematic decoupling index of the elbow joint is used as the optimal target of the elbow joint, in which $\xi_e = 0.1524$. When ξ_e is not more than 0.1524, the global kinematic decoupling performance is better.

Under the condition that the evaluation index of the global kinematic decoupling performance is better than the optimization target value, the distribution rule of sampling values of each parameter counted the sampling within the range of structural parameters, and the probability distribution of the structural parameters is obtained, as shown in Figure 6. It is clear from Figure 6 that the structure parameters are $R_{e1} = 90$ mm, $R_{e2} = 70$ mm, and $R_{e3} = 30$ mm, and the probability model of the structural parameters of the biomimetic robotic elbow joint is higher.

Table 1: The primary technical parameters of the biomimetic robotic elbow joint.

Design parameter	Technical index
Degree of freedom	2
Flexion	45°
Extension	45°
Internal rotation	50°
External rotation	45°
R_{e1}	90 mm
R_{e2}	70 mm
R_{e3}	30 mm
Motor	Maxon 273755
Coupling	Maxon 326665
Encoder	MR TL 256-1024 CPT

5. The Design of the Biomimetic Robotic Elbow Joint

Considering its processing and assembling process, the virtual prototype of the elbow joint is designed based on the optimized structure parameters, and primary technical parameters are shown in Table 1.

The virtual prototype model of the biomimetic robotic elbow joint is shown in Figure 7.

Servo motor 13 is installed on motor base 15, and servo motor 13 transmits the torque of the motor to carrier rod 23 through the planar four-bar mechanism. The other movement branch of the biomimetic robotic elbow joint is servo motor 7 mounted on elbow base 5. Servo motor 7 is fixedly connected with the rotating shaft on the bottom of connecting rod 17 through the mounting hole of coupling 8. Connecting rod 17 is connected to annular member 21 by a pair of coaxial rotating hinges 18 and 19. The other pair of coaxial rotary hinges 26 and 27 on annular member 21 is

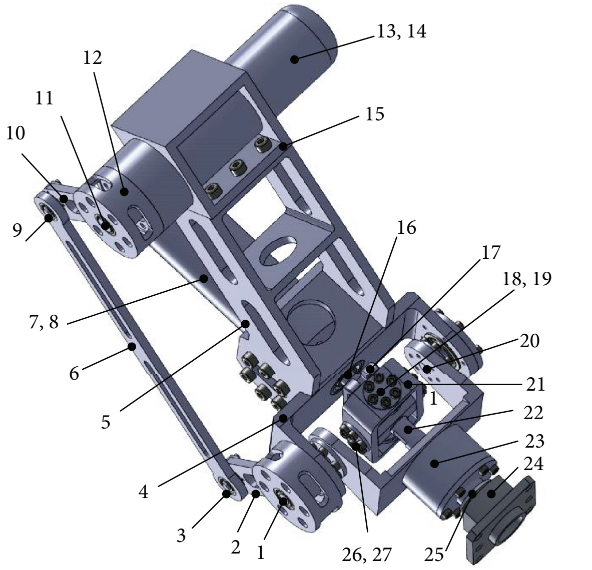

Figure 7: A novel biomimetic robotic elbow joint virtual prototype. 1, 3, 9, 11, 16, 18, 19, 20, 25, 26, and 27—revolute joints; 2 and 10—short bars; 4—frame; 5—upper arm; 6—long bar; 7 and 13—motor; 8 and 14—connectors; 12–15—motor bases; 17 and 23—connecting rods; 21—annular member; 22—moving platform; and 24—arm connector.

connected to moving platform 22. Arm connector 24 is fixedly connected to the bottom of the moving platform.

6. Simulation Experimental Analyses

6.1. Kinematic Simulation Experiment. In order to verify the correctness of the kinematic equations of the elbow joint mechanism, the results of the theoretical solution of the elbow joint and the simulation of the kinematic model are compared and analyzed. The movement trajectory of the biomimetic robotic elbow joint moving platform is expressed by

$$\begin{aligned} \gamma_e &= \sin(t)(\text{rad}), \\ \beta_e &= \cos(t)(\text{rad}). \end{aligned} \tag{21}$$

According to (11), under a given movement trajectory, the theoretical input angular velocity curve can be obtained by using MATLAB, as shown in Figure 8. A virtual prototype of the elbow joint is designed based on the optimized structure parameters, and the simulation value of the movement change curve of the input angle of the virtual prototype is obtained by using ADAMS movement simulation software, as shown in Figure 8. From Figure 8, the theoretical values and the simulation values are almost identical, which verifies the correctness of the modeling of the movement equation.

6.2. Kinematic Decoupling Simulation Experiment. A virtual prototype of the biomimetic robotic elbow joint is established, and a virtual simulation experiment is performed. Based on the Core software, the elbow joint is parametric designed. The parameter design range is the same as the parameter range in the spatial model theory. The parametric

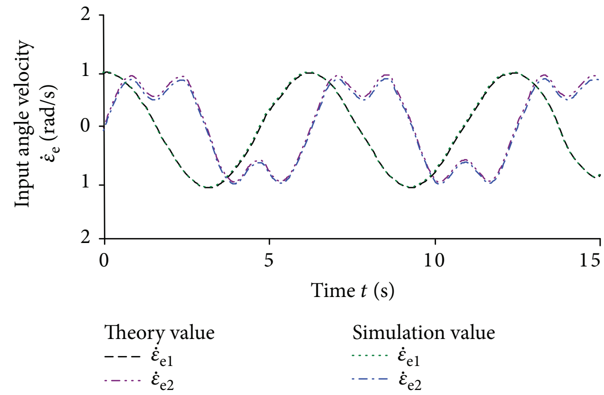

Figure 8: The input angle velocity curve of the elbow joint.

design variable increment is 5 mm, and 343 virtual prototypes of elbow joints with different structural dimensions were obtained.

The kinematic simulation of the reachable workspace is carried out for each prototype, and the total volume number of workspaces and the number volume of workspaces conforming to the kinematic decoupling index are recorded.

The structural parameters were obtained by optimizing the spatial model, which are 30 mm, 70 mm, and 90 mm. The kinematic decoupling workspace volume number is taken as the standard value W_{d0}, and the virtual prototype is defined by the standard prototype. The volume number of kinematic decoupling workspaces obtained by other different structural parameters is W_d. The kinematic decoupling workspace volume ratio Wds is defined as

$$\text{Wds} = \frac{W_d}{W_{d0}} \times 100\%. \tag{22}$$

The 343 elbow joint movement decoupling volume numbers are compared with the basic kinematic decoupling volume number. When one structural parameter is changed and the other parameters are unchanged in the standard prototype, the volume number of kinematic decoupling workspaces is acquired, and the influence curve of each structural parameter on the size of the elbow joint kinematic decoupling workspace is drawn, as shown in Figure 9.

In Figure 9, the kinematic decoupling volume ratio Wds increases with the increase of R_{e2} and R_{e3}, and with the increase of R_{e3}, the volume ratio of the kinematic decoupling workspace firstly increases and then decreases. The change trend is the same as that in Figure 6, the rationality of optimization of the structural parameters can be proved, and the kinematic decoupling analysis is correct.

7. Conclusion

The kinematic decoupling analysis of a novel biomimetic robotic elbow joint was performed. Analysis of the kinematic decoupling of the elbow joint is symmetrical in the workspace, and the motion is completely decoupling when driven by a single motor. The global kinematic decoupling performance of the elbow joint showed a linear distribution. With

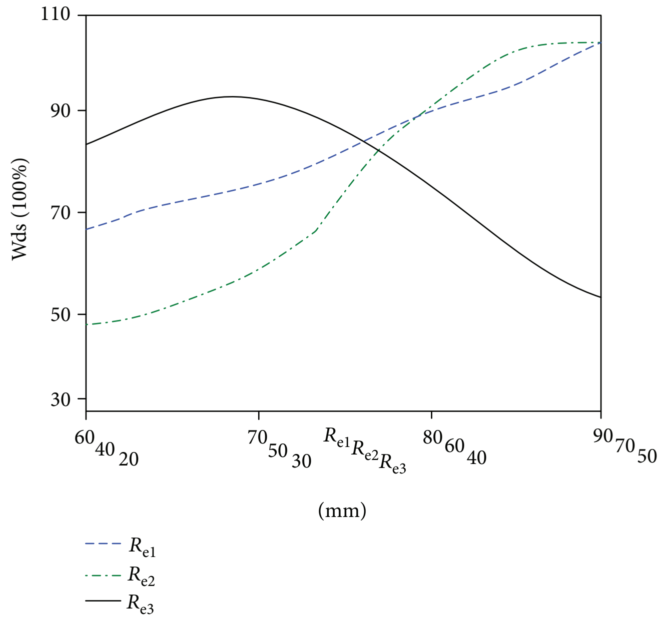

FIGURE 9: The influence curve of structural parameters on the kinematic decoupling workspace volume ratio.

the increase of R_{e3}, the decoupling decreased gradually. The structure parameters of the elbow joint were selected by the Monte Carlo method, which are$R_{e1} = 90$ mm, $R_{e2} = 70$ mm, and $R_{e3} = 30$ mm. Considering the process and the assembly process, the elbow joint prototype had been designed and developed. Finally, simulation experiments have verified the correctness of the kinematic equation and kinematic decoupling, as well as the rationality of the optimization use of spatial model parameters.

In summary, the biomimetic robotic elbow joint has two degrees of freedom and good decoupling characteristics, which can be applied in rehabilitation robot, biomimetic robot, industrial robot, humanoid robot arm, and other fields.

Conflicts of Interest

The authors declare that there is no conflict of interests regarding the publication of this paper.

Acknowledgments

This research was supported by the Chinese National Natural Science Fund (E51505124), Hebei Provincial Natural Science Foundation (E2017209252), Department of Education of Hebei Province (QN2015203 and 2015GJJG084), and Online Education Research Fund of Education Research Center of the Ministry of Education (2016YB117).

References

[1] H.-Y. Xu, Y.-L. Fu, S.-G. Wang, and J.-G. Liu, "Research on biomimetic robotics," *Robot*, vol. 26, no. 3, pp. 283–288, 2004.

[2] G. Wang, D. Chen, K. Chen, and Z. Zhang, "The current research status and development strategy on biomimetic robot," *Journal of Mechanical Engineering*, vol. 51, no. 13, pp. 27–44, 2015.

[3] L. D. Paulson, "Biomimetic robots," *Computer*, vol. 37, no. 9, pp. 48–53, 2004.

[4] Y. Lu, "The significance and development of bionics," *Scientific Chinese*, vol. 4, pp. 22–24, 2004.

[5] B. Tondu, "Modelling of the shoulder complex and application to the design of upper extremities for humanoid robots," in *5th IEEE-RAS International Conference on Humanoid Robots, 2005*, pp. 313–320, Tsukuba, Japan, December 2005, IEEE.

[6] B. Tondu, "Kinematic modelling of anthropomorphic robot upper limb with human-like hands," in *2009 International Conference on Advanced Robotics*, pp. 1–9, Munich, Germany, June 2009, IEEE.

[7] S. Hong, C. Cho, H. Lee, S. Kang, and W. Lee, "Joint configuration for physically safe human–robot interaction of serial-chain manipulators," *Mechanism and Machine Theory*, vol. 107, pp. 246–260, 2017.

[8] Y. B. Li, Z. L. Jin, S. M. Ji, and F. Gao, "Error analysis of a parallel anthropopathic shoulder," *Journal of Basic Science and Engineering*, vol. 17, no. 3, pp. 446–451, 2009.

[9] C. Li, S. Xie, H. Li, D. Wang, and J. Luo, "Design of bionic eye based on spherical parallel mechanism with optimized parameters," *Robot*, vol. 32, no. 6, pp. 781–786, 2010.

[10] J. Klein, S. Spencer, J. Allington, J. E. Bobrow, and D. J. Reinkensmeyer, "Optimization of a parallel shoulder mechanism to achieve a high-force, low-mass, robotic-arm exoskeleton," *IEEE Transactions on Robotics*, vol. 26, no. 4, pp. 710–715, 2010.

[11] L. Zhang and Z. Jin, "Analysis on driving characteristics of a robot shoulder joint based on parallel mechanism," *Energy Education Science and Technology Part A: Energy Science and Research*, vol. 32, no. 6, pp. 5073–5080, 2014.

[12] L. Sun, Y. Liu, and Y. Zhu, "Position analysis of a spherical 3-DOF parallel decoupling mechanism for wrist joints China," *Mechanical Engineering*, vol. 14, no. 10, pp. 0831–0834, 2003.

[13] B. Cui and Z. Jin, "Analysis of statics performance for a novel elbow joint of agricultural robot," *Transactions of the Chinese*

Society of Agricultural Engineering, vol. 27, no. 3, pp. 122–125, 2011.

[14] B. Cui, L. Chen, Z. Wang, Y. Zhao, Z. Li, and Z. Jin, "Design and dynamic analysis of a novel biomimetic robotics hip joint," *Applied Bionics and Biomechanics*, vol. 2015, Article ID 145040, 8 pages, 2015.

[15] X. Xu, L. Hou, X. Huang, and W. Zhang, "Design and research of a wearable robot for upper limbs rehabilitation based on exoskeleton," *Robot*, vol. 2, p. 003, 2014.

[16] G. S. Luo, J. W. Chen, and L. Y. Gu, "An elbow of 7-DOF hydraulic manipulator based on double-screw-pair transmission," *Robot*, vol. 36, no. 1, pp. 36–43, 2014.

[17] M. Hwang, U.-J. Yang, D. Kong et al., "A single port surgical robot system with novel elbow joint mechanism for high force transmission," *The International Journal of Medical Robotics and Computer Assisted Surgery*, vol. 13, no. 4, 2017.

[18] M. M. Stanišić and C. M. Goehler, "Reproducing human arm motion using a kinematically coupled humanoid shoulder–elbow complex," *Applied Bionics and Biomechanics*, vol. 5, no. 4, 185 pages, 2008.

[19] E.-C. Lovasz, D. T. Mărgineanu, V. Ciupe et al., "Design and control solutions for haptic elbow exoskeleton module used in space telerobotics," *Mechanism and Machine Theory*, vol. 107, pp. 384–398, 2017.

[20] H. Zou and F. Gao, *Progress of Modern Mechanism*, Higher Education Press, Beijing, China, 2007.

[21] J. Gong, Y. Zhang, and F. Gao, "Decoupling characteristics of parallel mechanism," *The Mechanical Engineering of China*, vol. 17, no. 14, pp. 1509–1511, 2006.

[22] H. Shen, L. Ma, X. Zhu, and T. Yang, "Analyses of kinematics and workspace for a 3-DOF fully decoupled parallel mechanism," *Transactions of the Chinese Society of Agricultural Machinery*, vol. 36, no. 11, pp. 130–133, 2005.

[23] Y. Xu, D. Zhang, J. Yao, and Y. Zhao, "Type synthesis of the 2R1T parallel mechanism with two continuous rotational axes and study on the principle of its motion decoupling," *Mechanism and Machine Theory*, vol. 108, pp. 27–40, 2017.

[24] T. Essomba and L. Nguyen Vu, "Kinematic analysis of a new five-bar spherical decoupled mechanism with two-degrees of freedom remote center of motion," *Mechanism and Machine Theory*, vol. 119, pp. 184–197, 2018.

[25] B. Y. Cui and L. W. Chen, "Analysis of kinematics and design of structure parameters for a bionic parallel leg," *Journal of Biomimetics, Biomaterials and Biomedical Engineering*, vol. 20, pp. 23–33, 2014.

[26] B. Y. Cui, L. W. Chen, Y. T. Xie, and Y. D. Hu, "Static decoupling performance analysis and design of bionic elbow joint," *Journal of Biomimetics, Biomaterials and Biomedical Engineering*, vol. 36, pp. 34–44, 2018.

[27] S.-D. Stan, M. Manic, V. Maties, and R. Balan, "Evolutionary approach to optimal design of 3 DOF translation exoskeleton and medical parallel robots," in *2008 Conference on Human System Interactions*, pp. 720–725, Krakon, Poland, May 2008.

[28] Y. B. Li, Z. L. Jin, and S. M. Ji, "Design of a novel 3-DOF hybrid mechanical arm," *Science in China Series E: Technological Sciences*, vol. 52, no. 12, pp. 3592–3600, 2009.

Hindawi
Applied Bionics and Biomechanics
Volume 2018, Article ID 9735979, 10 pages
https://doi.org/10.1155/2018/9735979

Research Article

Initial Clinical Trial of Robot of Endovascular Treatment with Force Feedback and Cooperating of Catheter and Guidewire

Yuhua Jiang, Keyun Liu, and Youxiang Li

Department of Interventional Neuroradiology, Beijing Neurosurgical Institute and Beijing Tiantan Hospital, Capital Medical University, Beijing 100050, China

Correspondence should be addressed to Keyun Liu; liukeyunsll@163.com and Youxiang Li; liyouxiang@263.net

Received 9 December 2017; Accepted 15 March 2018; Published 16 April 2018

Academic Editor: Liwei Shi

To evaluate the feasibility and safety of the robot of endovascular treatment (RobEnt) in clinical practice, we carried out a cerebral angiography using this robot system. We evaluated the performance of application of the robot system to clinical practice through using this robotic system to perform the digital subtraction angiography for a patient who was suspected of suffering intracranial aneurysm. At the same time, through comparing the postoperative head nuclear magnetic and blood routine with the preoperative examination, we evaluated the safety of application of the robot system to clinical practice. We performed the robot system to complete the bilateral carotid artery and bilateral vertebral arteriography. The results indicate that there was no obvious abnormality in the patient's cerebral artery. No obvious abnormality was observed in the examination of patients' check-up, head nuclear magnetism, and blood routine after the digital subtraction angiography. From this clinical trial, it can be observed that the robot system can perform the operation of cerebral angiography. The robot system can basically complete the related observation indexes, and its accuracy, effectiveness, stability, and safety basically meet the requirements of clinical application in neurointerventional surgery.

1. Introduction

With lifestyle changing, the population of "hypertension, hyperlipidemia, and hyperglycemia" is increasing year by year. The incidence of cardiovascular and cerebrovascular disease is increasing. At present, the morbidity, recurrence rate, and mortality of cardiovascular and cerebrovascular disease are very high [1, 2]. Endovascular treatment is a safe, effective, minimally invasive new method to be promoted in clinical treatment. It plays an increasingly important role in the treatment of vascular disease and gradually becomes the best treatment, while there are still some bottlenecks restricting the development of the endovascular treatment. For example, high demand of operation technique, stability and accuracy, radiation exposure, and long-term radiation exposure of vascular interventional surgeon may lead to leukocyte reduction and cell carcinogenesis, and so on. At the same time, there is a limit to the stability and precision of human hand operation.

Despite technology is progressing in vasointerventional materials and vascular intervention techniques, many of these procedures continue to be several hours in duration and require the use of significant amounts of fluoroscopy resulting in considerable radiation exposure to the vascular interventional surgeons [3, 4]. Although protective garments can protect parts of the vascular interventional surgeon's body from radiation scatter, such protective garments are heavy and uncomfortable resulting in increased surgeon fatigue during long procedures as well as physical stresses that will result in orthopedic injuries [5, 6]. And fatigue can reduce the stability and accuracy of surgical operations.

But the vascular intervention robot conforms to the clinical requirements. Robots have the following advantages: high accuracy, stability, and safety; the interventional surgeon can operate the robot outside the operating room, and the radiation damage is small. Other systems for vascular interventional surgery have been developed to the degree that allows the vascular interventional surgeon to control and direct catheter movement at a distance from the patient [7–13]. These systems allow the vascular interventional surgeon to be removed from radiation exposure without the use of cumbersome protective garments. However, these systems are expensive and complex, and the product positioning is relatively unitary, it can only be used for the single type of vascular disease, but not various types of vascular disease.

In view of the above deficiencies, cooperating with the Beijing Institute of Technology, we have developed a master-slave cardiovascular and cerebrovascular interventional surgical robotic system—the robot of endovascular treatment (RobEnt). The robot system increases the accuracy of force feedback measurement, improves the accuracy of catheter push and rotation, reduces the damage to the surface of catheter and guidewire, and increases the true sense of operation at the same time. And the complex operation can be accomplished by the cooperative operation of the catheter and guidewire. Meanwhile, the system adopts master-slave operation mode, the master controller is located outside the operating room, and the slave manipulator is set in the operation room. Through the doctor operates the handle of the master controller, the control signal is transmitted to the slave, using the slave manipulator to complete the operation. By using master-slave operation, the doctor can avoid the operation directly under the radiation line and solve a series of problems caused by the long-term acceptance of radiation.

The robot system is equipped with a catheter controller and a guidewire controller on the slave end device, so that the catheter and the guidewire can be operated simultaneously, and it has tactile feedback system. The surgeon can feel the resistance of the catheter and the guidewire on the operating handle. It solves the problem that the existing robot is difficult to complete the cooperative operation of the catheter and guidewire and cannot intuitively feel the operative procedure. The slave manipulator takes the form of multiple platform-connecting blocks on one track; the platform-connecting blocks are used for fixing the catheter controller or guidewire controller and control the axial movement of the catheter and guidewire on a single track. Due to the use of a plurality of blocks running on the same track, running distance of each slider coincides. It can improve the safety and operability of interventional operation or angiography, and the structure is simple and easy to implement. The device can also be used for surgical simulation and training.

The robot system can perform multiple vascular interventional operations including cerebral arteriography, angiography of the heart, renal arteriography, and so on. At present, the robot system has completed the performance self-test and 10 animal experiments. The analysis of the experimental process and results indicated that the robot achieved the same operation quality as manual operation. Furthermore, we conducted a clinical trial using the robot system to verify its feasibility and safety applied to clinical practice. This report describes the vascular intervention robotic system's performance and safety in this clinical study.

2. Materials and Methods

2.1. Patient. Five inpatients aged from 20 to 60 years old were chosen in our hospital. All the patients were suspected of having intracranial aneurysms and needed to be determined by cerebral angiography. The exclusion criteria included the patients who were long time in bed, could not take care of oneself, could not cooperate with inspection, used antibiotics in two weeks, suffered from serious internal medicine diseases, chronic inflammatory diseases, acute cerebrovascular events (included ischemic stroke, cerebral hemorrhage, and subarachnoid hemorrhage) in six months, other cerebrovascular diseases, brain tumor, and other known neurological diseases, and could not sign informed consents.

In the end, we screened out the most appropriate patient according to exclusion criteria and after the contrast analysis. The participating patient gave informed consent for study participation. The study protocol was approved by the local ethics committee.

According to the requirements of preoperative examination of cerebral angiography in our hospital, we had carried out the related examinations, including chest X-ray, electrocardiogram, blood routine, various biochemical tests, and so on. Inspection results were diagnosed by two specialist neurointerventional surgeons under the double blind. They agreed that the patient had no contraindications for digital subtraction angiography (DSA), and the patient should have a DSA to make a clear diagnosis.

2.2. Experimental Instrument

(1) The robot of endovascular treatment mainly consists of two parts: the master controller console and the slave manipulator.

(2) Conventional surgical equipment and vascular intervention equipment and consumables are presented. The main consumables are as follows:

   (a) Femoral artery sheath module, 5F, DQ05113818, Y connector assembly, 5F, DMK-Y (Beijing Demax Medical Technology Co. Ltd.)

   (b) Angiographic catheter, 5F, head angle 135°, 451-514HO (Cordis Corporation)

   (c) 0.035-inch hydrophilic membrane guidewire, 150 cm, RF*GA35153M (Terumo Corporation)

   (d) Medical angiography X-ray machine, Artis zee III floor (Siemens)

(3) Drugs and reagents are the following:

   (a) 2% lidocaine hydrochloride injection (Beijing Yimin Pharmaceutical Co. Ltd.)

   (b) 5% glucose injection (Shanghai Baxter Healthcare Ltd.)

   (c) 0.9% saline injection (Shanghai Baxter Healthcare Ltd.)

(a) (b)

Figure 1

(d) Iohexol injection (Shanghai AXA Pharmaceutical Co. Ltd.)

(e) Low-molecular-weight heparin calcium injection (GlaxoSmithKline (Tianjin) Co. Ltd.)

2.3. Experimental Procedure

(1) After disinfection and sterilization, the robot system was installed in the operating room. The master controller console and the slave manipulator are fixed, respectively. We adjusted the angle of the slave manipulator and operated the handle of the master controller console. The performance of RobEnt was satisfactory (Figure 1).

(2) We connected the Y type valve assembly, 5F single bend angiographic catheter, and 150 cm hydrophilic membrane guidewire, respectively, to the system and operated the control platform handle to control the guidewire and catheter forward, backward, and rotation. The guidewire and catheter movement performance was good (Figure 2).

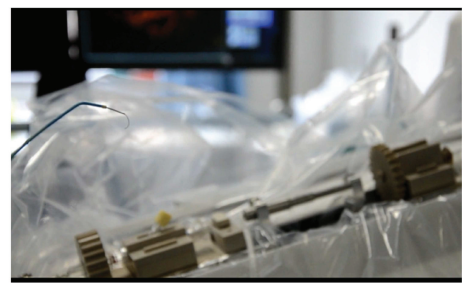

Figure 2

(3) The bilateral inguinal surgery area was disinfected with 0.5% iodophor for two times, and the routine operation sheet was given. The 5F femoral artery sheath was inserted into the femoral artery at the left side of the patient, and the Seldinger puncture was performed. 5F single bend angiographic catheter was injected with high-pressure heparin saline continuously, and the catheter was inserted into the artery sheath about 5 cm (Figure 3).

Figure 3

(4) Adjusting the operating bed and making the guidewire and catheter exposed to the X-ray, the surgeon controlled the operation handle at the operating table, keeping the catheter position unchanged, advanced guidewire about 10 cm. X-rays showed that the guidewire had entered the left iliac artery; we rotated the guidewire tip pointing to the left, keeping the relative position between the guidewire and catheter unchanged, meanwhile advanced the guidewire and catheter. The guidewire and catheter were sent into the aortic arch along the abdominal aorta. Keeping the catheter position unchanged, the surgeon controlled the guidewire into the right carotid artery and pushed the catheter along the guidewire, then selected the appropriate position, withdrew the guidewire, and performed the right carotid artery angiography. The right vertebral artery, the left common carotid artery, and the left vertebral artery angiography were performed, respectively, and the three-dimensional angiography was performed on the right common carotid artery. The cerebral angiography showed good, and there was no obvious abnormality (Figure 4).

(5) After the angiography, we pulled out the catheter and femoral artery sheath. The puncture site was compressed for 15 minutes, pressure dressing on the puncture point (Figure 5).

(6) After withdrawing the robot system from the operating room, the catheter room was cleaned, and related disinfection was carried out.

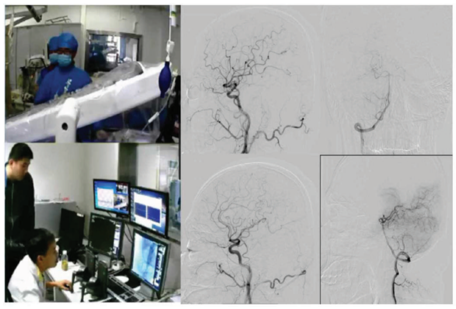

(a)

(b)

Figure 4

Figure 5

(7) After surgery, the changes of the patient's condition were closely monitored, and the blood routine and the head nuclear magnetism were reviewed.

3. Results

(1) Accuracy, effectiveness, and stability index are the following:

(a) The surgeon's console basically meet ergonomic and can provide the operating platform in line with the surgeon's operating habits.

(b) The master controller console can monitor the operation information of the catheter and guidewire (including microwire and microcatheter), the resistance condition of the catheter and guidewire, the position of the catheter and guidewire, and the contact of the catheter and guidewire with the blood vessel.

(c) The handle of the console is flexible and reliable, which can provide the force feedback for the operator. The doctor can feel the catheter state during the operation and carry out the operation according to the force information of the catheter.

(d) When the gear held the guidewire and the catheter, it had a good fit and will not damage the surface coating of the catheter and guidewire.

(e) The robot system can maintain the synchronization action with the doctor-operating lever.

(f) The robot system does not affect the operation of the equipment around the operating bed after installation and has good operability.

(g) Under the X-ray operation, the system can accurately and timely realize the movement of the single curved angiographic catheter and 150 cm super slide loach guidewire in the blood vessel forward, backward, and rotation, consistent with the master and the slave, and can accurately and timely reflect the operation of the master and the slave, and had achieved the following indicators:

(i) The maximum movement distance of the catheter and the guidewire is 0.9 m, the positioning accuracy of the axial position is not less than 0.2 mm, and the rotation accuracy is not less than 2 degrees. The maximum speed of linear motion can reach 90 cm/s, and the maximum rotation speed can reach 420°/s.

(ii) The sterilization time of robot system is less than 1 h.

(iii) The time of changing the catheter and the guidewire is less than 3 min.

(iv) The DSA device will not affect the stability of the robot system.

(v) The robot system can control the catheter and guidewire into any branch vessel with an inner diameter greater than 3 mm and an angle less than 90 degrees from the main vessel.

(h) From the slave manipulator, the catheter can be placed into the patient's blood vessel accurately and timely according to the doctor's instructions.

(2) Security index is as follows:

(a) After the whole brain angiography was carried out with the robot system, the elastic bandage of the puncture site of the patient was bandaged for 24 hours. The puncture site had no oozing of blood and exudate, and there was no swelling, heat pain, and other infection signs. After 24 hours, the patient can walk out of bed without discomfort symptoms.

日 期 20171103
样本号 S 3727
上机号
处理序号
标 本 全血
864
病人ID号 547731
病历号
姓 名 苏永平
年龄性别 37 岁 男
科 室 介入病房
病床号 183 9
诊 断 颅内动脉瘤
大 夫 穆士卿
检验者 李芬芬
审核者 柏景乔
申请时间 20171103 1056
采样时间 20171103 1114
送检时间 20171103 1127
核收时间 20171103 1127
检验时间
报告时间 20171103 1159
第1次打印
第2次打印
打印份数 0份
设备名称 门诊血型Diana
记录个数:11

项目：ABO血型
参考：
A型

ABO血型	A型		
RH	阳性		
*WBC	6.97	4.00-10.00	10E9/L
LY#	2.15	0.90-5.20	10E9/L
MONO#	0.37	0.16-1.00	10E9/L
NEUT#	4.22	2.00-7.50	10E9/L
EO#	0.21	0.00-0.80	10E9/L
BA#	0.02	0.00-0.20	10E9/L
LY	30.8	20.0-50.0	%
MO	5.30	2.00-8.00	%
GR	60.60	50.00-75.00	%
EO%	3.00	0.50-5.00	%
BA%	0.30	0.00-1.50	%
*RBC	4.86	3.50-5.50	10E12/L
*HGB	152	110-160	g/L
*HCT	43.80	37.00-50.00	%
*MCV	90.1	80.0-100.0	fl
*MCH	31.3	27.0-32.0	pg
*MCHC	347.0	320.0-360.0	g/L
RDW	42.00		fl
RDW-CV	12.8	10.1-16.0	%
*PLT	248	100-300	10E9/L
PDW	10.1	15.0-17.0	fL
MPV	9.5	7.0-11.0	fl
P-LCR	20.3		%
PCT	0.23		%

Figure 6: Preoperative blood routine examination.

(b) The time of complete cerebral angiography using the robotic system was about 40 minutes, which was almost the same as that of the interventional surgeons in our hospital.

(c) Routine blood test is as follows:

The patient underwent routine preoperative examination after admission. There was no obvious abnormality in blood routine. Blood routine examination was repeated 24 hours after operation, and no obvious abnormality was found. Moreover, the patient is generally in good condition, no fever, and other signs of discomfort (Figures 6 and 7).

(d) Head nuclear magnetic examination is as follows:

Intracranial aneurysm has been suspected after head MRI in the local hospital of the patient, and then the suspected has been overturned in our hospital after performing cerebral angiography. 48 hours after the operation, we performed 7.0 T nuclear magnetic resonance examination on the head of the patient in the Biophysics Institute of Chinese Academy of Sciences. The results showed that there were no new ischemic or hemorrhagic foci after the diagnosis of two interventional surgeons, and there was no obvious abnormality in the cerebral vessels (Figures 8 and 9).

4. Discussions

This clinical trial demonstrated that the robot system has the ability to complete cerebral angiography. The important precondition for complete cerebral angiography is to super select the guidewire and catheter to enter each branch of cerebral artery. In this clinical trial, we successfully operated

*WBC	7.50	4.00-10.00	10E9/L
LY#	1.89	0.90-5.20	10E9/L
MONO#	0.42	0.16-1.00	10E9/L
NEUT#	4.91	2.00-7.50	10E9/L
EO#	0.25	0.00-0.80	10E9/L
BA#	0.03	0.00-0.20	10E9/L
LY%	25.20	20.00-50.00	%
MO%	5.60	2.00-8.00	%
GR%	65.50	50.00-75.00	%
EO%	3.30	0.50-5.00	%
BA%	0.40	0.00-1.50	%
*RBC	4.99	3.50-5.50	10E12/L
*HGB	155	110-160	g/L
*HCT	44.30	37.00-50.00	%
*MCV	88.80	80.00-100.00	fl
*MCH	31.10	27.00-32.00	pg
*MCHC	350	320-360	g/L
RDW-SD	43.10		fl
RDW-CV	13.30	10.10-16.00	%
*PLT	251	100-300	10E9/L
PDW	11.1	15.0-17.0	fL
MPV	9.70	7.00-11.00	fl
P-LCR	23.0		%
PCT	0.240		%

Figure 7: Postoperative blood routine examination.

the robot to super select the catheter and guidewire into the main cerebral arteries. The operating time of the robot system was not significantly different from that of the interventional surgeons in our hospital. The speed and accuracy of the advancing, retreating, and rotating of the guidewire and the catheter can be continuously adjusted by the slave manipulator, and the catheter and the guidewire can cooperate with each other and deliver simultaneously. The feasibility, accuracy, and stability of the robot system are up to standard. Compared with hand operation, the robot system has better accuracy and stability and meets the requirements of clinical vascular interventional surgery.

Three aspect inspections have been used to estimate this system's security.

First, the femoral artery puncture site may produce additional damage by the process that the slave manipulator holds the guidewire and the catheter into the femoral artery through the femoral artery sheath, and the damage is mainly estimated by physical examination and the symptoms of the patient. After the operation, the puncture site has no errhysis, no seepage, no inflamed hot pain, and so on, and no masses have been found by palpation and no vascular murmur by auscultation. The patient can get off of the bed freely by himself 24 hours later after the operation, with no activities and sensory disturbance. Therefore, in this cerebral angiography, the robotic system did not cause additional damage to the puncture artery.

Secondly, another indicator to evaluate safety of the system is the effect of aseptic operation, mainly observing whether or not the patient has an infection after surgery. The robot system was installed in the surgical bed in a sterile environment after being strictly disinfected, and the sterile membrane had been used to cover the machine before operation. The contact area of the slave manipulator between the guidewire, catheter, and the femoral artery sheath was strictly disinfected again. Before operation, the patient had no fever, no abnormal blood routine, and no related infections. 24 hours later after the operation, there was no abnormality in the blood test. Vital signs had been checked every 12 hours after operation, and no fever or other discomforts occurred when the patient was discharged on the third day. It is indicated that this robot system is qualified for the aseptic operation of total cerebral angiography.

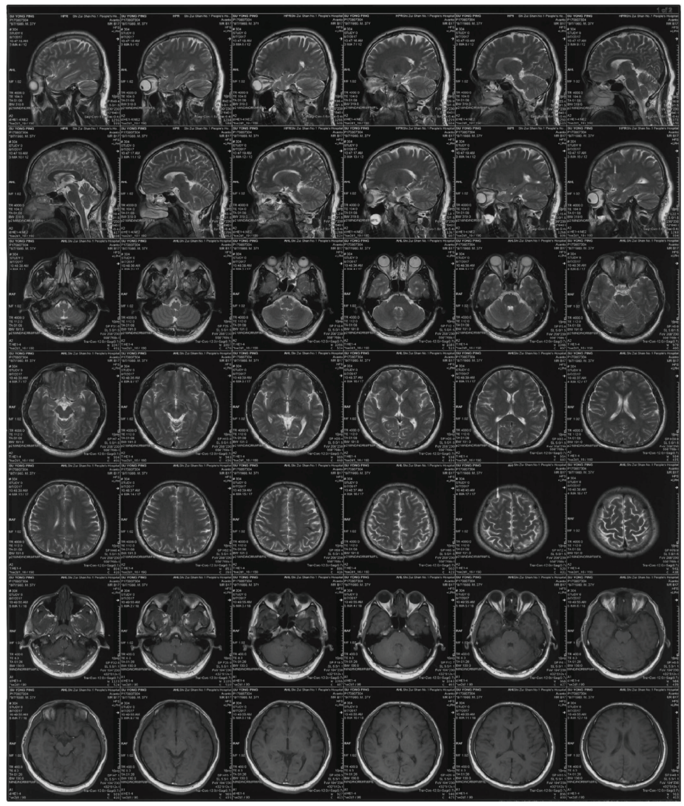

(a)

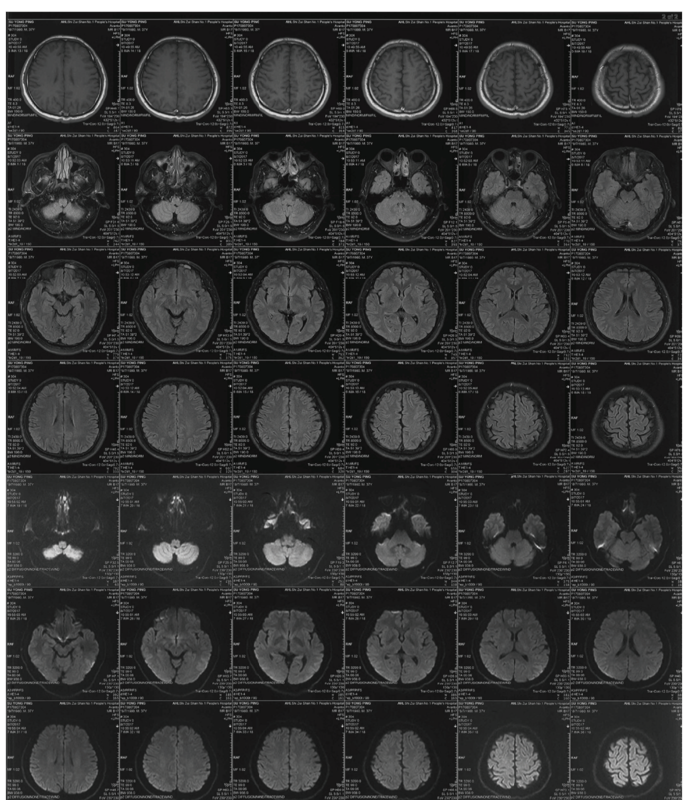

(b)

FIGURE 8: Preoperative head nuclear magnetic resonance examination.

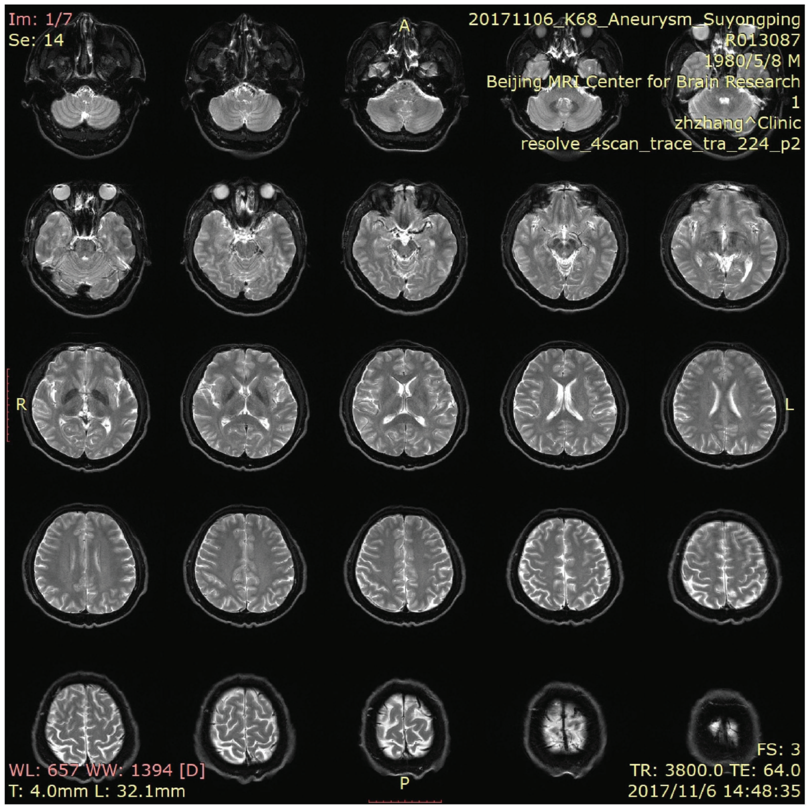

(a)

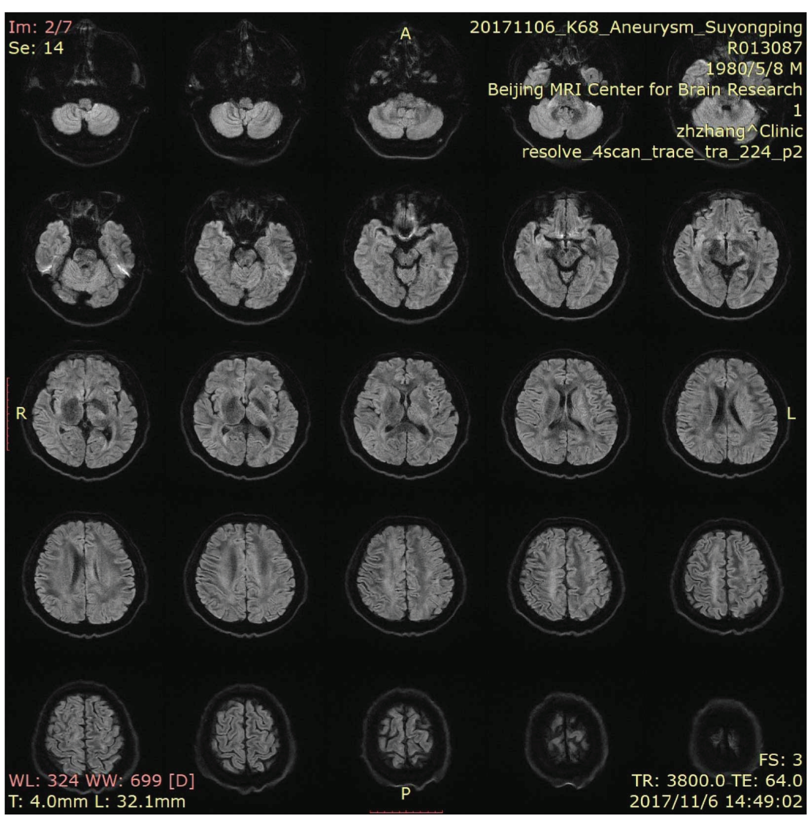

(b)

Figure 9: Postoperative head nuclear magnetic resonance imaging.

Finally, the most serious complication of cerebrovascular angiography is cerebrovascular events, and the occurrence of cerebrovascular events is an important index to evaluate the operation safety of the robot. Therefore, we have been completed the examination of head 7.0 T MRI for the patient 48 hours later after operation. The results of the cranial MRI were viewed by two professional neurointerventional surgeons; combined with the head MRI before operation, new focal ischemia or hemorrhage of intracranial had not been found. At the same time, 24 hours and 48 hours later after operation, the positive signs associated with cerebral vascular events of the patient had not been found, such as dizziness, headache, physical activity disorder, and sensory dysfunction. On the seventh day after the operation, we conducted a telephone follow-up to the patient, and the patient had no positive signs of the nervous system. This indicates that there are no related cerebral vascular complications in this operation of the robotic system for cerebral angiography. And this robot system is safe to be used in clinic.

In recent years, vascular interventional surgery has developed rapidly, and the progress of related technologies and the upgrading of supporting equipment have enabled interventional surgeons to perform more complicated vascular interventional procedures. However, because the accuracy and stability of hand operation are not enough, there is still a high risk of complex surgery. At the same time, the number of vascular interventional procedures is increasing, and the total operation time is also increasing. The amount of X-ray radiation and the strain caused by wearing protective equipment to the body also increased [3–6]. This mode of operation that the main end system outside the operating room manipulates the slave end system in the operating room to perform vascular interventional operation had successfully solved these problems. It allows the operator to perform vascular interventional procedures without radiation protection on the outside of the radiation field and has higher accuracy and stability.

At the same time, the robot system is equipped with a catheter controller and a guidewire controller on the slave end device, which can operate the catheter and guidewire simultaneously, and it has the tactile feedback system, which solves the problem that the existing technology is difficult to meet the requirements of the cooperative operation of the catheter and the guidewire and cannot directly feel the tactile information as the traditional surgical operation. It improves the safety and operability of vascular interventional operation, and the doctor can feel the power and achieve more precise operation. The device can also be used for the training of vascular interventional operation. There are other commercial vascular interventional catheter manipulation systems, but they are very different in terms of concept and design [14–17].

There are several deficiencies in this experiment and the robot system. We have only one clinical trial, which cannot be controlled by grouping, and the evaluation of each index of the robot system needs more clinical trials to verify the analysis. Cerebral angiography was performed only in this clinical trial without angiography of other important vessels and organs. Although cerebral angiography requires higher accuracy, stability, and safety, no angiography of other important vessels in the human body may bias the results. The tilt angle of the slave manipulator needs to be adjusted at the time of installation, and it is difficult to adjust the tilt angle in the process of experiment. Therefore, further optimization of the equipment is needed. Because the robot system is in the experimental research and development stage, there is no connection to the DSA device, and experimenter needs to operate DSA equipment under X-ray in the operating room. When this problem is solved, all operations can be performed outside the operating room.

5. Conclusions

The result of this clinical trial shows that the robotic system has completed a cerebral angiography with accuracy, stability, and security. The robot system can realize the coordinated operation of the catheter and the guidewire. Meanwhile, the surgeon can perceive the manipulation power and achieve more accurate effect by the equipped force feedback system. We used the robotic system to operate the catheter and guidewire from the femoral artery to the aortic arch and then entered the major cerebral arteries and completed the cerebral angiography. According to the operation effect, the clinical manifestations and examination result of patient, we conclude that the accuracy, effectiveness, stability, and safety of this robot system reach the standard.

Conflicts of Interest

The authors declare that there are no conflicts of interest.

Acknowledgments

This research is supported by the National High Technology Research and Development Program (863) (Grant no. 2015AA043202) and the Scientific and Technological Projects of Science and Technology Commission of Beijing (Grant no. Z161100002616002).

References

[1] F. Jokar, H. Yousefi, A. Yousefy, and M. Sadeghi, "Begin again and continue with life: a qualitative study on the experiences of cardiac rehabilitation patients," *The Journal of Nursing Research*, vol. 25, no. 5, pp. 344–352, 2017.

[2] J. Yong, L. Xiao-Yan, H. Nan, H. Zheng-Jing, and W. Fan, "Epidemiologic characteristics of cerebrovascular disease mortality in China, 2004-2005," *Zhonghua Yu Fang Yi Xue Za Zhi*, vol. 44, no. 4, pp. 293–297, 2010.

[3] Center for Devices and Radiological Health (CDRH), U.S. Food and Drug Administration (FDA), *Initiative to Reduce Unnecessary Radiation Exposure from Medical Imaging*, FDA, Silver Spring, MD, USA, 2010.

[4] K. P. Kim, D. L. Miller, S. Balter et al., "Occupational radiation doses to operators performing cardiac catheterization procedures," *Health Physics*, vol. 94, no. 3, pp. 211–227, 2008.

[5] L. W. Klein, D. L. Miller, S. Balter et al., "Occupational health hazards in the interventional laboratory: time for a safer

environment," *Journal of Vascular and Interventional Radiology*, vol. 20, no. 2, pp. 147–152, 2009.

[6] N. L. Hughes, A. Nelson, M. W. Matz, and J. Lloyd, "AORN ergonomic tool 4: solutions for prolonged standing in perioperative settings," *AORN Journal*, vol. 93, no. 6, pp. 767–774, 2011.

[7] C. Pappone, G. Vicedomini, F. Manguso et al., "Robotic magnetic navigation for atrial fibrillation ablation," *Journal of the American College of Cardiology*, vol. 47, no. 7, pp. 1390–1400, 2006.

[8] V. Y. Reddy, P. Neuzil, Z. J. Malchano et al., "View-synchronized robotic image-guided therapy for atrial fibrillation ablation: experimental validation and clinical feasibility," *Circulation*, vol. 115, no. 21, pp. 2705–2714, 2007.

[9] B. Schmidt, K. R. J. Chun, R. R. Tilz, B. Koektuerk, F. Ouyang, and K. H. Kuck, "Remote navigation systems in electrophysiology," *Europace*, vol. 10, Supplement 3, pp. iii57–iii61, 2008.

[10] P. Kanagaratnam, M. Koa-Wing, D. T. Wallace, A. S. Goldenberg, N. S. Peters, and D. W. Davies, "Experience of robotic catheter ablation in humans using a novel remotely steerable catheter sheath," *Journal of Interventional Cardiac Electrophysiology*, vol. 21, no. 1, pp. 19–26, 2008.

[11] B. Schmidt, R. R. Tilz, K. Neven, K. R. Julian Chun, A. Furnkranz, and F. Ouyang, "Remote robotic navigation and electroanatomical mapping for ablation of atrial fibrillation: considerations for navigation and impact on procedural outcome," *Circulation: Arrhythmia and Electrophysiology*, vol. 2, no. 2, pp. 120–128, 2009.

[12] O. M. Wazni, C. Barrett, D. O. Martin et al., "Experience with the Hansen robotic system for atrial fibrillation ablation—lessons learned and techniques modified: Hansen in the real world," *Journal of Cardiovascular Electrophysiology*, vol. 20, no. 11, pp. 1193–1196, 2009.

[13] R. Bai, L. di Biase, M. Valderrabano et al., "Worldwide experience with the robotic navigation system in catheter ablation of atrial fibrillation: methodology, efficacy and safety," *Journal of Cardiovascular Electrophysiology*, vol. 23, no. 8, pp. 820–826, 2012.

[14] M. Schiemann, R. Killmann, M. Kleen, N. Abolmaali, J. Finney, and T. J. Vogl, "Vascular guide wire navigation with a magnetic guidance system: experimental results in a phantom," *Radiology*, vol. 232, no. 2, pp. 475–481, 2004.

[15] W. Saliba, J. E. Cummings, S. Oh et al., "Novel robotic catheter remote control system: feasibility and safety of transseptal puncture and endocardial catheter navigation," *Journal of Cardiovascular Electrophysiology*, vol. 17, no. 10, pp. 1102–1105, 2006.

[16] E. M. Khan, W. Frumkin, G. A. Ng et al., "First experience with a novel robotic remote catheter system: Amigo™ mapping trial," *Journal of Interventional Cardiac Electrophysiology*, vol. 37, no. 2, pp. 121–129, 2013.

[17] M. N. Faddis, W. Blume, J. Finney et al., "Novel, magnetically guided catheter for endocardial mapping and radiofrequency catheter ablation," *Circulation*, vol. 106, no. 23, pp. 2980–2985, 2002.